EVALUATION AND STRUCTURAL BEHAVIOR OF DETERIORATED PRECAST, PRESTRESSED CONCRETE BOX BEAMS

by

Ryan T. Whelchel

A Dissertation

Submitted to the Faculty of Purdue University

In Partial Fulfillment of the Requirements for the degree of

Doctor of Philosophy

Lyles School of Civil Engineering

West Lafayette, Indiana

December 2019

THE PURDUE UNIVERSITY GRADUATE SCHOOL
STATEMENT OF COMMITTEE APPROVAL

Dr. Robert J. Frosch, Co-Chair

Lyles School of Civil Engineering

Dr. Christopher S. Williams Co-Chair

Lyles School of Civil Engineering

Dr. Mark D. Bowman

Lyles School of Civil Engineering

Dr. Randall W. Poston

Senior Principal, Pivot Engineers, Austin, TX

Approved by:

Dr. Dulcy Abraham

Head of the Graduate Program

To my parents, for their boundless devotion to my success and

To Emily, for your patience and unending support

ACKNOWLEDGMENTS

I am eternally grateful for the lessons that have been learned through the course of this research. To Dr. Robert Frosch and Dr. Christopher Williams, whom with great patience took the time to guide me through this research, I owe a great dept of gratitude. To the members of my committee, Dr. Mark Bowman and Dr. Randall Poston, I would like to express my appreciation for the perspectives of the research that have been provided. I would also like to thank Dr. Santiago Pujol, who was the first of many to teach me the difference between thinking and knowing. The lessons and perspectives I have gained through this research have shaped how I approach engineering and will continue to guide me throughout my career.

I am indebted to Ryan Molley. His insatiable curiosity and passion for exploring new ideas has provided constant inspiration for me to seek out alternatives and quest for better solutions. Our collaboration on this research provided me the beginnings of my understanding of deteriorated structures and motivated me to learn more. I wish all the best to my friend and colleague.

The experimental testing of deteriorated box beams posed unique challenges that were overcome through the support of the Bowen Laboratory staff. I would like to thank, Harry Tidrick, Molly Stetler, Tom Bradt, and Kevin Brower, for their assistance throughout the experimental phase of the research.

Through the course of this research, I was assisted by many of my peers whom stopped to lend me hand on the lab floor, asked me about my research, told me about their research, and offered solutions to the various issues that arise during experimental testing. Thank you, Ahmed Alimran, Bridget Crowley, David Derks, Eric Fleet, Bobby Jacobs, Alana Lund, Jon Pevey, Will Pollalis, Aishwarya Puranam, Will Rich, Prateek Shah, Kinsey Skillen, Andi Vicksman, Hwa Ching Wang, and Ting-Wei Wang, you all were instrumental in the completion of this research.

This project was supported by the Joint Transportation Research Program (JTRP). I am very thankful for the provided support and guidance throughout the course of this research.

Ryan Whelchel

TABLE OF CONTENTS

LIST OF TABLES

LIST OF FIGURES

ABSTRACT

Author: Whelchel, Ryan, T. Ph.D.
Institution: Purdue University
Degree Received: December 2019
Title: Evaluation and Structural Behavior of Deteriorated Precast, Prestressed Concrete Box Beams
Committee Co-Chair: Robert J. Frosch
Committee Co-Chair: Christopher S. Williams

Adjacent precast, prestressed box beam bridges have a history of poor performance and have been observed to exhibit common types of deterioration including longitudinal cracking, concrete spalling, and deterioration of the concrete top flange. The nature of these types of deterioration leads to uncertainty of the extent and effect of deterioration on structural behavior. Due to limitations in previous research and understanding of the strength of deteriorated box beam bridges, conservative assumptions are being made for the assessment and load rating of these bridges. Furthermore, the design of new box beam bridges, which can offer an efficient and economical solution, is often discouraged due to poor past performance. Therefore, the objective of this research is to develop improved recommendations for the inspection, load rating, and design of adjacent box beam bridges. Through a series of bridge inspections, deteriorated box beams were identified and acquired for experimental testing. The extent of corrosion was determined through visual inspection, non-destructive evaluation, and destructive evaluation. Non-destructive tests (NDT) included the use of connectionless electrical pulse response analysis (CEPRA), ground penetrating radar (GPR), and half-cell potentials. The deteriorated capacity was determined through structural testing, and an analysis procedure was developed to estimate deteriorated behavior. A rehabilitation procedure was also developed to restore load transfer of adjacent beams in cases where shear key failures are suspected. Based on the understanding of deterioration

developed through study of deteriorated adjacent box beam bridges, improved inspection and load rating procedure are provided along with design recommendations for the next generation of box beam bridges.

CHAPTER 1. INTRODUCTION

1.1 Background

According to the Federal Highway Administration's (FHWA) LTBP InfoBridge database (FHWA 2019) there are over 43,000 prestressed, precast adjacent box beam bridges in the United States. Over 4,000 of these bridges are located in Indiana and account for approximately 25% of Indiana's bridge inventory. The first adjacent box beam bridges were constructed in the 1950's (NCHRP 2009), and as early as the late 1970's, premature distress and failures were observed in adjacent box beam bridges in Indiana, Illinois, and Pennsylvania (Molley 2017; Naito et al. 2011).

A study of the evolution and performance of adjacent box beam bridges in Indiana was conducted by Molley (2017). The study found that box beam bridges are prone to several types of deterioration including leaking shear keys, longitudinal cracking, concrete spalling at the longitudinal joint, and deterioration of the concrete top flange. These common types of deterioration were primarily observed in the bottom flange of box beams and at the longitudinal connection between box beams that facilitates the distribution of load between beams. Water and deicing salts were also noted as accumulating in the voids of the beams.

Load rating a box beam exhibiting common types of deterioration requires knowledge of the correlation between visual signs of deterioration and actual structural damage. The nature of these types of deterioration leads to uncertainty of the extent and effect of deterioration. For example, longitudinal cracks may indicate strand corrosion, but the extent of corrosion along the length of the strand in addition to corrosion of the adjacent strands is uncertain. Without knowledge of the extent of actual deterioration, load rating calculations must make the most conservative assumptions to account for the uncertainty in the extent of deterioration. Furthermore, the impact of corroded strand on structural capacity and deformation capacity remain uncertain.

1.2 Behavior of Deteriorated Box Beams

The following studies present the current understanding of the deteriorated behavior of adjacent box beam bridges. These studies focused on structural testing of box beams with longitudinal cracking and corroded strands, forensic investigation of decommissioned box beams, and live-load distribution of full-scale adjacent box beam bridges.

1.2.1 Structural Testing

Beginning in the 1990's, structural tests of individual box beams were conducted to determine the effect of longitudinal cracking and concrete spalling observed in the bottom flange of prestressed, precast concrete box beams (Shenoy and Frantz 1991; Miller and Parekh 1994; Hawkins and Fuentes 2003; Harries et al. 2006; Kasan and Harries 2011; Attanayake and Aktan 2011). In total, eight beams with visible bottom flange deterioration were tested, but a clear correlation between visual deterioration and structural capacity was not observed.

1.2.1.1 Shenoy and Frantz

Shenoy and Frantz (1991) tested a pair of decommissioned box beams that were constructed in 1960 with 7/16 in. diameter strands. The beams were tested in four-point bending with load points at approximately one third of the span from each support. The first beam was observed with staining and evidence of minor cracking and concrete spalling in the bottom flange. The other beam was observed with only staining from water leakage through the longitudinal joint between beams. Both structural tests were concluded prior to failure, but each beam was believed to have reached flexural capacity. The results of the structural tests showed that both beams achieved the design load without loss of ductility indicating that the observed deterioration had little to no effect on the structural capacity.

1.2.1.2 Miller and Parekh

Miller and Parekh (1994) tested a 76.8 ft long deteriorated box beam that was constructed in 1980 with ½ in. diameter strands. The beam was tested in four-point bending with load points at 28.8 ft from each support. Deterioration of the beam consisted of three corroded prestressing strands (one broken strand and two exposed strand) on the edge of the bottom flange located at approximately 25.5 ft from the support. The test results were compared to an undamaged beam constructed prior to testing to match the cross-section geometry and span of the deteriorated beam. The results of the structural tests showed that the loss of three strands at the edge of the section caused a reduction in both strength and ductility. The loss of edge strands also caused out-of-plane deformations that led to a further reduction in strength.

1.2.1.3 Hawkins and Fuentes

Hawkins and Fuentes (2003) tested two decommissioned box beams that were constructed in 1968 with 7/16 in. diameter strands. The beams were tested in four-point bending with load points at approximately one third of the span from each support. Deterioration of the first beam consisted of longitudinal cracking and concrete spalling along the edge of the bottom flange for the length of the beam. The section exhibiting the most deterioration consisted of three exposed strands on one corner of the bottom flange and concrete spalling from the corners of the top flange within 2 ft of midspan. The second beam was observed with minor deterioration consisting of primarily water staining on the bottom flange and evidence of leakage through the longitudinal joint on the sides of the beam. Failure of the first beam was caused by crushing of the top flange at the section of greatest deterioration. The test results showed that the reduced strength of the beam was consistent with the visually observed deterioration. The test of the second beam was concluded prior to failure but was observed to achieve the capacity of the first beam without signs of concrete crushing or strand fracture.

1.2.1.4 Harries et al.

Harries et al. (2006) tested two 84 ft decommissioned box beams that were constructed in 1960 with 3/8 in. diameter strands. The beams were tested in four-point bending with each load point located 2 ft from midspan. Deterioration of the first beam consisted of concrete spalling on the edge and middle of the bottom flange resulting in 12 corroded strands (6 broken and 6 exposed strands) located near midspan. The second beam was constructed with a barrier rail and was observed with concrete spalling at various locations along the edges of the bottom flange. The section of greatest deterioration (6 exposed strands) was located at approximately midspan. The test results indicated that the moment capacity of the first beam was overestimated by 15% assuming 12 ineffective strands. A post-failure investigation revealed that 6 additional strands were corroded at the same section but were not exposed prior to testing. The moment capacity of the second beam, estimated assuming 6 ineffective strands, was consistent with the test results.

Based on the test results from the two beams, two recommendations were made for the load rating of box beams. First, assume any corroded strand to be ineffective for the length of the span based on uncertainty of the redevelopment length. Second, assume an additional 25% of section loss for any visual indication of strand corrosion.

1.2.1.5 Kasan and Harries

The uncertainty of strand corrosion affecting the development length of uncorroded strand away from the location of deterioration led to a study of strand redevelopment by Kasan and Harries (2011). Strand redevelopment was tested by monitoring the strain in pretensioned strands embedded in a decommissioned box beam. Strands were intentionally cut at specified distances from the point of strain measurement to simulate corrosion induced strand fracture. The results showed that cuts located further than the transfer length away from the point of strain measurement caused no change in strain. This study indicated that prestress is preserved in undeteriorated regions located outside the transfer length from strand deterioration.

It should be noted that the test was conducted on a single girder under the action of self-weight. Redevelopment of strand strength corresponding to the flexural capacity of a beam remains unclear.

1.2.1.6 Attanayake and Aktan

Attanayake and Aktan (2011) tested a 45 ft decommissioned box beam that was constructed in 1957 with 3/8 in. diameter strands. The beam was tested in four-point bending with each load point located 2 ft from midspan. Deterioration consisted of two large longitudinal cracks along the length of the beam within the middle portion of the bottom flange with staining resembling corrosion. Due to stroke limitations of the loading jacks, the structural test was concluded prior failure. The tests results, however, showed that the design capacity of the beam was exceeded during the test. In addition, the strands at the longitudinal cracks were observed without corrosion.

1.2.2 Forensic Studies

In addition to structural tests of deteriorated box beams, a series of forensic investigations were conducted at Lehigh University (Naito et al. 2010, Naito et al. 2011). These studies focused on developing an understanding of box beam deterioration and providing load rating recommendations to the Pennsylvania Department of Transportation.

1.2.2.1 Naito et al.

Naito et al. (2010) conducted a forensic investigation of eleven deteriorated box beams reinforced with 3/8 in. diameter strand from the Lake View Drive bridge in Pennsylvania of which an exterior girder failed under self-weight due to corrosion induced strand fractures. The investigation included a review of the 1960 design and construction of the bridge, extensive materials testing, and strand corrosion identification. Materials testing included a concrete strength assessment, petrographic examination, air void analysis, carbonation analysis, and chloride analysis. The results of the forensic investigation determined that strand corrosion was attributed to runoff of deicing salts penetrating the longitudinal joint onto the web and bottom flange of the beams. These findings led to the following recommendations regarding the correlation between visible deterioration and structural capacity.

- For every exposed strand, 125% of the strand area should be deducted from structural capacity calculations.
- All strands intersecting or located adjacent to a crack should be considered ineffective only within the immediate region of deterioration.
- Longitudinal cracks may cause corrosion of the strand above the crack and the strands to either side of the crack. In this case, a parametric study was recommended to determine the influence of the number of strand considered ineffective on the structural capacity.

1.2.2.2 Naito et al.

Naito et al. (2011) collected a total of seven decommissioned box beams reinforced with 3/8 in. diameter strand from three bridges constructed in Pennsylvania between 1956 and 1961. For the research study, only a portion of the full span of each of the seven box beams was recovered from the decommissioned bridges. The box beam sections were thoroughly examined using visual, non-destructive, and destructive inspection techniques. The non-destructive tests included half-cell potential mapping of each strand along the length of the beam sections. The value of the half-cell potential reading correlated with the level of strand corrosion but with a coefficient of variation between 25% and 56% depending on the level of corrosion. Therefore, the method was not recommended for indicating the level of strand corrosion.

Material testing was performed on extracted strand with various levels of deterioration. The test results showed that the strand strength was dependent on the severity of corrosion. For strands observed with light corrosion, pitting, or heavy pitting, the strength of the strand relative to an assumed strength of 270 ksi was 100%, 79.9% and 71.4%. Based on the inspection and material testing results, the following load rating recommendations were made.

- Where longitudinal cracks are observed in the bottom flange, reduce the cross-sectional area of all strands in the beam by at least 5%.
- If strands align with a crack or are located within 3 in. of a longitudinal crack, the cross-sectional area of these strands should be reduced by 25%.
- The effect of deterioration should be considered within two development lengths, along the span of the beam, as estimated by the ACI 318 (2008) equation for development length.

1.2.3 Live-Load Distribution

Load tests have been conducted by Steinburg et al. (2011) and Kassner and Balakumaran (2016) to determine the load distribution of adjacent box beam bridges exhibiting signs of shear key deterioration. The studies found that evidence of a leaking shear key may not indicate any loss of load distribution. It should be noted that these studies were conducted on bridges constructed with bituminous wearing surfaces. Load test data of bridges constructed with composite or non-composite concrete decks along with evidence of leaking shear keys is not available.

1.2.3.1 Steinburg et al.

Steinburg et al. (2011) conducted load tests on the center span of a three-span adjacent box beam bridge constructed in 1967 with spans of 47 ft 10 in. Deterioration of the center span consisted of delaminated concrete in the top flange in the exterior beams and minimal efflorescence at the longitudinal joints. Results of the load tests showed that the measured distribution factors were consistent with the distribution factors estimated using equations from AASHTO LRFD (2010).

1.2.3.2 Kassner and Balakumaran

Kassner and Balakumaran (2016) conducted a series of load tests on one span of an existing adjacent box beam bridge constructed in 1959 with five spans (consisting of a combination of 40.75 ft and 41.5 ft individual spans) and a bituminous wearing surface. Deterioration of the bridge consisted of efflorescence at the longitudinal joint and isolated concrete spalling on two beams due to poor consolidation. The efflorescence at the longitudinal joint indicated that the shear keys were leaking. The results of the load tests showed that the measured distribution factors were consistent with the distribution factors estimated using equations from AASHTO LRFD (2012).

1.2.4 Limitations of Previous Research

The recommendations based on previous research are not in general agreement. Structural tests of box beams with longitudinal cracking found that, despite the presence of longitudinal cracks, the beams achieved their full design strength (Shenoy and Frantz 1991; Attanayake and Aktan 2011). These results conflict with the load rating recommendations developed by Harries et al. (2006), Naito et al. (2010) and Naito et al. (2011) regarding longitudinal cracking which state that a reduced area of strand should be assumed for strands at and adjacent to longitudinal cracks. In addition, Miller and Parekh (1994) and Hawkins and Fuentes (2003) found that the structural capacity estimated based on visible deterioration was consistent with test results, whereas Harries et al. (2006) observed that corroded strands may be obscured by concrete cover.

Load tests of adjacent box beam bridges have shown adequate load distribution between beams with minor deterioration. Due to the uncertainty of determining the shear key condition, however, many states require that load distribution be discounted when leaking shear keys are observed. The loss of load distribution can significantly reduce the load capacity of a bridge.

Based on review of previous research, there exists a need for further study of deteriorated adjacent box beam bridges. An improved correlation between visual signs of deterioration and structural damage is necessary to develop an accurate method for estimating the capacity of deteriorated beams. Structural testing is also required to verify the redevelopment of strands away from deterioration at ultimate strength.

1.3 Objective and Scope

Due to limitations in previous research and understanding of the strength of deteriorated box beam bridges, conservative assumptions are being made for the assessment and load rating of these bridges. This can have significant implications for communities especially in cases where a bridge posting may be required. Furthermore, the design of new box beam bridges, which can offer an efficient and economical solution, is often discouraged due to poor past performance. Therefore, the objective of this research is to develop improved recommendations for the inspection, load rating, and design of adjacent box beam bridges. Research focused on the following:

1. Conduct bridge inspections to observe common types of deterioration and identify deteriorated box beams for experimental study (Chapter 2).
2. Determine the extent of deterioration through visual inspection, non-destructive evaluation, and destructive evaluation (Chapter 3).
3. Determine the capacity of deteriorated beams (Chapter 4).
4. Develop a rehabilitation procedure to restore load transfer (Chapter 5).
5. Develop an analytical approach for the calculation of the capacity of deteriorated box beams (Chapter 6).
6. Develop design recommendations for the next generation of box beam bridges (Chapter 7)

CHAPTER 2. DETERIORATED CONCRETE BOX BEAMS

2.1 Introduction

A series of decommissioned bridge beams were acquired to study the extent of actual deterioration in precast, prestressed concrete box beams. The beams were acquired through coordination with INDOT, county highway departments, bridge contractors, and bridge engineering firms to identify adjacent box beam bridge replacement projects. Box beam candidates for experimental testing were further identified by the presence of common deterioration. Common types of deterioration were identified by Molley (2017) and further investigated through additional bridge inspections that were conducted as part of the process of acquiring beam specimens to include in the experimental program. The inspections of these bridges and those bridge beams selected for experimental testing are presented in this chapter.

2.2 Background

According to Molley (2017), there are seven common types of deterioration of adjacent box beam bridges, and they are classified as follows:

- Leaking shear key joint
- Torsion of the exterior beam
- Clogged drain holes
- Spalling at longitudinal joint
- Longitudinal cracking in bottom flange
- Corrosion of reinforcement
- Top flange damage

The first two types of deterioration primarily affect the durability and live-load distribution of the bridge. Leaking shear key joints compromise durability by allowing chloride-laden water through the joint onto the box beam thus creating a corrosive environment for the steel reinforcement. A leaking shear key joint also calls into question the capacity of the shear key to provide load transfer between beams for adequate live-load distribution. Torsion of the exterior beam causes transverse tension at the shear key, which may lead to cracking of the shear key and all the problems related to leaking shear key joints.

The remaining five types of deterioration primarily affect the durability and capacity of the individual box beam exhibiting the deterioration. These types of deterioration are of primary interest for specimen acquisition as they can be studied in the laboratory based on individual beam tests. Furthermore, these types of deterioration can be studied without load testing the in-situ bridge. The search for box beam specimens focused primarily on identifying bridges with clogged drain holes, longitudinal cracking, spalling at the longitudinal joint, and corroding reinforcement. Top flange damage was not a primary focus because 93 percent of box beam bridges have a wearing surface obstructing the inspection of the top flange (Molley 2017).

2.3 Bridge Inspections

All the box beam bridges inspected were county bridges. There was no intention of disregarding state bridges; the number of county bridges (4206) simply outweighed the number of state bridges (187) such that many more county bridges were identified for replacement than state bridges. State and county bridge statistics were generated from the Indiana Bridge Inspection Application System (BIAS) in July 2019. A summary of the bridges that were inspected is provided in Table 2.1, and the locations of each bridge are shown in Figure 2.1.

Table 2.1: Bridge Inspection Summary

Bridge Name	Structure Number	NBI Rating (superstr.)	Operating Rating (HS-20)	Inventory Rating (HS-20)	Inventory Rating (H-20)	Load Rating Method	Official Inspection Date	Research Team Inspection Date
Daviess 95	14-00095	5	0.89	0.67	0.90	LFR	27 Jun. 2017	24 Jan. 2017
Daviess 160	14-00160	5	1.29	0.94	1.00	LFR	20 Jun. 2017	24 Jan. 2017
Elkhart 102*	20-00102	4	0.96	0.69	0.80	LFR	24 Aug. 2016	9 Jan. 2018
Elkhart 385	20-00385	6	1.00	1.00	1.00	EJ†	14 Aug. 2018	27 Jan. 2017
Elkhart 404	20-00404	7	0.98	0.72	1.00	LFR	22 Aug. 2018	27 Jan. 2017
Elkhart 406	20-00406	5	1.00	0.75	1.00	LFR	22 Aug. 2018	27 Jan. 2017
Elkhart 409*	20-00409	5	0.80	0.58	0.80	LFR	24 Aug. 2016	27 Jan. 2017
Elkhart 410	20-00410	4	0.67	0.47	0.65	LFR	8 Aug. 2018	27 Jan. 2017
Greene 8	28-00008	3	0.38	0.28	0.40	LFR	25 Jul. 2018	24 Jan. 2017
Kosciusko 18	43-00018	4	0.80	0.78	0.80	EJ†	22 Mar. 2018	9 Jan. 2018
Lake 61	45-00061	3	0.82	0.61	0.80	LFR	8 Aug. 2016	9 Jan. 2018
Lake 264	45-00264	3	0.71	0.53	0.75	LFR	20 Aug. 2018	9 Jan. 2018
Newton K5*	56-000K5	4	0.51	0.47	0.60	LFR	20 Sept. 2016	8 May 2017
Newton 56*	56-00056	4	0.80	0.75	0.95	LFR	19 Sept. 2016	8 May 2017
Tippecanoe 115	79-00115	4	1.02	0.75	0.95	LFR	26 Sept. 2017	19 Feb. 2018
Tippecanoe 244*	79-00244	4	1.29	0.97	1.25	LFR	26 Sept. 2017	8 Nov. 2017
Tippecanoe 504	79-00504	4	0.91	0.67	1.00	LFR	26 Sept. 2017	8 Nov. 2017
Wells 79*	90-00079	3	1.00	1.00	1.00	EJ†	25 Oct. 2016	27 Jul. 2016

*Source bridge for box beam specimens

†Engineering Judgement

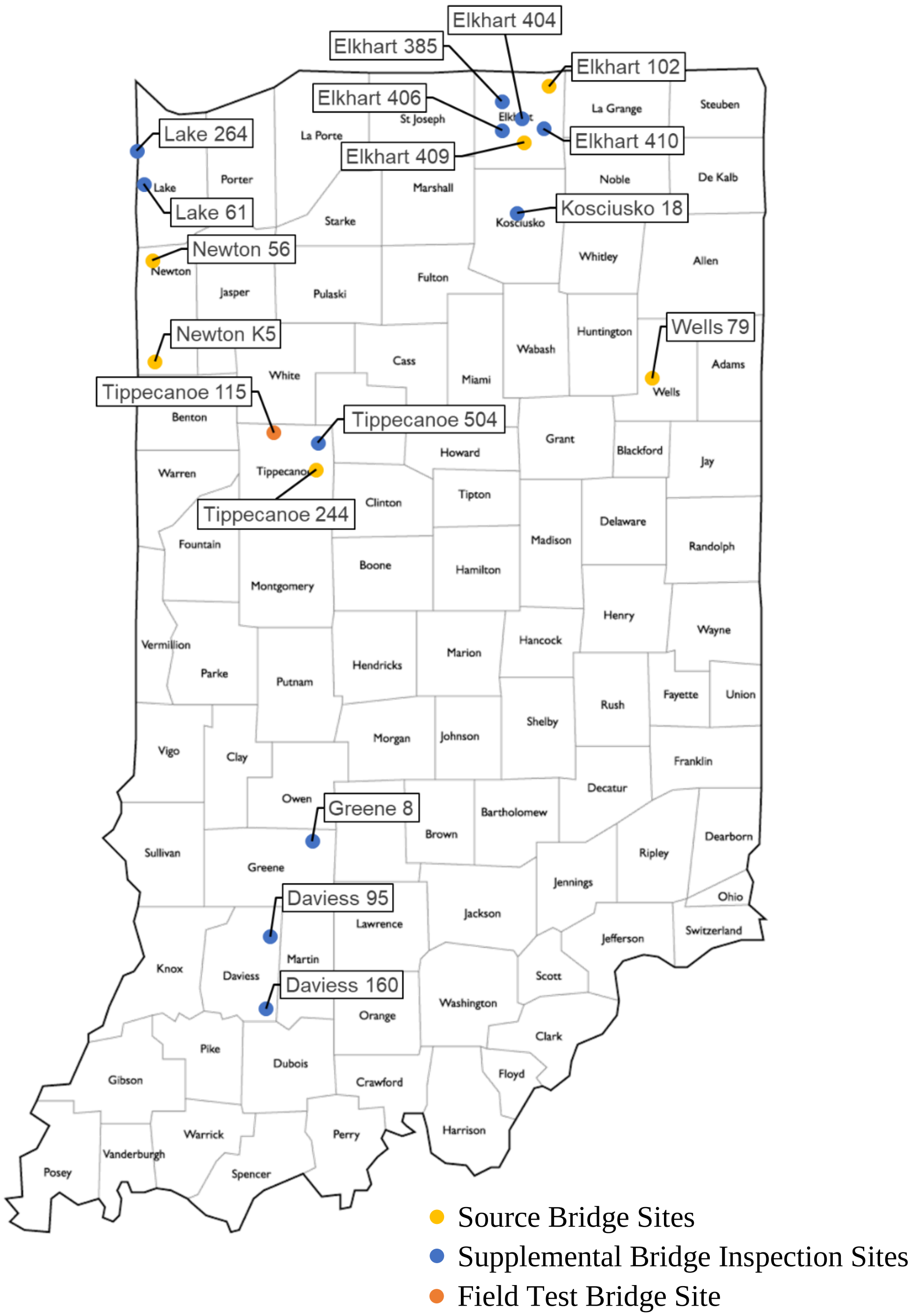

Figure 2.1: Mapped Bridge Locations

In Indiana, all county bridges are given a unique structure number consisting of a two-digit number and a five-digit number separated by a dash. The first number is the county number (numbers assigned alphabetically), and the second number is the bridge number. For example, when all the counties in Indiana are sorted alphabetically, Daviess County is the 14th county in the resulting list. Therefore, structure number 14-00095 corresponds to Bridge 95 in Daviess County. For the purpose of easily identifying the bridge location and number, the structure number will be referred to as the county name followed by the county bridge number. As such, 14-00095 will be referred to as Daviess 95.

In addition to the bridge name and structure number, Table 2.1 lists the NBI superstructure condition rating, load ratings for the HS-20 design truck and H-20 design truck, load rating method, date of the official inspection, and date of inspection by the research team. Table 2.2 presents the descriptions associated with the NBI condition ratings (FHWA 1995). The date of the official inspection is as noted in the bridge inspection report. An official inspection is defined here as the inspection of a bridge by a certified bridge inspector. Part 1 of the Bridge Inspection Manual defines the qualifications necessary to inspect bridges (INDOT 2017). All bridge inspection reports for the bridges discussed here are cited in Appendix A.

Table 2.2: FHWA Condition Ratings and Descriptions

Rating	Condition	Description
9	Excellent	-
8	Very Good	No problems noted.
7	Good	Some minor problems.
6	Satisfactory	Structural elements show some signs of deterioration.
5	Fair	All primary structural elements are sound but may have minor section loss, cracking, spalling, or scour.
4	Poor	Advanced section loss, deterioration, spalling, or scour.
3	Serious	Loss of section, deterioration, spalling, or scour have seriously affected primary structural components. Local failures are possible. Fatigue cracks in steel or shear cracks in concrete may be present.
2	Critical	Advanced deterioration of primary structural elements. Fatigue cracks in steel or shear cracks in concrete may be present or scour may have removed substructure support. Unless closely monitored it may be necessary to close the bridge until corrective action is taken.
1	Imminent Failure	Major deterioration or section loss present in critical structural components or obvious vertical or horizontal movement affecting structure stability. Bridge is closed to traffic, but corrective action may put back in light service.
0	Failed	Out of service - beyond corrective action.
N	Not Applicable	-

2.4 Concrete Box Beam Specimens

Eighteen bridges were inspected through the course of identifying deteriorated box beam specimens for laboratory study. After extensive coordination with INDOT, county highway departments, and several bridge contactors, 6 of the 18 bridges were selected as source bridges for deteriorated box beam specimens. These bridges were selected based on two criteria. The first and foremost was that they were scheduled for replacement during the period of specimen acquisition for the project. Many of the bridges inspected were scheduled for replacement, but the timing of the replacement was subject to change. In some cases, the timing of the replacement was delayed by more than a year only a few months before the project was set to begin. The second criterion was based on type and severity of deterioration. The type of deterioration sought has been discussed previously. A range in the severity of deterioration was also sought. By studying both mild and severe deterioration, a threshold may be established that defines when a given type of deterioration has become critical.

A total of 15 bridge beams were salvaged from the six source bridges. Table 2.3 provides a summary of the salvaged beams and specimen identification (specimen ID) for each beam. The specimen ID was created to summarize the source bridge, beam number, and state of strand deterioration into one, easy to reference, identification (Figure 2.2) The first number of the specimen ID is the county bridge number of the source bridge. For brevity, the county name has been omitted. Each of the six source bridges have different county bridge numbers; therefore, there is no need to include the county name in the specimen ID. The second number is the beam number. The beam number was assigned to the specimen upon arrival to the laboratory. The two letters at end of the specimen ID describe the state of strand deterioration in the specimen and is defined as one of four states (listed from no discernable deterioration to most deteriorated): undamaged (UD), presence of a longitudinal crack (LC), exposed strand (ES), and broken strand (BS). The abbreviations for each deterioration state are used in the specimen ID to identify the most advanced state of strand deterioration in the specimen.

Table 2.3: Specimen Identification

Bridge	Year Built	Specimen ID	Source Bridge Beam Number
Tippecanoe 244	1960	244-1-LC	6
Elkhart 409	1962	409-1-ES	B9
		409-2-UD	B8
Newton K5	1965	K5-1-LC	1
		K5-2-LC	7
Wells 79	1966	79-1-UD	B2
		79-2-UD	A6
		79-3-UD	A1
		79-4-LC	A7
Newton 56	1968	56-1-LC	A6
		56-2-ES	B1
Elkhart 102	1970	102-1-BS	C7
		102-2-BS	C5
		102-3-BS	B8
		102-4-BS	B7

$$\underbrace{409}_{\text{County bridge number}} - \overbrace{1}^{\text{Beam number}} - \underbrace{\text{ES}}_{\text{Most advanced state of deterioration}}$$

Figure 2.2: Specimen Identification

The descriptions of source bridges and their deterioration are provided in the following sections ordered by age, oldest to youngest. Each bridge was inspected to document the condition of the bridge while in service and determine which beams were most suitable for experimental study. Deterioration maps were included to summarize the deterioration observed during the bridge inspections. Table 2.4 provides a key to identify common types of deterioration. Please note that each deterioration map was drawn with the correct geometrical proportions.

Table 2.4: Key for Deterioration Maps

Deterioration Type	**Map Symbol**	
Shear key showing signs of deterioration		
Longitudinal cracking	 Cracking 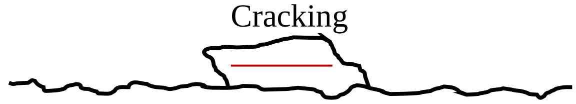 Cracking with exposed strand	
Concrete spalling	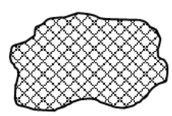 Spalling	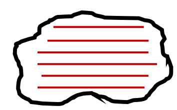 Spalling with Exposed Strands
Concrete spalling on one side of shear key	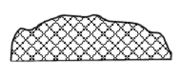 Spalling	 Spalling with Exposed Strands
Drain hole	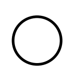 Unclogged	 Clogged
Staining	Blue Water Staining	Red Rust Staining

The remaining bridge inspections are presented after the source bridges as supplemental bridge inspections with exception to Tippecanoe 115, which is discussed in detail in Chapter 5 on live-load distribution.

2.4.1 Tippecanoe 244

2.4.1.1 Bridge Information

Tippecanoe 244 (79-00244) was a 44.1 ft long single-span bridge built in 1960 over Buck Creek (Figure 2.3). The total width is 26.3 ft and is comprised of seven 21 in. deep, 45 in. wide beams. The bridge was built with 10 in. tall, 11 in. wide concrete curbs. This type of curb is very common for this bridge type and will hereafter be referred to as a standard curb. The curbs did not have outlets along the span, but deck drains were installed at the ends of the exterior beams. Each deck drain consisted of a 6 in. diameter metal pipe cast in the beam to allow water from the deck surface to drain through the beam onto the rip-rap below the bridge. The bituminous wearing surface was approximately 6 in. thick at the time of inspection. A single line of transverse tie rods was located at midspan.

Figure 2.3: Tippecanoe 244

2.4.1.2 Bridge Deterioration

Tippecanoe 244 was inspected by the research team on 8 November 2017. The observed deterioration is summarized in Figure 2.4. Every joint between beams was found with water staining or efflorescence (Figure 2.5). The wearing surface was also observed to have reflective cracks along the length of the bridge. Two large longitudinal cracks were observed in Beam 6 (Specimen 244-6-LC). The crack at midspan was observed to be leaking during the inspection (Figure 2.6). Green staining covered most of the bottom flanges of Beam 1 (Figure 2.7) and Beam 7. The stain also partially extended onto the flange of Beam 6. In addition, spider web cracks were observed on the southeast corner of the bridge on the side of Beam 1 at the abutment (Figure 2.8). No drain holes were found in any of the beams.

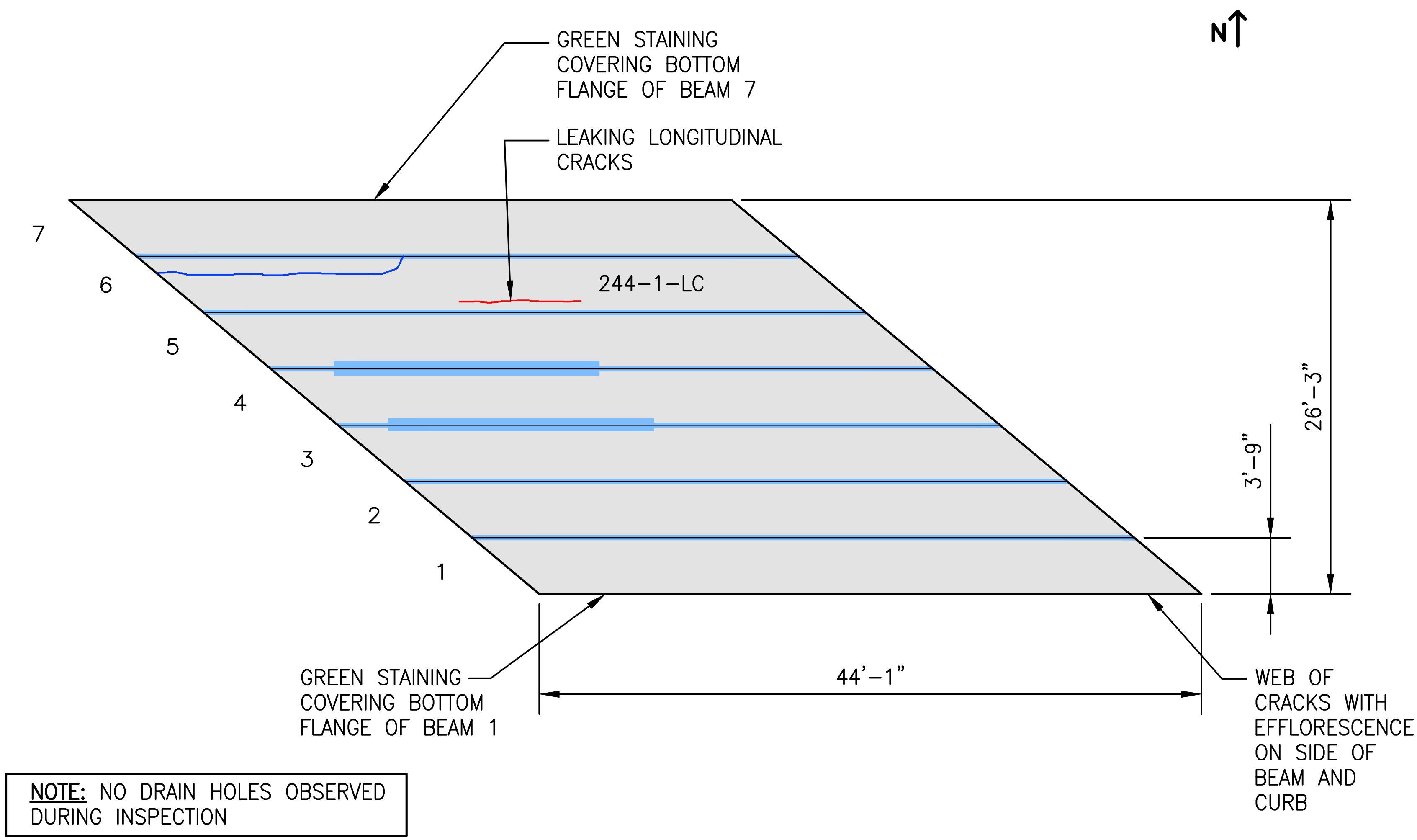

Figure 2.4: Tippecanoe 244 Deterioration Map

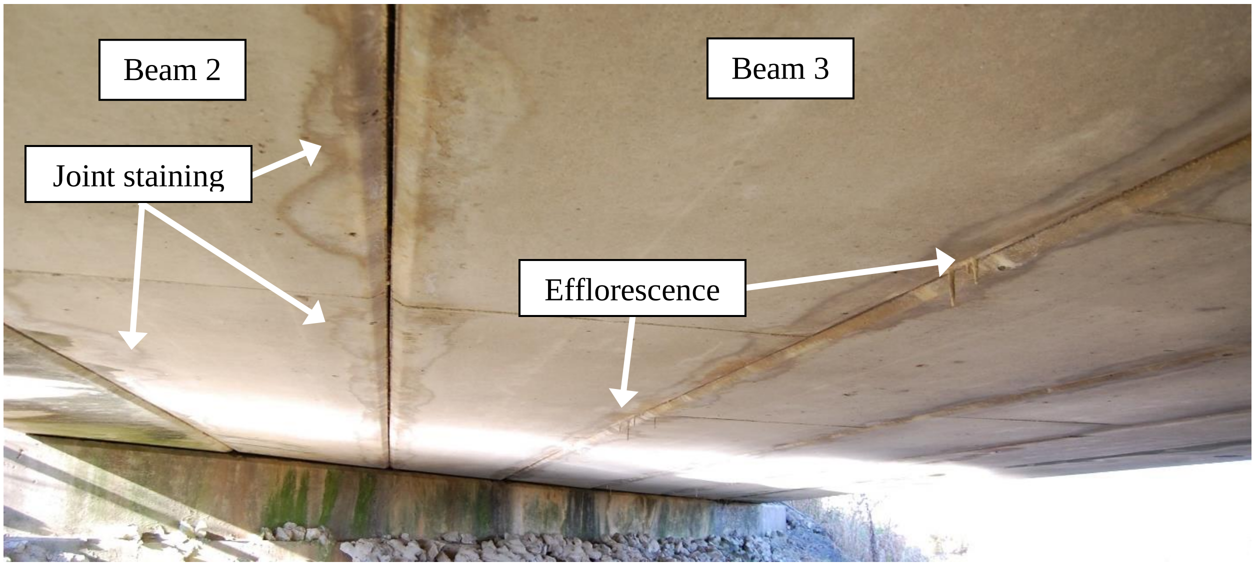

Figure 2.5: Joint Staining and Efflorescence

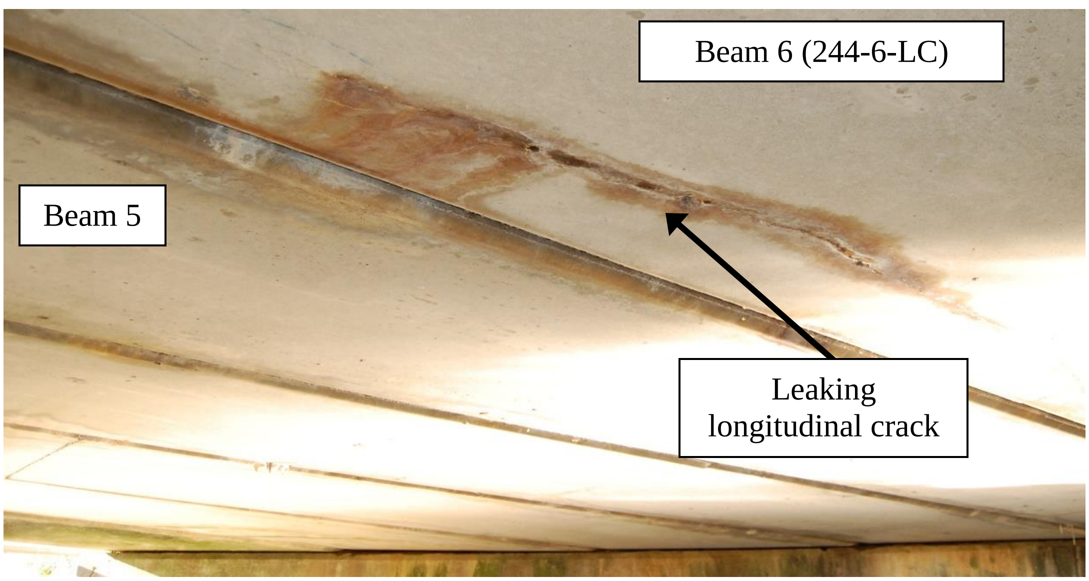

Figure 2.6: Leaking Longitudinal Crack in Beam 6 (244-1-LC)

Figure 2.7: Green Staining on Beam 1

Figure 2.8: Spider Web Cracking on East End of Beam 1

2.4.1.3 Beam Specimen Information

In 2018, the bridge was replaced with a new adjacent box beam bridge. As part of the bridge replacement, Beam 6 (Specimen 244-1-LC) was salvaged and transported to the Bowen Laboratory. During the salvage process, the bituminous wearing surface was removed, and a large hole was found in the top flange of Specimen 244-1-LC at midspan. The hole was approximately 14 in. long and 12 in. wide after removal of the gravel in and around the hole (Figure 2.9). No additional deterioration was observed after the beam was transported to the laboratory. Drain holes were drilled into each of the voids with a 5/8 in. concrete drill bit. Two drain holes were installed approximately 3 ft from each end of the beam. Once the drain holes were cleared, water drained from three of the four drain holes for approximately two to five minutes (Figure 2.10).

(a) Before removal of gravel **(b) After removal of gravel**

Figure 2.9: Hole in Top Flange of Specimen 244-1-LC (Beam 6)

(a) Northeast drilled drain hole

(b) Southeast drilled drain hole

(c) Southwest drilled drain hole

Figure 2.10: Water Filled Voids in Specimen 244-1-LC (Beam 6)

2.4.2 Elkhart 409

2.4.2.1 Bridge Information

Elkhart 409 (20-00409) was a four-span bridge over the Elkhart River built in 1962 (Figure 2.11). The total bridge span of 204.8 ft was divided into four equal 51.2 ft spans. Each span consisted of nine 27 in. deep, 36 in. wide beams for a total width of 27 ft. The bituminous wearing surface was estimated to be 2 in. thick. The bridge was constructed with standard curbs on the exterior beams. The curbs had scuppers installed near the ends of each span to drain water off the bridge deck. In each span, transverse tie rods were located at midspan.

Figure 2.11: Elkhart 409

2.4.2.2 Bridge Deterioration

The bridge was inspected by the research team on 27 January 2017. The observed deterioration is summarized in Figure 2.12. Due to access restrictions, photos of the deteriorated sections could not be taken, and only a small portion of the bridge could be inspected. Much of the information presented in Figure 2.12 is based on the official inspection report.

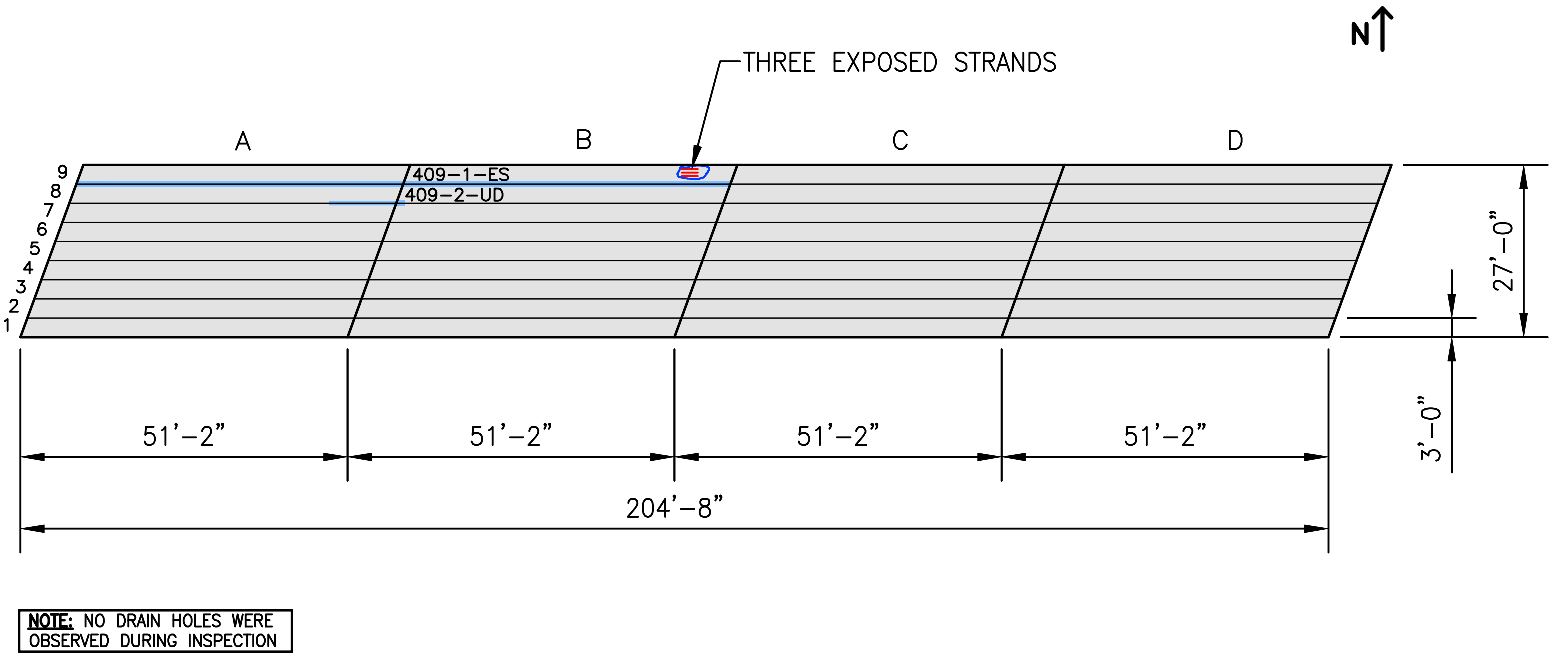

Figure 2.12: Elkhart 409 Deterioration Map

2.4.2.3 Beam Specimen Information

In 2017, the bridge was replaced with a concrete slab girder bridge using prestressed concrete bulb-tees. As part of the replacement, the bridge contractor agreed to donate the transportation of two bridge girders to the Bowen Laboratory. Through coordination with the contractor, the bituminous wearing surface was removed from the bridge, and Beam B8 (Specimen 409-2-UD) and Beam B9 (Specimen 409-1-ES) were selected for salvage. Upon arrival to the laboratory, the beams were found to have an additional 2.5 in. thick concrete topping slab (Figure 2.13), and the curb from Specimen 409-1-ES had been removed. As shown in Figure 2.12, Specimen 409-1-ES had a concrete spall exposing three strands (Figure 2.14). Specimen 409-2-UD did not exhibit any visual signs of deterioration and was thus considered a control specimen.

Figure 2.13: Topping Slab on Specimen 409-2-UD (Beam B8)

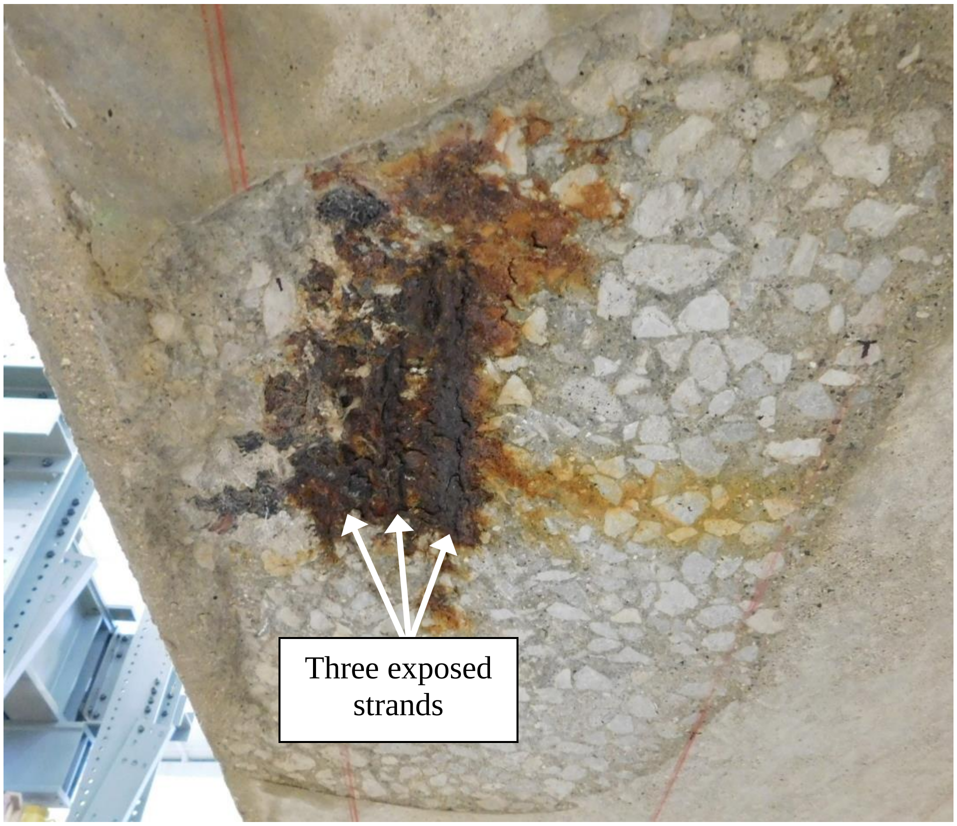

Figure 2.14: Exposed Strands in Specimen 409-1-ES

2.4.3 Newton K5

2.4.3.1 Bridge Information

Newton K5 (56-000K5) was a 35 ft single-span bridge over Kent Ditch (Figure 2.15). The bridge was built in 1965 using six 27 in. deep, 36 in. wide beams and two 21 in deep, 45 in. wide beams for a total width of 25.5 ft. The two 45 in wide beams were placed on the exterior edges of the bridge and were built with standard curbs. The curbs did not have outlets along the span, and deck drains through the bridge were not installed. All water was drained to the ends of the bridge. The bituminous wearing surface was approximately 3 in thick. Transverse tie rods were located at midspan.

Figure 2.15: Newton K5

2.4.3.2 Bridge Deterioration

Newton K5 was inspected by the research team on 8 May 2017. A summary of the observed deterioration is provided in Figure 2.16. Two longitudinal cracks and joint staining were found in and around Beam 1 (Specimen K5-1-LC) with one of the longitudinal cracks extending from near the west support into midspan (Figure 2.17). Three rust-stained longitudinal cracks were observed in Beam 7 (Specimen K5-2-LC) along with spalling around the drain holes (Figure 2.18). In addition, reflective cracking was found in the wearing surface across the bridge (Figure 2.19). Please note that thin black lines have been drawn to the right of the actual cracks in Figure 2.19 to highlight the location of the cracks in the wearing surface.

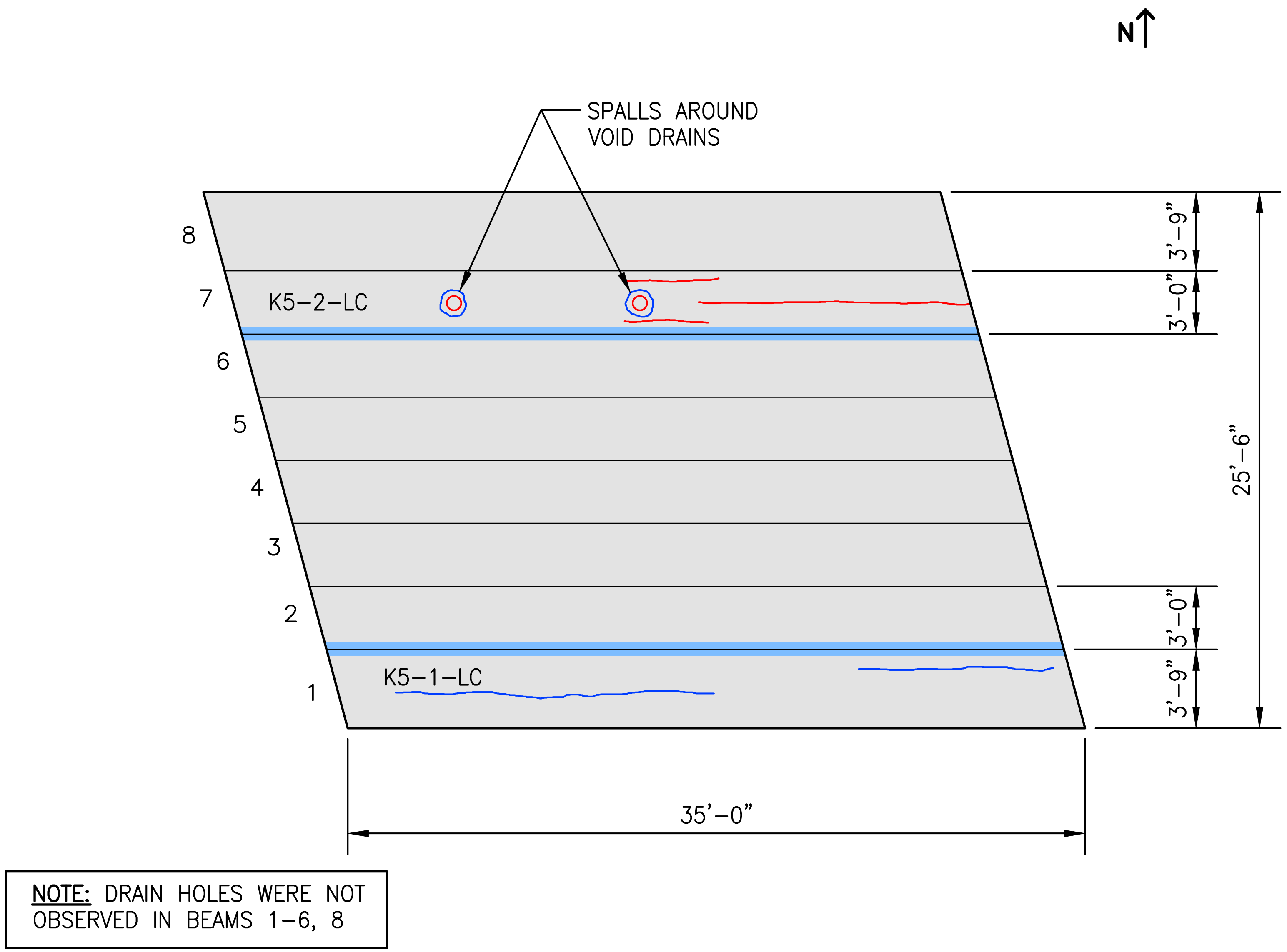

Figure 2.16: Newton K5 Deterioration Map

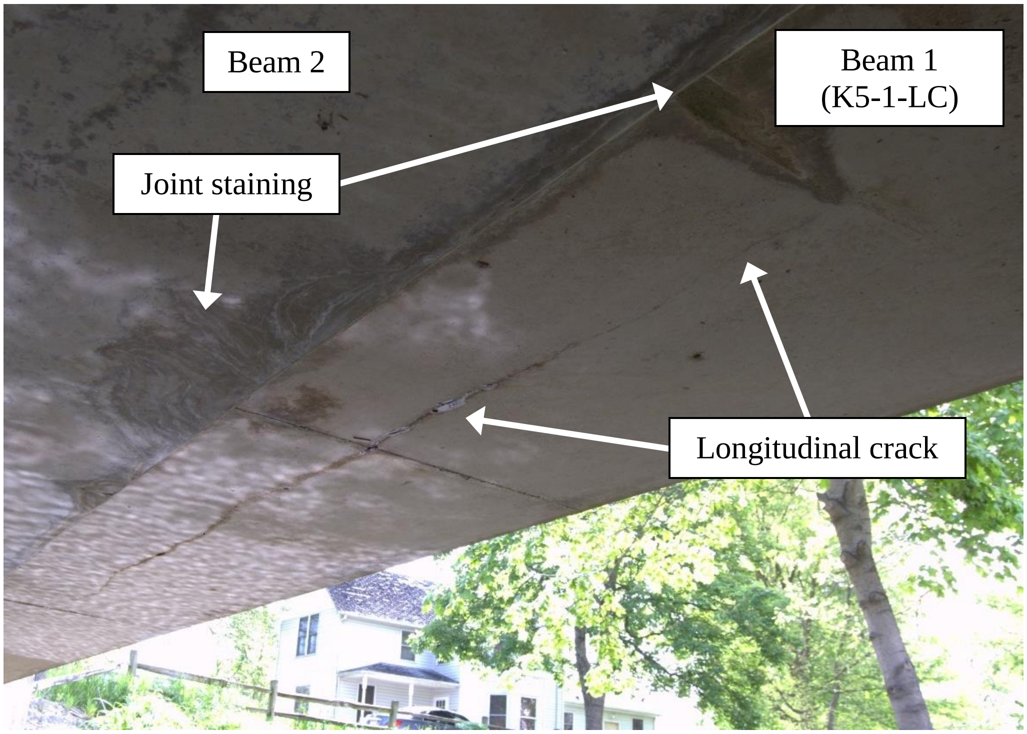

Figure 2.17: Beam 1 (Specimen K5-1-LC) Deterioration

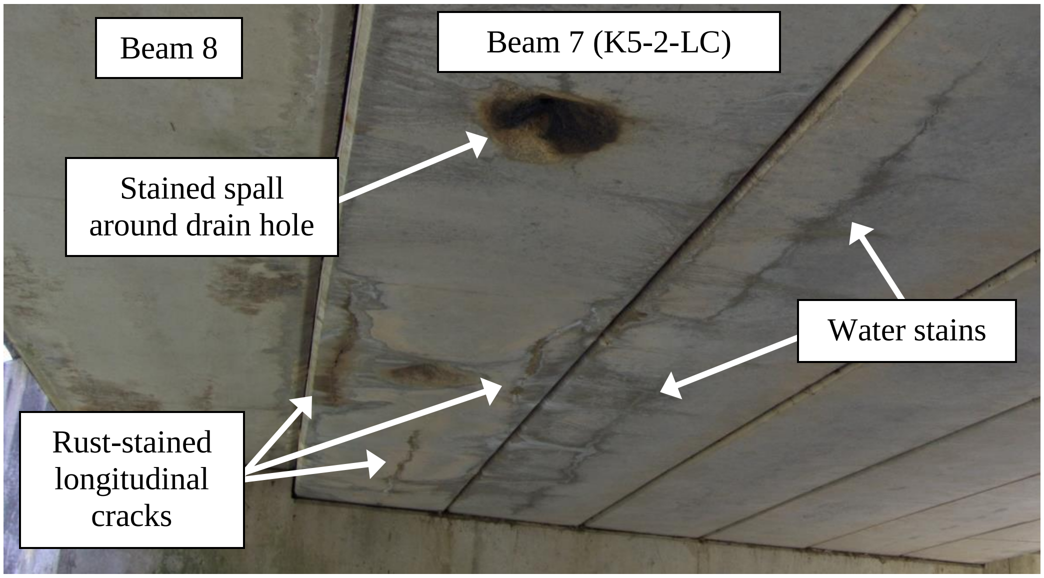

Figure 2.18: Beam 7 (Specimen K5-2-LC) Deterioration

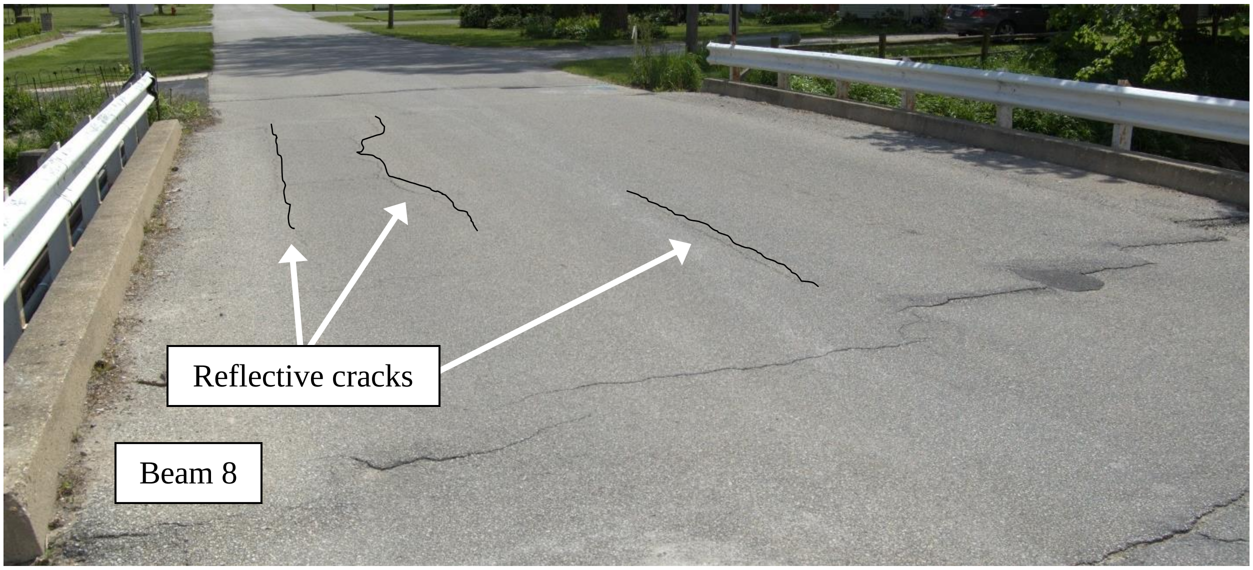

Figure 2.19: Reflective Cracks in Wearing Surface

2.4.3.3 Beam Specimen Information

In 2018, the bridge was replaced with a new adjacent box beam bridge. As part of the bridge replacement, Beam 1 (Specimen K5-1-LC) and Beam 7 (Specimen K5-2-LC) were salvaged and transported to the Bowen Laboratory. During the salvage process, the wearing surface was removed, and scaling of the top flange of Specimen K5-2-LC (Beam 7) was observed (Figure 2.20). The top flange deterioration location corresponded with the locations of the three longitudinal cracks in the bottom flange. No additional deterioration was observed in Specimen K5-1-LC (Beam 1), but no drain holes were found in the bottom flange. Drain holes were drilled into the bottom flange of each void using a 5/8 in. concrete drill bit at approximately 3 ft from both ends of the beam. After the drain holes were drilled into the east end of the beam, water drained from the south drain hole for approximately two minutes (Figure 2.21).

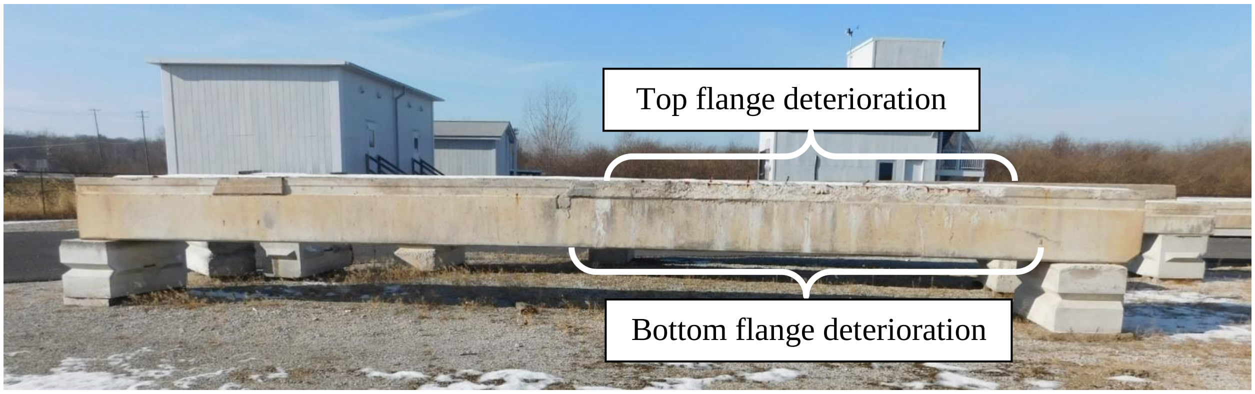

(a) Location of the flange deterioration

(b) Concrete scaling and corroded reinforcement

Figure 2.20: Specimen K5-2-LC (Beam 7) Top Flange Deterioration

Figure 2.21: Water Draining from K5-1-LC (Beam 1)

2.4.4 Wells 79

2.4.4.1 Bridge Information

Wells 79 (90-00079) was a three-span bridge built in 1966 over Rock Creek (Figure 2.22). The main span was 36 ft long, and the approach spans were each 28.5 ft long. Each of the three spans were comprised of five 17 in. deep, 48 in. wide beams and two 17 in. deep, 36 in. wide beams. The 36 in. wide beams were the exterior beams of the bridge and were constructed with standard curbs. Small 3 in. diameter holes were drilled into the bottom of the curbs as scuppers for deck drainage. Each scupper was located toward the end of each span. The bituminous wearing surface was approximately 2 in. thick. Transverse tie rods for each span were located at midspan.

Figure 2.22: Wells 79

2.4.4.2 Bridge Deterioration

Wells 79 was inspected by the research team on 27 July 2016. The observed deterioration is summarized in Figure 2.23. Longitudinal cracks were found in six beams. The longitudinal cracks in Beam A7 (Specimen 79-4-LC) and Beams C2 and C6 were localized to the ends of the beams supported by the abutments (Figure 2.24 and Figure 2.25). The cracks in Beams B6 and C7 extended from the east support of each beam into midspan (Figure 2.26 and Figure 2.27). The crack in Beam C7 covered almost the entire length of the beam. When the wearing surface was inspected, a hole was found in the top flange of Beam C1 (Figure 2.28). The hole was filled with water, and vegetation was growing around the hole. When the bottom flange was inspected, no drain holes were present. In addition, reflective cracks were found in the wearing surface. The location of the reflective cracks corresponded with the joint between the adjacent beams below.

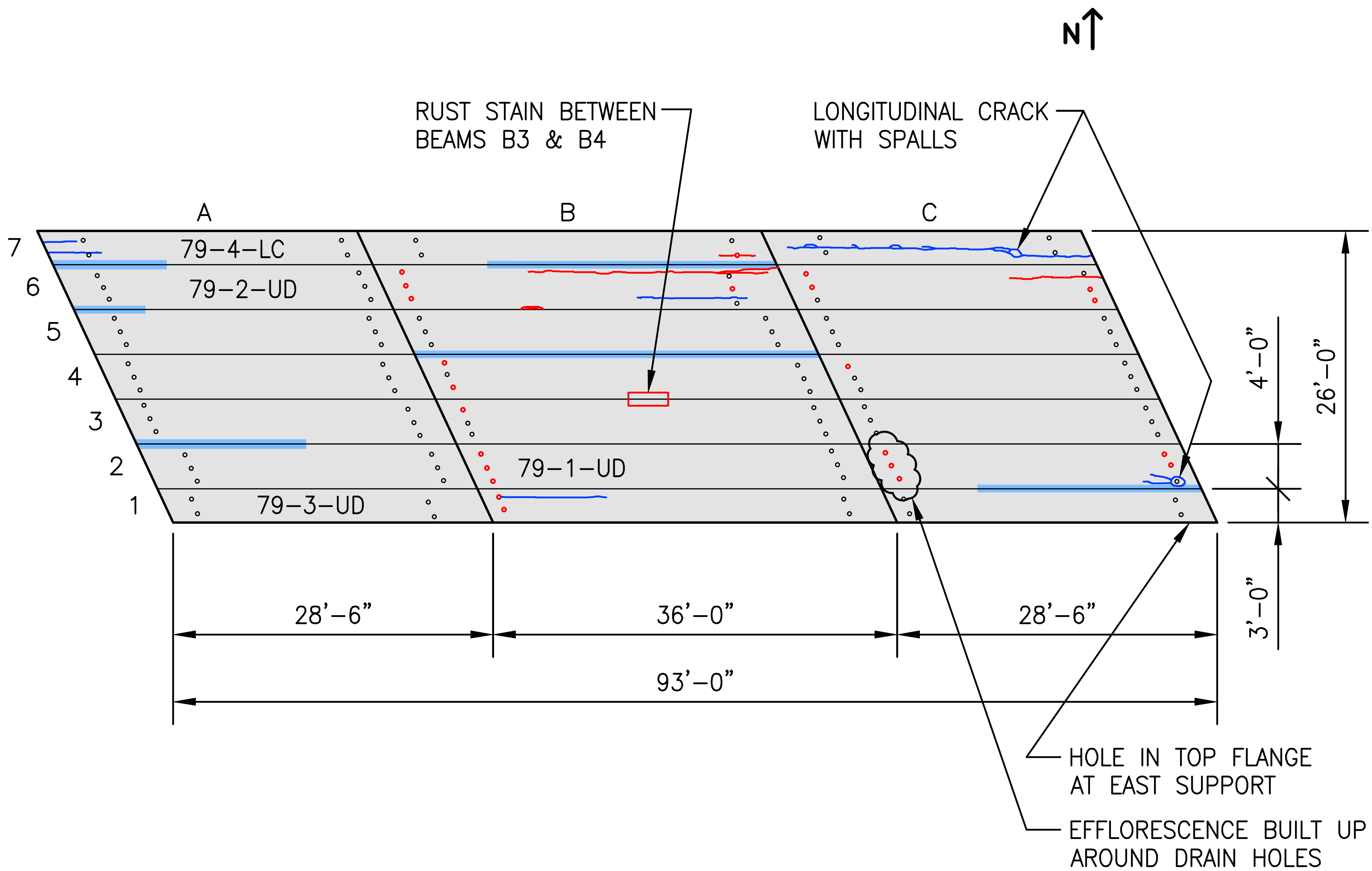

Figure 2.23: Wells 79 Deterioration Map

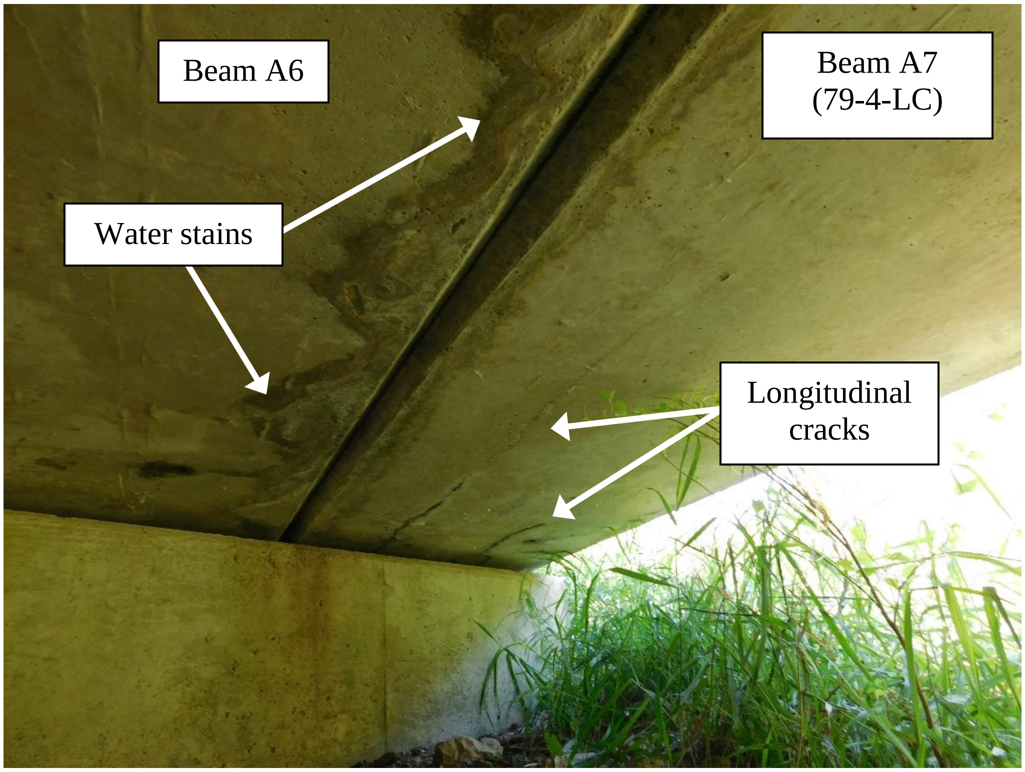

Figure 2.24: Beam A7 (specimen 79-4-LC) Deterioration

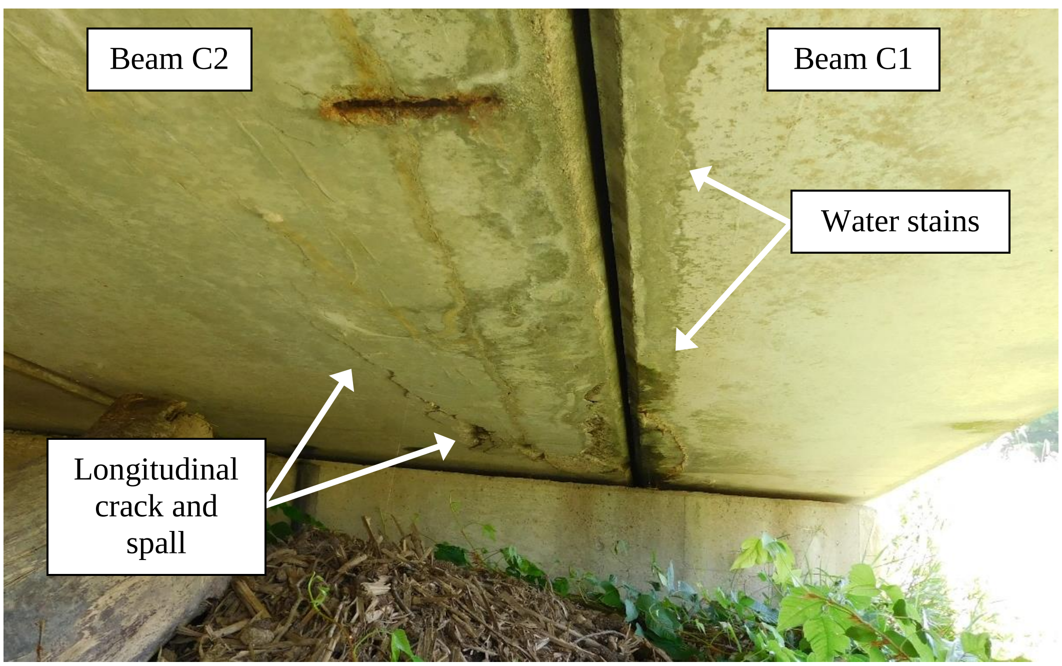

Figure 2.25: Beam C2 Deterioration

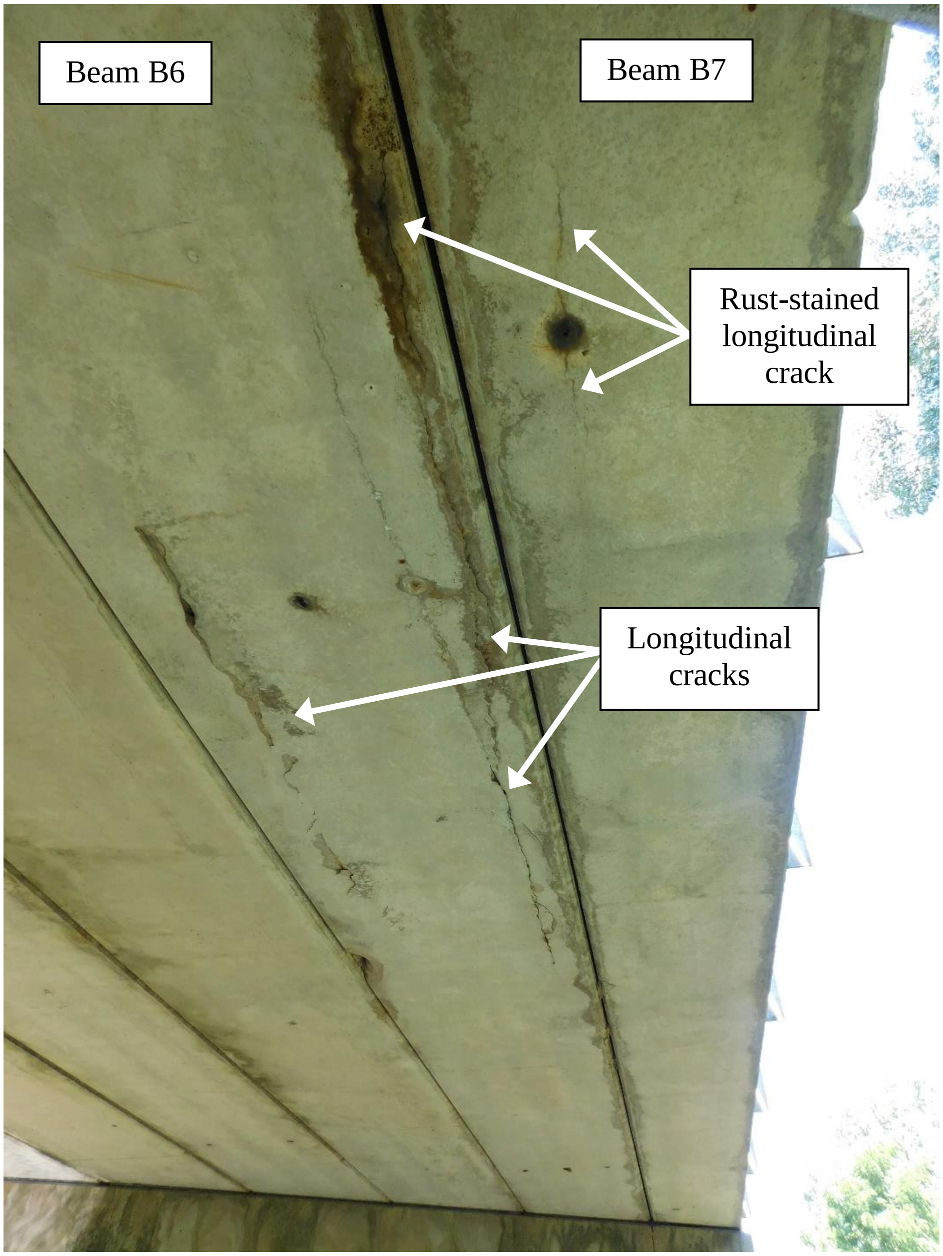

Figure 2.26: Beam B6 Deterioration

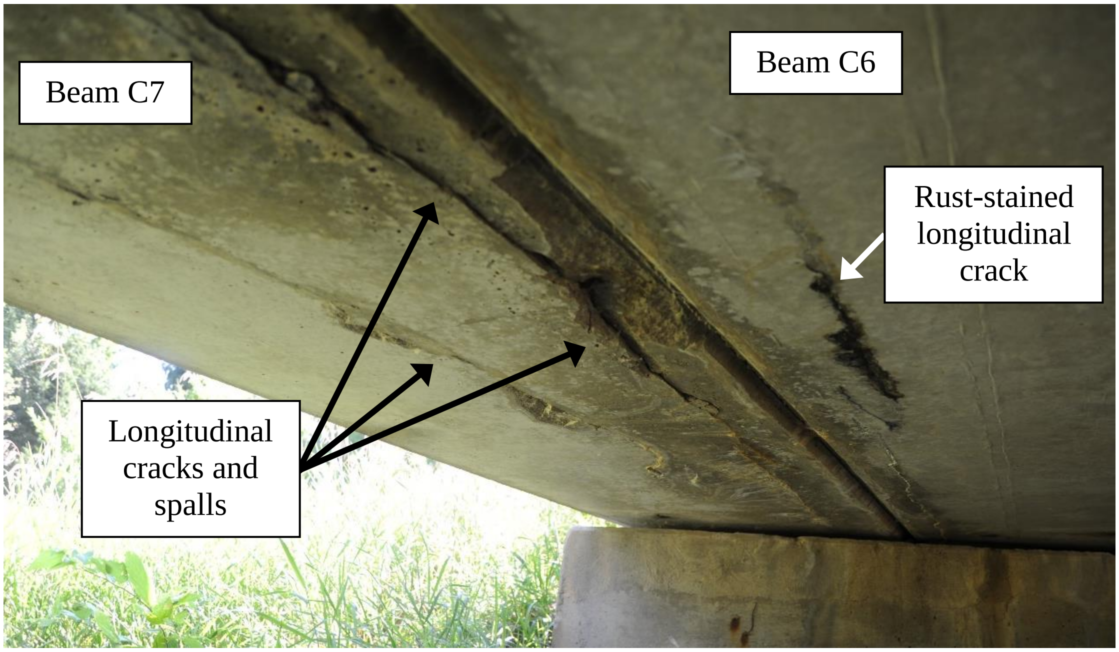

Figure 2.27: Beams C6 and C7 Deterioration

Figure 2.28: Hole in Top Flange of Beam C1

2.4.4.3 Beam Specimen Information

In 2017, the bridge was replaced with a new adjacent box beam bridge. During the demolition phase of the replacement project, four beams were salvaged. Due to a miscommunication with the demolition contractor, the four beams that were salvaged did not correspond to those desired for the project. Beams B2, A6, A1, and A7 (Specimens 79-1-UD, 79-2-UD, 79-3-UD, and 79-4-LC) were salvaged in place of Beams B6, C1, C6, and C7. As shown in Figure 2.23, the beams received showed minor signs of deterioration. As such, the beams were considered as good control specimens for the experimental study.

2.4.5 Newton 56

2.4.5.1 Bridge Information

Newton 56 (56-00056) was a three-span bridge over Beaver Lake Ditch built in 1968 (Figure 2.29). The main span was 36 ft long, and the two approach spans were each 27.5 ft long. The total width of the bridge was 24 ft and comprised of six 17 in. deep, 48 in. wide beams. The exterior beams were built without curbs or deck drains; therefore, water drained off the bridge over the sides of the exterior beams. The bituminous wearing surface was estimated to be 7 in. thick, and transverse tie rods were located at midspan in all three spans.

Figure 2.29: Newton 56

2.4.5.2 Bridge Deterioration

The bridge was inspected by the research team on 8 May 2017. The observed deterioration is summarized in Figure 2.30. Many of the joints showed signs of water leakage as staining around the joints between many of the beams. Examples of the observed staining is provided in Figure 2.31. The joint between Beams B5 and B6 had a large rust stain located near midspan. Because no spalling was observed on the bottom flanges of either beam, the rust was assumed to have originated from the transverse tie rod. A short longitudinal crack was observed in Beam A6 (Specimen 56-1-LC) at the west support (Figure 2.32). Beam B1 (Specimen 56-2-ES) was the most heavily deteriorated; nearly the entire exterior side of the beam had spalled off (Figure 2.33). Many stirrups were exposed, and a single strand was exposed at midspan (Figure 2.34). As shown in Figure 2.30, a majority of the drain holes were found to be rust stained or clogged (Figure 2.35). In addition, reflective cracking was observed in the bituminous wearing surface (Figure 2.36). Please note that a thin black line has been drawn to the right of the crack to highlight the location.

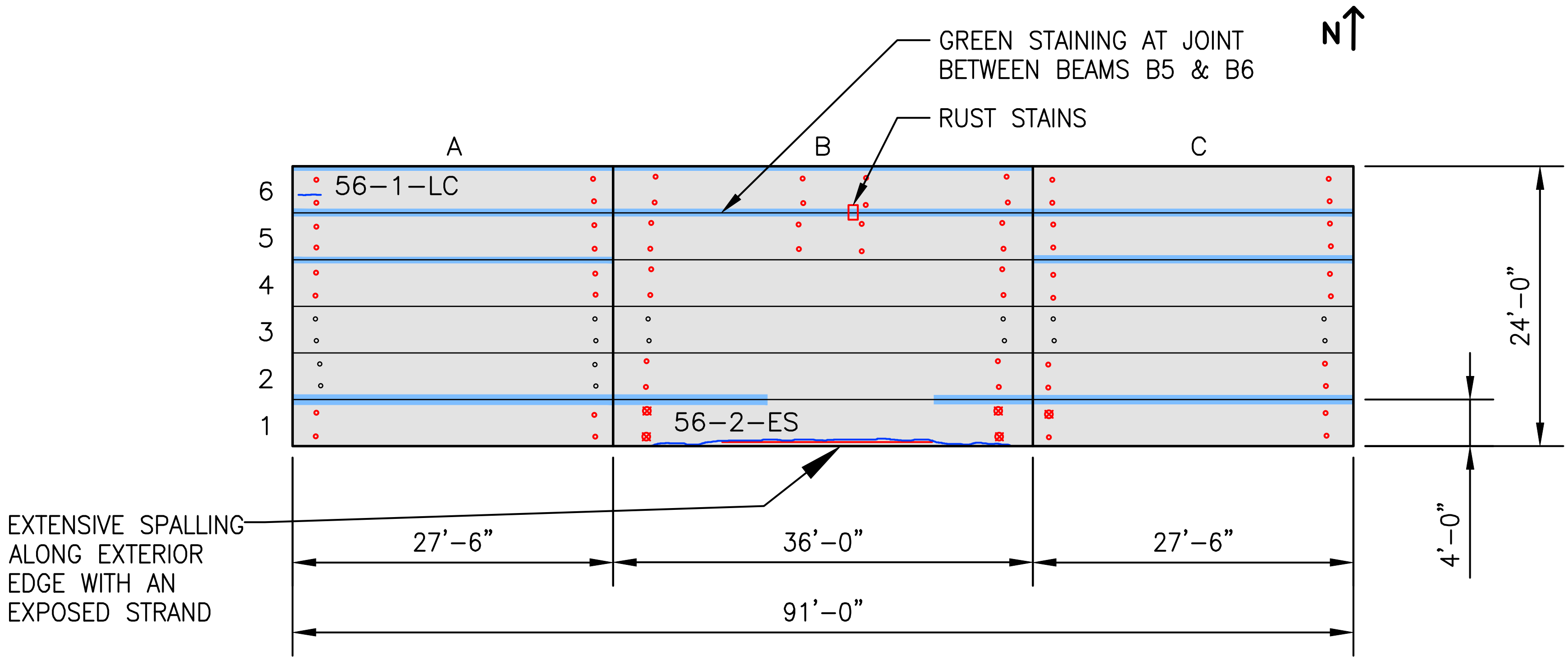

Figure 2.30: Newton 56 Deterioration Map

(a) Joint stains between Beams B5 and B6

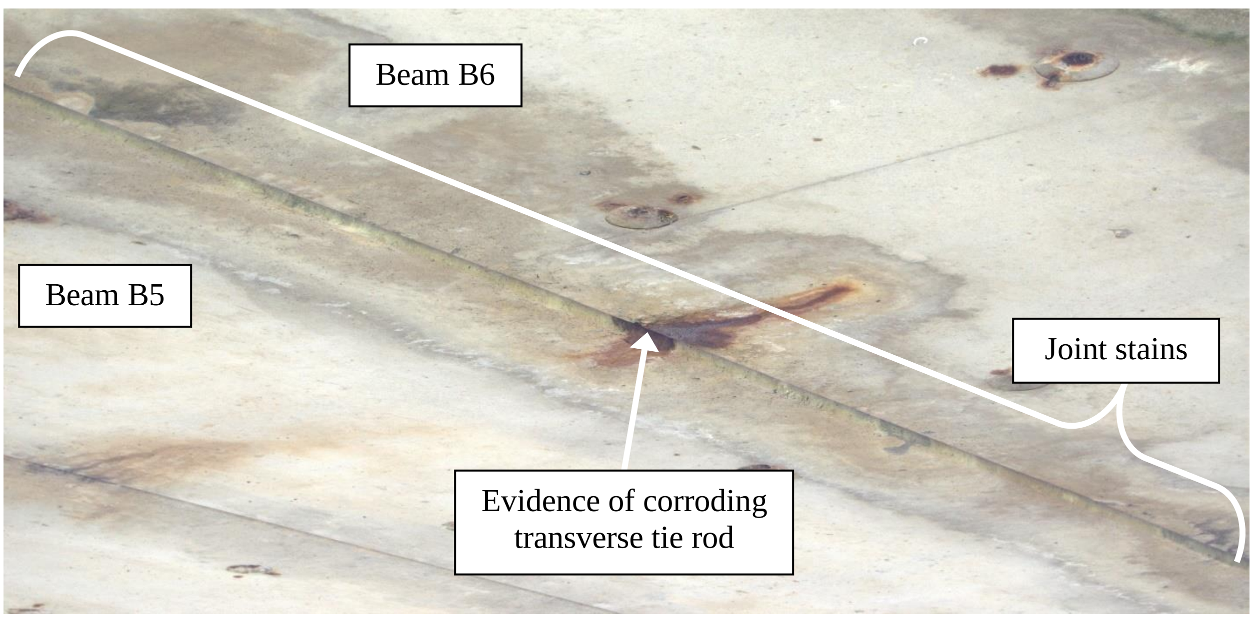

(b) Joint stains between Beams B5 and B6

Figure 2.31: Joint Staining

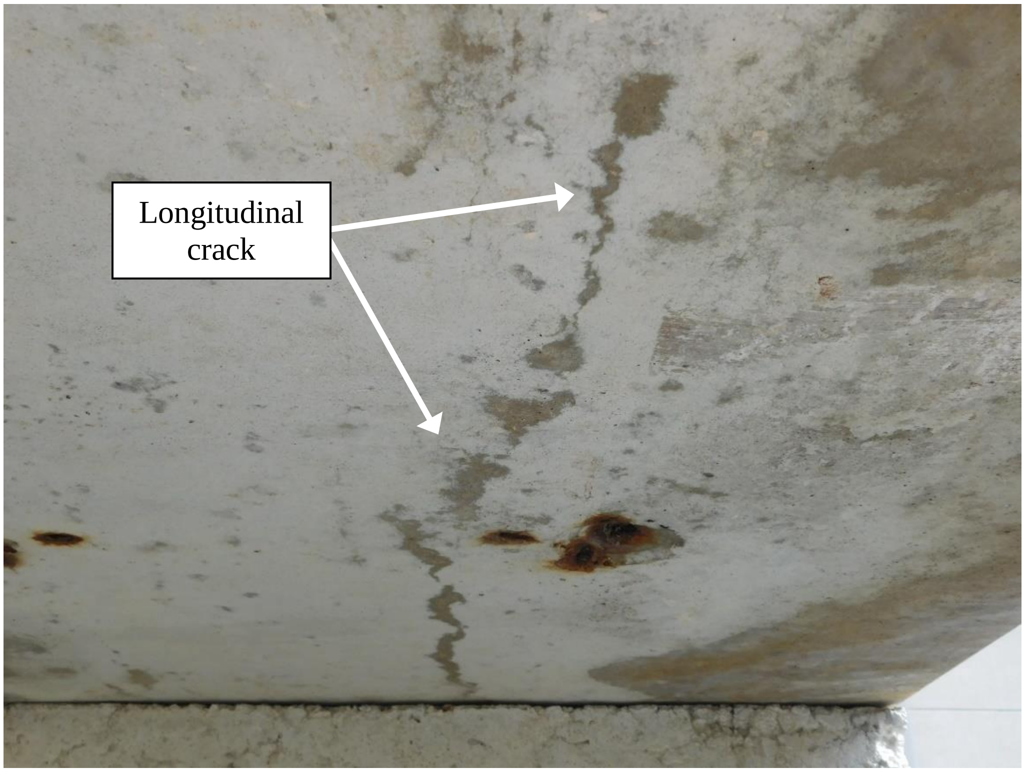

Figure 2.32: Longitudinal Crack in Beam A6 (Specimen 56-1-LC)

Figure 2.33: Spalling on Beam B1 (Specimen 56-2-ES)

Figure 2.34: Photo looking from above on the exterior side of Beam B1 (specimen 56-2-ES)

Figure 2.35: Rust-Stained and Clogged Drain Hole

Figure 2.36: Reflective Cracks at Joint between Beam A5 and Beam A6 (Specimen 56-1-LC)

2.4.5.3 Beam Specimen Information

In 2018, the bridge was replaced with a new adjacent box beam bridge. As part of the demolition of the bridge, Beam A6 (Specimen 56-1-LC) and Beam B1 (Specimen 56-2-ES) were salvaged and transported to Bowen Laboratory. To salvage the beams, the wearing surface had to be removed. The milling machine used to remove the wearing surface ground off approximately 2 in. of the top flange of Specimen 56-2-ES (Beam B1) (Figure 2.37). The research team was informed by the bridge contractor that deteriorated concrete is nearly as easy to mill as bituminous materials, and the similarity in hardness causes milling machine operators to have difficulty when determining where the bituminous wearing surface ends and the deteriorated concrete begins. As such, the bridge contractor believed that the top 2 in. of Specimen 56-2-ES (Beam B1) was deteriorated.

Figure 2.37: Top Flange Removed by Milling Machine

2.4.6 Elkhart 102

2.4.6.1 Bridge Information

Elkhart 102 (20-00102) was a three-span bridge over the Little Elkhart River built in 1970 (Figure 2.38). The bridge span consisted of three equal spans of 35 ft. Each span consisted of eight 48 in. wide box beams for a total width of 32 ft. The bridge was built without curbs or deck drains. Water simply drained off the sides of the bridge. The bituminous wearing surface was approximately 2-4 in. thick. A transverse tie rod was installed at midspan in each of the three spans.

Figure 2.38: Elkhart 102

2.4.6.2 Bridge Deterioration

Elkhart 102 was inspected by the research team on 9 January 2018. The observed deterioration is summarized in Figure 2.39. In general, the bridge was in an advanced state of deterioration; only one beam out of the 24 total beams did not show any signs of deterioration. A total of 16 beams had exposed or broken strands. Examples of the deterioration are provided in Figure 2.40 to Figure 2.43. In Figure 2.40, Beam B7 (Specimen 102-3-BS) and Beam B8 (Specimen 102-3-BS) are shown with broken strands and wet edge staining. In Figure 2.41, Beam C5 (Specimen 102-2-BS) and Beam C6 are shown with longitudinal cracks, exposed strand, and broken strand. In Figure 2.42, Beam C6 and Beam C7 (Specimen 102-1-BS) are shown with a broken strand and a longitudinal crack. Notably, all observed deterioration was localized to the edges of each beam, and where the corner of the section had not cracked, there was evidence of water leaking onto the bottom flange (Figure 2.43). In addition, reflective cracks were observed in the wearing surface.

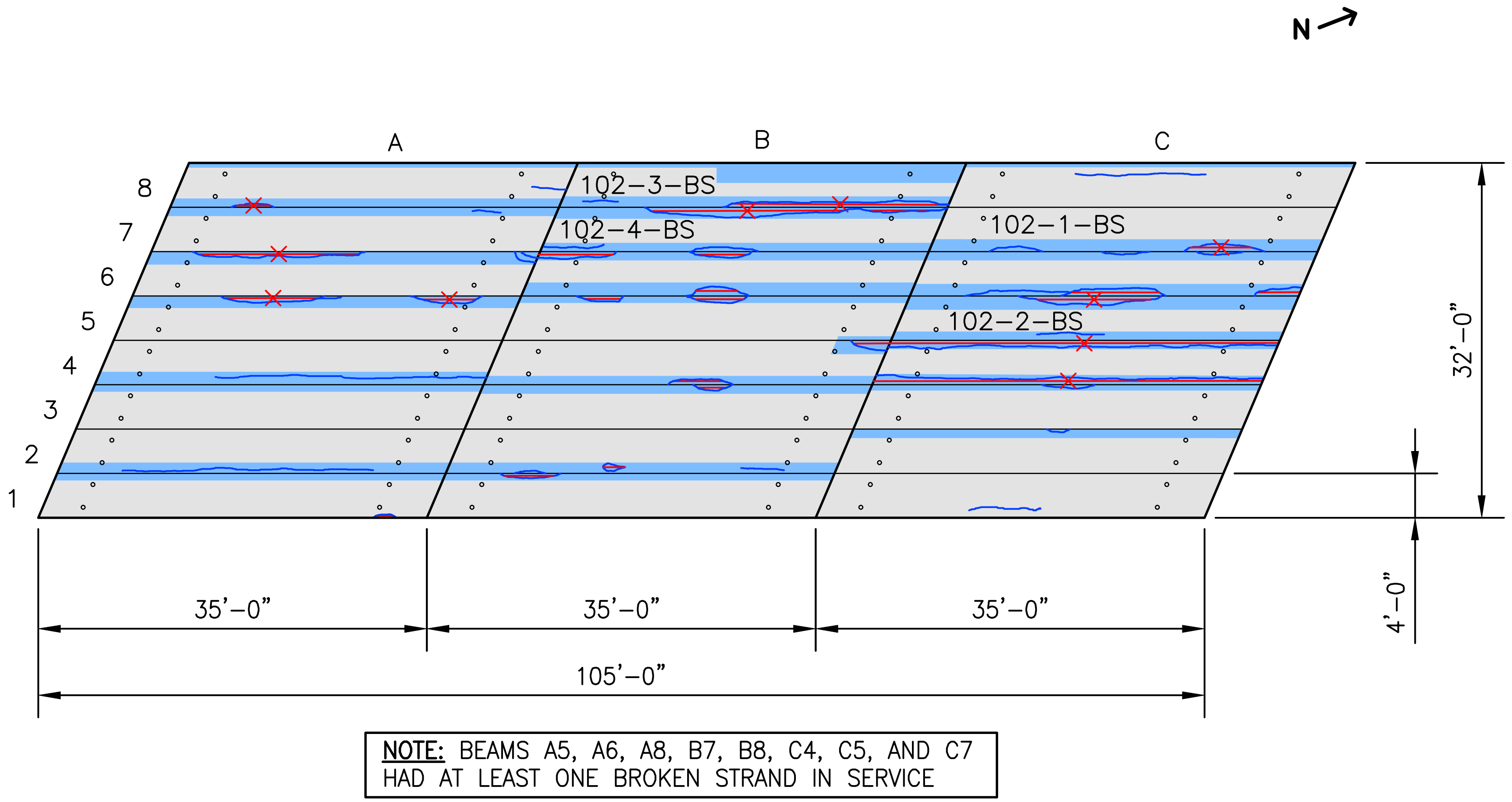

Figure 2.39: Elkhart 102 Deterioration Map

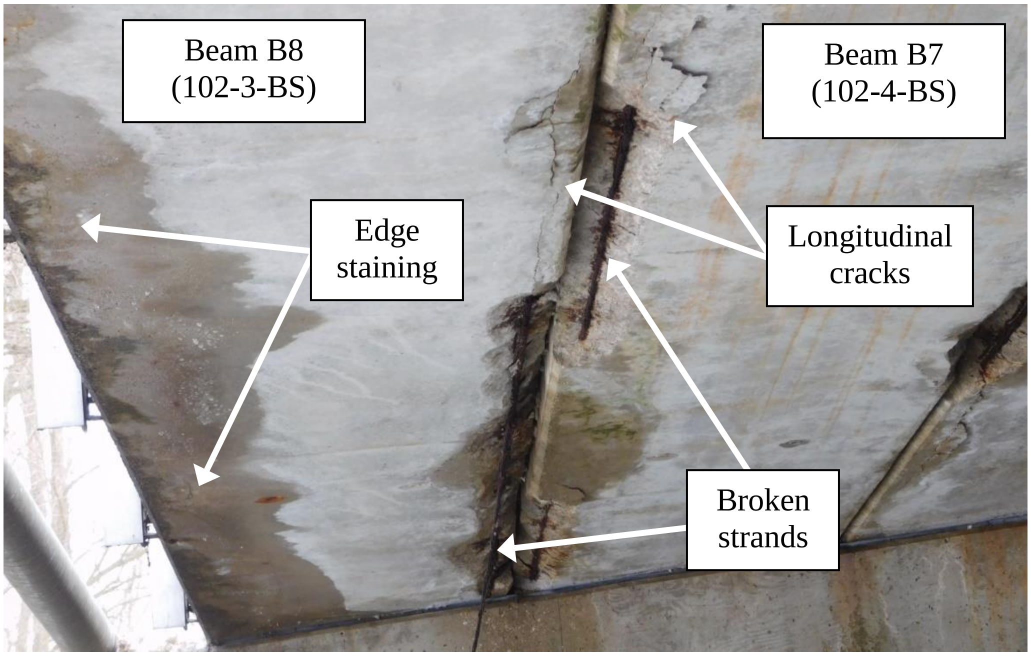

Figure 2.40: Deterioration of Beams B7 and B8 (Specimens 102-3-BS and 102-4-BS)

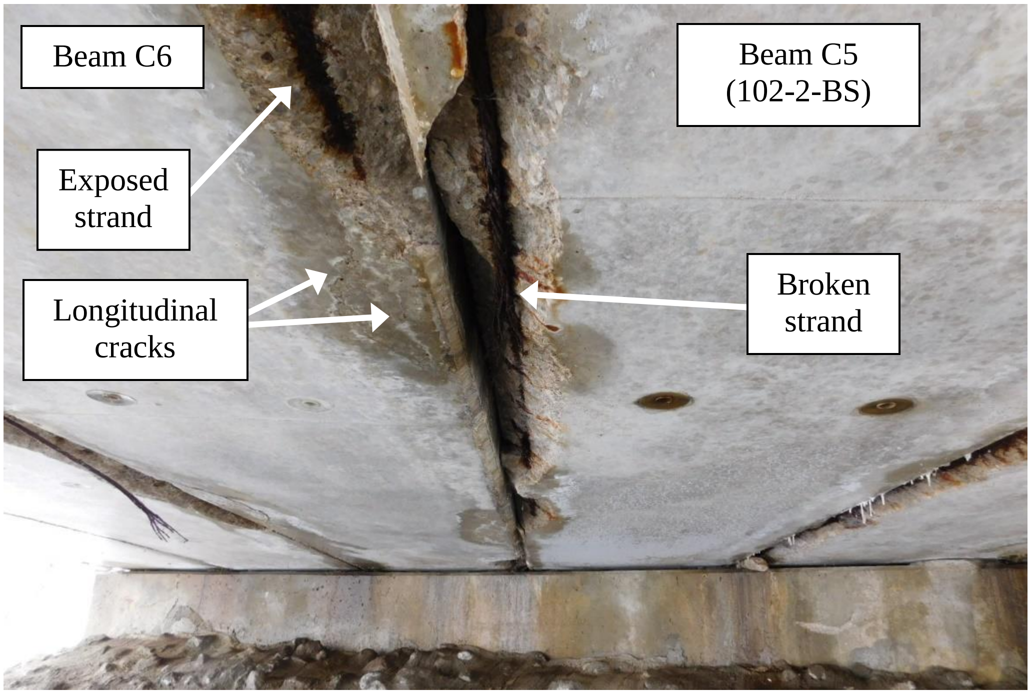

Figure 2.41: Deterioration of Beam C5 and Beam C6 (Specimen 102-2-BS)

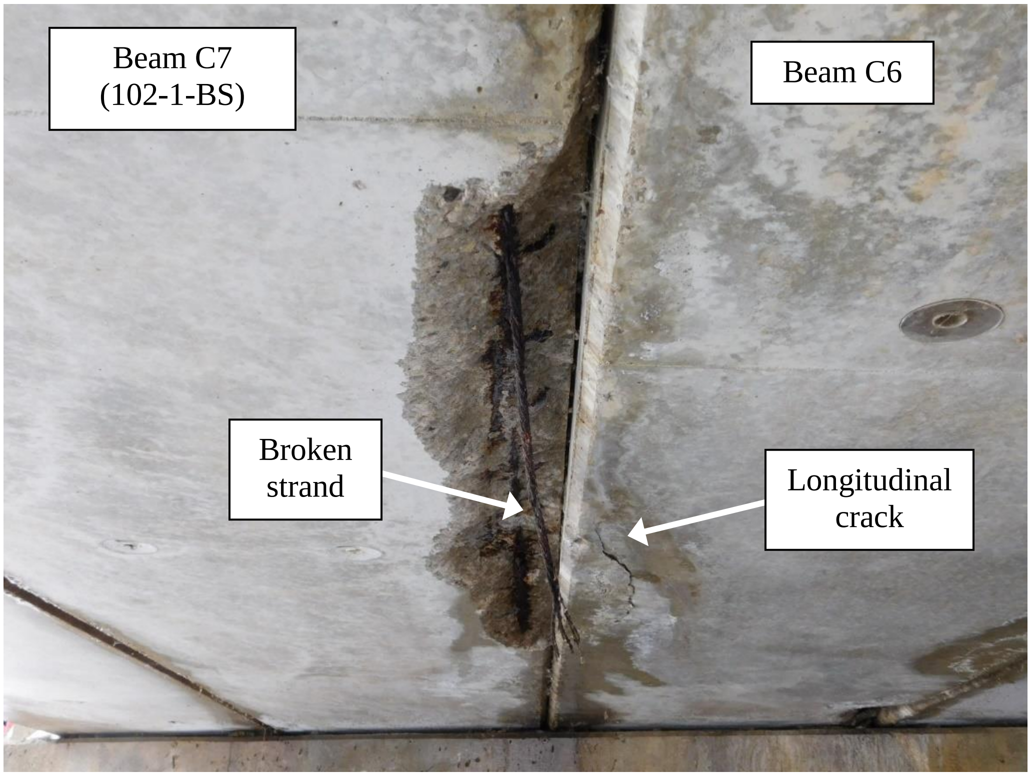

Figure 2.42: Deterioration of Beam C6 and Beam C7 (Specimen 102-1-BS)

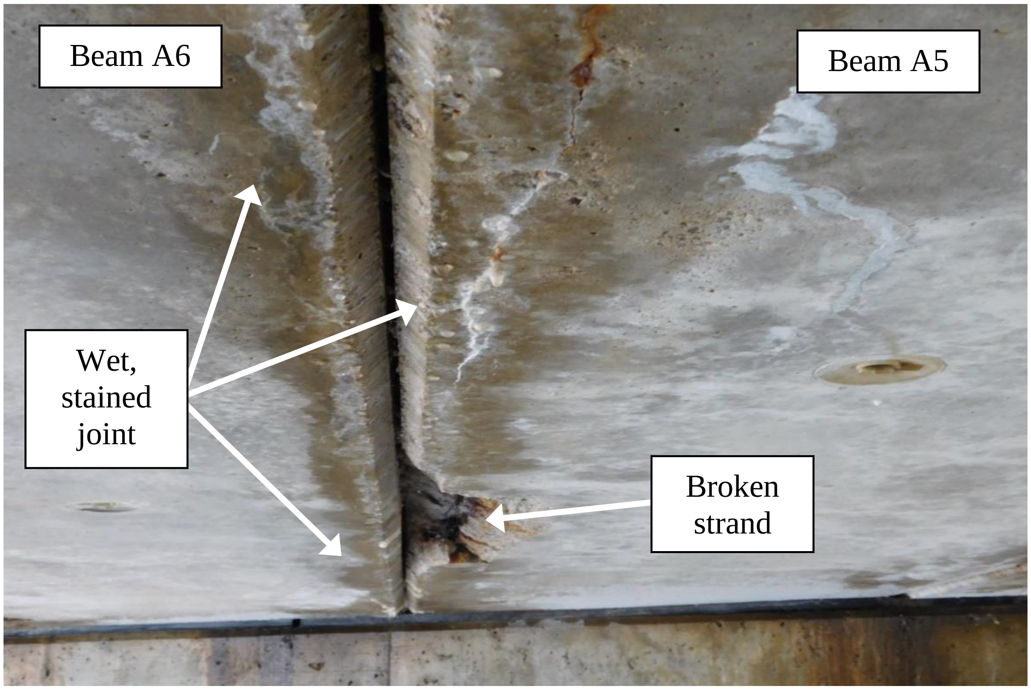

Figure 2.43: Leaking Shear Key between Beams A5 and A6

2.4.6.3 Beam Specimen Information

In 2018, the bridge was replaced with a slab-girder type bridge with a concrete deck and steel beams. As a part of the bridge replacement project, Beams C7, C5, B8, and B7 (Specimens 102-1-BS, 102-2-BS, 102-3-BS, and 102-4-BS) were salvaged and transported to the Bowen Laboratory. Upon arrival, no additional deterioration was observed in any of the specimens.

2.5 Supplemental Bridge Inspections

The 11 supplemental bridge inspections that were conducted through the course of searching for laboratory specimens are presented in the following sections (order by structure number). Each bridge inspection provided information to augment the understanding of box beam deterioration. This understanding forms the basis of the recommended changes to the design of box beam bridges.

2.5.1 Daviess 95

2.5.1.1 Bridge Information

Daviess 95 (14-00095) is a three-span bridge over North Fork Prairie Creek built in 1962 (Figure 2.44). The main span is 44 ft with two approach spans of 37 ft. The total width of the bridge is 28 ft, which consists of seven 48 in. wide beams. The bridge has a 2 in. thick bituminous wearing surface and standard 10 in. tall curbs on the exterior beams. The curbs have water outlets along the length of the bridge that allow water to drain from the bridge deck onto the side of the exterior beams. No transverse tie rods were found during the inspection.

Figure 2.44: Davies 95

2.5.1.2 Bridge Deterioration

Daviess 95 was visited by the research team on 24 January 2017. The observed deterioration is summarized in Figure 2.45. A longitudinal crack in Beam A1 extended from the west beam support into the middle portion of the beam and showed signs of water leaking through the crack (Figure 2.46). Beam A1 also showed signs of clogged drain holes (Figure 2.47). A hairline longitudinal crack was found in Beam A6 in the middle third of the span. Staining was observed between the exterior beam and first interior beam on both sides of the bridge along the length of all three spans. The staining was characterized by a greenish color and efflorescence (Figure 2.48). Longitudinal reflective cracks were also observed in the wearing surface (Figure 2.49). Please note that a black line has been drawn next to the reflective crack to highlight the crack location in Figure 2.49.

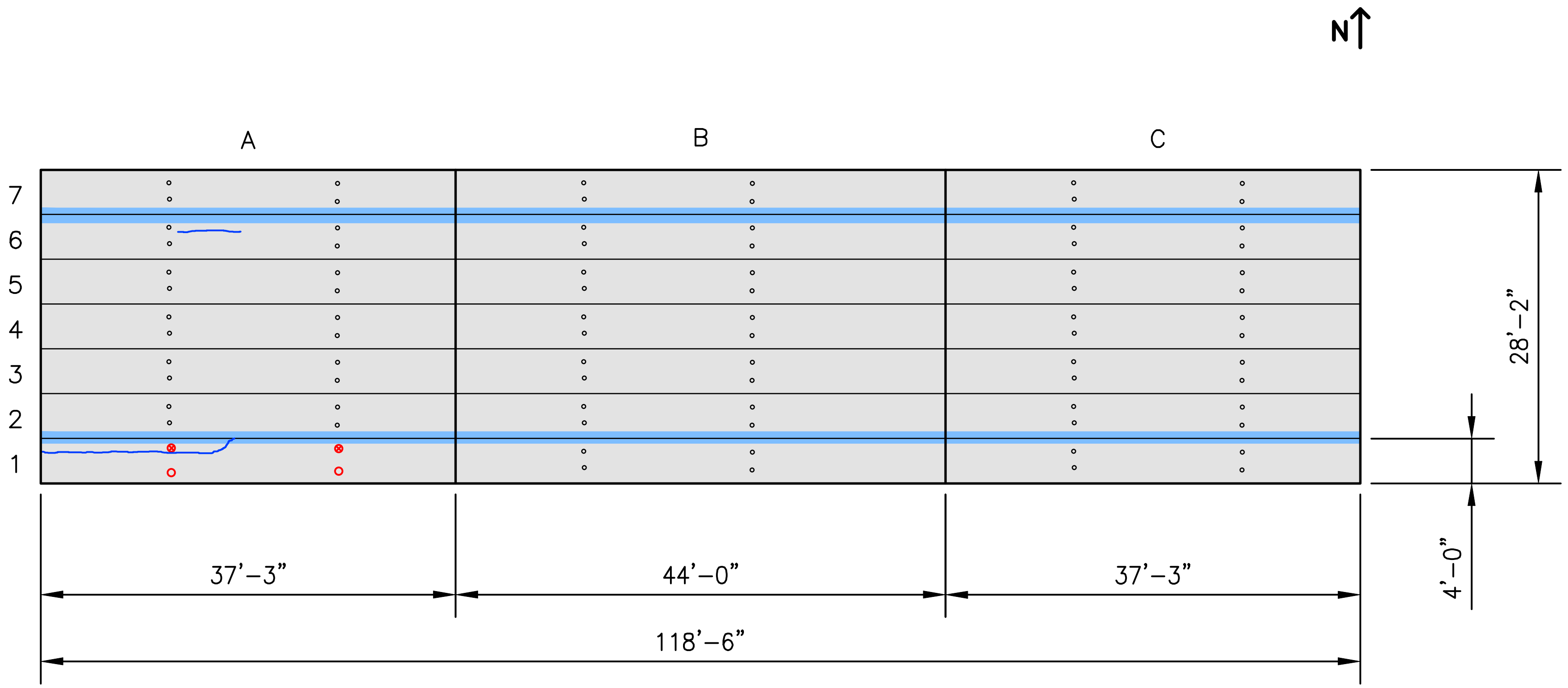

Figure 2.45: Daviess 95 Deterioration Map

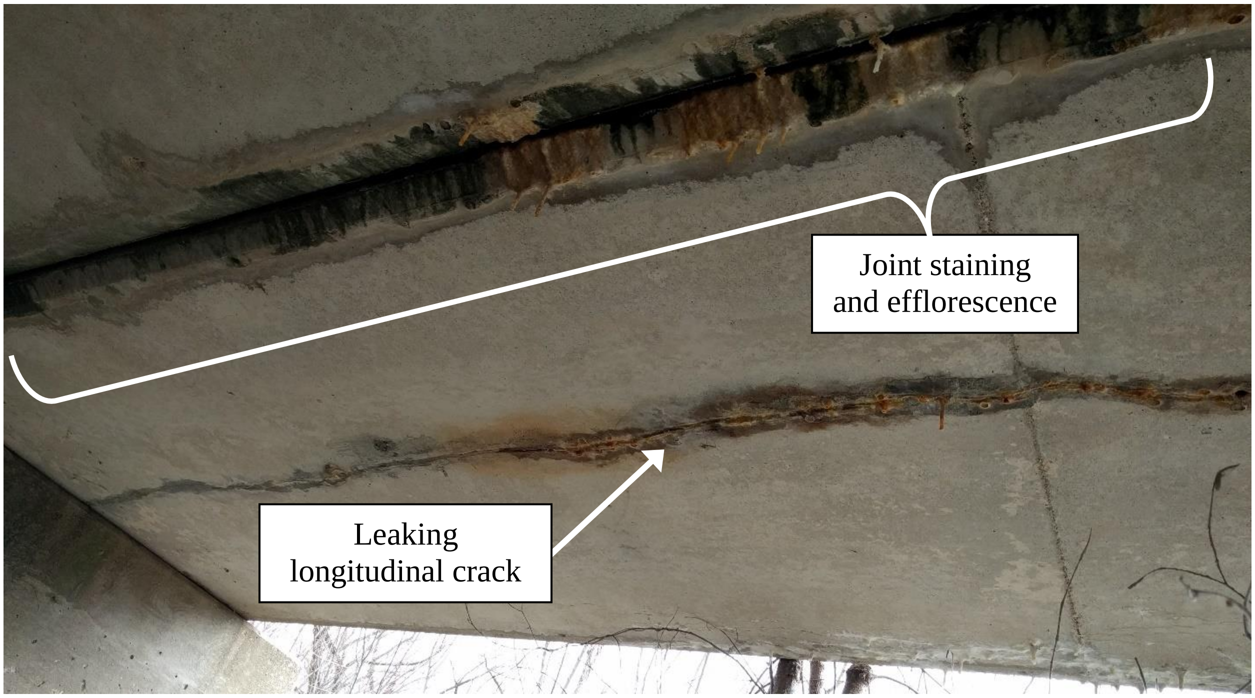

(a) West portion of the longitudinal crack on Beam A1

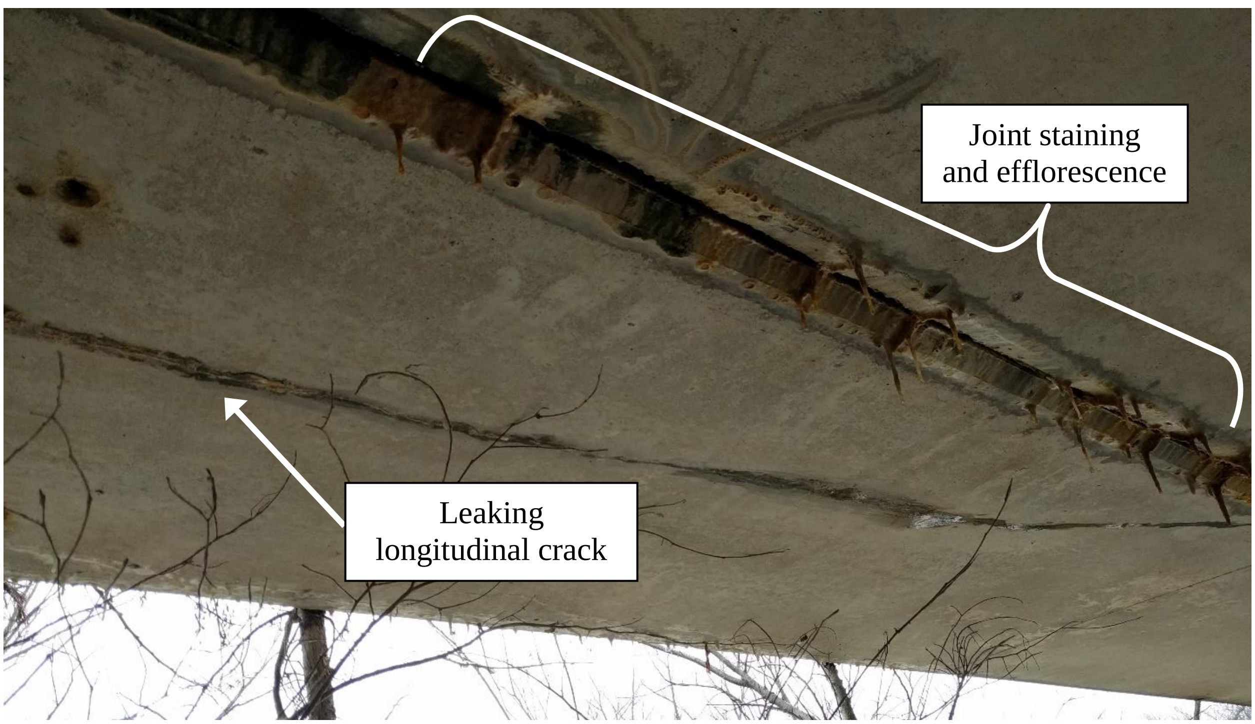

(b) East portion of the longitudinal crack on Beam A1

Figure 2.46: Beam A1 Deterioration

Figure 2.47: Clogged Drain Hole in Beam A1

Figure 2.48: Staining between Beam A1 and A2

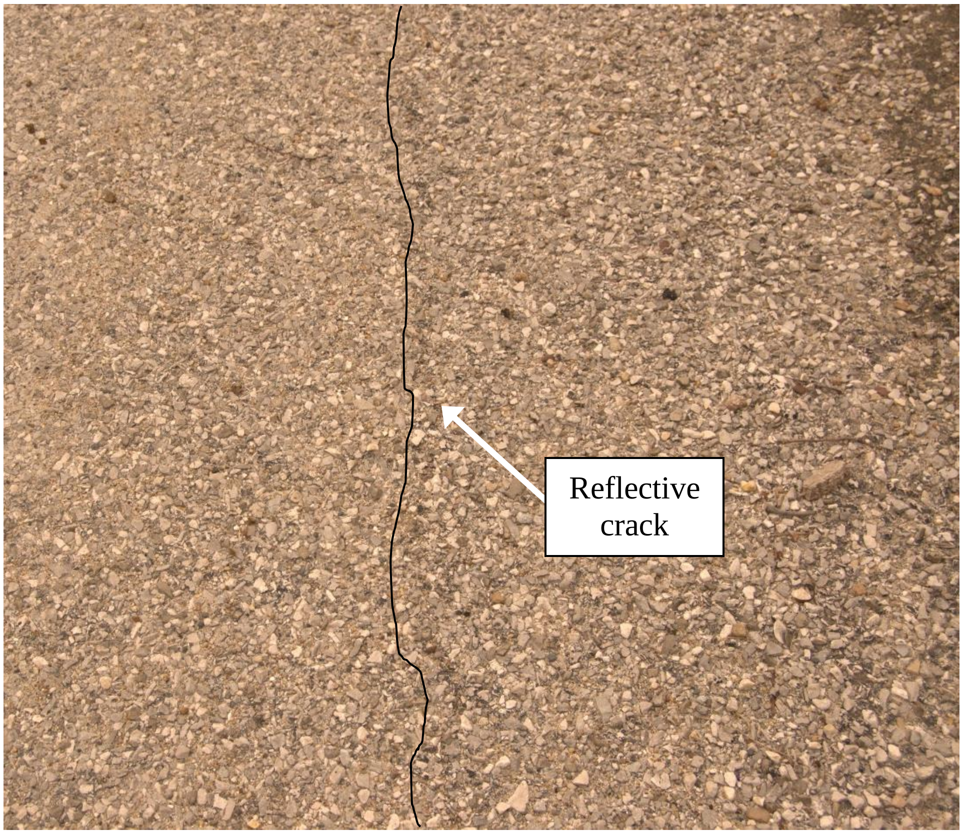

Figure 2.49: Reflective Crack through Wearing Surface

2.5.2 Daviess 160

2.5.2.1 Bridge Information

Built in 1965, Daviess 160 (14-00160) is a 56 ft long, single-span bridge over Sugar Creek (Figure 2.50). Seven 48 in. wide beams make up the total bridge width of 28 ft. The wearing surface of the bridge is bituminous and approximately 1 in. thick. The concrete barriers on each exterior beam are 39 in. tall with no water outlets along the span. All water from the bridge deck is drained to the ends of the bridge. Transverse tie rods are located at third points along the span.

Figure 2.50: Davies 160

2.5.2.2 Bridge Deterioration

Daviess 160 was inspected by the research team on 24 January 2017. The observed deterioration is summarized in Figure 2.51. Beam 1 was observed to have a longitudinal crack on the bottom flange and green staining at the joint (Figure 2.52). Beam 7 had similar deterioration to Beam 1 but exhibited more extensive longitudinal cracking and green staining at the joint (Figure 2.53). The wearing surface was also observed to have reflective cracks between Beams 2 and 3 (Figure 2.54). A black line has been drawn on Figure 2.54 next to the reflective crack to highlight the crack's location.

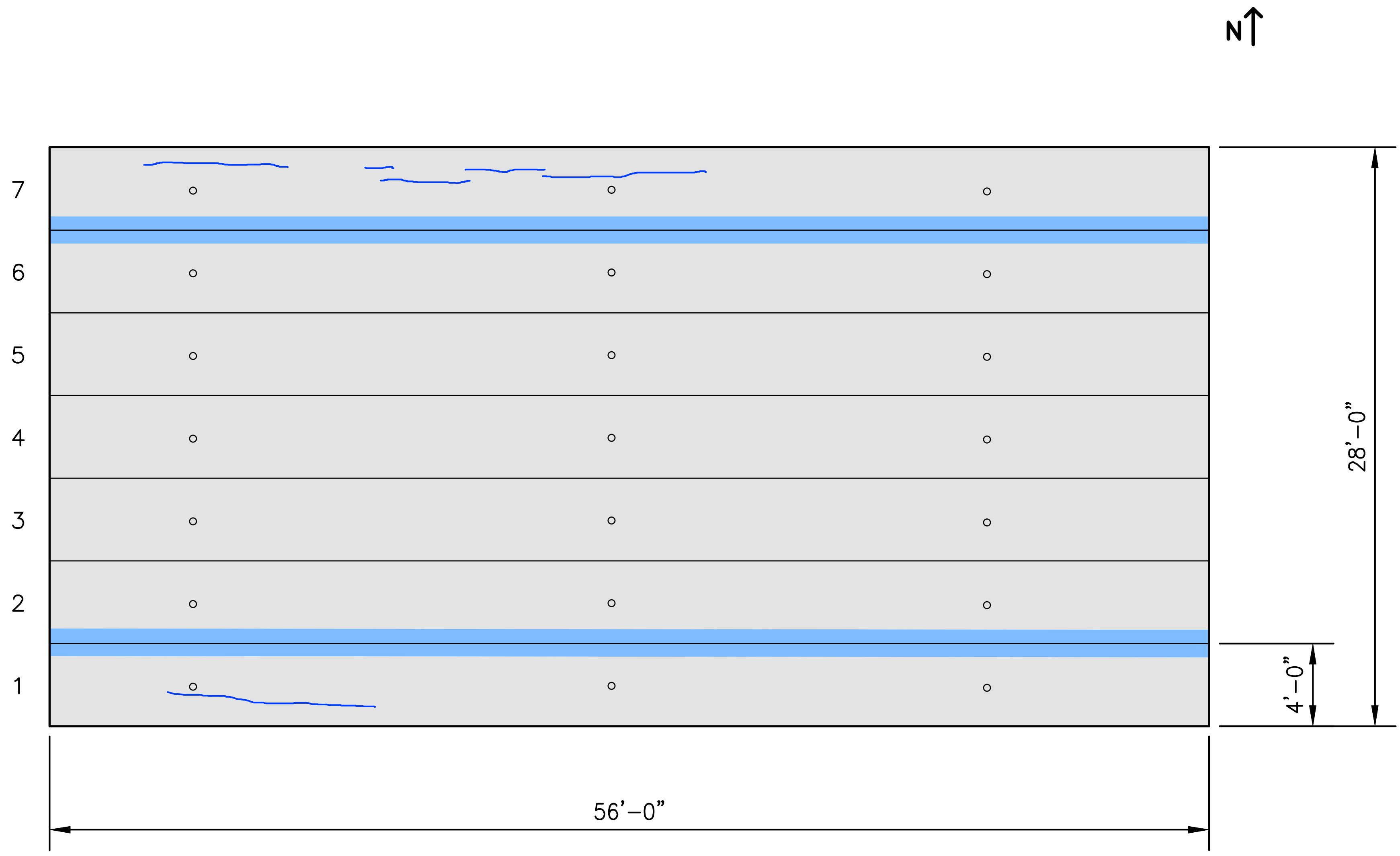

Figure 2.51: Daviess 160 Deterioration Map

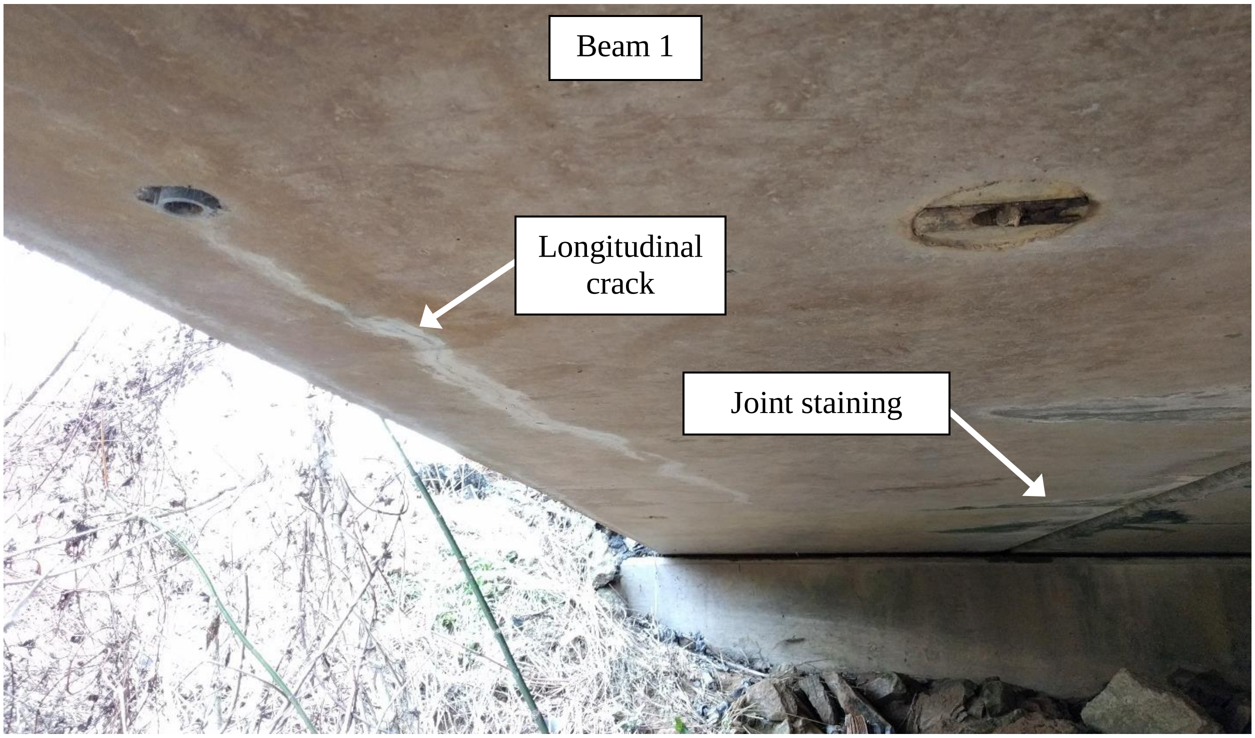

Figure 2.52: Beam 1 Deterioration

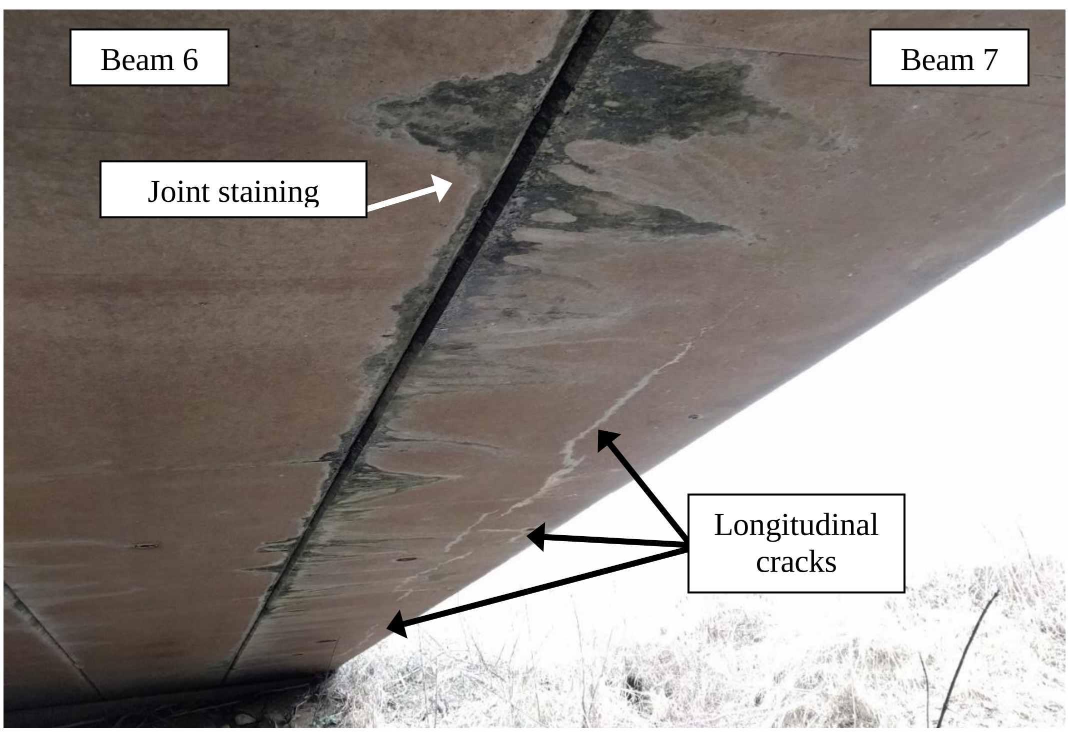

Figure 2.53: Deterioration of Beams 6 and 7

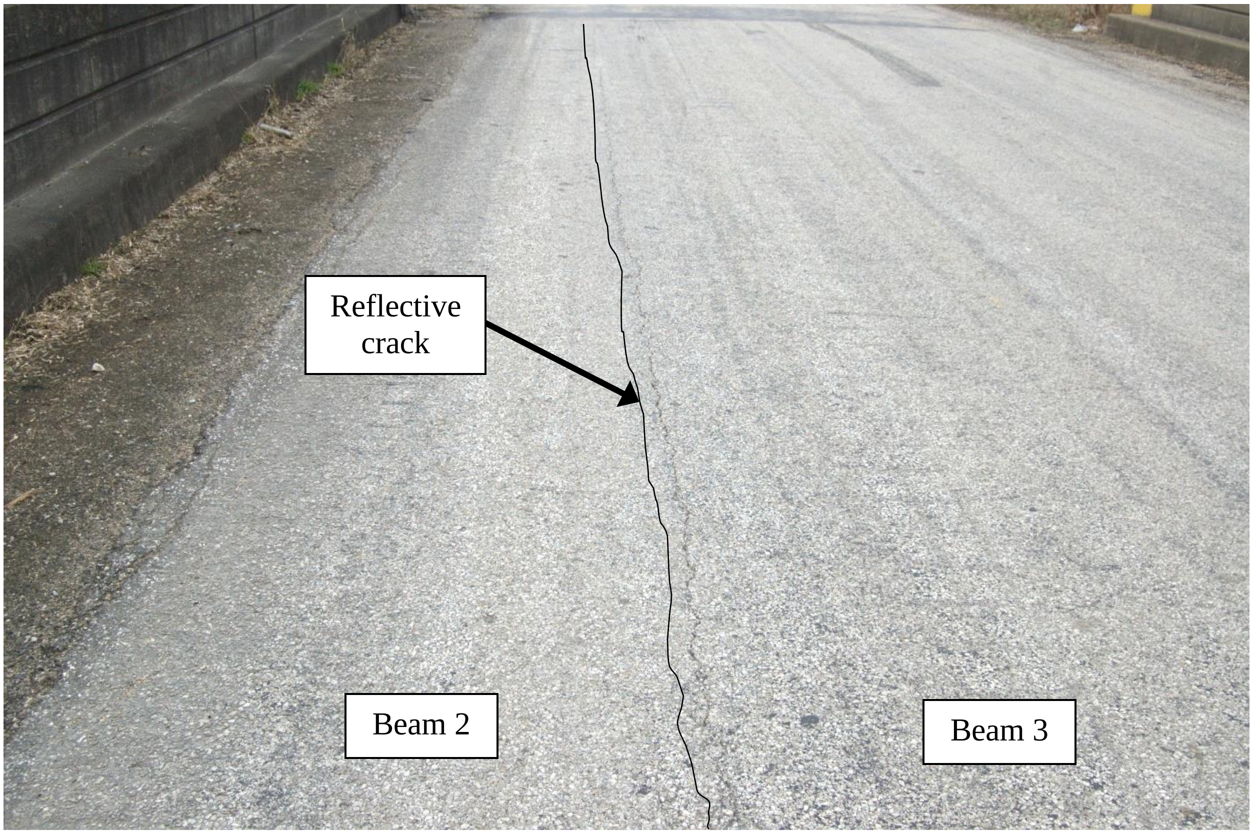

Figure 2.54: Reflective Crack in the Wearing Surface between Beams 2 and 3

2.5.3 Elkhart 385

2.5.3.1 Bridge Information

Elkhart 385 (20-00385) is a single-span bridge that spans 41.5 ft over Yellow Creek (Figure 2.55). The bridge was built in 1958. Original construction consisted of seven 48 in. wide beams for a total width of 28 ft. During the service life of the bridge, two 48 in. beams were added to the exterior to widen the bridge to 34 ft. The bridge was constructed without curbs. Water drains off the bridge deck onto the exterior beams along the length of the span. No transverse tie rods were found during the inspection. The original 28 ft width may include tie rods but could not be inspected because of the added exterior beams. At the time of inspection, the bridge had a 4-5 in. thick concrete deck with a chip and seal wearing surface.

Figure 2.55: Elkhart 385

2.5.3.2 Bridge Deterioration

Elkhart 385 was inspected by the research team on 27 January 2017. The observed deterioration is summarized in Figure 2.56. A rust stained longitudinal crack was found at midspan on Beam 3 (Figure 2.57). The joints between Beams 2 and 3 and Beams 7 and 8 were stained from water leaking through the shear key. These locations are interesting as they are the locations of the first joint in the original configuration of the bridge prior to the addition of the new exterior beams. Small sections of efflorescence were also observed at the joint between Beams 3 and 4. No reflective cracks were observed in the wearing surface or concrete deck.

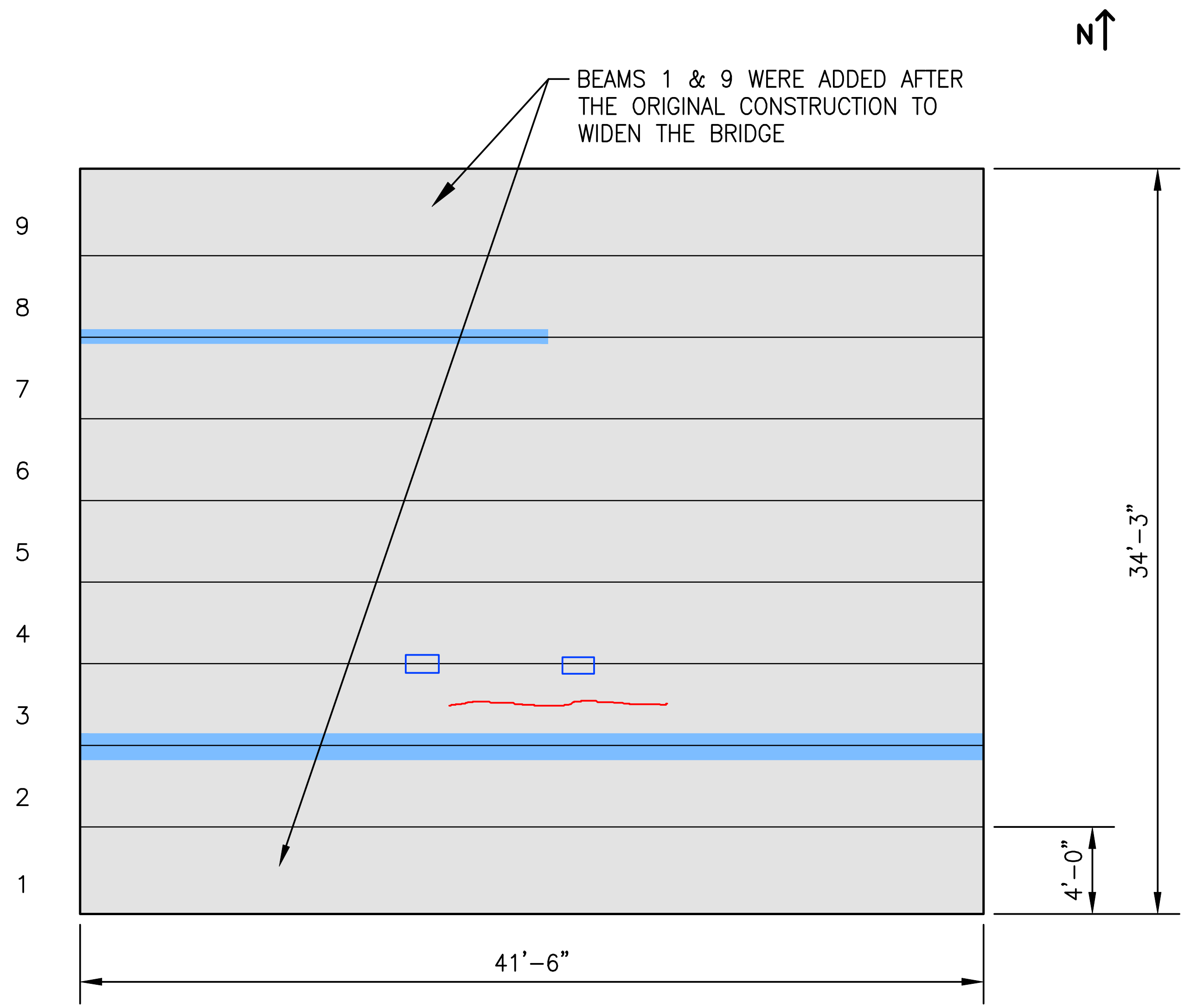

NOTE: NO DRAIN HOLES WERE OBSERVED DURING INSPECTION

Figure 2.56: Elkhart 385 Deterioration Map

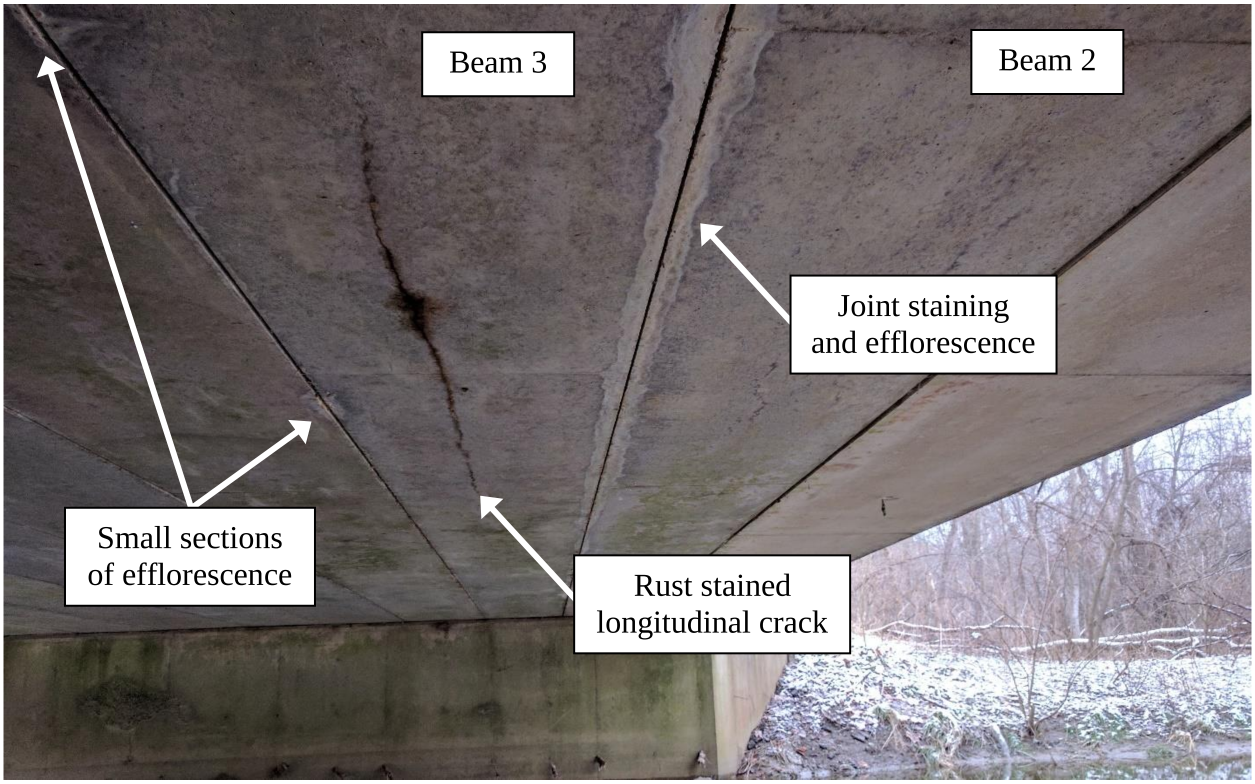

Figure 2.57: Elkhart 385 Deterioration

2.5.4 Elkhart 404

2.5.4.1 Bridge Information

Elkhart 404 (20-00404) is a 51.5 ft single-span bridge built in 1979 over Rock Run Creek (Figure 2.58). The bridge consists of seven 48 in. wide beams making up the total width of 28 ft. At the time of inspection, the bridge had a 4 to 5 in. thick concrete deck with no additional wearing surface. The bridge was constructed without curbs allowing water to drain onto the sides of the exterior beams. No transverse tie rods were observed during the bridge inspection.

Figure 2.58: Elkhart 404

2.5.4.2 Bridge Deterioration

Elkhart 404 was inspected by the research team on 27 January 2017. The observed deterioration is summarized in Figure 2.59. As shown in Figure 2.58, the bridge was constructed with a sidewalk south of Beam 1. The sidewalk was placed on a beam separated from the road bridge (Figure 2.60). A single exposed strand on the west end of Beam 1 and staining on the exterior edge of Beam 1 were the only deterioration found (Figure 2.61). No reflective cracks in the wearing surface were observed by the research team, but hairline cracks were noted in the official inspection report.

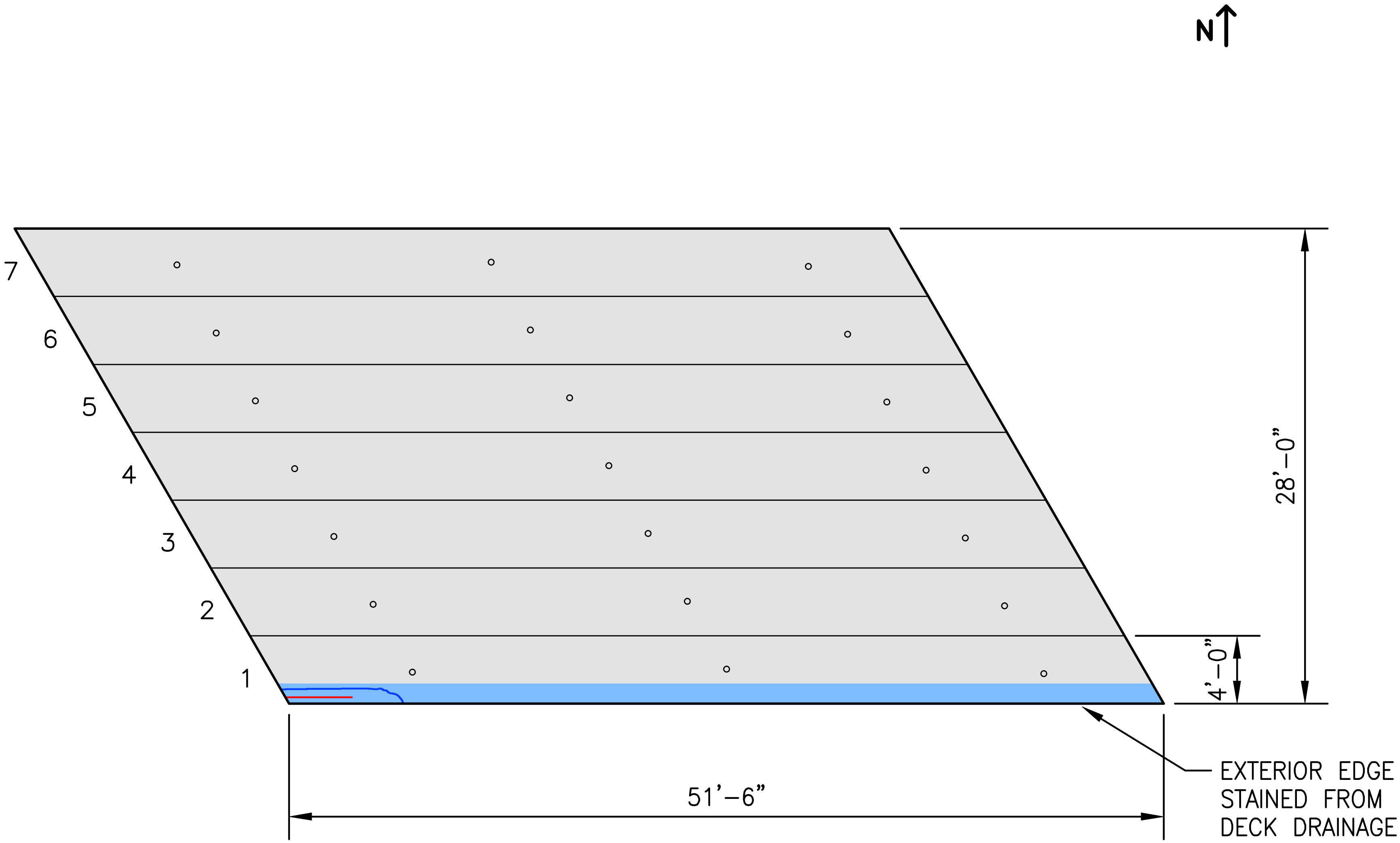

Figure 2.59: Elkhart 404 Deterioration Map

Figure 2.60: Separation between Road Bridge and Footbridge

Figure 2.61: Beam 1 Deterioration

2.5.5 Elkhart 406

2.5.5.1 Bridge Information

Built in 1980 over Rock Run Creek, Elkhart 406 (20-00046) is a single-span bridge with a span of 51.5 ft (Figure 2.62). Eight 48 in. wide beams make up the 32 ft total width of the bridge. The reported width does not include the two footbridges on the west and east sides of the bridge which are structurally separated. The wearing surface is a concrete deck approximately 4 to 5 in. thick. Similar to Elkhart 385 and Elkhart 404, the bridge deck was detailed without curbs, and no transverse tie rods were observed during the bridge inspection.

Figure 2.62: Elkhart 406

2.5.5.2 Bridge Deterioration

Elkhart 406 was visited by the research team on 27 January 2017. The observed deterioration is summarized in Figure 2.63. The deterioration of Elkhart 406 is localized to the exterior beams. Beam 1 and Beam 8 were both observed to have spalling with an exposed strand. A spall extending from the north support to midspan on Beam 1 exposed three strands (Figure 2.64), and a spall on Beam 8 exposed a single strand near the north support (Figure 2.65). No longitudinal cracks were found in the concrete deck. In addition, the footbridge beams on either side of the bridge were in excellent condition. Neither were found with any deficiencies.

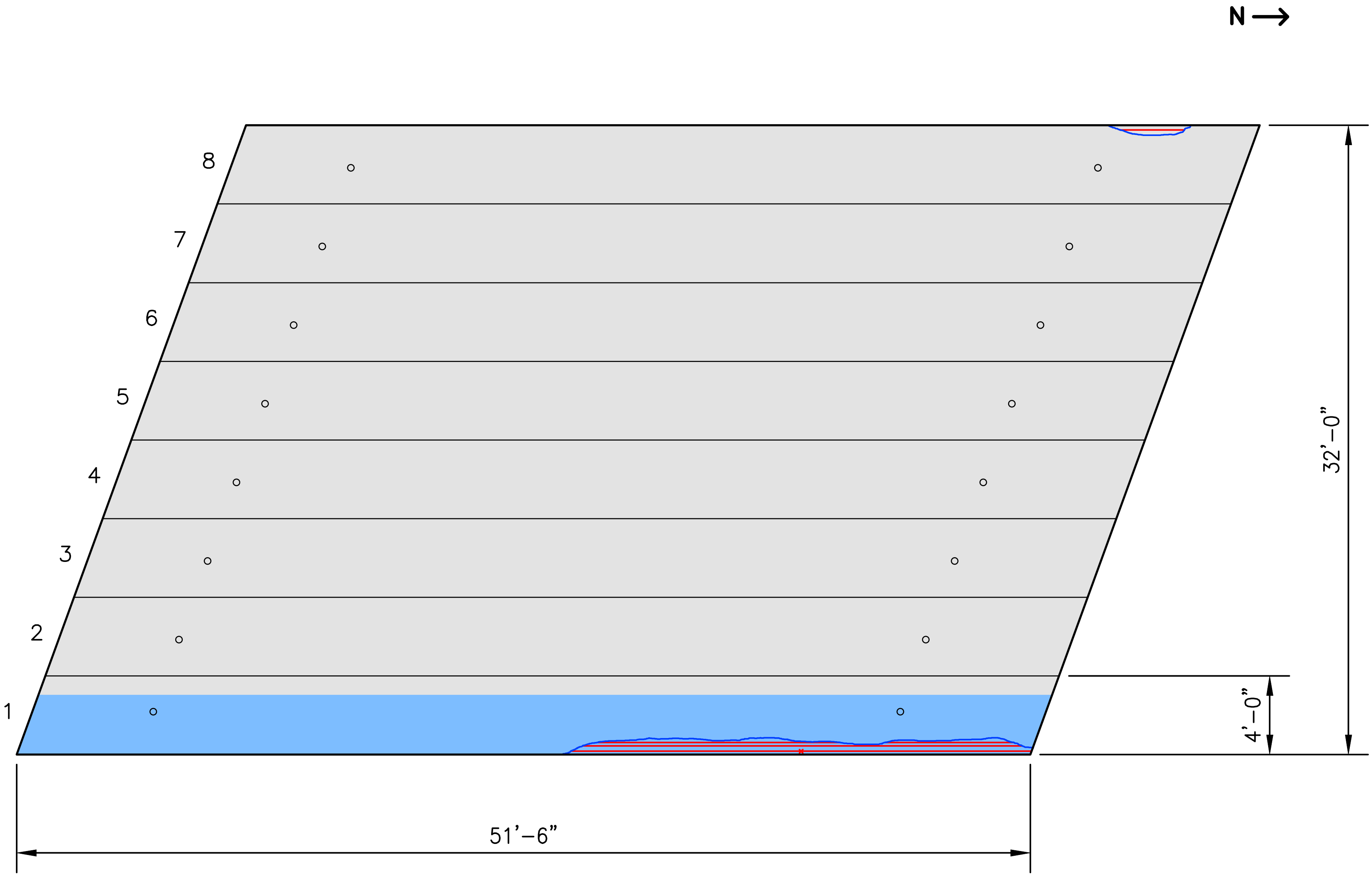

Figure 2.63: Elkhart 406 Deterioration Map

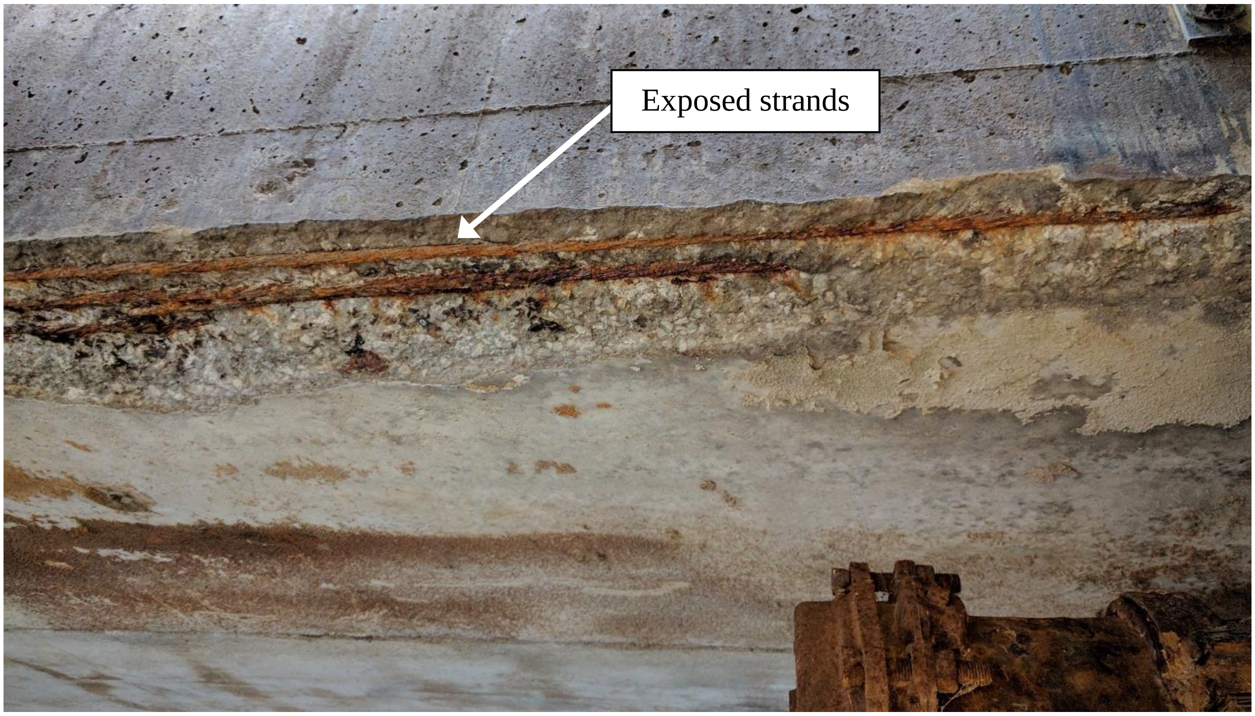

(a) Spalling on Beam 1 with three exposed strands

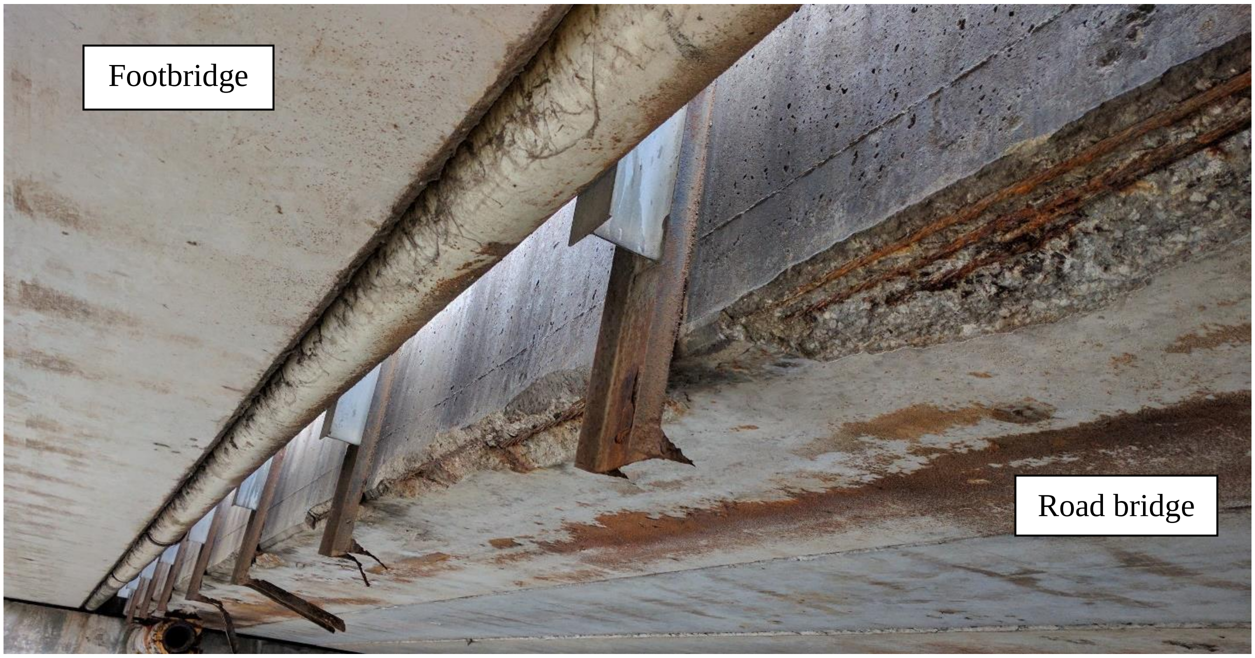

(b) Strands exposed up to midspan of Beam 1

Figure 2.64: Deterioration of Beam 1

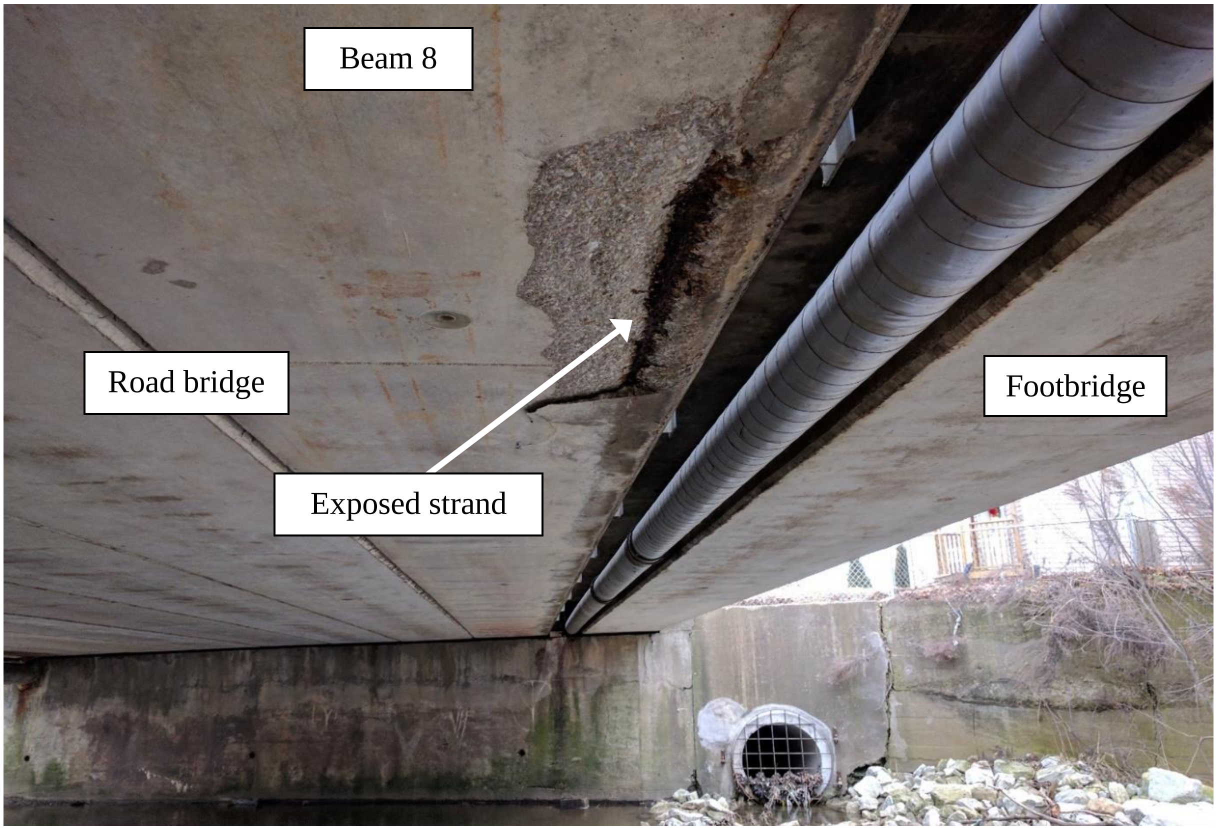

Figure 2.65: Beam 8 Deterioration

2.5.6 Elkhart 410

2.5.6.1 Bridge Information

Elkhart 410 (20-00410) is a single-span bridge built in 1959 and reconstructed in 1973 (Figure 2.66). The beams built in 1959 span 46.4 ft across Horn Ditch. Three beams were added to either side of the bridge in 1973 to widen the roadway. The additional six beams span an extra 10 ft from each end of the original abutments for a total span of 66.4 ft. Together, the nine 36 in. wide beams from 1959 and six 48 in. wide beams from 1973 form a total bridge width of 51 ft. The bituminous wearing surface is approximately 2 in. thick and is separated from the beams by a membrane (Figure 2.67). The bridge was built without curbs. The 1973 reconstruction used a single transverse tie rod at midspan. The use of a tie rod in the 1959 construction could not be verified.

Figure 2.66: Elkhart 410

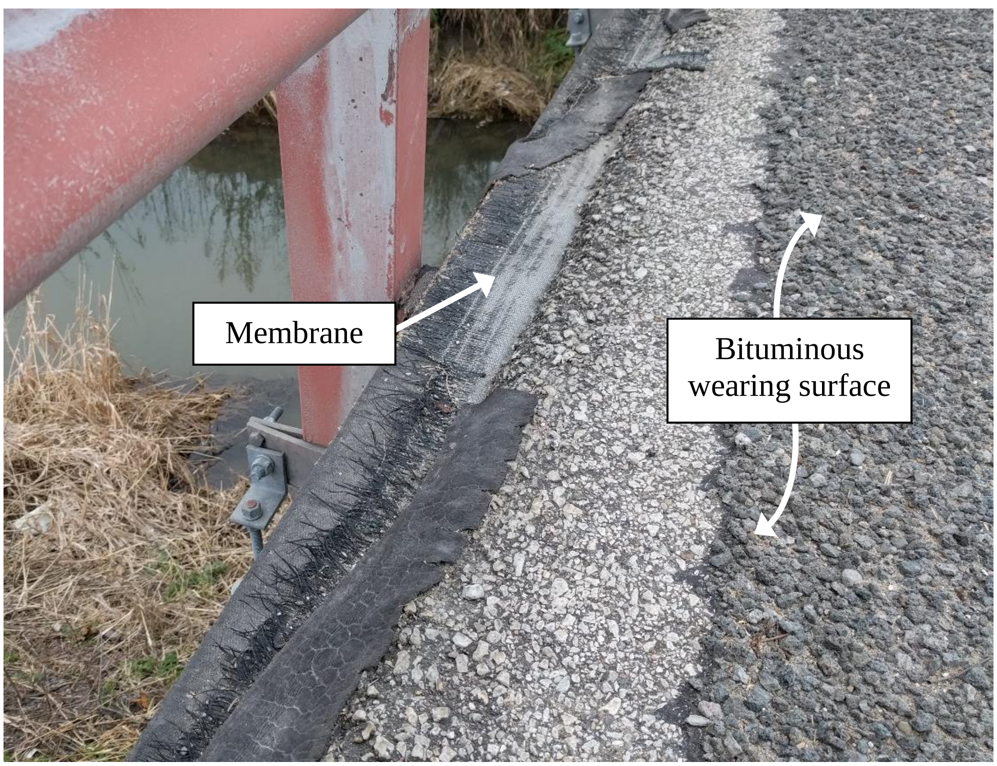

Figure 2.67: Membrane under the Bituminous Wearing Surface

2.5.6.2 Bridge Deterioration

Elkhart 410 was inspected by the research team on 27 January 2017. A summary of the observed deterioration is provided in Figure 2.68. Overall, the bridge exhibited extensive deterioration in the form of longitudinal cracking and spalling which exposed strand. Examples of this deterioration are provided in Figure 2.69 and Figure 2.70.

A comparison between the 1959 beams and 1973 beams (Figure 2.68) revealed that more of the 1973 beams were deteriorated. The direct cause of this discrepancy in deterioration is unknown, but the roadway is only two lanes (24 ft wide) which creates a very wide shoulder that is carried by the beams added during the 1973 reconstruction (Figure 2.71). During the winter there is potential for plowed snow to accumulate on the edges of the bridge. When the snow is removed from the traffic lane, road salts may be carried with the snow onto the edge of the bridge. If the snow is not removed from the bridge, the resulting chloride laden snow melt could be carried through the shear keys to the beams below. Over time, chlorides in the snow melt could reach the strand and induce corrosion. The described mechanism of deterioration implies, however, that the membrane between the wearing surface and the beams has failed and is not effective.

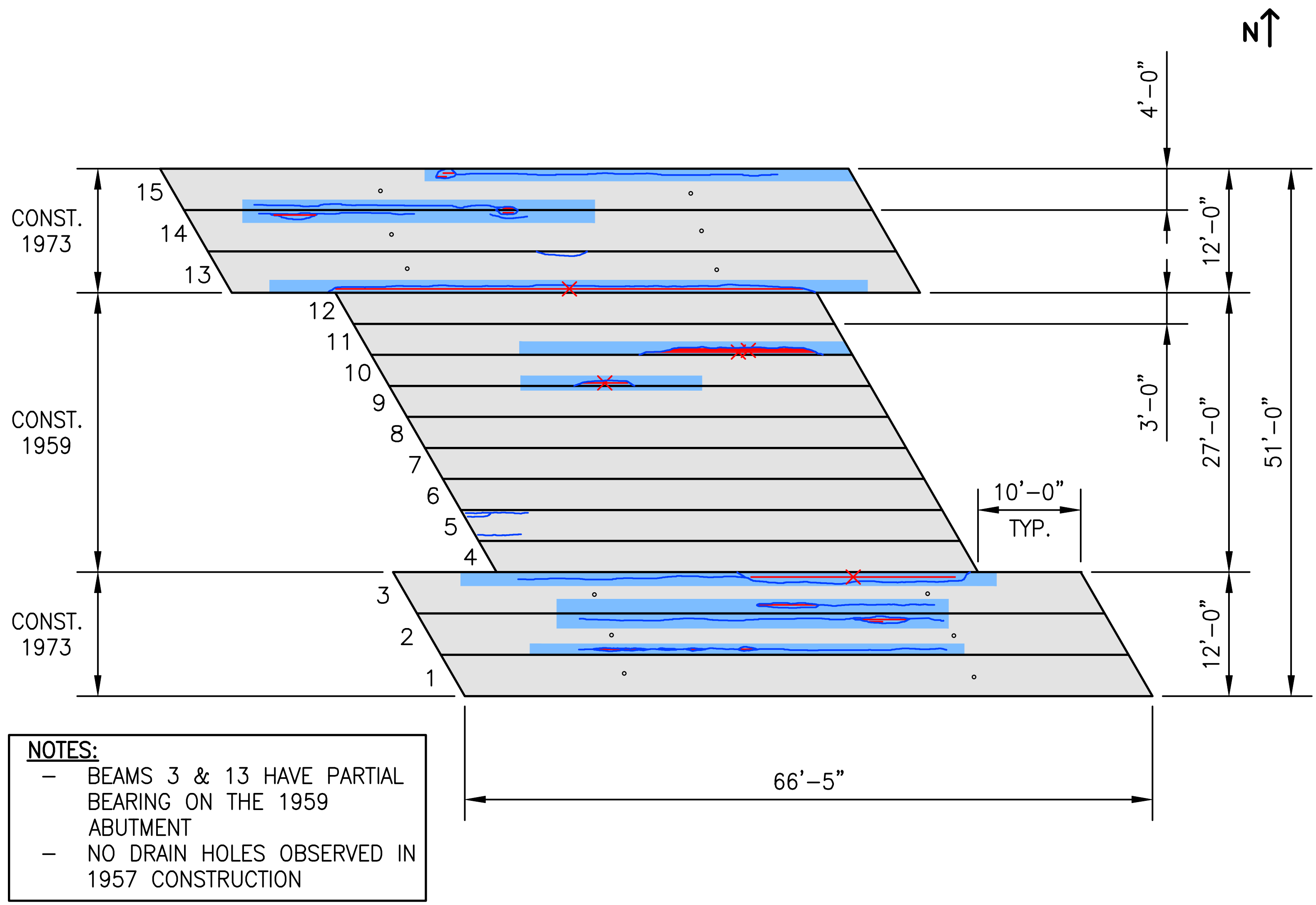

Figure 2.68: Elkhart 410 Deterioration Map

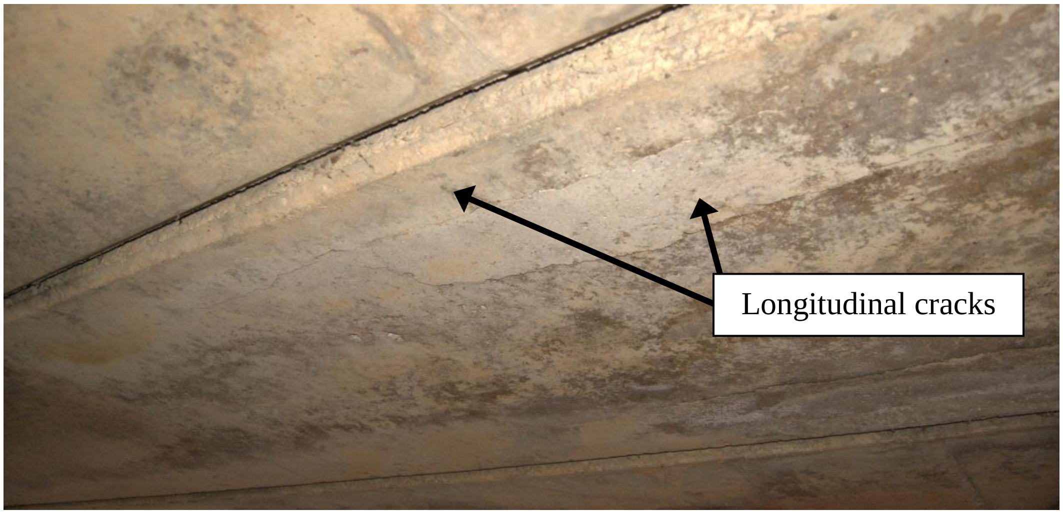

(a) Beam 5 (1959) deterioration

(b) Beam 11 (1959) deterioration

Figure 2.69: 1959 Construction - Example Longitudinal Cracking and Exposed Strands

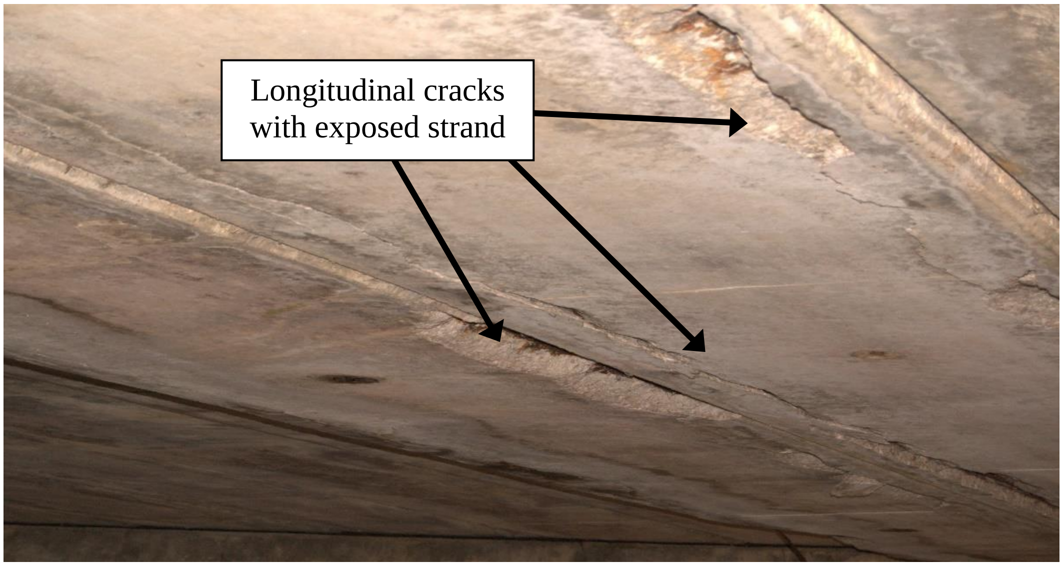

(a) Beam 2 (1973) deterioration

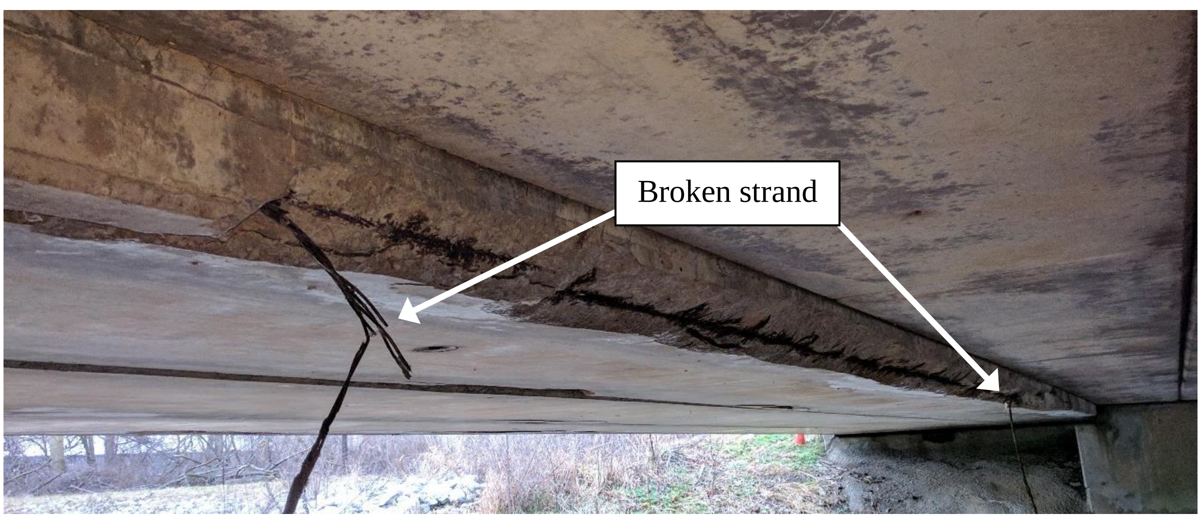

(b) Beam 15 (1973) deterioration

Figure 2.70: 1973 Reconstruction - Example Longitudinal Cracking with Exposed Strand

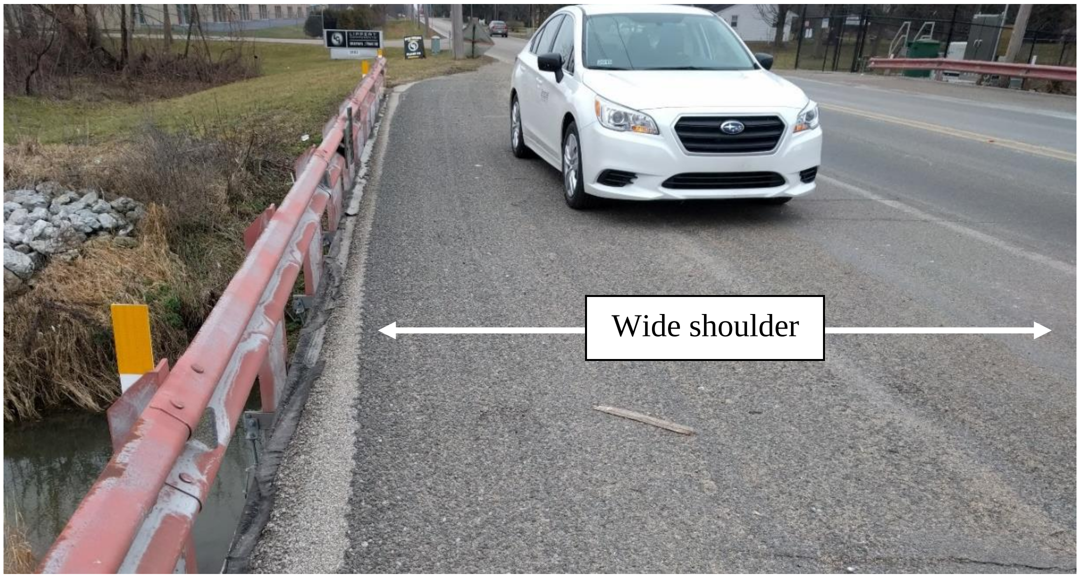

Figure 2.71: Large shoulder Width Carried by the 1973 Beams

2.5.7 Greene 8

2.5.7.1 Bridge Information

Greene 8 (28-00008) is a 58.3 ft single-span bridge over Richland Creek (Figure 2.72). The bridge was built in 1969 using four 36 in. wide beams and one 48 in. wide beam. The 16 ft total width allows for only one legal lane of traffic. The bituminous wearing surface is approximately 5 in. thick. Transverse tie-rods are located at the third points along the span. The standard curbs have no outlets along the span; all water is drained to the ends of the bridge.

Figure 2.72: Greene 8

2.5.7.2 Bridge Deterioration

The bridge was inspected by the research team on 24 January 2017. The observed deterioration is summarized in Figure 2.73. Staining was observed at each of the exterior joints (Figure 2.74). One of the longitudinal cracks extending from the end of Beam 3 was rust stained for a length of approximately 1 ft (Figure 2.75). Two longitudinal cracks were observed in Beam 5 at midspan. The longitudinal crack on the west side of Beam 5 is believed to extend through the corner of the section to join the corner crack that was observed on the exterior of Beam 5 (Figure 2.76).

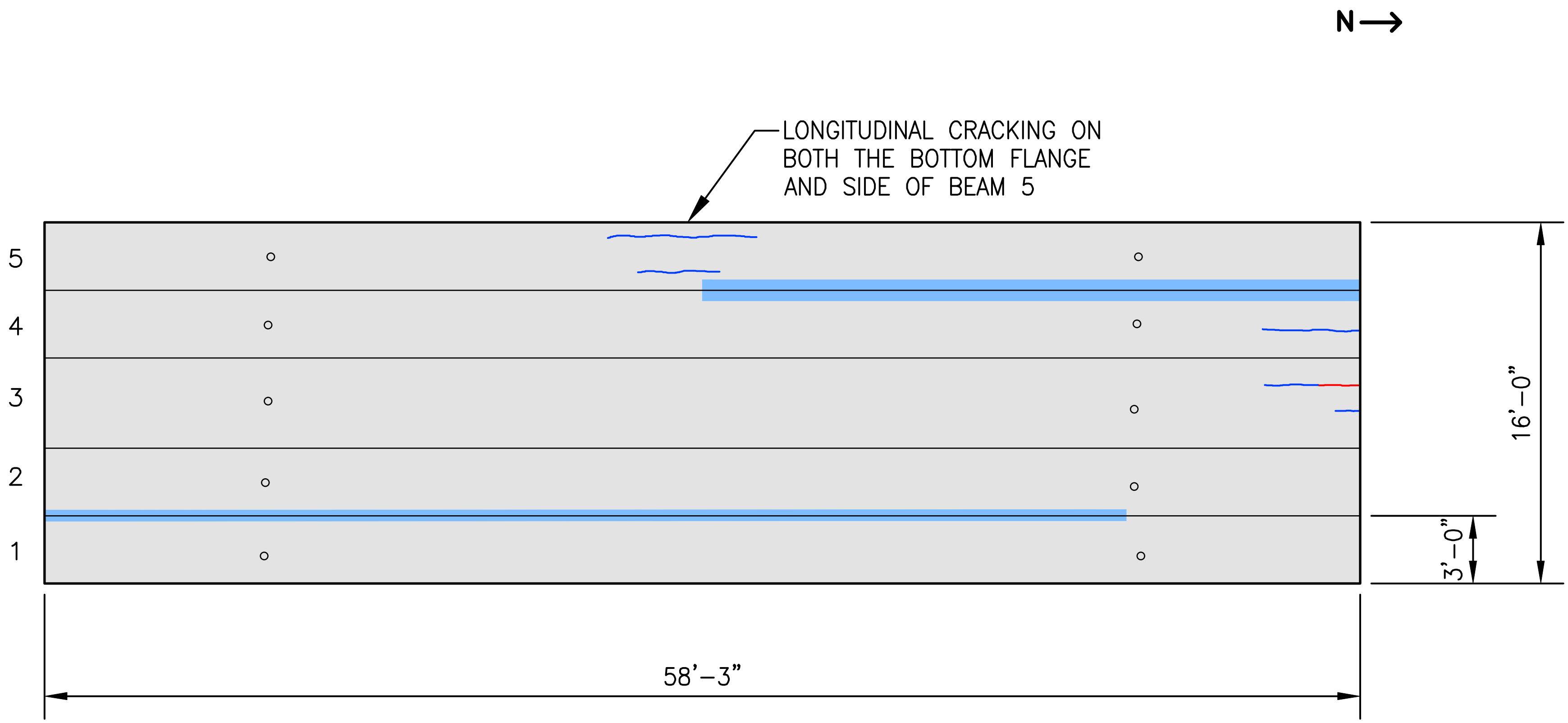

Figure 2.73: Greene 8 Deterioration Map

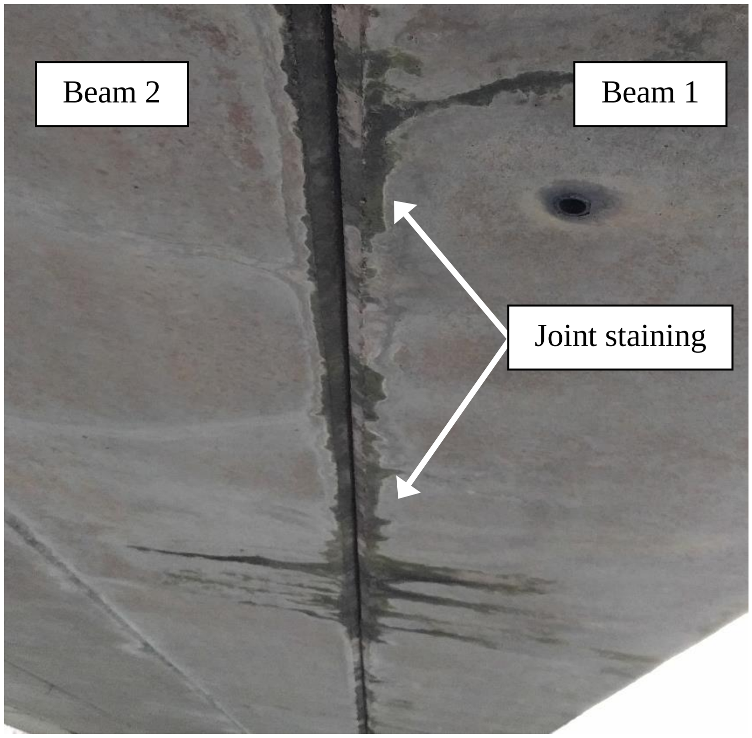

Figure 2.74: Stained Joint between Beams 1 and 2

Figure 2.75: Stained Longitudinal Crack in Beam 3

Figure 2.76: Corner Cracks in Beam 5

2.5.8 Kosciusko 18

2.5.8.1 Bridge Information

Kosciusko 18 (43-00018) is a three-span bridge over Tippecanoe River built in 1980 (Figure 2.77). Each of the three spans are 30 ft long and 28 ft wide. The width of the bridge is comprised of seven 48 in. wide beams. The bituminous wearing surface is approximately 5 in. thick. The bridge was constructed without curbs allowing water to drain onto the sides of the exterior beams along the span. No transverse tie rods were found during the bridge inspection.

Figure 2.77: Kosciusko 18

2.5.8.2 Bridge Deterioration

The research team inspected Kosciusko 18 on 9 January 2018. A summary of the deterioration is provided in Figure 2.78. Beams A1, A7, and B1 were all found to have exposed and broken strands located on the exterior corner of the respective sections (Figure 2.79). Longitudinal cracks were observed in Beams A1 and C6 (Figure 2.80). Melting frost was observed at the joint between Beams 1 and 2 over the pier between Spans A and B (Figure 2.81). The melting frost at the joint indicated that water from the bridge deck above was leaking into the joint and curling onto the bottom flange of the beams.

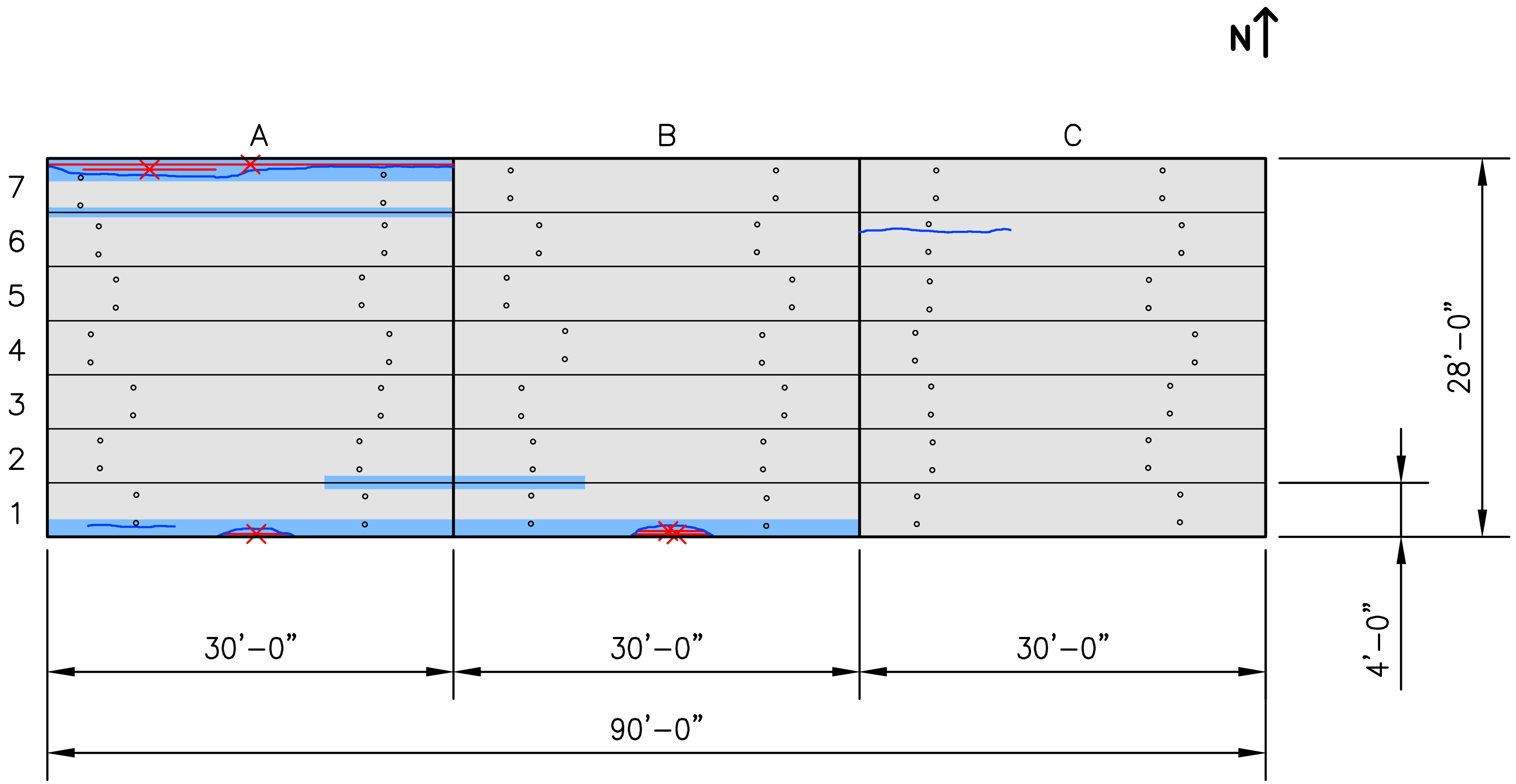

Figure 2.78: Kosciusko 18 Deterioration Map

(a) Broken strand Beam A1

(b) Broken strand Beam A7

(c) Broken strands Beam B1

Figure 2.79: Deterioration of Beams A1, A7, and B1

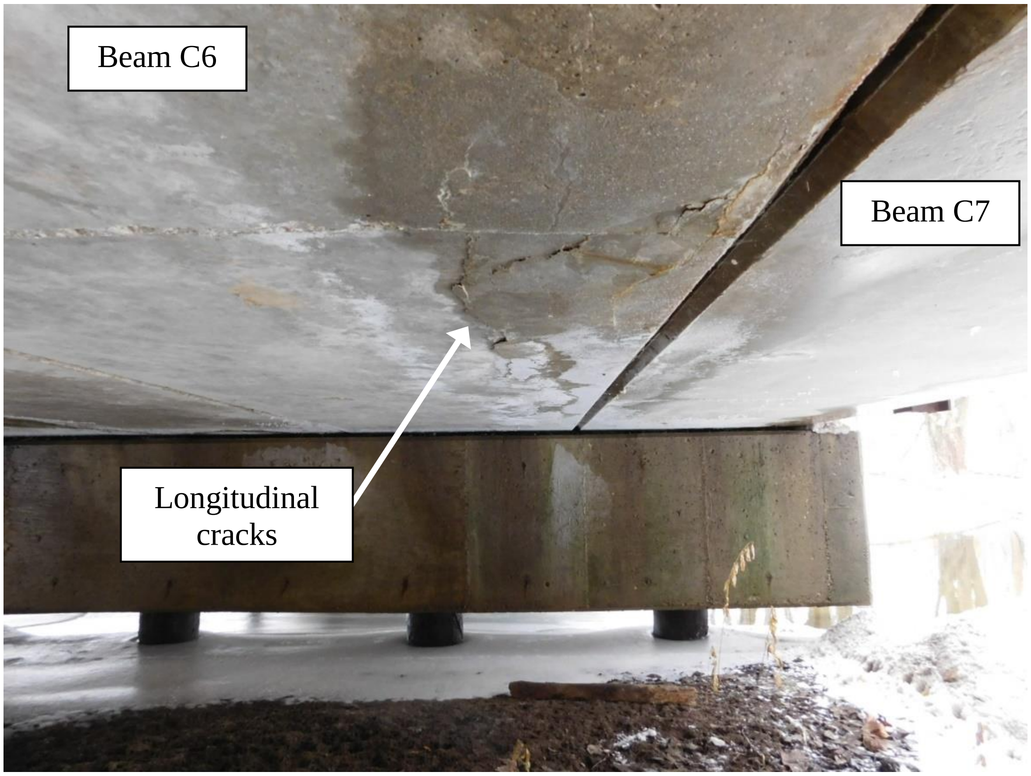

Figure 2.80: Beam C6 Deterioration

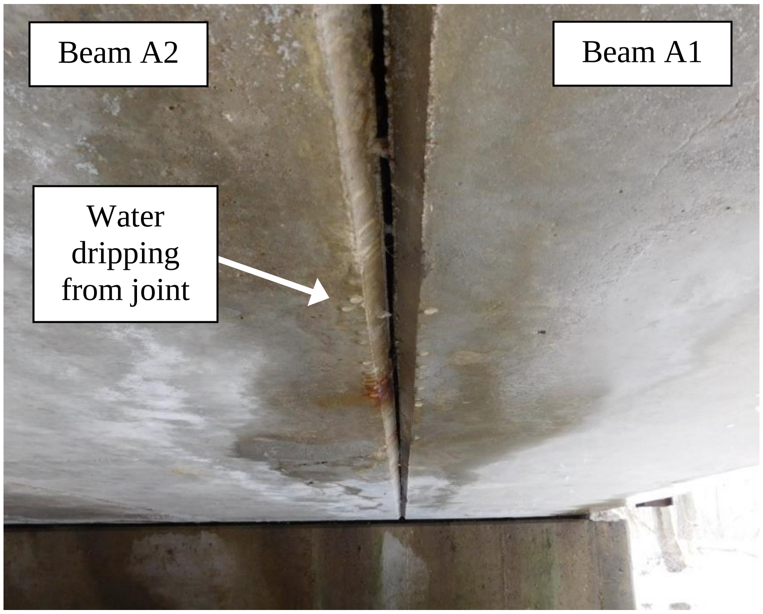

Figure 2.81: Leaking Shear Key between Beams A1 and A2

2.5.9 Lake 61

2.5.9.1 Bridge Information

Lake 61 (45-00061) is a single-span bridge that spans 46.5 ft over West Creek (Figure 2.82). The bridge was built in 1970. The total bridge width of 26.3 ft is made up of seven 45 in. wide beams. The bituminous wearing surface of the bridge is approximately 7 in. thick. The bridge has standard 10 in. tall curbs on each exterior beam in addition to a single tie rod at midspan.

Figure 2.82: Lake 61

2.5.9.2 Bridge Deterioration

Lake 61 was inspected by the research team on 9 January 2018. A summary of the observed deterioration is provided in Figure 2.83. As shown, Beams 4 and 5 were found with multiple exposed and broken strand in addition to longitudinal cracks near the corners of the beams (Figure 2.84). Longitudinal cracks were also observed in Beams 1, 3, and 7 near the edges of the beams. Beam 1 exhibited a rust stained crack and spall next to a stained joint near the west support (Figure 2.85). Large drain pipes were cast into the beams for drainage. A single hole approximately 6 in. in diameter was also observed at midspan of Beam 7 (Figure 2.86). The shape of the hole indicates that a coring machine was used to create the hole. No explanation or documentation of this work was available in the official inspection reports.

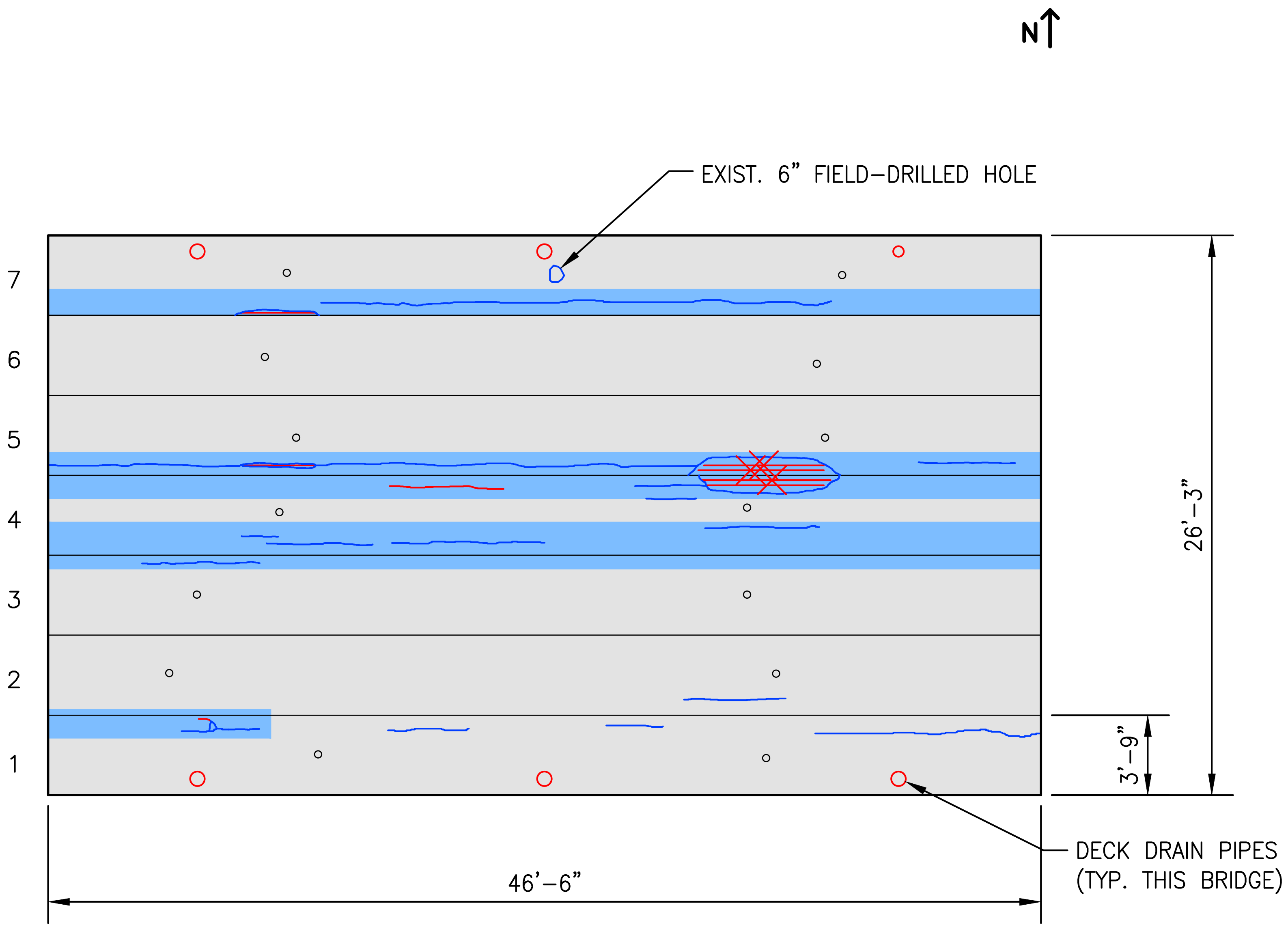

Figure 2.83: Lake 61 Deterioration Map

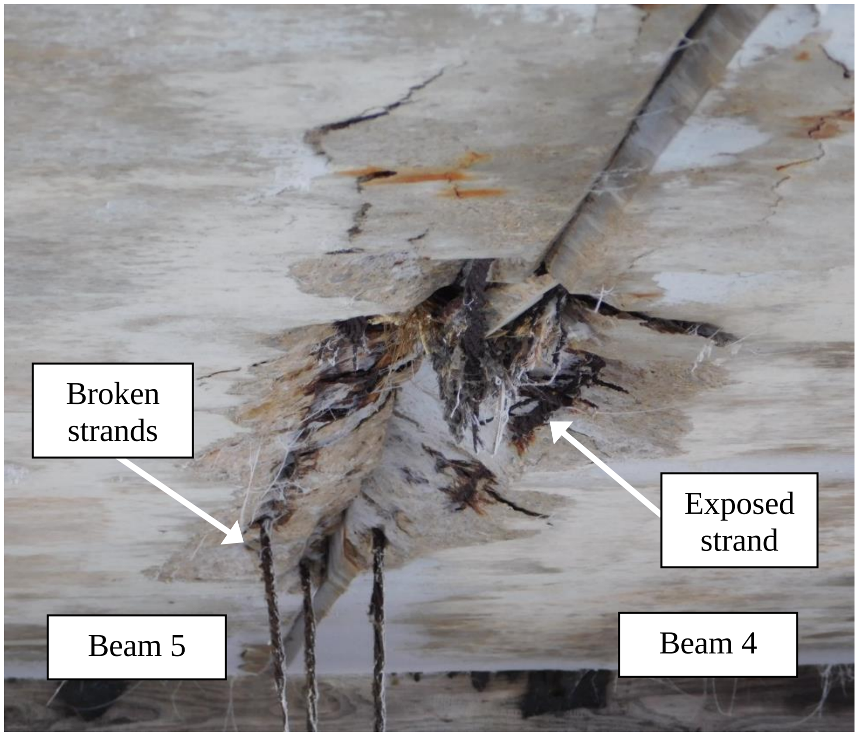

Figure 2.84: Deterioration of Beams 4 and 5

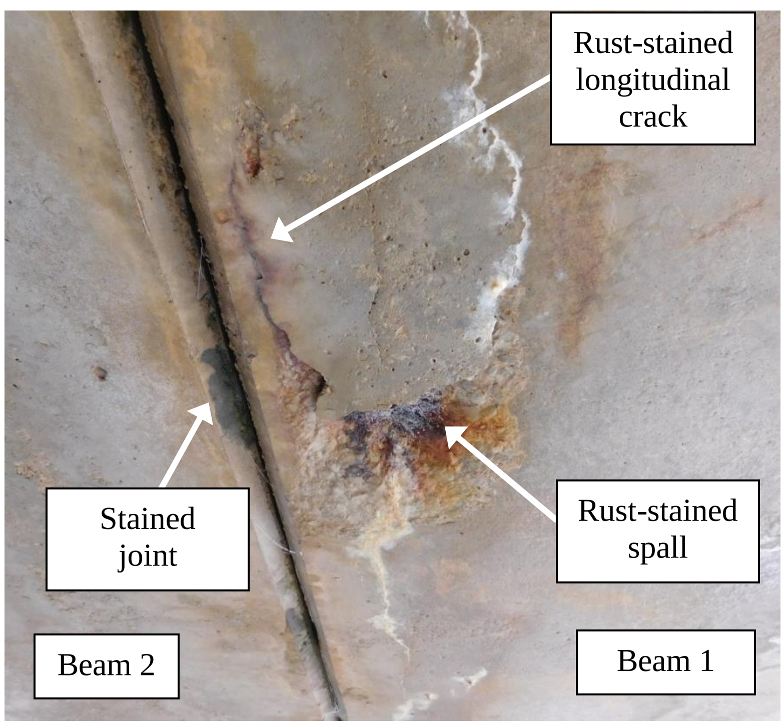

Figure 2.85: Deterioration of Beam 1

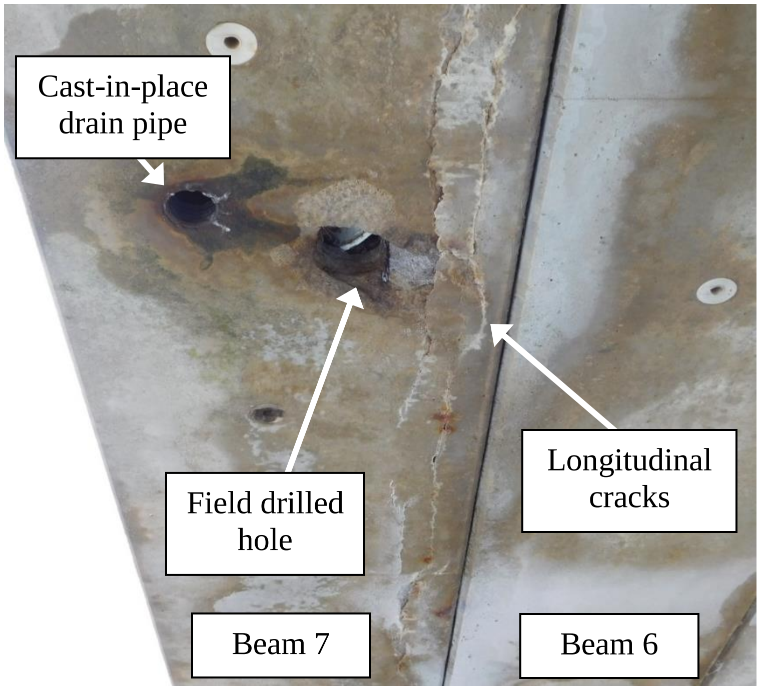

Figure 2.86: Deterioration of Beam 7

2.5.10 Lake 264

2.5.10.1 Bridge Information

Lake 264 (45-00264) is a single-span bridge over Hart Ditch and was built in 1970 (Figure 2.87). The bridge is 44 ft wide and comprises of 11 beams, each 48 in. wide. The exterior beams carry concrete sidewalks that are approximately 5 ft wide. A metal barrier rail is attached to the top of the standard curbs on the outside of the sidewalk on each exterior beam. The bituminous wearing surface thickness is approximately 2 to 4 in. thick. Transverse tie rods for the bridge are located at the third points along the span.

Figure 2.87: Lake 264

2.5.10.2 Bridge Deterioration

The research team visited Lake 264 on 9 January 2018. A summary of the observed deterioration is presented in Figure 2.88. Beams 3, 4, 9, and 10 were found with exposed edge strands, and Beams 3 and 9 were both found with broken strands (Figure 2.89). In addition to the exposed corner strand, Beam 10 was found with a large spall around the deck drain (Figure 2.90). Longitudinal cracks were observed in Beams 5, 6, 7, and 8. The longitudinal crack in Beam 5 was rust stained (Figure 2.91). Clogged drain holes in Beams 2 and 3 were also noted.

The lack of deterioration on beams 1 and 11 and in the joints between beams 1 and 2 and beams 10 and 11 may be due, in part, to the concrete sidewalk. The side walk is 5 ft wide and covers the both the exterior beams and the joint between the exterior beam and first interior beam. Concrete sidewalk provides a much greater resistance to cracking and moisture migration than the bituminous wearing surface. The difference in porosity between the two materials may have resulted in greater durability of the exterior beams.

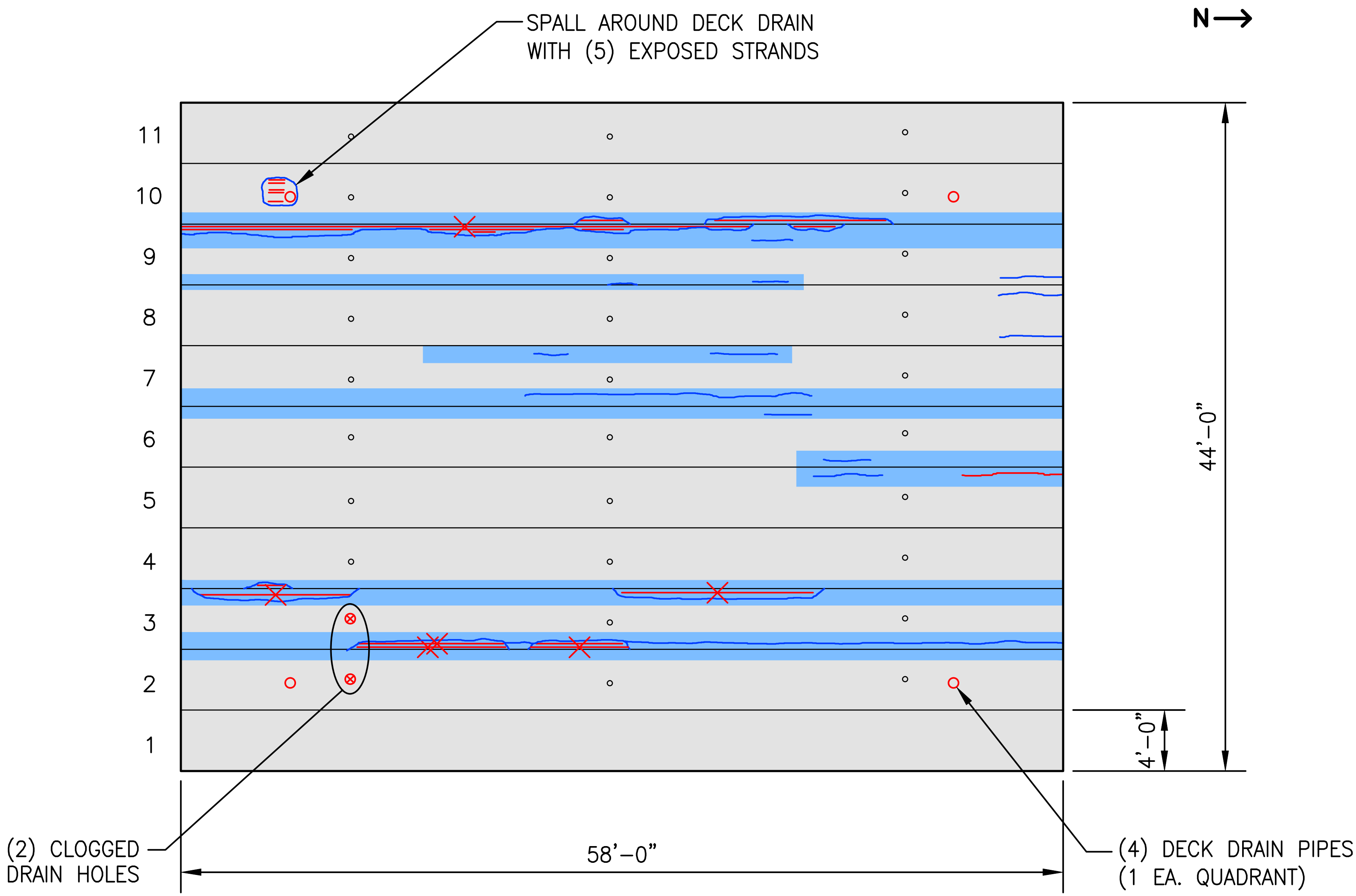

Figure 2.88: Lake 264 Deterioration Map

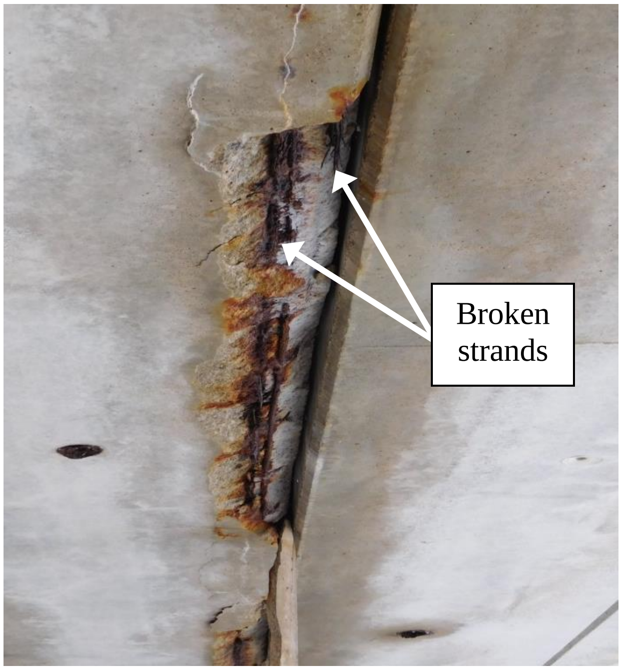

(a) Broken strands in Beam 3

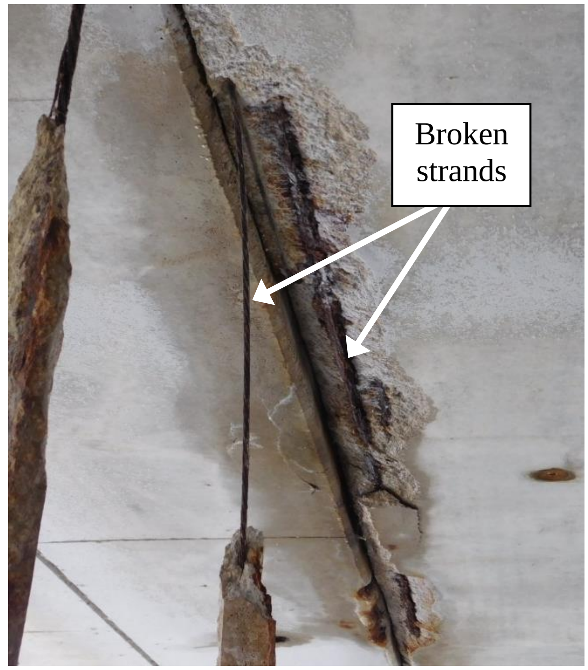

(b) Broken strands in Beam 9

Figure 2.89: Deterioration of Beams 3 and 9

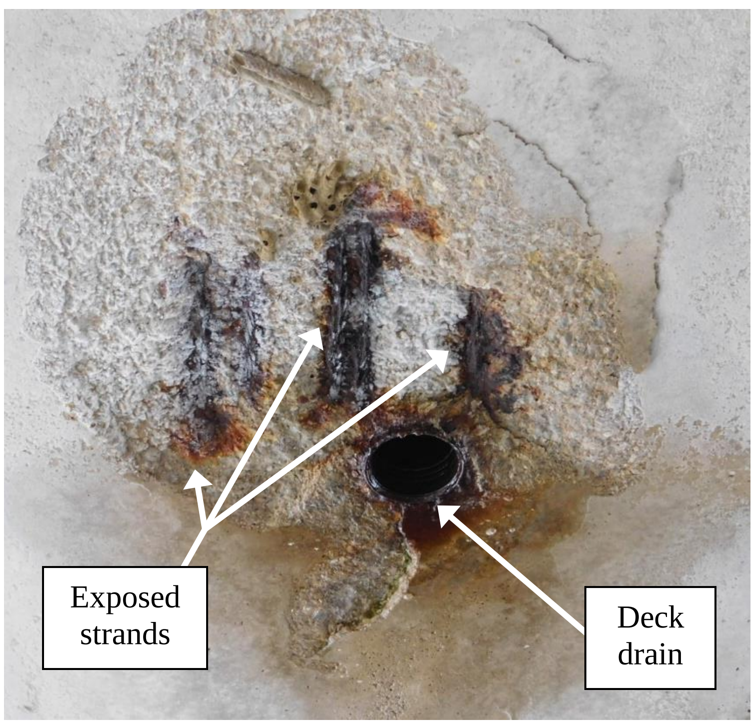

Figure 2.90: Beam 10 Deterioration

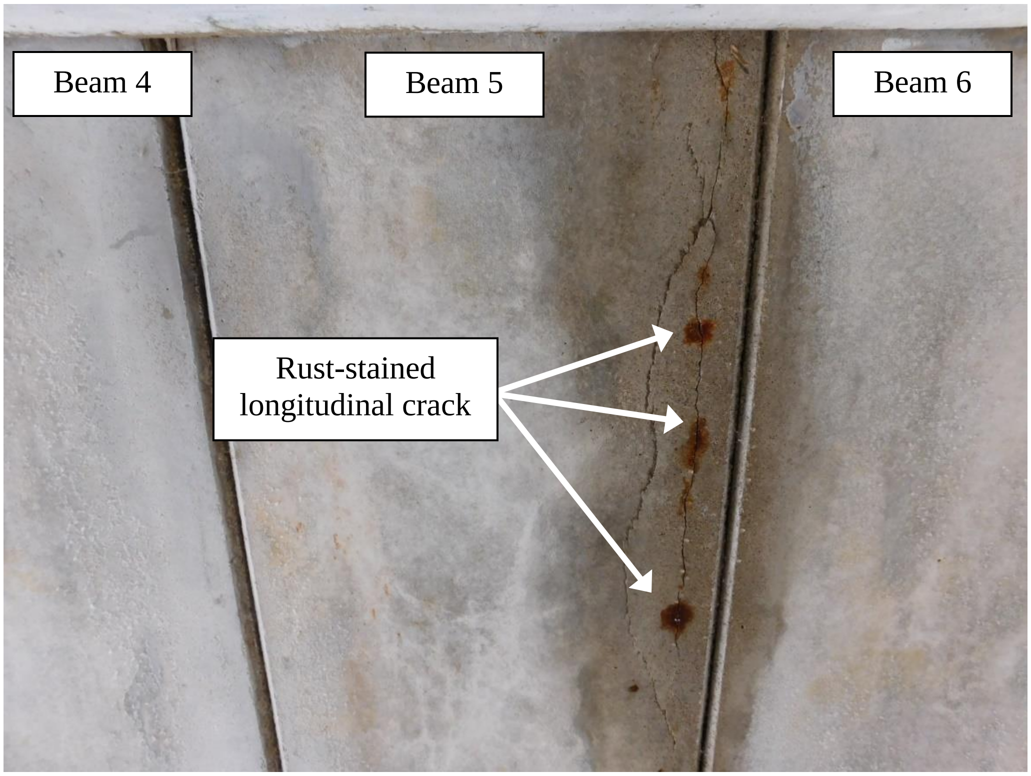

Figure 2.91: Beam 5 Deterioration

2.5.11 Tippecanoe 504

2.5.11.1 Bridge Information

Tippecanoe 504 (79-00504) is a 36.5 ft long single-span bridge over Buck Creek (Figure 2.92). The bridge was built in 1963 using seven 45 in. wide beams for a total width of 26.25 ft. The exterior beams have concrete barriers approximately 3 ft tall. The barriers do not have outlets along the span for water drainage. The bituminous wearing surface is approximately 7 in. thick. A transverse tie rod for the bridge is located at midspan.

Figure 2.92: Tippecanoe 504

2.5.11.2 Bridge Deterioration

Tippecanoe 504 was inspected by the research team on 8 November 2018. A summary of the observed deterioration is presented in Figure 2.93. All beams in the bridge exhibited some form of longitudinal cracking with the exception of Beam 7. Beams 2 and 6 were observed to have spider web cracks at the south support of each beam (Figure 2.94). In addition to the spider web cracking, portions of the west edge of Beam 6 had spalled without exposing strand (Figure 2.95). Efflorescence was common at the exterior and first interior joints from both sides of the bridge (Figure 2.96).

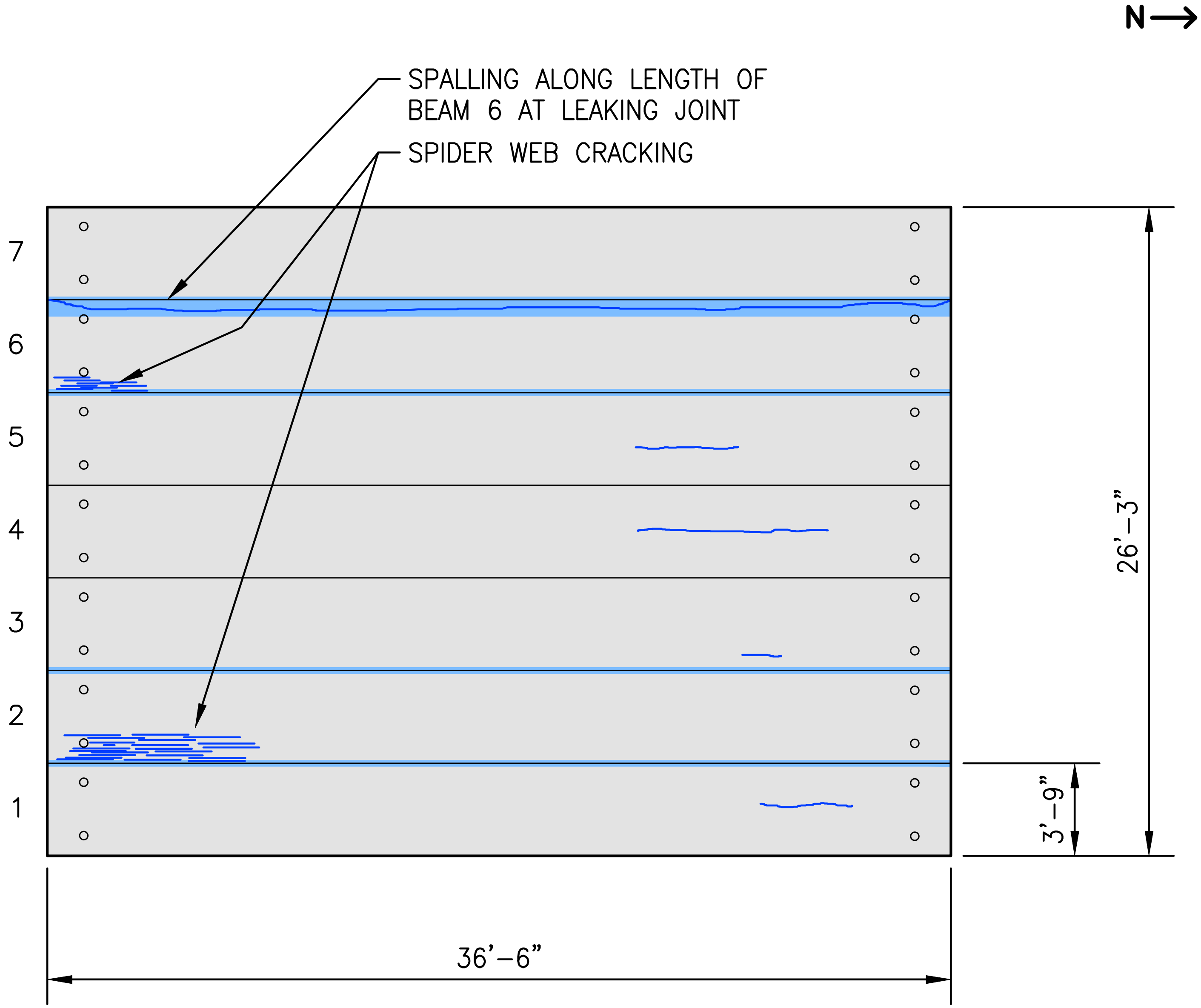

Figure 2.93: Tippecanoe 504 Deterioration Map

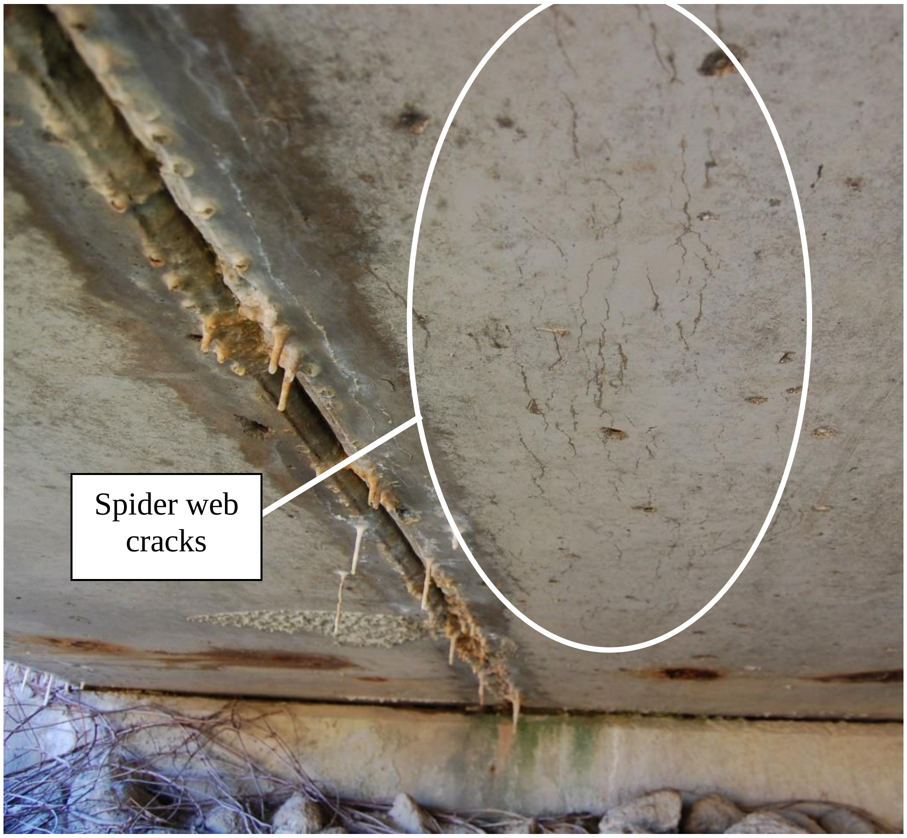

Figure 2.94: Beam 2 Deterioration

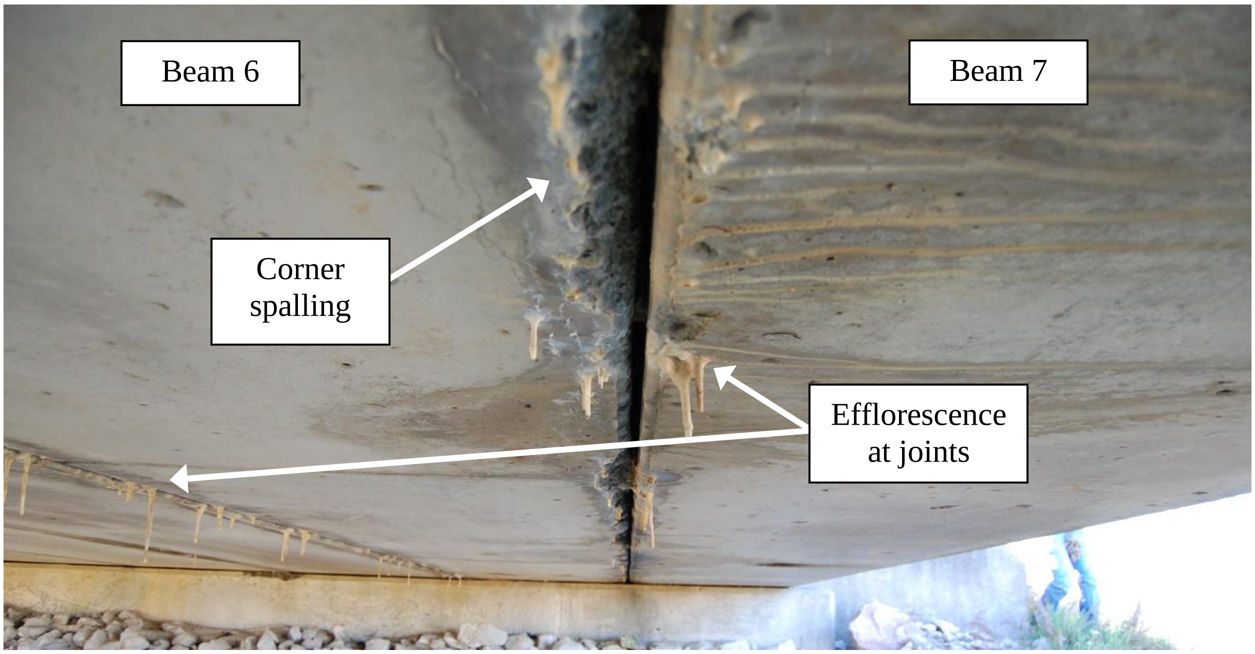

Figure 2.95: Spalling on West Side of Beam 6

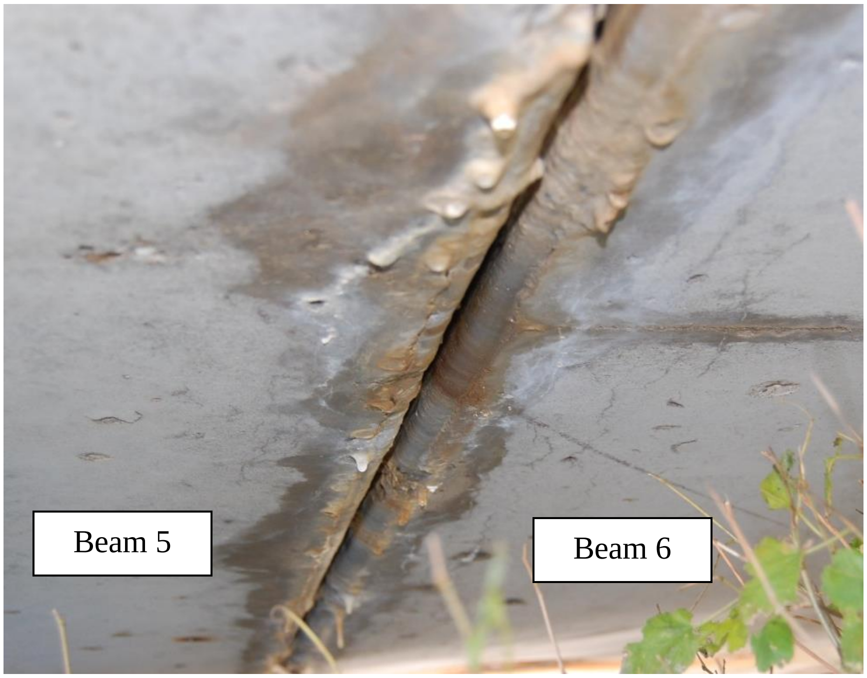

Figure 2.96: Efflorescence at joint between Beams 5 and 6

2.6 Deterioration Mechanisms

A review of all the bridge inspections confirm the findings of Molley (2017) and reveal three predominant deterioration mechanisms. The first mechanism is related to the partial depth shear key detail used in adjacent box beam bridges. The second mechanism is related to the ingress of water into the voids of the box beams. The third mechanism is related to the damage observed in the top flange of box beams.

2.6.1 Leaking Shear Key

The shear key connection allows water to infiltrate the longitudinal joint between adjacent beams. There are several causes of water infiltration. First, shrinkage of the shear key grout or concrete causes debonding between the beam and shear key and creates a gap for water to pass around the shear key. Second, the shear key detail includes a crack-like imperfection at the base of the shear key (Figure 2.97). From fracture mechanics, crack-like imperfections can propagate a crack in the direction perpendicular to the greatest tensile stress. Traffic loading and temperature effects have been shown to cause transverse tensile stresses to occur across the shear key joint (Hucklebridge and El-Esnawi 1997, Miller et al. 1999, Dong 2002, Halbe et al. 2014, and Yuan and Greybeal 2016). Tensile stresses in the shear key promote the propagation of cracks through the shear key and can also cause reflective cracking through the wearing surface. Third, the wearing surface materials used on adjacent box beam bridges are not impervious. Bituminous surfaces are quite porous and allow moisture to easily penetrate through the thickness of the wearing surface. Concrete is significantly less porous than bituminous overlays but are not impervious and will allow moisture migration to occur.

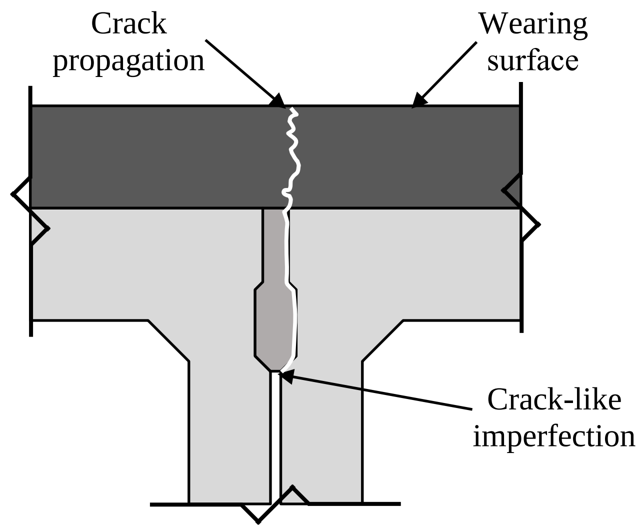

Figure 2.97: Shear Key Crack Propagation

Once water has infiltrated the longitudinal joint, it is free to drain down the sides of the box beams. Surface tension between the water and concrete surface allow the water to curl onto the bottom flanges of the box beams on either side of the longitudinal joint. If the bridge deck is treated with deicing salts, as is common practice during the winter in Indiana, the water carries the salt through the shear key and deposits form on the sides and bottoms of the box beams. The chlorides from the salt slowly penetrates through the concrete cover to the reinforcement resulting in the formation of chloride-induced corrosion.

When strands begin to corrode, the expansive corrosion process causes small cracks to form along the length of the strand (Figure 2.98(a)). These cracks grow toward the surface of the concrete and are observed as longitudinal cracking in the edges of the box beams (Figure 2.98(b)). The cracks continue to grow until the concrete spalls away fully exposing the corroding strand (Figure 2.98(c)). At this point, the strand has been heavily pitted by corrosion and may eventually rupture under the stress of the prestress force in the strand. Figure 2.99 shows an example of a heavily pitted and ruptured strand. If the deterioration develops from the end of the beam, the longitudinal cracks typically release the prestress in the strand and prevent rupture of the strand.

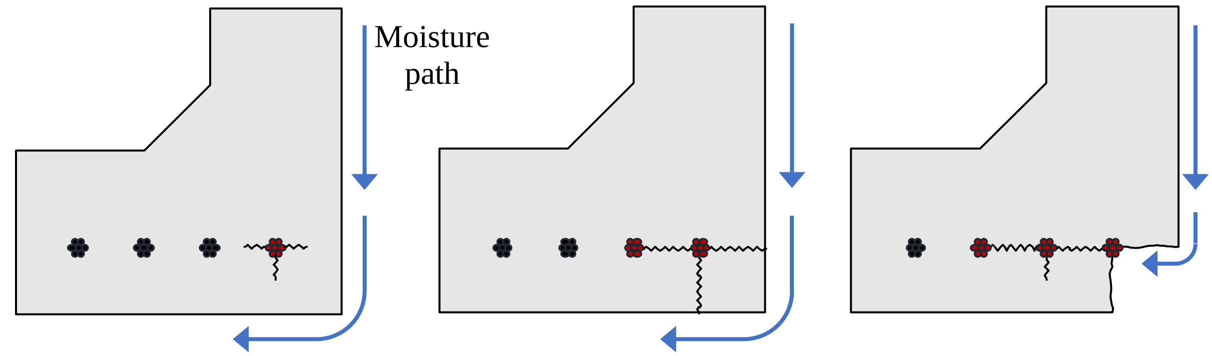

(a) Initial crack formation **(b) Crack propagation** **(c) Spall forms exposing strand**

Figure 2.98: Strand Corrosion

Figure 2.99: Heavily Pitted and Ruptured Strand

The described deterioration mechanism summarizes the formation of the following common types of deterioration:

- Leaking shear key joints
- Concrete spalling adjacent to longitudinal joints
- Longitudinal cracking in bottom flange (edge cracks only)
- Corrosion of reinforcement

Leaking shear key joints were observed in nearly all the bridges that were inspected. Elkhart 404 and Elkhart 406 were the only two bridges inspected that did not have joint stains.

Both bridges were constructed with a 4 to 5 in. thick concrete deck. Elkhart 385 was also built with a 4 to 5 in. thick concrete deck but was found with minor stains at two of the longitudinal joints. All other bridges had bituminous wearing surfaces. It should be noted that only one bridge (Elkhart 410) was inspected that had a waterproofing membrane installed, and leaking of these joints was also observed.

Longitudinal edge cracks were observed in 11 of the bridges inspected (Newton K5, Wells 79, Newton 56, Elkhart 102, Elkhart 404, Elkhart 406, Elkhart 410, Greene 8, Kosciusko 18, Lake 61, and Lake 264), and concrete spalls and corroded strands were found in 9 bridges (Elkhart 409, Newton 56, Elkhart 102, Elkhart 404, Elkhart 406, Elkhart 410, Kosciusko 18, Lake 61, and Lake 264).

In addition, bridges built without curbs or other water drainage systems, frequently exhibited deterioration similar to that which is caused by leaking shear keys (Newton 56, Elkhart 102, Elkhart 404, Elkhart 406, Elkhart 410, and Kosciusko 18) (Figure 2.100). In all of these bridges, longitudinal cracking, exposed strand, or broken strand were observed at the edge of the exterior beams. Bridges with curbs or other water drainage systems did not exhibit these types of deterioration unless there were scuppers or other water outlets that allowed water onto the side and bottom flange of the beams.

A series of examples of deterioration related to leaking shear keys and water drainage over the side of the exterior beam is provided in Appendix B.

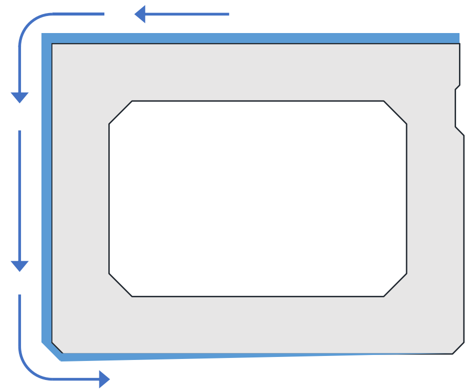

Figure 2.100: Exterior Beam Moisture Path

2.6.2 Ingress of Water into Box Beam Void

The shear key deterioration mechanism does not address the formation of longitudinal cracks in the middle of the bottom flange away from the support as observed in Tippecanoe 244 (Figure 2.6), Newton K5 (Figure 2.17 and Figure 2.18), Wells 79 (Figure 2.26 and Figure 2.27), Daviess 95 (Figure 2.46), Daviess 160 (Figure 2.52 and Figure 2.53), Elkhart 385 (Figure 2.57), and Elkhart 410 (Figure 2.69(a)). If the longitudinal crack forms away from the edge of the section and the support, it is theorized that the source of the cracking is the void.

Ingress of water into the void of box beams is a known phenomenon. As early as the 1960s, box beams have been cast with drain holes to prevent the voids from filling with water (Molley 2017). Precast box beams built in the 1950s and 1960s used cardboard to form the void in the box beam. Over time, the cardboard in the void degrades and clogs the drain holes. If the drain hole is clogged, the void will slowly fill with water.

Retained water in the void has the potential to cause two problems in addition to the additional weight that must be resisted. First, the chloride-laden water in the void can saturate the bottom flange and cause strand corrosion, resulting in longitudinal cracking. Second, water in the void can freeze. When ice forms in the filled void, the box beam is subjected to bursting stresses exerted by the expanding water (Figure 2.101), which can cause cracking in the longitudinal direction. The bottom flange is a likely location of cracking due to its lower tensile strength. The transverse reinforcement detail shown in Figure 2.101 was commonly used in box beams designed using the INDOT standard drawings between 1961 and 1965. The lack of transverse reinforcement in the bottom flange may cause large crack widths because crack redistribution is not possible without reinforcement in the flange.

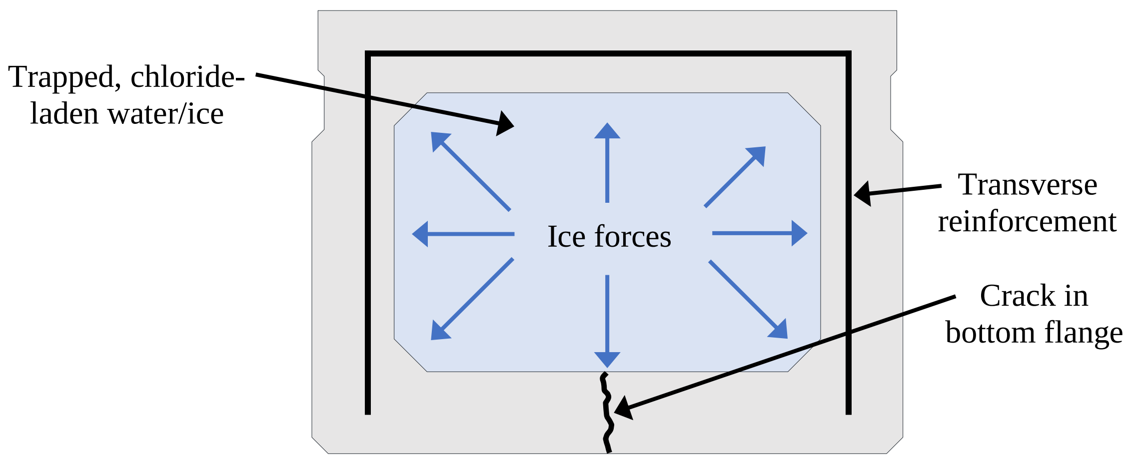

Figure 2.101: Ice Forces on Box Beam Section

The current practice of the design of concrete box beams in Indiana no longer uses cardboard to the form the void, but rather uses expanded polystyrene (EPS), a closed-cell insulation material. The use of EPS eliminates the potential of clogging drain holes with the void forming material and prevents the entirety of the void from filling with water. If the drain holes do become clogged, only a thin layer of water can accumulate around the EPS void form. A thin layer of water when frozen will deform the EPS void form.

Both potential deterioration mechanisms from entrapped water in the void explain the formation of longitudinal cracks that develop away from the edges of the box beam section and beam supports. This discussion also explains the effect of clogged drain holes. Examples of these deterioration mechanisms are provided in Appendix C.

The discussed deterioration mechanisms do not, however, fully explain the formation of longitudinal cracks extending from the beam support. According to 1961-1971 era standard drawings from INDOT, an 18 in. thick concrete diaphragm was cast at the support of each beam. The lack of a void at the support would prevent saturation as well as longitudinal cracks related to freezing of the void from forming at the support and extending into the span. Longitudinal cracking at the ends of the beams, as observed in Wells 79, Newton 56, and others, may be related in part to the release of the pretension force during the fabrication of the precast, prestressed beams and propagated by corrosion of the strands. Cracking at release, which may only result in hairline cracks, can still provide a path for chloride-laden water to access the strand.

2.6.3 Top Flange Damage

Top flange damage was observed in Tippecanoe 244 (Figure 2.9) and Newton K5 (Figure 2.20) after the bituminous wearing surfaces had been removed and in Wells 79 (Figure 2.28) during the bridge inspection. In all cases, the bituminous wearing surface had no membrane, and reflective cracking was observed in the wearing surface. In agreement with Molley (2017), the lack of a membrane and the formation of reflective cracks allowed salt water onto the top surface of the beam, which resulted in corrosion of the reinforcement in the top flange. Furthermore, moisture ingress through the bituminous surface that cannot easily free-drain off the deck causes saturation of the top flange of the beams. This saturation can cause scaling of the concrete, freeze-thaw damage, and corrosion of the reinforcement. This type of deterioration can be prevented by using either wearing surfaces with low permeability such as concrete or through the use of waterproofing membranes. Regular bridge deck maintenance using deck sealers and crack sealers should also be provided to maintain water resistance of the deck.

2.7 Conclusions

A total of 18 bridges were inspected in the process of acquiring decommissioned bridge beams for experimental study. Six of the 18 bridges inspected were identified as source bridges for 15 prestressed, precast box beam specimens. In addition to finding and acquiring specimens for experimental study, understanding of the deterioration of adjacent box beam bridges gained through field observation of in-service bridges informed the following conclusions:

1. Deck systems need to prevent moisture migration through the joint and prevent saturation of the top flange of the beam. Based on this investigation, concrete decks demonstrated greater durability of the box beam system than bituminous wearing surfaces.
2. Deicing salts are the primary cause of deterioration at longitudinal joints due to water seepage at the joint and on exterior beams due to water drainage over the side of the exterior beam. The connection of adjacent box beams needs to be improved to prevent leaking through the shear key and the initiation of reflective cracks through the wearing surface.
3. The current practice of using expanded polystyrene to form the void in tandem with drain holes prevents water from filling the void. Eliminating the potential of retained water prevents longitudinal cracking of the bottom flange through either corrosion of the saturated bottom flange or freezing of the retained water.
4. Top flange deterioration is caused by (1) saturation of the concrete due to saturation of the wearing surface as provided by bituminous wearing surfaces, and (2) chloride-

induced corrosion of the reinforcement in the top flange. This deterioration can be prevented by using either wearing surfaces with low permeability, such as concrete, or through the use of waterproofing membranes. Regular bridge deck maintenance using deck sealers and crack sealers should also be provided to maintain water resistance of the deck.

CHAPTER 3. EXTENT OF DETERIORATION

3.1 Introduction

The extent of deterioration in each of the acquired box beam specimens was determined in two parts. First, each specimen was scanned using three non-destructive test methods to estimate the extent of deterioration. Second, the strand at the locations of visual deterioration were extracted to determine the actual extent of deterioration. The extraction procedure was conducted after structural testing for each beam. The extent of deterioration observed in each specimen provides data necessary to develop a more accurate correlation between both visual signs of deterioration and deterioration identified by non-destructive test methods and actual damage.

3.2 Visual Inspection

As discussed in the previous chapter, 15 box beam specimens were acquired for experimental study (Table 3.1). The beams exhibited common types of deterioration ranging from hairline longitudinal cracks to extensive spalling and broken strands. Table 3.2 provides a list of common deterioration and the corresponding symbol used on the deterioration map.

An inspection of each specimen was conducted after arrival to the lab to determine the location and extent of visual indications of deterioration. All stains, longitudinal cracks, concrete spalls, exposed strands, and broken strands were considered visual indications of deterioration. The location and extent of visual deterioration was measured using a tape measure to develop visual deterioration maps. The visual deterioration map, drawn approximately to scale, of each beam is provided in Figure 3.1 to Figure 3.15. Please note that the cardinal directions labeled in the deterioration maps correspond to the beam specimen’s orientation in the laboratory and not to the orientation of the beam specimen in the source bridge.

Table 3.1: Box Beam Specimens

Bridge	Year Built	Specimen ID	Source Bridge Beam Number
Tippecanoe 244	1960	244-1-LC	6
Elkhart 409	1962	409-1-ES	B9
		409-2-UD	B8
Newton K5	1965	K5-1-LC	1
		K5-2-LC	7
Wells 79	1966	79-1-UD	B2
		79-2-UD	A6
		79-3-UD	A1
		79-4-LC	A7
Newton 56	1968	56-1-LC	A6
		56-2-ES	B1
Elkhart 102	1970	102-1-BS	C7
		102-2-BS	C5
		102-3-BS	B8
		102-4-BS	B7

Table 3.2: Key for Deterioration Maps

Deterioration Type	Map Symbol	
Shear key showing signs of deterioration	 Water Staining	Rust-Colored Staining
Longitudinal cracking	 Cracking 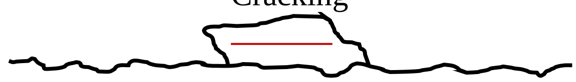 Cracking with exposed strand Blue Crack = Water Stained Red Crack = Rust Stained	
Corner Cracking	cc	
Concrete spalling	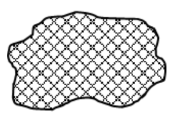 Spalling	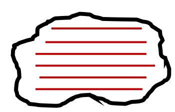 Spalling with Exposed Strands
Concrete spalling on one side of shear key	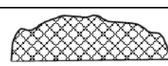 Spalling	 Spalling with Exposed Strands
Drain hole	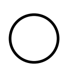 Unclogged	 Clogged

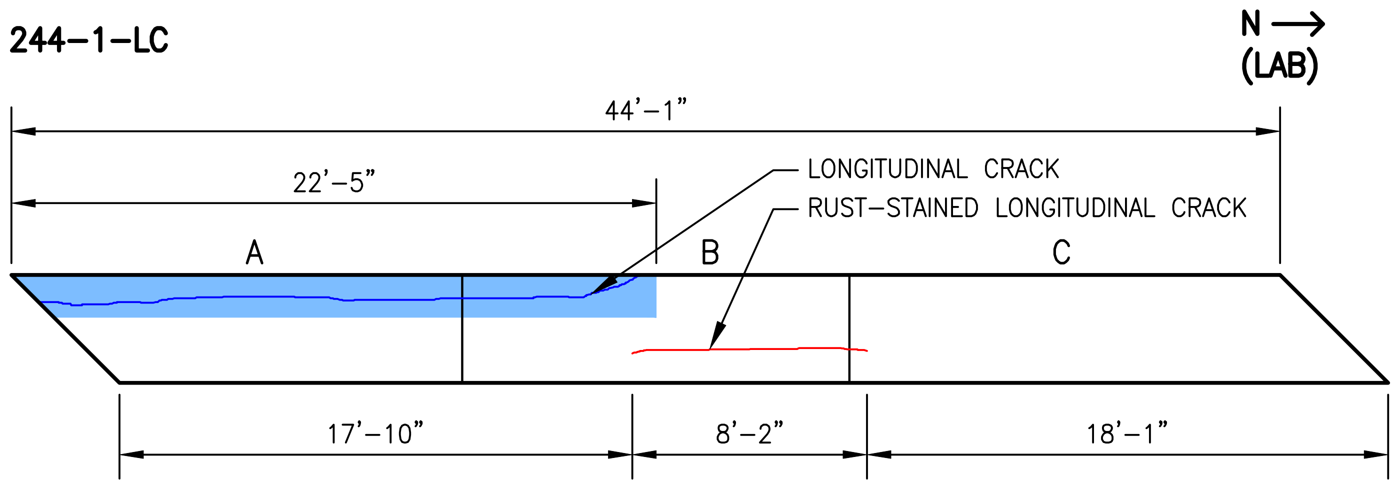

GREEN STAINING AROUND SOUTH LONGITUDINAL CRACK EXTENDS 10 IN. FROM BEAM EDGE.

Figure 3.1: Specimen 244-1-LC Visual Deterioration Map

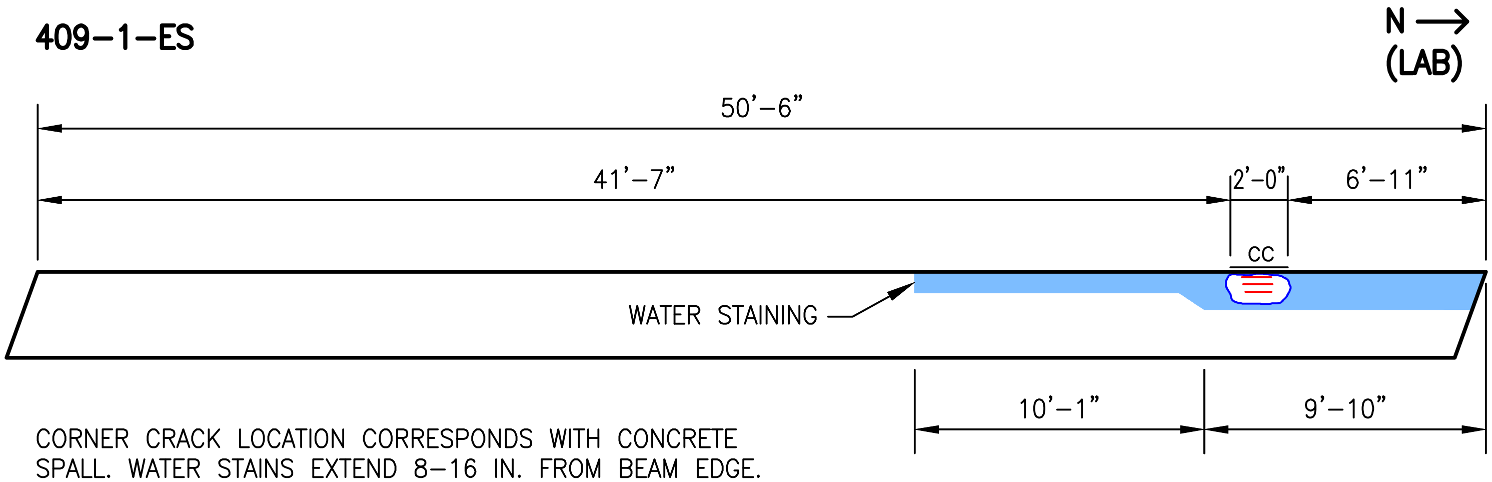

Figure 3.2: Specimen 409-1-ES Visual Deterioration Map

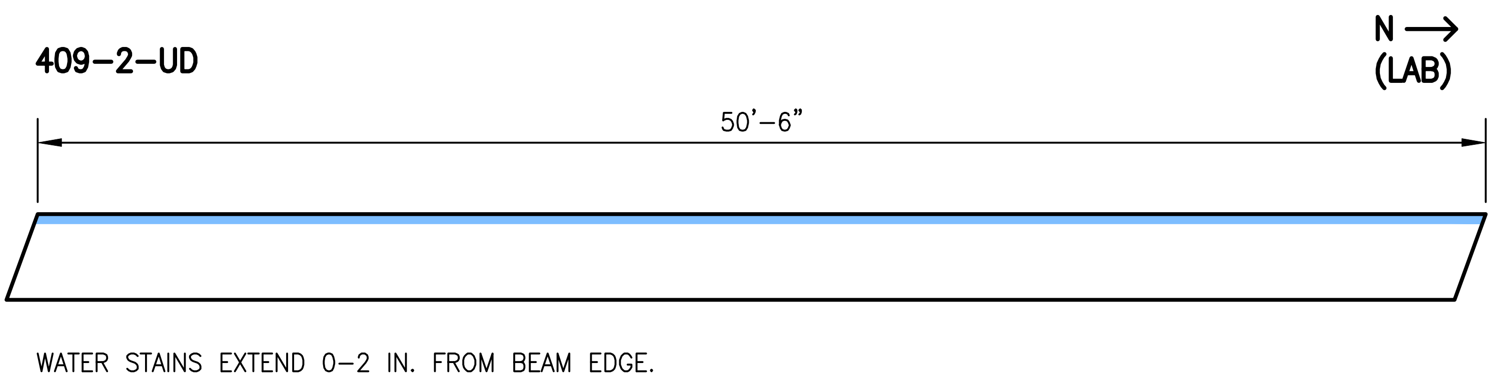

Figure 3.3: Specimen 409-2-UD Visual Deterioration Map

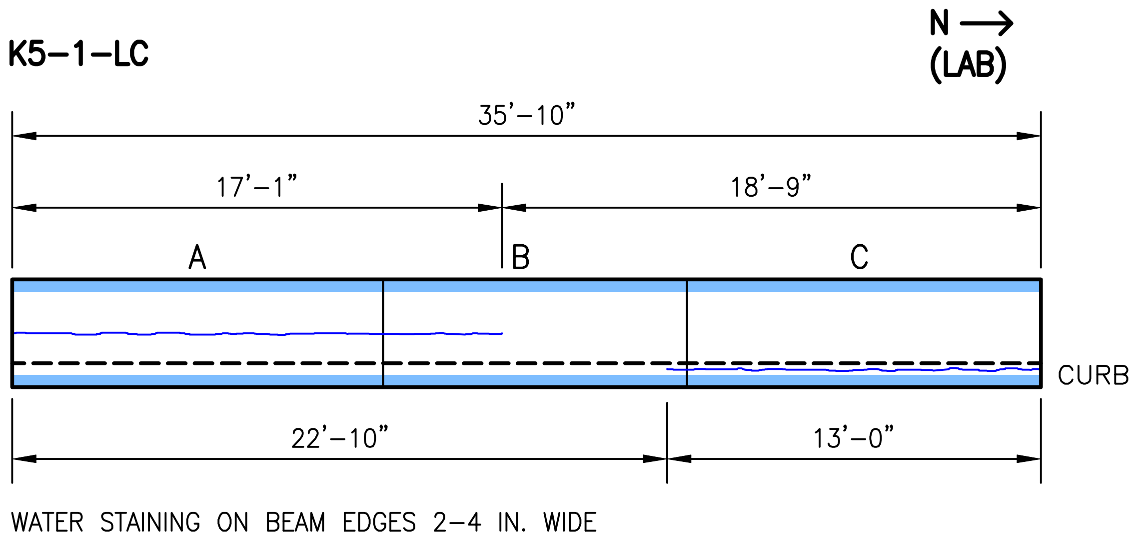

Figure 3.4: Specimen K5-1-LC Visual Deterioration Map

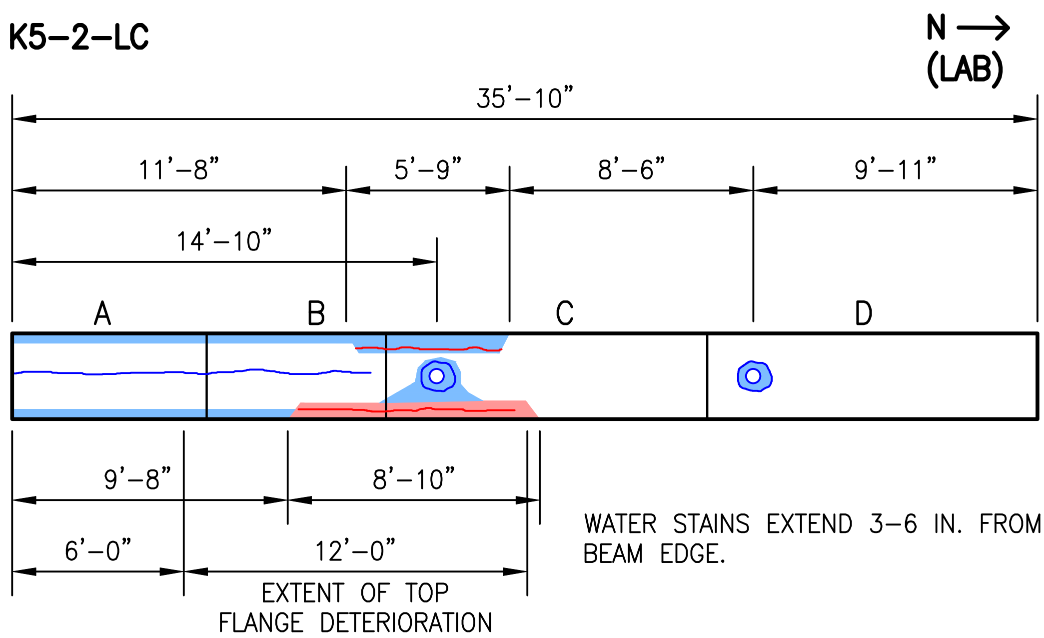

Figure 3.5: Specimen K5-2-LC Visual Deterioration Map

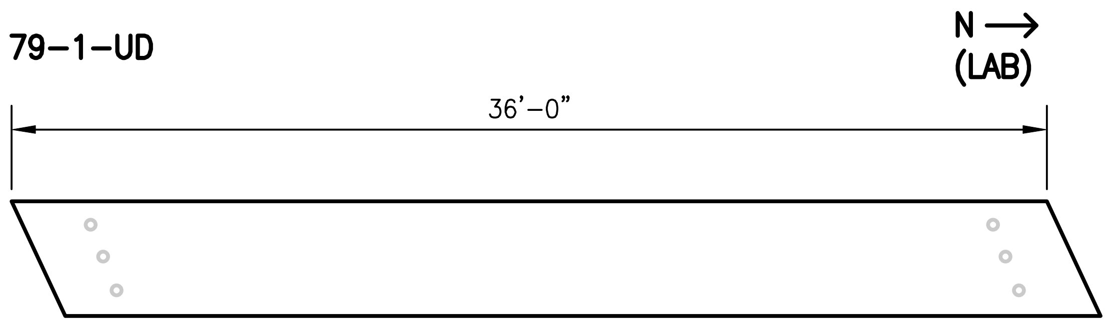

Figure 3.6: Specimen 79-1-UD Visual Deterioration Map

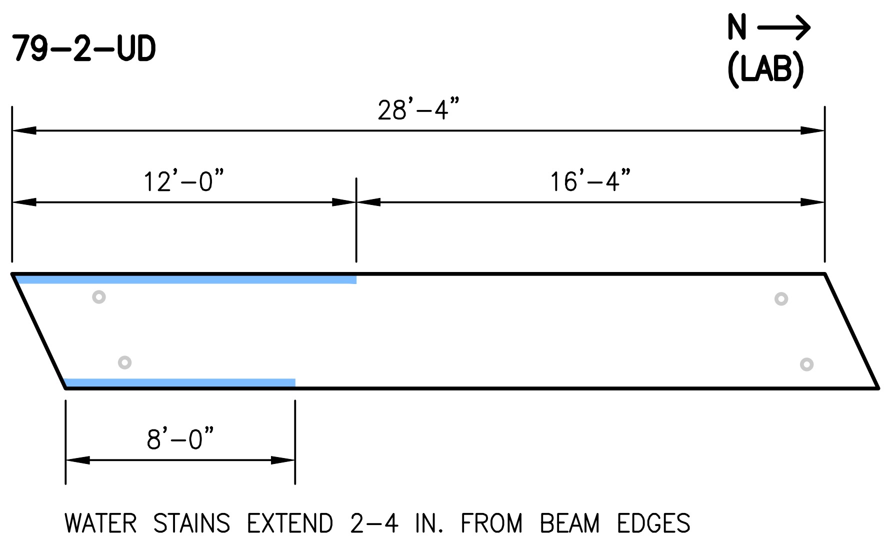

Figure 3.7: Specimen 79-2-UD Visual Deterioration Map

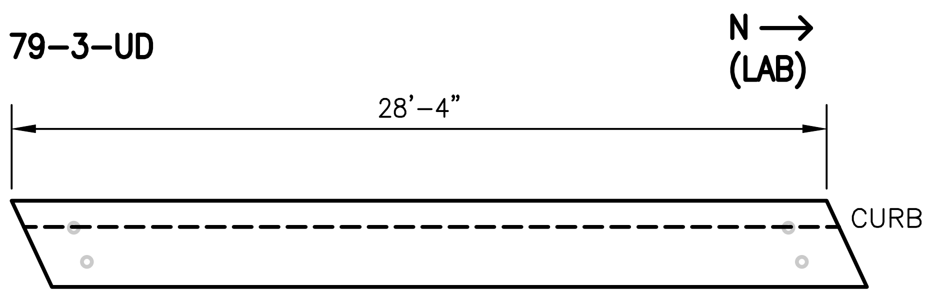

Figure 3.8: Specimen 79-3-UD Visual Deterioration Map

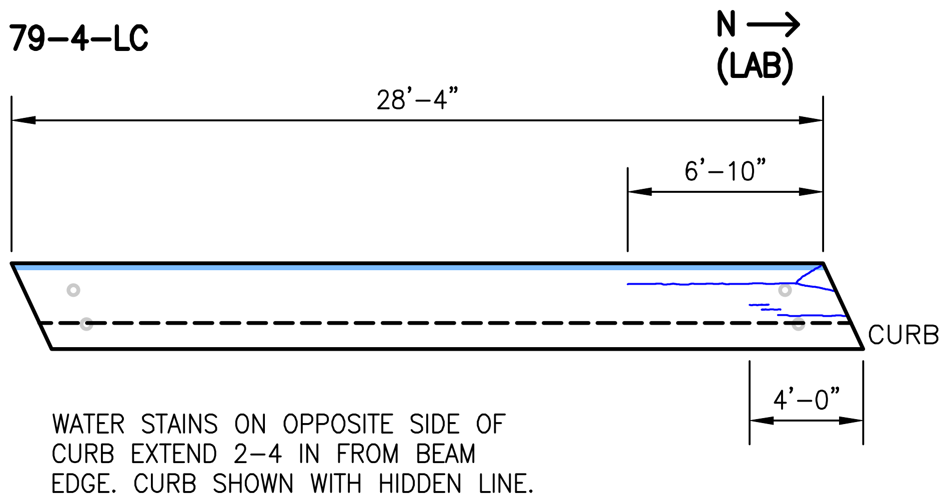

Figure 3.9: Specimen 79-4-LC Visual Deterioration Map

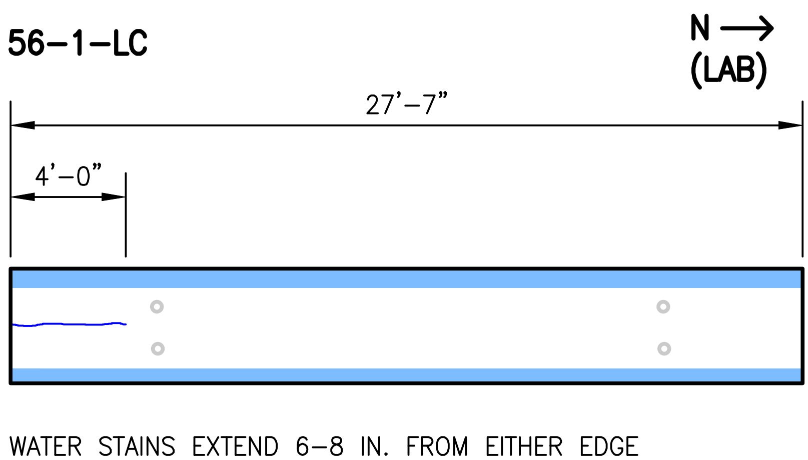

Figure 3.10: Specimen 56-1-LC Visual Deterioration Map

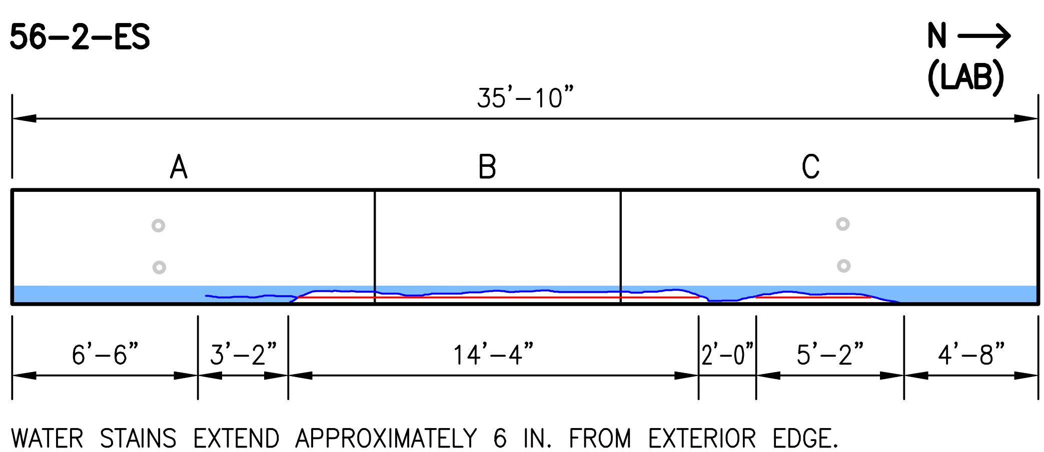

Figure 3.11: Specimen 56-2-ES Visual Deterioration Map

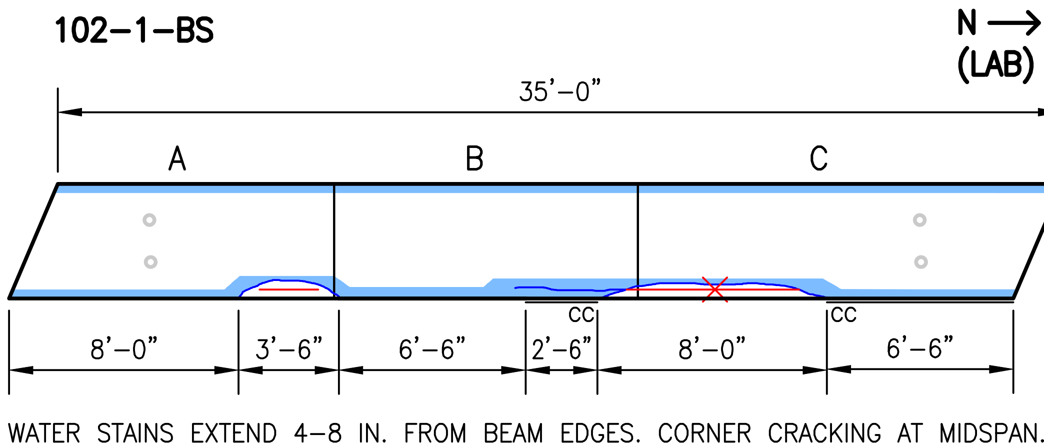

Figure 3.12: Specimen 102-1-BS Visual Deterioration Map

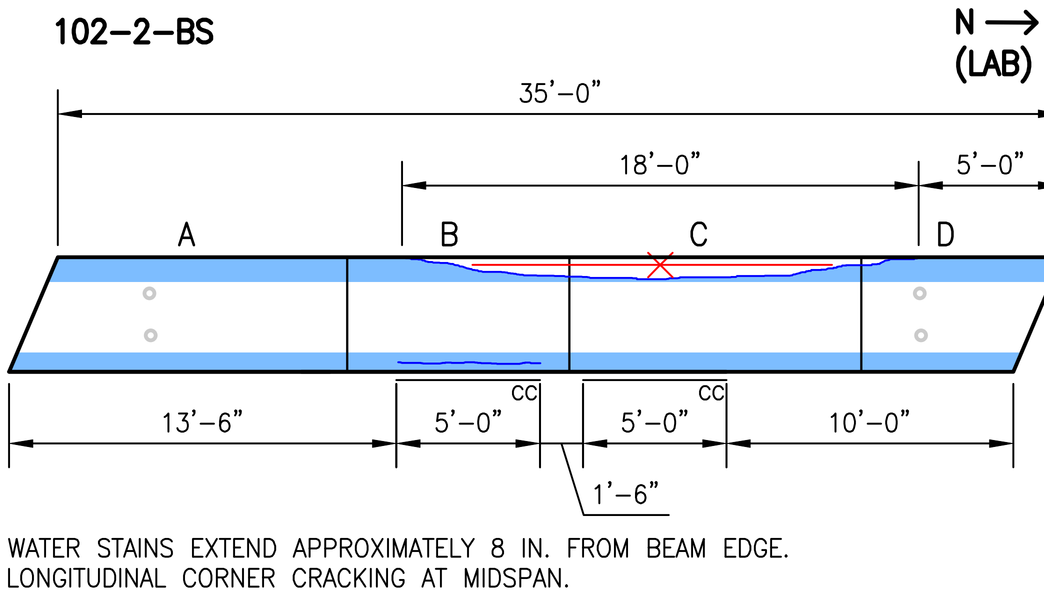

Figure 3.13: Specimen 102-2-BS Visual Deterioration Map

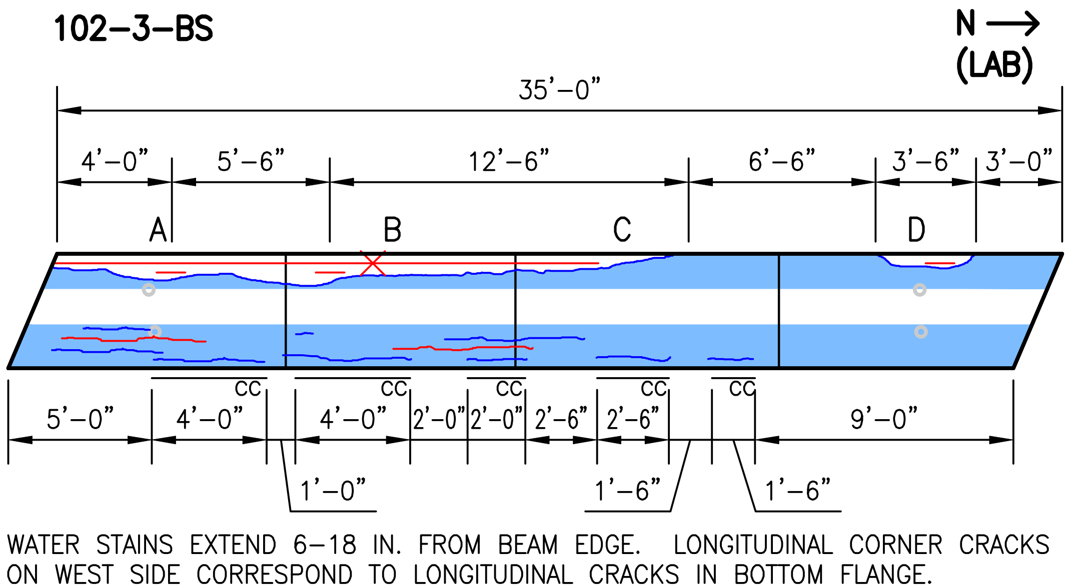

Figure 3.14: Specimen 102-3-BS Visual Deterioration Map

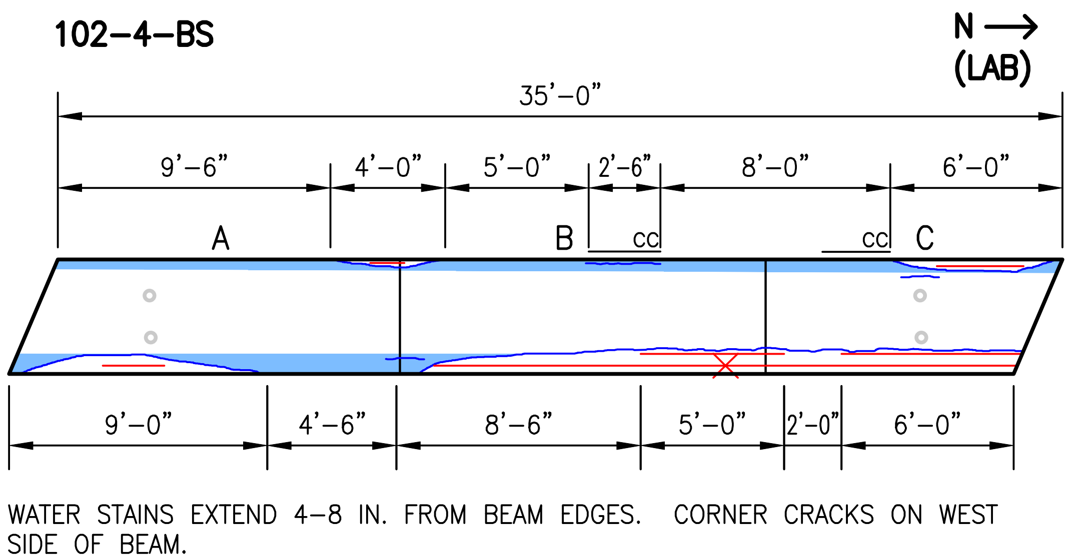

Figure 3.15: Specimen 102-4-BS Visual Deterioration Map

3.3 Nondestructive Test Methods

Non-destructive test (NDT) methods have been widely used to inspect concrete structures. The goal of NDT in this study was to assess the ability of commercially available devices to correlate visual signs of deterioration with the extent of deterioration in concrete box beams. The assessment of commercially available devices allows a device with positive results to be immediately implemented by state and county bridge inspectors. Two NDT methods were chosen for assessment: connectionless electrical pulse response analysis (CEPRA) and ground penetrating radar (GPR). CEPRA and GPR were selected because both technologies do not require a direct connection to the reinforcement. In addition, both NDT methods are portable and can be easily used upside down to evaluate the underside of a concrete box beam. To demonstrate the use of each device upside down, all box beam specimens were scanned while supported on concrete blocks. This allowed the specimens to be scanned in the same orientation as they were in the field and as would be used by inspectors.

The CEPRA device was manufactured by Giatec Scientific Inc. and is a wireless NDT corrosion detection device. If reinforcement is corroding, the device measures the rate of corrosion. The GPR unit used for this study was manufactured by Geophysical Survey Systems Inc. (GSSI). The device was used primarily to locate the reinforcement within the box beam specimens, but using the BridgeScan™ software package available from GSSI, the condition of reinforcement was also estimated. A third NDT method was employed to provide a reference to which the CEPRA and GPR results could be compared.

Half-cell potential measurements are commonly used in NDT applications to assess the potential for corrosion within a reinforced concrete member. The procedure for taking measurements has been standardized since 1977 by ASTM International (ASTM C876-15). The standard use of half-cell potential measurements for over 40 years makes the method an ideal reference for comparison against the CEPRA and GPR results. This method, however, requires a direct connection to the reinforcement for measurements to be taken. Therefore, bridge inspectors would be required to remove concrete cover to make a connection with the prestressing strand. Removing cover from prestressed strands can lead to deterioration and should generally be avoided. The destructive component of the half-cell measurement technique makes this method unsuitable for widespread use on prestressed box beam bridges and is therefore considered as a reference in this study.

Previous studies have been conducted to identify NDT methods for use on adjacent box beam bridges (Jones et al. 2010 and Fernandes et al. 2012). These studies determined that magnetic flux leakage (MFL) may be applied to adjacent box beam bridges with success. The MFL systems used by Jones et al. (2010) and Fernandes et al. (2012), however, are not well suited for widespread use on in-service bridges. The system used by Jones et al. (2010) was used in a laboratory on individual box beams, and for ease, each beam was turned upside down to facilitate scanning of the bottom flange. Fernandes et al. (2012) installed a track system on an existing bridge to allow the MFL system to scan the bottom flanges of the bridge. The MFL system currently on the market, however, was designed for use on slabs. The unit weighs over 120 lb and therefore, must be mounted on a track system for use on existing bridges. Considering the feasibility of assembling a track system for every bridge inspection, the MFL system was not included in this study.

The following sections describe each NDT method and summarize the testing procedure that was carried out on each specimen. The NDT results are presented together for comparison in Section 3.5.

3.3.1 Connectionless Electrical Pulse Response Analysis (CEPRA)

Giatec Scientific Inc. developed and patented the CEPRA method for determining the corrosion rate of steel reinforcement embedded in concrete (Ghods et al. 2017). The method is based on determining the corrosion intensity, I_{corr}. According to Fahim et al. (2019a and b), I_{corr} is calculated using the following expression:

$$I_{corr} = \frac{\beta}{A * R_p} \tag{3-1}$$

where:

I_{corr}	=	corrosion intensity (μA/cm^2)
β	=	Tafel constant, typically 27 mV
A	=	area polarized by the applied current (cm^2)
R_p	=	ratio of the change in voltage to the change in current (Ω)

The corrosion rate, in μm/year, is then determined by multiplying I_{corr} by a factor of 10.

The corrosion rate output from the CEPRA device is assumed to be the corrosion rate at the time of measurement. Considering that the rate of steel corrosion is not constant with time, the corrosion rate measurements provided by the CEPRA device are assumed to provide an indication of corrosion rather than a quantification of section loss.

3.3.1.1 CEPRA Scanning Procedure

The CEPRA device used in this study was the Giatec iCOR™ (Figure 3.16). The device has a diameter of approximately 10 in. and weighs approximately 2 lb. Using Bluetooth®, the device wirelessly connects to a tablet with the CEPRA software for recording and processing data. The device is completely controlled by the tablet, and although the device does not come with an extension pole, one could be manufactured for easier scanning of the bottom flange of box beams in service. An extension pole for a GPR unit is shown in Figure 3.17 as an example.

Figure 3.16: CEPRA Device (Giatec iCOR^{TM})

Figure 3.17: Extension Pole (GSSI)

Use of the device requires the location of the reinforcement and the thickness of the concrete cover to be known as accurately as possible. GPR was used to determine the location of the strands and the thickness of the concrete cover to within ±1/4 in.

Each beam was scanned at 5 ft intervals along the length of the beam. According to the user manual, very dry concrete surfaces will affect measurements (iCOR User Manual). In practice, when very dry concrete surfaces were scanned, an error was returned by the device and no data was collected. Therefore, the bottom flange of each specimen was wetted with tap water using a spray bottle approximately 20 minutes before scans were taken. If any excess water was still present on the concrete surface (small droplets), the water was removed with a rag and scans were taken after an additional 10 minutes.

The CEPRA device measured the corrosion rate of the strand in each box beam specimen. A four-part scale for determining the classification of the corrosion rate values was developed for 1/4 in. diameter (7 mm) steel wire reinforcement by Andrade and Alonso (1996) and is provided in Table 3.3. No tests have been performed on prestressed strands using CEPRA to determine if the correlation is the same for 7-wire strand as steel bars. The data provided by scanning the prestress concrete beam specimens acquired from the field will be used to verify the correlation with 7-wire strand.

Table 3.3: CEPRA Corrosion Rate Scale

Color Code	Corrosion Rate, C_r (µm/year)	Classification of Corrosion
Green	$C_r < 1.1$	Passive/Low
Yellow	$1.1 \leq C_r < 2.2$	Uncertain
Orange	$2.2 \leq C_r < 10$	Visible
Red	$C_r \geq 10$	Severe
Black	No available data	

Temperature and relative humidity have been reported to influence corrosion rate measurements (Alonso et al. 1988, Andrade and Alonso 1996, and Millard and Gower 1992). The corrosion rate measurements in μm/year from the CEPRA device are automatically corrected for temperature and relative humidity within the software developed by the manufacturer.

3.3.1.2 CEPRA Results

The corrosion rate measurement results for each specimen are provided in Figure 3.18. The results are displayed using the color coding from Table 3.3. A full scan of Specimens 56-2-ES, 102-1-BS, 102-2-BS, 102-3-BS, and 102-4-BS could not be completed because the device could not be used over concrete spalls or on exposed strand. The concrete spall in Specimen 409-1-ES was also not scanned, but the area of the beam adjacent to the spall was scanned. In addition, if the probes of the device were placed on either side of a crack wider than 1/16 in. no data could be collected. In regions with large cracks, scans were taken on one side of the crack. Where a scan could not be taken, the unscanned length of strand was omitted from Figure 3.18.

The missing results from Specimen 244-1-LC are a result of repeated scan errors from the device. These locations were scanned multiple times on different days. Each time, the device produced an error for these locations. The source of the error is unknown as no difficulty was encountered while scanning other areas of the specimen. The initial results for Specimen 102-3-BS were invalidated by an instrument error that was realized after completion of the strand extraction. Specimen 102-3-BS was scanned again after the extraction, but because some strand had been removed, a portion of the results in Figure 3.18(c) is missing.

In general, the CEPRA results interpreted using Table 3.3 indicate much more corrosion than the visible signs of deterioration would suggest. A comparison between the CEPRA results and the results of the strand extraction is provided in Section 3.5.

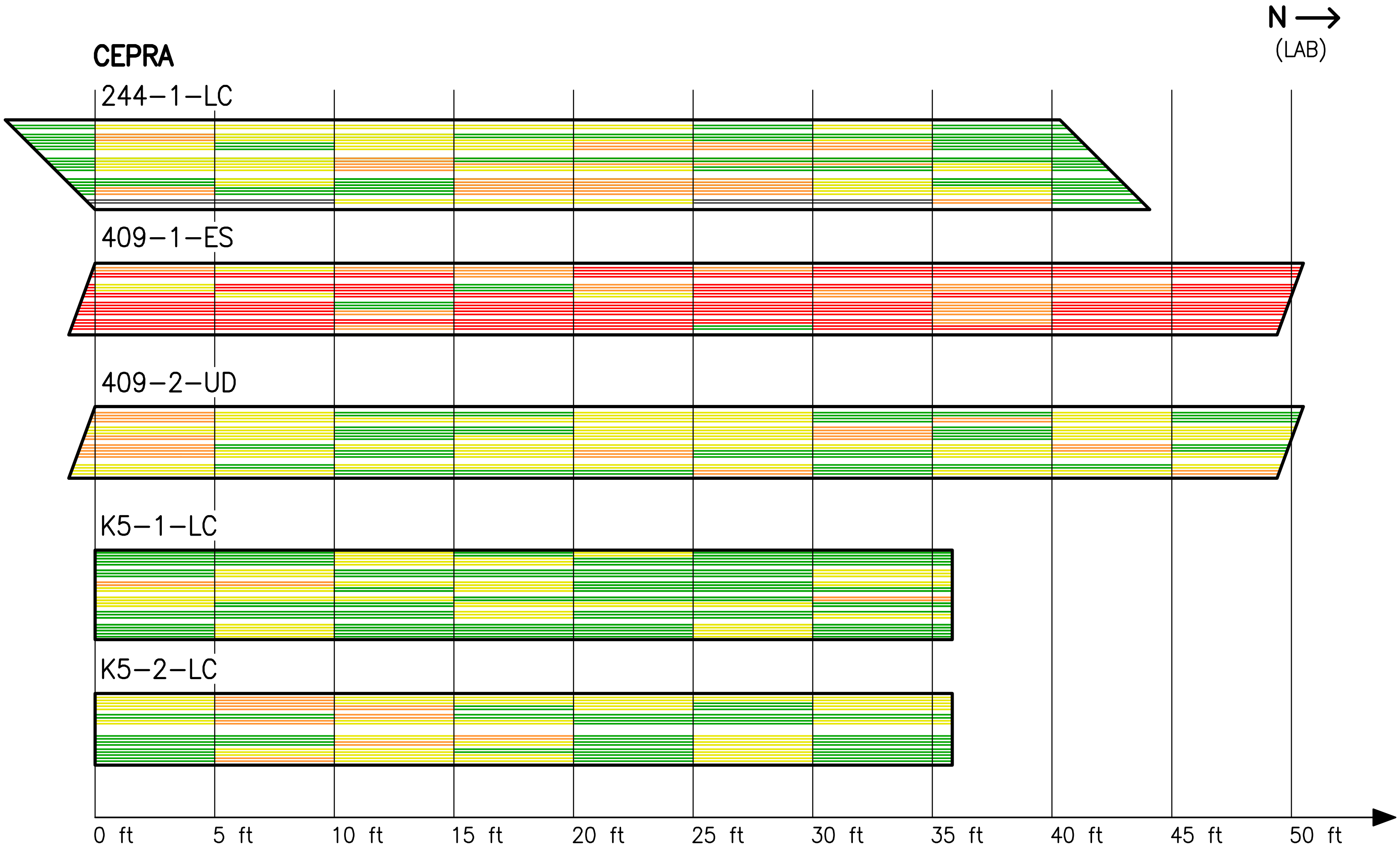

(a) Specimens 244-1-LC, 409-1-ES, 409-2-UD, K5-1-LC, and K5-2-LC

Figure 3.18: CEPRA Results

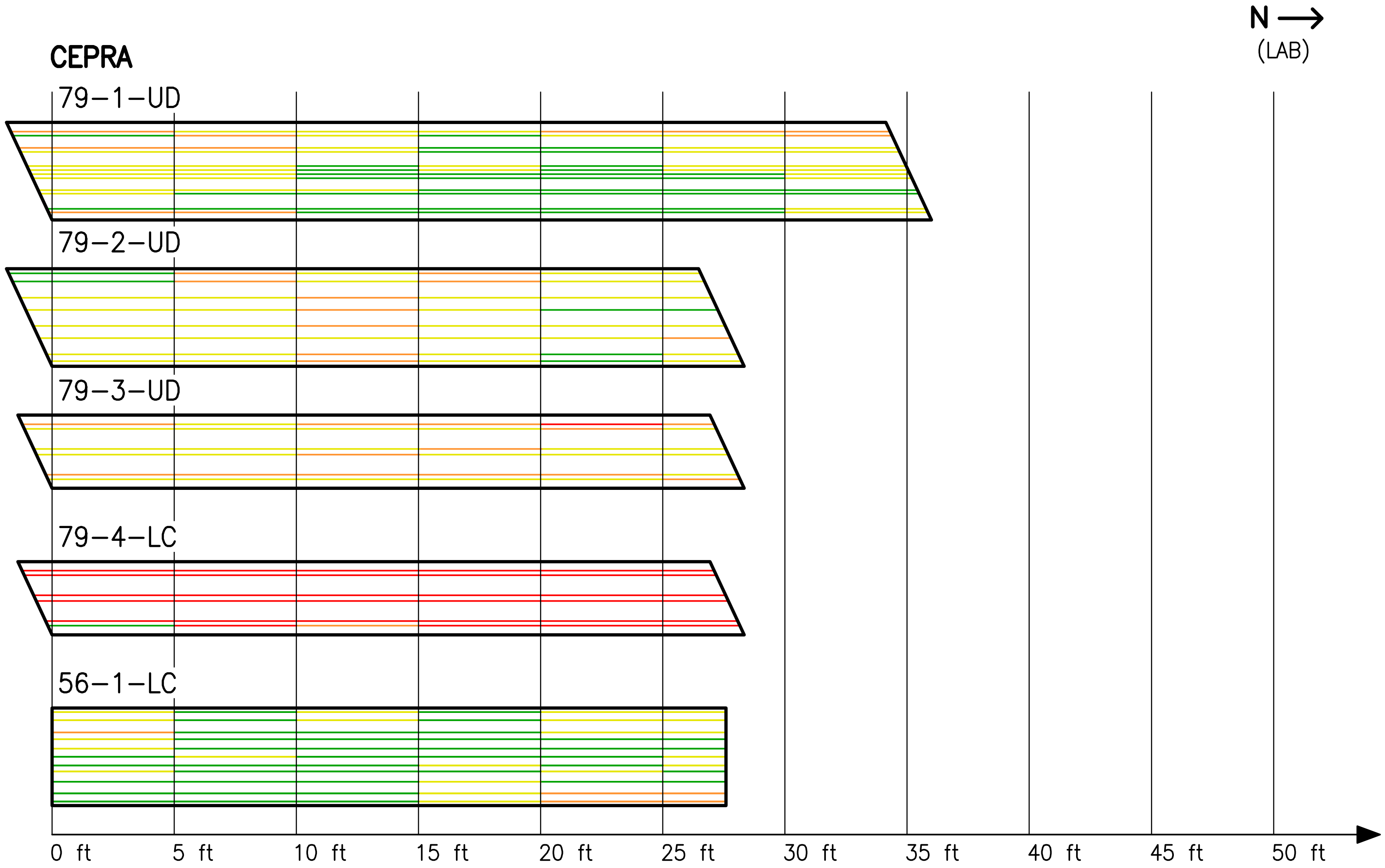

(b) Specimens 79-1-UD, 79-2-UD, 79-3-UD, 79-4-LC, and 56-1-LC

Figure 3.18: Continued

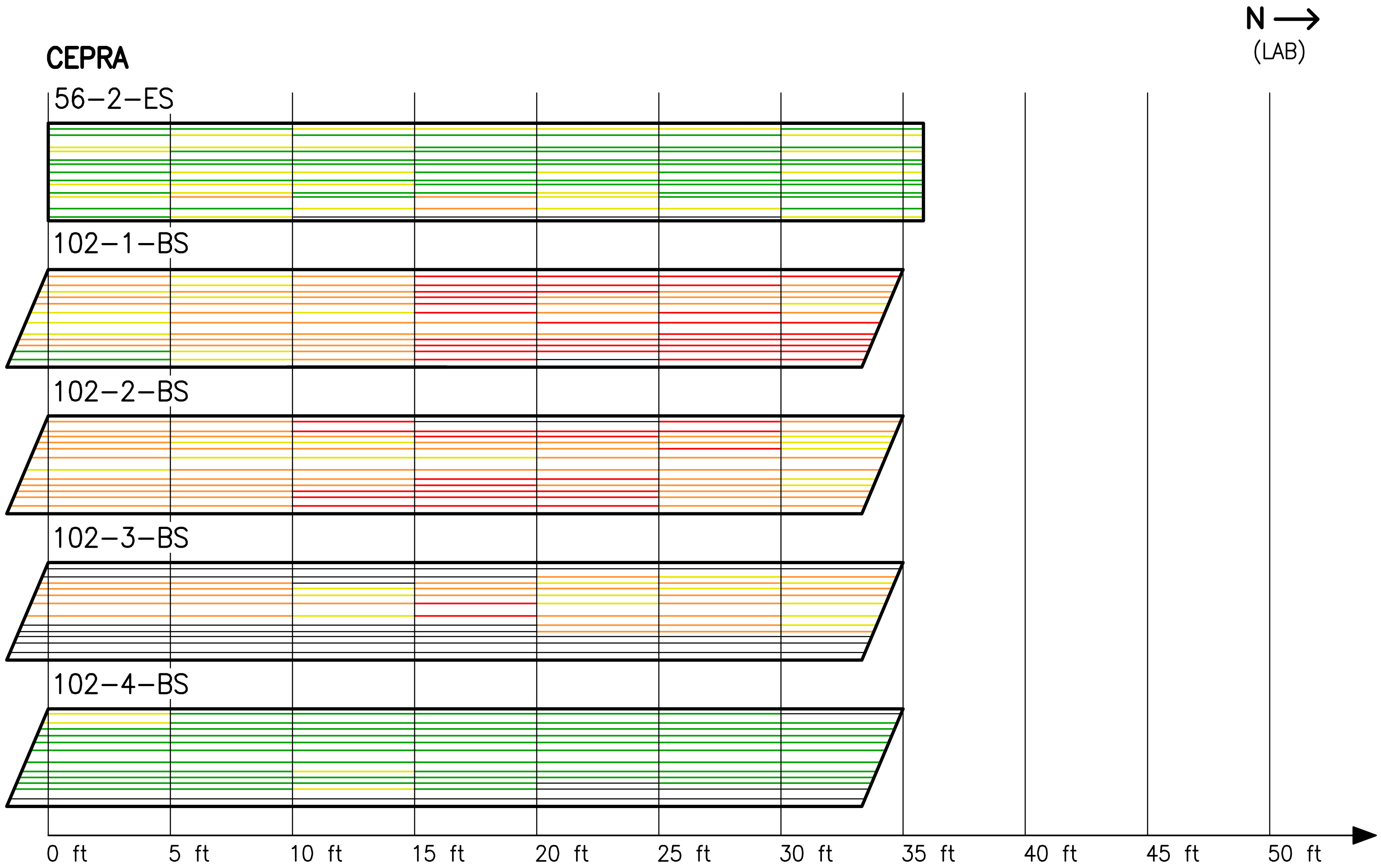

(c) Specimens 56-2-ES, 102-1-BS, 102-2-BS, 102-3-BS, and 102-4-BS

Figure 3.18: Continued

3.3.1.3 CEPRA Device User Notes

The CEPRA device user manual provided all the information needed to operate the device successfully. The software and scanning procedure were easy to follow but provided little aid when measurement errors were encountered. Further reading of literature provided on Giatec Scientific's webpage provided sufficient information to correct the conditions creating measurement errors.

The device was very sensitive to surface moisture and position relative to the strand. Dry concrete surfaces often prevented data collection. If the concrete surface was not prewetted with water, the device was unable to record any data. In addition, if the surface was wet enough to form water droplets, no data could be recorded.

When the device was used on concrete spalls, no data could be collected. Similarly, when the device was positioned across cracks larger than 1/16 in. wide, no data could be collected.

3.3.2 Ground Penetrating Radar (GPR)

A GPR unit consists of two antennas: a transmitter and a receiver. When a medium is scanned with GPR, electromagnetic (EM) waves are emitted from the transmitter into the medium. Depending on composition, the waves may pass through the medium or be reflected to the receiver. Materials within the medium that have dielectric constants greater than 80, such as water, are considered conductive and reflect EM waves. Metallic materials are highly conductive and are assumed to be perfect reflectors of EM waves. Air and concrete have dielectric constants ranging between 1 and 15, depending on moisture content, and have low conductivity. Due to the low conductivity of concrete, a GPR unit can be used to scan through the thickness of a concrete member to search for highly reflective materials such as steel reinforcement. The depth of the reinforcement in concrete is determined by a correlation between the dielectric constant of concrete and the elapsed time between transmission and reception of the EM wave reflected off the reinforcement. Therefore, any change in the dielectric constant will change the depth calculation of the reinforcement.

An example GPR scan of box beam bottom flange is shown in Figure 3.19. The vertical axis represents the depth of the scan into the bottom of the beam, and the horizontal axis represents the distance across the section perpendicular to the depth of the scan (i.e. distance along the transverse axis of the beam). The hyperbolas in the figure indicate the presence of strong reflectors, and the peak of each hyperbola corresponds to the location of each strong reflector indicated by a yellow dot. The type of strong reflector depends on knowledge of the object scanned. For the box beam specimens, the strong reflector is steel prestressing strand.

In Figure 3.19, a single row of strands is shown for Specimen 56-1-LC which was reinforced with a single row of strand. Scans of the specimens with multiple rows of strands (Specimens 244-1-LC, 409-1-ES, and 409-2-UD) did not show the second row of strands. The close proximity of the strands in the first row prevented detection of the second row of strands. Figure 3.20 shows a scan of Specimen 244-1-LC. The detected strands are highlighted with yellow dots, and the undetected strands are marked with red dots.

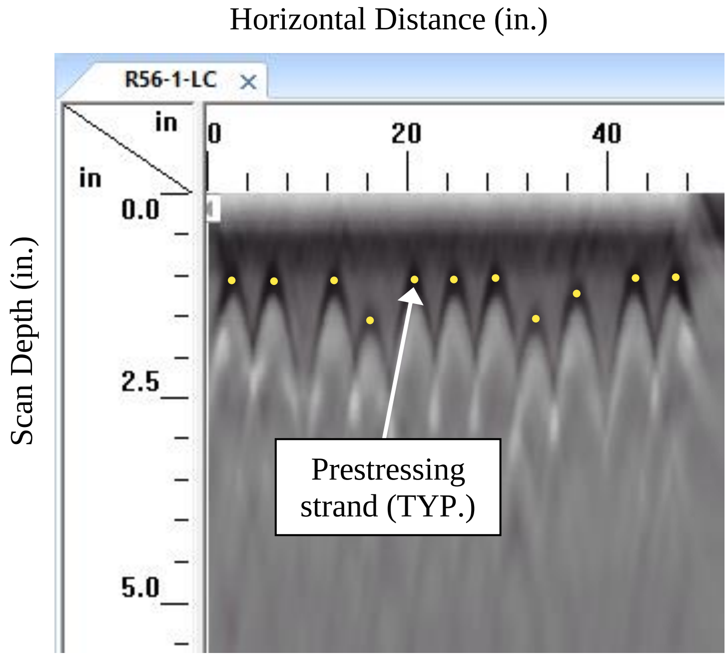

Figure 3.19: Example GPR Scan of Specimen 56-1-LC

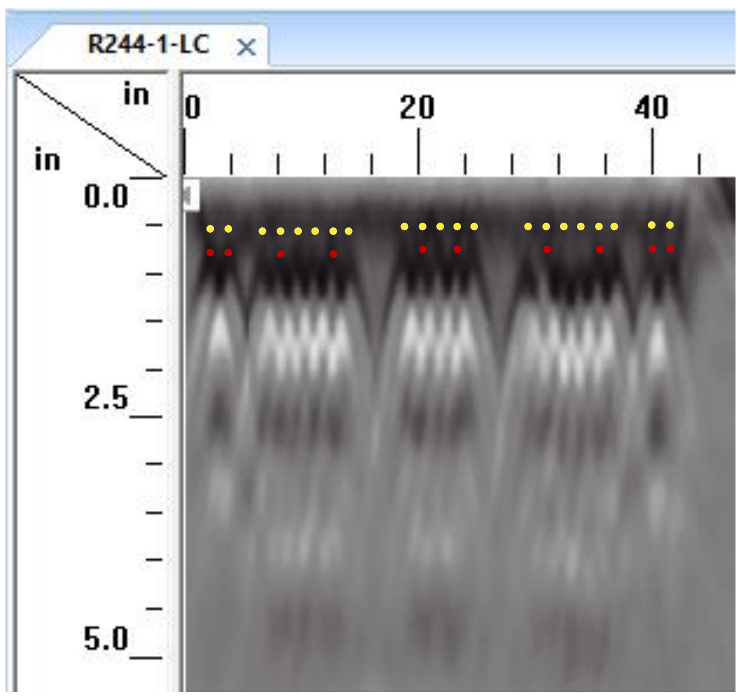

Figure 3.20: GPR Scan of Specimen 244-1-LC

Using GPR, the horizontal location and concrete cover of the strands in each specimen could be determined. The location and concrete cover information are required for proper use of the CEPRA and Half-Cell Potentials methods because the methods do not provide accurate results unless the scans are performed at the location of the reinforcement and the thickness of concrete cover is known. In addition, the equipment used for CEPRA and Half-Cell Potentials is not capable of locating reinforcement.

The dielectric constant of a material also influences the amplitude of the reflected EM wave. As the wave travels through a medium, the amplitude decreases. As the dielectric constant increases, the loss in amplitude also increases. This phenomenon is used to map deterioration in reinforced concrete structures because the dielectric constant of deteriorated concrete is relatively higher than undeteriorated concrete in the same structure. Therefore, in areas of deterioration, the measured amplitude is lower than the amplitude measured in areas without deterioration. Please note that the amplitude of the reflected wave is measured in decibels (dB).

ASTM D6087 (2015) employs the amplitude of the reflected GPR signal to determine the probability of deterioration. The standard states that deterioration is typically found where the measured reflection amplitude is 6 to 8 dB below the maximum measured reflection amplitude. The threshold of 6 dB was conservatively used for this study. The GPR results were color coded to indicate deteriorated and undeteriorated strands based on ASTM D6087 (Table 3.4).

Table 3.4: GPR Deterioration Threshold

Color Code	Measurement	Deterioration Classification	Source
Green —	≥ 6 dB threshold	No deterioration	ASTM D6087 (2015)
Red —	< 6 dB threshold	Deterioration	
Black —	No reading available		

3.3.2.1 GPR Scanning Procedure

A StructureScan Pro GPR unit equipped with a 2.6 GHz antenna system was used to scan each specimen (Figure 3.21). The small cart shown is handheld and weighs less than 5 lb. The SIR 4000, weights around 15 lb. and was used with a carry harness that allowed the unit to be carried while keeping both hands free to scan with the handcart. The handcart also is available with an extendable pole (Figure 3.17) that allows the device to be used on the bottom flanges of box beams in service.

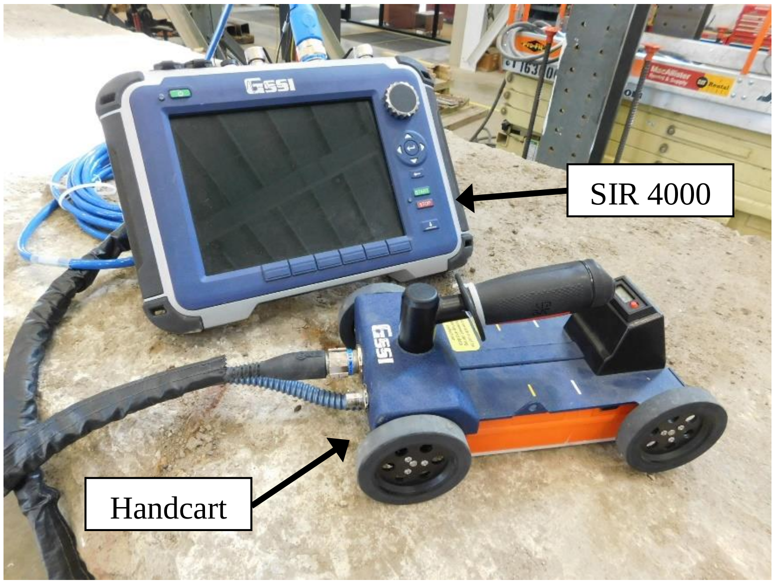

Figure 3.21: GSSI StructureScan Pro

Each specimen was scanned at 5 ft intervals along the length of the beam. The scan data from each specimen was processed using the BridgeScan software package of RADAN 7, a computer program developed by GSSI to analyze GPR data. The program processes each scan to determine the location of the strand. Figure 3.22 shows a comparison of the GPR scan before and after processing. The image on the left shows the raw GPR scan. The band of white then black at the top of the image is the concrete surface of the beam. The image on the right shows the GPR scan after processing. Note that the surface of the beam has been adjusted to correspond with the vertical 0.0 in. mark in the image. The small yellow dots represent the location of the strand within the box beam specimen.

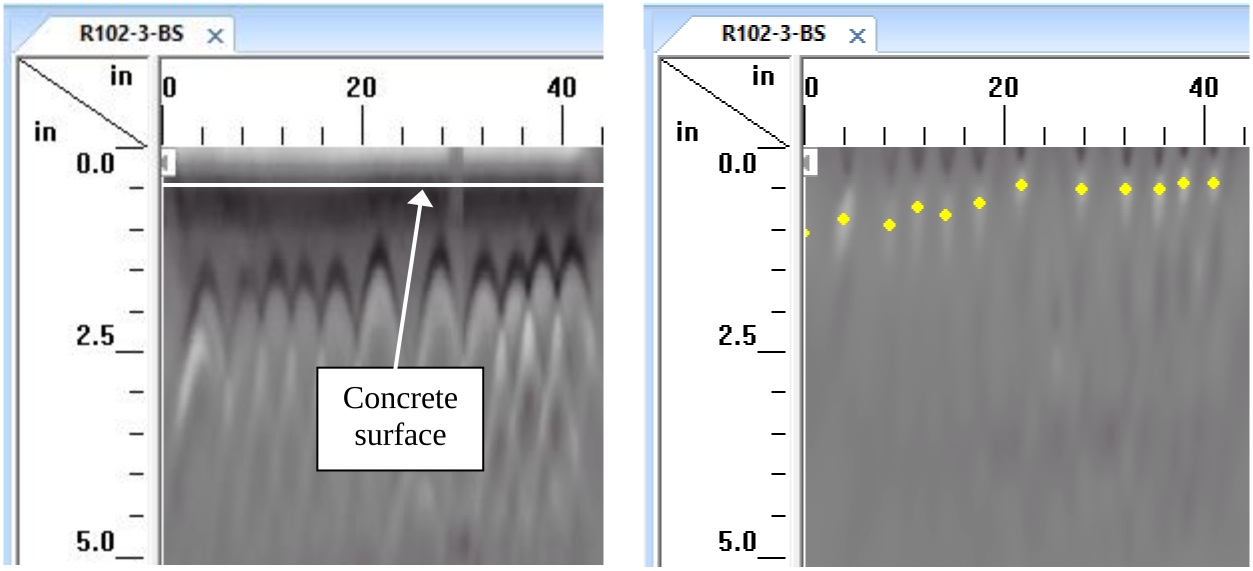

(a) Raw GPR scan **(b) Processed GPR scan**

Figure 3.22: GPR Signal Processing

The location of the identified strand (yellow dot) is editable to allow users to manually select the location of the strand in the event the program cannot properly locate the strand. In many cases, the strand location provided by the program was in error. Manual adjustments relied on determining the location of the hyperbola peak. After the locations of the strand were determined for each scan, the reflected GPR signal amplitudes of the strands were exported from RADAN 7 and processed using the procedure recommended by ASTM D6087.

3.3.2.2 GPR Results

The GPR deterioration mapping results are provided in Figure 3.23. The results are displayed using the color coding from Table 3.4. Scans taken over exposed or broken strands were not processed. The unprocessed length of strand for Specimens 56-2-ES, 102-1-BS, 102-2-BS, 102-3-BS, and 102-4-BS are shown as black lines in Figure 3.23. The concrete spall in Specimen 409-1-ES was not directly scanned, but the area of the beam adjacent to the spall was scanned. A comparison of the GPR results and the results from the strand extraction is provided in Section 3.5

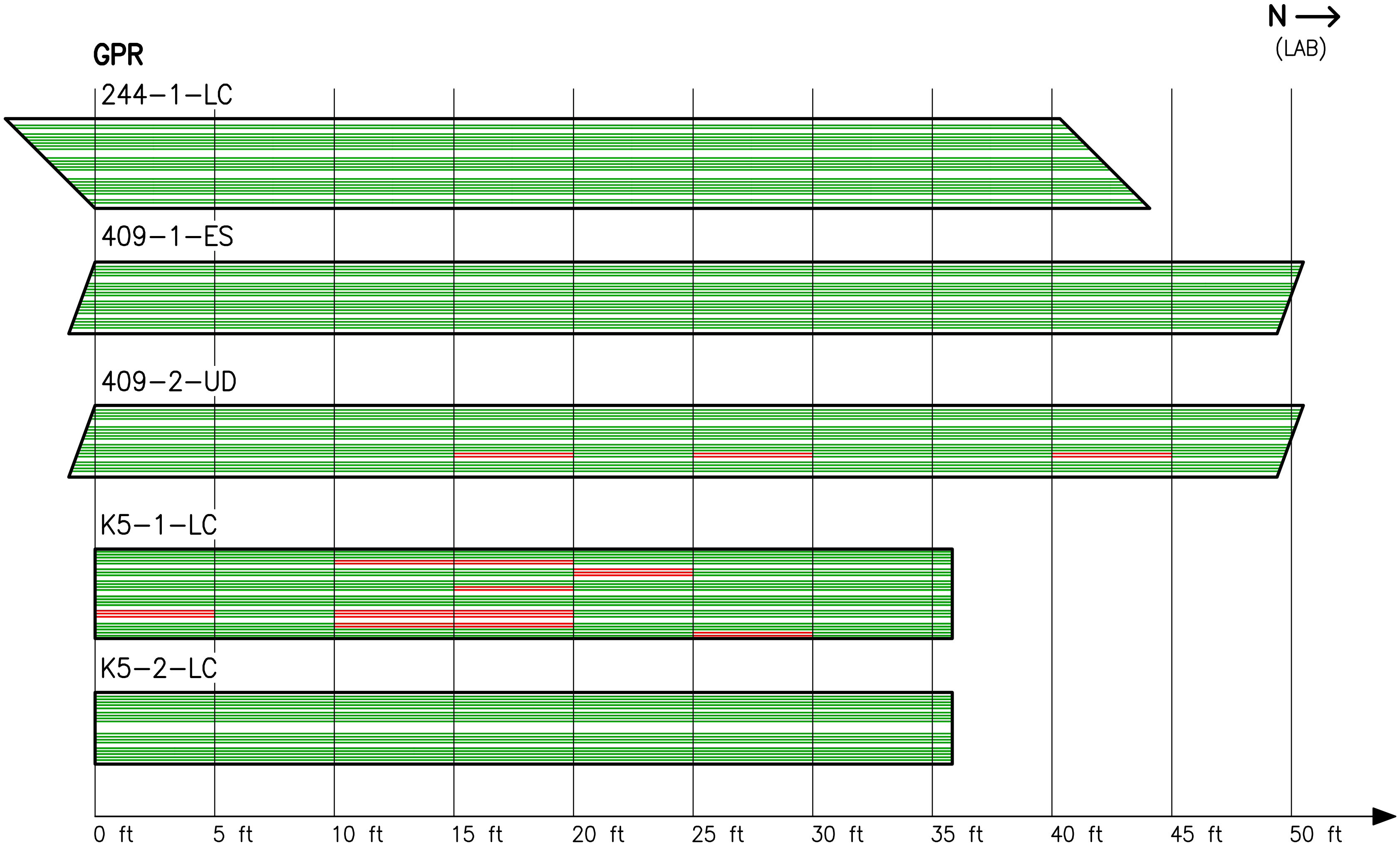

(a) Specimens 244-1-LC, 409-1-ES, 409-2-UD, K5-1-LC, and K5-2-LC

Figure 3.23: GPR Results

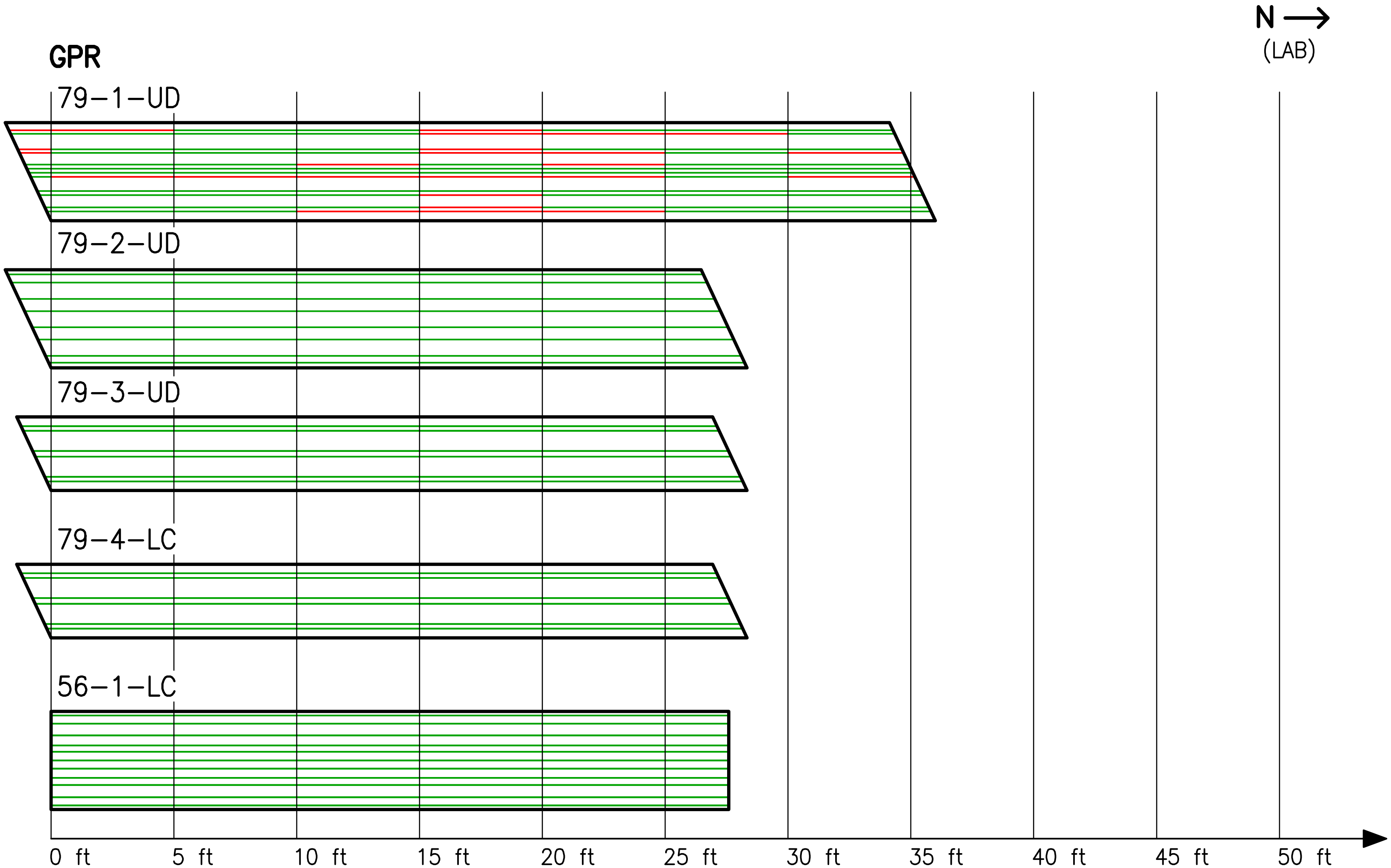

(b) Specimens 79-1-UD, 79-2-UD, 79-3-UD, 79-4-LC, and 56-1-LC

Figure 3.23: Continued

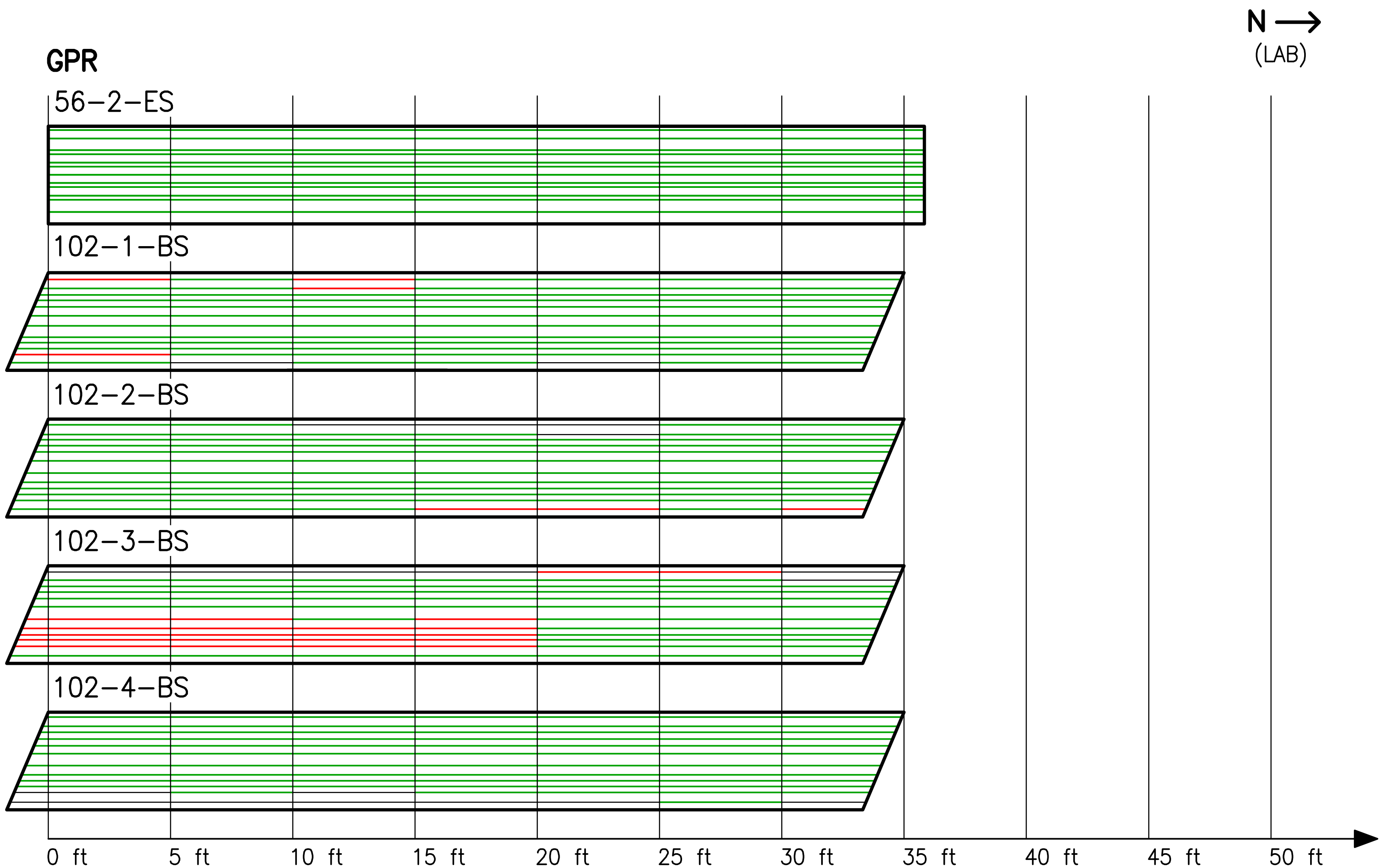

(c) Specimens 56-2-ES, 102-1-BS, 102-2-BS, 102-3-BS, and 102-4-BS

Figure 3.23: Continued

3.3.2.3 GPR Device User Notes

A training course provided by the manufacturer (GSSI) was taken in preparation for using the GPR unit (StructureScan Pro) to scan for reinforcement location and deterioration. Without the training course, the operation of the unit and interpretation of the data would not have been possible. It is strongly recommended that a training course be taken prior to the use of the equipment.

Once the settings of the unit are understood, scanning for reinforcement location and deterioration were conducted with little effort. Scanning for reinforcement location could be made much easier by using a handheld device with the processing unit on-board. Such a device is available from GSSI but with only the capability to scan for reinforcement location. Deterioration mapping is only available on the larger unit that was used in this research program.

3.3.3 Half-cell Potentials

Corrosion in reinforced concrete structures is an electrochemical process where a galvanic cell is formed between two portions of steel reinforcement. The electric potential field that forms when steel reinforcement corrodes can be measured by the half-cell potentials method. The method is based on comparing the voltage potential of a standard half-cell electrode to the voltage potential of the reinforced concrete specimen under evaluation. A full description of the formation of voltage potentials in corroding reinforcement embedded in concrete may be found in Carino (1998).

3.3.3.1 Half-Cell Potential Measurement Procedure

The half-cell potentials method used in this study utilized an M.C. Miller copper-copper sulfate R5-U reference electrode with a 40 MΩ Fluke 76 True RMS Multimeter to measure voltage potentials (Figure 3.24). A copper plated steel clamp was used to attach to the strand exposed at the end of each box beam specimen. Strands were exposed using a jackhammer. Sandpaper was used on the exposed strands to clean the areas were the clamp attached to the strand.

Each box beam specimen was scanned at the same 5 ft interval as the CEPRA and GPR methods. Readings were taken in accordance with ASTM C876 (2015). A damp sponge was attached to the end of the reference electrode to form a coupling between the electrode and concrete surface. Once the electrode was in position on the concrete surface, the voltage was monitored until a stable reading was observed. Readings were recorded to the nearest 0.01 V. In the case that a stable reading was not observed after a few minutes, the surface was prepared using the same prewetting procedure used with the CEPRA device.

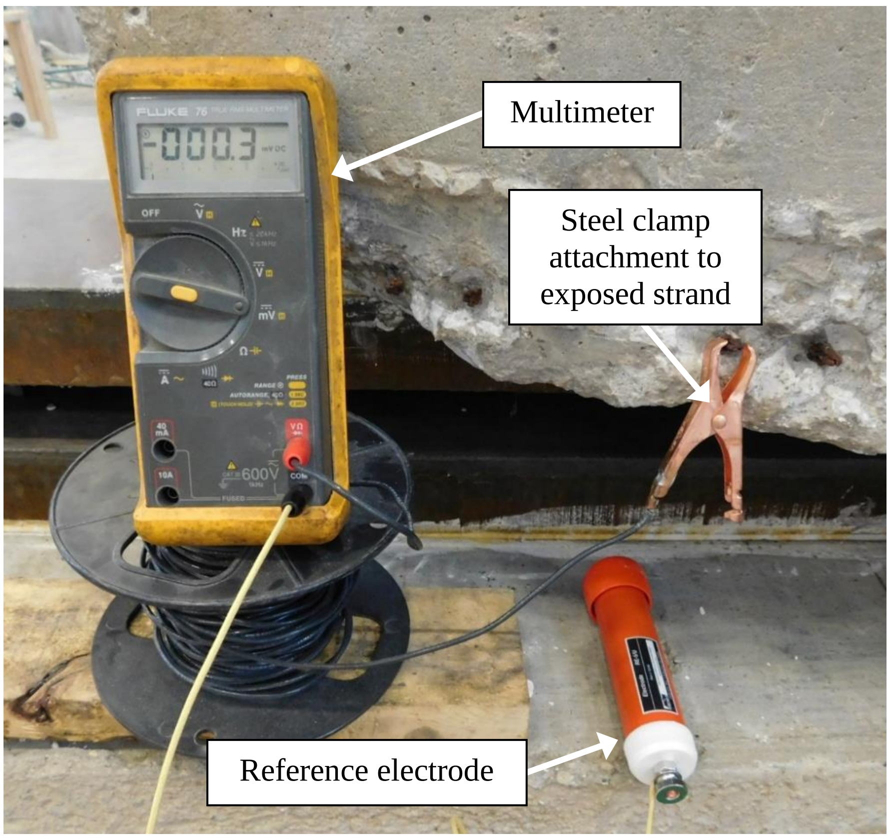

Figure 3.24: Half-Cell Potentials Measurement Equipment

ASTM C876 provides a correlation between the measured voltage, V_m, and the probability of corrosion as given in Table 3.5.

Table 3.5: ASTM C876 Probability of Corrosion Correlation

Color		Voltage Measurement, V_m (V)	Probability of Corrosion
Green	—	$V_m > -0.20$	90% probability of no corrosion
Yellow	—	$-0.20 \geq V_m \geq -0.35$	Probability of corrosion is uncertain
Red	—	$V_m < -0.35$	90% probability of corrosion
Black	—	No reading available	

The values of V_m presented in Table 3.5 correspond to readings taken with a copper-copper sulfate reference electrode at 72°F. ASTM C876 recommends correcting the voltage readings using Equation 3-2 if measurements are taken outside the range of 72°F ± 10°F. The temperature correction factor, *CF*, for copper-copper sulfate reference electrodes is 0.0005 V/°F for the range from 32°F to 120°F with 72°F taken as the reference temperature.

$$V_{m_{cor}} = V_m + CF * (T_{ref} - T) \tag{3-2}$$

where:

$V_{m_{cor}}$	=	temperature corrected voltage measurement (V)
V_m	=	voltage measurement (V)
CF	=	correction factor for the reference electrode (V/°F)
T_{ref}	=	reference temperature for the reference electrode (°F)
T	=	temperature at the time of measurement (°F)

The temperature was recorded with a thermometer before measurements were taken on each specimen. Equation 3-2 was used to correct each measurement. It should be noted that a change of 20°F is needed to change the voltage by 0.01 V. Therefore, the change in temperature that may have occurred while measurements were taken was considered negligible.

3.3.3.2 Half-Cell Potentials Results

The half-cell potentials results are provided in Figure 3.25. The results are displayed using the color coding from Table 3.5. The exposed strands in Specimens 409-1-ES, 56-2-ES, 102-1-BS, 102-2-BS, 102-3-BS, and 102-4-BS were not directly scanned. If the area adjacent to the exposed strand was not spalled, the strand was scanned. Results for Specimen 409-1-ES include the results from the area adjacent to the exposed strands. No suitable areas for scanning were available in portions of Specimens 56-2-ES, 102-1-BS, 102-2-BS, 102-3-BS, and 102-4-BS. The locations where no scan could be taken are indicated in Figure 3.25 by coloring the strand black.

In general, the half-cell potential results correlate well with the visual deterioration observed. A complete comparison between the half-cell potentials results and the results from the strand extraction is provided in Section 3.5.

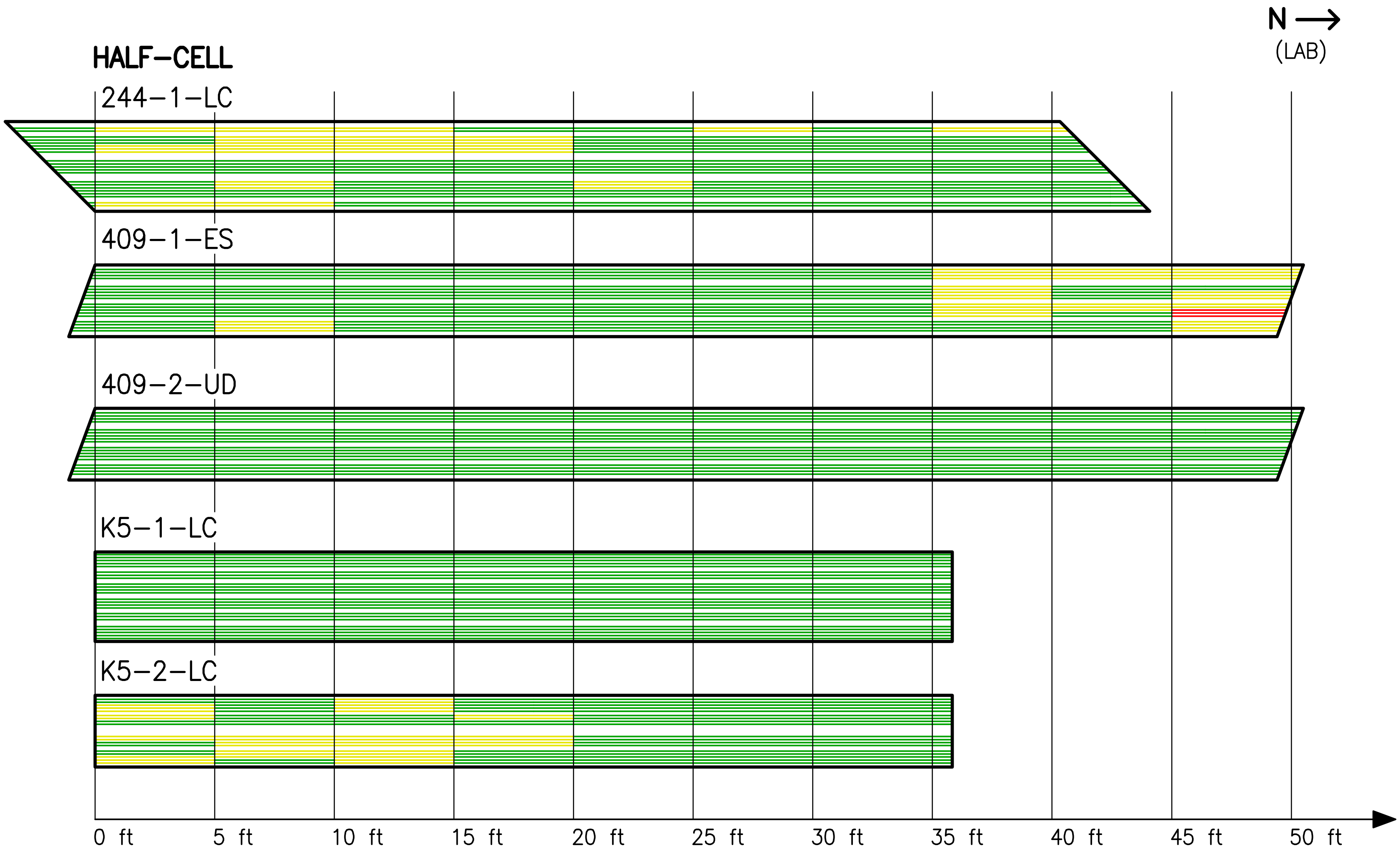

(a) Specimens 244-1-LC, 409-1-ES, 409-2-UD, K5-1-LC, and K5-2-LC

Figure 3.25: Half-Cell Potential Results

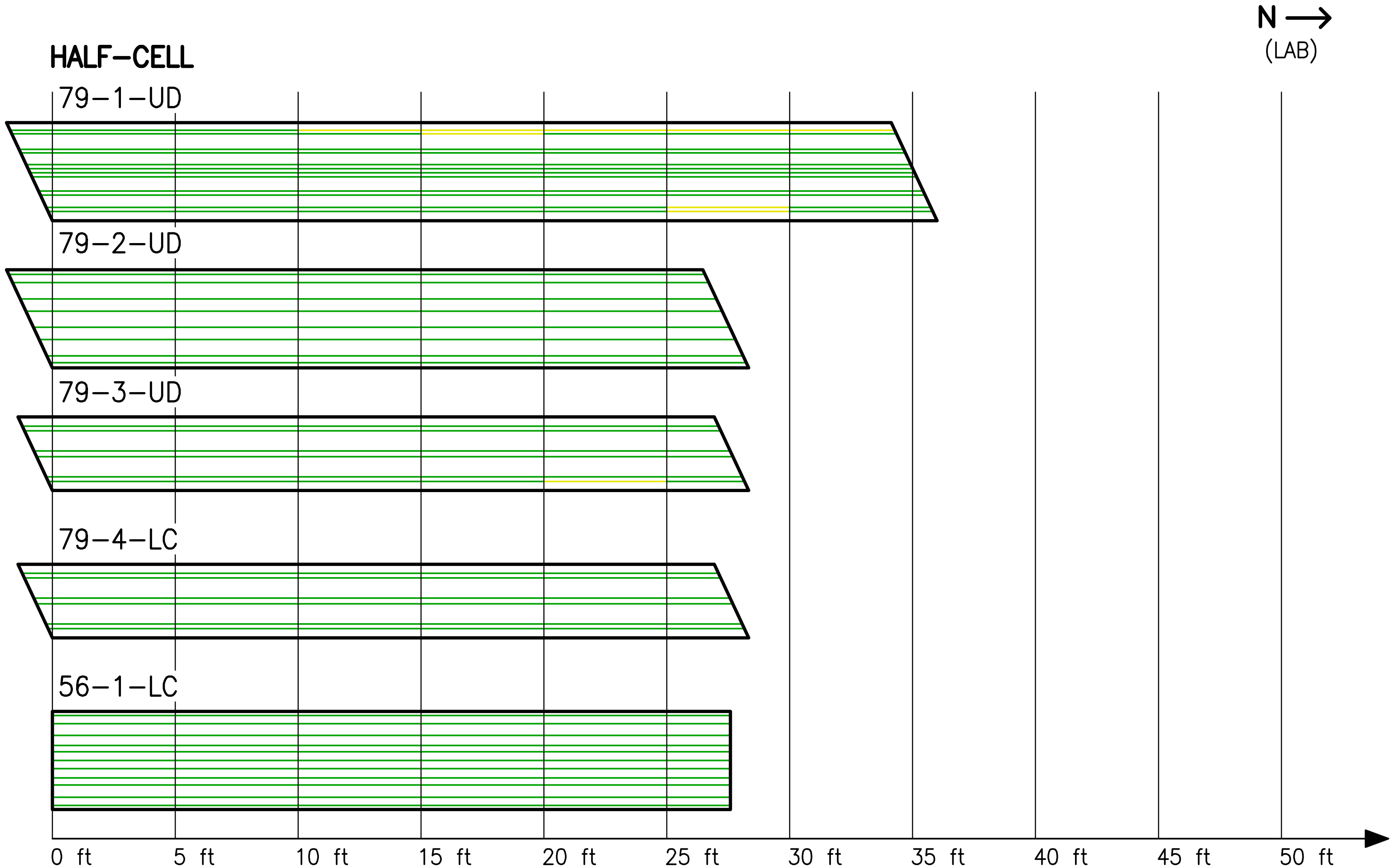

(b) Specimens 79-1-UD, 79-2-UD, 79-3-UD, 79-4-LC, and 56-1-LC

Figure 3.25: Continued

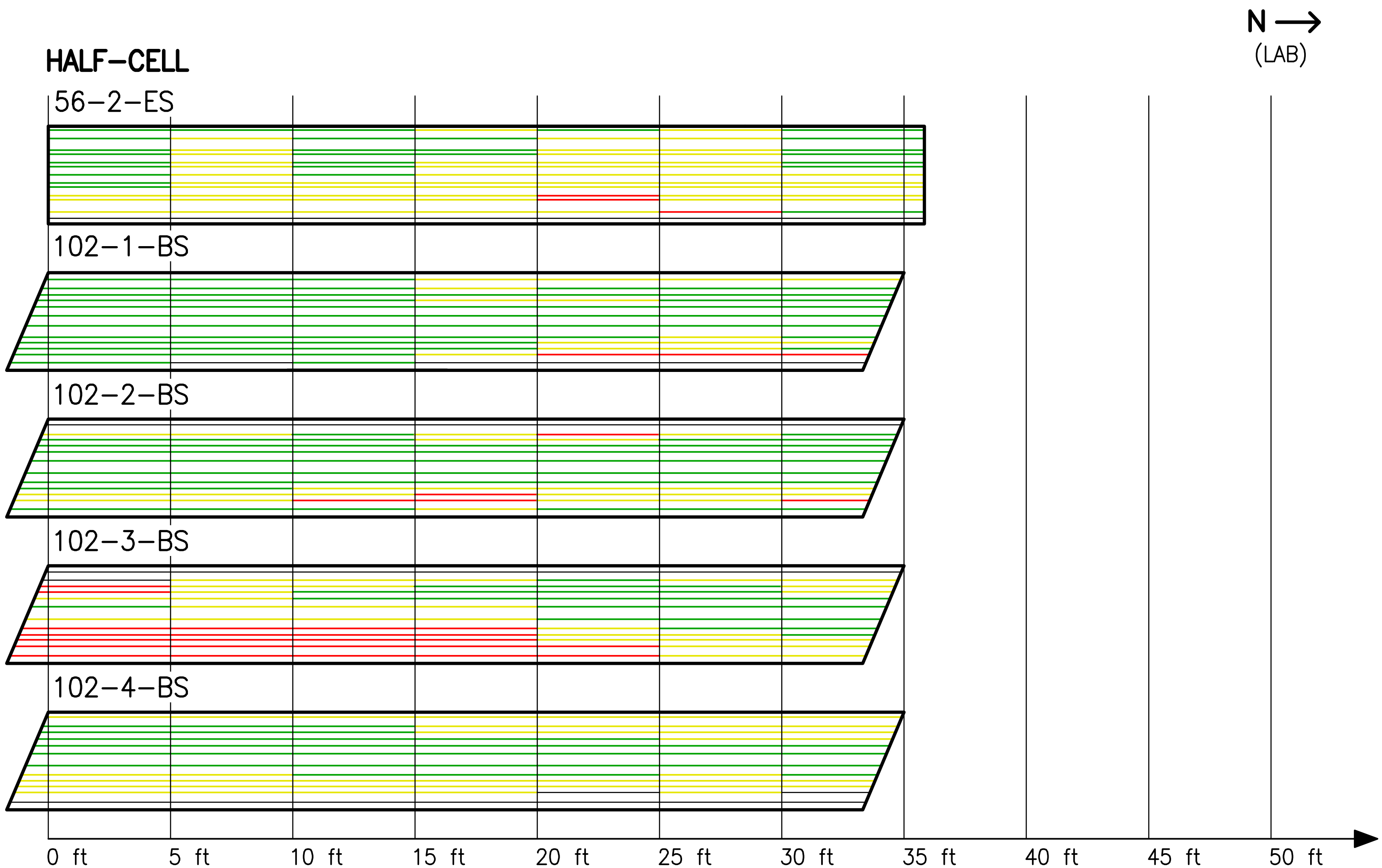

(c) Specimens 56-2-ES, 102-1-BS, 102-2-BS, 102-3-BS, and 102-4-BS

Figure 3.25: continued

3.3.3.3 Half-Cell Potentials User Notes

ASTM C876 (2015) provides all information needed to successfully conduct half-cell potentials measurements. The only error encountered during the use of the equipment was no readings could be taken directly over longitudinal cracks or on the rough surface of concrete spalls. When the reference electrode was positioned over a crack or on a spall, the voltage reading did not stabilize after approximately 5 minutes. The same result was found when the surface was treated in accordance with ASTM C876. When this error occurred, the electrode was positioned immediately adjacent to the longitudinal crack. If the reading did not stabilize after moving the position of the electrode, no reading was recorded.

3.4 Strand Extraction

To determine the actual extent of deterioration, the strands at and adjacent to the location of deterioration were extracted. The strands were extracted by removing the concrete cover using a combination of a jackhammer and a handheld concrete saw. Where corrosion was found on the strand, further cover was removed to determine the extent of corrosion. A summary of the corroded strands found in each specimen is provided in Section 3.5.

In the beam deterioration maps (Figure 3.1 to Figure 3.15), specimens with extensive deterioration were divided into segments labeled “A”, “B”, “C”, or “D” to further identify the location of deterioration. These segments correspond to cuts that were made through the depth of the beam to allow the beam pieces to be transported out of the laboratory for outdoor storage.

The strand extraction procedure was documented for each of the specimens with visual signs of deterioration. As discussed previously, two primary deterioration mechanisms resulted in corrosion of the prestressed strands in the bottom flange of box beams: leaking shear keys and water ingress to the box beam void. In the following sections, the extent of strand deterioration is examined for both deterioration mechanisms.

3.4.1 Leaking Shear Key Deterioration

Six beam specimens were observed with deterioration at the edges of the bottom flange (409-1-ES, 56-2-ES, 102-1-BS, 102-2-BS, 102-3-BS, and 102-4-BS). In the previous chapter, this type of deterioration was attributed to leaking shear key joints or the lack of curbs to prevent water from draining over the side of the bridge. In the following, the strand extraction procedure for the noted beam specimens is presented to determine the extent of deterioration associated with this type of deterioration.

3.4.1.1 Specimen 409-1-ES

In service, Specimen 409-1-ES was an exterior beam. The west side of the beam noted in Figure 3.26 corresponds to the side of the beam that faced the exterior. The region of deterioration shown corresponds to the location of a scupper drain where water drained from the bridge deck onto the side of the beam and curled onto the bottom flange. In Figure 3.2, the beam is shown with a spall and three exposed strands. Figure 3.26 shows the condition of the strands adjacent to the three exposed strands (Strands 2 to 4).

As shown in Figure 3.26(b), Strand 1 is completely corroded in addition to the exposed strands. Strand 1 was not exposed by the concrete spall, but deterioration was indicated by longitudinal cracking shown in Figure 3.26(a) and corner cracking shown in Figure 3.27. The corrosion of Strands 1 to 4 extended approximately 6 in. to the north and south of where the strands were exposed. Strand 5, located 4 in. east of Strand 4, has no observable corrosion. The measured bottom cover for all the strands was 1 in.

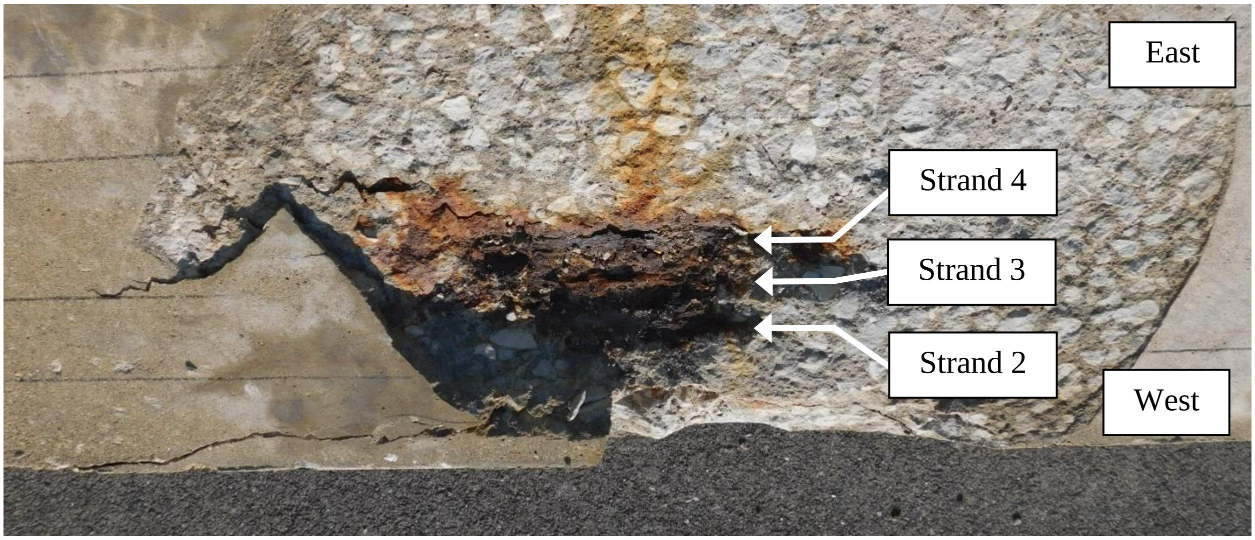

(a) Before cover was removed

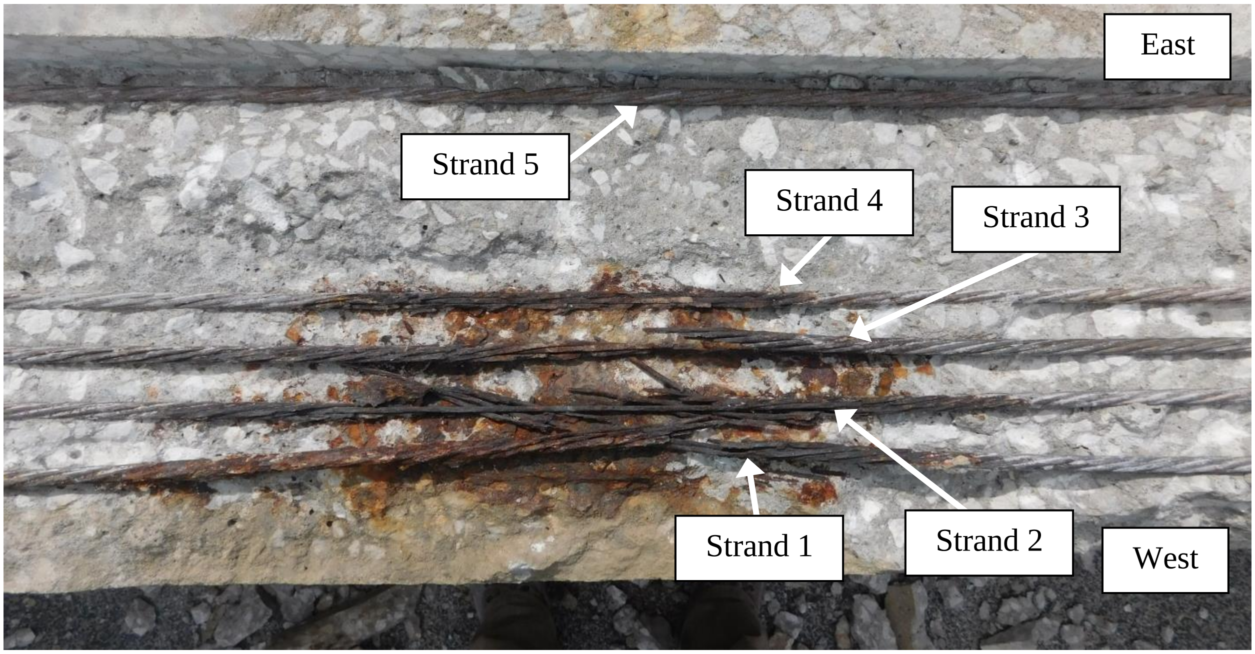

(b) After cover was removed

Figure 3.26: Strand Condition at Spall in Specimen 409-1-ES

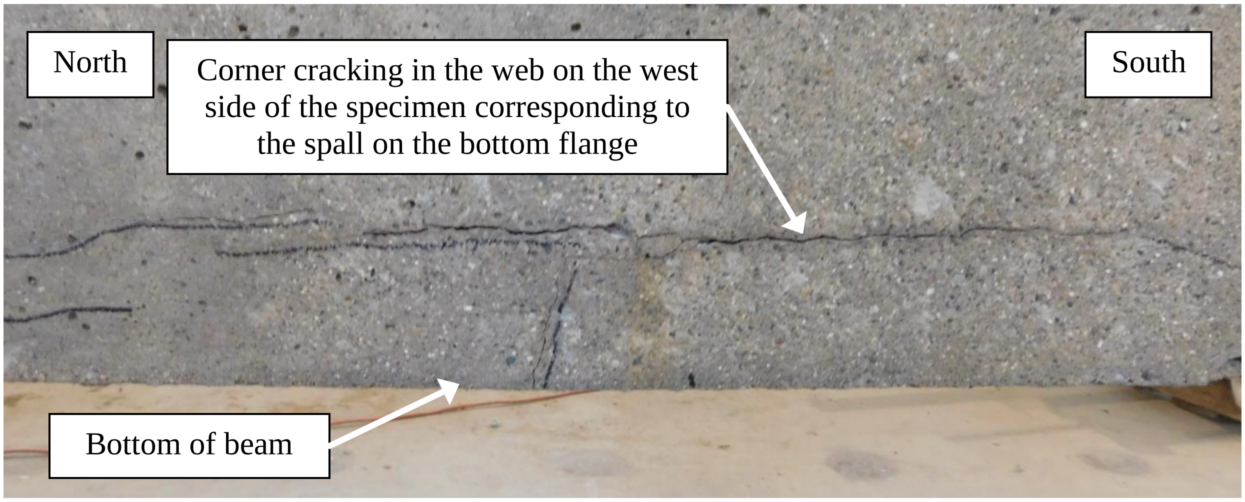

Figure 3.27: Corner Cracking at Concrete Spall in Specimen 409-1-ES

3.4.1.2 Specimen 56-2-ES

All deterioration of Specimen 56-2-ES was concentrated on the east side of the specimen (Figure 3.11). In service, Specimen 56-2-ES was an exterior beam with no curbs or other deck drains. The east side of the beam corresponds to the exterior side of the beam while in service. Figure 3.28 shows the representative condition of the strands adjacent to the exposed strand. As shown, Strand 12 (the strand adjacent to the exposed strand (Strand 13)) shows a small amount of surface corrosion but no pitting. The location of the exposed strand in Figure 3.28(b) is provided as a dashed white line for reference. Strand 11, shown in Figure 3.28(c) and located 6 in from Strand 12, was found without any observable corrosion. The measured bottom cover for all strands was 1-3/8 in.

Corrosion was observed on Strand 13 outside of the exposed region of the strand where a longitudinal crack extended from the concrete spall (Figure 3.29). Where the longitudinal crack ended, no corrosion of Strand 13 was observed. Only the length of strand at the longitudinal crack was corroded. No corrosion of Strand 13 was observed where no cracking or concrete spalling was observed.

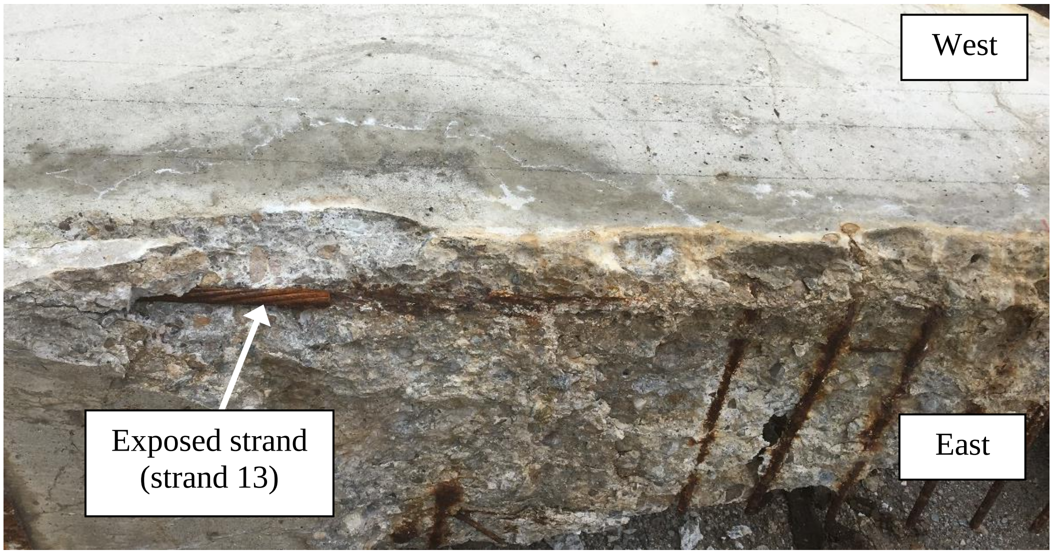

(a) Before cover was removed

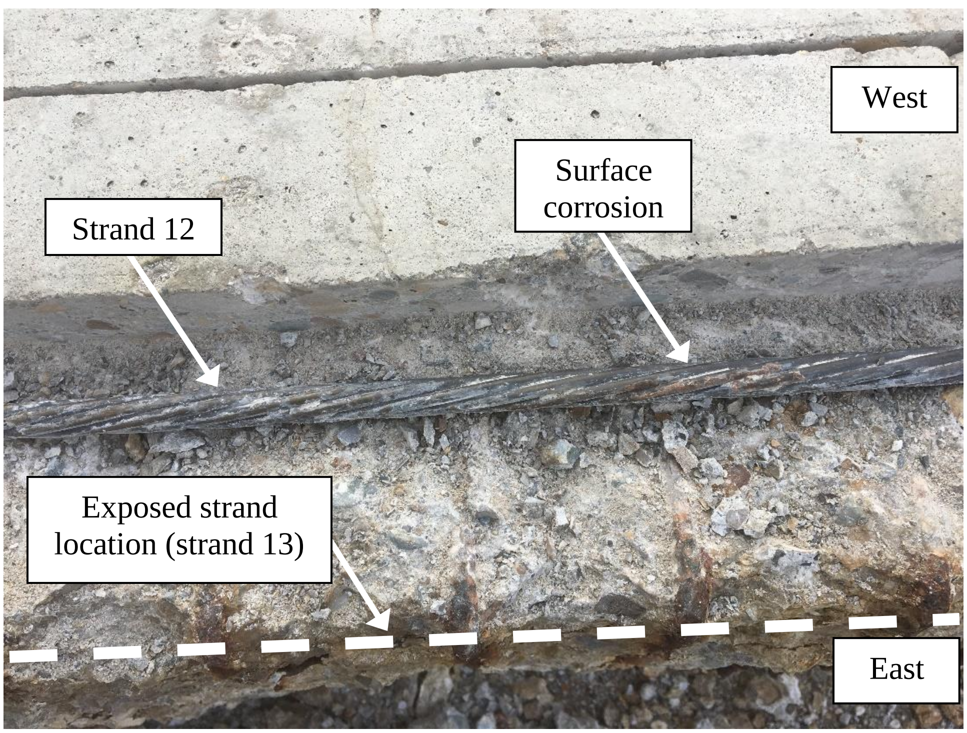

(b) After cover was removed from strand 12

Figure 3.28: Representative Condition of Strands Adjacent to the Exposed Strand in Specimen 56-2-ES

(c) After cover was removed from strand 11

Figure 3.28: Continued

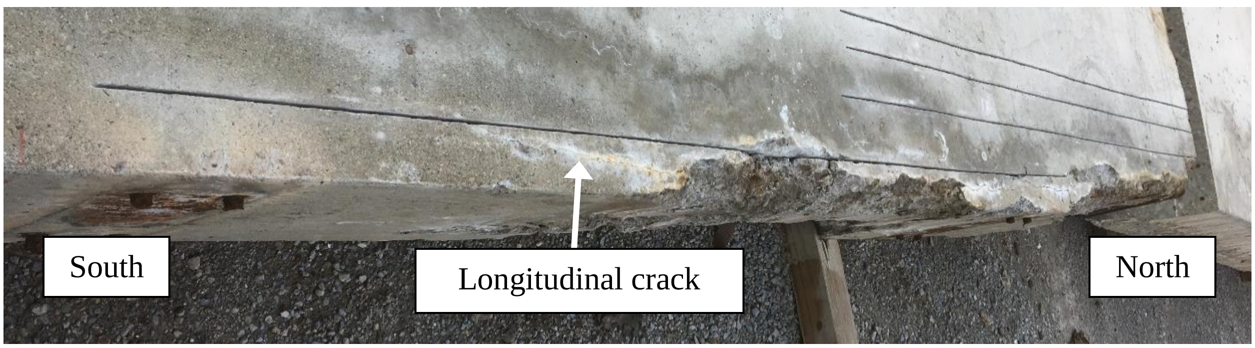

(a) Before cover was removed

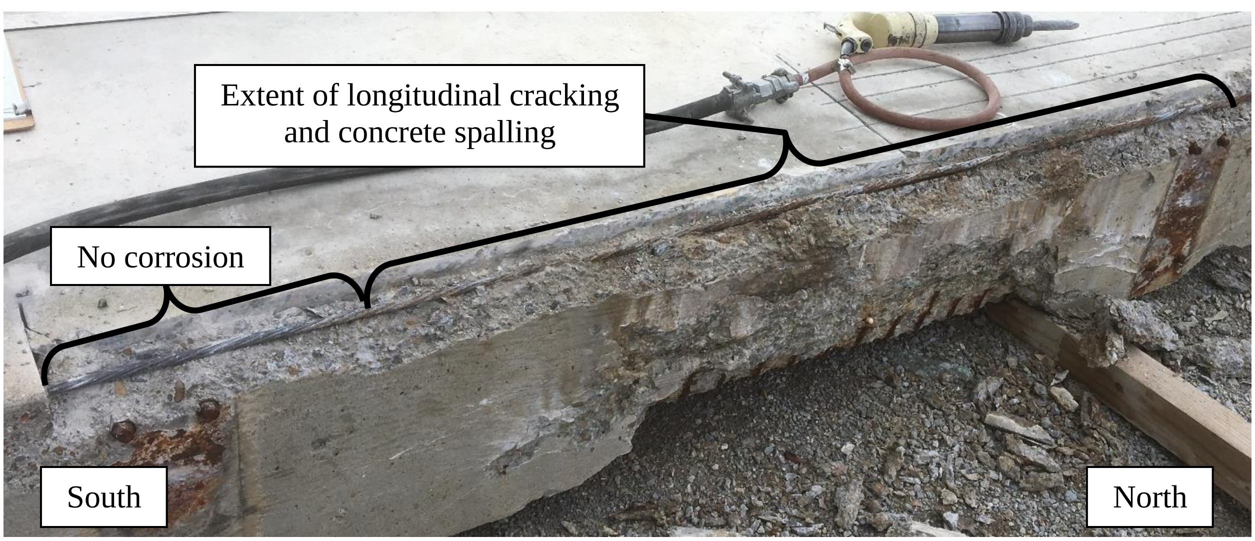

(b) After cover was removed

Figure 3.29: Extent of Corrosion in Exposed Strand in Specimen 56-2-ES

3.4.1.3 Specimen 102-1-BS

Specimen 102-1-BS was an interior beam while in-service. The deterioration of the specimen was concentrated on the east edge of the bottom flange at the longitudinal joint (Figure 3.12). The deterioration consisted of longitudinal cracking, an exposed strand, and a broken strand.

Figure 3.30 to Figure 3.32 show the condition of Strand 11 which is adjacent to the corroded edge strand. As shown in Figure 3.30(a), the corrosion on Strand 12 in Segment A extended approximately 2 in. from the exposed region of the strand. In Figure 3.32, a dashed white line represents the original location of the broken strand (Strand 12). Corrosion of Strand 11 was only observed in Segment C, where the strand was adjacent to the broken portion of Strand 12. In addition, at the location of the broken strand, no corrosion was observed on Strand 10. The corrosion on Strand 12 in Segment C was limited to the length of the longitudinal cracks and corner cracks extending north and south from the exposed region of Strand 12 (Figure 3.12). Notably, Strand 11 was located 4 in. from Strand 12, and Strand 10 was located 3 in. from Strand 11.

As shown in Figure 3.30 to Figure 3.32, a nonprestressed #3 bar was found at each location of deterioration. The bar was assumed to have been used during construction of the beam to support the transverse reinforcement. The location of the bar in Figure 3.31 indicates that the lack of side cover at that location (1 in.) may have resulted in premature deterioration of Strand 12. In the other locations, however, the bar was located between Strands 11 and 12 and had adequate side cover. The measured bottom cover for all strands and nonprestressed reinforcement was 1-1/2 in.

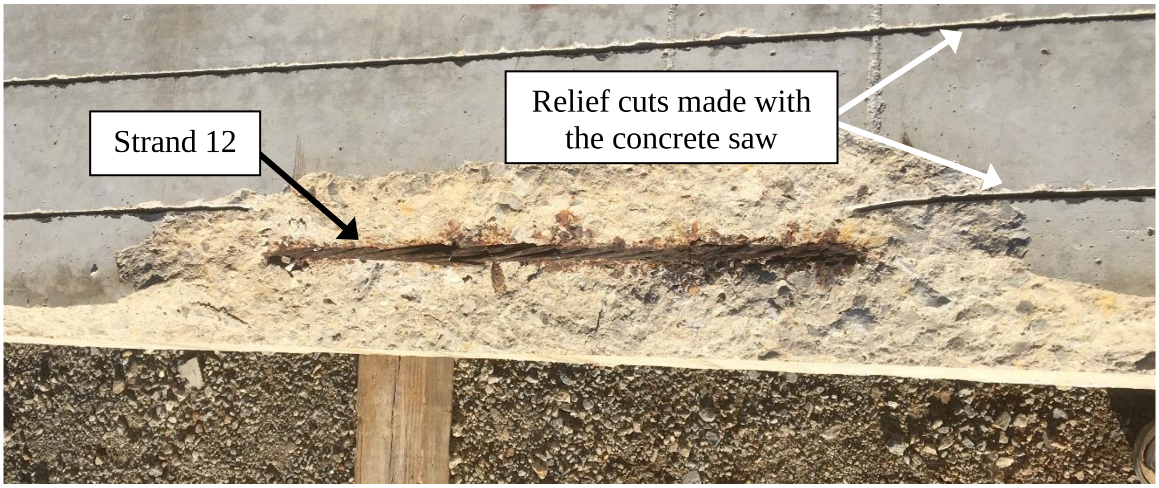

(a) Before cover was removed

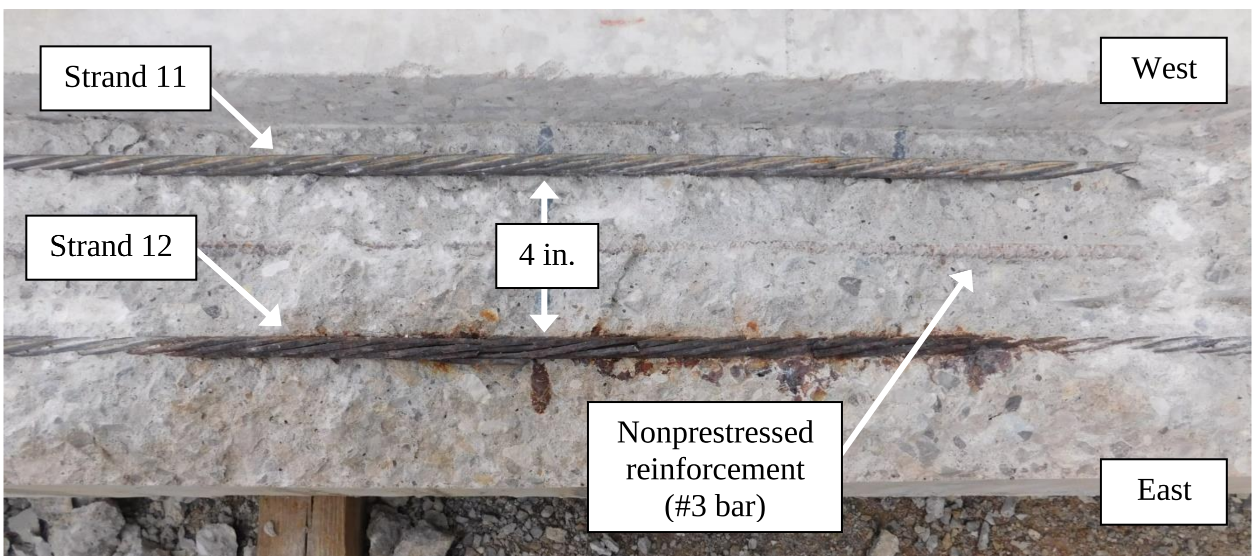

(b) After cover was removed

Figure 3.30: Strand Condition at Exposed Strand in Segment A of Specimen 102-1-BS

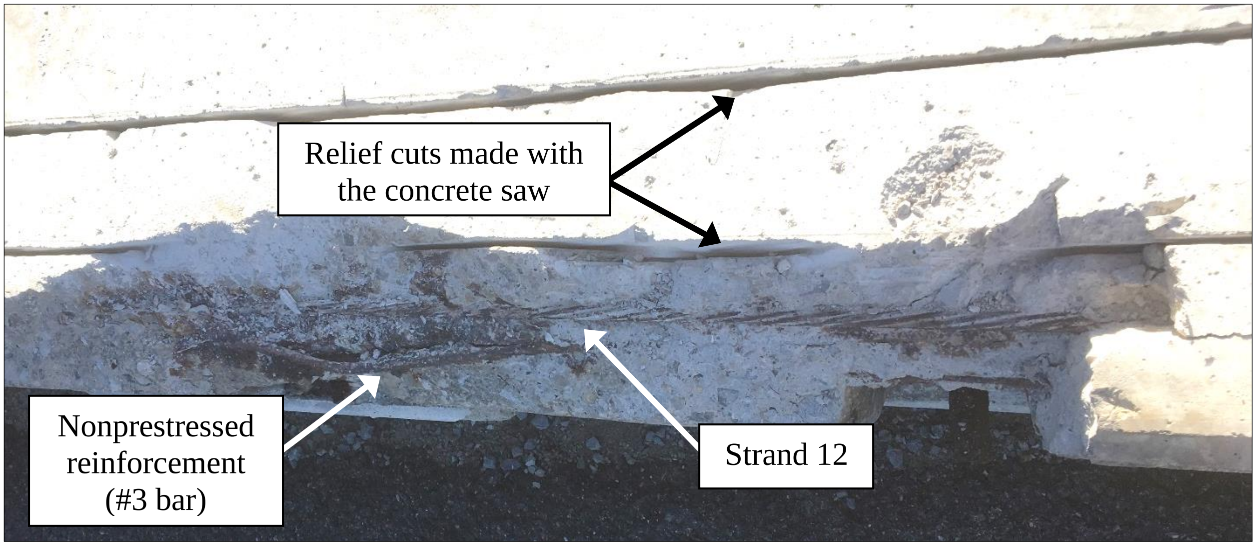

(a) Before cover was removed

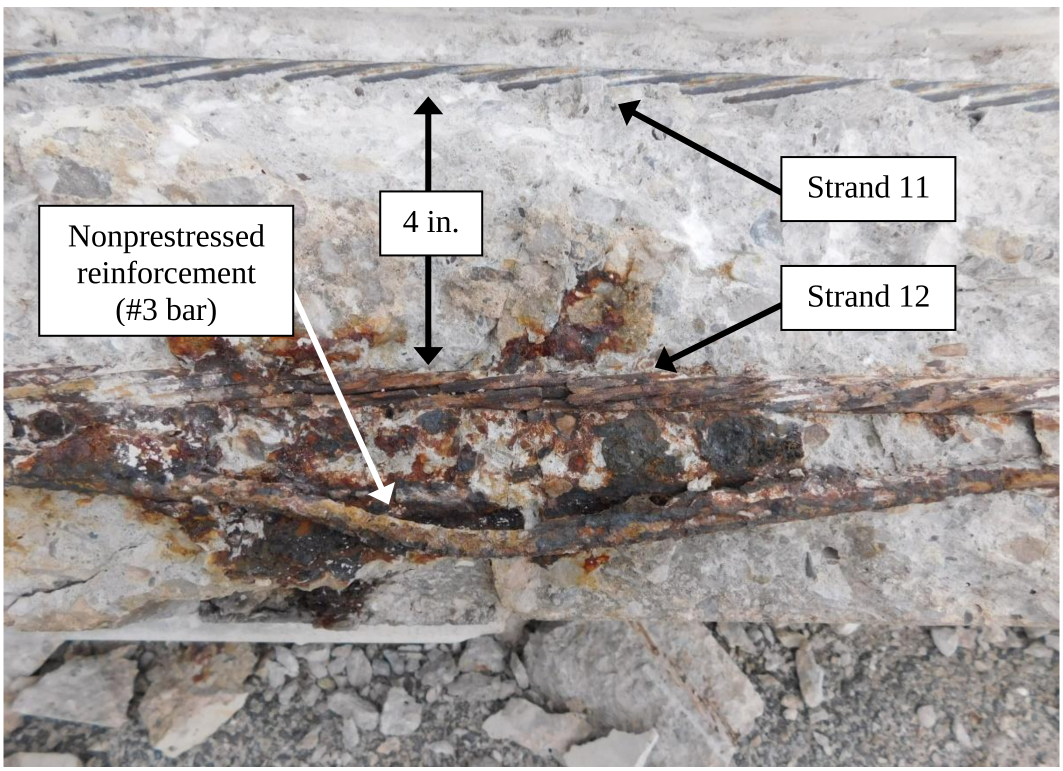

(b) After cover was removed

Figure 3.31: Strand Condition at Corner Crack in Segment B of Specimen 102-1-BS

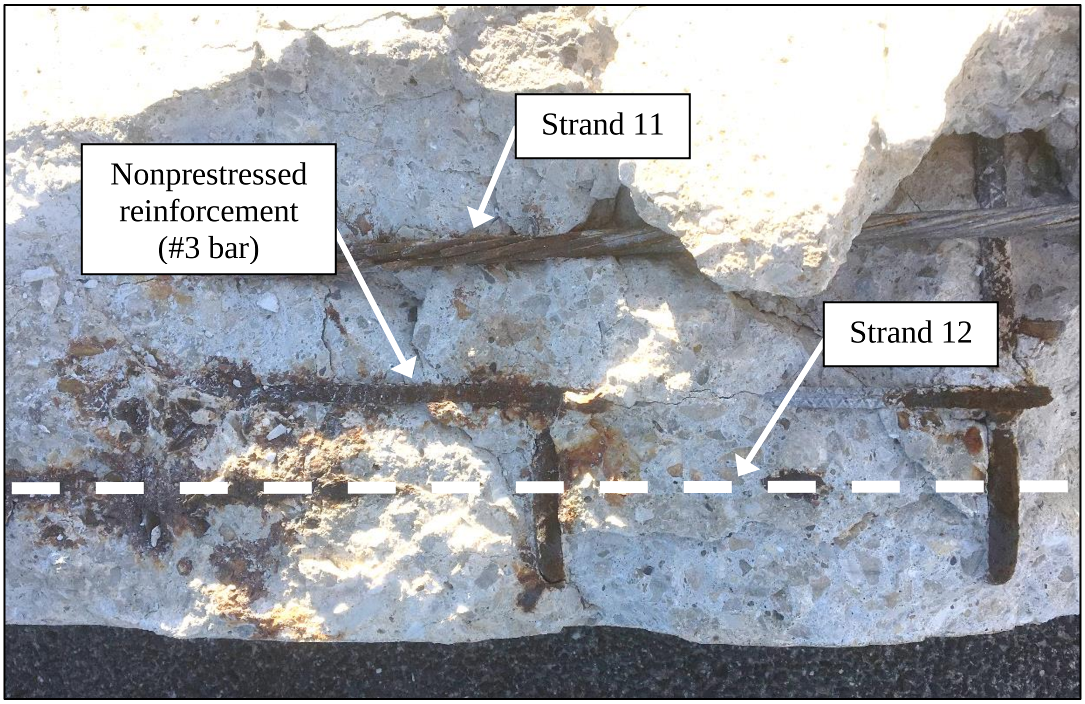

(a) Before cover was removed (note partial cover removal from structural test)

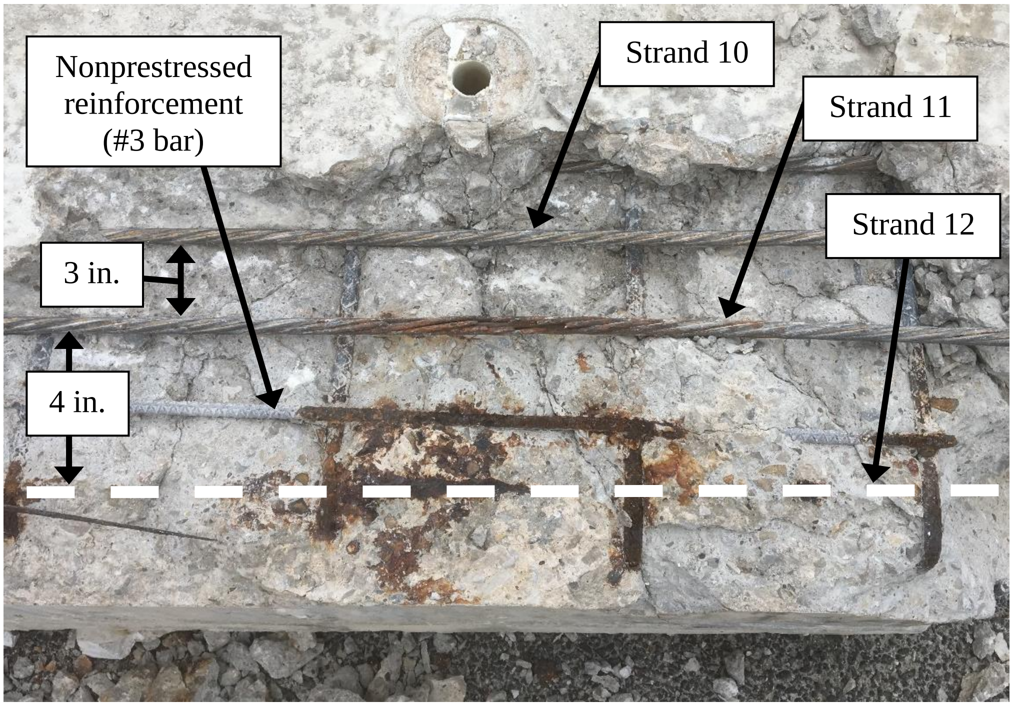

(b) After cover was removed

Figure 3.32: Strand Condition at Broken Strand Location in Segment C of Specimen 102-1-BS

3.4.1.4 Specimen 102-2-BS

Specimen 102-2-BS was an interior beam in-service. In Figure 3.13, 102-2-BS is shown with a broken strand on the west beam edge and longitudinal cracks on the east beam edge. The condition of the strands at the locations of deterioration are shown in Figure 3.33 for longitudinal cracking in Segment B and Figure 3.34 for the exposed and broken strand in Segment C. In Segment B, Strand 12 was observed with severe corrosion while Strand 11, located 4 in. from Strand 12, was found with no corrosion. Strand 2 in Segment C was located 5 in. from Strand 1 (the broken strand) and was observed to have no corrosion. The measured bottom cover of all the reinforcement was 1-5/8 in.

The longitudinal extent of the corrosion of Strand 1 was limited to the exposed length of the broken strand. Similar to Strand 1, the extent of corrosion along the length of Strand 12 was limited to the extent of the longitudinal cracking shown in Figure 3.13 (Figure 3.33(b)).

A #3 bar was found next to the edge strands (Strands 1 and 12) in 102-2-BS. Similar to 102-1-BS, the bars were assumed to have been used for construction. For both beam edges, the #3 bar was corroded, and the first interior strands (Strands 2 and 11) were not.

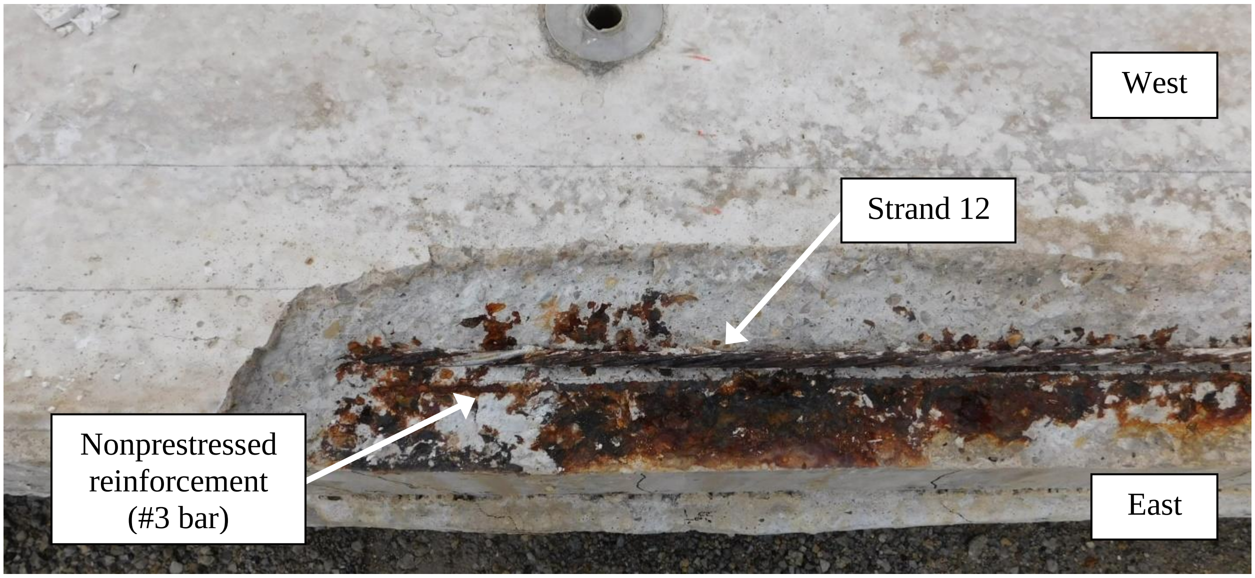

(a) Before cover was removed (portion of cover fell off during structural test)

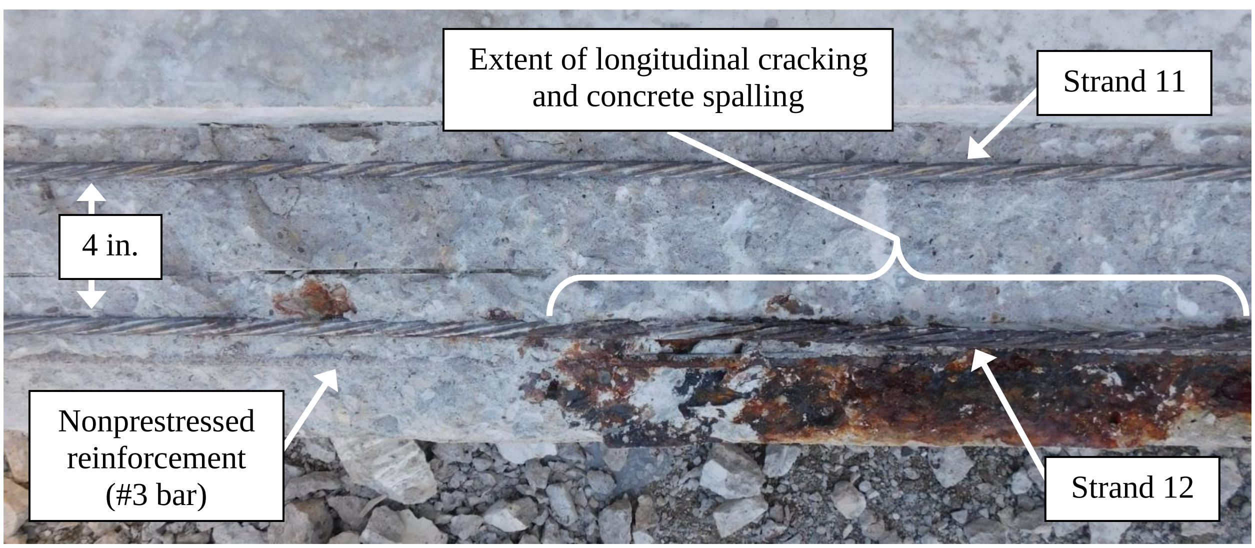

(b) After cover was removed

Figure 3.33: Strand Condition at Longitudinal Cracks in Segment B of Specimen 102-2-BS

(a) Before cover was removed

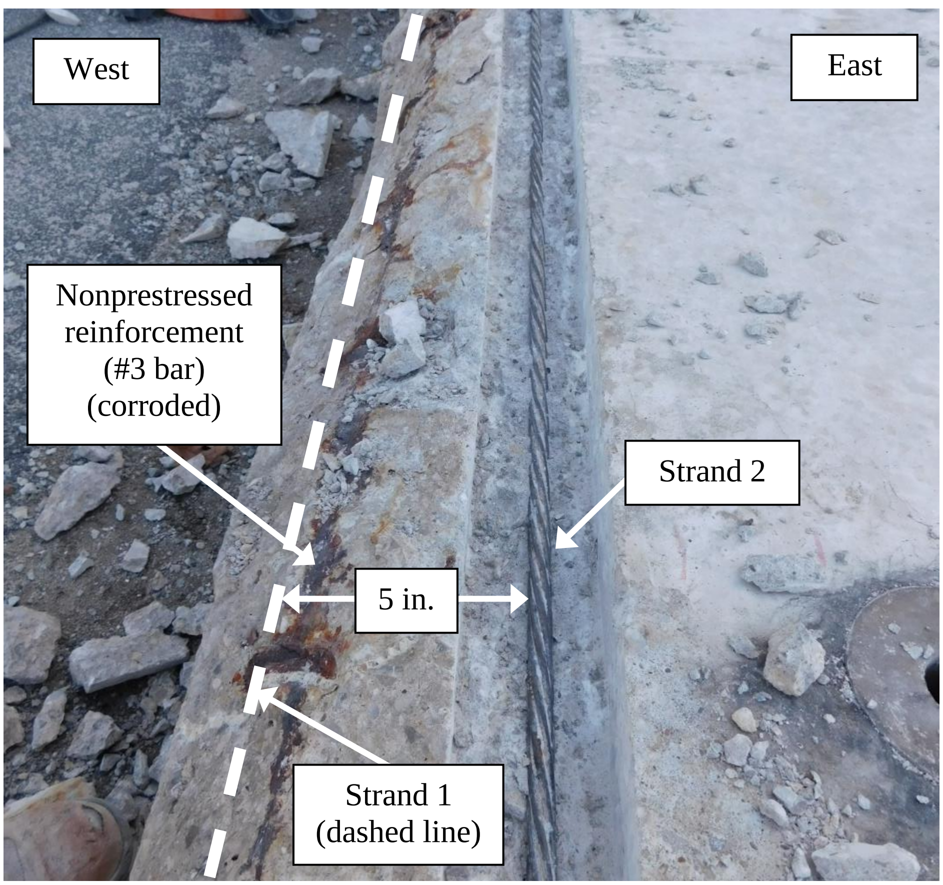

(b) After cover was removed

Figure 3.34: Strand Condition at Broken Strand in Segment C of Specimen 102-2-BS

3.4.1.5 Specimen 102-3-BS

In service, 102-3-BS was an exterior beam without a curb or other drainage system. The deterioration shown in Figure 3.14 consists of exposed and broken strands on the west side of the beam and longitudinal cracking on the east side of the beam. The east side of the beam corresponds to the exterior side of the beam while in service. During the bridge inspection, the exterior side of the beam was wet while the interior side was dry (Figure 3.35). In Figure 3.36, longitudinal cracks were observed prior to structural testing within the wet region shown in Figure 3.35. The representative condition of the strands at the locations of deterioration is provided in Figure 3.37 to Figure 3.39.

In Figure 3.37, longitudinal cracks are noted on the east side of Segment A. The approximate locations of Strands 9 to 12 have been indicated in Figure 3.37(a) with white dotted lines. Strands 9 to 12 were found corroded in the region shown in Figure 3.37(b), and Strand 8 was observed with surface corrosion. The strand spacing between Strands 11 and 12 was 4-1/4 in. The corroded strands correspond to the region of the beam that was cracked and heavily stained.

In Figure 3.38 and Figure 3.39, the same trend in deterioration was observed as in the previous specimens. No corrosion was observed on the strands adjacent to corroded strands at longitudinal cracks, and a large spacing was measured between strands. The strand spacing was 4 in. between Strands 1 and 2, and 3 in. between Strands 2 and 3.

The longitudinal extent of corrosion associated with longitudinal cracking corresponded to the extent of the longitudinal crack. For exposed strands (Strands 1 and 2), corrosion was observed to extend approximately 1 to 2 in. past the concrete spall on either end of the exposed region.

The measured bottom cover for all reinforcement was 1-1/2 in. The side cover to the edge strands was 4 in. on the west edge and 3 in. on the east edge.

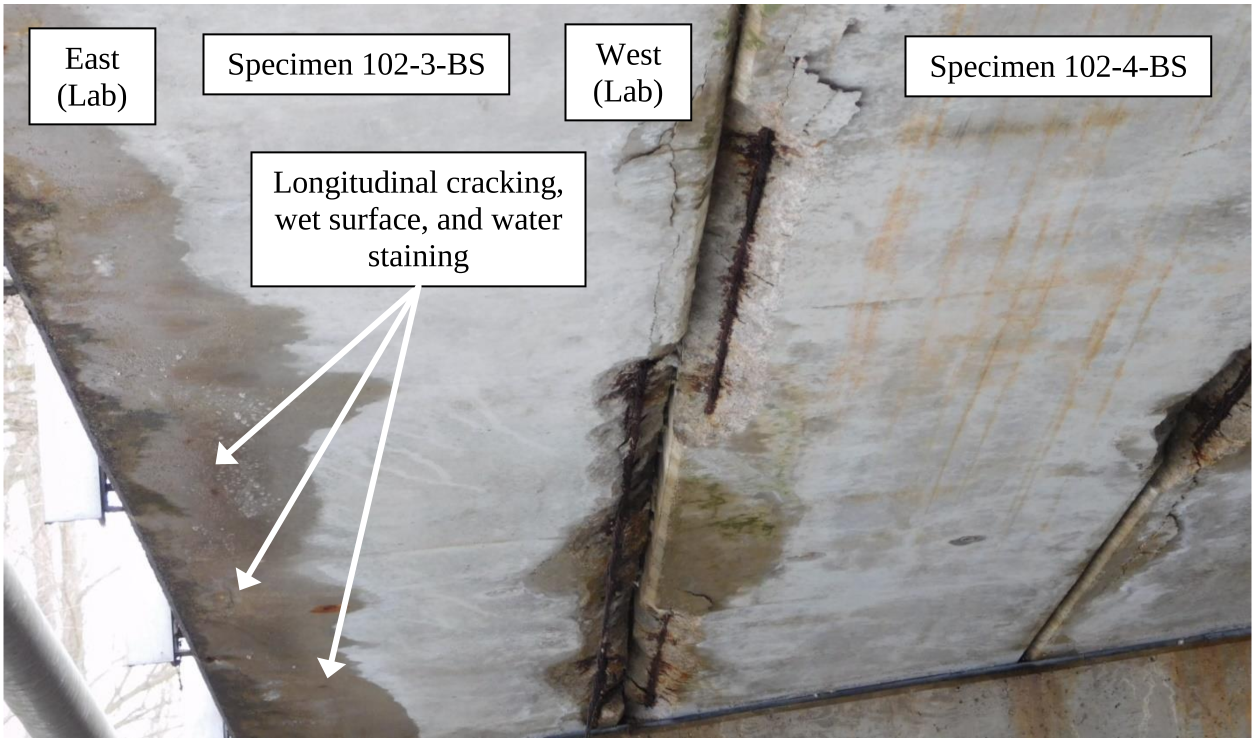

Figure 3.35: Condition of Specimen 102-3-BS in Service

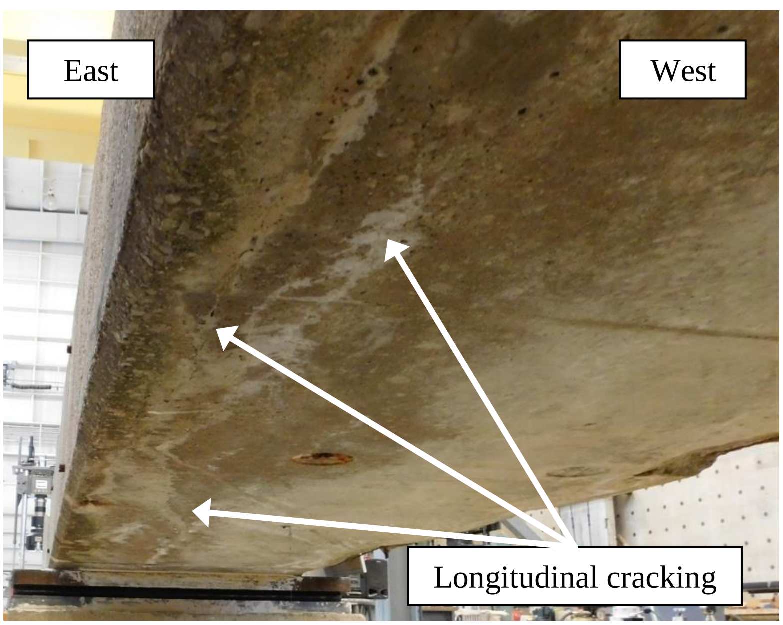

Figure 3.36: Longitudinal Cracking in Specimen 102-3-BS Prior to Structural Testing

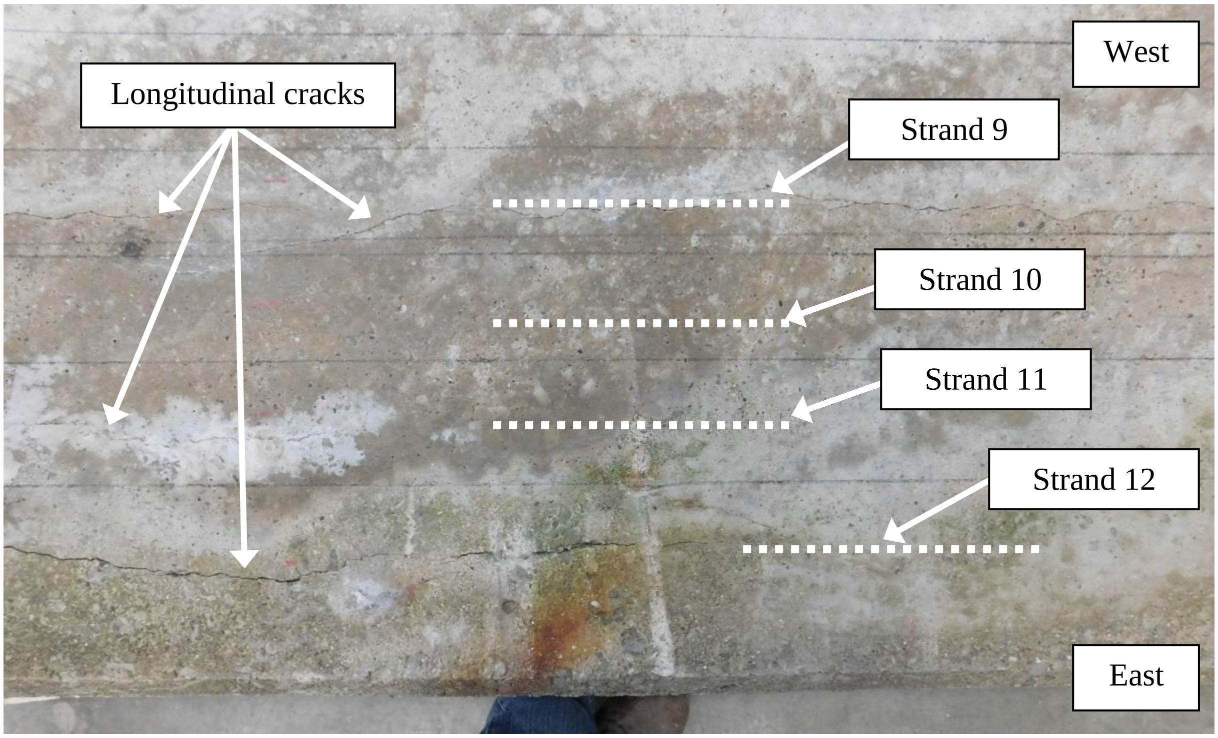

(a) Before cover was removed

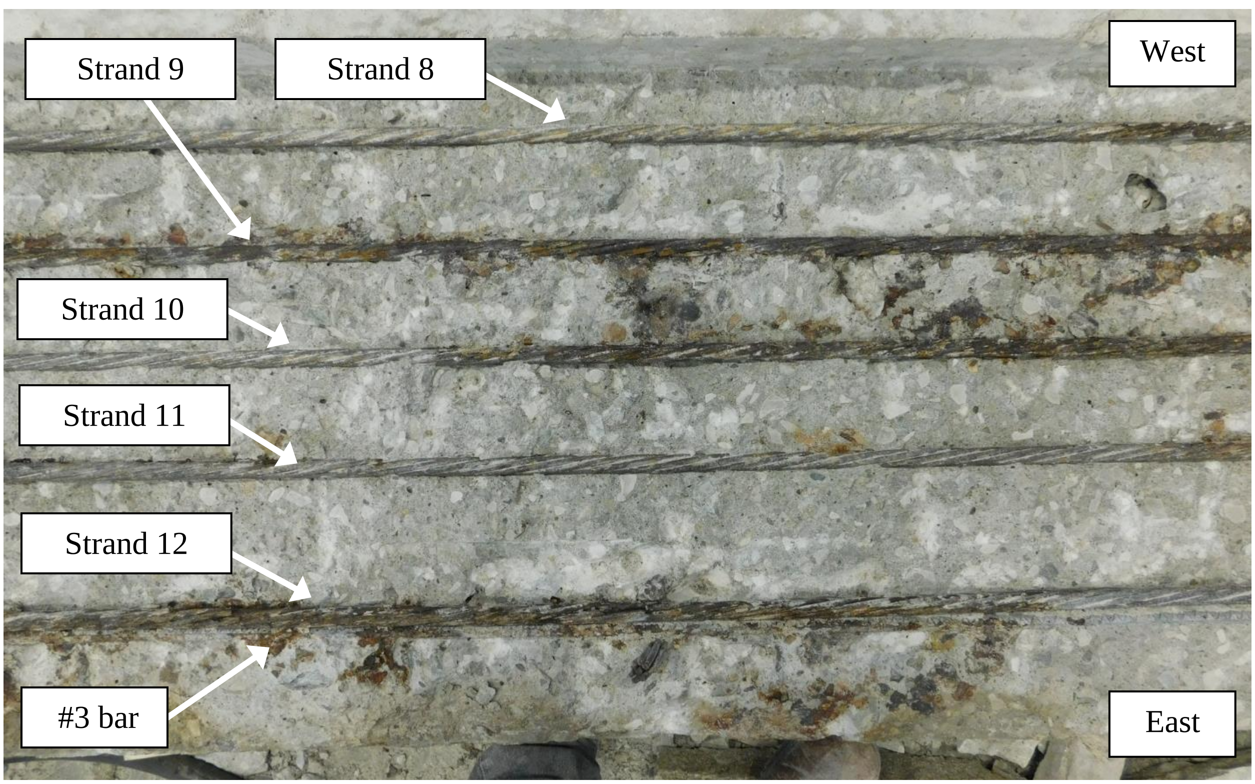

(b) After cover was removed

Figure 3.37: Strand Condition at Longitudinal Cracks in Segment A of 102-3-LC

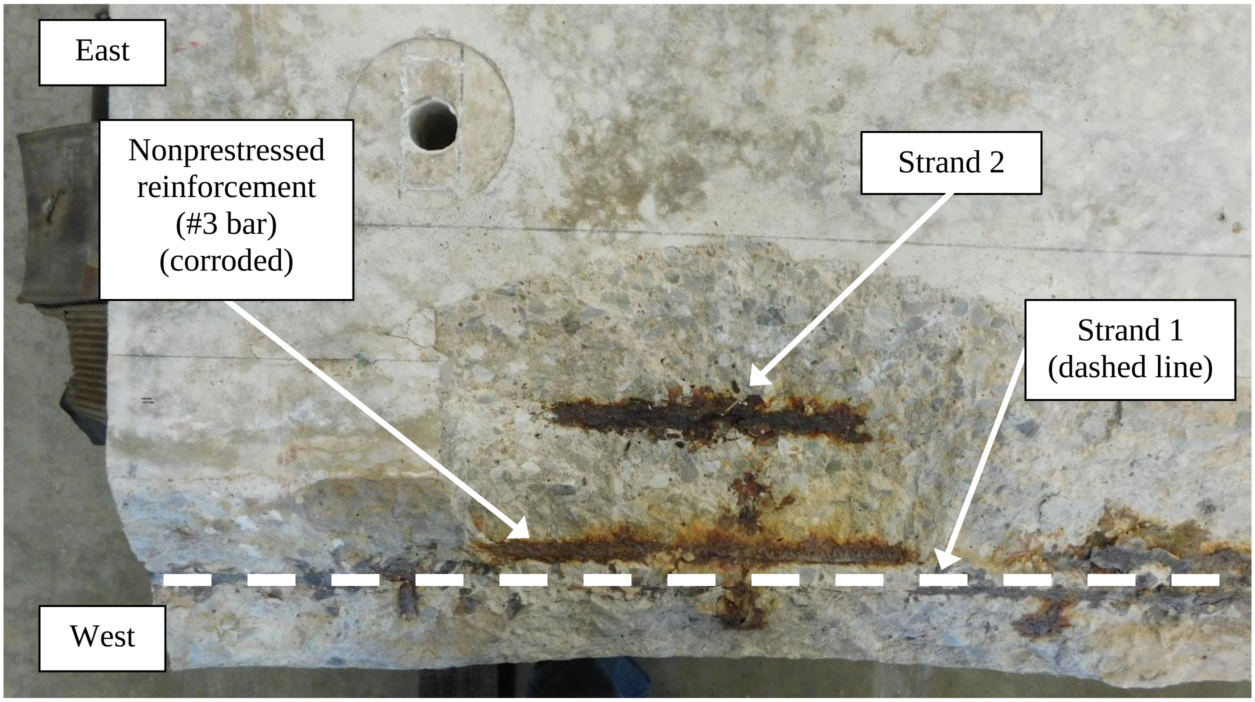

(a) Before cover was removed

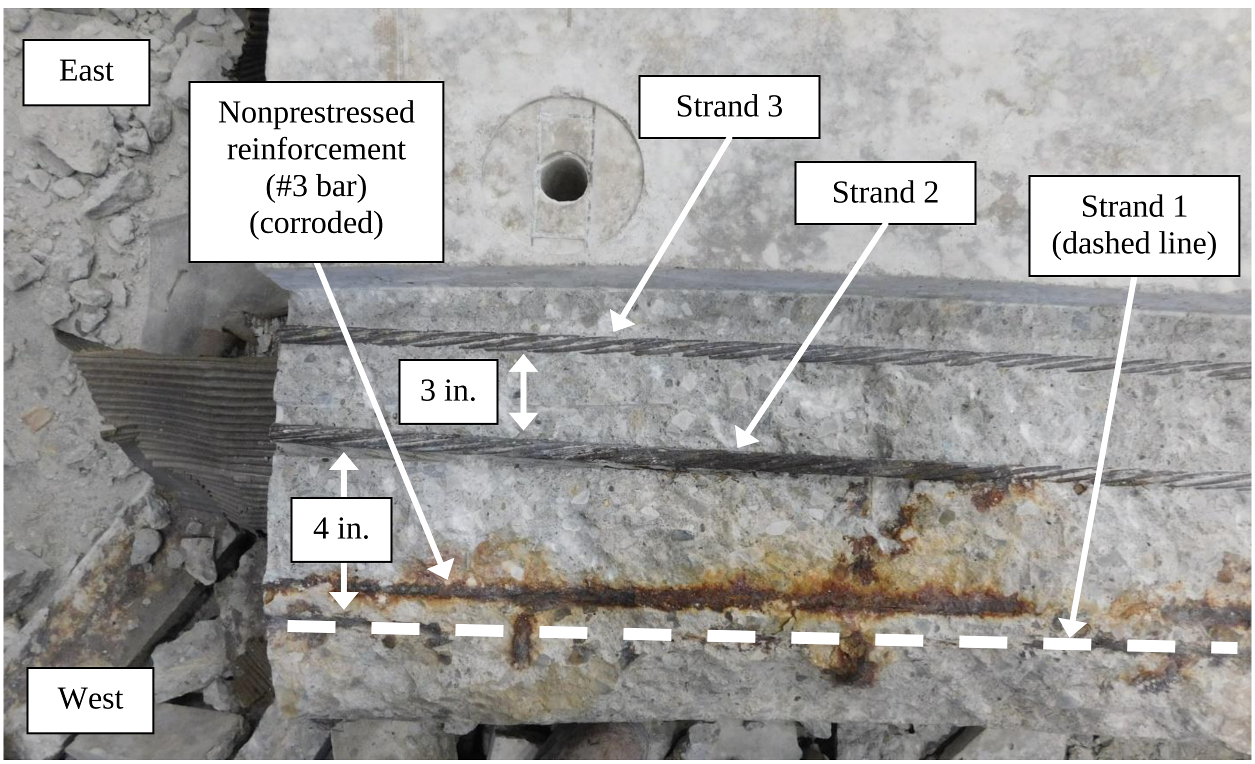

(b) After cover was removed

Figure 3.38: Strand Condition at Exposed and Broken Strands in Segment B of Specimen 102-3-BS

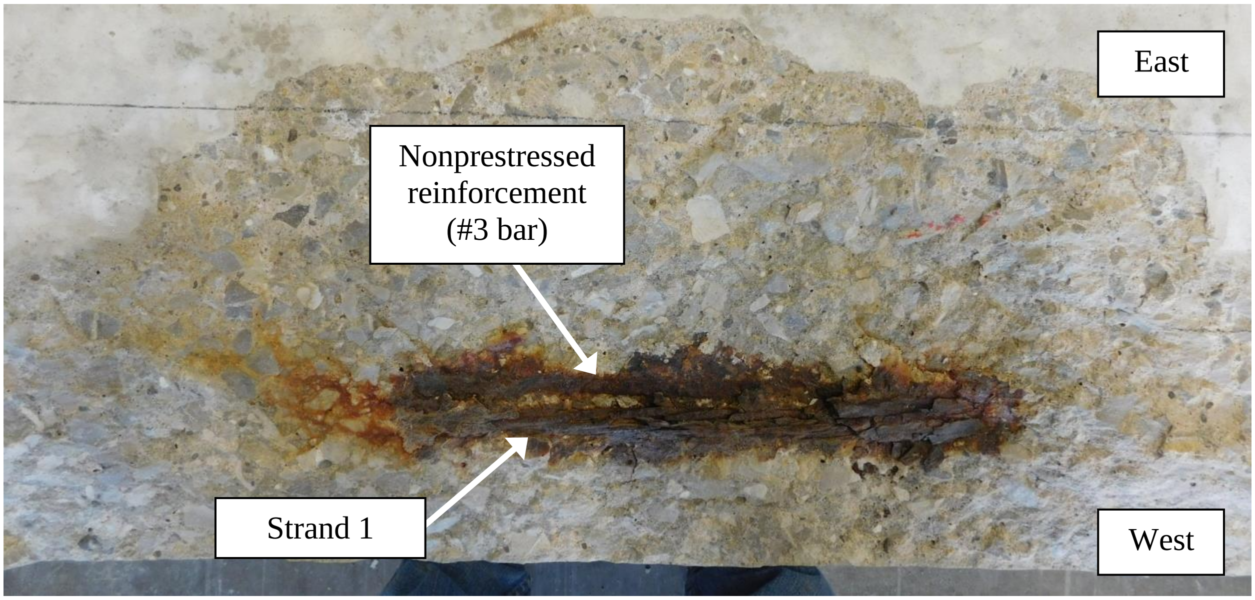

(a) Before cover was removed

(b) After cover was removed

Figure 3.39: Strand Condition at the Exposed Strand in Segment D of Specimen 102-3-BS

3.4.1.6 Specimen 102-4-BS

Specimen 102-4-BS was an interior beam while in service. In Figure 3.15, Specimen 102-4-BS is shown with longitudinal cracks and exposed strands the west and east edges of the bottom flange. A broken strand is also located on the east side of the bottom flange. The representative condition of the strands at the location of deterioration is provided in Figure 3.40 to Figure 3.46.

In the northeast end of Segment B, there was an exposed strand (Strand 11) adjacent to a broken strand (Strand 12) (Figure 3.40(a)). When cover was removed from Strand 10, no corrosion was observed (Figure 3.40(b)). The spacing of strands was 3-1/4 in. between Strands 10 and 11 and 4-3/4 in. between Strands 11 and 12.

The exposed strand (Strand 12) in the southeast end of Segment B was further exposed during the structural test (Figure 3.41(a)). When cover was removed from Strand 11, a small section of corrosion was found, and delamination of the concrete was observed when the cover was chipped away. Cover was then removed from Strands 8 to 10 to determine the extent of the delamination (Figure 3.41(b)). Strands 9 and 10 were found with sections of corrosion and Strand 8 was found with no corrosion. The corrosion on Strand 9 corresponds to the existing longitudinal crack shown in Figure 3.42. The corrosion on Strands 10 and 11 correspond to a transverse crack observed prior to testing (Figure 3.43). It should be noted that the light corrosion at the crack was localized and consisted of mainly surface rust.

The exposed strand (Strand 1) in Figure 3.44(a) was exposed during the structural test. Prior to the structural test, deterioration was indicated by longitudinal cracks in the bottom flange and side of the beam at the level of the strand (Figure 3.45). When cover was removed, only Strand 1 was found to be corroded. No corrosion was found on Strand 2.

The exposed strand (Strand 1) in Figure 3.46 was located in the southwest portion of Segment B. After cover was removed from Strands 1 to 3, surface corrosion was observed on

Strand 2 (Figure 3.46(b)). Prior to the removal of cover, the concrete spall extended to Strand 2 but had not exposed the strand.

The longitudinal extent of corrosion was found to be consistent with the specimens previously discussed. Corrosion related to longitudinal cracking corresponded to the extent of the crack. Outside of the cracked region, no corrosion was observed. Corrosion in exposed strands extended approximately 1 to 2 in. outside of the concrete spalling.

The side cover for the edge strands was measured to be 2-3/4 in. on the west edge and 3-1/2 in. on the east edge. The measured bottom cover for all reinforcement was 1-1/2 in.

(a) Before cover was removed

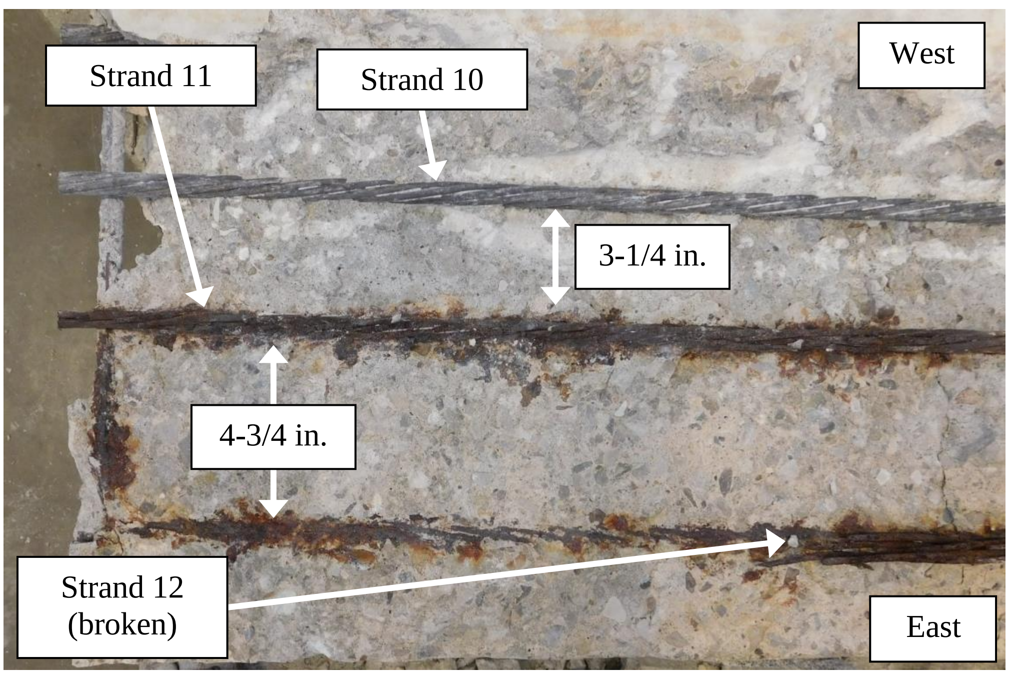

(b) After cover was removed

Figure 3.40: Strand Condition at North Exposed and Broken Strand in Northeast Portion Segment B of Specimen 102-4-BS

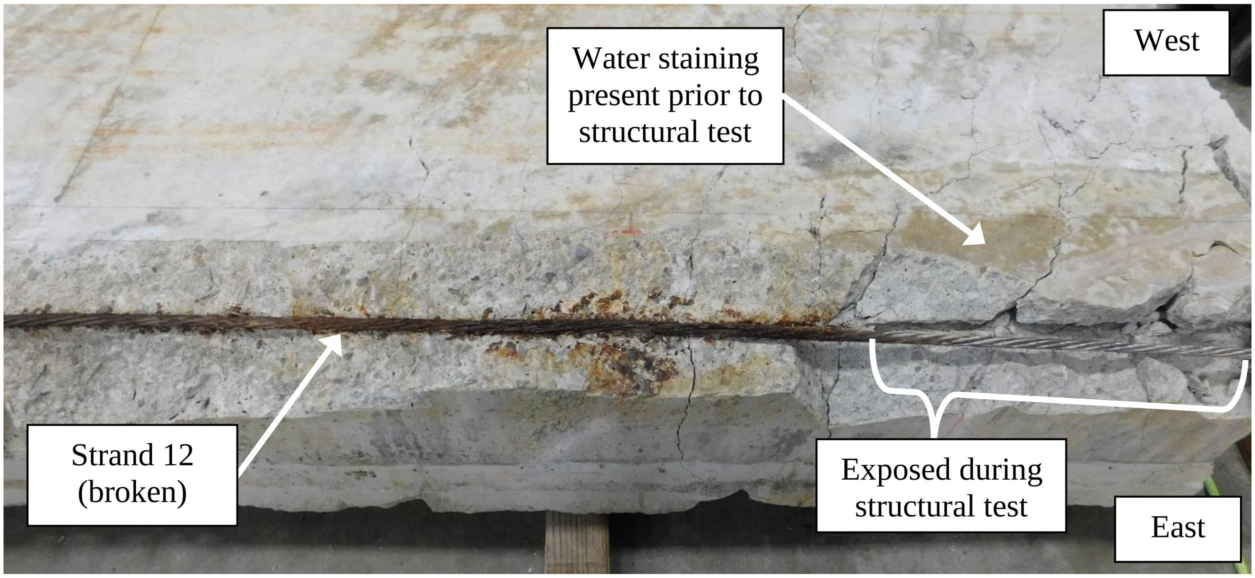

(a) Before cover was removed (partial removal occurred during structural test)

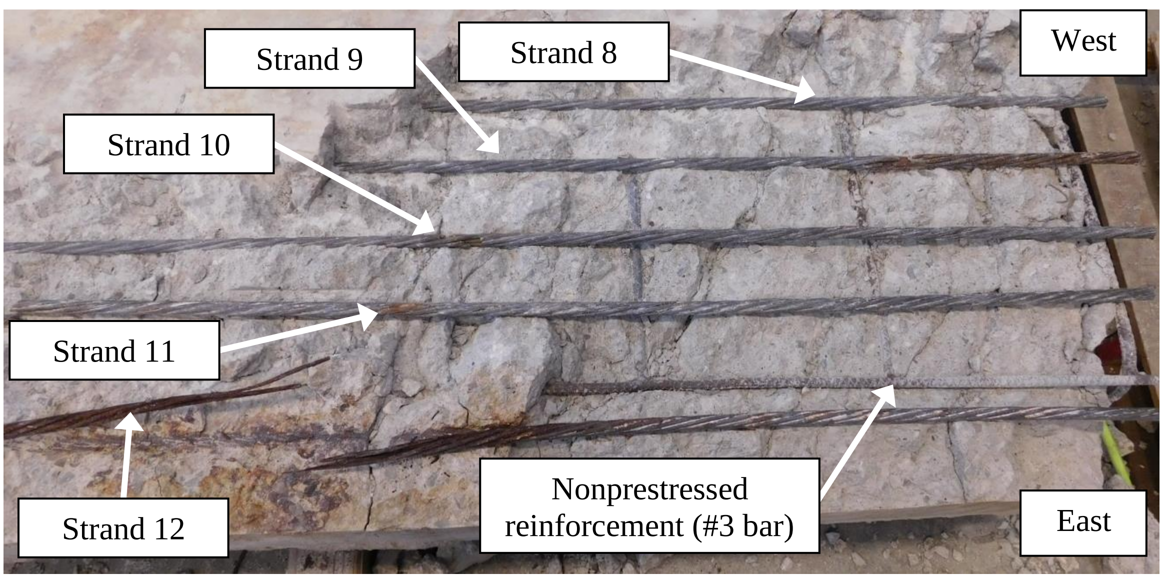

(b) After cover was removed

Figure 3.41: Strand Condition at South Exposed Strand in Southeast Portion of Segment B of Specimen 102-4-BS

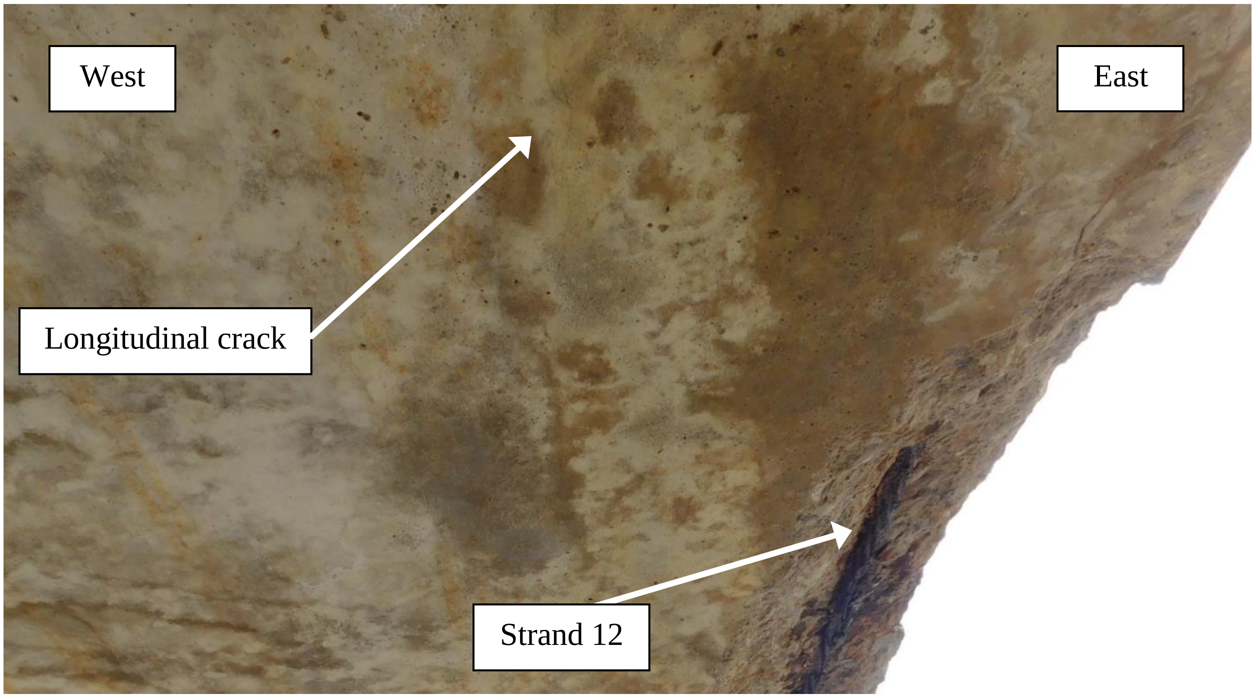

Figure 3.42: Longitudinal Cracking in Specimen 102-4-BS

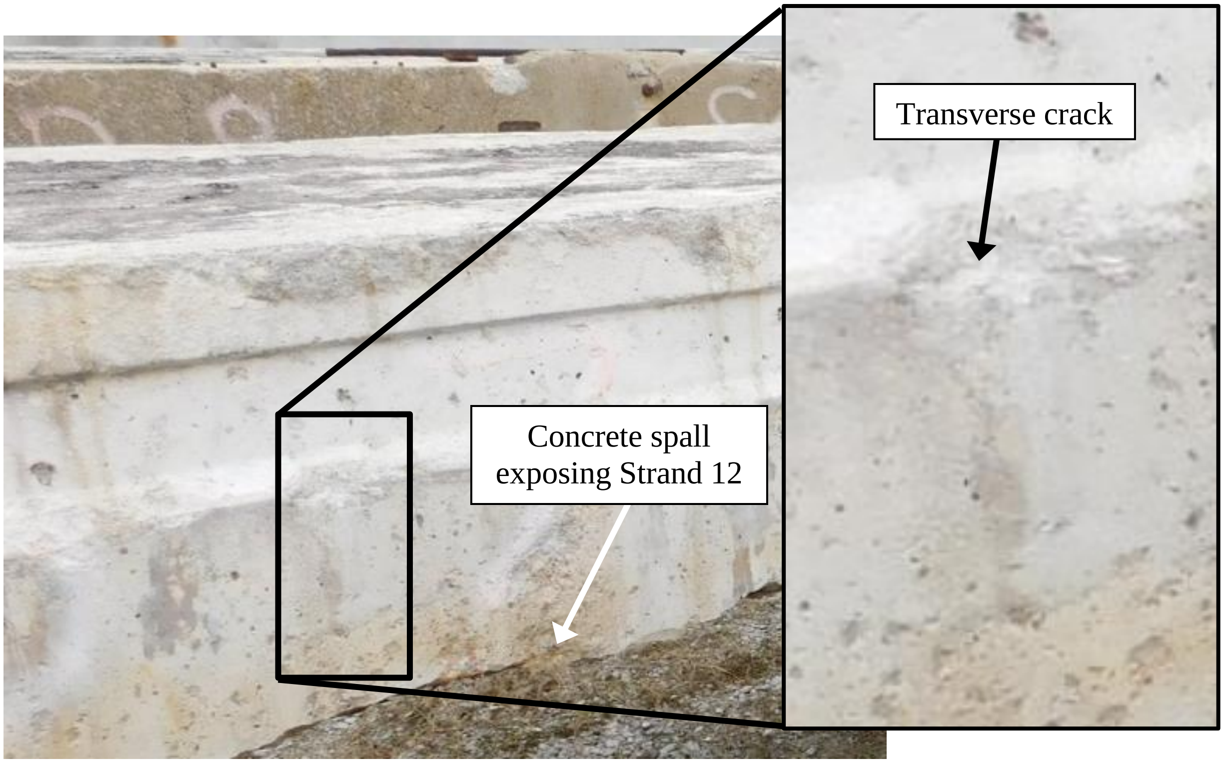

Figure 3.43: Existing Transverse Crack on East Side of Specimen 102-4-BS

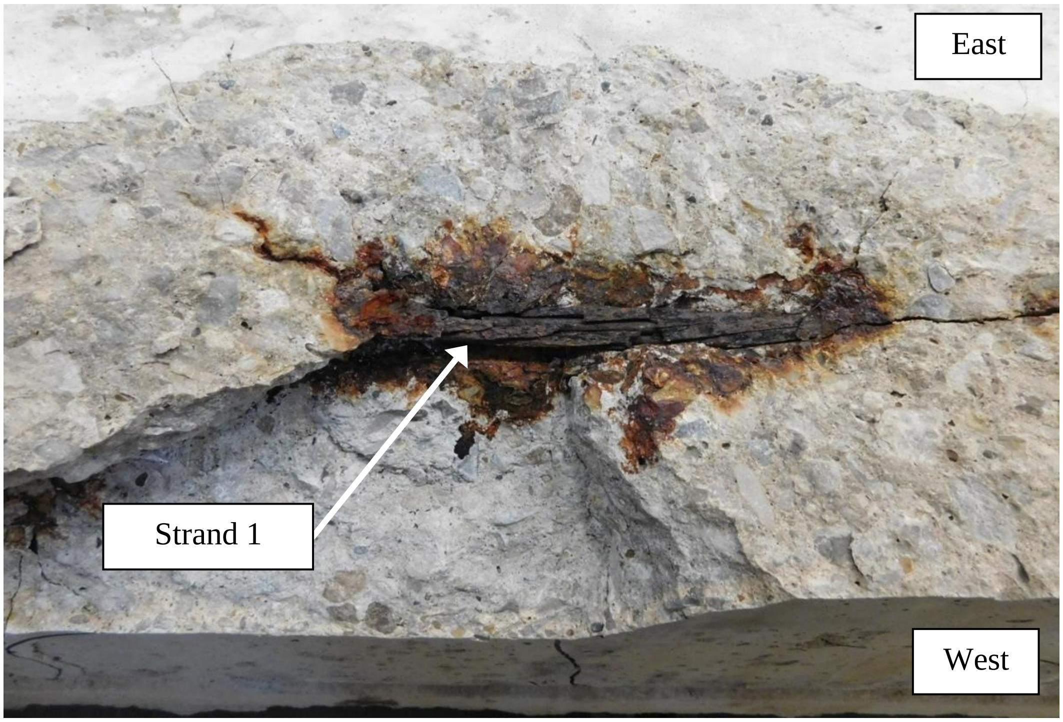

(a) Before cover was removed (strand exposed during structural test)

(b) After cover was removed

Figure 3.44: Strand Condition at Corner Crack in Segment B of 102-4-BS

Figure 3.45: Longitudinal Cracking in Northwest Portion of Segment B in Specimen 102-4-BS

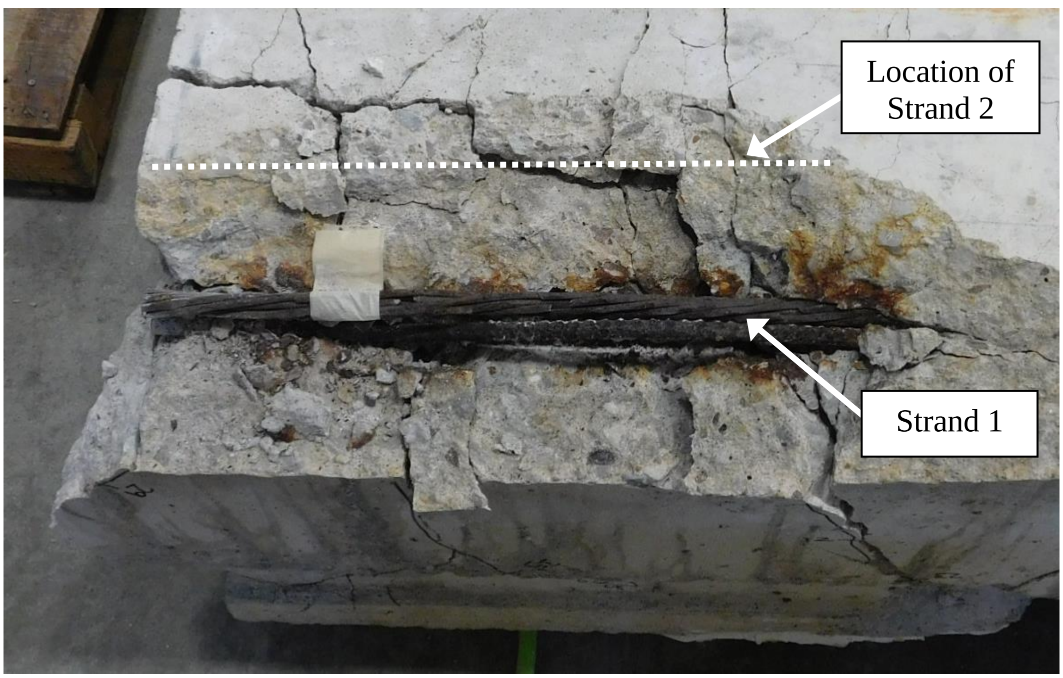

(a) Before cover was removed

Figure 3.46: Strand Condition in Southwest Portion of Segment B of Specimen 102-4-BS

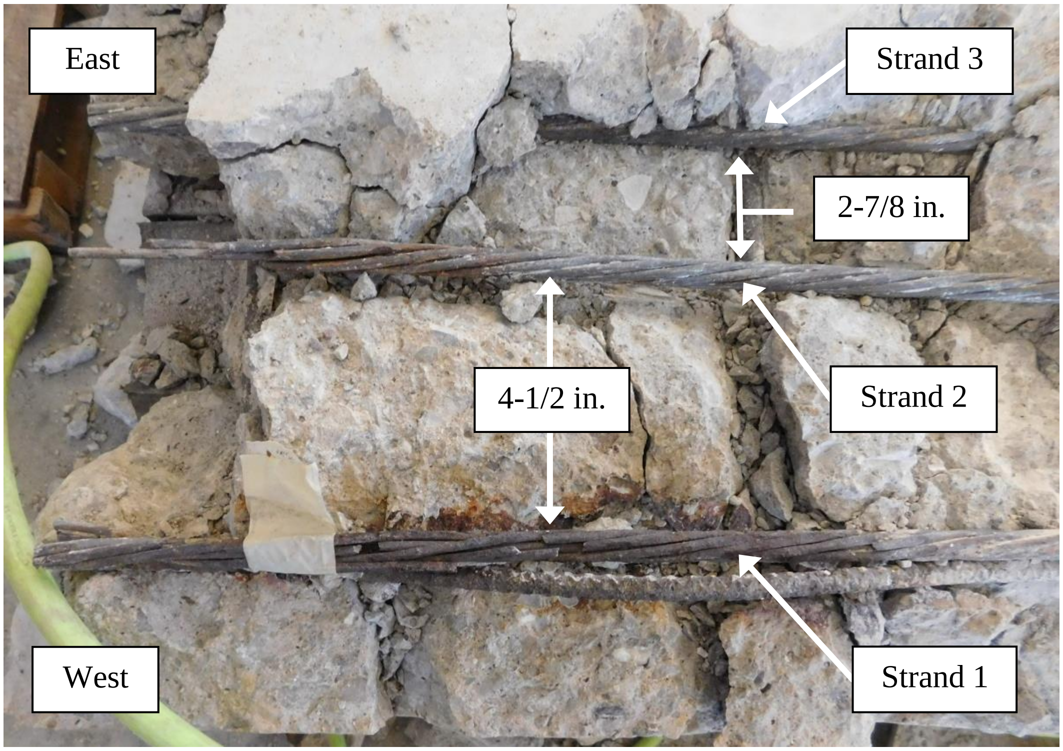

(b) After cover was removed

Figure 3.46: Continued

3.4.1.7 Summary

Six beam specimens were observed with edge deterioration consisting of a combination of longitudinal cracking along the strands, exposed strand, and broken strand. All deterioration was observed to originate at the edge stand and move toward the middle of the bottom flange as discussed in Section 2.6.1 (Figure 2.97).

The extent of strand corrosion for the common types of deterioration associated with leaking shear keys and water shedding over the exterior beam edge are summarized as follows:

- Leaking shear key joint (concrete staining) - In specimens 102-3-BS and 102-4-BS, corroded strands were found at stains that were accompanied by longitudinal cracks, transverse cracks, or concrete spalls. No corrosion was found at stains where no other deterioration was present.

- Longitudinal cracking in bottom flange - In all specimens, a longitudinal crack indicated that the strand at the crack was corroded.
- Spalling at longitudinal joint/corrosion of reinforcement - Any strand at a concrete spall was found corroded. Each strand adjacent to a strand at a concrete spall was located at least 2-7/8 in. from the exposed strand. Where no longitudinal cracking was observed in addition to concrete spalling, all strands adjacent to strands at concrete spalls were observed with no corrosion. Where longitudinal cracking was observed at strands adjacent to concrete spalling, the spacing between strands was as small as 2-1/4 in.

In general, the extent of corrosion associated with the ingress of salt-water to the bottom flange can be summarized as follows:

1. Where longitudinal cracks existed, strands at the longitudinal cracks were corroded.
2. Where strands were located at concrete spalls (exposed or not exposed), the strands were corroded.
3. Where staining was present in addition to transverse cracking, the strands at the transverse crack were corroded. Corrosion was localized at the crack and consisted of mainly surface rust.

3.4.2 Water Ingress into Box Beam Void Deterioration

Five beam specimens were observed with longitudinal cracks located away from the edge of the bottom flange (244-1-LC, K5-1-LC, K5-2-LC, 79-4-LC, and 56-1-LC). In the previous chapter, this type of deterioration was attributed to retention of water in the internal void. In the following, the strand extraction procedure for each of the noted beam specimens is presented to determine the extent of strand corrosion associated with this type of deterioration.

3.4.2.1 Specimen 244-1-LC

As shown in Figure 3.1, 244-1-LC had two large longitudinal cracks located away from the edges of the bottom flange. A section taken through each crack revealed that the cracks formed through the thickness of the bottom flange (Figure 3.47). In addition, the cardboard used to form the void was found to have disintegrated (Figure 3.48).

The strands at the rust-stained crack in the northeast portion of Segment B (Figure 3.1) are shown in Figure 3.49 and Figure 3.50. A black line has been drawn in Figure 3.49(b) next to Strand 17 to locate the through-thickness crack. Notably, the strands were in good condition and extensive corrosion was not observed. Light surface corrosion was observed on the strands at the crack. Corrosion of Strand 17 was observed approximately 4 ft from the location in Figure 3.49 (Figure 3.50). Along the length of the crack, corrosion of the adjacent strands was not observed.

Figure 3.51 shows the strand condition at the longitudinal crack in the northwest portion of Segment A. Strand 5 was located at the longitudinal crack, and as shown in Figure 3.51(b), corrosion and minor section loss was observed. Corrosion of the adjacent strands was only observed at the locations where the strands were located at the longitudinal crack.

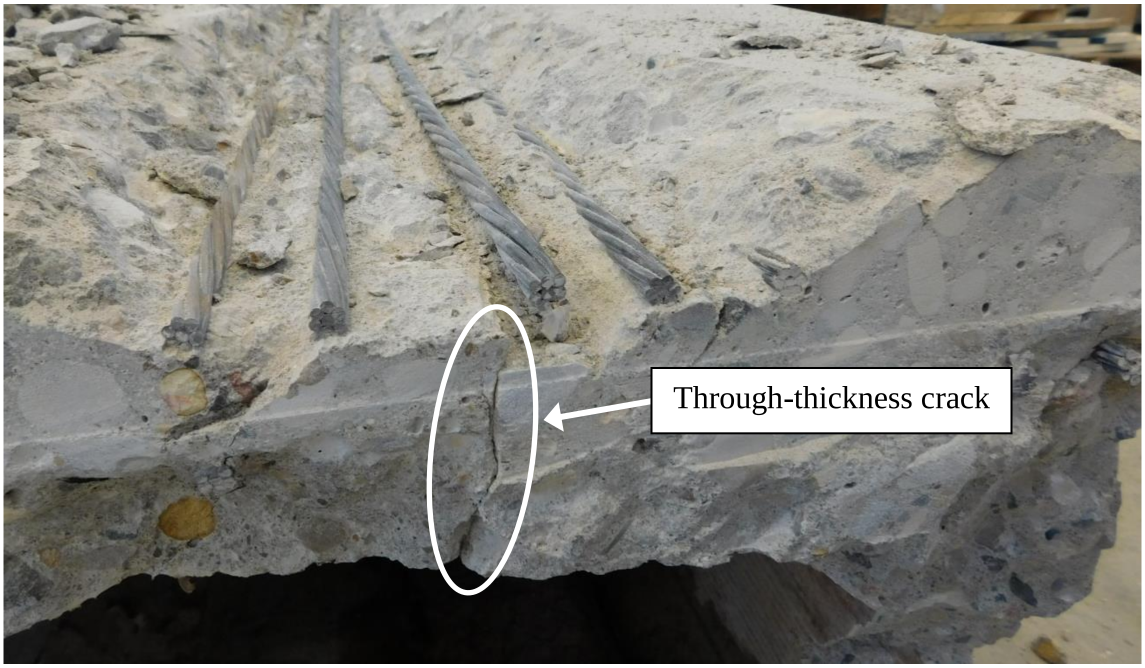

(a) Section at midspan through the rust-stained longitudinal crack

(b) Section at 12 ft from the south support through the south longitudinal crack

Figure 3.47: Through-Thickness Cracks in 244-1-LC

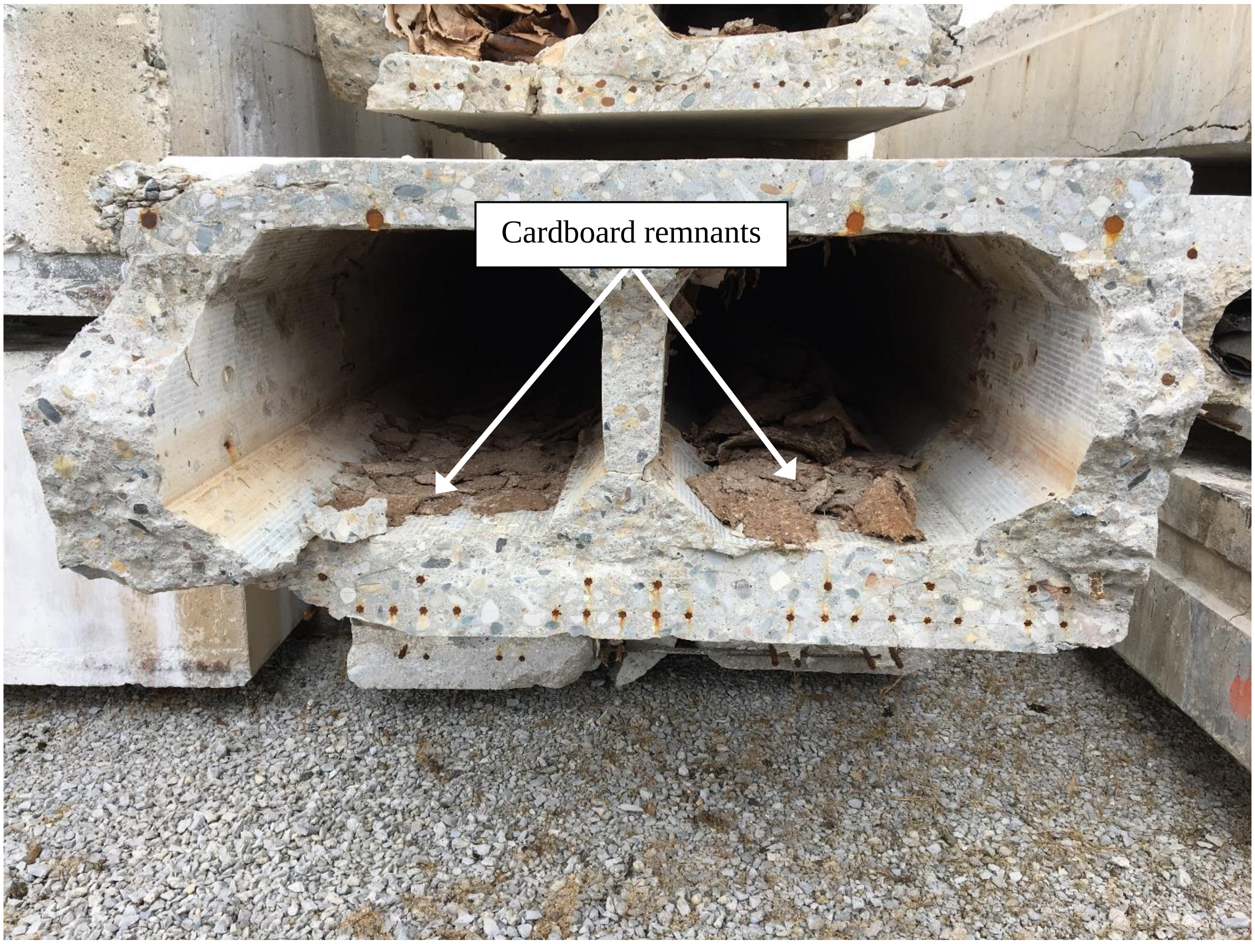

Figure 3.48: Disintegrated Cardboard Form

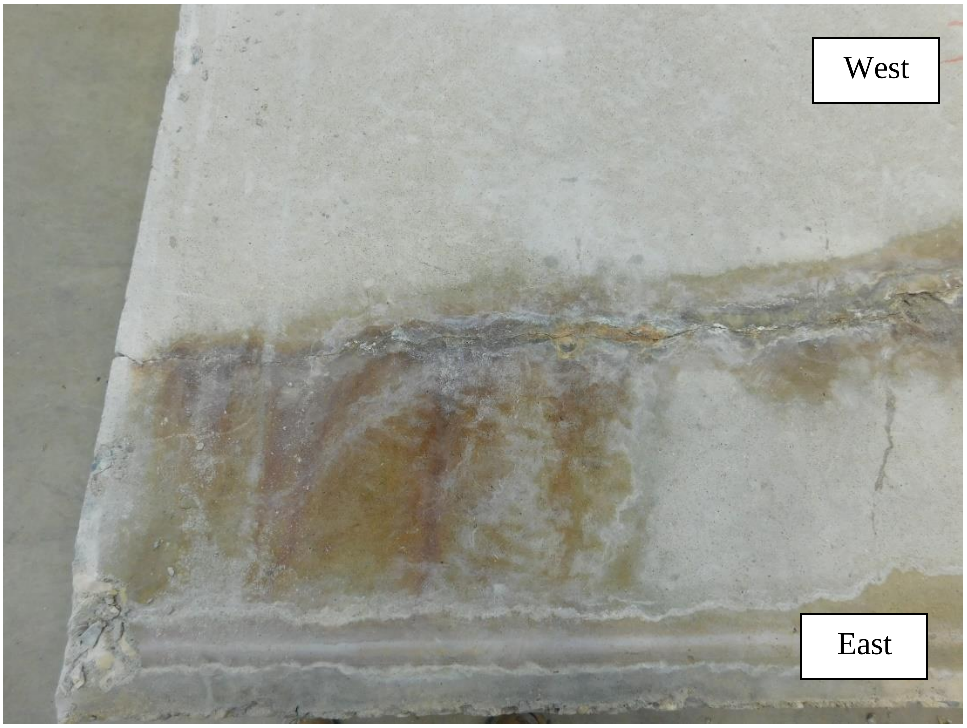

(a) Before cover was removed

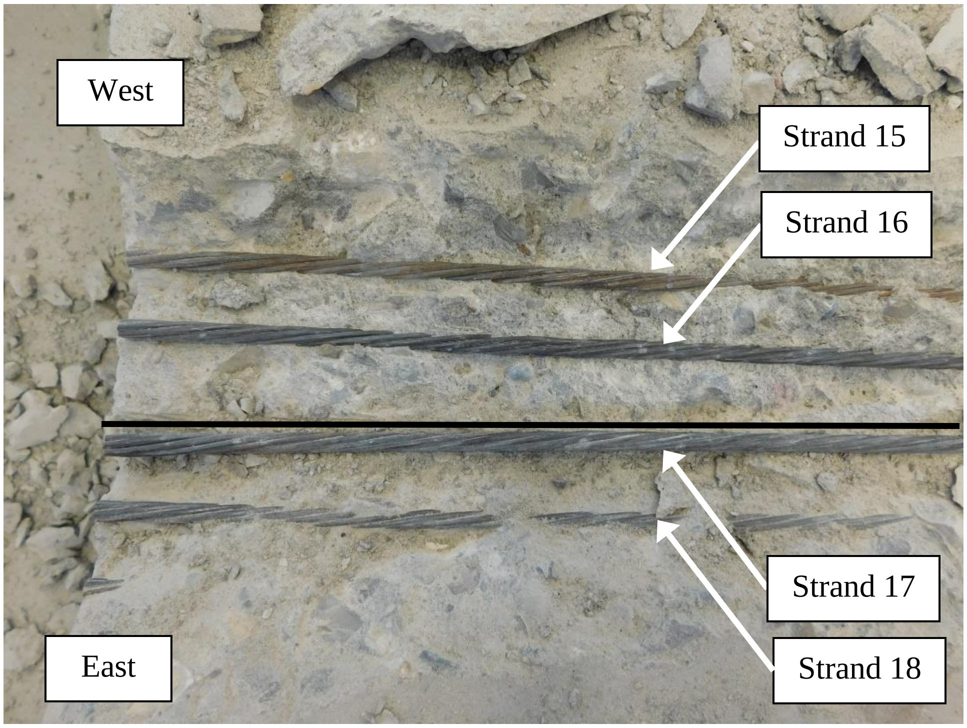

(b) After cover was removed

Figure 3.49: Strand Condition at Stained Longitudinal Crack in Northeast Portion of Segment B of Specimen 244-1-LC

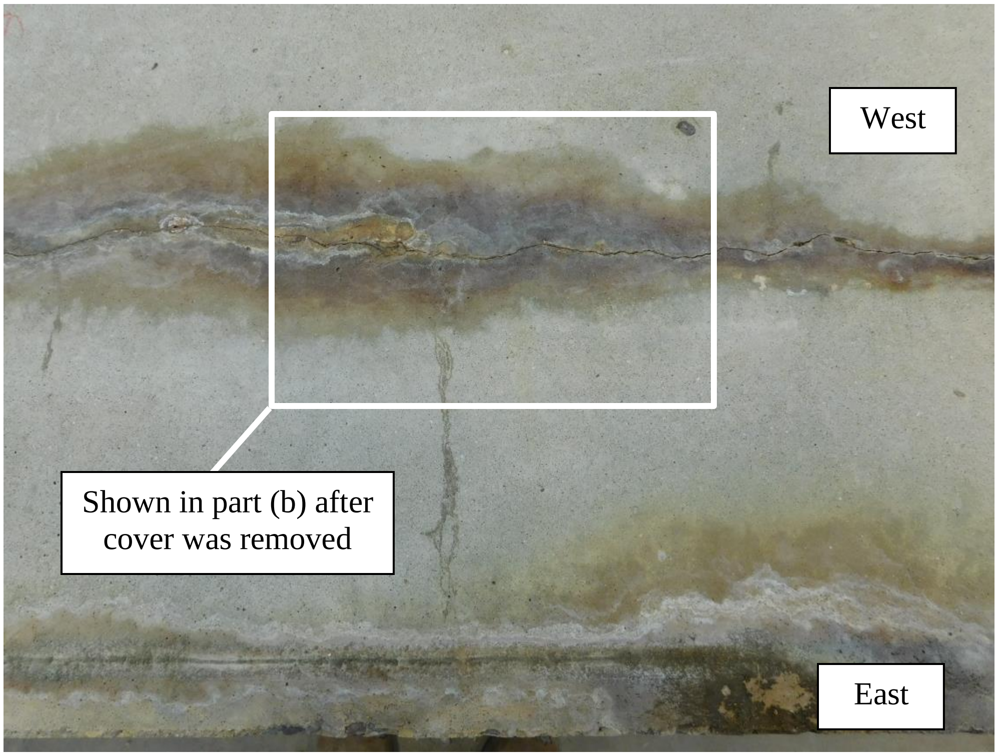

(a) Before cover was removed

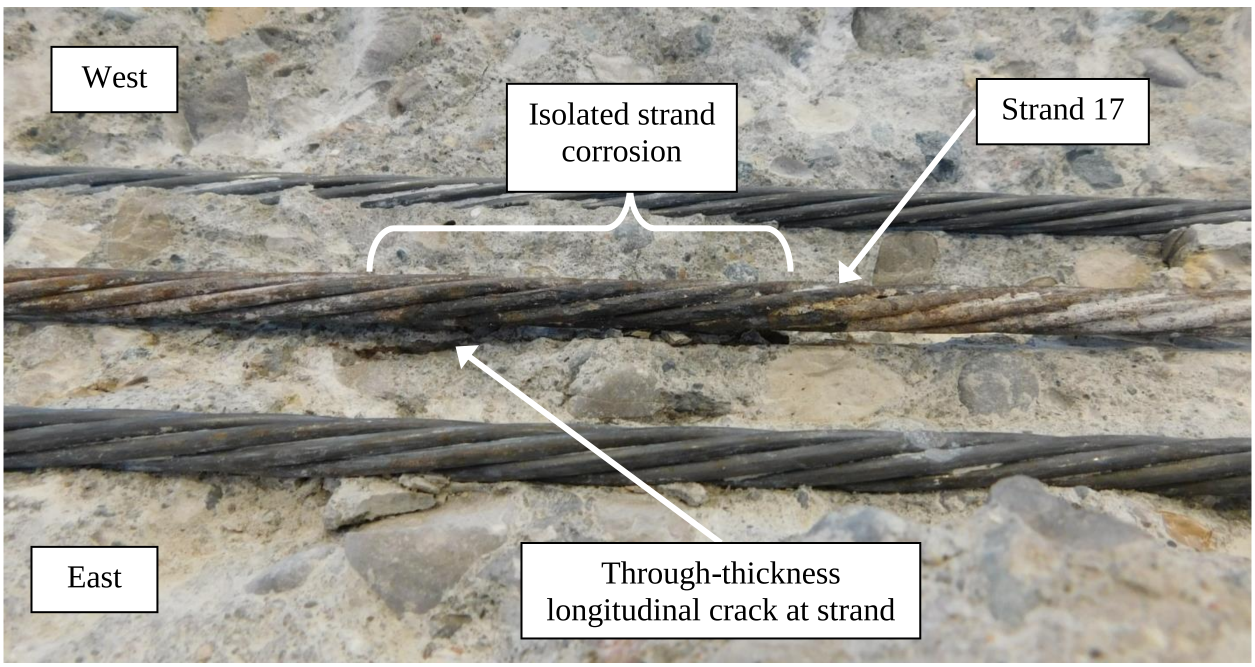

(b) After cover was removed

Figure 3.50: Isolated Corrosion of Strand 17 in 5 ft from the North end of Segment B of Specimen 244-1-LC

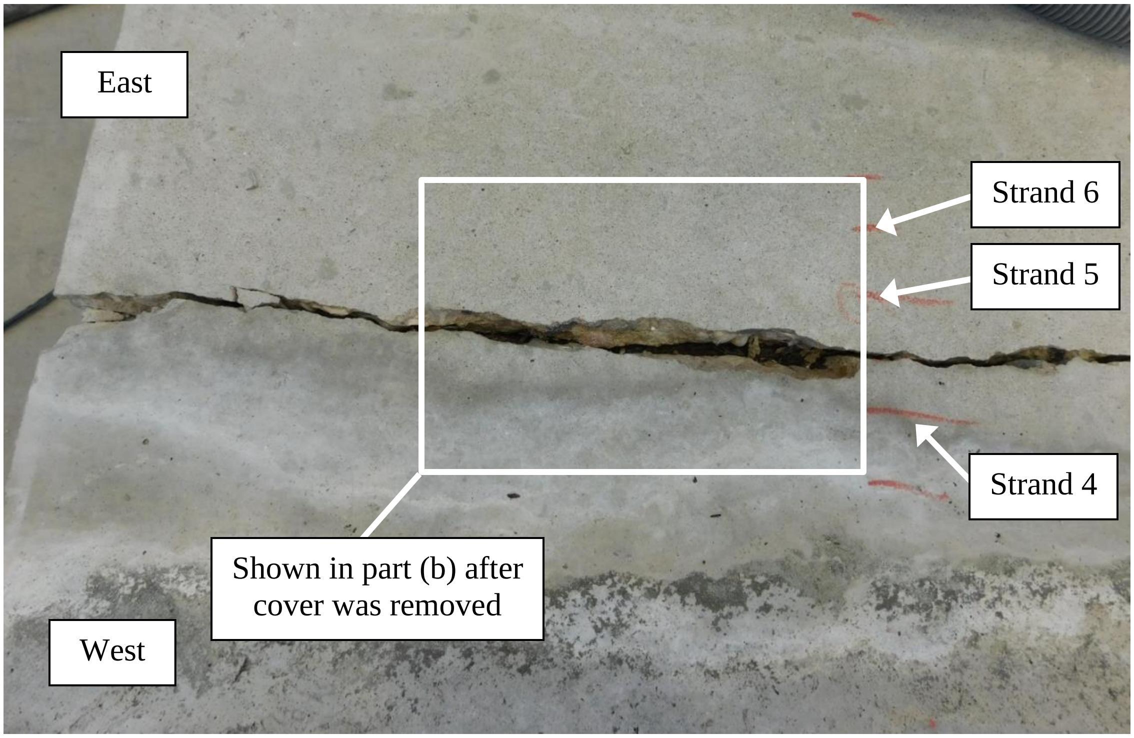

(a) Before cover was removed

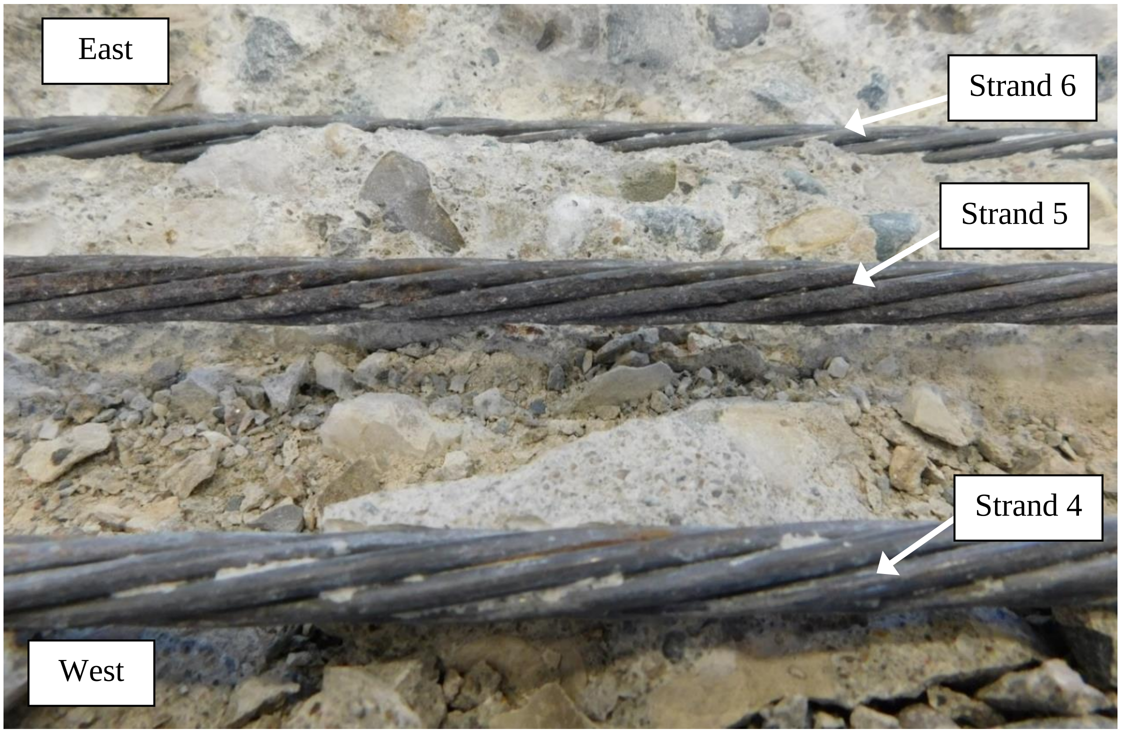

(b) After cover was removed

Figure 3.51: Strand Condition at Longitudinal Crack in Northwest Portion of Segment A of Specimen 244-1-LC

3.4.2.2 Specimen K5-1-LC

The deterioration of K5-1-LC consisted of two longitudinal cracks each extending from opposite ends of the beam and located away from the edge of the beam (Figure 3.4). A section was taken through the south longitudinal crack to investigate the extent of cracking (Figure 3.52). As shown, the crack extends through the thickness of the flange into the empty void. The strands at the north longitudinal crack (Figure 3.53) have surface corrosion due to 5 months of outdoor exposure after completion of the structural test. Strand 5 (located at the longitudinal crack), however, was observed with corrosion and minor section loss. At the south longitudinal crack (Figure 3.54), corrosion of Strands 10 and 11 was limited to the locations of the strands at the cracks, and no corrosion was observed on Strands 9 and 12. A black line has been drawn in Figure 3.54 to illustrate the location of the through-thickness crack.

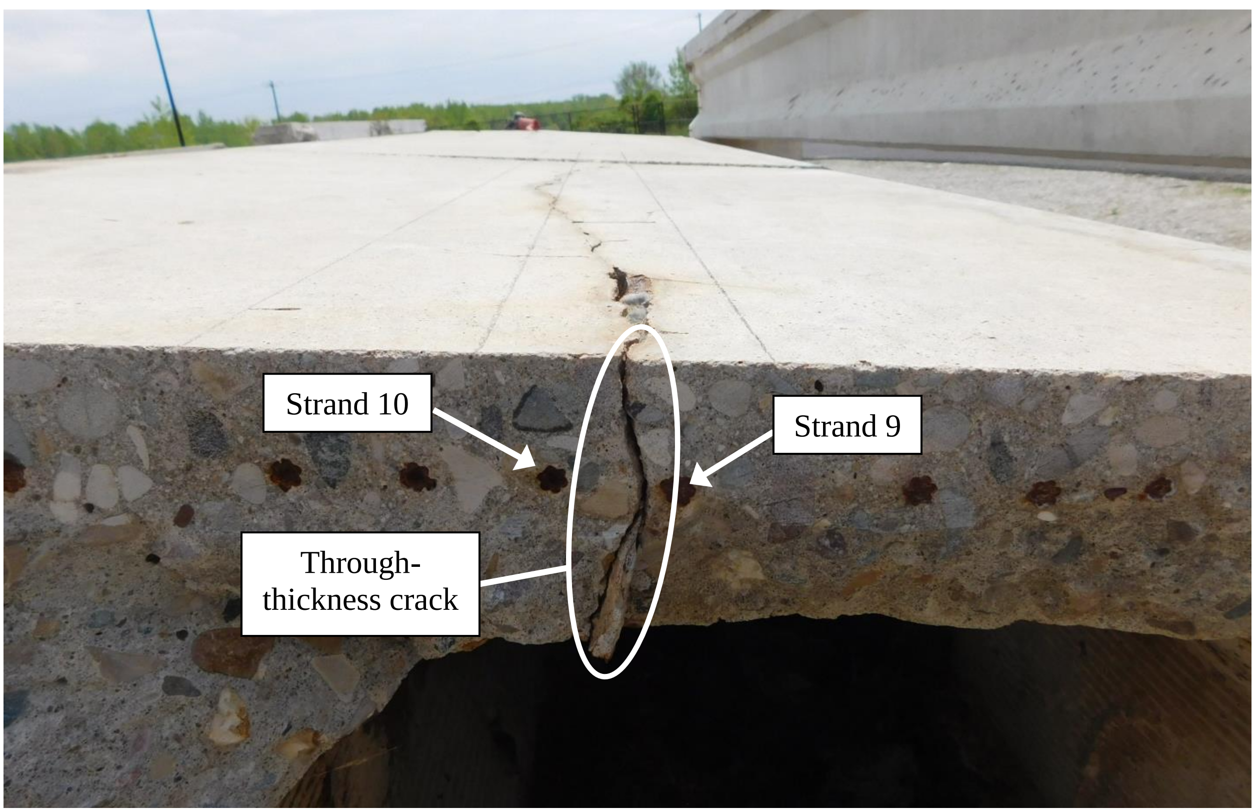

Figure 3.52: Through-thickness Crack in South Portion of K5-1-LC

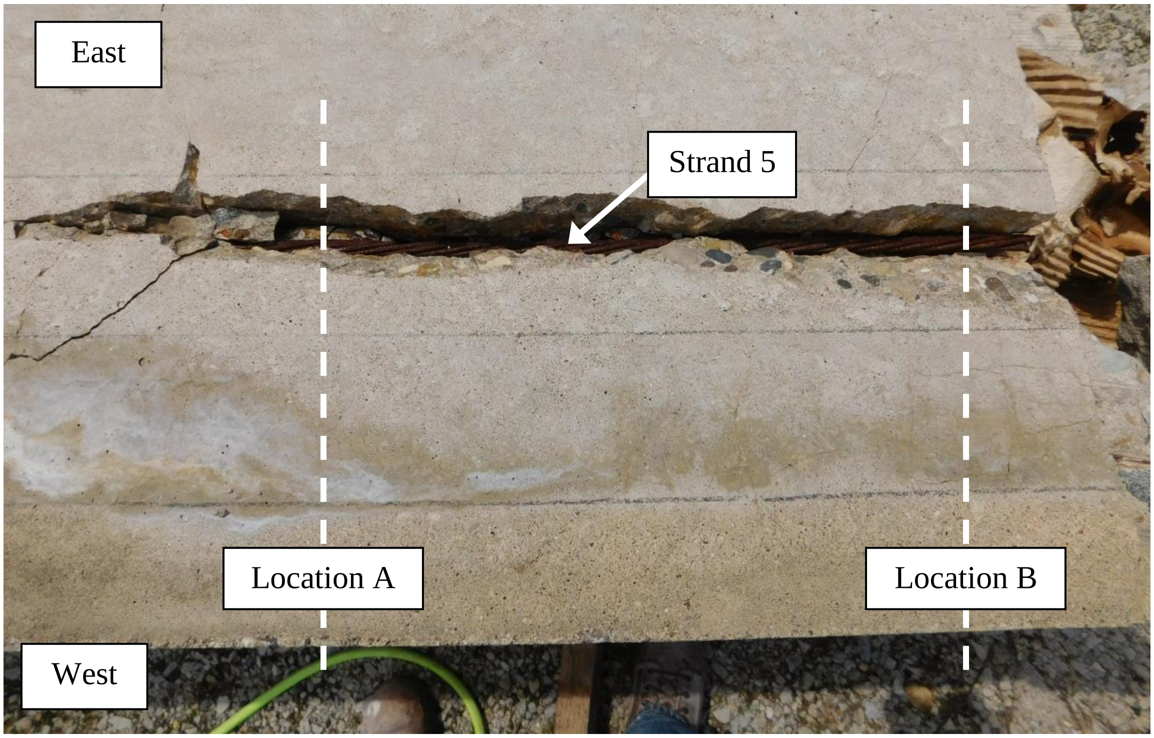

(a) Before cover was removed

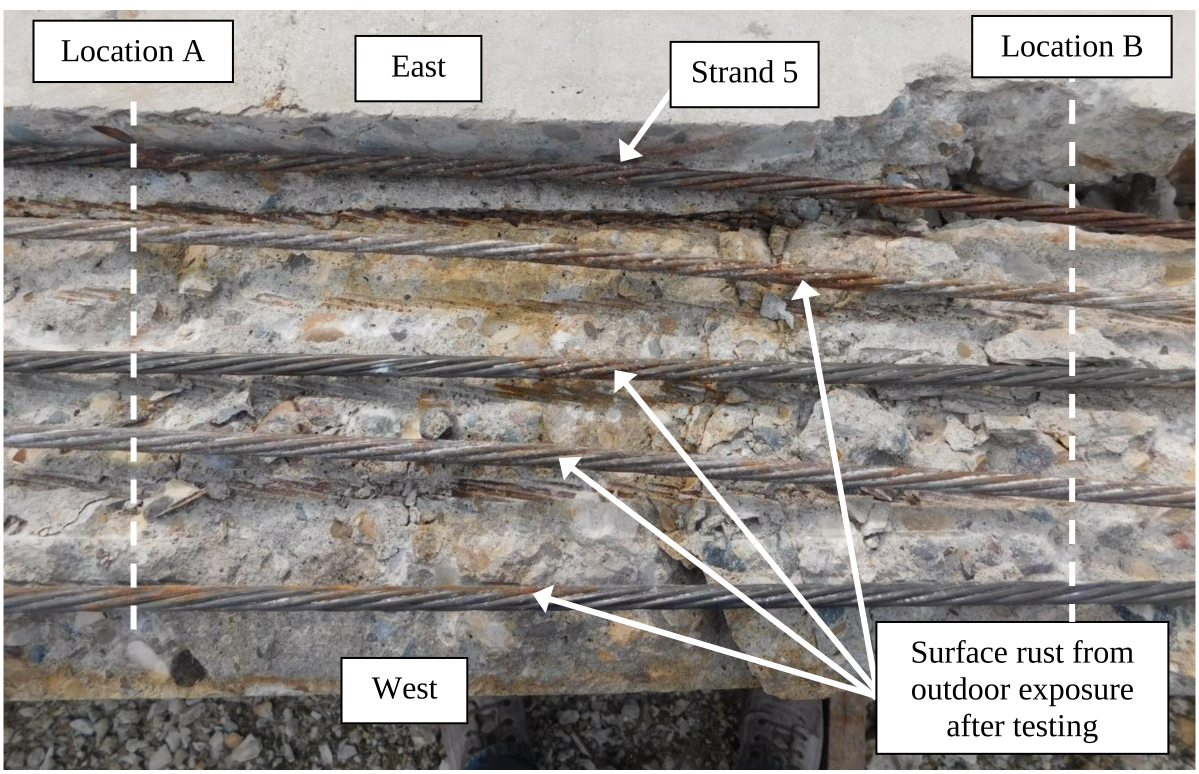

(b) After cover was removed

Figure 3.53: Strand Condition at North Longitudinal Crack in K5-1-LC

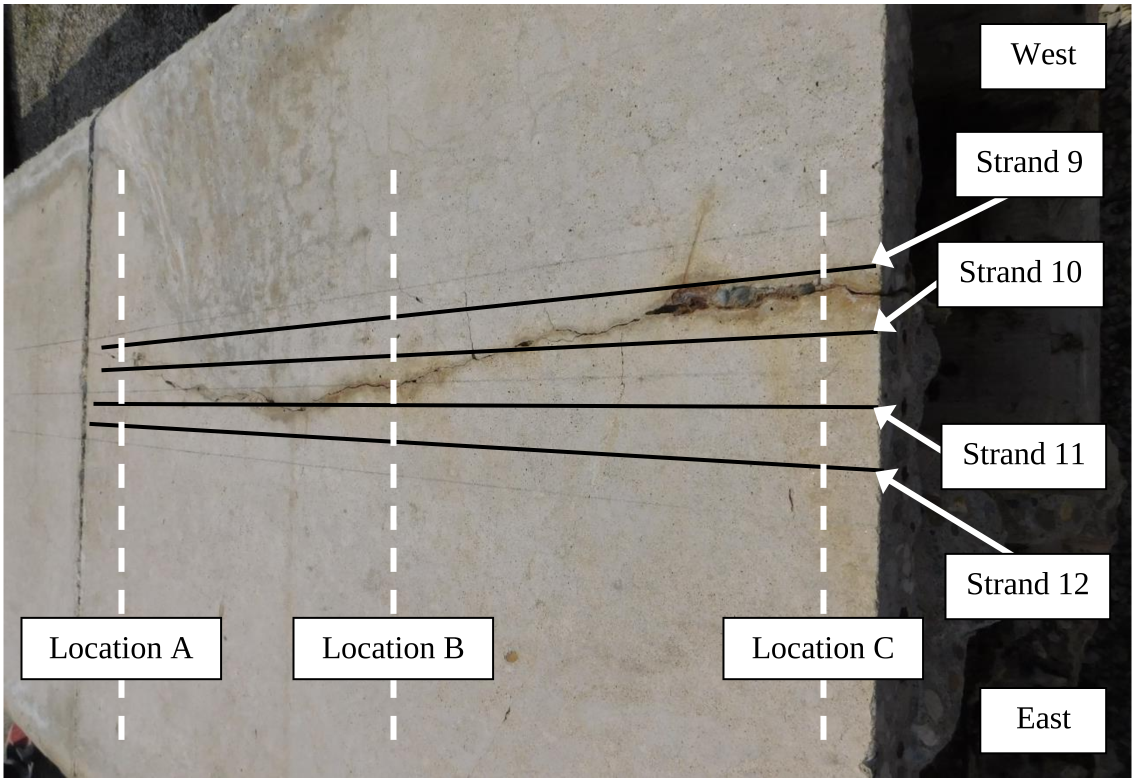

(a) Before cover was removed

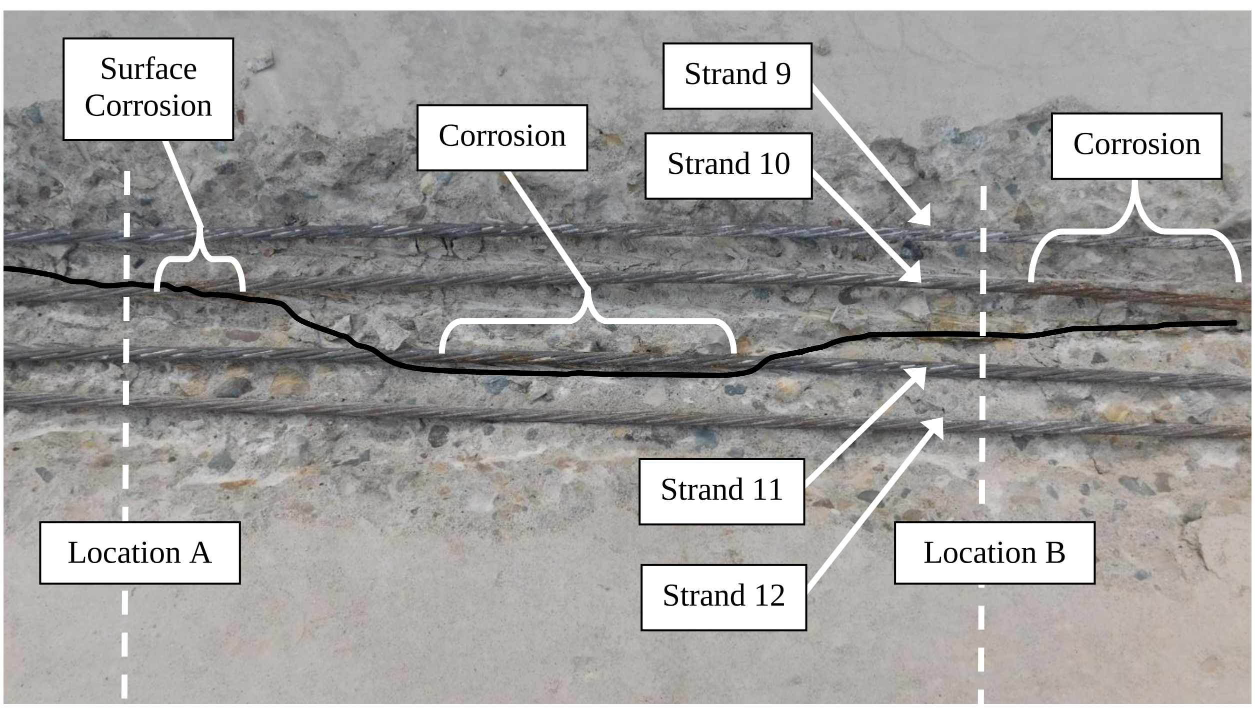

(b) After cover was removed

Figure 3.54: Strand Condition at South Longitudinal Crack in K5-1-LC

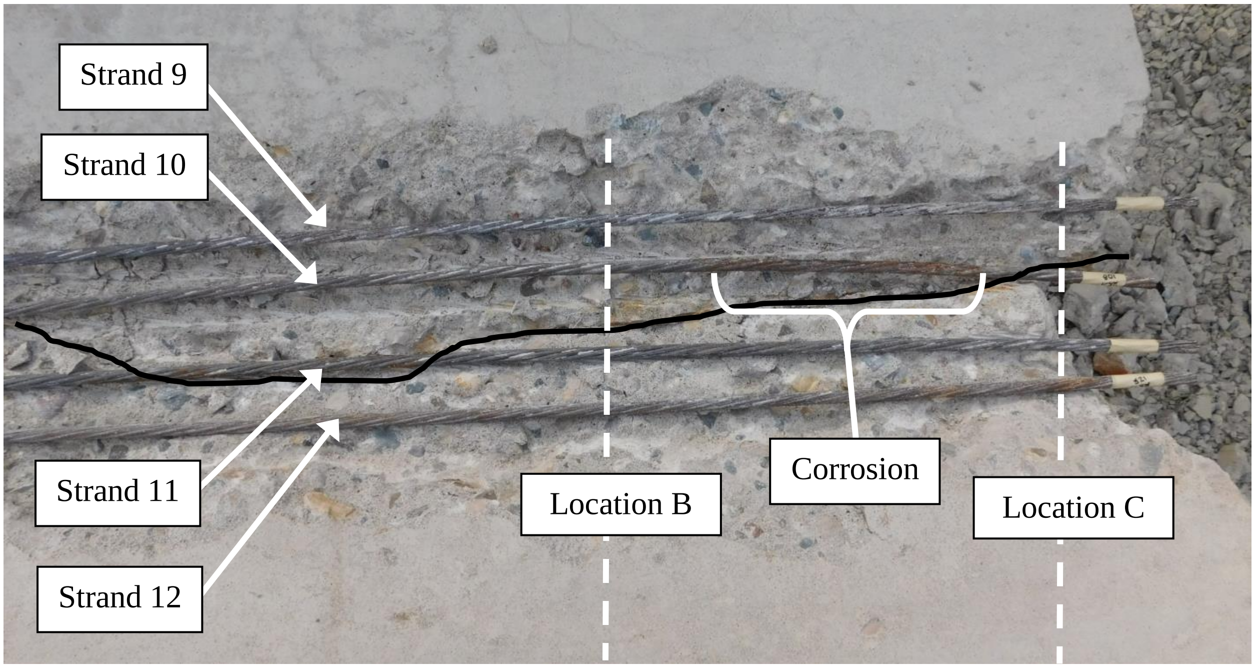

(c) After cover was removed

Figure 3.54: Continued

3.4.2.3 Specimen K5-2-LC

3.4.2.3.1 Structural Patch

To investigate the extent of corrosion in K5-2-LC, the beam was cut into four segments (Figure 3.5). When the segments were separated, the void in the southern portion of the beam was found filled with a combination of bituminous material and cementitious fill (Figure 3.55). The top flange was also observed to have been patched. Records of this work while Newton K5 was in service were not available. It is assumed that the top flange failed during a routine resurfacing of the bridge. To repair the top flange, the void was filled with sand and cementitious fill as formwork for a structural concrete patch. To provide a comparison between the original and patched cross-section, the original cross-section is shown in Figure 3.56. The original cross-section was also observed with an empty void indicating that the cardboard used to form the void had disintegrated (Figure 3.56).

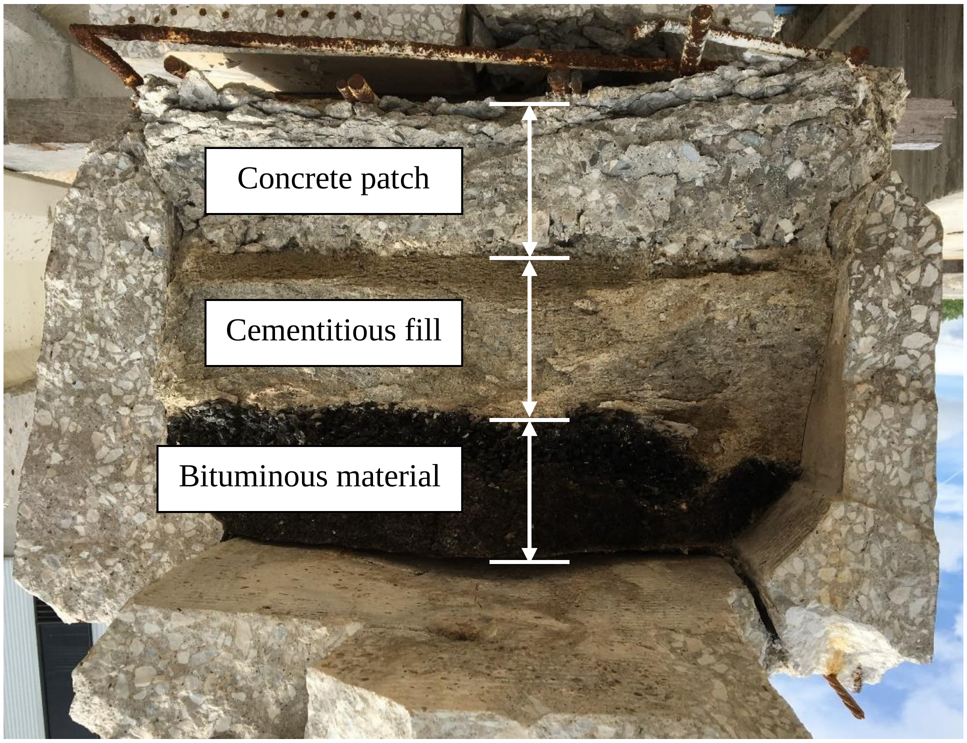

Figure 3.55: Patched Cross-Section of K5-2-LC

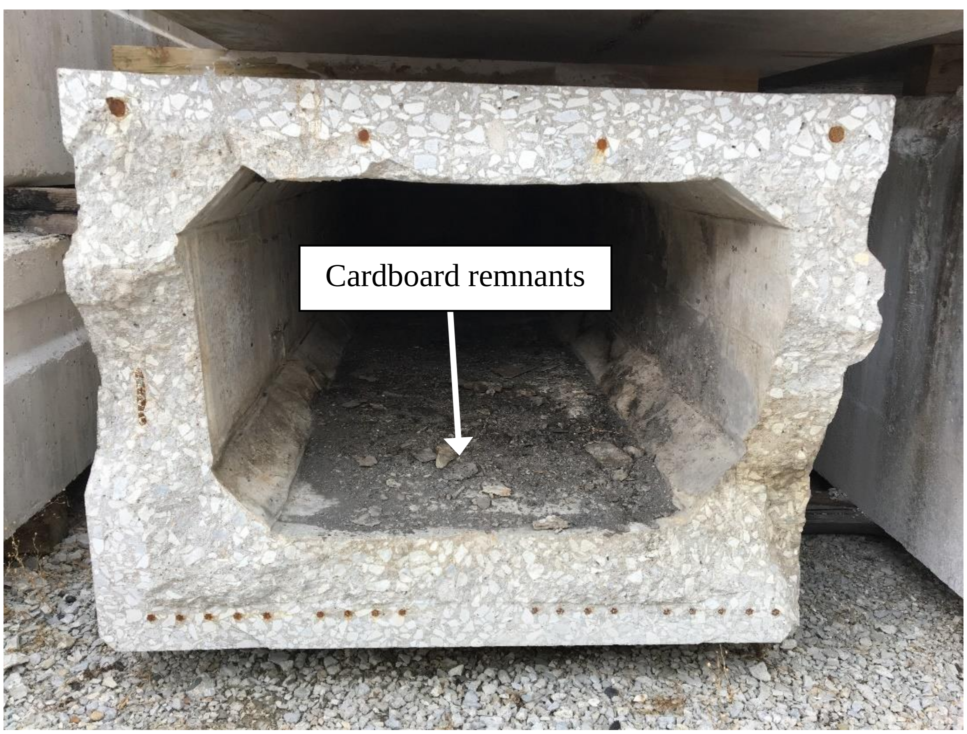

Figure 3.56: Original Cross-Section of K5-2-LC

3.4.2.3.2 Bottom Flange Deterioration

The deterioration of the bottom flange included three longitudinal cracks (Figure 3.5). Each of the longitudinal cracks were observed to extend through the thickness of the flange into the void (Figure 3.57).

When Segment B was rolled onto its top flange to facilitate extraction of the strands, the beam split open longitudinally (Figure 3.58). As shown, no transverse steel was present in the bottom flange of the beam to hold the segment together, and the crack did not cross or align with any of the strand in the longitudinal direction. When the longitudinal crack was further investigated in Segment A, no corrosion of the strands was observed (Figure 3.59). This crack formation indicates that freezing of water in the void is the likely cause of bottom flange cracking.

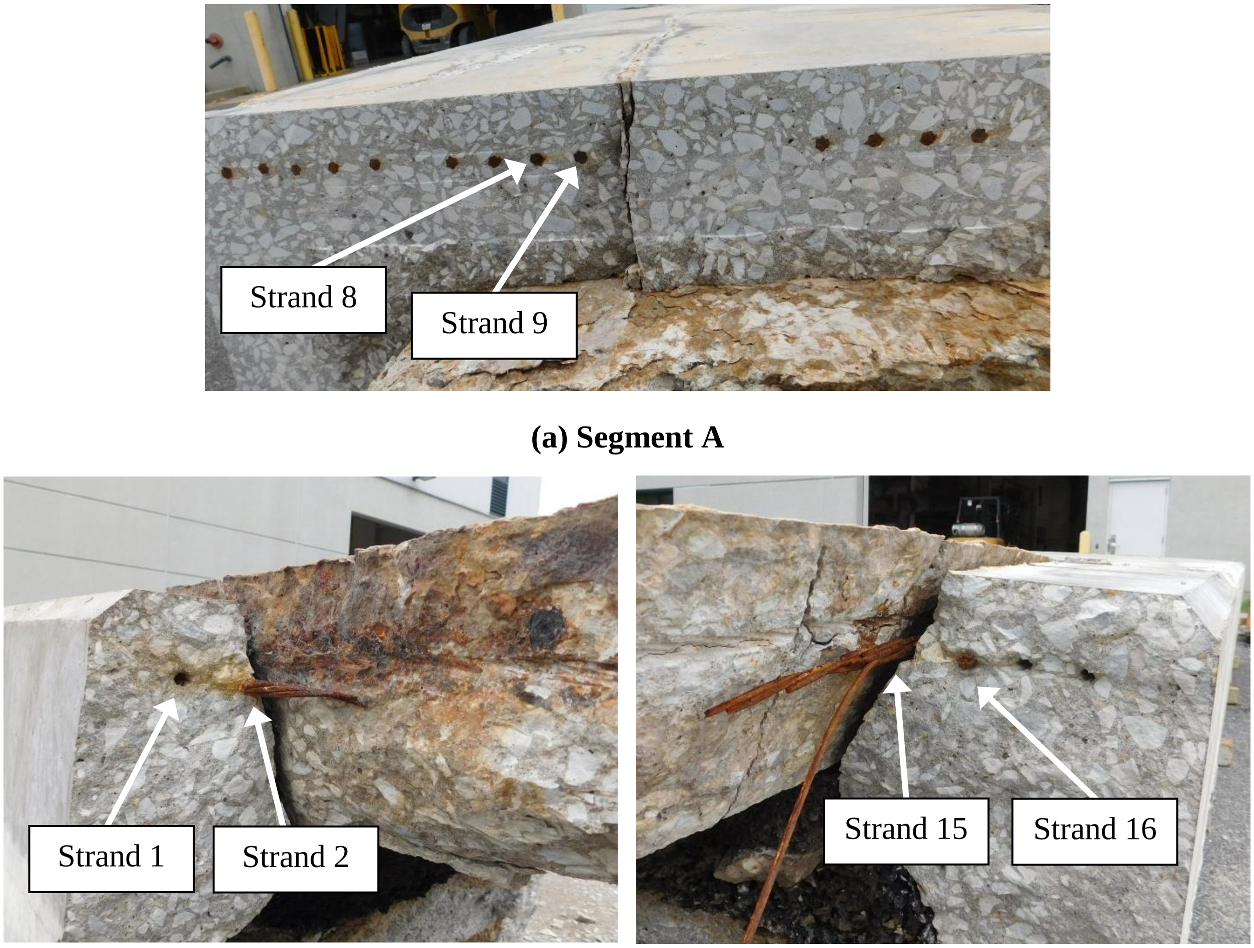

(a) Segment A

(b) West side of Segment C **(c) East side of Segment C**

Figure 3.57: Through-Thickness Cracks in K5-2-LC

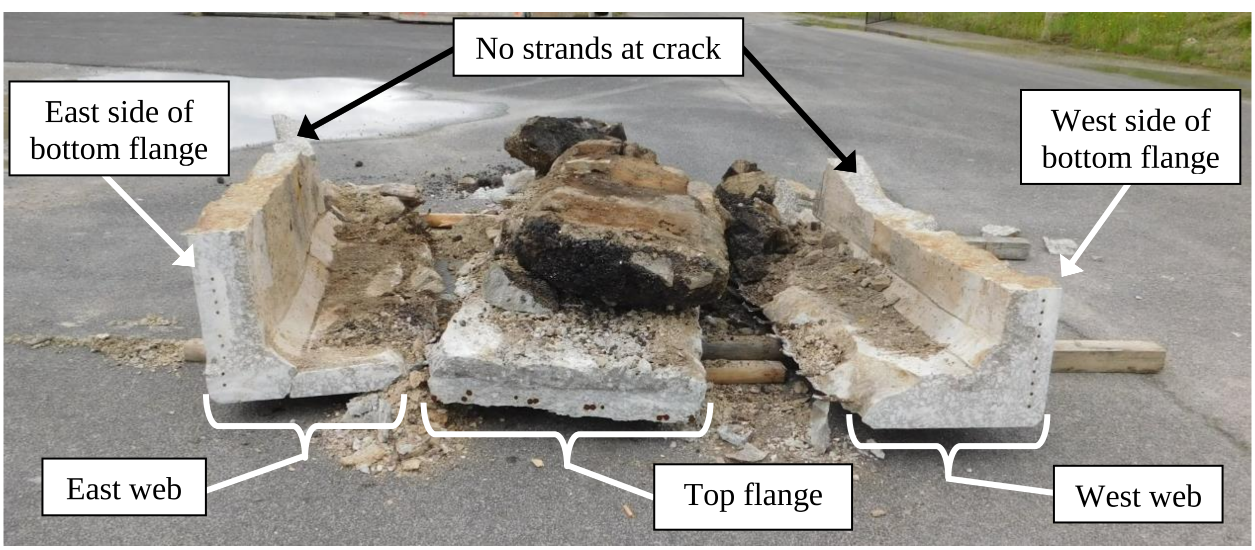

Figure 3.58: Beam Segment B of K5-1-LC

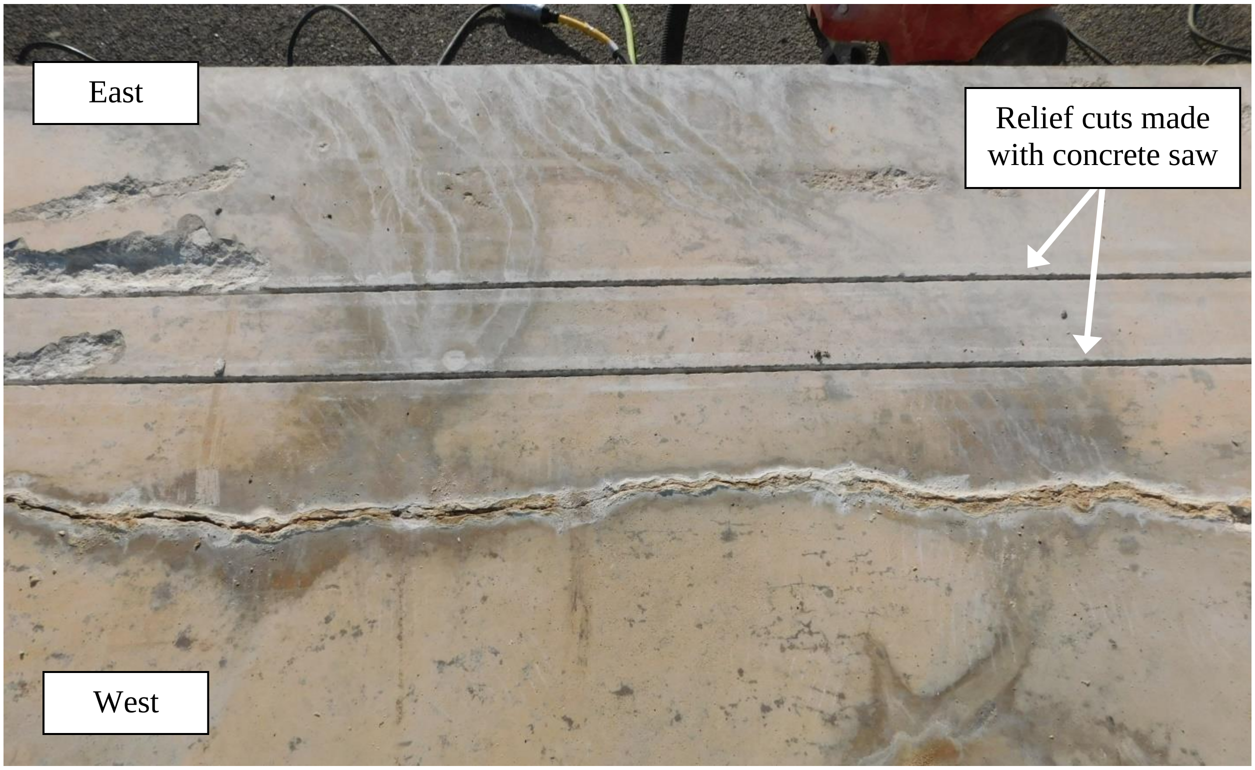

(a) Before cover was removed

(b) After cover was removed

Figure 3.59: Strand Condition at Longitudinal Crack in Segment A of K5-2-LC

The strands at the longitudinal cracks on either side of the drain hole spall in Segment C were observed to have isolated corrosion at the longitudinal cracks (Figure 3.60 to Figure 3.62). In addition to the corroded strand in Figure 3.57 (Strand 2), corrosion was observed on Strand 3 in Figure 3.61. The surface rust present on Strands 4 and 5 in Figure 3.61 was due to outdoor exposure of the flexural crack that formed during the structural test. Surface rust on Strands 14-18 at localized cracks shown in Figure 3.62 were also due to outdoor exposure following the structural test. Based on review of the specimen, all longitudinal cracks in K5-2-LC were observed with corrosion. Corrosion was limited to the locations where the cracks aligned with the strand.

Figure 3.60: Longitudinal Cracks in Segment C of K5-2-LC Before Cover was Removed

(a) After cover was removed from east longitudinal crack

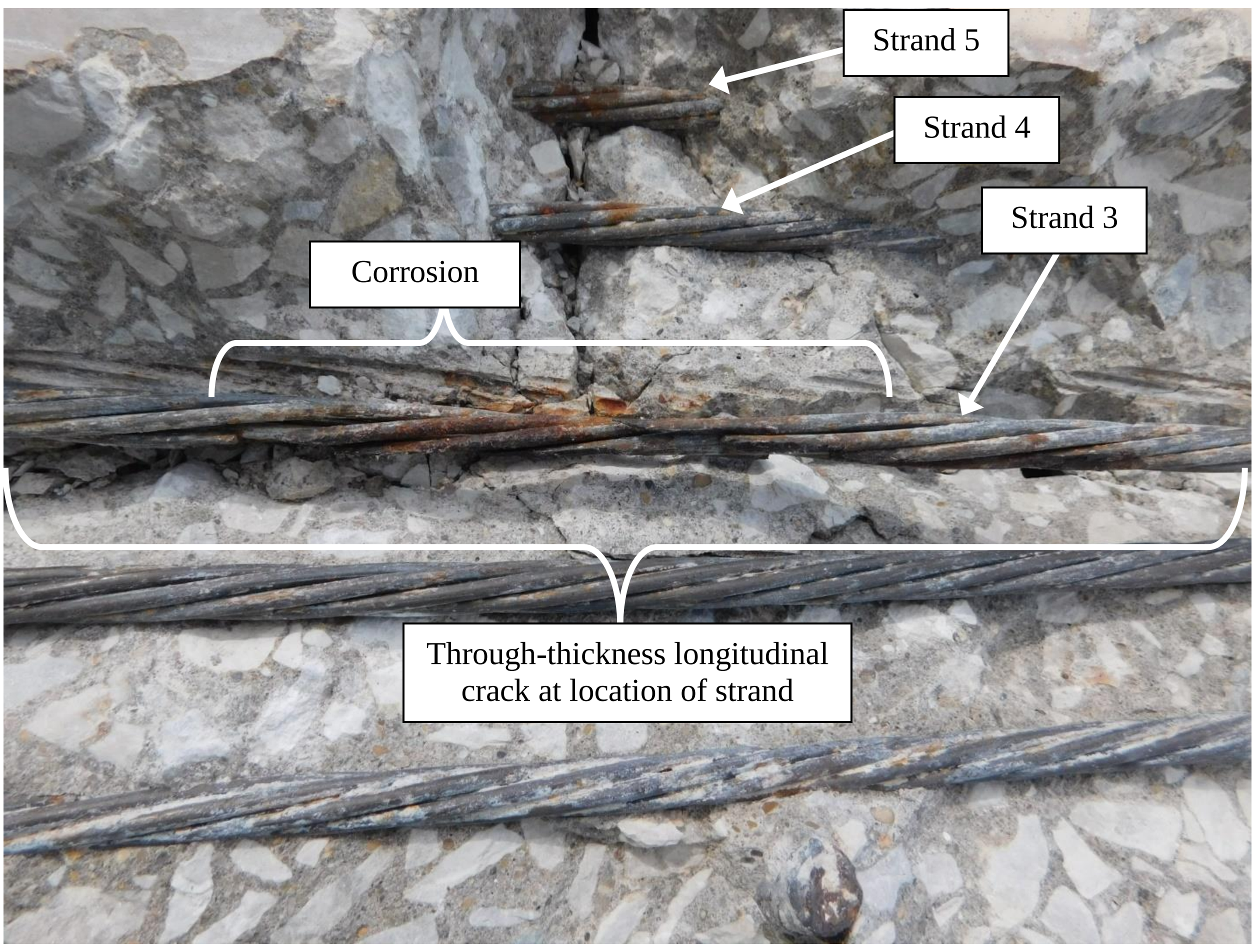

(b) Close-up view of strand corrosion

Figure 3.61: Strand Condition at West Longitudinal Crack in Segment C of K5-2-LC

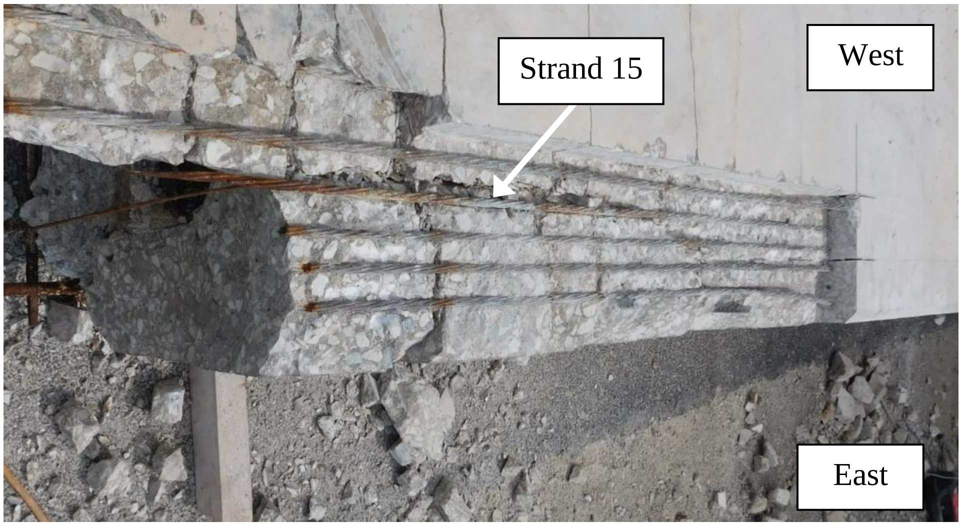

(a) After cover was removed

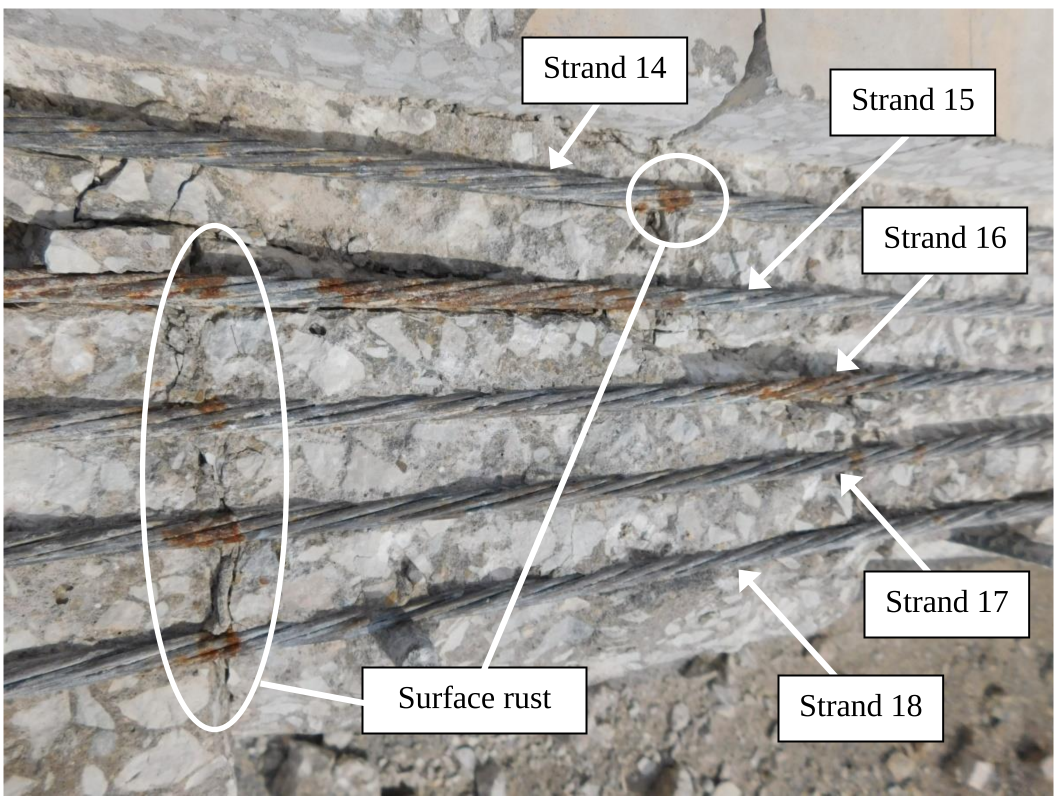

(b) Close up view of strand corrosion

Figure 3.62: Strand Condition at East Longitudinal Crack in Segment C of K5-2-LC

3.4.2.4 Specimen 79-4-LC

Two longitudinal cracks were observed on the north end of 79-4-LC (Figure 3.9). When the concrete cover was removed, corrosion was found on Strands 1 to 4 where the strands were located at the cracks (Figure 3.63(b)). No other strand corrosion was observed. The voids of the box beam were formed with cardboard sonotubes, and upon inspection of the voids, the cardboard was found to have disintegrated (Figure 3.64). This indicates that water was retained in the void and froze causing the longitudinal cracks.

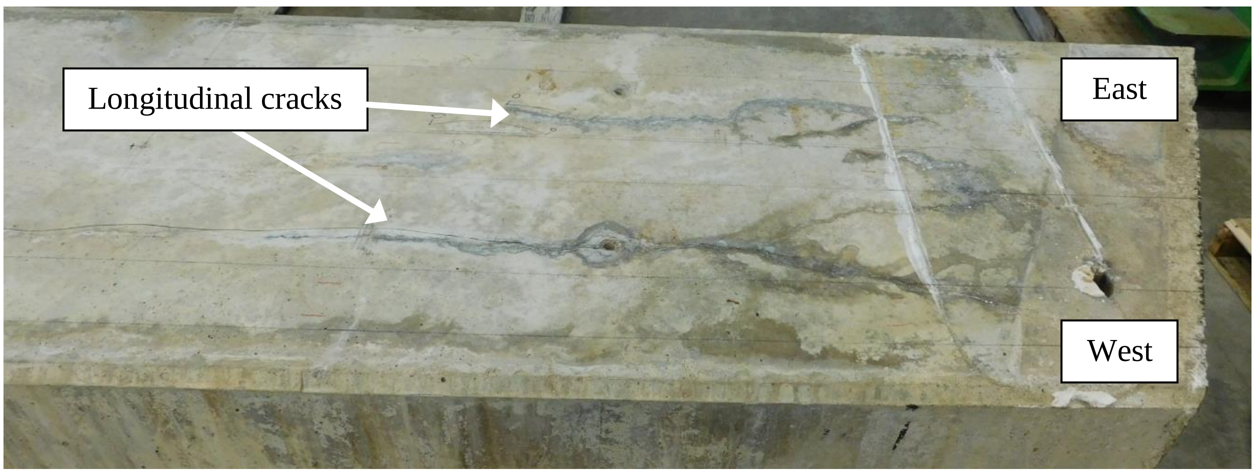

(a) Before cover was removed

Figure 3.63: Strand Condition at Longitudinal Cracks in 79-4-LC

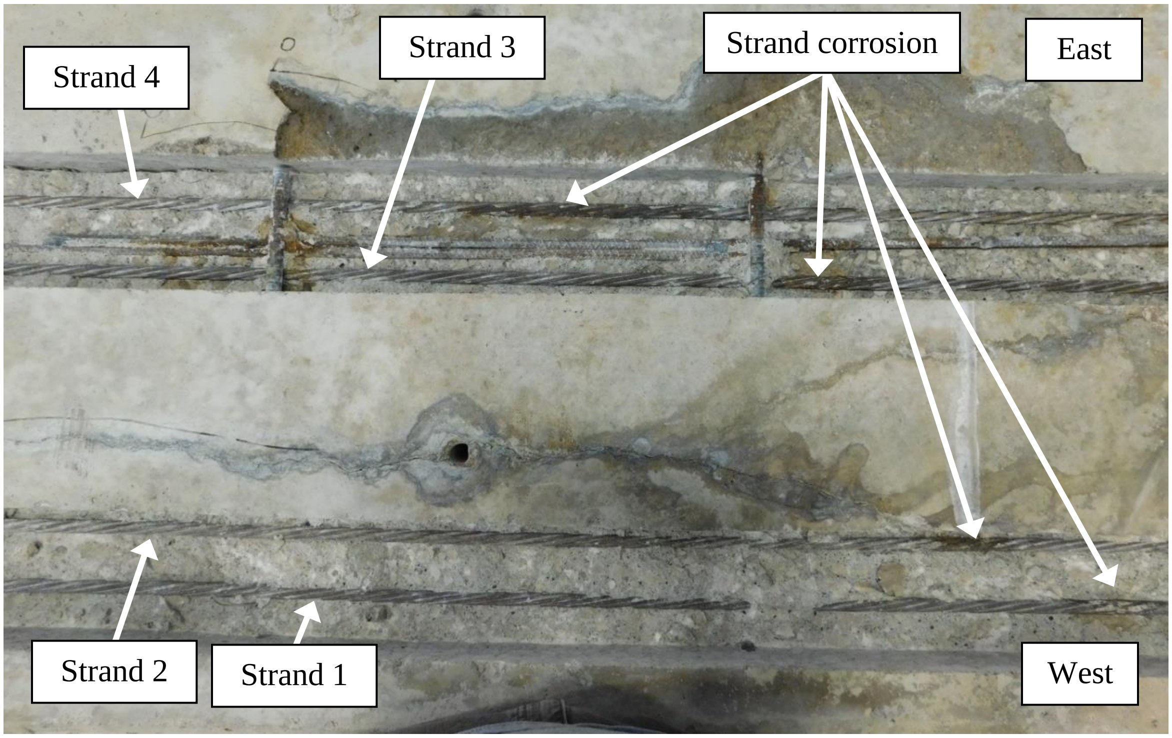

(b) After cover was removed

Figure 3.63: Continued

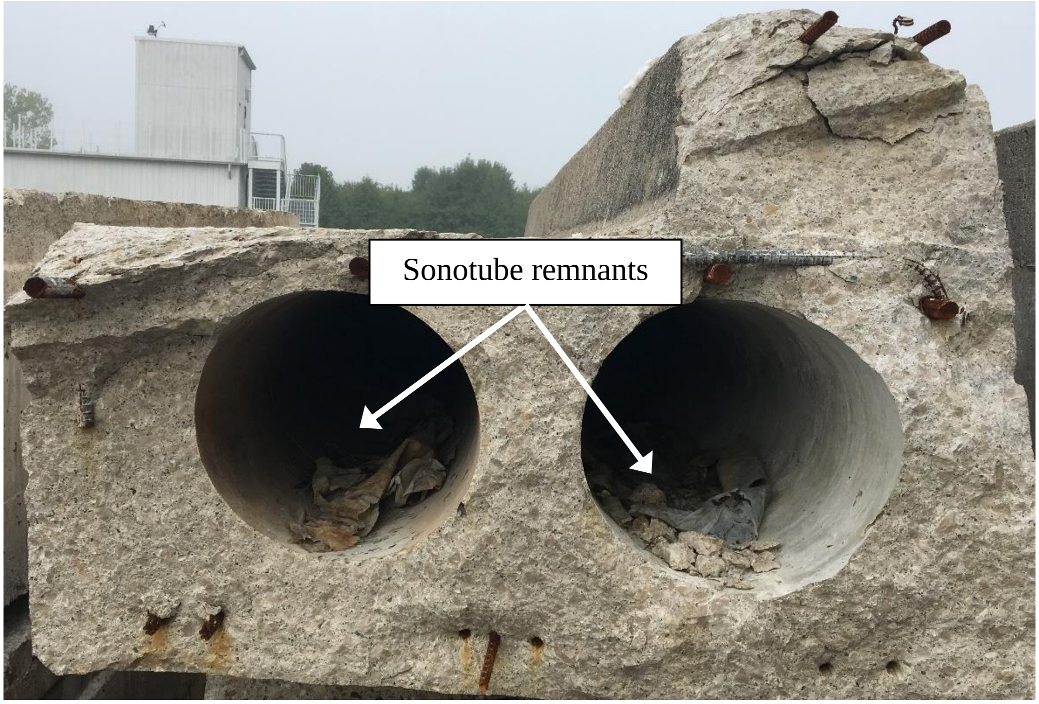

Figure 3.64: Disintegrated Cardboard Sonotubes

3.4.2.5 Specimen 56-1-LC

A single hairline longitudinal crack was observed in 56-1-LC at the end of the beam (Figure 3.10). The crack was located over Strand 6, and no corrosion was observed when the concrete cover was removed (Figure 3.65(b)). After removal of Strand 6, the extent of cracking was investigated, and the crack was not observed to continue through the thickness of the bottom flange. The formation of the longitudinal crack was assumed to be related to stresses induced at release of the strands after initial concrete curing.

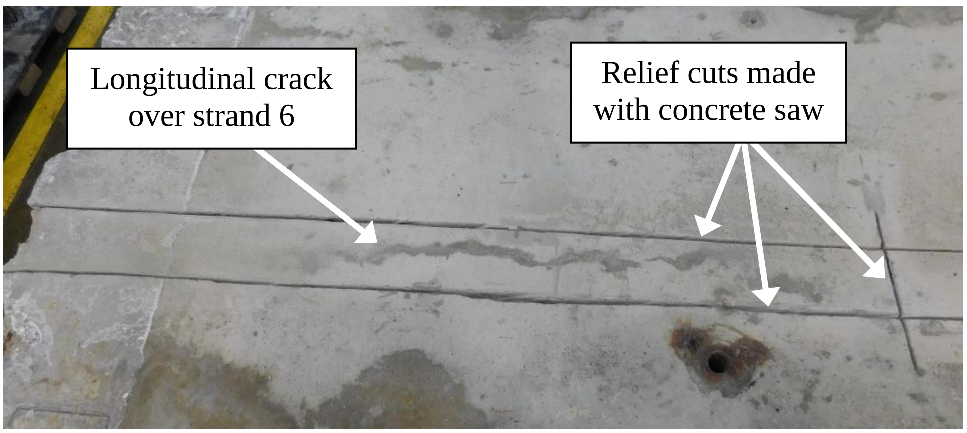

(a) Before cover was removed

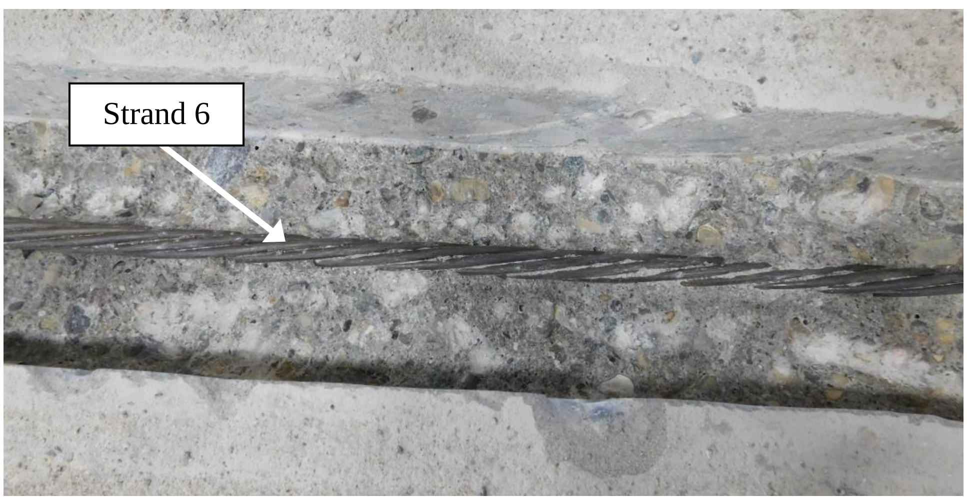

(b) After cover was removed

Figure 3.65: Strand Condition at the Longitudinal Crack in 56-1-LC

3.4.2.6 Summary

Four of the five beam specimens were observed with longitudinal cracks that extended through the thickness of the bottom flange (Specimens 244-1-LC, K5-1-LC, K5-2-LC, and 79-4-LC). The longitudinal cracks in each of the four beams mentioned were observed to wander through the bottom flange, crossing strand in no discernable pattern. In the case of Specimen K5-2-LC, the crack occurred away from the strands, toward the middle of the bottom flange. These observations paired with the fact that each beam was observed to have evidence of water ingress to the void indicates that the longitudinal cracks were formed by water freezing in the void. Saturation of the bottom flange due to retention of water in the voids did not play a role in corrosion due to moisture ingress. If the cracks were initiated by strand corrosion, the cracks would have been observed following a path along the length of the strand as observed in Specimens 102-1-BS, 102-2-BS, 102-3-BS, and 102-4-BS.

The extent of deterioration was the same in each of the four beam specimens (244-1-LC, K5-1-LC, K5-2-LC, and 79-4-LC). Corrosion of the strand was observed to be limited to only the location where the longitudinal crack was aligned with the strand. Evidence of corrosion in strands adjacent to the strands at longitudinal cracks was not found.

3.5 NDT Results

Colors have been used to designate the correlation of the numerical results from the NDT methods to corrosion as specified from the literature or respective ASTM standard. Table 3.6 provides a summary of this color correlation. In some locations, cracks and concrete spalls prevented the use of the NDT devices and no reading was available. In these locations in the NDT deterioration maps, no reading is indicated by a black line.

To compare the results of the NDT methods against the corrosion found in each of the beam specimens, the NDT results have been mapped to correspond with the locations of the strand within each beam (Figure 3.66 to Figure 3.80). In the figures, the visual deterioration map from Section 3.2 is noted as “visual”, and the results from the strand extraction from Section 3.4 are noted as “strand”. Corrosion found during the strand extraction procedure has been mapped to provide a visual summary of actual strand corrosion. The deterioration noted in the strand corrosion maps follows the key provided in Table 3.7.

Table 3.6: NDT Results Color Key

NDT Method	Color Code	Measurement	Deterioration Classification	Source
CEPRA	Green —	$C_r < 1.1$ µm/yr	Passive/low corrosion	Andrade and Alonso (1996)
	Yellow —	$1.1 \leq C_r < 2.2$ µm/yr	Uncertain	
	Orange —	$2.2 \leq C_r < 10$ µm/yr	Visible corrosion	
	Red —	$C_r \geq 10$ µm/yr	Severe corrosion	
GPR	Green —	≥ 6 dB threshold	No deterioration	ASTM D6087 (2015)
	Red —	< 6 dB threshold	Deterioration	
Half-Cell	Green —	$V_m > -0.20$ V	90% probability of no corrosion	ASTM C876 (2015)
	Yellow —	$-0.20\text{ V} \geq V_m \geq -0.35$ V	Probability of corrosion is uncertain	
	Red —	$V_m < -0.35$ V	90% probability of corrosion	
All	Black —	No reading available		

Table 3.7: Deterioration Key for Strand Corrosion Maps

Deterioration Type	Map Symbol
Shear key showing signs of deterioration	Water Staining; Rust-Colored Staining
Longitudinal cracking	Cracking Cracking with exposed strand Blue Crack = Water Stained Red Crack = Rust Stained
Corner Cracking	cc
Concrete spalling	Spalling; Spalling with Exposed Strands
Concrete spalling on one side of shear key	Spalling; Spalling with Exposed Strands
Strand	No corrosion on strand Strand with corrosion

A review of Figure 3.66 to Figure 3.80 should be conducted with the understanding that the CEPRA and half-cell potential methods could not be used to scan directly over most longitudinal cracks, and all three methods cannot used to scan exposed strand. Therefore, the goal of each method was to identify corrosion occurring adjacent to signs of deterioration that could not be observed visually.

As an example, the deterioration and NDT results of Specimen 244-1-LC are shown in Figure 3.66. As shown, strand corrosion was limited to the longitudinal cracks based on a review of the "Visual" and "Strand" deterioration maps. Comparing these maps with the NDT results provides correlation between indicated and actual strand corrosion. The CEPRA method indicated "visible" corrosion in the strands adjacent to the rust stained crack at midspan, and around the south longitudinal crack, the indicated corrosion of the adjacent strands ranged from passive to visible. These results are understood as the corrosion of the strands adjacent to the longitudinal cracks was minimal, but there is much noise in the data. The GPR results indicated that there was no corrosion in the specimen. The half-cell potential readings indicated an uncertain probability of corrosion in the strands adjacent to both longitudinal cracks. These readings are understood to indicate minimal to no corrosion adjacent to the longitudinal cracks.

As a supplemental example, the deterioration and NDT results of Specimen 102-2-BS are shown in Figure 3.78. The "Visual" and "Strand" deterioration maps show that strand corrosion was limited to the broken strand and strand at the longitudinal cracks and corner cracks. No readings were available at the broken strand; therefore, the strand is colored black in that location. The CEPRA results indicate "visible" corrosion throughout most of the specimen except for strands adjacent to the broken strand and longitudinal and corner cracks, where severe corrosion is indicted. These results are understood as corrosion of the adjacent strands is highly likely. The GPR results indicate corrosion on the strand at the corner crack at midspan and no corrosion throughout the rest of the specimen. Half-cell potentials indicated corrosion adjacent to the broken strand and in the strands adjacent to the longitudinal and corner cracking. These readings are understood to indicate corrosion in the adjacent strands.

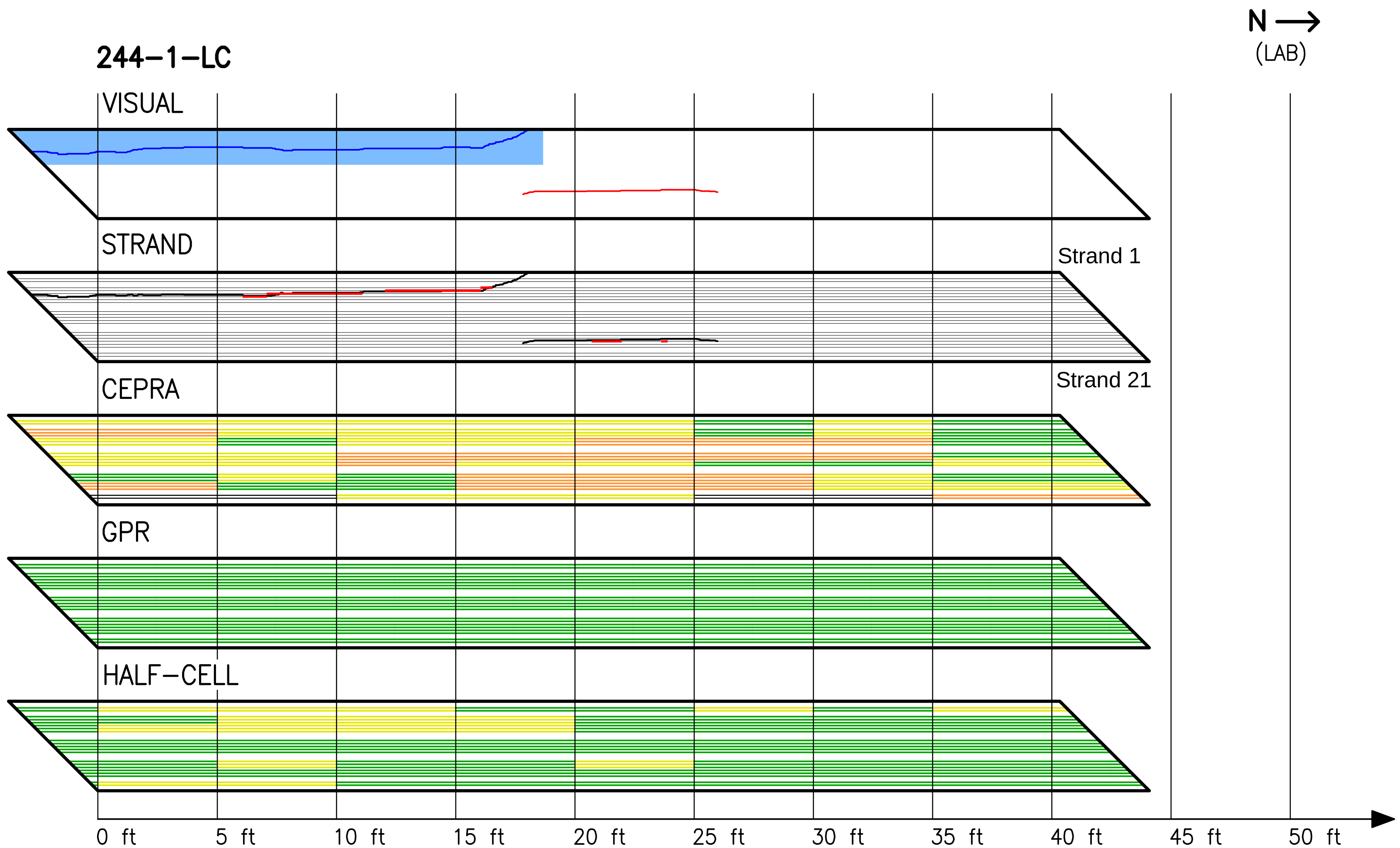

Figure 3.66: 244-1-LC Deterioration Map

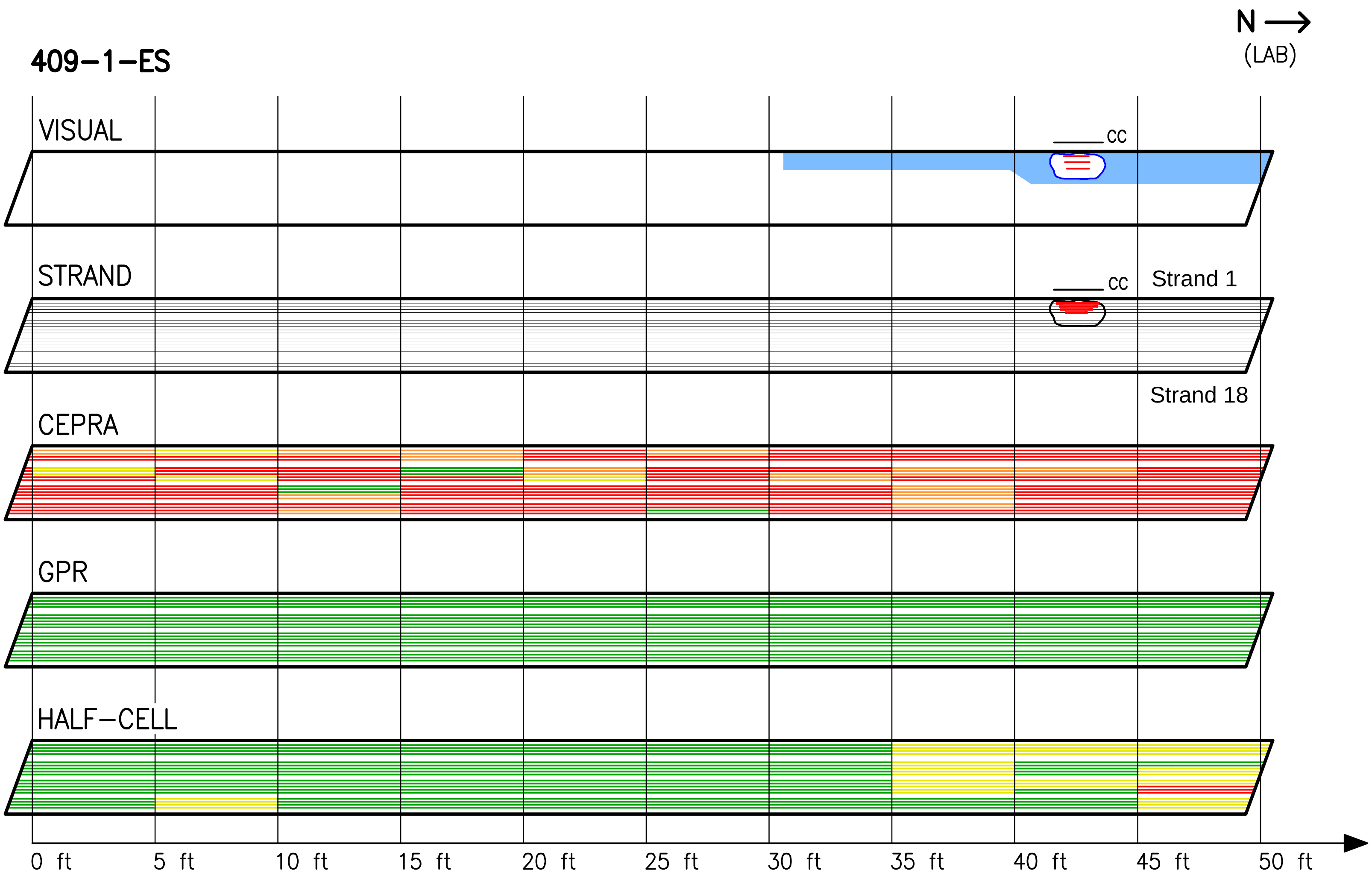

Figure 3.67: 409-1-ES Deterioration Map

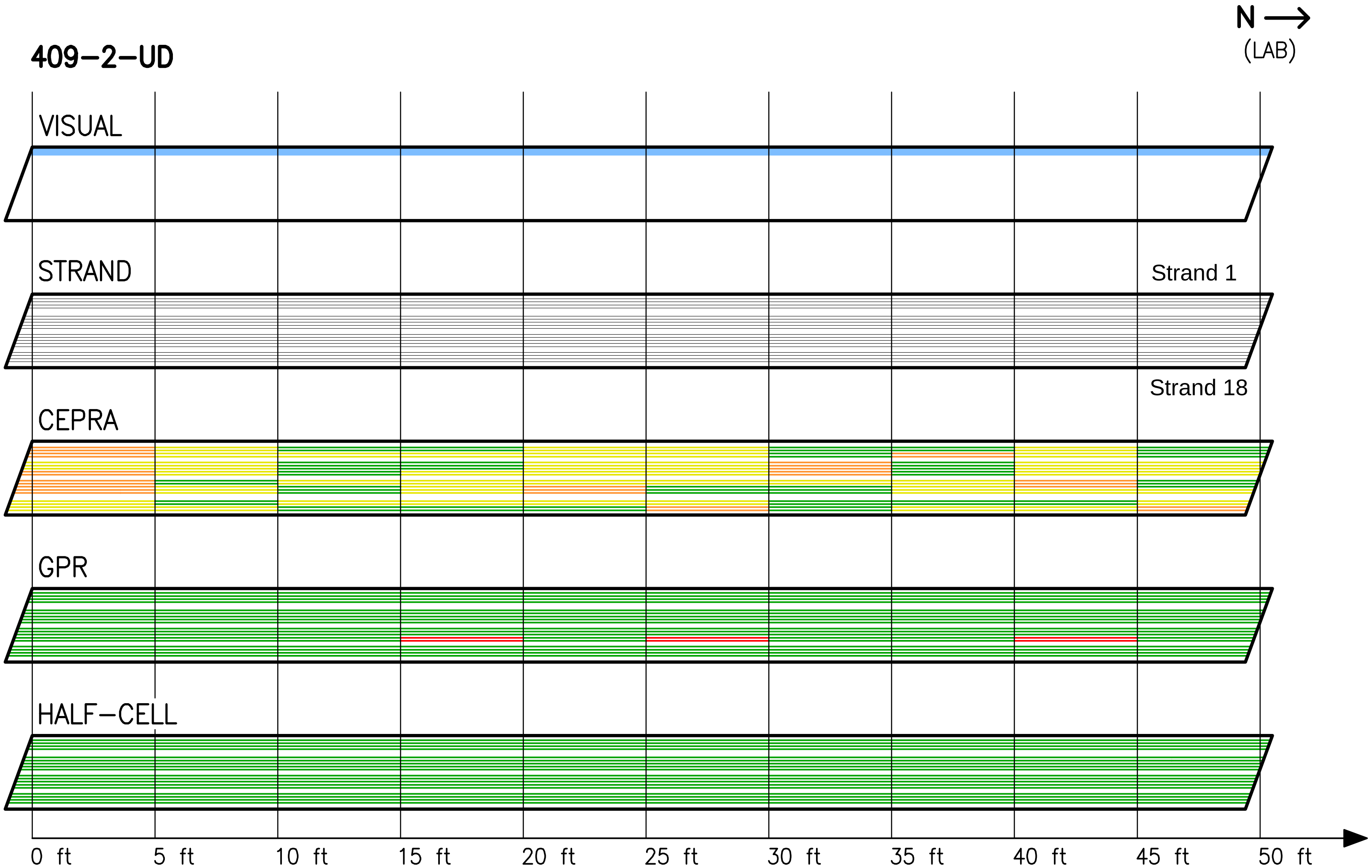

Figure 3.68: 409-2-UD Deterioration Map

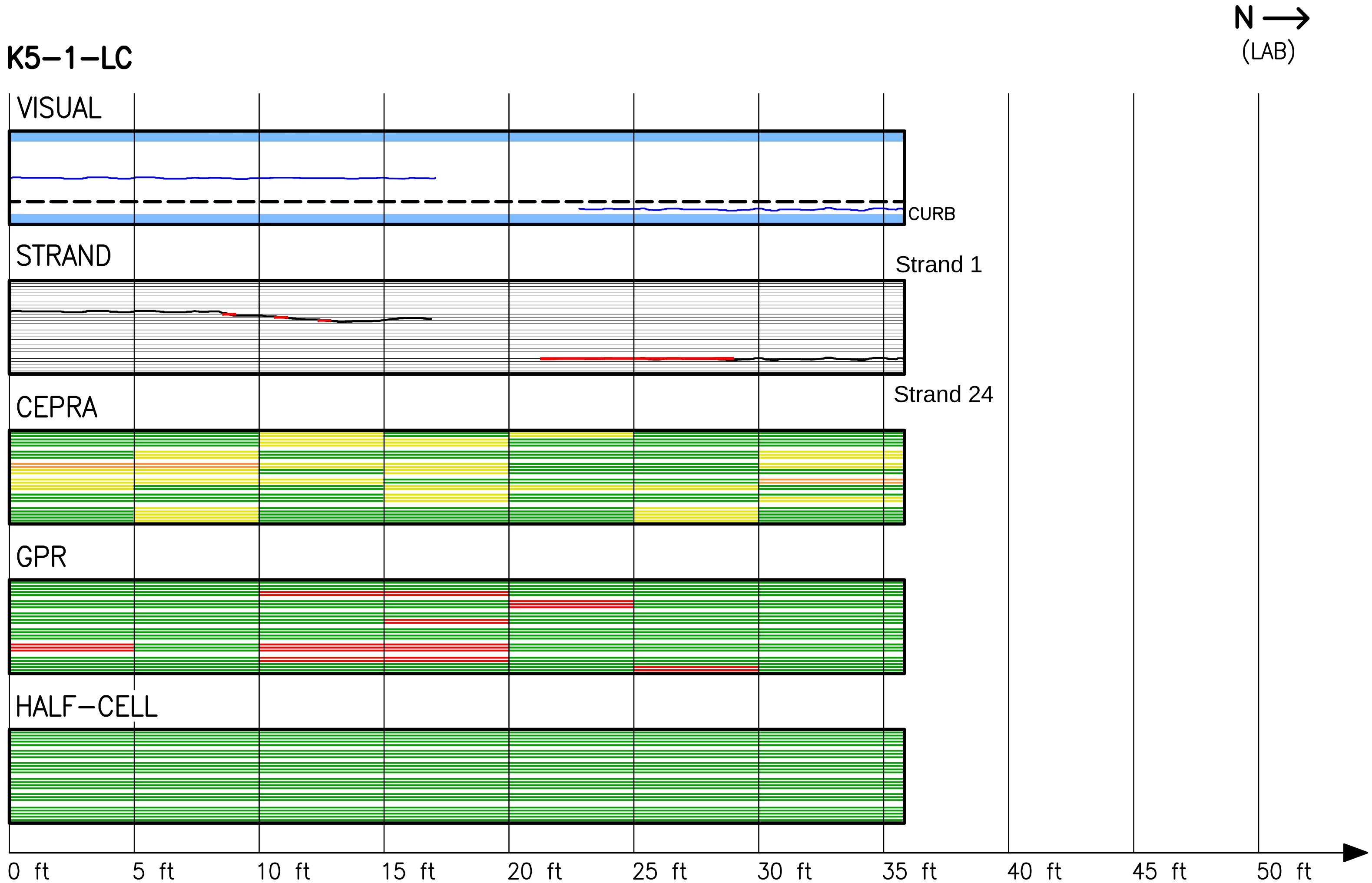

Figure 3.69: K5-1-LC Deterioration Map

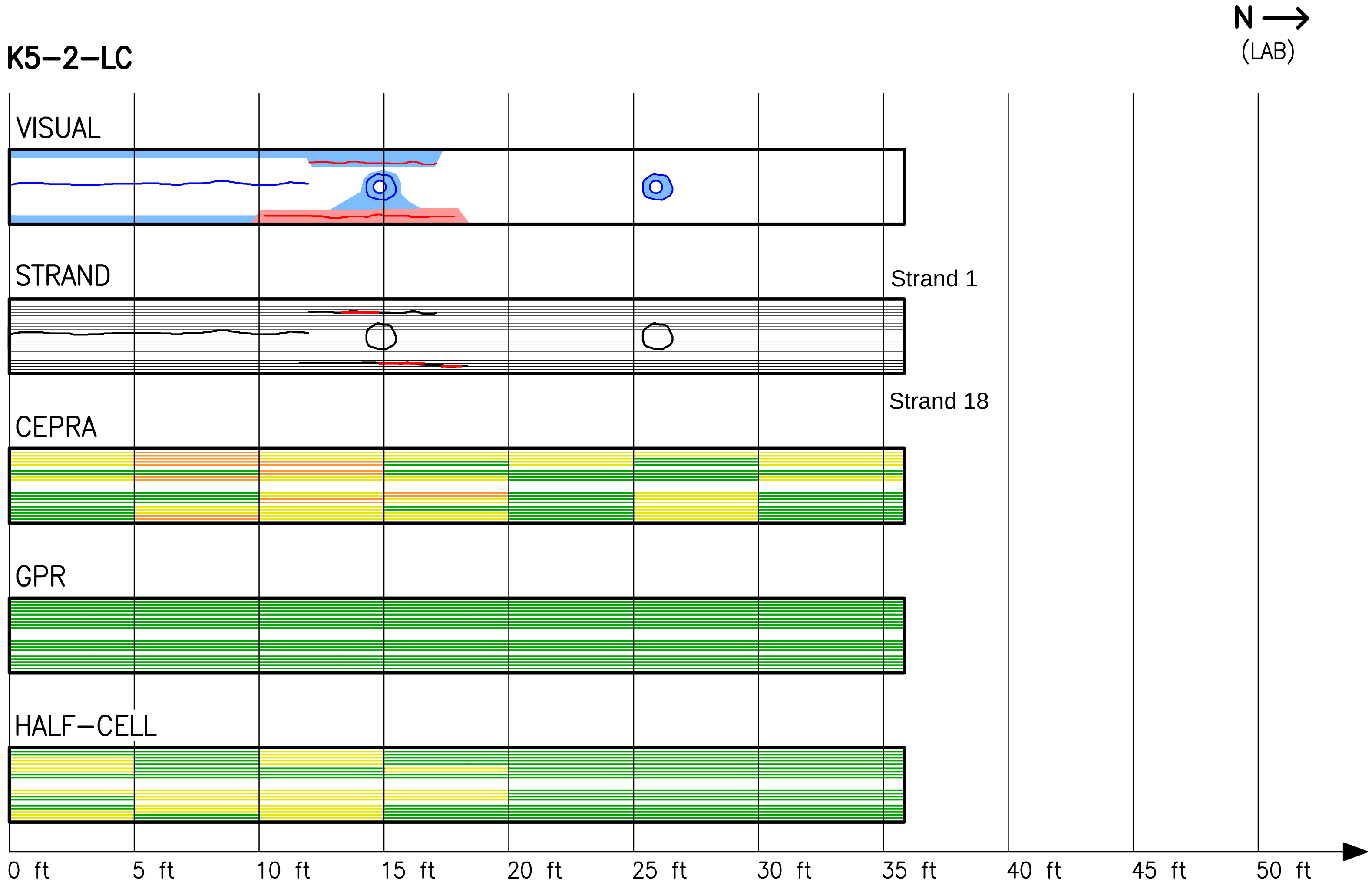

Figure 3.70: K5-2-LC Deterioration Map

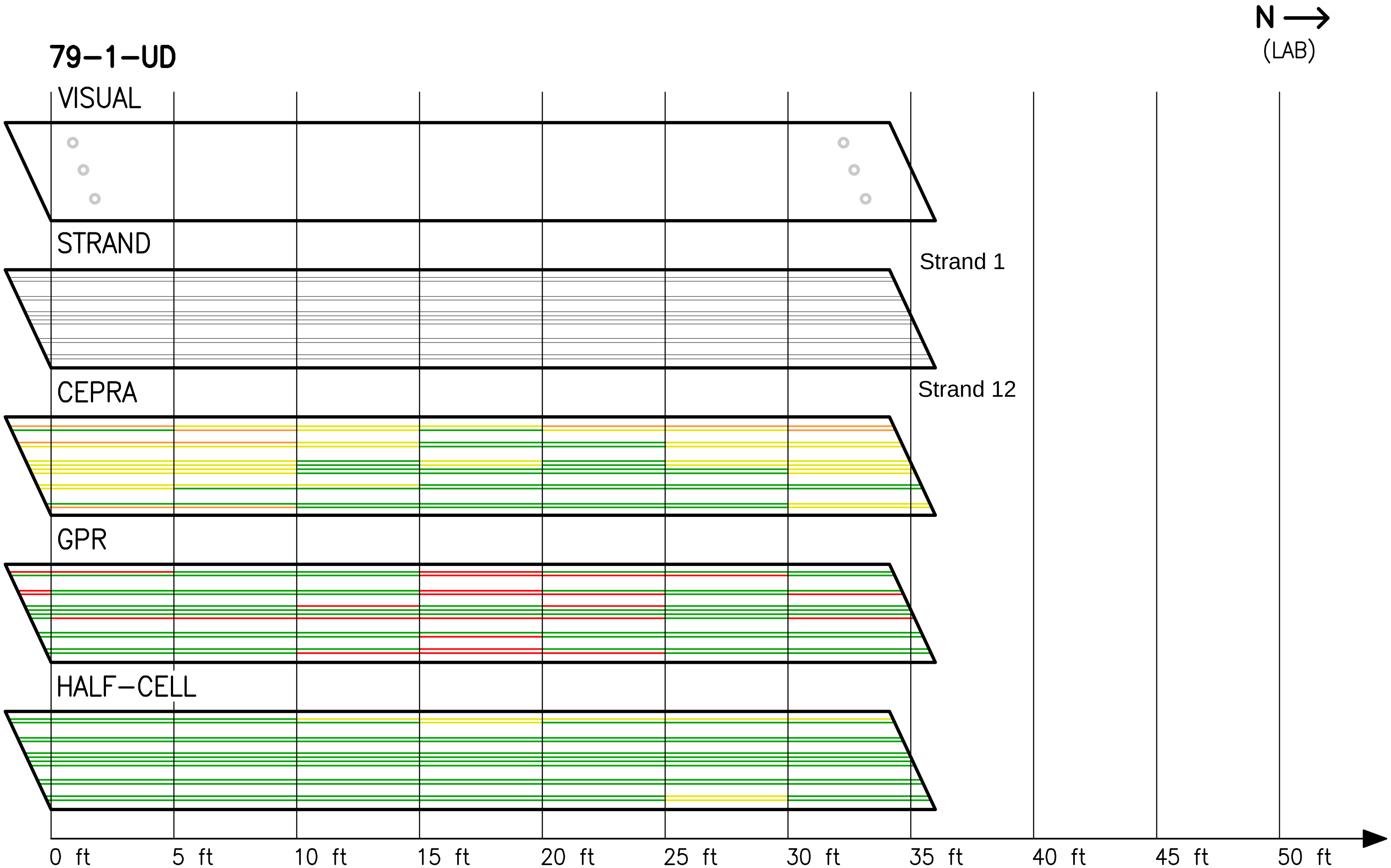

Figure 3.71: 79-1-UD Deterioration Map

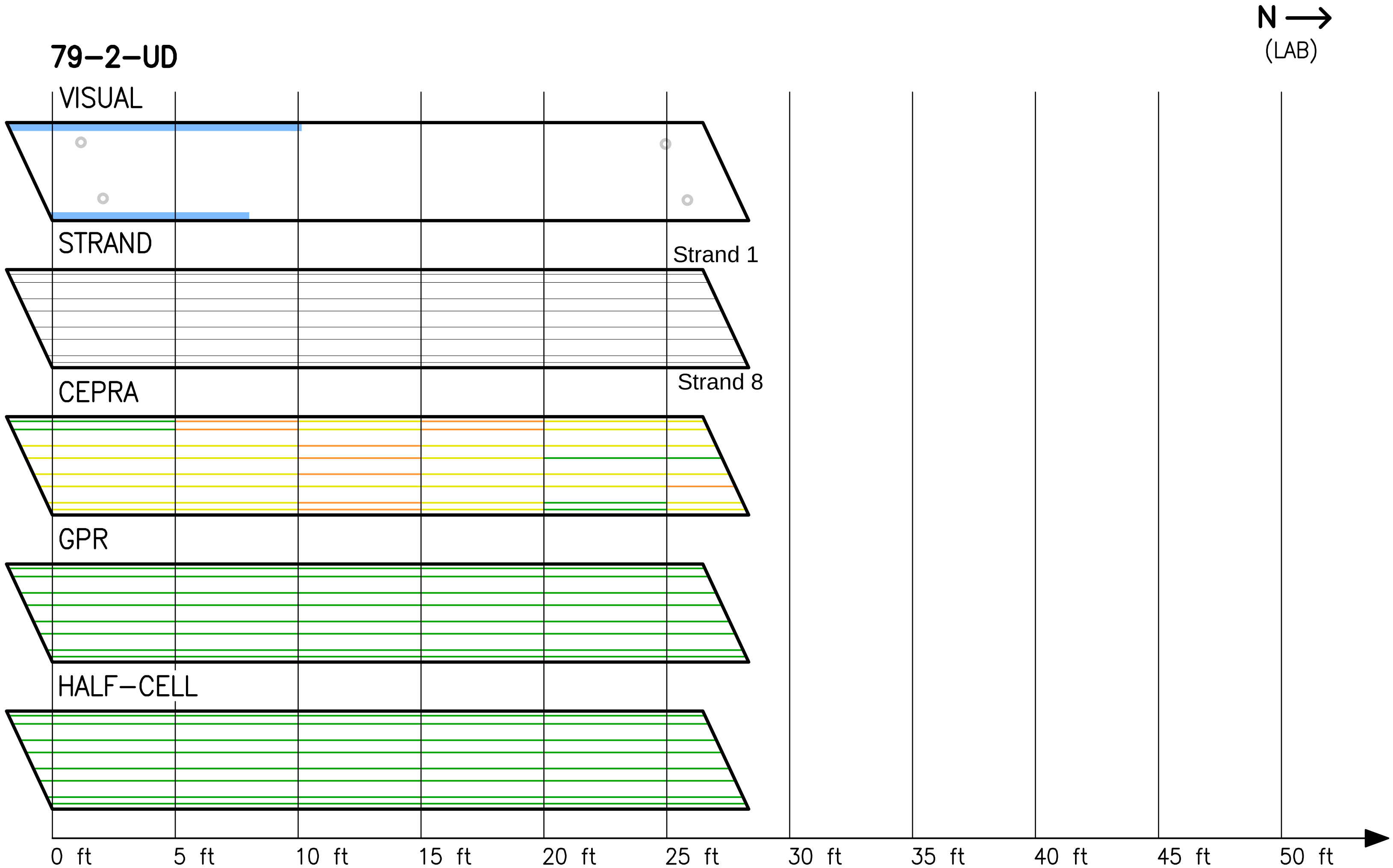

Figure 3.72: 79-2-UD Deterioration Map

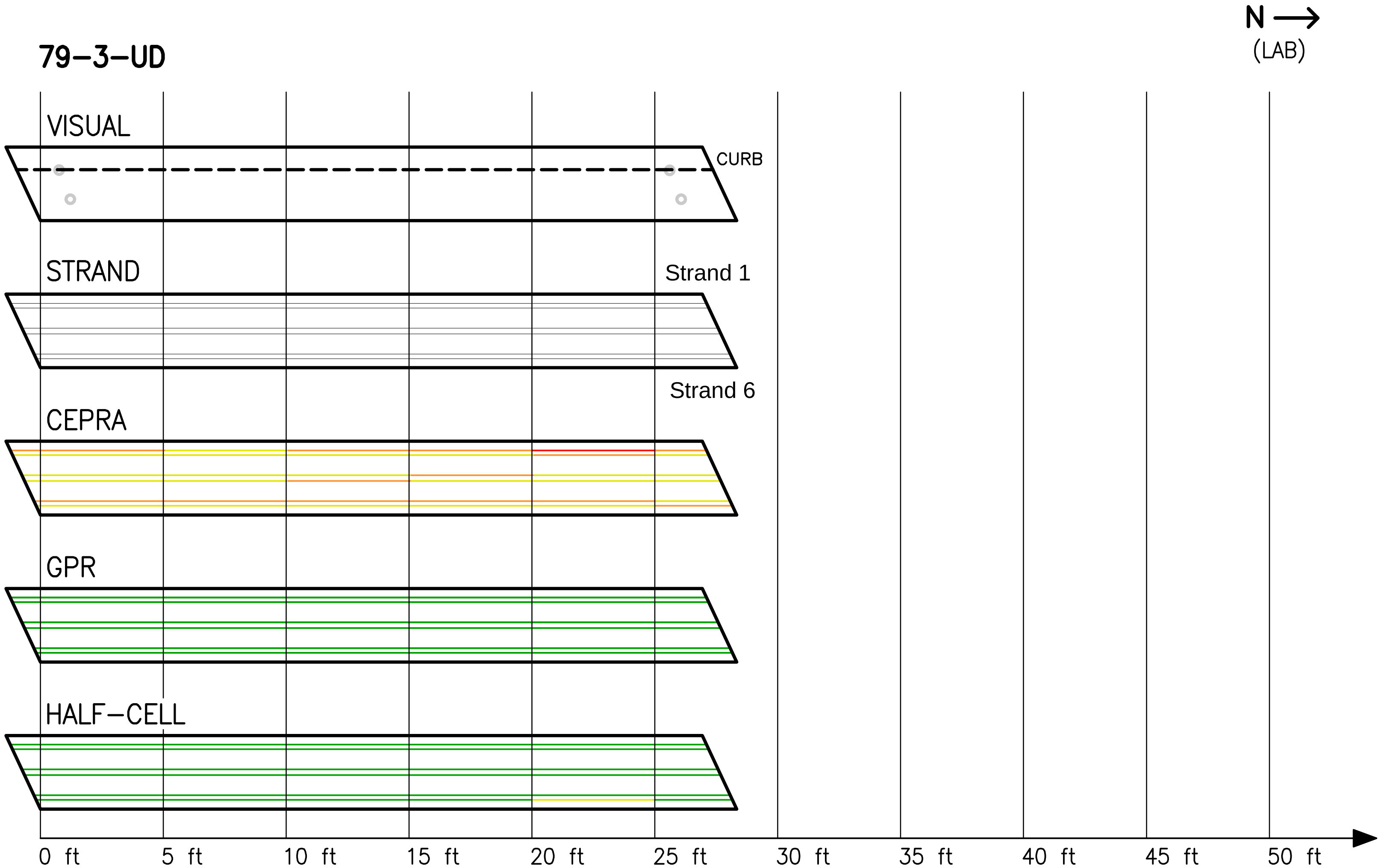

Figure 3.73: 79-3-UD Deterioration Map

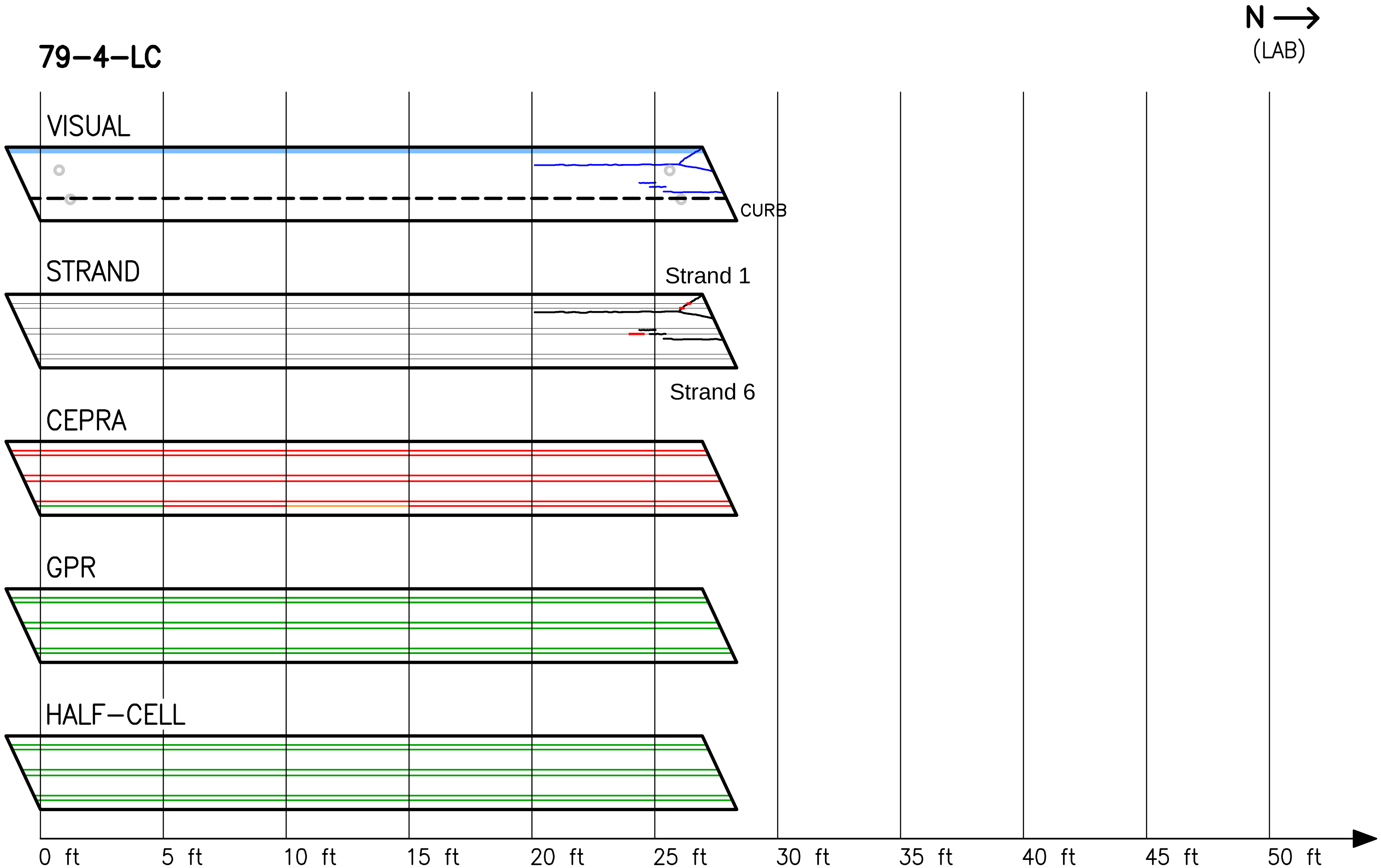

Figure 3.74: 79-4-LC Deterioration Map

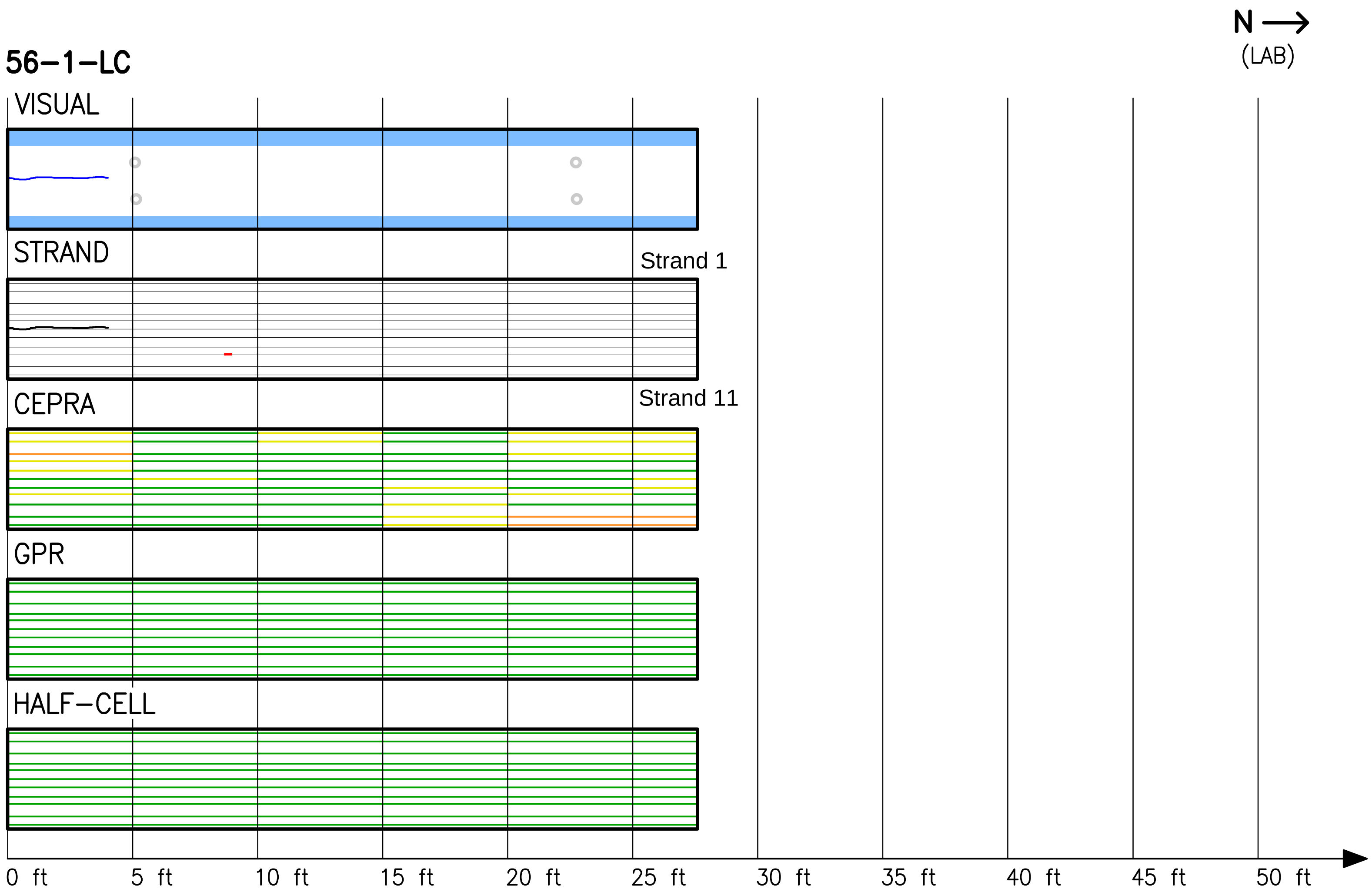

Figure 3.75: 56-1-LC Deterioration Map

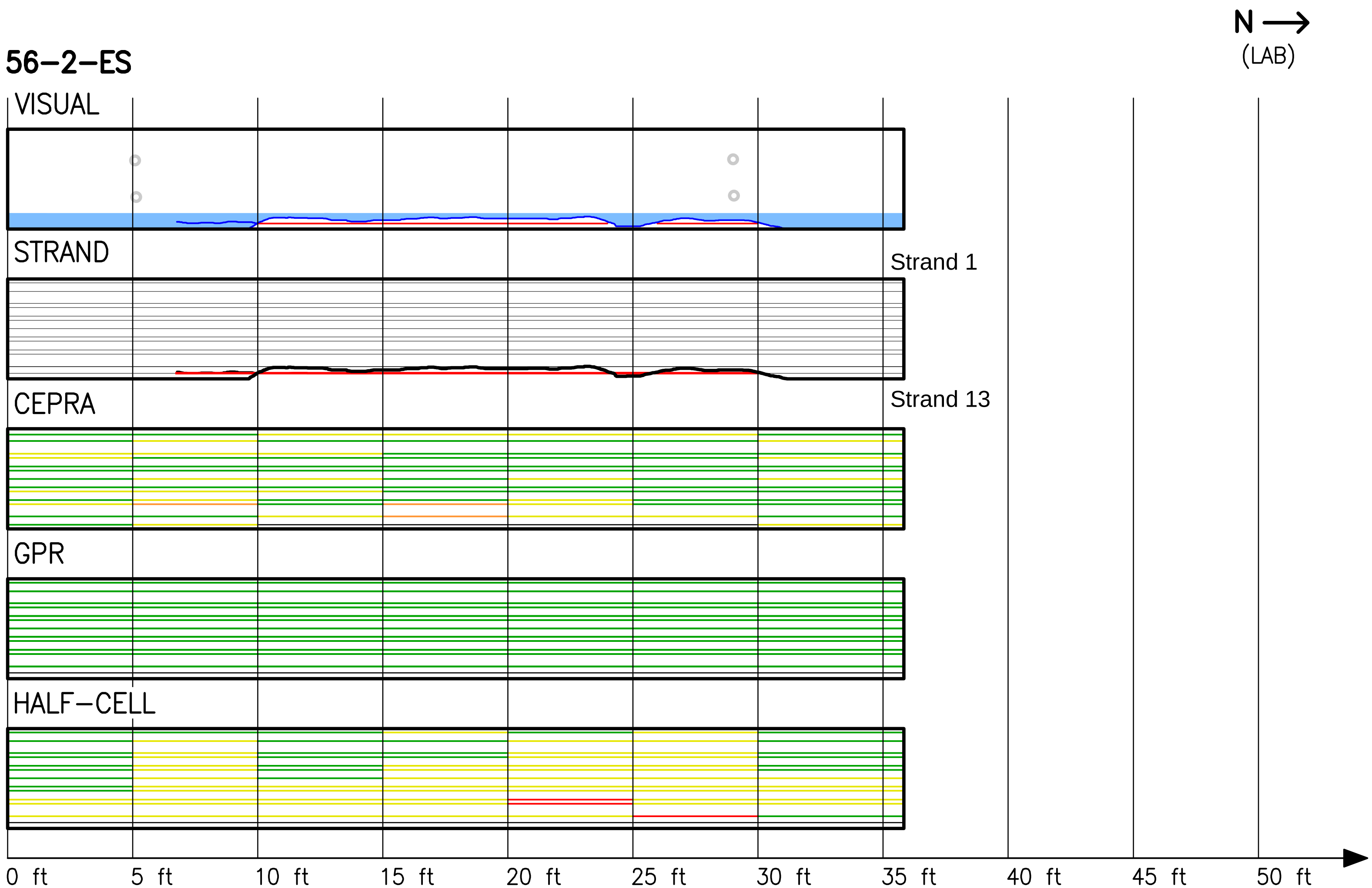

Figure 3.76: 56-2-ES Deterioration Map

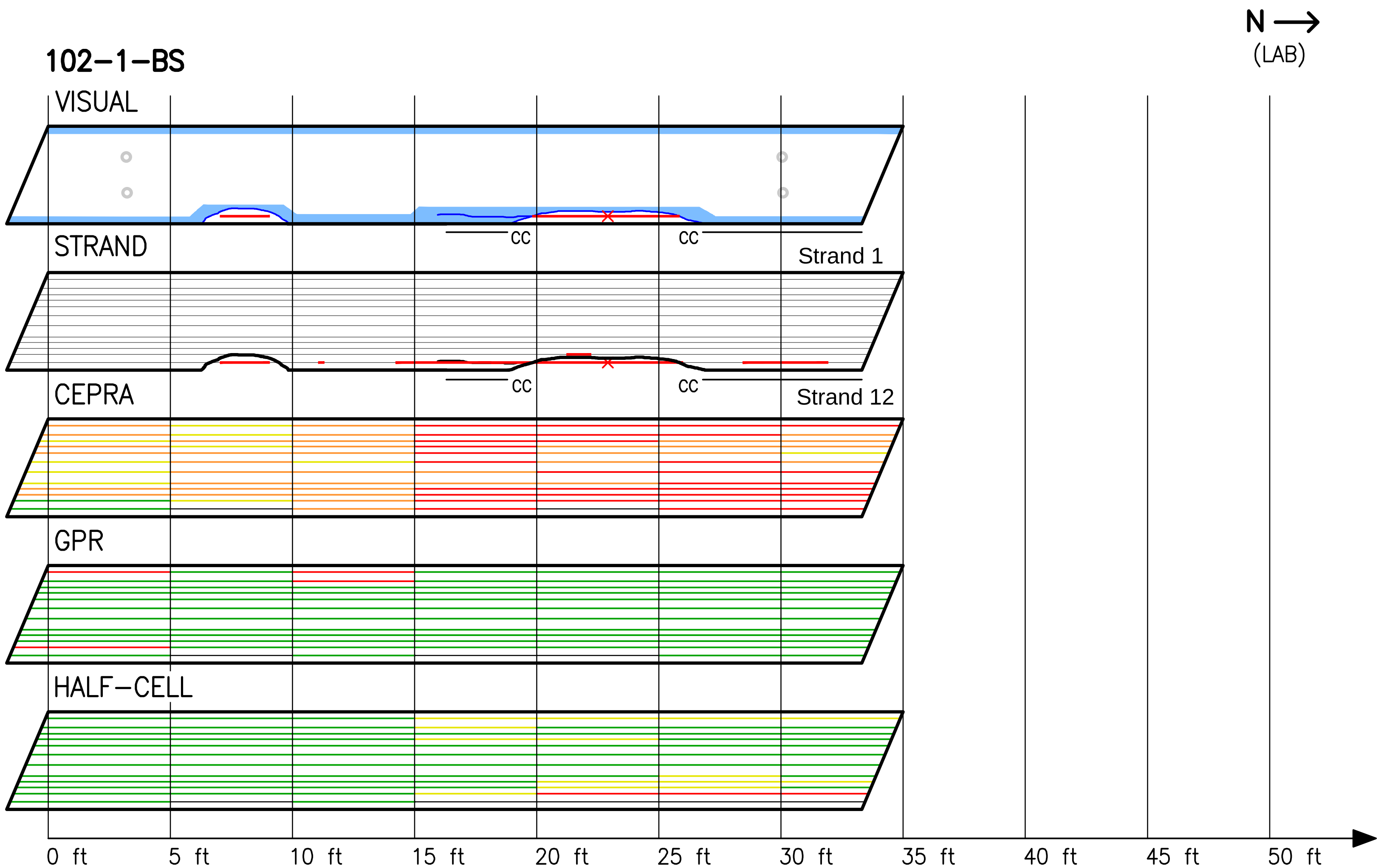

Figure 3.77: 102-1-BS Deterioration Map

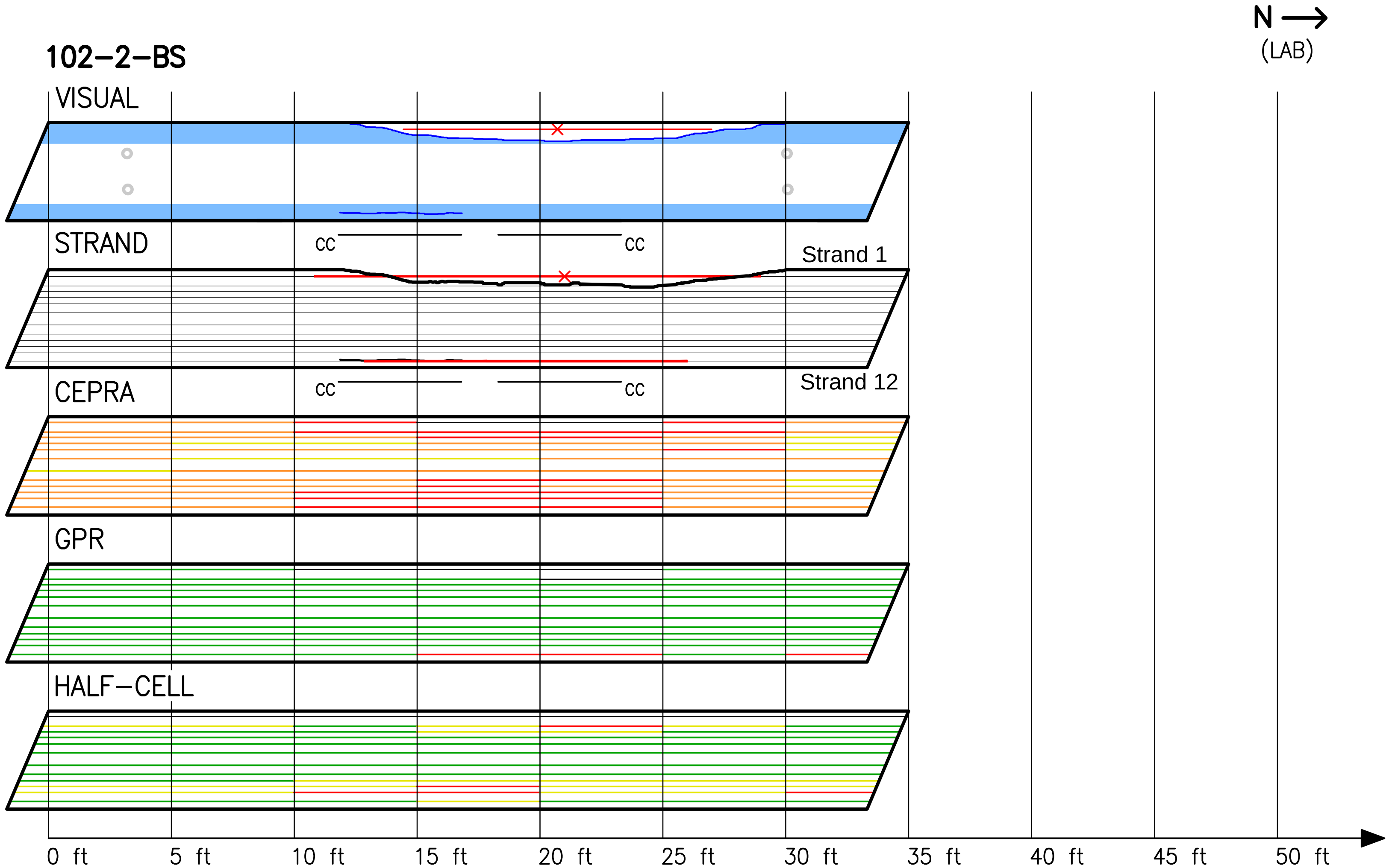

Figure 3.78: 102-2-BS Deterioration Map

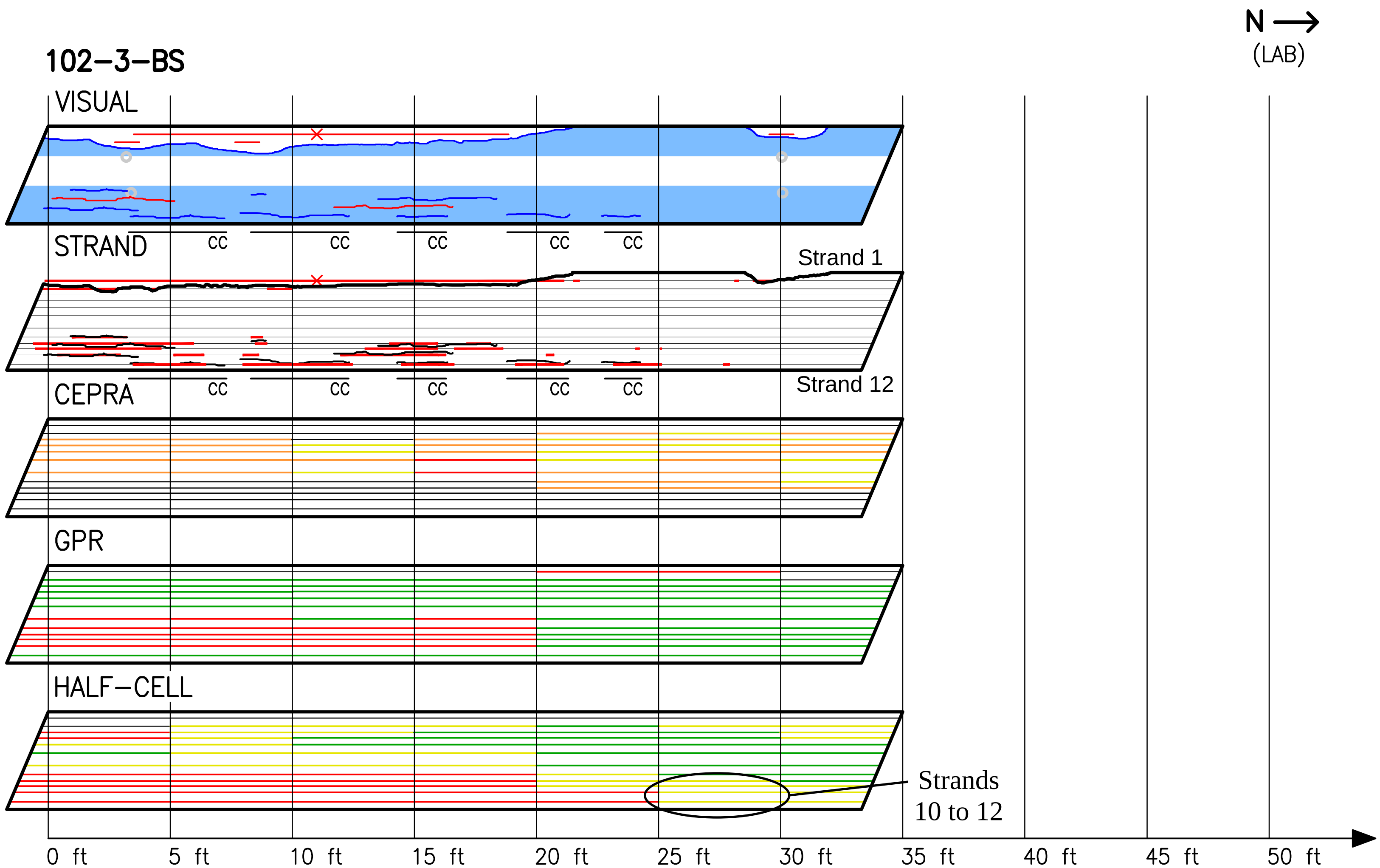

Figure 3.79: 102-3-BS Deterioration Map

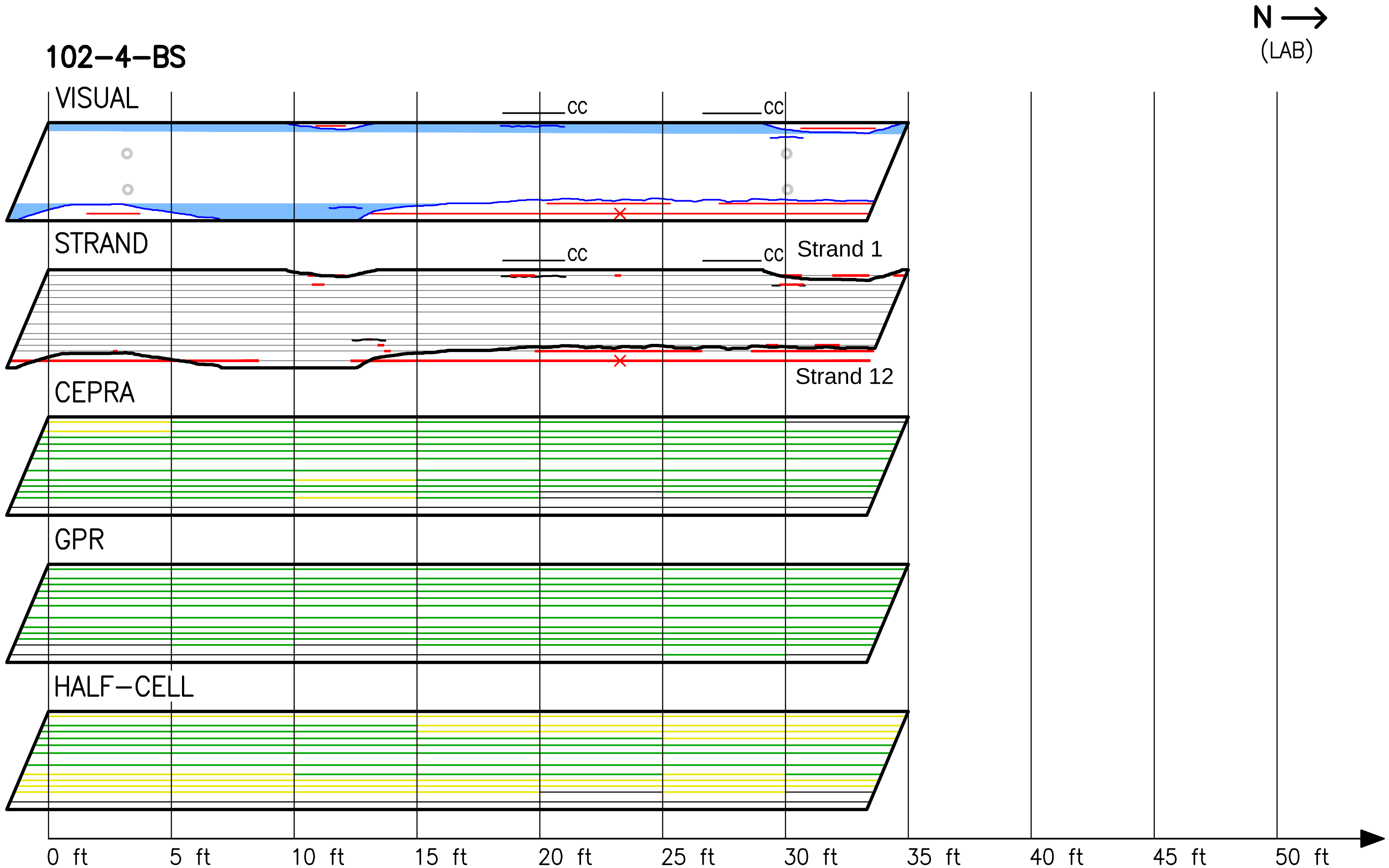

Figure 3.80: 102-4-BS Deterioration Map

3.6 Comparison of NDT Results

A review of each comparison presented in Figure 3.66 to Figure 3.80 shows that, in general, the Half-Cell Potentials method provided the best estimation of strand corrosion as compared to the CEPRA and GPR methods. The CEPRA method overestimated the level of corrosion, and the GPR method underestimated the number of corroded strands. In the following sections, the results of CEPRA, GPR, and half-cell potentials are discussed.

3.6.1 CEPRA

A review of the CEPRA results and actual strand corrosion in Figure 3.66 to Figure 3.80 indicates that the corrosion rates provided by the CEPRA device, in general, overestimated the amount of corrosion. The CEPRA results in Figure 3.74 indicate "severe" corrosion (red) along the length of every strand with exception to the eastern most strand which had two lengths of strand indicated to have "passive" (green) and "visible" (orange) corrosion. Figure 3.81 provides the condition of the two west edge strands on the north end of the specimen. As shown, the strands exhibit no corrosion. The CEPRA results also indicated "visible" corrosion (orange) in Strands 3 to 5 between 25 ft and 30 ft in Figure 3.77. When cover was removed, no corrosion was observed (Figure 3.82).

Figure 3.81: West Edge Strand Condition at North End of Specimen 79-4-LC

Figure 3.82: Strand Condition of North End Strands in Specimen 102-1-BS

Based on the observations made between actual strand corrosion and indicated strand corrosion, an adjustment to the CEPRA data was considered necessary. The adjustment in the interpretation of the CEPRA data was determined by considering the development of the four-part scale by Andrade and Alonso (1996) (Table 3.3). As mentioned previously, the measured corrosion rate is inversely proportional to the surface area of the bar polarized by the applied current (Equation 3-1). Table 3.3 was developed based on the surface area of steel wire reinforcement, but seven-wire strand has significantly more surface area than steel wire with similar cross-sectional area. For example, the surface area ratio of 3/8 in. strand to #3 bar or 3/8 in. diameter wire is 2.25, and the surface area ratio of 1/2 in. strand to #4 bar or 1/2 in. diameter wire is 2.3. Considering the difference in surface area, corrosion rate measurements of strand may appear artificially higher as observed in Figure 3.66 to Figure 3.80. Therefore, an adjustment factor of 2.3 was applied to the CEPRA data to be consistent with these surface ratios. The adjusted scale is provided in Table 3.8, and the adjusted results are shown in Figure 3.83 to Figure 3.97. As shown, the adjusted results provide better correlation with the actual corrosion observed in the strands.

Table 3.8: Adjusted CEPRA Corrosion Rate Scale

Color Code		Corrosion Rate, C_r (µm/year)	Classification of Corrosion
Green	—	$C_r < 2.5$	Passive/Low
Yellow	—	$2.5 \leq C_r < 5.1$	Uncertain
Orange	—	$5.1 \leq C_r < 23$	Visible
Red	—	$C_r \geq 23$	Severe
Black	—	No available data	

The adjustment made to the four-part scale provides a simple correction to the data without altering the CEPRA software. Please note that this correction is only considered applicable to 3/8 in. and 1/2 in. nominal strand diameters entered in the CEPRA software as #3 bars for 3/8 in. strand and #4 bars for 1/2 in. strand. It should be noted that the surface area ratio for 1/2 special strand to a #4 bar is 2.41 and the surface area ratio for a 0.6 in. diameter strand to a 0.6 in. diameter solid wire is 2.3. This indicates that the 2.3 adjustment factor may apply to other commonly used strand diameters. Further research, however, is needed to verify the correlations between larger strand diameters and the corresponding reinforcement bar sizes.

In addition to the adjusted four-part scale, a two-part scale was developed to investigate the potential of using a single value of corrosion rate as the threshold between corroded and uncorroded strands. The two-part scale is provided in Table 3.9. The threshold for corrosion is the same as the four-part scale threshold for "severe" corrosion, 23 μm/year. As shown in Figure 3.83 to Figure 3.97, use of the two-part scale provides a quick interpretation of the results but prevents the identification of areas of corrosion potential. As an example, the two-part scale for Specimen 102-1-BS (Figure 3.94) indicates corrosion on strands in the north end of the specimen but leads the inspector to believe that the rest of the specimen has no issues. The indication of "visible" corrosion, as shown in the adjusted four-part scale, may indicate strands that are likely to corrode in the future.

Table 3.9: Two-Part CEPRA Corrosion Rate Scale

Color Code		Corrosion Rate (μm/year)	Classification of Corrosion
Green	—	< 23	No corrosion
Red	—	≥ 23	Corrosion

.

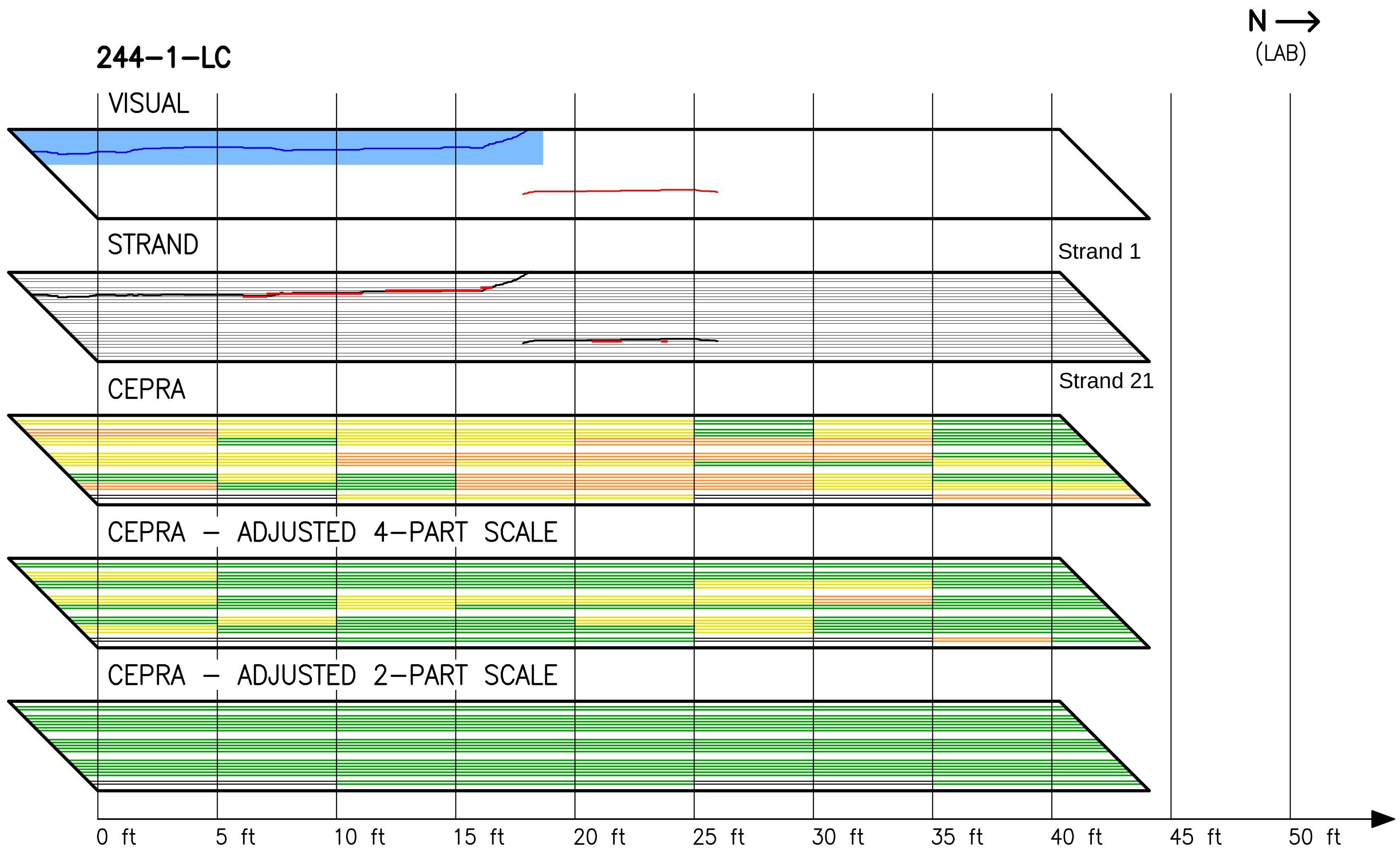

Figure 3.83: 244-1-LC Deterioration Map (CEPRA)

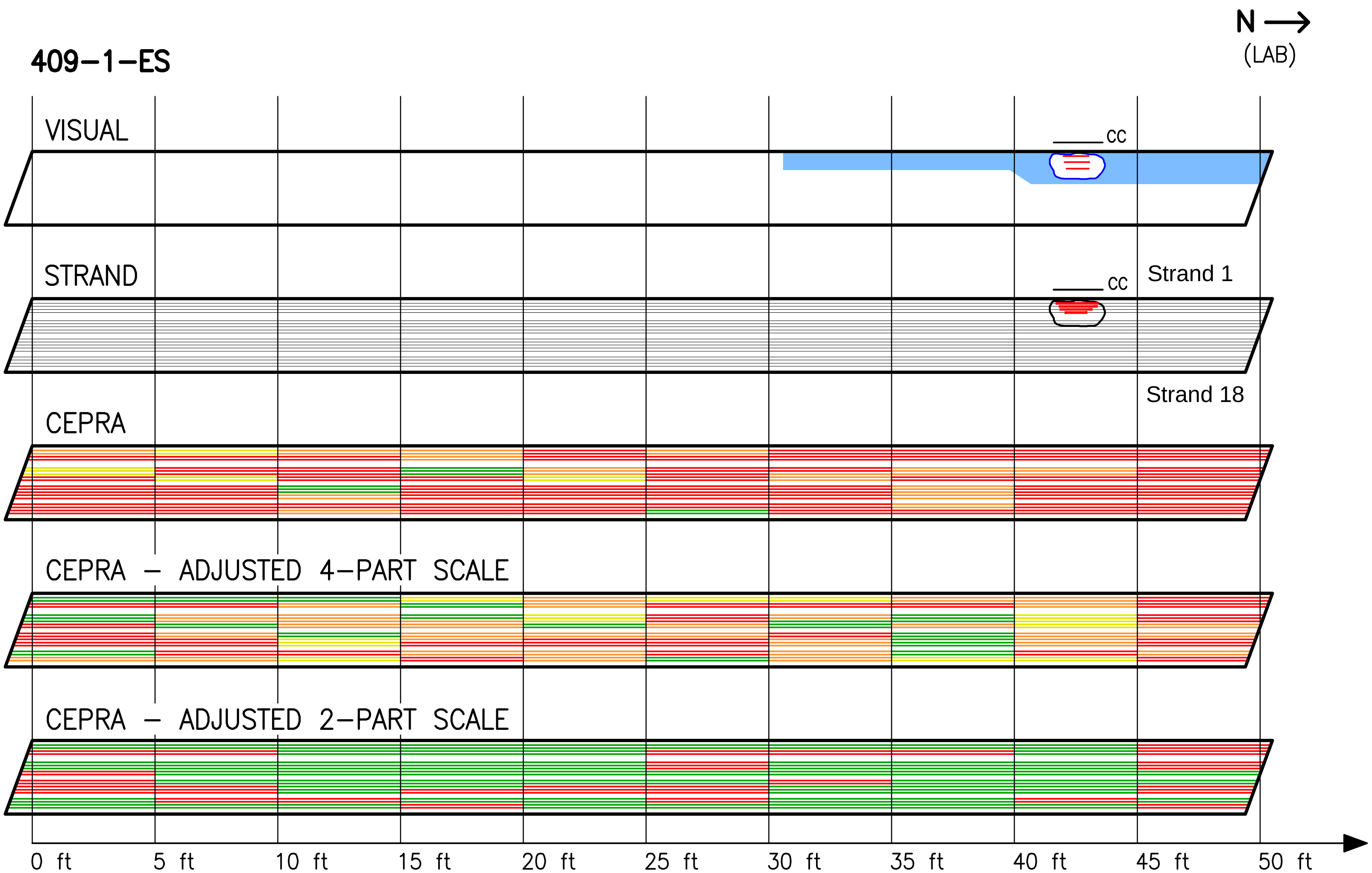

Figure 3.84: 409-1-ES Deterioration Map (CEPRA)

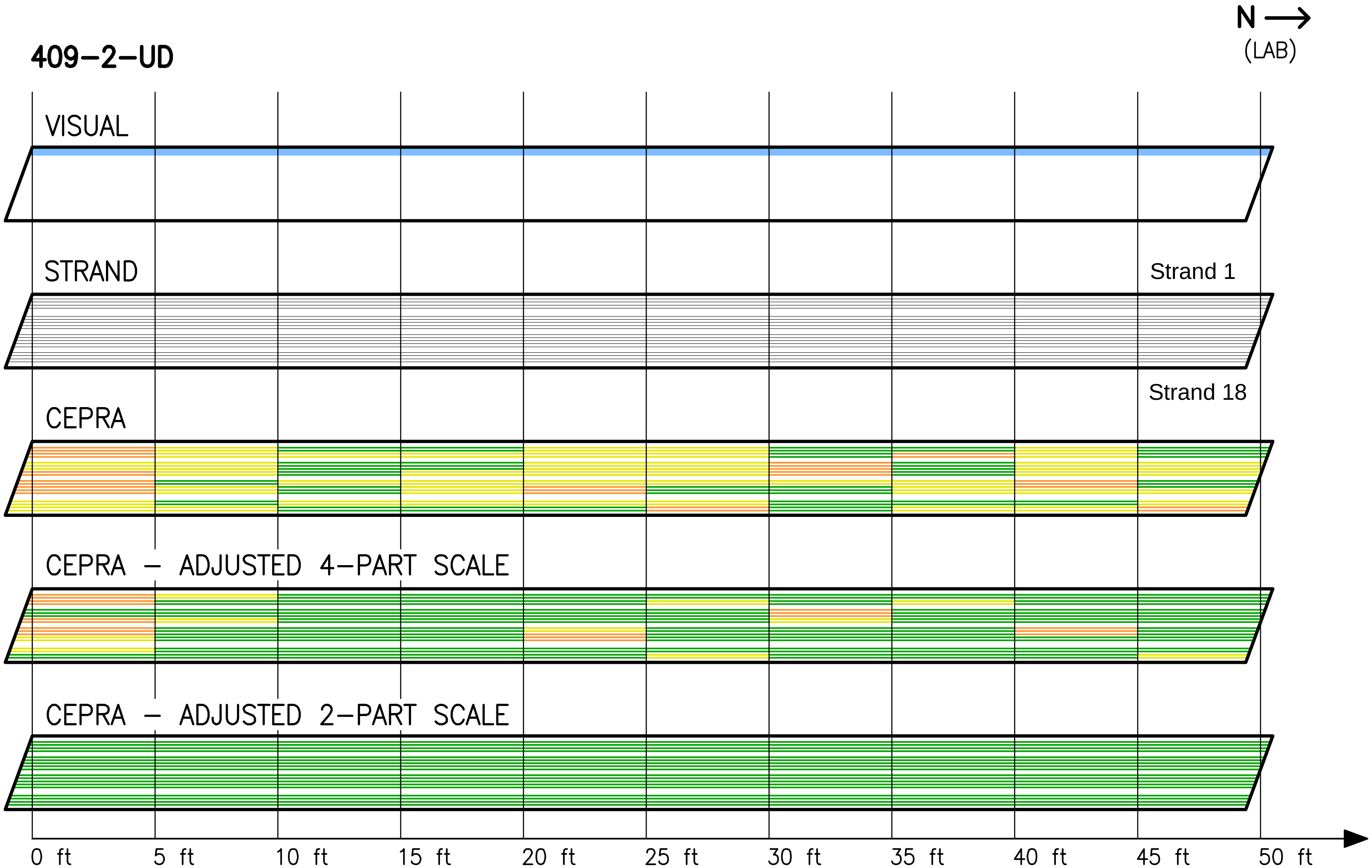

Figure 3.85: 409-2-UD Deterioration Map (CEPRA)

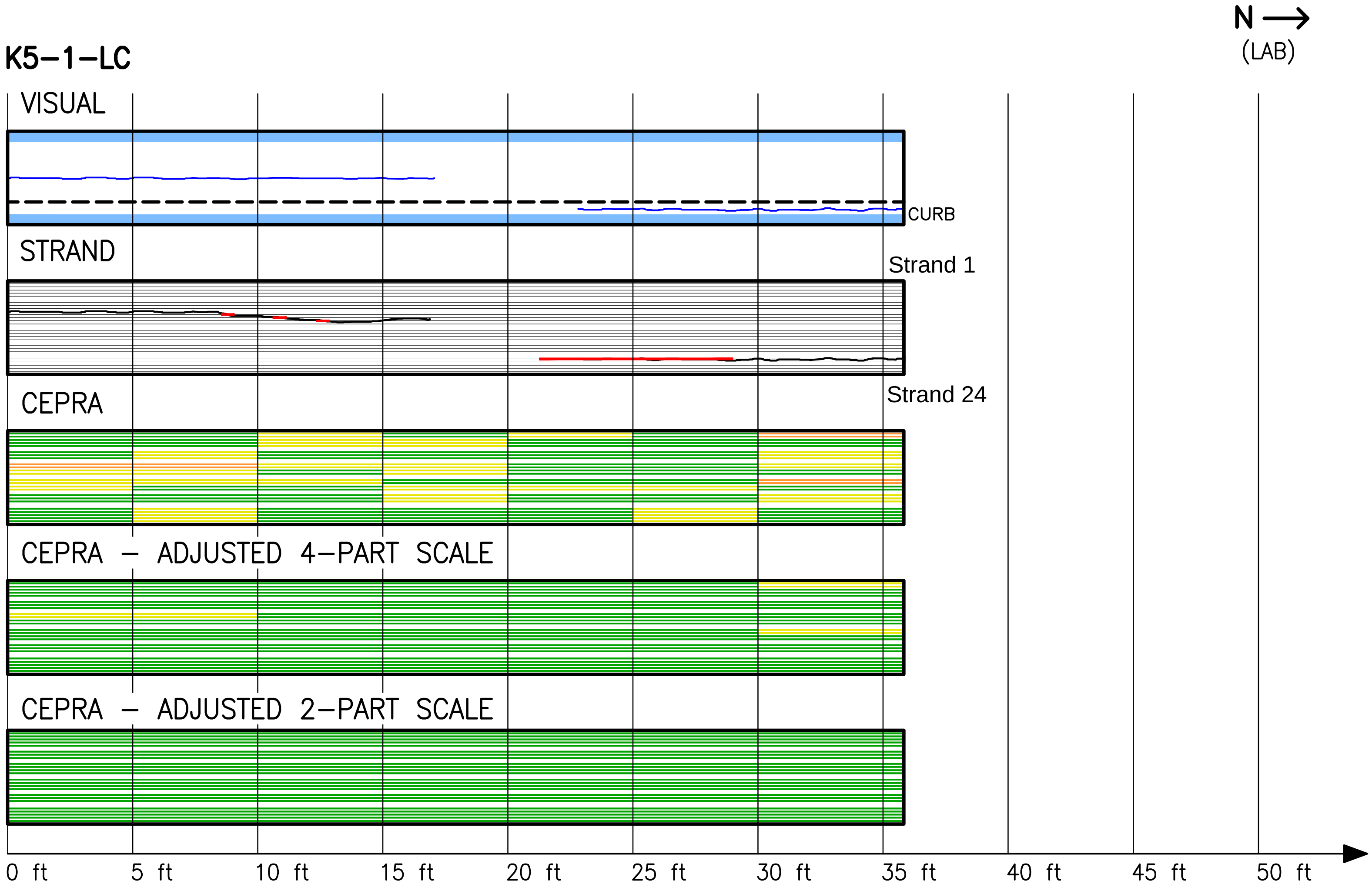

Figure 3.86: K5-1-LC Deterioration Map (CEPRA)

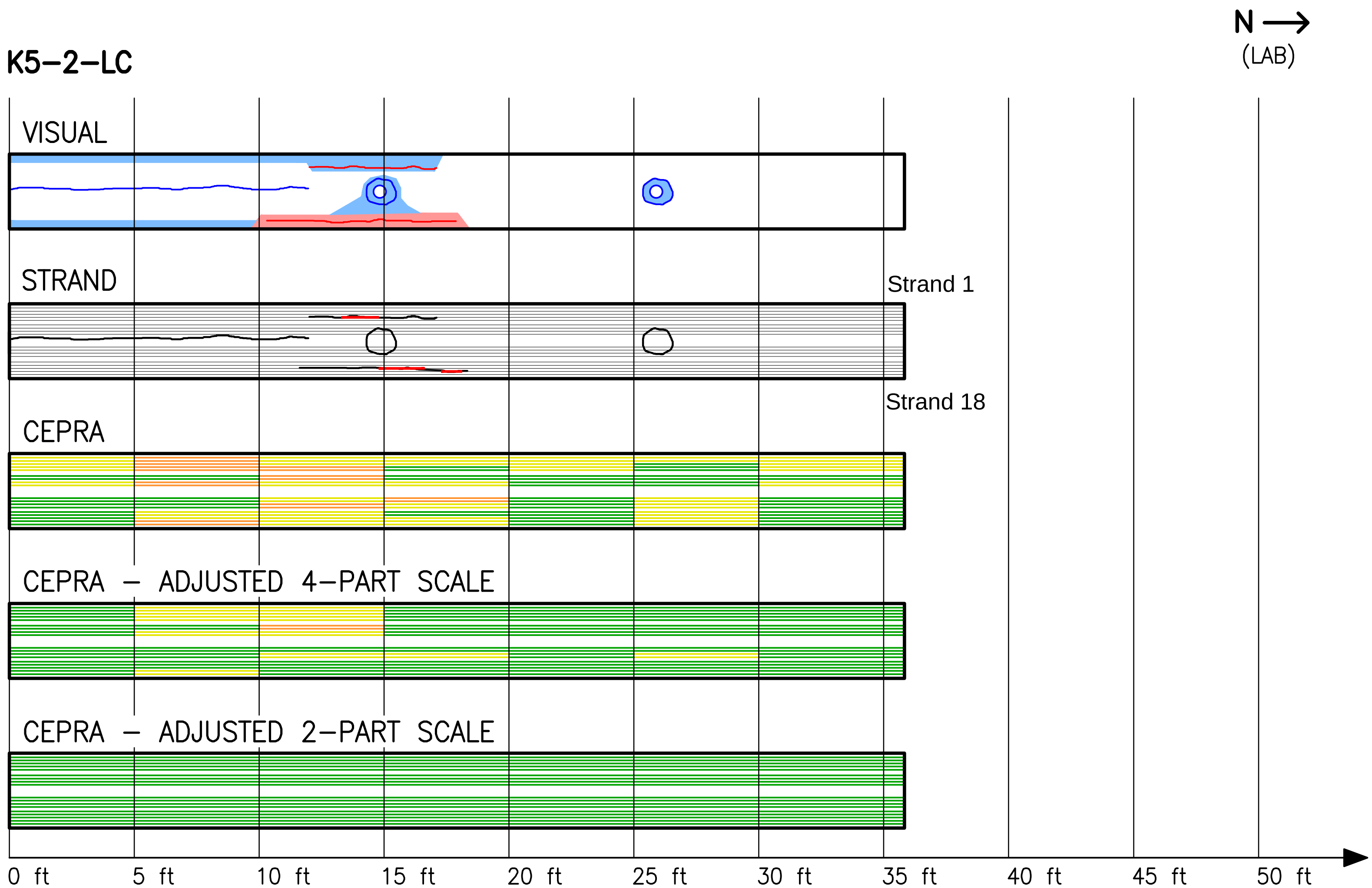

Figure 3.87: K5-2-LC Deterioration Map (CEPRA)

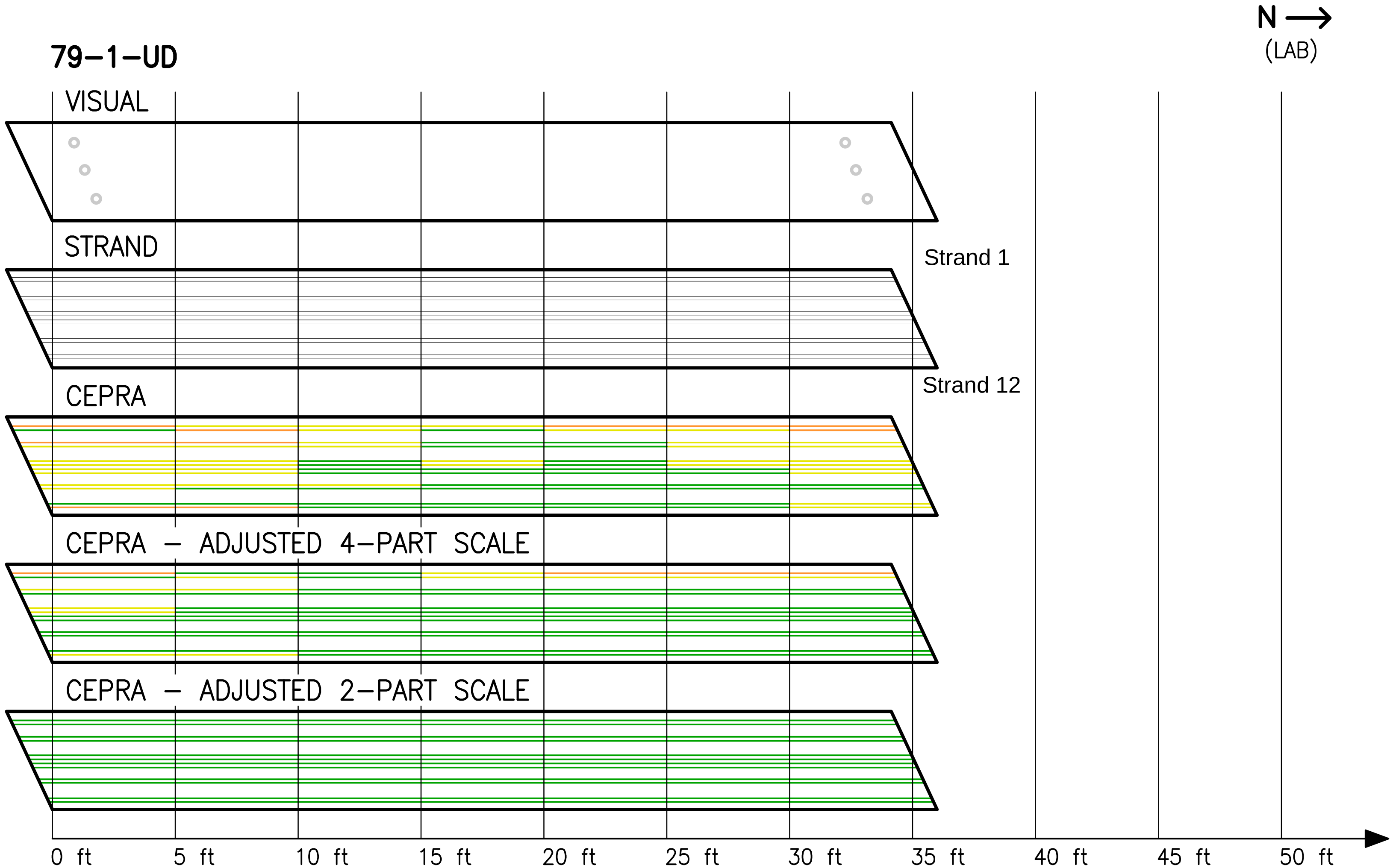

Figure 3.88: 79-1-UD Deterioration Map (CEPRA)

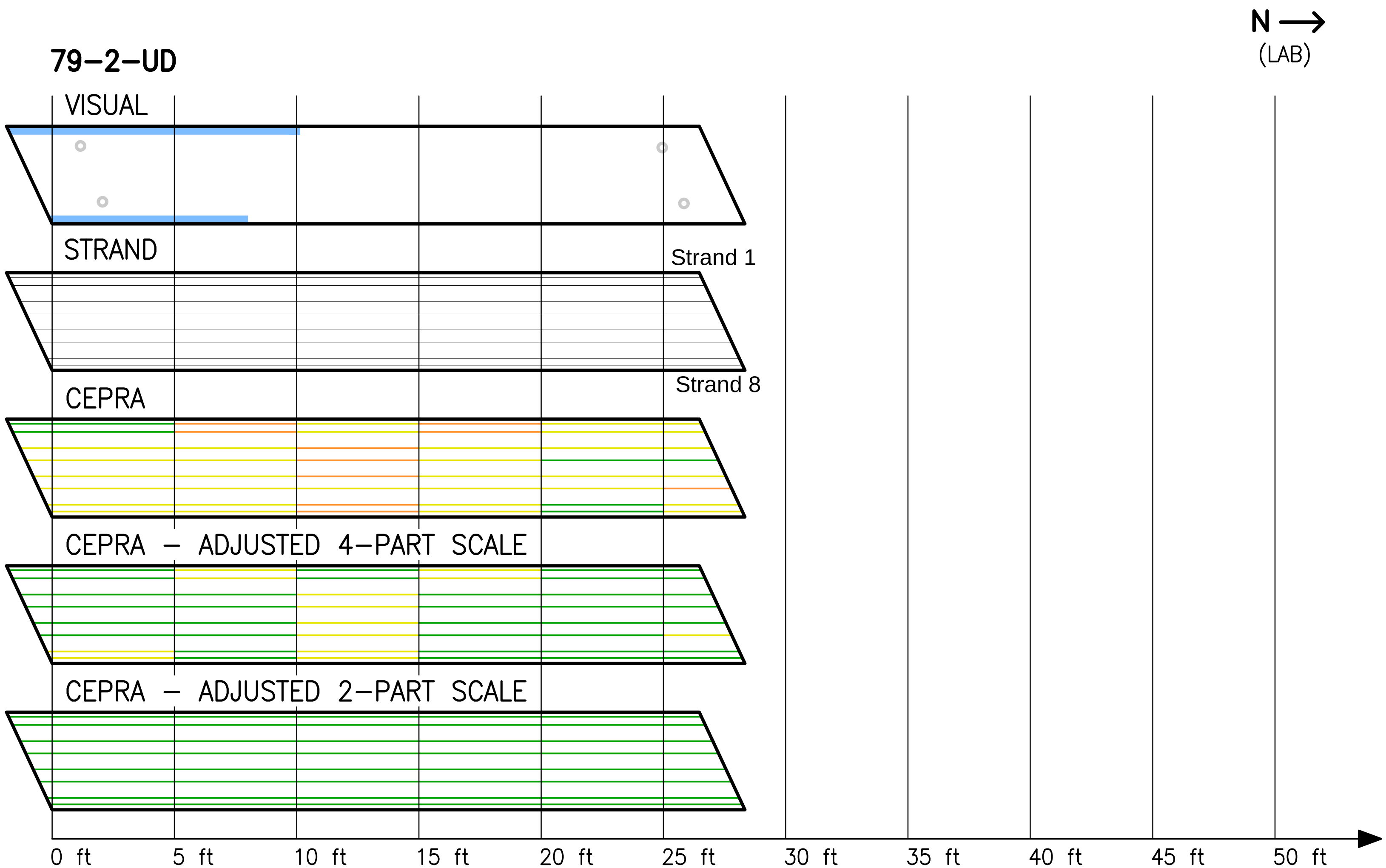

Figure 3.89: 79-2-UD Deterioration Map (CEPRA)

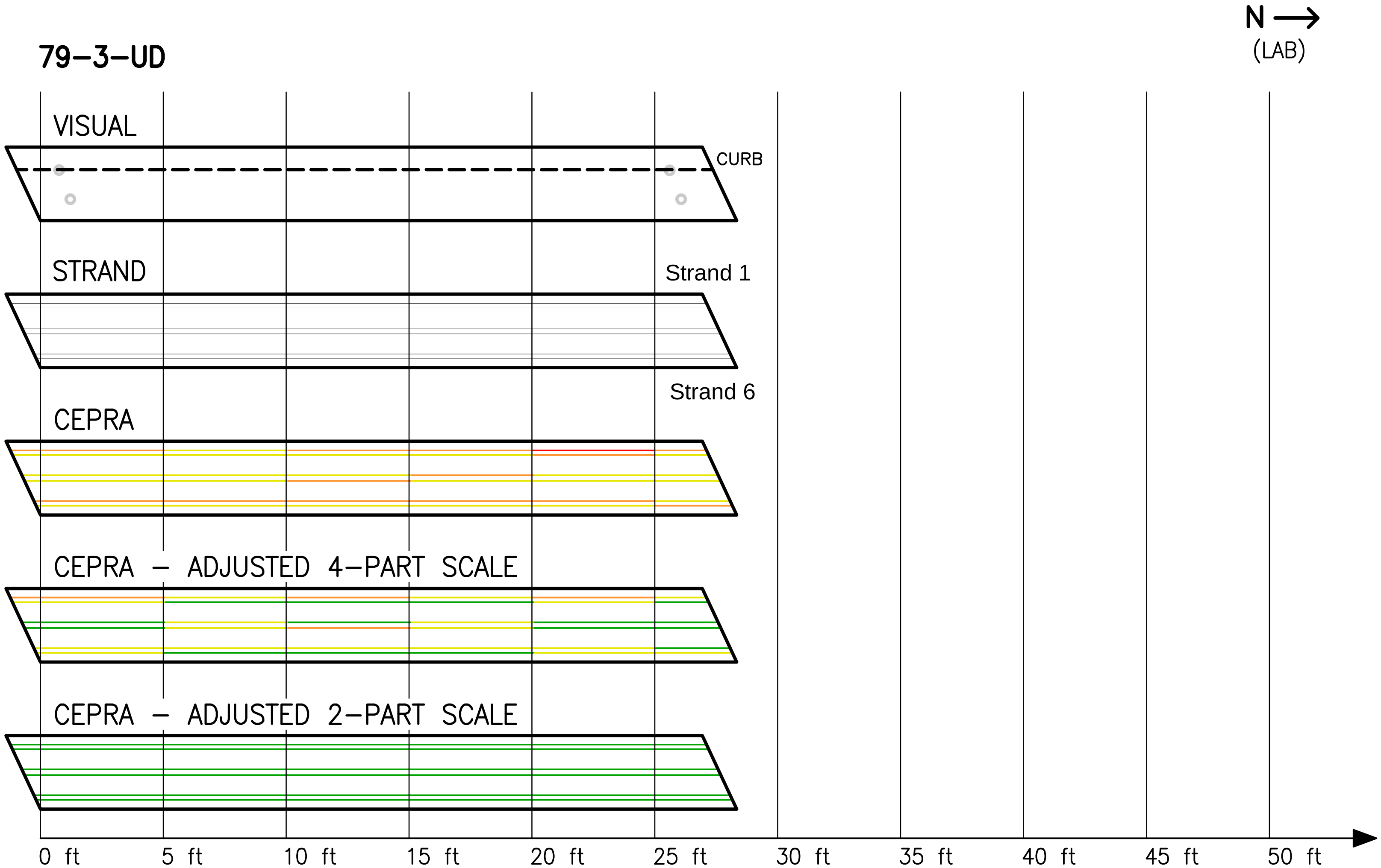

Figure 3.90: 79-3-UD Deterioration Map (CEPRA)

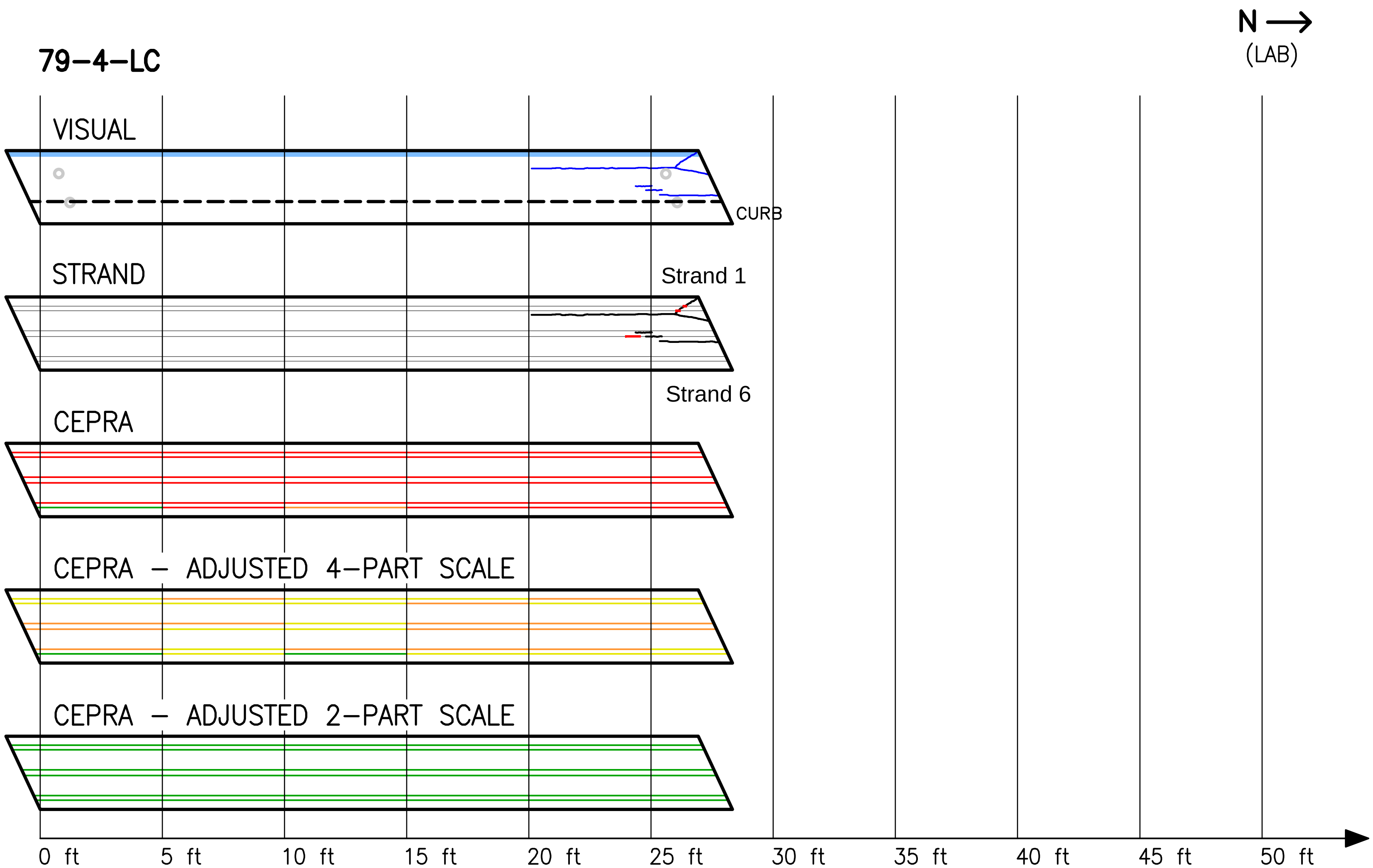

Figure 3.91: 79-4-LC Deterioration Map (CEPRA)

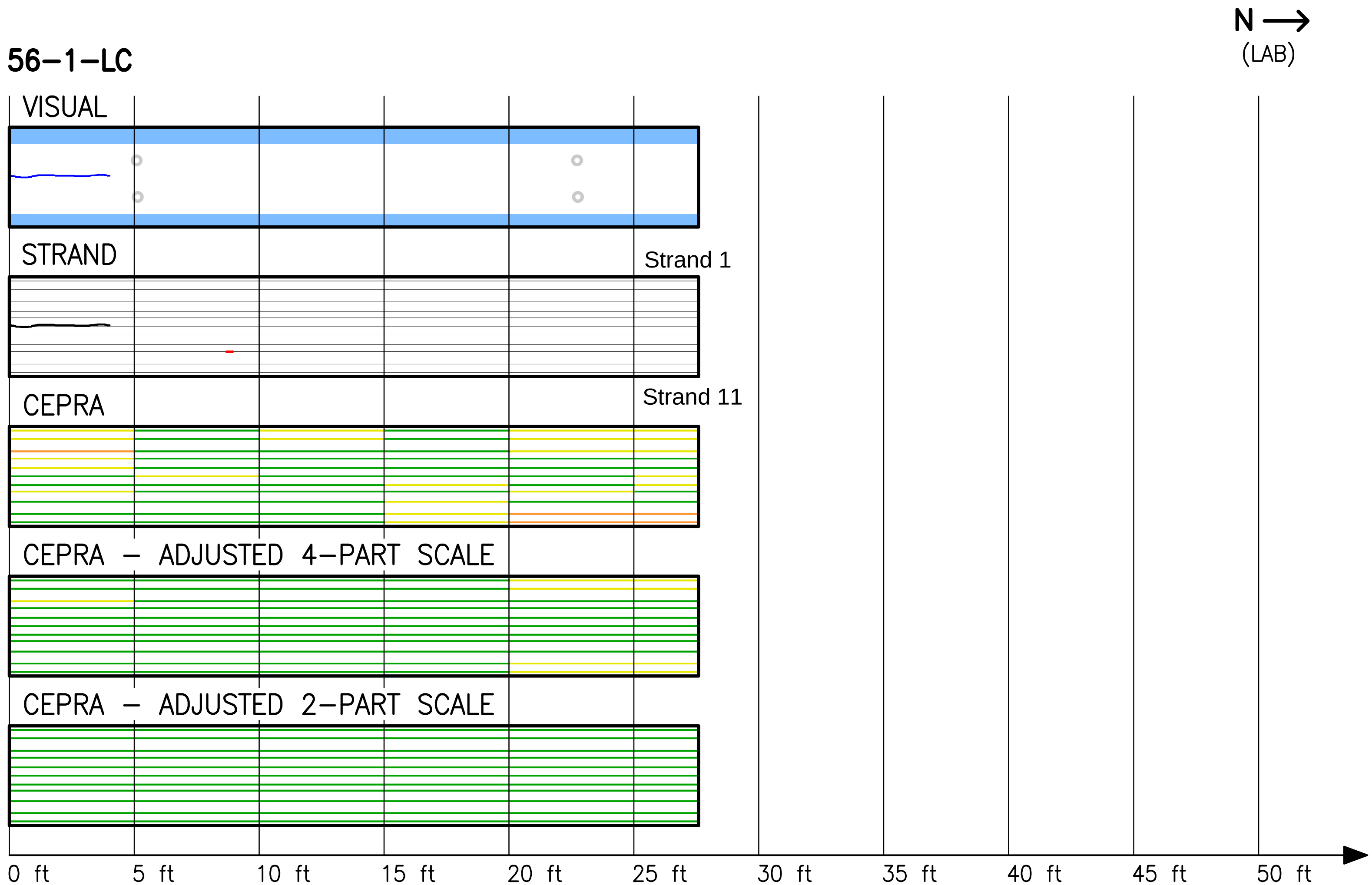

Figure 3.92: 56-1-LC Deterioration Map (CEPRA)

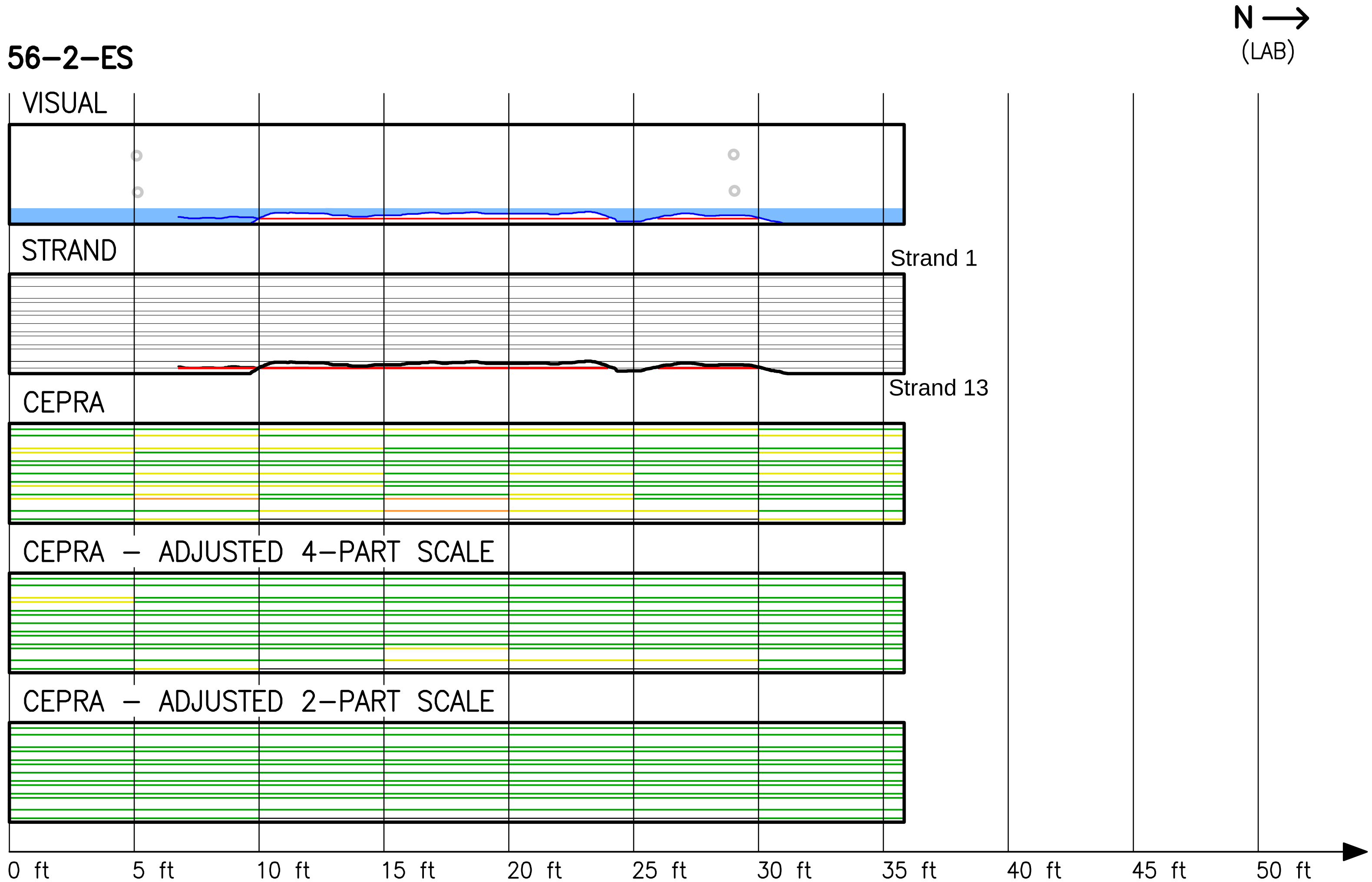

Figure 3.93: 56-2-ES Deterioration Map (CEPRA)

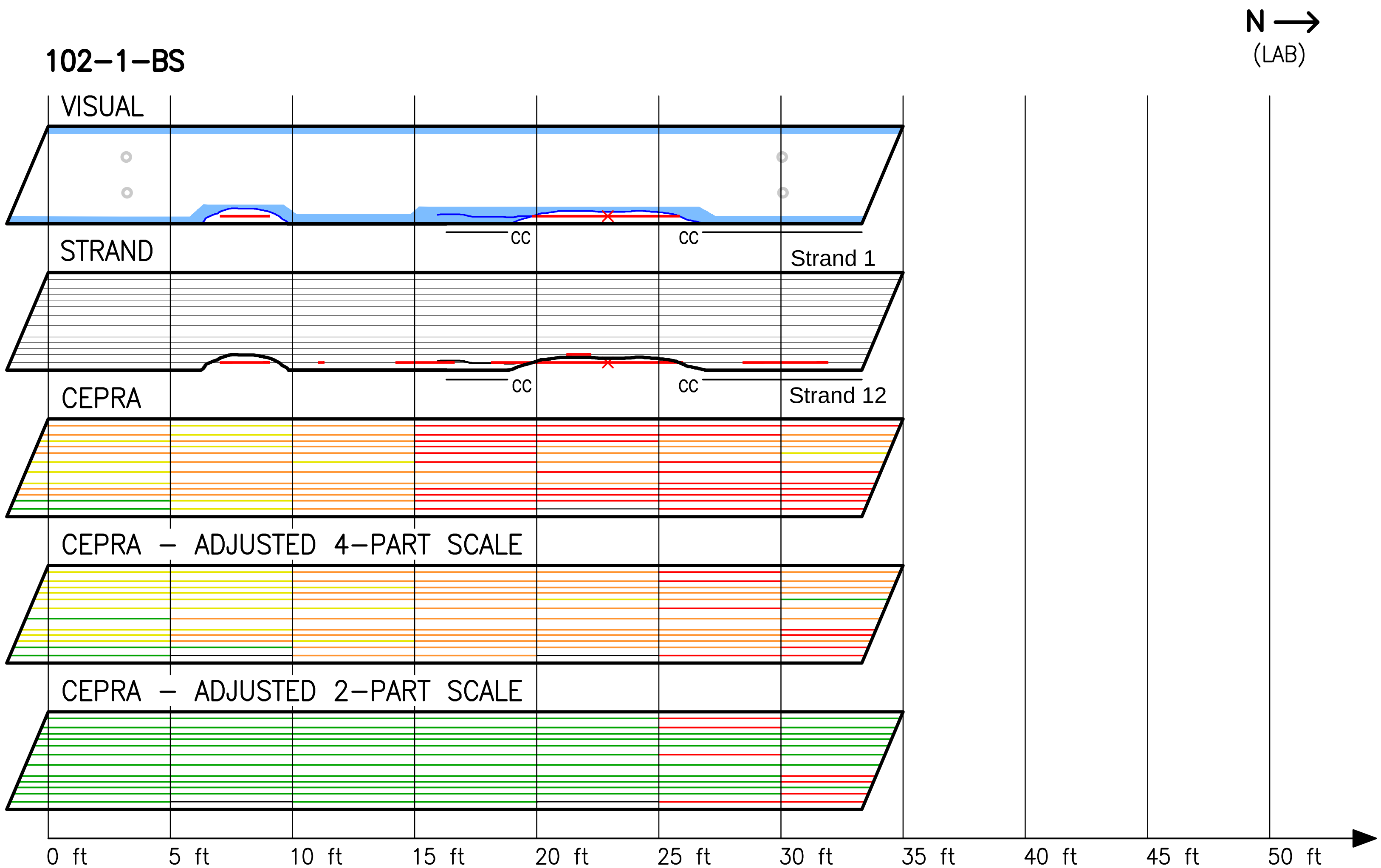

Figure 3.94: 102-1-BS Deterioration Map (CEPRA)

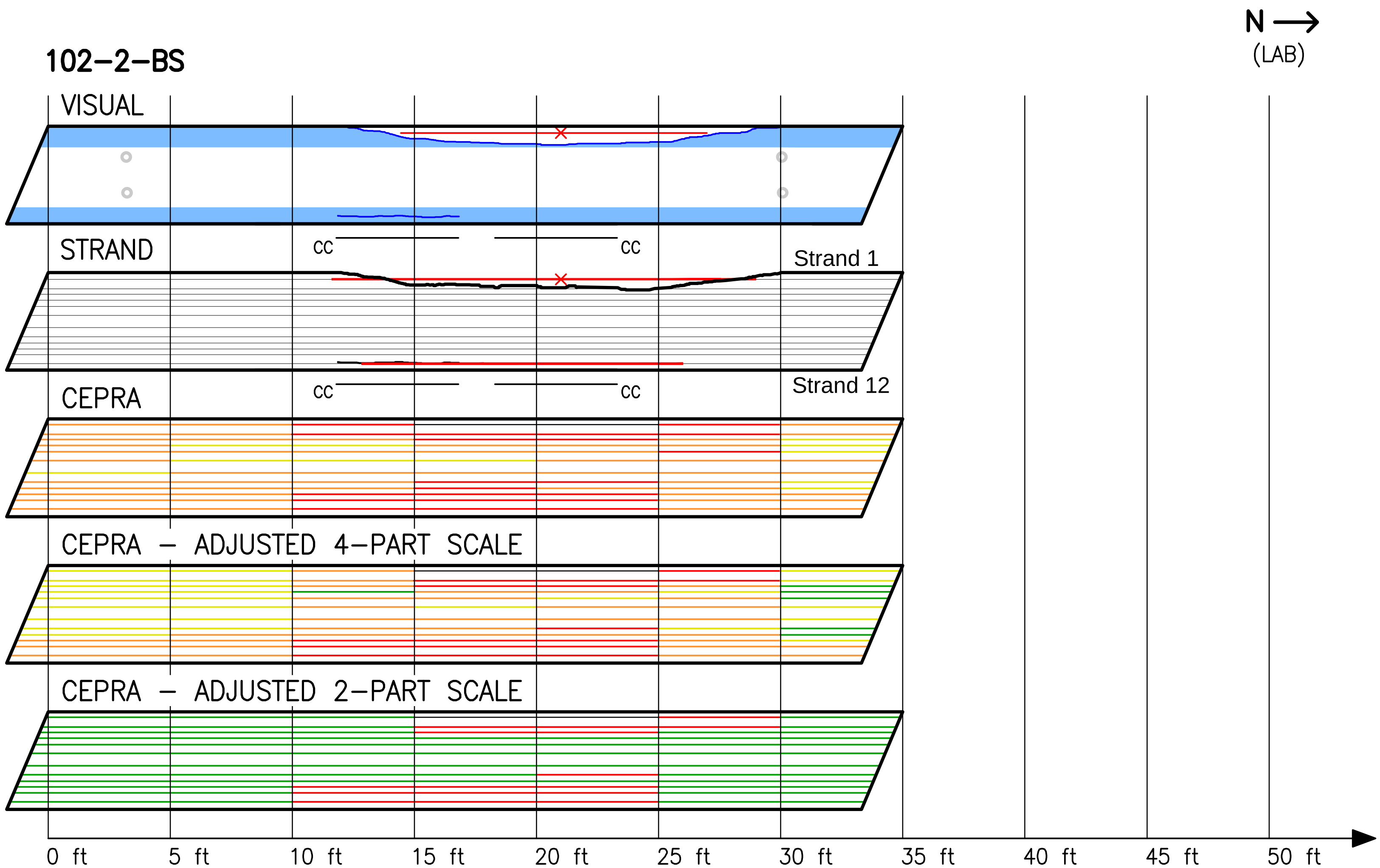

Figure 3.95: 102-2-BS Deterioration Map (CEPRA)

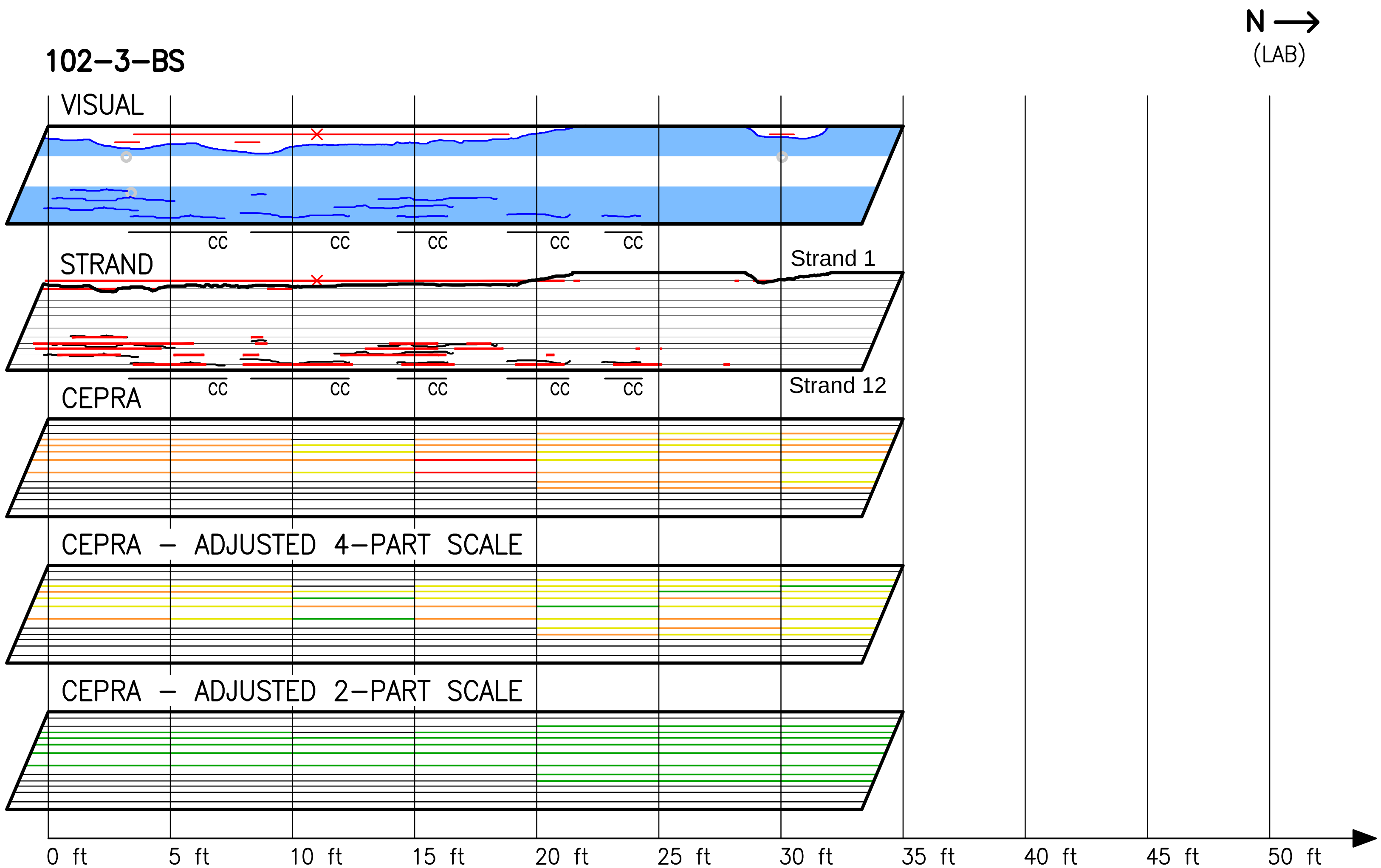

Figure 3.96: 102-3-BS Deterioration Map (CEPRA)

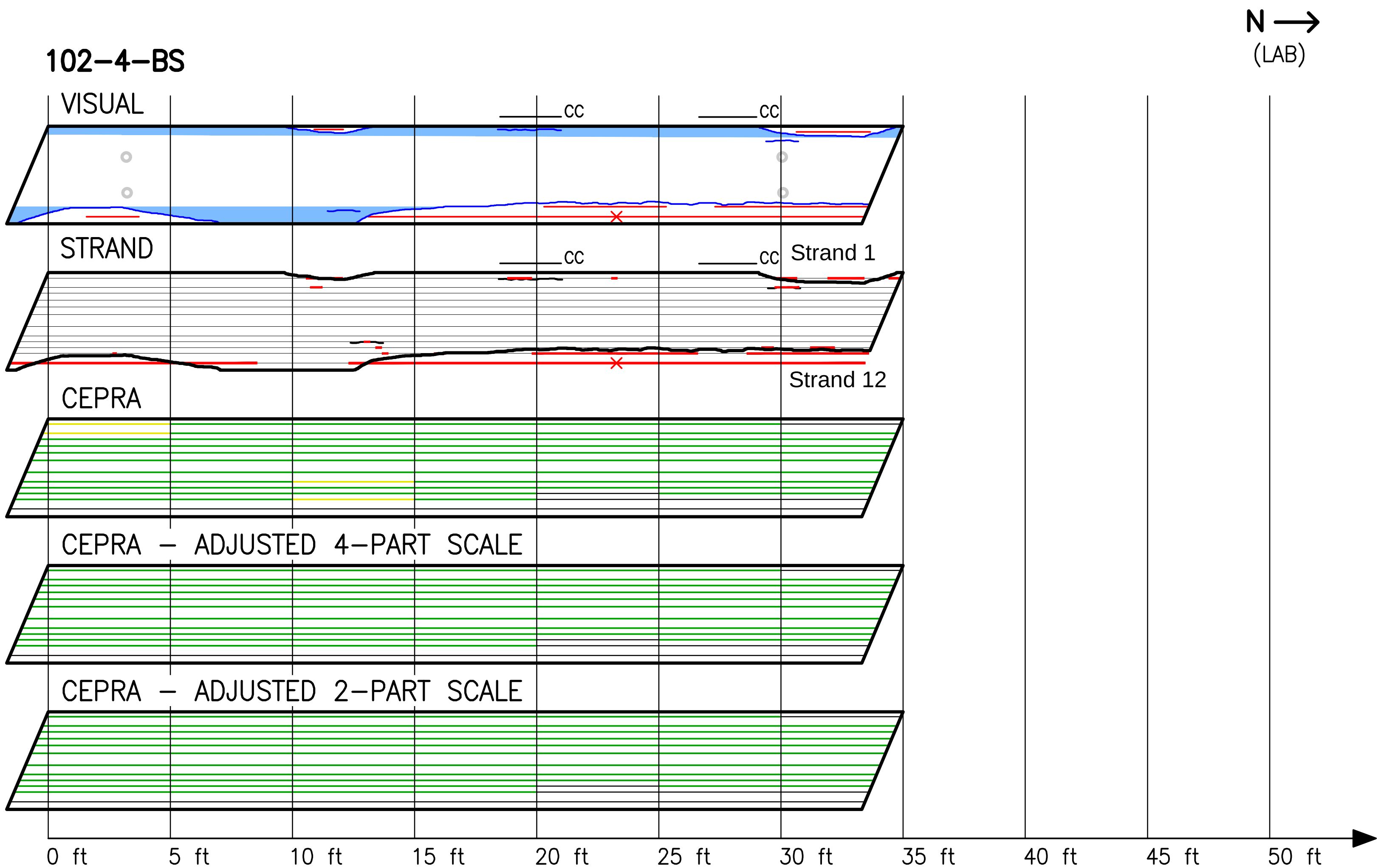

Figure 3.97: 102-4-BS Deterioration Map (CEPRA)

3.6.1.1 Discussion of the Adjusted Results

After the adjusted four-part scale was applied to the CEPRA data, the corrosion rate measurements were found to provide a reasonable indication of strand deterioration. Locations where "severe" corrosion rates were measured (red strand in figures); corroded strand with section loss was often observed. As shown in Figure 3.94 and Figure 3.95, corrosion was detected at the longitudinal cracks in Specimen 102-1-BS (adjusted four-part scale between 25 ft and 35 ft in Figure 3.94) and 102-2-BS (adjusted four-part scale between 10 ft and 25 ft in Figure 3.95). Corrosion of Strand 12 in Specimen 102-1-BS after cover was removed is shown in Figure 3.31(b), and corrosion of Strand 12 in Specimen 102-2-BS after removal of cover is presented in Figure 3.33(b). It should be noted that Specimen 102-2-BS was an interior beam in Elkhart 102. Therefore, the corner cracking noted in Figure 3.13 would not have been visible to a bridge inspector because the sides of interior box beams cannot be inspected due to the small gap between beams. This shows that CEPRA provided indication of corrosion where visual inspection would have indicated no strand corrosion.

In Specimen 102-4-BS (Figure 3.97), no corrosion was indicated at the longitudinal crack on the northwest side of the bottom flange where corrosion was observed during the strand extraction (Figure 3.44). This is the only instance where CEPRA gave no indication of corrosion where corrosion was observed after strands were extracted. It should be noted that this was observed prior to adjusting the corrosion rate scale and after adjustment.

Where the CEPRA corrosion rate indicated "visible" corrosion (orange strand in figures), the strands were often found with no corrosion, or surface rust and no pitting. In Specimens 102-1-BS and 102-2-BS, "visible" corrosion was indicated on many of the strands adjacent to exposed strand (Figure 3.94 and Figure 3.95). For Specimen 102-1-BS, "visible" corrosion was detected on Strand 11 and at the locations where the strands were adjacent to exposed strands (adjusted four-part scale between 15 ft and 30 ft in Figure 3.94), but no corrosion was observed in Strand 11, as shown in Figure 3.30(b) and Figure 3.31(b), or in Strand 10, as shown in Figure 3.32(b). In addition, corrosion was detected on Strand 11 in Specimen 102-2-BS (adjusted four-part scale between 10 ft and 25 ft in Figure 3.95), but no corrosion was observed as shown in Figure 3.33(b).

In locations where the adjusted corrosion rate indicated “passive” or “uncertain” corrosion (green or yellow strand in figures), strands were found with no corrosion. In Specimen 102-1-BS (Figure 3.94), “passive” corrosion was indicated on Strand 12 (adjusted four-part scale between 0 ft and 5 ft), and no corrosion was observed when cover was removed (Figure 3.98). In Specimen 56-2-ES (Figure 3.93), “uncertain” corrosion was indicated on Strand 12 (adjusted four-part scale between 15 ft and 20 ft), and no corrosion was observed when cover was removed (Figure 3.99).

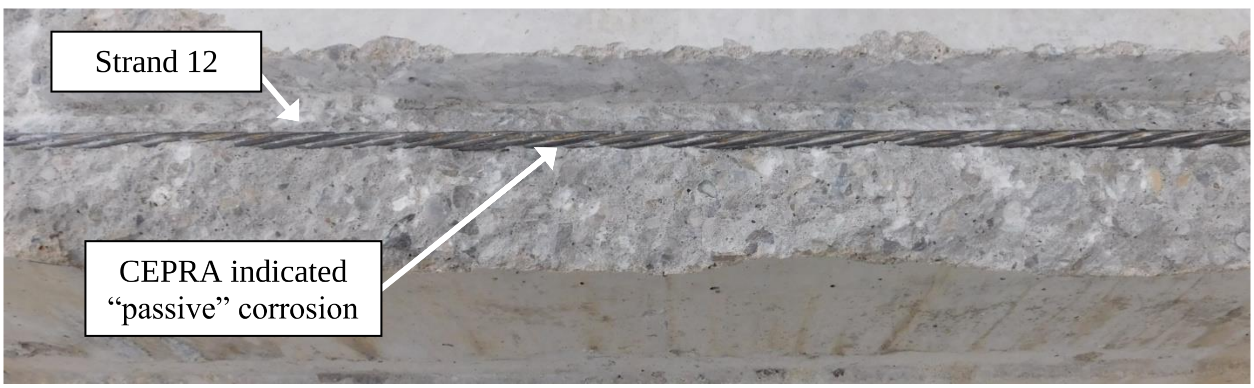

Figure 3.98: Condition of Strand 12 in Specimen 102-1-BS

Figure 3.99: Condition of Strand 12 in Specimen 56-2-ES

Considering the lack of corrosion observed where “visible” or “uncertain” corrosion (orange or yellow) was indicated, a two-part corrosion rate scale (Table 3.9) provides an easy way to highlight the areas of corrosion. It should be noted, however, that the areas where “visible” corrosion was indicated (using the adjusted four-part scale) were usually adjacent to areas of strand corrosion. The deterioration of Specimens 102-1-BS and 102-2-BS was caused by leaking longitudinal joints which has the potential to cause on-going corrosion of strands beginning with the edge strands and working toward the middle of the section. The indication of “visible” corrosion may signal the next strands to start corroding. Therefore, the two-part scale may be of most benefit in situations where only the current condition of the strands is important. The overestimation of corrosion in strands adjacent to heavily corroded strands may also be caused by a halo effect of the corroding strand.

Overall, the CEPRA method provided a general indication of strand condition using a simple and easy-to-use device. In addition, the CEPRA method was able to identify strand corrosion where the only visual sign of deterioration would have been obscured by the proximity of an adjacent beam. A comparison of the CEPRA results to the actual strand condition showed that, with adjustment, corrosion rate measurements provided information on the condition of the strands in areas adjacent to visual signs of deterioration. The CEPRA results were also observed to overestimate strand corrosion around heavily corroded strands. This halo effect of strand corrosion prevented the accurate assessment of strands immediately adjacent to strands with severe corrosion. This effect was primarily observed for specimens exhibiting deterioration related to leaking longitudinal joints or water draining over the side of the exterior beam. Considering the progression of corrosion for this type of deterioration, the observed halo effect due to strand corrosion may also be an indication of future corrosion.

3.6.1.2 Data Discrepancies

The corrosion rate measurements of Specimen 409-1-ES (Figure 3.84) were not consistent with the actual corrosion observed. Severe corrosion was indicated by CEPRA data where no strand corrosion was indicated in the visual inspection or by half-cell potential readings (Figure 3.67). In addition, strands extracted in a test area on the beam showed no signs of corrosion where severe corrosion was indicated by CEPRA (Figure 3.100). The measurements for 409-1-ES were repeated several times without significant change in the readings. The inconsistencies between the CEPRA results and the observed corrosion may have been caused by a combination of scatter in the measurements and irregularities in the concrete. The cause of discrepancies, however, could not be determined.

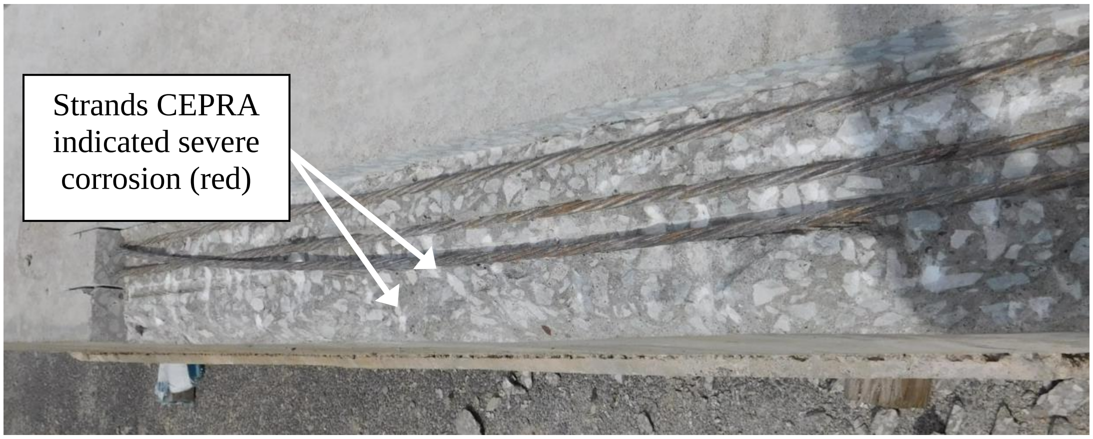

Figure 3.100: Condition of Strand at North Support of Specimen 409-1-ES

3.6.2 GPR

GPR was used primarily to locate reinforcement to allow accurate CEPRA measurements to be made. The strand location accuracy of the GPR was found to be within the ±1/4 in. accuracy reported by the manufacturer for smooth concrete surfaces.

Deterioration mapping with GPR was most successful in delaminated areas of the bottom flange (Specimens 102-2-BS (Figure 3.78) and 102-3-BS (Figure 3.79)). For Specimen 102-2-BS, the GPR results indicated strand deterioration between 15 ft and 25 ft in Figure 3.78 where the only visual indication of deterioration was a corner crack. As discussed previously, a corner crack would not be visible to a bridge inspector. Therefore, in this case, GPR provided indication of corrosion that would not have been otherwise visually detected.

Regions without delaminated areas, however, did not provide a large enough change in the dielectric constant to produce changes in the reflection amplitude. This was especially apparent in the results for specimens with corroded strands at longitudinal cracks away from the edge of the bottom flange where no corrosion was detected by the GPR (Specimens 244-1-LC (Figure 3.66), K5-2-LC (Figure 3.70), and 79-4-LC (Figure 3.74)). In each specimen, corrosion was observed in the strands at the longitudinal crack, but GPR provided no indication of deterioration.

For Specimens K5-1-LC and 79-1-UD, the GPR results in Figure 3.69 and Figure 3.71 indicate deterioration at scattered locations throughout the bottom flanges of either specimen. ASTM C6087 (2015) states that the threshold for deterioration may be between 6 to 8 dB. When 8 dB was used as the threshold for deterioration for Specimens K5-1-LC and 79-1-UD (Figure 3.101 and Figure 3.102), the GPR results showed little indication of deterioration, which is consistent with the visual inspection, adjusted CEPRA results, and half-cell potential results. However, if the 8 dB threshold is applied to the GPR results for Specimens 102-2-BS and 102-3-BS (Figure 3.103 and Figure 3.104) the indicated deterioration is lost. This indicates that the 8 dB threshold is not suitable for detecting strand corrosion, and that some noise in the data may be encountered when using the 6 dB threshold.

Overall, GPR was only capable of providing good correlation between indicated deterioration and actual strand corrosion in areas of delaminated concrete. Considering the lack of strand condition information provided by GPR data, GPR is most useful for locating reinforcement. However, it can be useful in investigating corner cracking due to the delamination detection and other regions that might be susceptible to delamination.

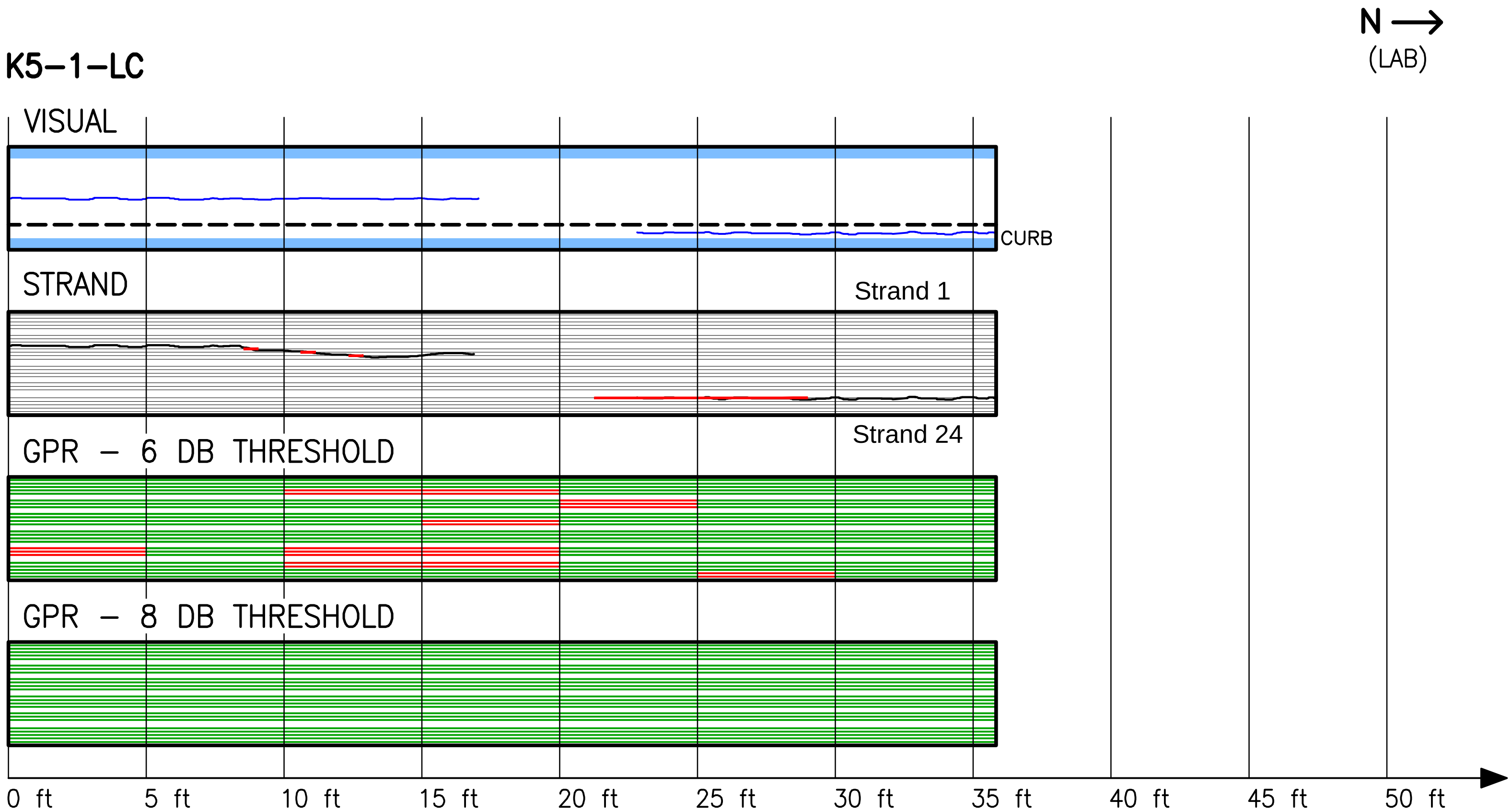

Figure 3.101: Specimen K5-1-LC Adjusted GPR Deterioration Map

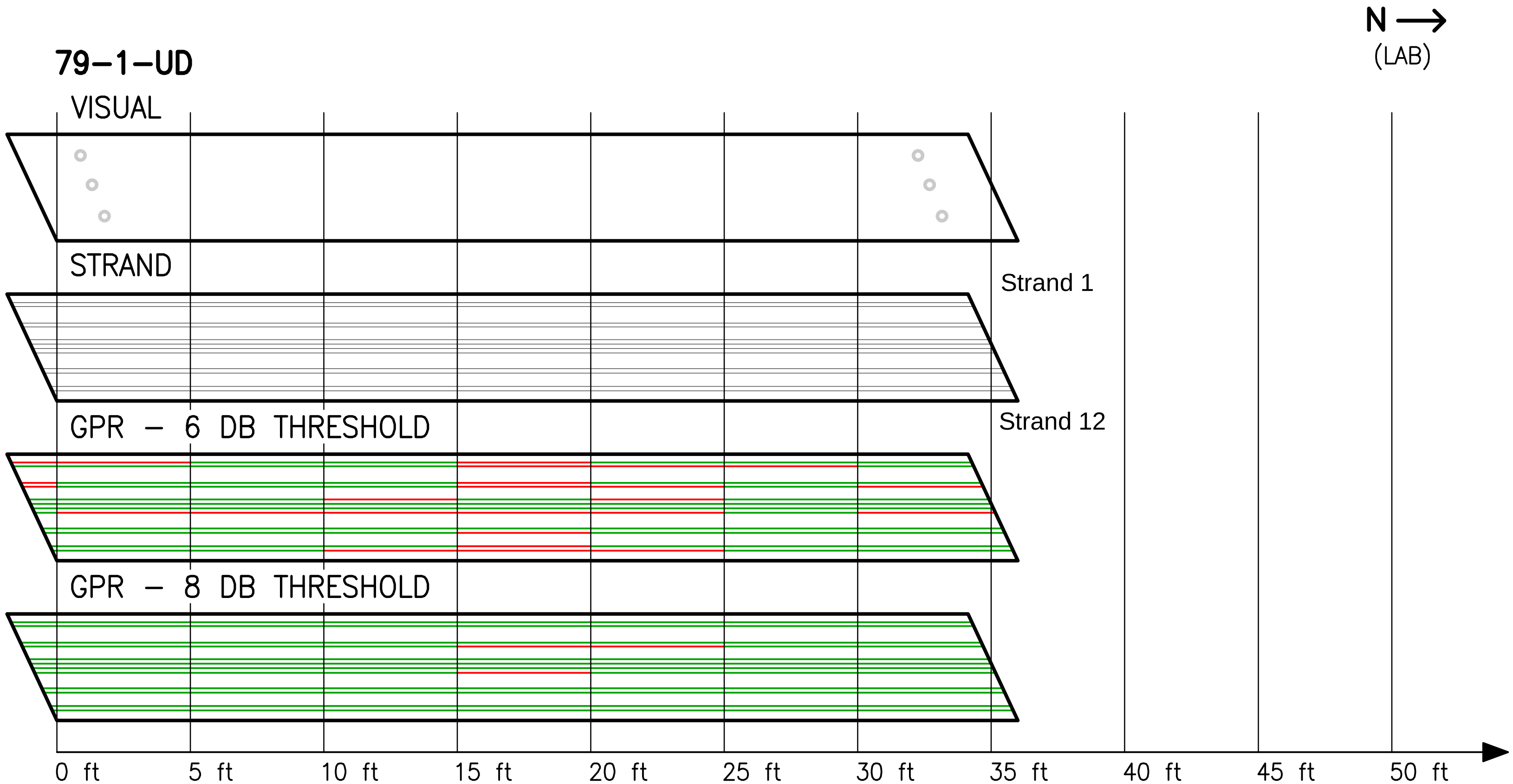

Figure 3.102: Specimen 79-1-UD Adjusted GPR Deterioration Map

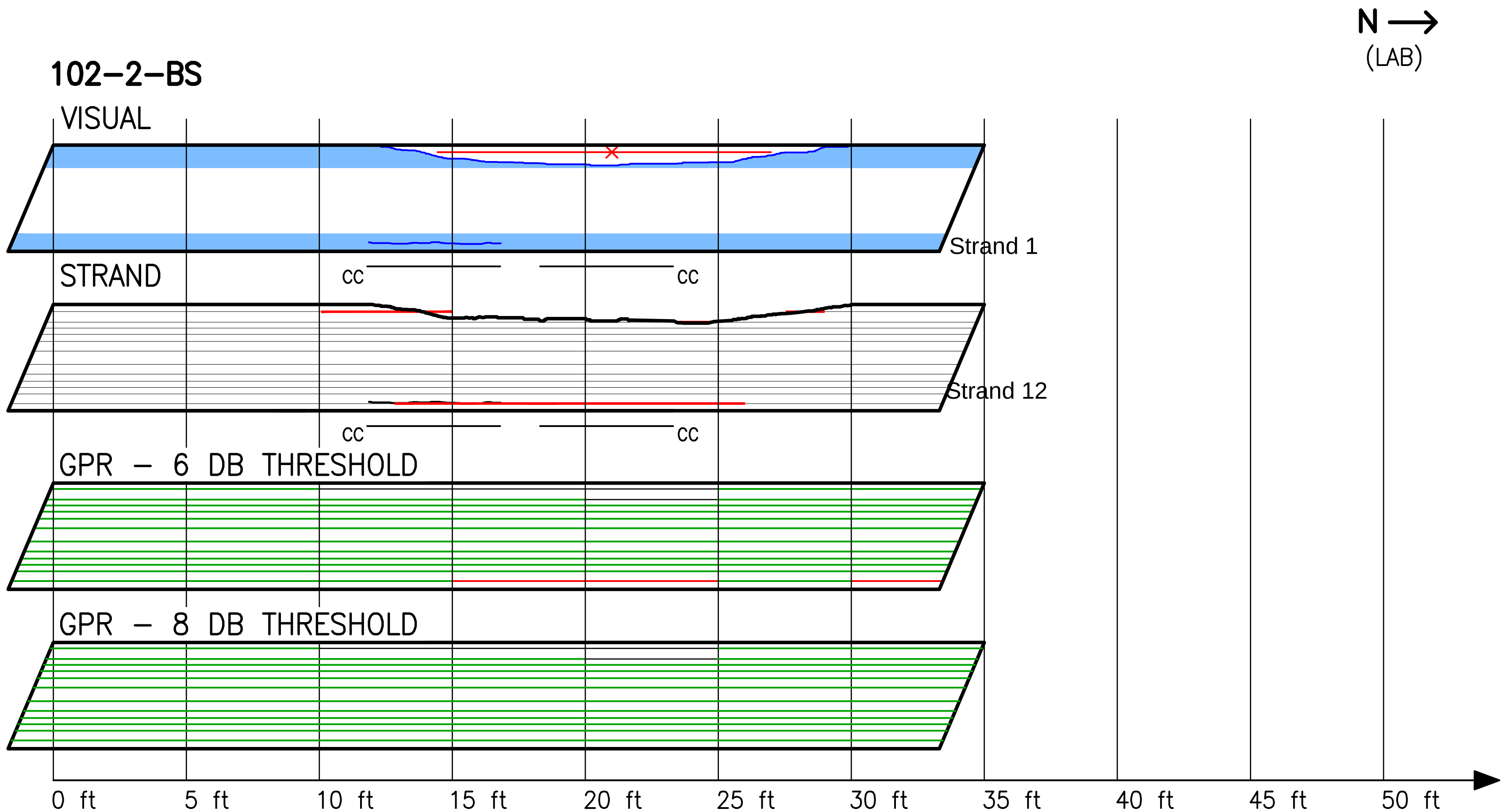

Figure 3.103: Specimen 102-2-BS Adjusted GPR Deterioration Map

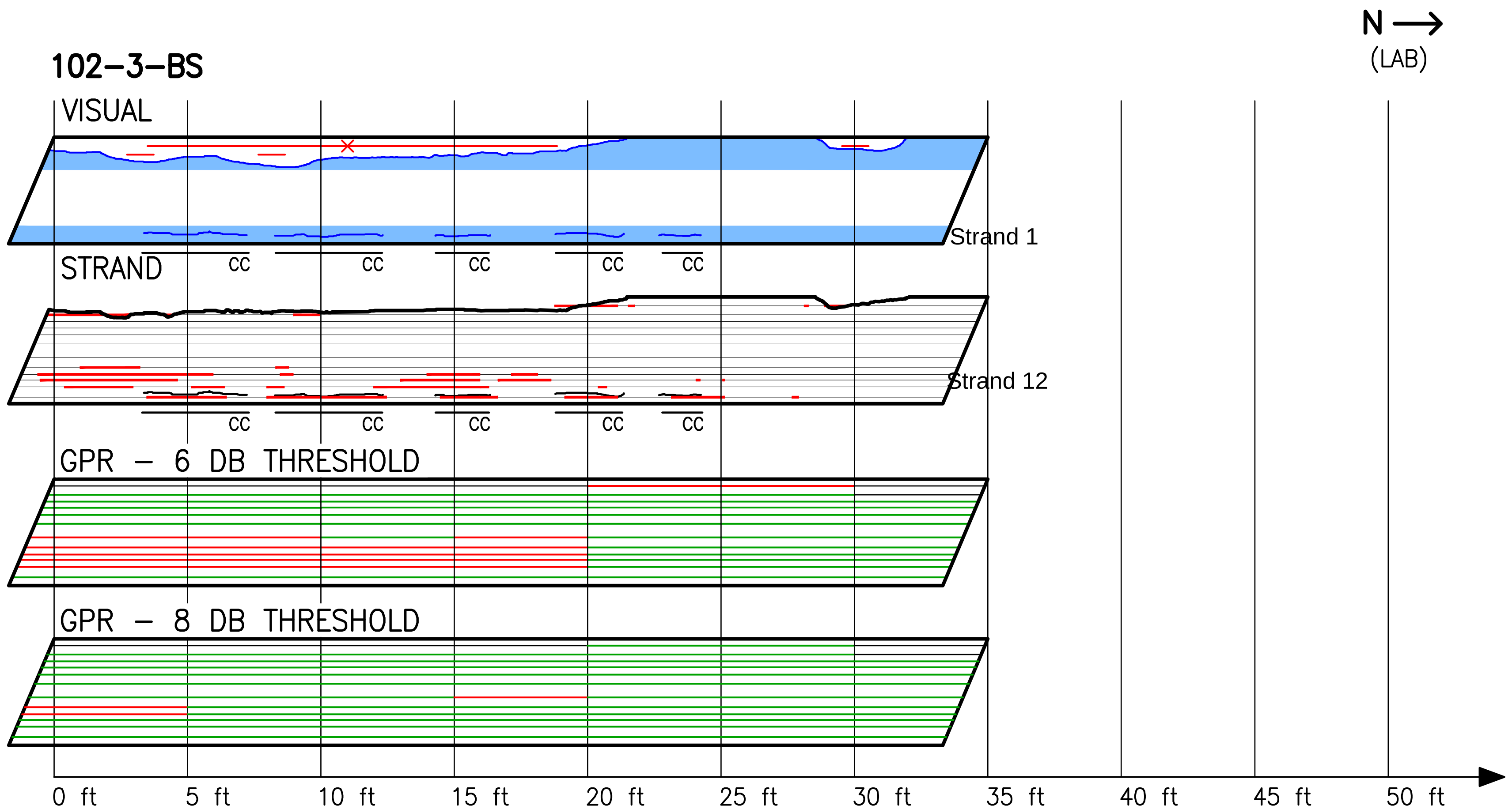

Figure 3.104: Specimen 102-3-BS Adjusted GPR Deterioration Map

3.6.3 Half-Cell Potentials

The half-cell potential results provided good indication of strand corrosion. Although half-cell potential readings could not be taken directly over a crack or on concrete spall, the readings of adjacent strands provided an accurate assessment of the extent of corrosion. Therefore, the assessment of the half-cell potential method is focused on the indicated condition of the strands adjacent to visual signs of deterioration.

In Specimens K5-1-LC (Figure 3.69), 79-4-LC (Figure 3.74) and 56-1-LC (Figure 3.75), half-cell potential readings indicated no corrosion (green strand in figures) of the strands adjacent to longitudinal cracks as was observed during the strand extraction.

Where the half-cell potential readings indicated uncertain corrosion (yellow strand in figures), uncorroded strands were observed. In Figure 3.66 at the locations of the longitudinal cracks in Specimen 244-1-LC (half-cell readings between 5 ft and 15 ft on the west side of the specimen and between 20 ft and 25 ft on the east side of the specimen), uncertain corrosion was indicated for the strands adjacent to the longitudinal cracks. As shown in Section 3.4.2.1, no corrosion was observed on strands adjacent to longitudinal cracks. Uncertain corrosion was also detected in Strands 11 and 12 in Specimen 56-2-ES (Figure 3.76 between 10 ft and 15 ft on the east side of the specimen). As shown in Figure 3.28(b) and (c), Strand 11 was observed without any corrosion, and Strand 12 was found with only surface corrosion. In Specimen 102-3-BS (Figure 3.79 between 25 ft and 30 ft and the southeast portion of Segment D in Figure 3.14), Strands 10 to 12 were classified with uncertain corrosion. As shown in Figure 3.105, when cover was removed from Strands 10 to 12, in the southeast portion of Segment D, no corrosion was observed.

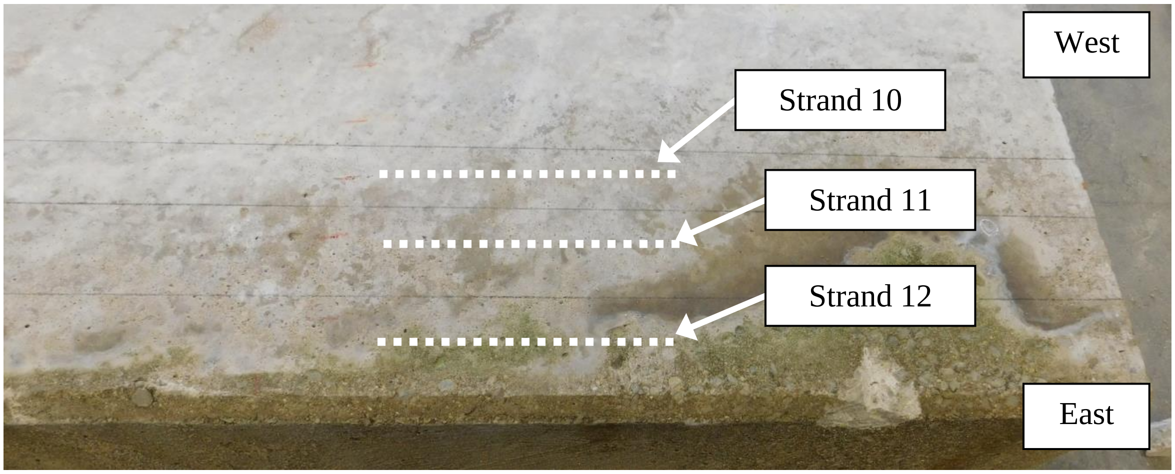

(a) Before cover was removed

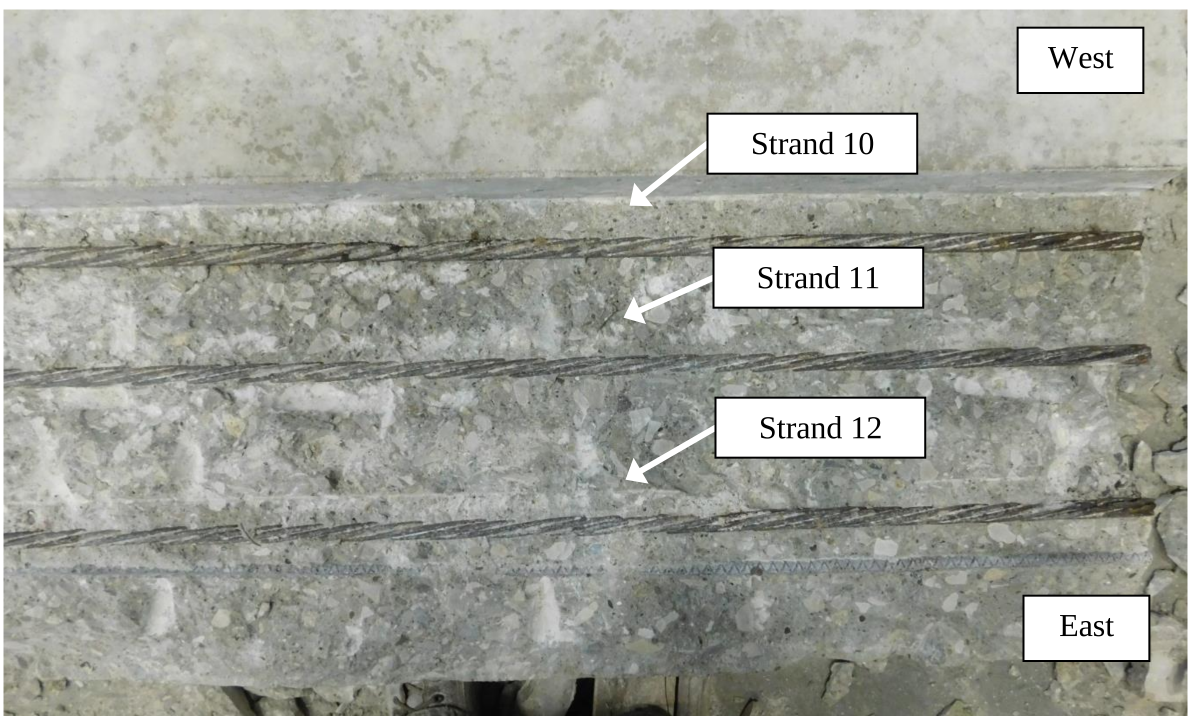

(b) After cover was removed

Figure 3.105: Condition of Strands Classified with Uncertain Corrosion in Specimen 102-3-BS

Where corrosion was indicated by the half-cell potential readings, corrosion was often observed. In Specimen 102-1-BS, corrosion was indicated on the strand adjacent to the broken strand (Strand 11) on the east side of the specimen (Figure 3.77 between 20 ft and 35 ft). When cover was removed from Strand 11, corrosion was observed (Figure 3.32(b)). In Specimen 102-3-BS, corrosion was indicated on the Strands 9 to 12 located at the longitudinal cracks between 0 ft and 25 ft (Figure 3.79). When cover was removed from Strands 9 to 12, corrosion was observed (Figure 3.37(b)). It should be noted that corrosion was indicated on the strands at the longitudinal cracks in Specimen 102-3-BS even though the readings had to be taken adjacent to the cracks.

Corrosion was also indicated by the half-cell potential readings where no corrosion was observed. These readings were observed for strands located adjacent to visual signs of deterioration. In Specimen 102-2-BS, on the east side of the specimen between 10 ft and 20 ft in Figure 3.78, corrosion was indicated on Strand 11, located adjacent to the corner cracks and longitudinal crack. When cover was removed, no corrosion was observed on Strand 11 (Figure 3.33(b)).

The only locations where no corrosion was indicated but corrosion was observed during the strand extraction occurred at locations with visual signs of deterioration.

Considering the observed condition of the strands indicated with uncertain corrosion, the ASTM C879 three-part scale was condensed to a two-part scale with no corrosion (green strands) for voltage potential readings greater than or equal to -0.35 V and corrosion (red strands) for voltage potential readings less than -0.35 V. The condensed scale is provided in Table 3.10. The two-part scale was used with the results for Specimens 409-1-ES, 56-2-ES, 102-1-BS, 102-2-BS, 102-3-BS, and 102-4-BS and presented in Figure 3.106 to Figure 3.111. As shown, the two-part scale provides a “hotspot” view of the data.

Table 3.10: Two-Part Corrosion Correlation Scale

Color		Voltage Measurement, V_m (V)	Corrosion Classification
Green	—	$V_m \geq -0.35$	no corrosion
Red	—	$V_m < -0.35$	corrosion
Black	—	No reading available	

Overall, the half-cell potential method provided an indication of the condition of strands adjacent to visual signs of deterioration. The half-cell method was not capable of consistently providing an accurate assessment of strands at longitudinal cracks. Good correlation, however, was observed between the indicated strand condition and actual corrosion of strands adjacent to visual signs of deterioration. Similar to the CEPRA method, the half-cell readings were also observed to be influenced by heavily corroded strands. This halo effect was observed for specimens exhibiting deterioration related to leaking longitudinal joints or water draining over the side of the exterior beam but to less extent than was observed for the CEPRA method. Considering that corrosion propagates from strand to strand for this type of deterioration, the observed halo effect may also be an indication of future corrosion.

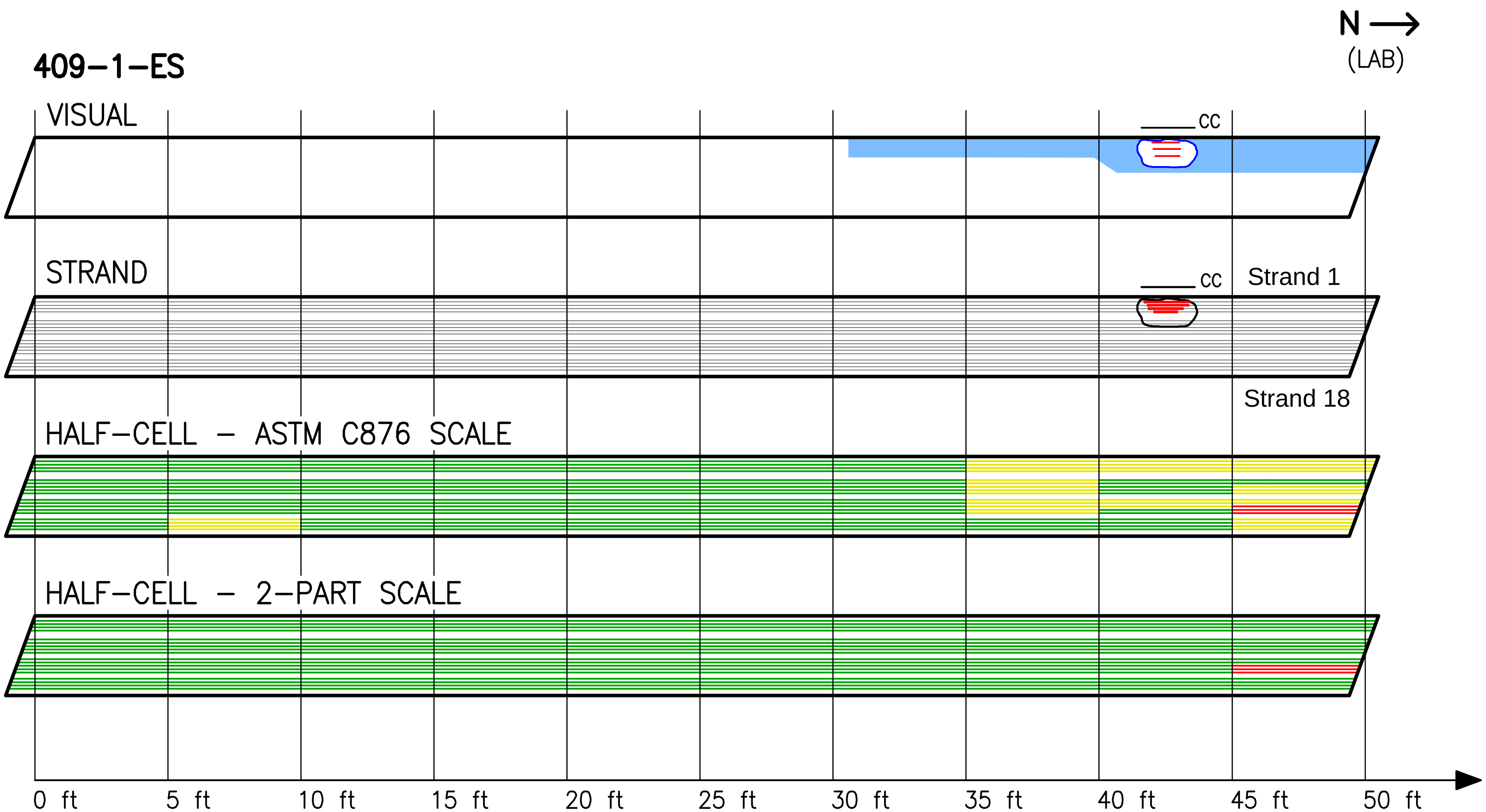

Figure 3.106: Specimen 409-1-ES Adjusted Half-Cell Potential Results

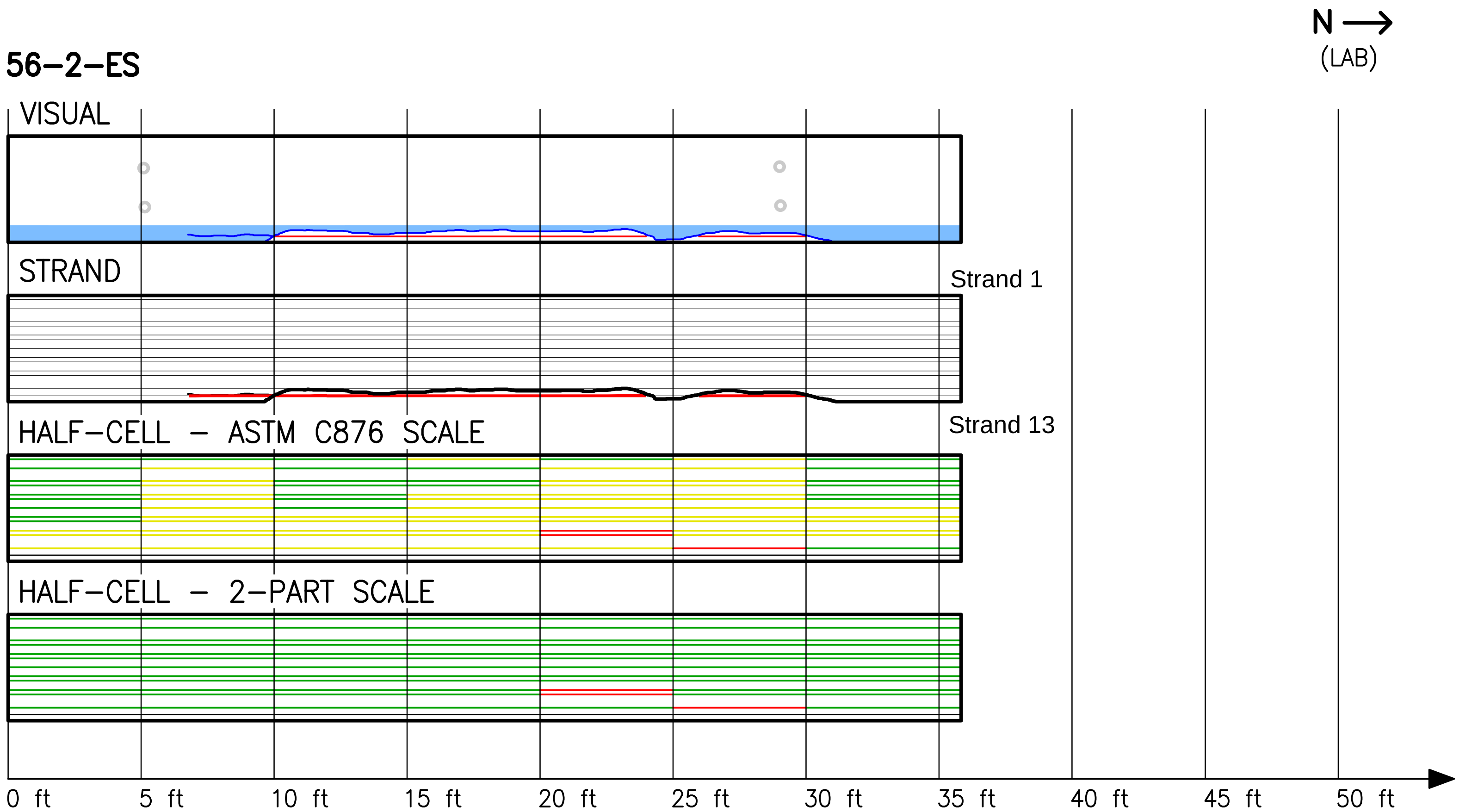

Figure 3.107: Specimen 56-2-ES Adjusted Half-Cell Potential Results

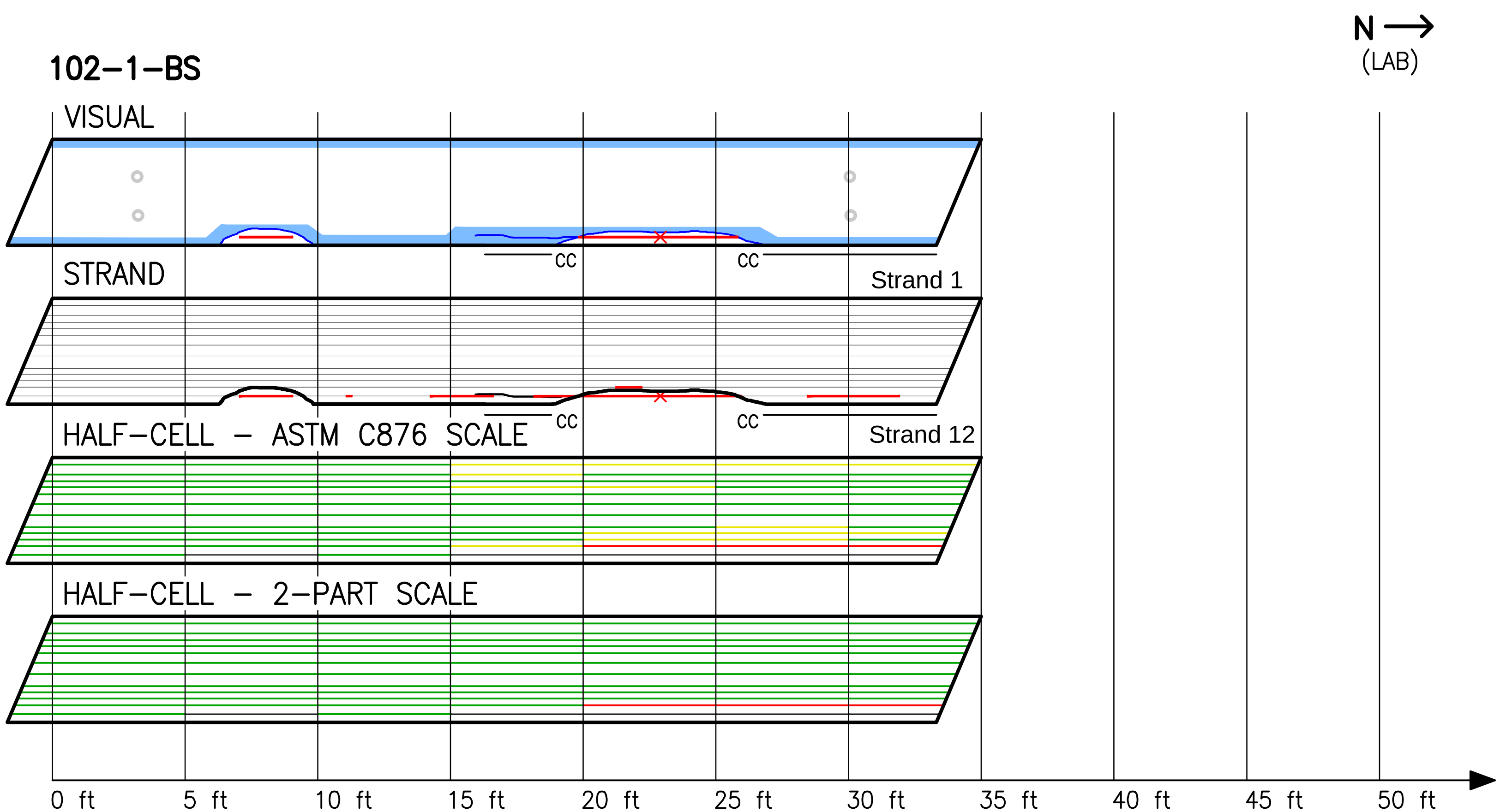

Figure 3.108: Specimen 102-1-BS Adjusted Half-Cell Potential Results

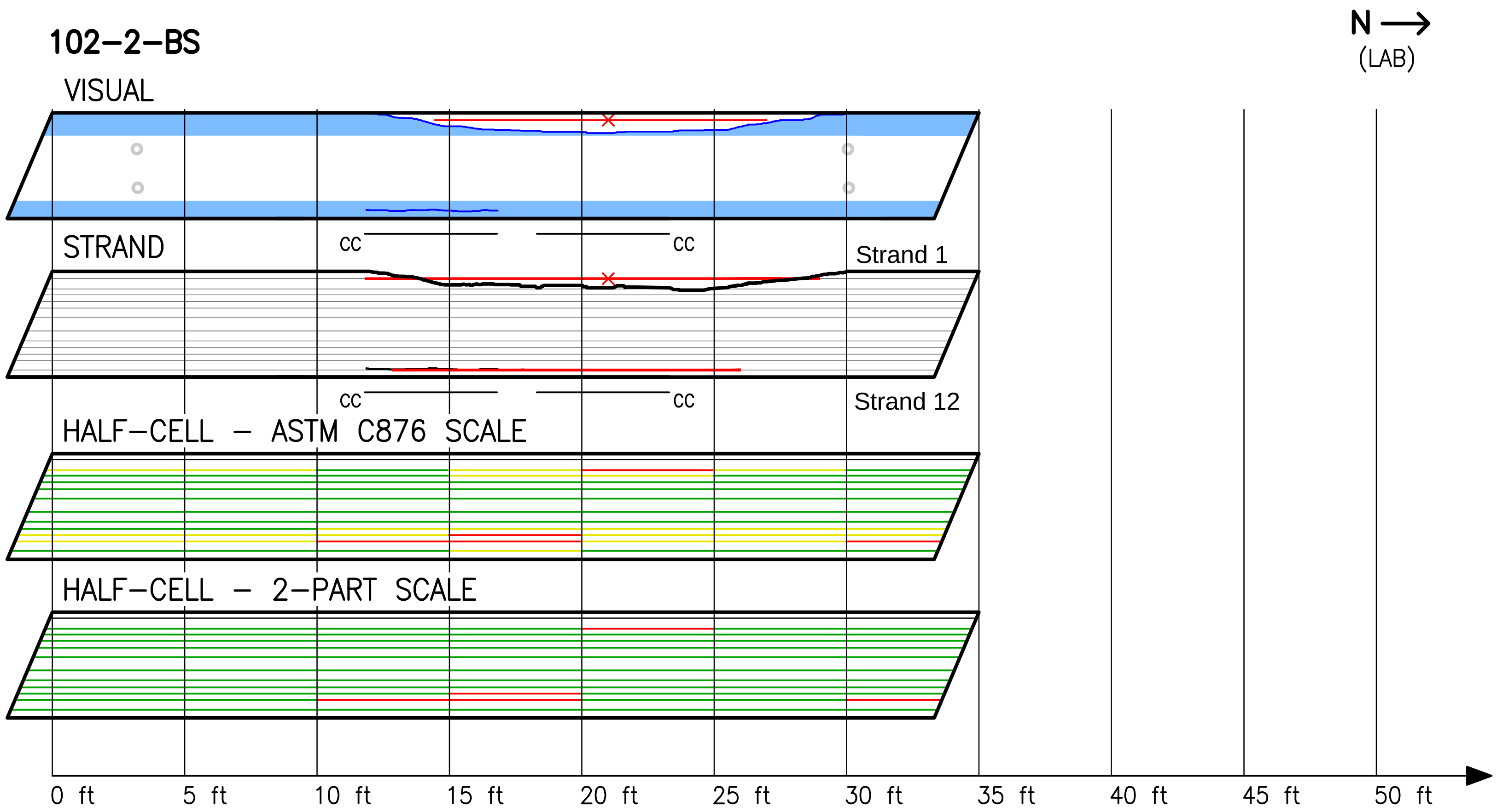

Figure 3.109: Specimen 102-2-BS Adjusted Half-Cell Potential Results

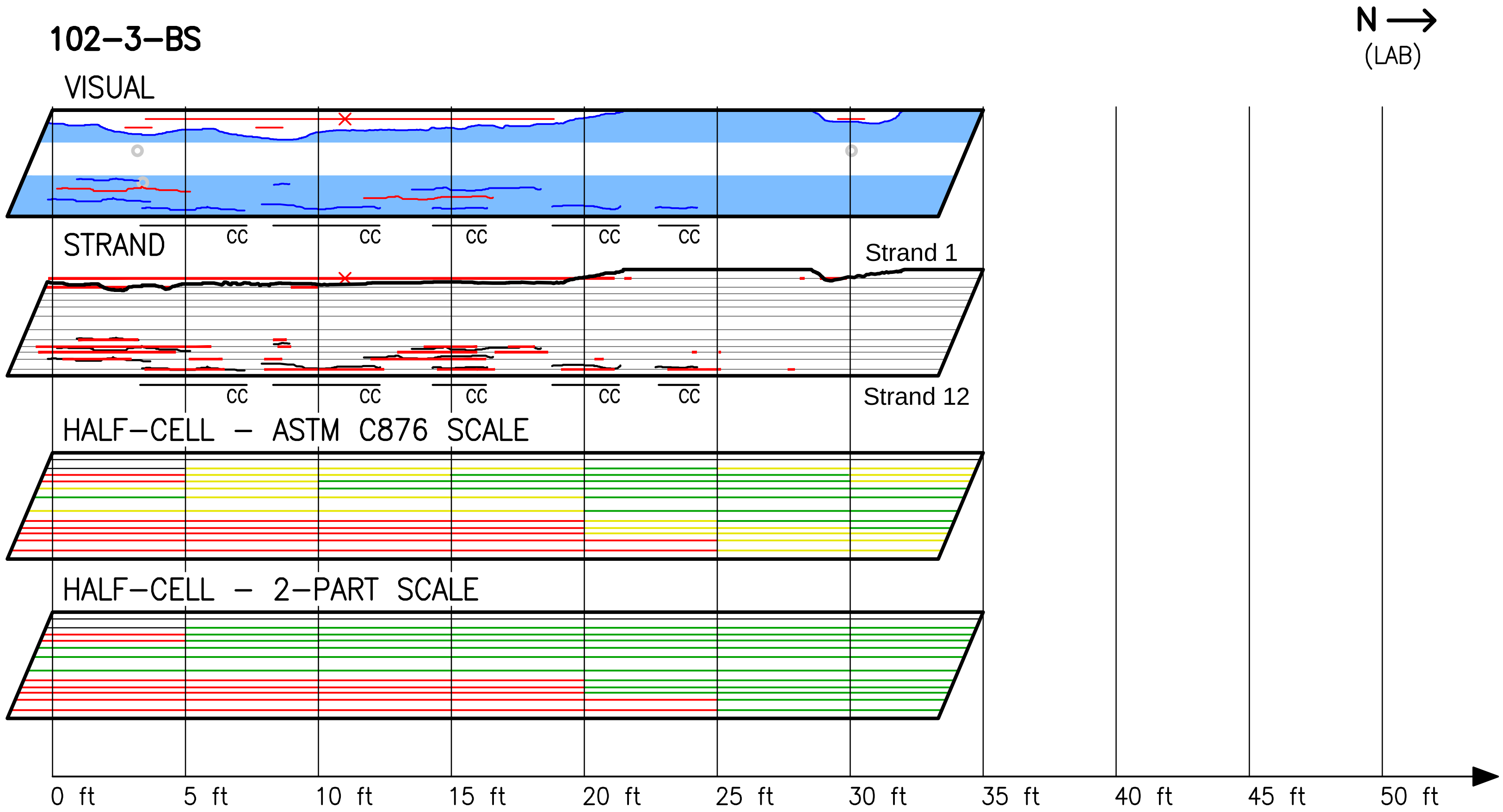

Figure 3.110: Specimen 102-3-BS Adjusted Half-Cell Potential Results

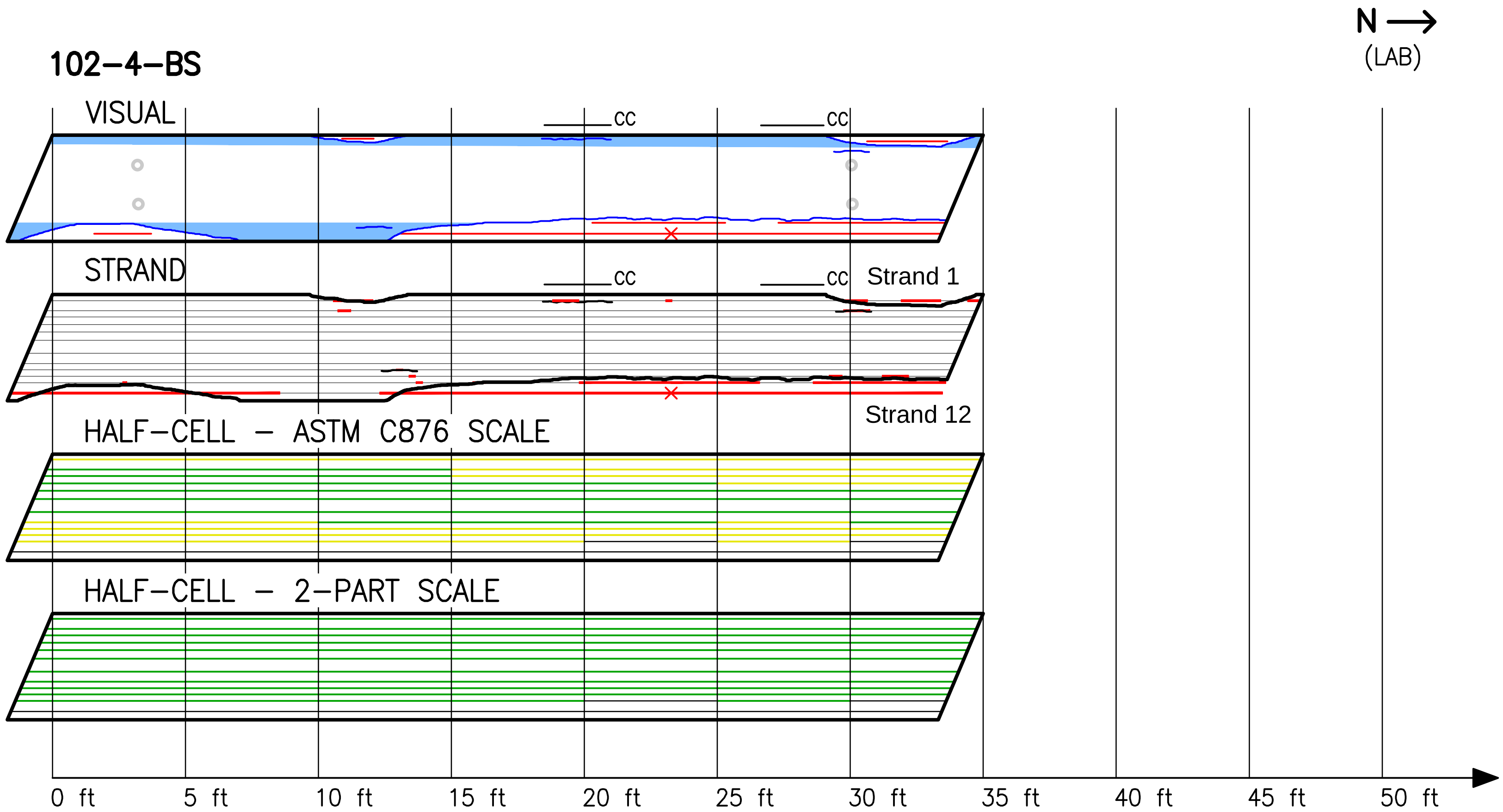

Figure 3.111: Specimen 102-4-BS Adjusted Half-Cell Potential Results

3.7 Summary and Conclusions

The visual deterioration of 15 box beam specimens acquired from decommissioned bridges was documented. Each specimen was tested using three NDT methods: connectionless electrical pulse response analysis (CEPRA), ground penetrating radar (GPR), and half-cell potentials. After completion of the nondestructive evaluation, strands in the location of visual signs of deterioration, as well as several "hot spots" detected by NDT, were removed to determine the actual extent of deterioration. The NDT results were then compared to the strand corrosion observed. The extent of deterioration and the comparison between the NDT results and strand corrosion is summarized as follows:

3.7.1 Visual Inspection

1. Visible inspection provided an excellent means of identifying the locations of corroded strand. Corrosion was limited to regions exhibiting visual distress such as cracking, spalling, and delamination.
2. Longitudinal cracks near the edge of the beam were observed to correspond with strand corrosion along the length of the crack. Corrosion only extended a few inches beyond the end of the visible crack.
3. Longitudinal cracks in the middle of the box were caused by water freezing in the void and do not generally align with the strand. The crack was often observed to meander and not be completely longitudinally aligned with the axis of the beam. Corrosion in this case was observed to be localized to the intersection of strands with the crack and any locations where the strand aligned with the crack.

4. Flexural cracking was observed in several beams. Strands intersecting flexural cracks were observed to be corroded only at the intersection with the flexural crack.
5. Strands at concrete spalls and delamination (exposed or not exposed) were observed to be corroded.
6. Corner cracks which are only visible for exterior girders were observed to correspond with strand corrosion over the length of the crack. For interior joints, this crack would not be visible; the only potential visible indicator would be rust staining at the joint.

3.7.2 NDT Inspection

3.7.2.1 CEPRA

1. CEPRA was capable of determining corrosion where visual inspection would not have observed deterioration.
2. CEPRA did not demonstrate an ability to accurately assess the condition of strands adjacent to corrosion. Often, heavily corroded strands influenced the readings of adjacent strands causing overestimations of the indicated corrosion which may be a halo effect of the adjacent corroded strand. This effect was primarily observed for specimens exhibiting deterioration related to leaking longitudinal joints or water draining over the side of the exterior beam. Considering the progression of corrosion for this type of deterioration, the observed halo effect may also be an indication of future corrosion.
3. Correlation between corrosion rate measurements and severity of corrosion as noted in the literature did not correspond well with the test results. For the strand in the box beam specimens (3/8 in. and 1/2 in.), modifying the thresholds by a factor of 2.3 (the ratio of surface area of strand to bar reinforcement) resulted in significantly improved

correlation. Further research is needed to verify the appropriate CEPRA modification factor for use on structures reinforced with strands with a nominal diameter other than 3/8 in. or 1/2 in.

4. Using a threshold of 23 μm/year, where strands are considered corroded if measurements are above the threshold, provided adequate correlation between corrosion rate measurements and corroding strand. This "hot spot" analysis may be useful to inspectors, but information regarding regions of distress may be lost.
5. CEPRA provides a simple tool to augment visual inspection. The system is lightweight and easy to operate with minimal training.

3.7.2.2 GPR

1. GPR provides an accurate method to locate strand embedded in concrete and is recommended for this purpose.
2. GPR is not recommended for general deterioration mapping of the bottom flange of box beams. GPR can locate areas of delaminated concrete which are likely locations of corrosion. This system can be helpful in locating corrosion due to corner cracking or other regions where delaminated concrete is suspected. Outside of these regions, corrosion could not be detected.
3. The 8 dB threshold provided poor correlation to delaminated areas of concrete, whereas the 6 dB threshold provided good correlation. Therefore, the 6 dB threshold is recommended for delamination detection.

3.7.2.3 Half-Cell Potentials

1. Good correlation was observed between indicated strand corrosion and actual strand corrosion of strands adjacent to visual signs of deterioration. Measurements were not possible directly over longitudinal cracks or on the rough surfaces at concrete spalls.
2. Similar to the CEPRA method, the half-cell potential readings were observed to be influenced by heavily corroded strand. This halo effect was observed for specimens exhibiting deterioration related to leaking longitudinal joints or water draining over the side of the exterior beam but to less extent than was observed for the CEPRA method. Considering that corrosion propagates from strand to strand for this type of deterioration, the observed halo effect may also be an indication of future corrosion.
3. The ASTM C879 correlation between voltage potential and corrosion corresponded well with the test results, but strand corrosion was only observed where corrosion was indicated. Therefore, a condensed scale using a threshold of -0.35 V, where corrosion is indicated for voltage potentials less than the threshold, also provided adequate correlation to the observed corrosion and simplified data interpretation.
4. While half-cell potentials require access to select locations of the reinforcement and is not fully non-destructive, it provided the best results related to identifying the corrosion of strands adjacent to visual signs of deterioration.

3.7.3 Overall Findings

1. The ingress of salt-water to the bottom flange of box beams from leaking joints or drainage over the side of the bridge results in corrosion of the strands at the edge of the box section. Where longitudinal cracks or spalls exist, strands at the longitudinal cracks

or concrete spalls were corroded. Where staining was present in addition to transverse cracks, the strands at the cracks were also corroded.

2. Longitudinal cracks located away from the edge of the bottom flange of box beams were caused by water freezing in the void. Cracks were observed in many cases away from reinforcement. Furthermore, corrosion was not observed on the longitudinal strand except at localized locations where the longitudinal crack traversed the strand. These findings indicate that corrosion was not the cause of longitudinal cracking. Evidence of corrosion in strands adjacent to the strands at longitudinal cracks was not found.
3. Based on the findings of the visual inspections and NDT method evaluation, visual inspection of bottom flange deterioration proved to provide the most reliable method for determining the extent of deterioration. The NDT methods may be used to augment visual inspection. For example, GPR may be used to locate reinforcement such that the number of strands intersecting or aligning with a crack may be determined. Also, CEPRA and GPR may be used to identify corrosion at the edge of a bottom flange where delamination may be suspected.
4. GPR is extremely useful to identify the number strands actually provided in the section especially when construction drawings are not available.

CHAPTER 4. STRUCTURAL TESTING

4.1 Introduction

Current load rating practice follows a simple set of assumptions to provide estimates of the deteriorated structural capacity of prestressed concrete box beams. To improve the current load rating practice, the load-deflection behavior of deteriorated box beams must be understood. In this chapter, the structural tests of 15 box beam specimens is presented, and an analytical model to estimate the load-deflection behavior of each specimen is developed. Using the results from the structural tests, the analytical model is evaluated.

4.2 Specimen Geometry

The cross-section dimensions of the beam specimens were measured and compared to the dimensions of the INDOT standard sections. This comparison is made because load rating calculations are often performed for box beam bridges assuming the beams have the geometry and reinforcement provided in the standard drawings. Table 4.1 provides a summary of the standard sections that were compared to each beam specimen. The as-built cross-section geometry of each specimen, the associated INDOT standard section, and a photo of the cross-section are provided in Appendix D. Please note that each figure was drawn with the correct proportions.

In Table 4.1, Specimen 244-1-LC (constructed in 1960) is paired with the 1961 standard section. The earliest available standard drawings were produced in 1961, and it is considered that this standard shape is consistent with earlier construction.

Table 4.1: Box Beam Specimens

Bridge (Year Built)	Specimen ID	Source Bridge Beam Number	INDOT Standard Section
Tippecanoe 244 (1960)	244-1-LC	6	1961 - B-21-3-9
Elkhart 409 (1962)	409-1-ES	B9	1961 - B-27
	409-2-UD	B8	
Newton K5 (1965)	K5-1-LC	1	1965 - B-21-3-9
	K5-2-LC	7	1965 - B-27
Wells 79 (1966)	79-1-UD	B2	1961 - B-17-3-9
	79-2-UD	A6	1971 - WS-17
	79-3-UD	A1	1961 - B-17
	79-4-LC	A7	
Newton 56 (1968)	56-1-LC	A6	1965 - WS-17
	56-2-ES	B1	
Elkhart 102 (1970)	102-1-BS	C7	1970 - WS-17
	102-2-BS	C5	
	102-3-BS	B8	
	102-4-BS	B7	

Specimen K5-2, as discussed in Chapter 3, was found with a repaired section. The original section and repaired section are shown in Figure D.5 and Figure D.6. To determine the additional dead load from the filler material, the dimensions shown Figure D.6(a) were used. The unit weight of the cementitious fill was assumed to be 145 lb/ft^3, and based on AASHTO (LRFD 2017), the unit weight of the bituminous material was assumed to be 140 lb/ft^3.

Specimen 79-1-UD (Figure D.7) was observed with three circular voids and a width of 48 in. The INDOT standard section 1965 B-17-3-9 has two rectangular voids which is not consistent with the as-built section. The INDOT standard section 1961 B-17-3-9 has three circular voids but a width of 45 in. A comparison of the as-built and standard drawing shows that 1.5 in. was added to the outer webs to achieve the 48 in. width. It is likely that the bridge designer specified the standard section to be 3 in. wider to accommodate the required width of the bridge. Based on the agreement in geometry between Specimen 79-1-UD and the 1961 standard drawing, Specimens 79-3-UD and 79-4-LC were assumed to correspond with the 1961 standard drawings as well.

Specimen 79-2-UD (Figure D.8) was observed to have expanded polystyrene (EPS) voids and reinforced with 1/2 in.-special strands. The combination of EPS voids and 1/2 in. special strand led to the assumption that Specimen 79-2-UD was a replacement beam. Information regarding any work prior to salvage of the beams in 2017 was not available. The most recent changes to the INDOT standard drawings for box beams were made in 2006 and 2010 (Molley 2017). The latest revision to the standard drawings prior 2006 was issued in 1971. The beam was assumed to have been replaced between 1971 and 2006. Therefore, the cross-section geometry of Specimen 79-2-UD is compared to the 1971 standard section.

Specimen 56-2-ES, as discussed in Chapter 2, arrived at the laboratory with partial loss of the concrete section. The section loss resulted in a variable cross-section along the length of the beam. The dimensions in Figure D.12(a) provide the maximum and minimum dimensions of the deteriorated portions of the section. All calculations were carried out using the minimum dimensions provided in Figure D.12(a).

4.2.1 As-Built Sections vs. INDOT Standard Sections

To compare the differences in geometry between the as-built sections and INDOT standard sections, Table 4.2 is provided. The year column provides the year of issue for the standard section drawing or the year of construction for the as-built section. The overall height of the section h, width of the section b, thickness of the top flange t_{tf}, thickness of the bottom flange t_{bf}, and web thickness t_w are also provided. The web thickness is reported as two, three, or four numbers separated by commas. Each number refers to a web thickness, and the number of thicknesses refers to the number of webs in the section. The order of the web dimensions is provided from left to right in reference to the cross sections shown in Appendix D.

A review of Table 4.2 reveals that the overall height and width of the as-built sections were very consistent with the standard sections. The web and flange dimensions, however, varied by up to 3 in. The large variance in geometry was caused by void movement during concrete placement. The movement of the void trended upwards and toward the middle of the section. The as-built top flange thickness of 10 out of 15 beams was less than the standard section thickness It should be noted that the topping slab on Specimens 409-1-ES and 409-2-UD was not included in the top flange thickness listed in Table 4.2. In all cases with multiple voids, the as-built middle web thickness was equivalent or less than the dimension provided for the standard section.

Table 4.2: Summary of Section Geometry- As-built and Standard Sections

Specimen	Year	Section	h (in.)	b (in.)	t_{tf} (in.)	t_{bf} (in.)	t_w (in.)
244-1-LC	1961	B-21-3-9	21	45	4	3.5	4, 3, 4
	1960	As-built	21	45	2.25	5.375	3.375, 2.375, 5.25
409-1-ES	1961	B-27	27	36	5.5	5.5	5, 5
	1962	As-built	27	36	3.75	6	5, 4.25
409-2-UD	1961	B-27	27	36	5.5	5.5	5, 5
	1962	As-built	27	36	2.5	7	5, 4.25
K5-1-LC	1965	B-21-3-9	21	45	4	4	4, 3, 4
	1965	As-built	21	45	3.5	4	4.75, 1.5, 4
K5-2-LC	1965	B-27	27	36	5.5	5.5	5, 5
	1965	As-built	27	36	4	5.875	5, 4.25
79-1-UD	1961	B-17-3-9	17	48	5.5	4.5	4, 2.75, 2.75, 4
	1966	As-built	17	48	3	3.5	5.5, 2.75, 2.75, 5.5
79-2-UD	1971	WS-17	17	48	5.5	4.5	4, 3, 4
	N/A*	As-built	17	47.75	3	3.5	5.5, 0, 5.5
79-3-UD	1961	B-17	17	36	3.25	3.25	4.75, 5.5, 4.75
	1966	As-built	17	36	3.4	3	4.25, 5, 5.75
79-4-LC	1961	B-17	17	36	3.25	3.25	4.75, 5.5, 4.75
	1966	As-built	17	36	1.75	4.75	4.75, 3.625, 6.375
56-1-LC	1965	WS-17	17	48	5.5	4.5	4, 3, 4
	1968	As-built	17	47.75	4.375	5.625	4.25, 2.75, 4
56-2-ES	1965	WS-17	17	48	5.5	4.5	4, 3, 4
	1968	As-built	17	47.75	6	4.5	3.5, 3, 3.5
102-1-BS	1970	WS-17	17	48	5.5	4.5	4, 3, 4
	1970	As-built	17	48	6	4	5.5, 0.5, 4.25
102-2-BS	1970	WS-17	17	48	5.5	4.5	4, 3, 4
	1970	As-built	17	48	5.5	4.25	4.5, 1.5, 4.75
102-3-BS	1970	WS-17	17	48	5.5	4.5	4, 3, 4
	1970	As-built	17	48	5.625	4.25	5.375, 1, 4.75
102-4-BS	1970	WS-17	17	48	5.5	4.5	4, 3, 4
	1970	As-built	17	48	5.625	4.375	5.5, 1, 4.625

*Construction date unavailable - assumed between 1971 and 2006

A comparison of the reinforcement in the as-built and standard sections was made by using the reinforcement information summarized in Table 4.3. The compression reinforcement, strand diameter, number of strands, and span were determined by direct measurement of the beam specimens. The transverse reinforcement spacing was determined using a GPR survey of each beam. The bar size of the transverse reinforcement was determined by removing cover from the bars after completion of the structural test. The transverse reinforcement ratio ρ_t, given in percent, was calculated by dividing the area of transverse reinforcement per foot by the area of concrete perpendicular to the transverse reinforcement per foot.

A review of Table 4.3 shows that the provided number of strands for a given span was always conservative relative to the standard section. In most cases, the number of strands in the as-built section were equal to the number provided in the standard drawing. The compression reinforcement was found to be consistent with the standard sections as well. Only four specimens had any deviation from the standard section. For Specimens 409-1-ES, 409-2-UD, and K5-2-LC, the same number of bars were used, but a slightly smaller bar was substituted for half of the bars. For Specimen 56-1-LC, the same bar size was used but the number of bars was reduced from five to three.

Table 4.3: Summary of Reinforcement- As-Built and Standard Sections

Specimen	Year	Section	Transverse Reinf.	ρ_t (%)	Compression. Reinf.	Strand (Dia.)-No.	Span
244-1-LC	1961	B-21-3-9	#4 @ 9"	0.40	(5) #5	(3/8)-31	43'
	1960	As-built	#4 @ 12"	0.36	(5) #5	(3/8)-31	43'-7"
409-1-ES	1961	B-27	#4 @ 16"	0.27	(4) #6	(3/8)-20	49'
	1962	As-built	#3 @ 12"	0.18	(2) #5-(2) #6	(3/8)-20	50'
409-2-UD	1961	B-27	#4 @ 16"	0.28	(4) #6	(3/8)-20	49'
	1962	As-built	#3 @ 12"	0.18	(2) #5-(2) #6	(3/8)-20	50'
K5-1-LC	1965	B-21-3-9	#4 @ 18"	0.22	(5) #5	(3/8)-16	35'
	1965	As-built	#3 @ 14"	0.14	(5) #5	(3/8)-24	35'-4"
K5-2-LC	1965	B-27	#4 @ 18"	0.24	(4) #5	(3/8)-16	47'
	1965	As-built	#3 @ 14"	0.16	(2) #3-(2) #5	(3/8)-18	35'-6"
79-1-UD	1961	B-17-3-9	#4 @ 9"	0.27	(5) #5	(1/2)-12	35'
	1966	As-built	#4 @ 10"	0.36	(5) #5	(1/2)-12	35'-4"
79-2-UD	1971	WS-17	#4 @ 9"	0.40	(5) #5	(1/2)-8	27'
	N/A*	As-built	#4 @ 9"	0.40	(5) #5	(1/2 sp.)-8	27'-10"
79-3-UD	1961	B-17	#4 @ 18"	0.15	(4) #5	(1/2)-6	27'
	1966	As-built	#4 @ 12"	0.22	(4) #5	(1/2)-6	27'-10"
79-4-LC	1961	B-17	#4 @ 18"	0.15	(4) #5	(1/2)-6	27'
	1966	As-built	#4 @ 12"	0.22	(4) #5	(1/2)-6	27'-10"
56-1-LC	1965	WS-17	#4 @ 9"	0.40	(5) #5	(1/2)-8	27'
	1968	As-built	#3 @ 3"	0.67	(3) #5	(1/2)-11	27'-2"
56-2-ES	1965	WS-17	#4 @ 9"	0.44	(5) #5	(1/2)-10	35'
	1968	As-built	#3 @ 3"	0.67	(5) #5	(1/2)-13	35'-4"
102-1-BS	1970	WS-17	#4 @ 9"	0.43	(5) #5	(1/2)-12	35'
	1970	As-built	#4 @ 10"	0.36	(5) #5	(1/2)-12	34'-4"
102-2-BS	1970	WS-17	#4 @ 9"	0.41	(5) #5	(1/2)-12	35'
	1970	As-built	#4 @ 10"	0.36	(5) #5	(1/2)-12	34'-6"
102-3-BS	1970	WS-17	#4 @ 9"	0.40	(5) #5	(1/2)-12	35'
	1970	As-built	#4 @ 10"	0.36	(5) #5	(1/2)-12	34'-4"
102-4-BS	1970	WS-17	#4 @ 9"	0.40	(5) #5	(1/2)-12	35'
	1970	As-built	#4 @ 10"	0.36	(5) #5	(1/2)-12	34'-4"

*Construction date unavailable - assumed between 1971 and 2006

The transverse reinforcement found in the as-built sections varied much more from the standard section than the other reinforcement properties. In 10 of 15 beams, the provided transverse reinforcement was less than the amount provided in the standard drawings, but in 5 of the 10 instances, the provided amount was only less by ρ_t = 0.04% or less. The maximum difference in reinforcement ratio was ρ_t = 0.1%.

Each standard section is associated with a specific range of design span lengths provided for each standard section. The transverse reinforcement noted for a given standard section applies to the entire range of span lengths. Therefore, the difference between the standard section and as-built transverse reinforcement ratios is assumed to be a result of designing each constructed beam for the actual span length. Small changes between the transverse reinforcement noted in the standard section drawings and the actual beam are consistent with this assumption.

4.2.2 Summary

A comparison between the as-built and standard sections showed that, in general, the as-built sections were similar to the standard sections. The variance in section geometry observed in the flange and web thicknesses was caused by void movement during concrete placement. In most cases, the void shifted upwards and toward the middle of the section, reducing the top flange thickness and, if the section had multiple voids, the middle web thickness.

Variance in the reinforcement was observed mainly in the transverse reinforcement, where 10 of 15 beams had transverse reinforcement ratios less than the standard sections by up to ρ_t = 0.1%. It is assumed that the specific beam was designed for the actual span length. Therefore, small changes between the transverse reinforcement noted in the standard section drawings and the actual beam are expected.

4.3 Materials

Material testing was performed to determine the compression strength of the concrete in each beam and the tensile properties of the prestressing strand. Concrete cores were taken from each beam for compression tests, and tension tests were conducted on strand extracted from each beam specimen.

4.3.1 Concrete

Three 4 in. diameter concrete cores were taken from the end diaphragm of each beam specimen. For the specimens with curbs (K5-1-LC, 79-3-UD, and 79-4-LC), three additional cores were extracted directly from the curb of each specimen. An additional series of 2-3/4 in. diameter cores were taken from the flanges of Specimens 244-1-LC and 56-2-ES and from the structural repair on Specimen K5-2-LC. The cores from Specimens 244-1-LC and 56-2-ES were taken to investigate the concrete strength near the failure region of the beam. The cores taken from the repair region in Specimen K5-2-LC could not be tested based on the condition of the concrete cores. The delaminated concrete from freeze-thaw damage penetrated through over half the flange repair thickness of Specimen K5-2-LC (Figure 4.1).

(a) Core 1 **(b) Core 2** **(c) Core 3**

Figure 4.1: Delamination in the Flange Repair Cores from K5-2-LC

Each core was obtained according to ASTM C42 (2018). A 600-kip Forney compression testing machine with a CA-0396 automatic control system interface was used to conduct each compression test according to ASTM C39 (2018). To capture the compressive strain up to peak compressive stress, a digital image correlation (DIC) system was used (Figure 4.2). The DIC system relied on two speckled targets glued to the specimen to capture the deformation of the concrete core (Figure 4.3). The speckled targets were used in place of a speckle pattern on the concrete surface to avoid issues associated with using DIC on cylindrical objects. Prior to testing, the ends of each core were ground smooth and parallel using a Marui Co., LTD. Hi-Kenma cylinder end grinder.

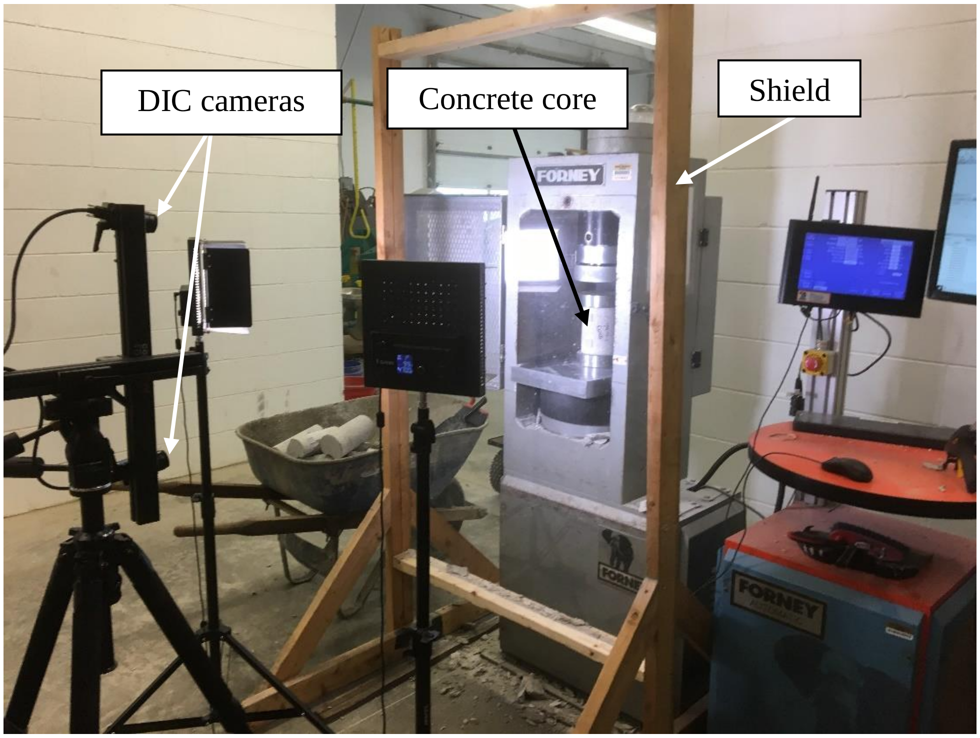

Figure 4.2: DIC Setup for Compression Testing

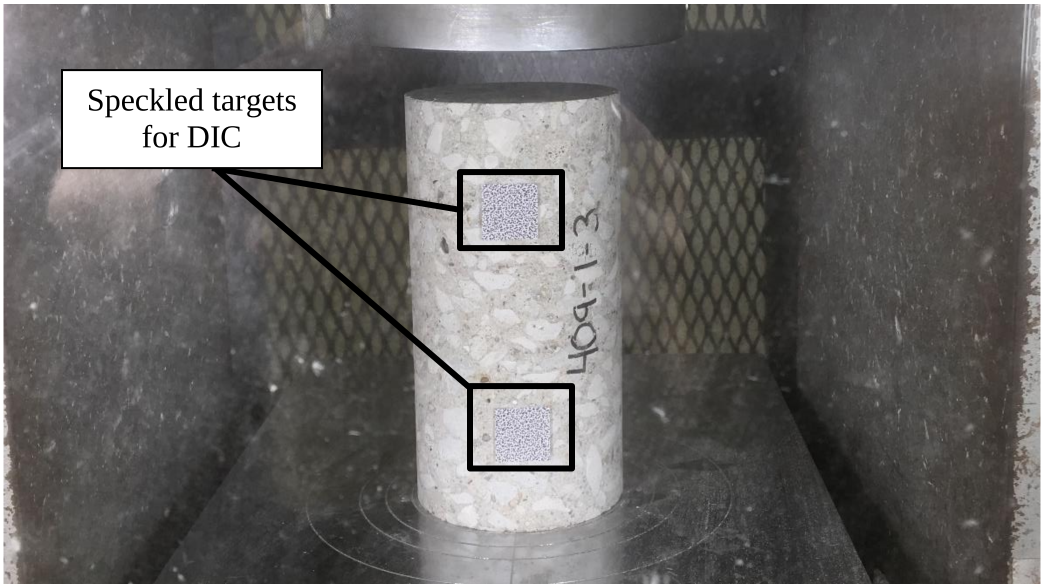

Figure 4.3: Concrete Core with Speckled Targets

The results from the compression tests are summarized in Table 4.4. The results from cores taken from the either a curb or flange have been labeled with a "C", for curb, or an "F", for flange, at the end of the specimen ID. The strain at peak stress measured by the DIC system for each core is also reported in Table 4.4. The DIC error noted for Cores 1 to 3 taken from the flange of Specimen 56-2-ES was caused by the very short height of the cores (3 in. to 3.32 in.).

The Hognestad (1951) and Thorenfeldt (Thorenfeld et al. 1987) concrete models were compared to the test data to determine the appropriate model for analysis. A description of each concrete model is provided in Section 4.6.1.1. A representative comparison of the two models is shown in Figure 4.4. The stress-strain curve generated from each model is provided with the compression test data for each beam specimen in Appendix E. In general, the Hognestad model was observed to provide the best representation of the test results.

Prior to structural testing, a James Instruments rebound hammer was used to estimate the concrete strength of each beam according to ASTM C805 (2013). The estimated strength values are reported in Table 4.4. As shown, the rebound hammer provided conservative estimates for the concrete strength for every specimen.

The coring procedure did not always produce cores free of any steel reinforcement. To conform to ASTM C42, the reinforced portions were cut off. In some cases, the length to diameter ratio (L/D) could not be maintained at 2.0 ± 0.1. In these cases, adjustment factors provided by ASTM C42 were used to calculate adjusted compressive strength values (Table 4.5). As shown, even in the cases of adjustments (underlined values), the adjustment is minor. The adjusted strengths are approximately the same as the tested strength and for practical purposes can be ignored.

Table 4.4: Compression Test Results

Specimen	Age (years)	Compressive Strength (psi)				Rebound Hammer (psi)	Strain at peak stress				Fracture Pattern		
		Cores					Cores				Cores		
		1	2	3	Average		1	2	3	Average	1	2	3
244-1-LC	59	13,100	12,700	13,400	**13,100**	7,500	0.0026	0.0021	0.0031	**0.0026**	2	1	1
244-1-LC-F	59	9,700	11,700	10,700	**10,700**	5,500	0.0023	0.0026	0.0023	**0.0024**	3	4	2
409-1-ES	57	8,400	9,300	9,400	**9,000**	7,250	0.0032	0.0035	0.0025	**0.0031**	3	3	2
409-2-UD	57	13,600	13,000	12,800	**13,100**	8,500	0.0032	0.0019	0.0029	**0.0026**	1	4	4
K5-1-LC	54	12,000	12,000	12,300	**12,100**	6,000	0.0029	0.0032	0.0039	**0.0033**	1	4	1
K5-1-LC-C	54	11,700	13,600	11,000	**12,100**	5,000	0.0018	0.0026	0.0025	**0.0023**	4	1	2
K5-2-LC	54	16,700	16,400	16,600	**16,600**	7,500	0.0026	0.0026	0.0027	**0.0026**	1	1	1
79-1-UD	53	11,100	12,200	11,100	**11,500**	6,500	0.0030	0.0029	0.0025	**0.0028**	3	1	3
79-2-UD	- -	10,600	10,600	10,500	**10,500**	7,000	0.0027	0.0024	0.0020	**0.0024**	5	1	2
79-3-UD	53	11,900	11,600	11,400	**11,600**	7,500	0.0028	0.0026	0.0030	**0.0028**	3	1	3
79-3-UD-C	53	10,700	10,600	10,600	**10,600**	5,500	0.0027	0.0025	0.0028	**0.0027**	3	3	1
79-4-LC	53	11,800	11,600	11,800	**11,700**	5,000	0.0032	0.0029	0.0032	**0.0031**	3	3	3
79-4-LC-C	53	10,200	10,300	10,900	**10,500**	6,500	0.0032	0.0028	0.0033	**0.0031**	5	3	3
56-1-LC	51	13,200	13,100	13,300	**13,200**	7,500	0.0035	0.0031	0.0030	**0.0032**	1	1	4
56-2-ES	51	13,600	10,400	12,000	**12,000**	8,500	0.0026	0.0024	0.0012	**0.0021**	1	2	3
56-2-ES-F	51	9,600	9,200	11,500	**10,100**	8,500	0.0038	0.0032	0.0038	**0.0036***	3	4	3
102-1-BS	49	8,100	7,500	7,200	**7,600**	7,000	0.0026	0.0019	0.0018	**0.0021**	3	3	3
102-2-BS	49	8,900	8,600	8,200	**8,600**	7,500	0.0020	0.0022	0.0038	**0.0027**	3	3	5
102-3-BS	49	10,100	9,500	9,900	**9,900**	7,000	0.0028	0.0031	0.0028	**0.0029**	2	1	1
102-4-BS	49	5,600	7,000	7,300	**6,600**	6,500	N/A*	0.0024	0.0024	**0.0024**	3	2	2

***DIC error**

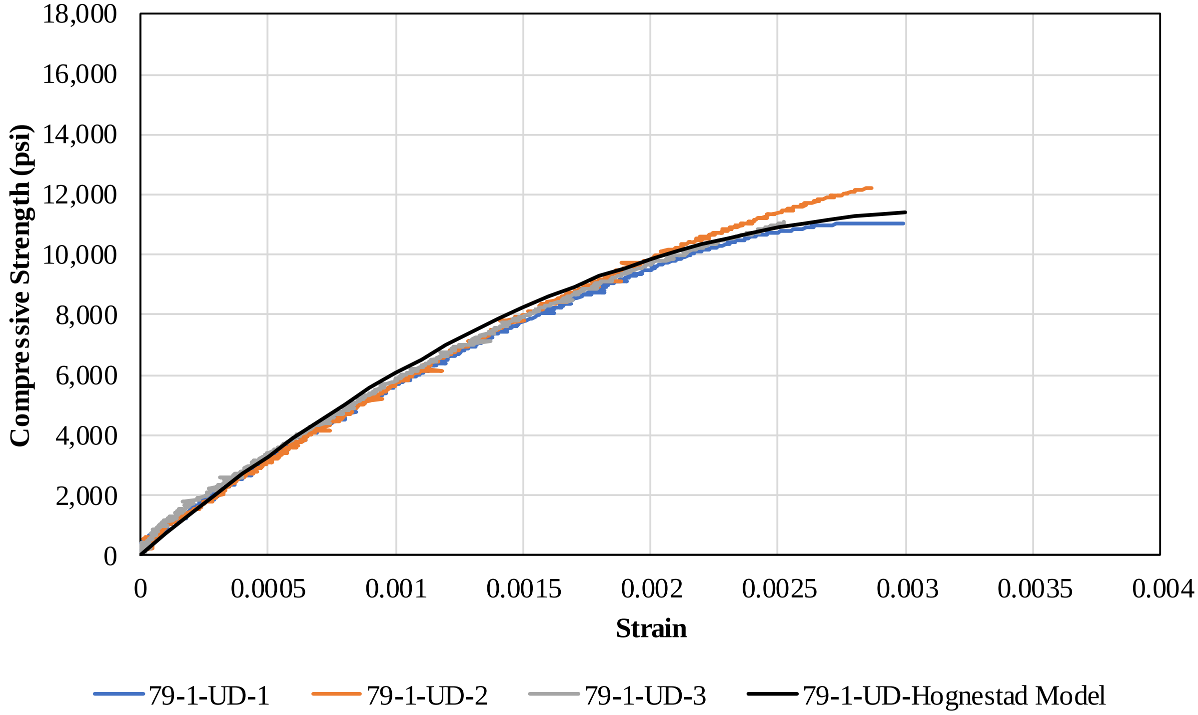

(a) Hognestad concrete model

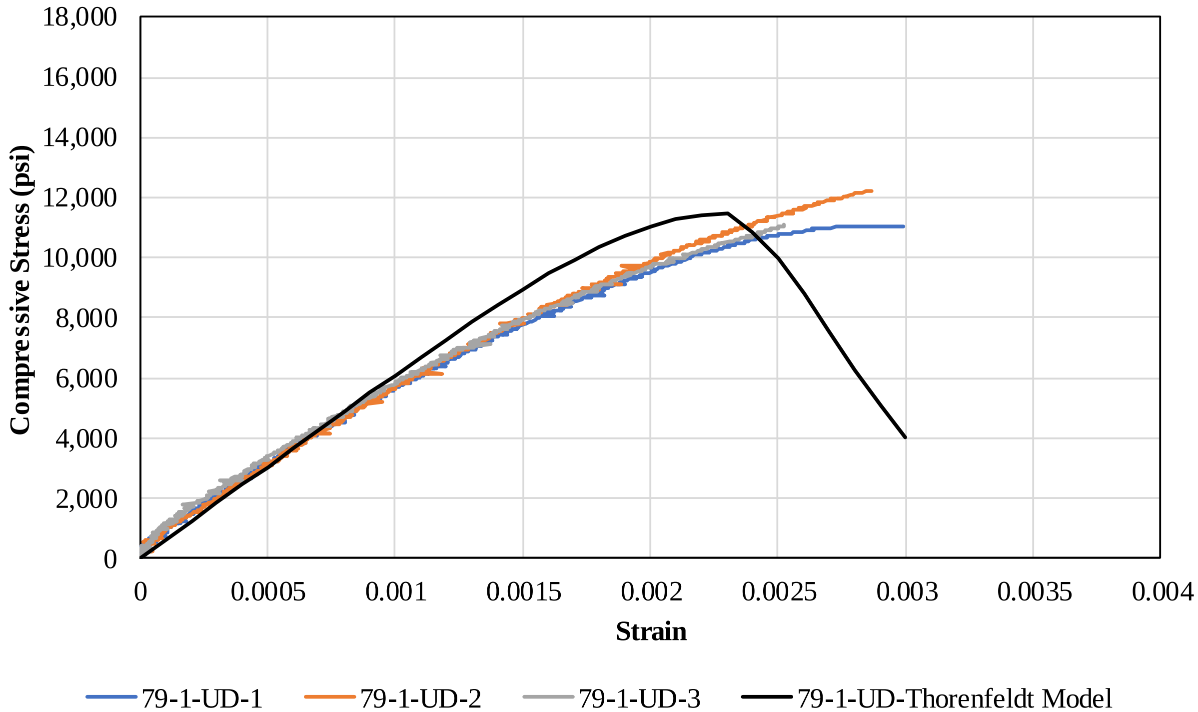

(b) Thorenfeldt concrete model

Figure 4.4: Representative Compressive Stress vs. Strain (Core Specimens 79-2-UD-1, 2, and 3)

Table 4.5: Adjusted Compression Strength Results

Specimen ID	L/D			Adjusted Strength (psi)				Average Strength without adjustment (psi)
	Cores			Cores				
	1	2	3	1	2	3	Average	
244-1-LC	1.95	1.96	1.94	13,100	12,700	13,400	**13,100**	**13,100**
244-1-LC-F	2.22	2.22	1.99	9,700	11,700	10,700	**10,700**	**10,700**
409-1-ES	1.47	1.16	1.95	8,100	8,600	9,400	**8,700**	**9,000**
409-2-UD	1.95	1.96	1.95	13,600	12,900	12,800	**13,100**	**13,100**
K5-1-LC	1.96	1.98	1.97	11,900	12,000	12,300	**12,100**	**12,100**
K5-1-LC-C	1.51	1.34	1.97	11,400	13,000	11,000	**11,800**	**12,100**
K5-2-LC	1.96	1.95	1.96	16,700	16,400	16,600	**16,600**	**16,600**
79-1-UD	1.96	1.95	1.96	11,100	12,200	11,100	**11,400**	**11,500**
79-2-UD	1.92	1.97	1.90	10,600	10,600	10,400	**10,500**	**10,500**
79-3-UD	1.97	1.97	1.97	11,900	11,700	11,400	**11,600**	**11,600**
79-3-UD-C	1.60	1.65	1.77	10,400	10,300	10,500	**10,400**	**10,600**
79-4-LC	1.73	1.98	1.98	11,400	11,800	11,800	**11,700**	**11,700**
79-4-LC-C	1.66	1.81	1.67	10,000	10,300	10,600	**10,300**	**10,500**
56-1-LC	1.91	1.98	1.93	13,100	13,100	13,300	**13,200**	**13,200**
56-2-ES	1.94	1.66	1.19	13,600	10,200	11,200	**11,700**	**12,000**
56-2-ES-F	1.23	1.09	1.14	9,100	8,500	10,800	**9,500**	**10,200**
102-1-BS	1.97	1.98	1.99	8,100	7,500	7,200	**7,600**	**7,600**
102-2-BS	2.02	1.98	1.99	8,900	8,600	8,200	**8,600**	**8,600**
102-3-BS	1.71	1.97	1.97	9,900	9,500	9,900	**9,800**	**9,900**
102-4-BS	1.97	1.50	1.83	5,600	6,700	7,300	**6,500**	**6,600**

4.3.2 Prestressing Strands

4.3.2.1 Strands without Corrosion

Three uncorroded prestressing strands were extracted from each specimen and cut to a length of 48 in. for tension testing. The strand specimens were tested using a 120-kip Baldwin testing machine equipped with an Instron hydraulic control system. Strain was measured using a DIC system with speckled targets glued to the strand (Figure 4.5). The targets were spaced 4 in. apart for a total gage length of 12 in. Four targets were used for redundancy in the event that any targets fell off during testing.

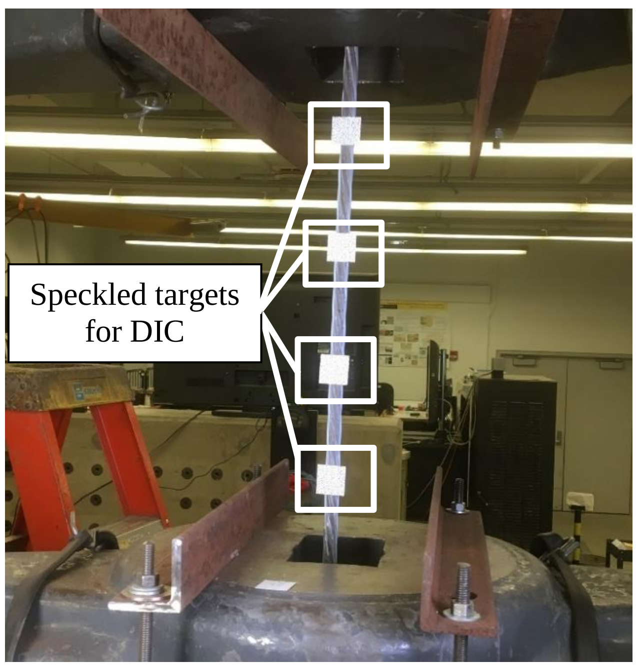

Figure 4.5: Tensile Test Specimen

Prestressing chucks designed for tension tests to failure of 7-wire strand (1/2 in. and 3/8 in. diameter (Figure 4.6)) were used as the gripping devices. Household aluminum foil was used as cushioning material to prevent the grips from biting into the strand to promote failure away from the grips. The chucks were installed with approximately 24 layers of aluminum foil wrapped around the ends of each strand (Figure 4.7).

Figure 4.6: Prestressing Chucks

Figure 4.7: Prestressing Chuck Installation

The stress-strain curve for each specimen is provided in Appendix F, and a representative curve is shown in Figure 4.8. The results are also summarized in Table 4.6 where the nominal diameter of the strand is reported with the specimen ID for each beam specimen. The stress in the strand was calculated by dividing the force applied to the strand by the nominal area (0.08 in.^{2} for 3/8 in. strand, 0.153 in.^{2} for 1/2 in. strand, and 0.167 in.^{2} for 1/2 in. special). The values of f_{pu}, f_{py} (0.2% offset), ε_{pu}, strain at fracture, and E_{ps} are also reported. The 0.2% offset yield stress and elastic modulus were calculated according to ASTM A1061 (2016). In addition, if the strand failed within 1/4 in. of the grip or within the grip, a "Y" is placed in the Failure within Grip column of Table 4.6. It should be noted that the strain at fracture was greater than ε_{pu} for all specimens that failed within the grip. This indicates that the failure location did not influence the measurement of ultimate tensile strength. Figure 4.9 shows a representative ductile strand fracture.

It should be noted that the measured strain at fracture for Strand 1 of Specimen 409-1-ES was significantly lower than that of Strands 2 and 3 of Specimen 409-1-ES. The failure mode of Strand Specimen 409-1-ES-1 was ductile although some surface rust was observed on the specimen (Figure 4.10). The difference in behavior of this strand is not clearly understood. Overall, all strands were capable of achieving strains greater than 0.04.

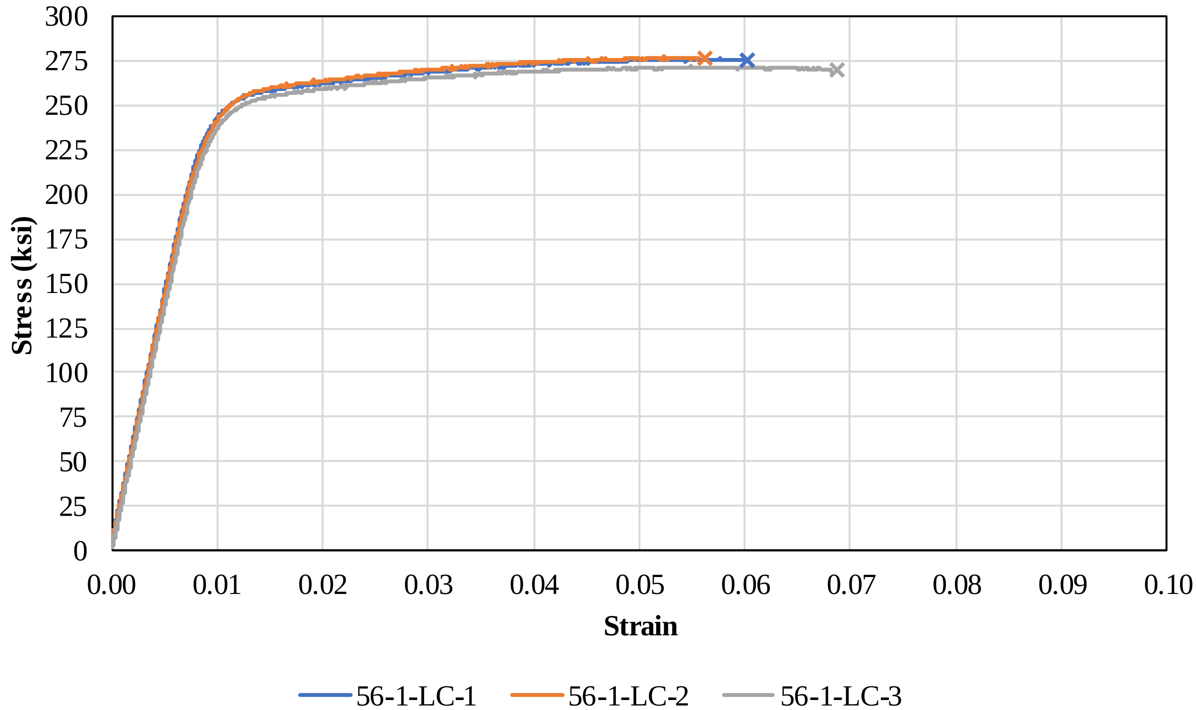

Figure 4.8: Representative Stress vs. Strain for Strand (Strand Specimens 56-1-LC-1, 2, and 3)

Figure 4.9: Ductile Strand Fracture (Strand Specimen 56-1-LC-3)

Table 4.6: Strand Test Results

Specimen ID (Strand Dia.)	Strand Specimen	Breaking Load (kip)	f_{pu} (ksi)	f_{py} (ksi)	ε_{pu}	Strain at fracture	E_{ps} (ksi)	Failure within Grip
244-1-LC (3/8 in.)	1	21,720	271.5	230.4	0.054	0.060	28,000	Y
	2	22,030	275.4	237.3	0.055	0.069	27,230	-
	3	22,010	275.1	238.7	0.052	0.059	27,770	-
	Average	**21,920**	**274.0**	**235.5**	**0.054**	**0.063**	**27,670**	
409-1-ES (3/8 in.)	1	22,100	276.2	259.5	0.024*	0.024	27,960	-
	2	22,130	276.6	255.6	0.052	0.055	28,170	-
	3	21,230	265.4	240.6	0.053	0.058	27,860	-
	Average	**21,820**	**272.7**	**251.9**	**0.043**	**0.046**	**28,000**	
409-2-UD (3/8 in.)	1	22,230	277.9	257.7	0.044	0.055	28,140	-
	2	22,150	276.8	254.8	0.056	0.059	28,190	-
	3	22,170	277.2	255.8	0.049	0.059	28,040	-
	Average	**22,180**	**277.3**	**256.1**	**0.049**	**0.058**	**28,120**	
K5-1-LC (3/8 in.)	1	21,300	266.3	237.3	0.048	0.055	26,570	-
	2	22,090	276.2	245.4	0.060	0.069	28,410	Y
	3	22,070	275.9	233.5	0.061	0.065	28,340	-
	Average	**21,820**	**272.8**	**238.8**	**0.056**	**0.063**	**27,770**	
K5-2-LC (3/8 in.)	1	22,340	279.2	246.5	0.048	0.049	28,120	-
	2	22,410	280.2	246.5	0.052	0.052	28,180	-
	3	22,410	280.1	246.0	0.053	0.064	27,750	-
	Average	**22,390**	**279.8**	**246.3**	**0.051**	**0.055**	**28,020**	

*Low value of strain was not associated with brittle type failure mode.

Table 4.6: Continued

Specimen ID (Strand Dia.)	Strand Specimen	Breaking Load (kip)	f_{pu} (ksi)	f_{py} (ksi)	ε_{pu}	Strain at fracture	E_{ps} (ksi)	Failure within Grip
79-1-UD (1/2 in.)	1	42,790	279.7	263.0	0.041	0.044	27,930	Y
	2	42,920	280.5	265.4	0.040	0.041	27,570	Y
	3	42,740	279.3	261.4	0.041	0.043	27,300	Y
	Average	**42,820**	**279.8**	**263.2**	**0.041**	**0.043**	**27,600**	
79-2-UD (1/2 in. special)	1	47,100	282.1	269.6	0.044	0.047	28,150	Y
	2	47,300	283.2	277.2	0.039	0.042	28,670	Y
	3	46,950	281.1	274.7	0.040	0.041	28,810	Y
	Average	**47,120**	**282.1**	**273.8**	**0.041**	**0.043**	**28,540**	
79-3-UD (1/2 in.)	1	42,590	278.4	253.2	0.038	0.039	27,710	-
	2	43,040	281.3	254.9	0.047	0.055	28,340	-
	3	42,920	280.5	256.2	0.041	0.042	28,370	-
	Average	**42,850**	**280.1**	**254.8**	**0.042**	**0.045**	**28,140**	
79-4-LC (1/2 in.)	1	43,020	281.2	255.3	0.055	0.063	26,410	-
	2	42,960	280.8	250.0	0.048	0.055	27,200	-
	3	40,710	266.1	221.9	0.054	0.055	28,070	-
	Average	**42,230**	**276.0**	**242.4**	**0.052**	**0.058**	**27,230**	
56-1-LC (1/2 in.)	1	42,290	276.4	249.4	0.058	0.060	27,960	-
	2	42,450	277.4	247.5	0.052	0.056	27,860	-
	3	41,610	271.9	245.5	0.055	0.068	27,180	-
	Average	**42,120**	**275.3**	**247.5**	**0.055**	**0.061**	**27,670**	

Table 4.6: Continued

Specimen ID (Strand Dia.)	Strand Specimen	Breaking Load (kip)	f_{pu} (ksi)	f_{py} (ksi)	ε_{pu}	Strain at fracture	E_{ps} (ksi)	Failure within Grip
56-2-ES (1/2 in.)	1	41,910	273.9	246.7	0.055	0.067	27,360	-
	2	41,670	272.4	248.5	0.054	0.057	27,440	-
	3	41,930	274.0	249.7	0.055	0.063	27,170	-
	Average	**41,840**	**273.4**	**248.3**	**0.055**	**0.062**	**27,320**	
102-1-BS (1/2 in.)	1	42,720	279.2	251.9	0.051	0.061	28,210	-
	2	41,150	269.0	234.9	0.048	0.050	28,330	-
	3	43,100	281.7	255.5	0.056	0.064	28,190	-
	Average	**42,320**	**276.6**	**247.4**	**0.052**	**0.058**	**28,240**	
102-2-BS (1/2 in.)	1	43,080	281.6	270.8	0.045	0.054	27,810	-
	2	43,400	283.7	274.9	0.026	0.026	27,180	-
	3	43,100	281.7	267.8	0.049	0.057	27,970	-
	Average	**43,190**	**282.3**	**271.2**	**0.040**	**0.046**	**27,650**	
102-3-BS (1/2 in.)	1	43,210	282.4	260.3	0.049	0.062	28,130	-
	2	43,260	282.8	258.3	0.051	0.058	28,660	-
	3	43,220	282.5	263.4	0.050	0.057	28,560	-
	Average	**43,230**	**282.5**	**260.7**	**0.050**	**0.059**	**28,450**	
102-4-BS (1/2 in.)	1	43,350	283.3	260.0	0.058	0.065	28,160	-
	2	43,400	283.7	261.6	0.048	0.055	28,780	-
	3	43,400	283.7	261.2	0.050	0.062	28,360	-
	Average	**43,380**	**283.6**	**261.0**	**0.052**	**0.061**	**28,430**	

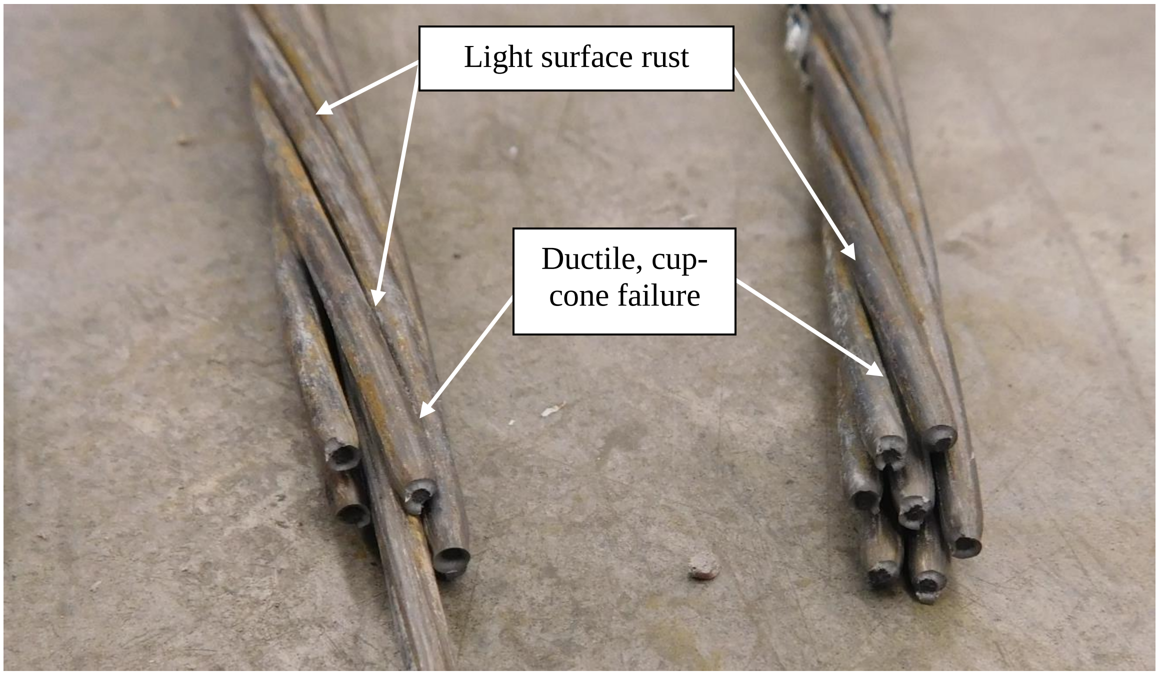

Figure 4.10: Strand Specimen 409-1-ES-1 After Tensile Testing

4.3.2.2 Corroded Strands

To investigate the remaining strength of a corroded strand, a series of 3/8 in. and 1/2 in. strands with a range of corrosion were tested. The 3/8 in. corroded strand specimens were taken from Specimens 244-1-LC and K5-1-LC. Other 3/8 in. strands were not available for testing as the corroded strands in Specimens 409-1-ES and K5-2-LC either fractured due to corrosion while in-service (Specimen 409-1-ES) or fractured during structural testing (Specimen K5-2-LC). The 1/2 in. corroded strand specimens were taken from Specimens 79-4-LC, 56-2-ES, and 102-3-BS to provide representative samples of the corrosion observed in 1/2 in. strands.

All corroded strand specimens were assigned strand numbers corresponding to their location, West to East, in the section followed by subscripted "cor". The corroded strand specimens from Specimen 102-3-BS, however, were labeled based on level of corrosion for comparison purposes. The location of each corroded strand specimen is provided in Appendix G.

The stress values reported in the following sections were calculated using the nominal area of the strand. The nominal area was used to facilitate comparison with the uncorroded strand test results.

4.3.2.2.1 Specimen 244-1-LC Corroded Strands

Two corroded strands were selected from Specimen 244-1-LC for tension testing. Both strands were located at a longitudinal crack that extended through-the-thickness of the bottom flange. Strand 5_{cor} (Strand 5 in Figure 3.51) is from Segment A, and Strand 6_{cor} is from Segment B (Figure G.1). Corrosion of each strand was relatively uniform along the length of the specimen and consisted of surface corrosion and minor pitting (Figure 4.11).

(a) Strand 5_{cor}

(b) Strand 6_{cor}

Figure 4.11: Specimen 244-1-LC Corroded Strands

Failure of each strand was characterized by a single-wire fracture at peak load (Figure 4.12). The breaking load, f_{pu}, ε_{pu}, and E_{ps} are reported in Table 4.7. The percent of full capacity was calculated considering the average uncorroded breaking load as full strength. The stress-strain curve for each specimen is presented in Figure 4.13.

(a) Strand 5_{cor}

(b) Strand 6_{cor}

Figure 4.12: Specimen 244-1-LC Corroded Strands After Failure

For comparison, the results from Strand Specimen 1 from Specimen 244-1-LC has been included in Table 4.7 and Figure 4.13. As shown, the corroded strand specimens had a capacity of at least 78% of the uncorroded strand capacity. In addition, the modulus of elasticity of the corroded strands was essentially the same as the uncorroded strands. The corroded strands, however, fractured before yielding occurred indicating that strand corrosion not only results in section loss but also in a loss of ductility. Brittle fracture of corroded strands is a known phenomenon attributed to a combination of corrosion, hydrogen embrittlement, and stress-corrosion cracking (ACI 222.2R-01).

Table 4.7: Specimen 244-1-LC Corroded Strand Test Results

Specimen ID (Strand Dia.)	Strand Specimen	Breaking Load (lb)	Percent of full capacity	f_{pu} (ksi)	ε_{pu}	E_{ps} (ksi)
244-1-LC (3/8 in.)	Uncorroded Average	21,920	100%	274.0	0.054	27,670
	5_{cor}	18,290	83%	228.7	0.012	26,450
	6_{cor}	17,050	78%	213.1	0.009	27,030

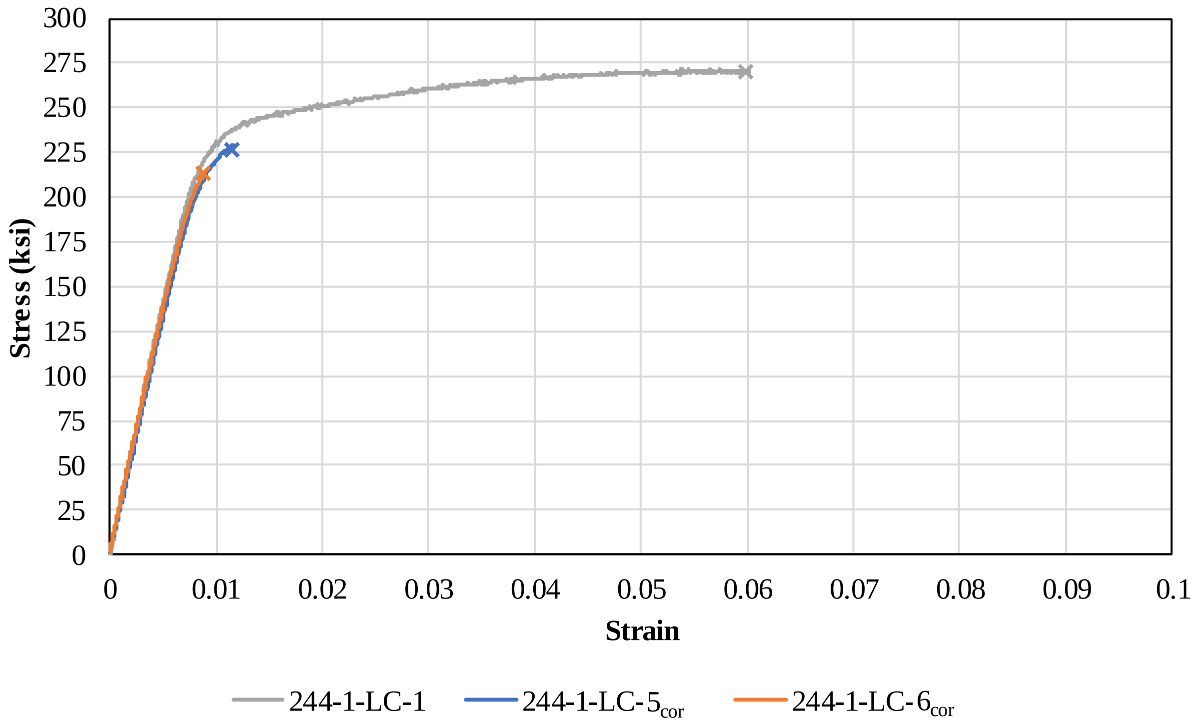

Figure 4.13: Stress vs. Strain for Specimen 244-1-LC Corroded Strand Specimens

4.3.2.2.2 Specimen K5-1-LC Corroded Strands

Two corroded strands were selected from Specimen K5-1-LC for tension testing. Both strands were located at a longitudinal through-thickness crack in Segment B of Specimen K5-1-LC (Figure G.2). Strand 10_{cor} and Strand 11_{cor} are Strands 10 and 11 in Figure 3.54. Corrosion of each strand was localized to a length of approximately 8-12 in. and consisted of surface corrosion and minor pitting (Figure 4.14).

(a) Strand 10_{cor}

(b) Strand 11_{cor}

Figure 4.14: Specimen K5-1-LC Corroded Strands

Similar to the corroded strands from Specimen 244-1-LC, failure of each strand was characterized by a single-wire fracture at peak load (Figure 4.15). The breaking load, f_{pu}, ε_{pu}, and E_{ps} are reported in Table 4.8, and the stress-strain curves are provided in Figure 4.16. As shown, the corroded strands were able to resist at least 78% of the average uncorroded breaking load with essentially the same modulus of elasticity. Strand 11_{cor} did begin to yield but fractured well before the uncorroded average of ε_{pu}. In general, both strands exhibited a lack of ductility characteristic of corroded prestressing strands.

(a) Strand 10_{cor}

(b) Strand 11_{cor}

Figure 4.15: Specimen K5-1-LC Corroded Strands After Failure

Table 4.8: Specimen K5-1-LC Corroded Strand Test Results

Specimen ID (Strand Dia.)	**Strand Specimen**	**Breaking Load (lb)**	**Percent of full capacity**	**f_{pu} (ksi)**	**ε_{pu}**	**E_{ps} (ksi)**
K5-1-LC (3/8 in.)	Uncorroded Average	21,820	100%	272.8	0.056	27,770
	10_{cor}	16,990	78%	212.3	0.008	27,950
	11_{cor}	19,170	88%	239.6	0.014	26,400

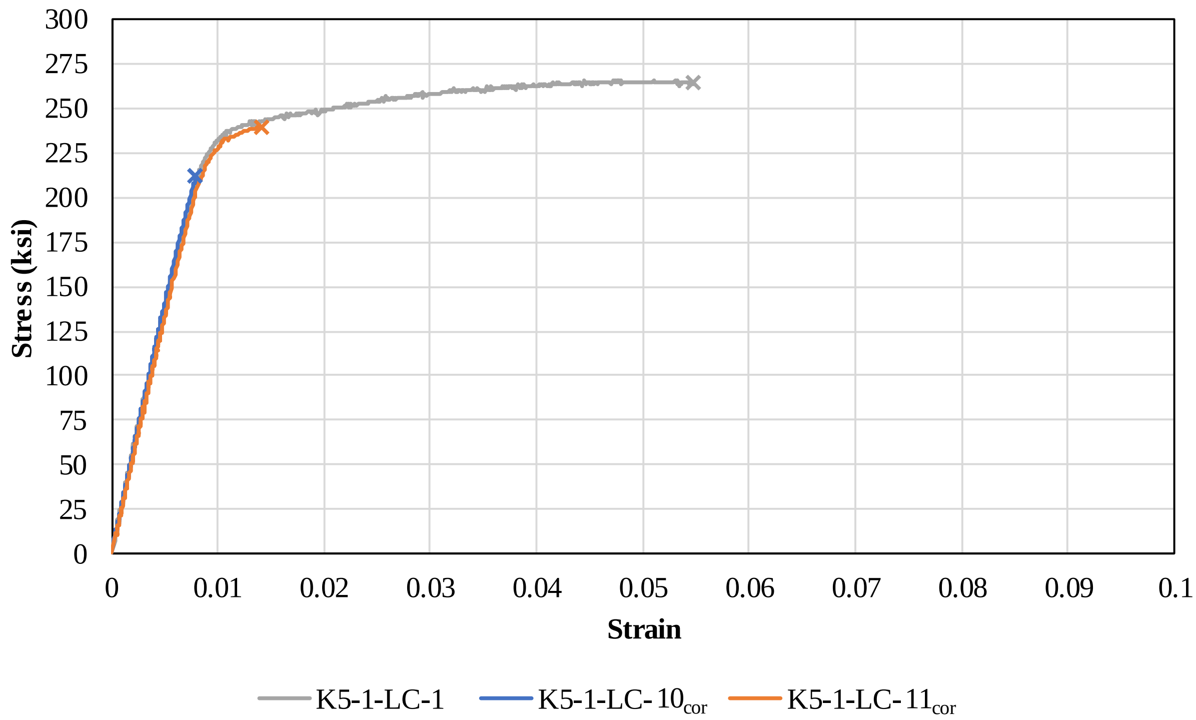

Figure 4.16: Stress vs. Strain for Specimen K5-1-LC Corroded Strand Specimens

4.3.2.2.3 Specimen 79-4-LC Corroded Strands

Four corroded strands were selected from Specimen 79-4-LC for testing. The strands were located in the end region with longitudinal cracks (Figure 3.63 and Figure G.3). Strands 1_{cor} through 4_{cor} are Strands 1 to 4 in Figure 3.63. Corrosion of each strand was limited to a localized area approximately 3 to 8 in. long and consisted of surface corrosion and minor pitting (Figure 4.17).

(a) Strand 1_{cor}

(b) Strand 2_{cor}

(c) Strand 3_{cor}

(d) Strand 4_{cor}

Figure 4.17: Specimen 79-4-LC Corroded Strand Specimens

The failure sections of each strand are shown in Figure 4.18. The test results of the four strands are summarized and compared to the average uncorroded strand results for Specimen 79-4-LC in Table 4.9, and the stress-strain curves are provided in Figure 4.19.

(a) Strand 1_{cor}

(b) Strand 2_{cor}

(c) Strand 3_{cor}

(d) Strand 4_{cor}

Figure 4.18: Specimen 79-4-LC Corroded Strand Specimens After Failure

Table 4.9: Specimen 79-4-LC Corroded Strand Test Results

Specimen ID (Strand Dia.)	Strand Specimen	Breaking Load (lb)	Percent of full capacity	f_{pu} (ksi)	ε_{pu}	E_{ps} (ksi)
79-4-LC (1/2 in.)	Uncorroded Average	42,230	100%	276.0	0.052	27,230
	1_{cor}	42,960	100%	280.8	0.019	28,910
	2_{cor}	37,720	89%	246.6	0.011	27,810
	3_{cor}	40,110	95%	262.2	0.018	27,770
	4_{cor}	39,510	94%	258.3	0.013	27,590

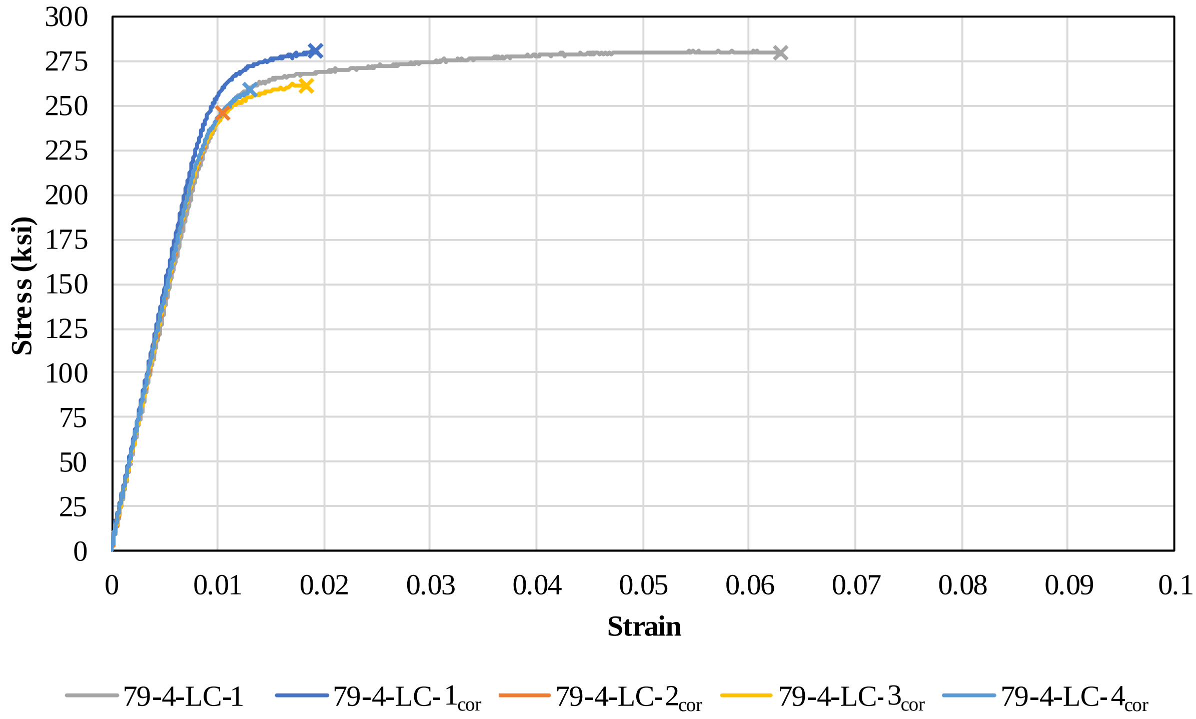

(a) Corroded strand stress-strain curves

Figure 4.19: Stress vs. Strain for Specimen 79-4-LC Corroded Strand Specimens

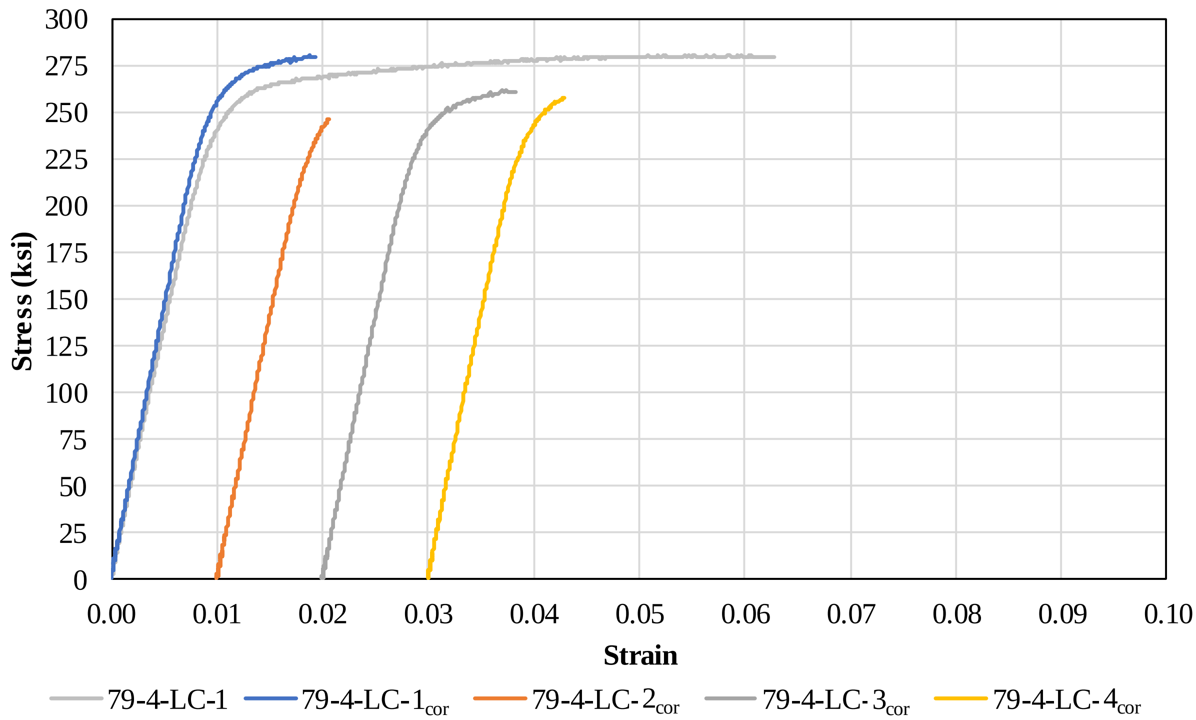

(b) Corroded strand stress-strain curve with 0.01 strain offset

Figure 4.19: Continued

All seven wires fractured at failure for Strand 1_{cor} (Figure 4.18(a)), and the breaking strength of Strand 1_{cor} was similar to the uncorroded strands. After yielding, the strand failed well short of the average value of ε_{pu} for uncorroded strand (Table 4.6 and Figure 4.19), providing further evidence of corrosion causing a decrease in ductility.

The failure of Strands 2_{cor} and 4_{cor} were characterized by single-wire fractures at failure (Figure 4.18(b) and (d)). Strand 2_{cor} and 4_{cor} resisted 89% and 94% of the average uncorroded breaking load but exhibited brittle behavior.

Two wires fractured at failure for Strand 3_{cor} (Figure 4.18(c)). As shown in Figure 4.19, yielding did occur and 95% of the breaking load was resisted, but fracture occurred very quickly after the onset of yielding with significantly reduced ductility.

4.3.2.2.4 Specimen 56-2-ES Corroded Strands

Strand 13_{cor} from Specimen 56-2-ES was cut from the exposed strand on the east side of the beam where extensive concrete spalling had occurred (Figure 3.11 and Figure G.4). Corrosion was relatively uniform along the exposed length of the strand and consisted of heavy pitting and minor section loss (Figure 4.20).

Figure 4.20: Strand 13_{cor} from Specimen 56-2-ES

The failure section of Strand 13_{cor} is presented in Figure 4.21. As shown, failure was characterized by three wires fracturing at failure. The test results for Strand 13_{cor} are reported in Table 4.10, and the stress-strain curve is provided in Figure 4.22. As shown, the strand exhibited brittle behavior and a reduced modulus of elasticity, but the corroded section was able to resist 77% of the average breaking load of the uncorroded strands. A reduction in modulus had not been observed until this specimen test indicating an additional impact of more severe strand corrosion.

Figure 4.21: Specimen 56-2-ES Strand 13_{cor} Failure

Table 4.10: Specimen 56-2-ES Corroded Strand Test Results

Specimen ID (Strand Dia.)	Strand Specimen	Breaking Load (lb)	Percent of full capacity	f_{pu} (ksi)	ε_{pu}	E_{ps} (ksi)
56-2-ES (1/2 in.)	Uncorroded Average	41,840	100%	273.4	0.055	27,320
	13_{cor}	32,180	77%	210.3	0.013	20,500

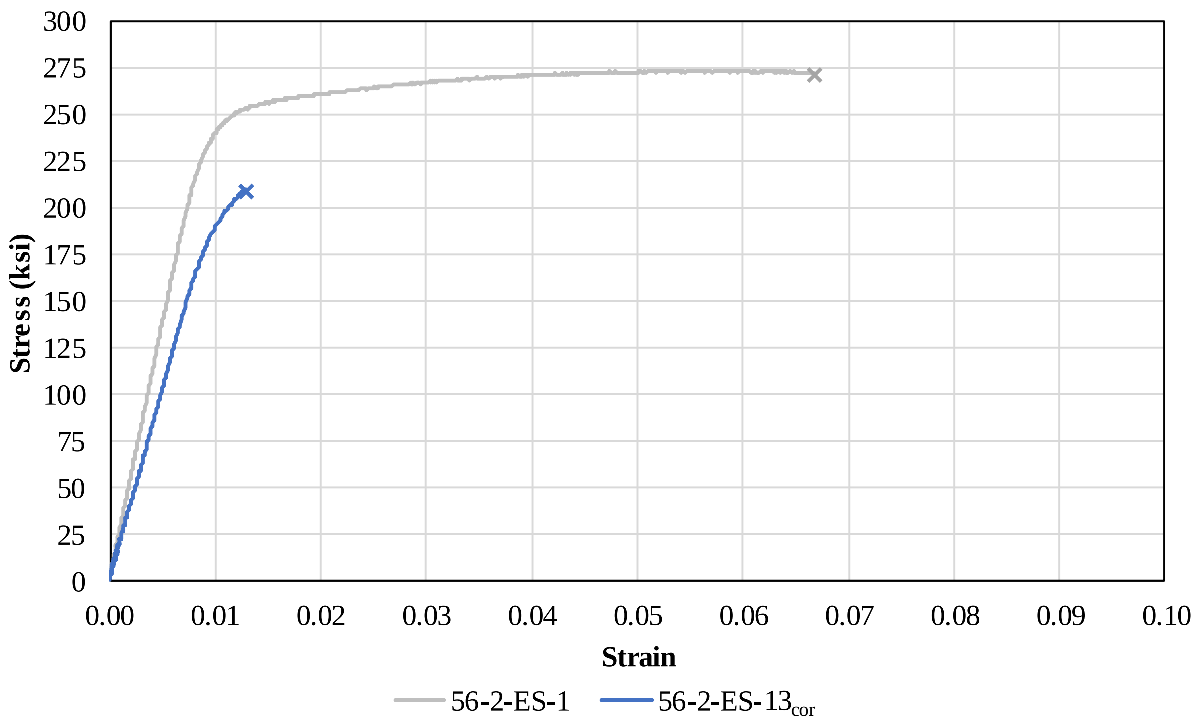

Figure 4.22: Stress vs. Strain Specimen 56-2-ES Corroded Strand Specimen

4.3.2.2.5 Specimen 102-3-BS Corroded Strands

A series of five corroded strand sections were selected from Specimen 102-3-BS for testing. All strands were taken from Segment A and B (Figure 3.14 and Figure G.5). The strands exhibited various levels of corrosion ranging from surface corrosion with minor pitting (a) to severe section loss and fractured wires (e). The strands were labeled Strand 1_{cor} to 5_{cor} based on the level of corrosion with Strand 1_{cor} having the lightest corrosion and Strand 5_{cor} having the heaviest corrosion (Figure 4.23). Table 4.11 provides the actual strands numbers corresponding to Strands 1_{cor} to 5_{cor}.

(a) Strand 1_{cor}

(b) Strand 2_{cor}

(c) Strand 3_{cor}

(d) Strand 4_{cor}

(e) Strand 5_{cor}

Figure 4.23: Specimen 102-3-BS Corroded Strand Specimens

Table 4.11: Strand Location Cross Reference

Corroded Strand Number	Actual Strand Number in Specimen 102-3-BS
Strand 1_{cor}	Strand 9 in Segment C
Strand 2_{cor}	Strand 9 in Segment D
Strand 3_{cor}	Strand 11 in Segment D
Strand 4_{cor}	Strand 2 in Segment C
Strand 5_{cor}	Strand 10 in Segment D

Strand 1_{cor} had surface corrosion with minor pitting along the length of the strand specimen (Figure 4.23(a)). Strand 2_{cor} had surface corrosion with localized pitting on three wires (Figure 4.23(b)). Strand 3_{cor} had minor surface corrosion with severe pitting of a single wire and no preexisting wire fractures (Figure 4.23(c)). Strand 4_{cor} was severely corroded with extensive pitting on four wires and no wire fractures prior to testing (Figure 4.23(d)). Strand 5_{cor} had severe section loss on six wires and three fractured wires before testing (Figure 4.23(e)). The wire fractures in Strand 5_{cor} occurred over a length of approximately 18 in. and could not be photographed all together.

The failure section of each strand is presented in Figure 4.24. The tests results are reported in Table 4.12, and the stress-strain curves are provided in Figure 4.25. Two wires fractured at failure of Strand 1_{cor} (Figure 4.24(a)). As shown in Figure 4.25, the strand failed as yielding was initiating. Strand 2_{cor} and Strand 3_{cor} exhibited three wire fractures at failure (Figure 4.24(b) and (c)). No yielding was observed in either strand before failure.

Failure of Strand 4_{cor} was characterized by four wires fracturing at peak load (Figure 4.24(d)). Initial loading of Strand 4_{cor} indicated the strand would exhibit a similar modulus of elasticity as the other corroded and uncorroded strands of Specimen 102-3-BS. At a stress (on the nominal cross-sectional area) of approximately 50 ksi, the stiffness of the strand softened slightly and continued at a constant but reduced stiffness to failure. The reduction in stiffness may have been caused by one of the wires fracturing before failure.

Strand 5_{cor}, which initially had three fractured wires, fractured an additional two wires at failure (Figure 4.25(e)). While 4 wires were intact, the remaining strength was only 20% of the uncorroded breaking load. Considering that 4 wires may theoretically carry 57% of the uncorroded breaking load, the low value of breaking strength indicates the effect of corrosion on the remaining strands. The stiffness of Strand 5_{cor} from initial loading to failure was constant and similar to the reduced stiffness observed in Strand 4_{cor} from 50 ksi to failure. Based on this similarity, the reduced stiffness in Strand 4_{cor} is believed to have been caused by wire fracture during the test. Overall, as the level of corrosion increased, a significant reduction in the tensile capacity of the strand occurred.

(a) Strand 1_{cor}

(b) Strand 2_{cor}

Figure 4.24: Specimen 102-3-BS Corroded Strand Specimens After Failure

(c) Strand 3cor

(d) Strand 4cor

(e) Strand 5cor

Figure 4.24: Continued

Table 4.12: Specimen 102-3-BS Corroded Strand Test Results

Specimen ID (Strand Dia.)	Strand Specimen	Breaking Load (lb)	Percent of full capacity	f_{pu} (ksi)	ε_{pu}	E_{ps} (ksi)
102-3-BS (1/2 in.)	Uncorroded Average	42,230	100%	276.0	0.052	27,230
	1_{cor}	36,900	85%	241.2	0.010	26,800
	2_{cor}	33,970	79%	222.0	0.008	27,630
	3_{cor}	32,760	76%	214.1	0.009	26,480
	4_{cor}	18,500	43%	120.9	0.008	14,360
	5_{cor}	8,780	20%	57.4	0.004	13,080

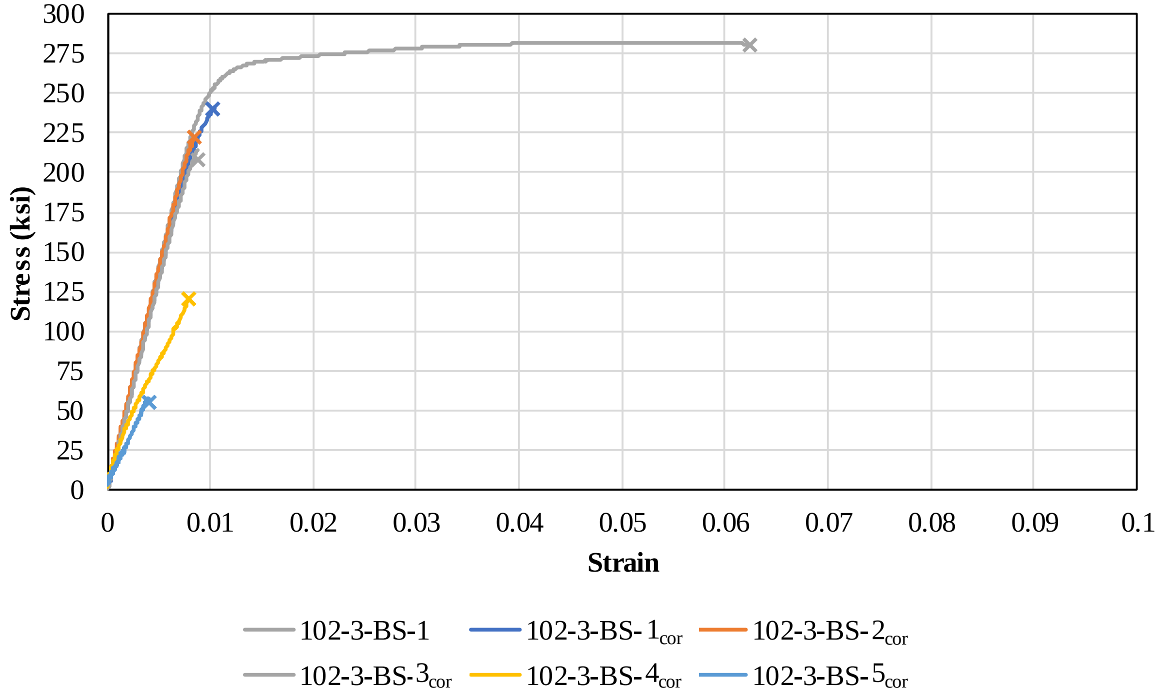

(a) Corroded strand stress-strain curves

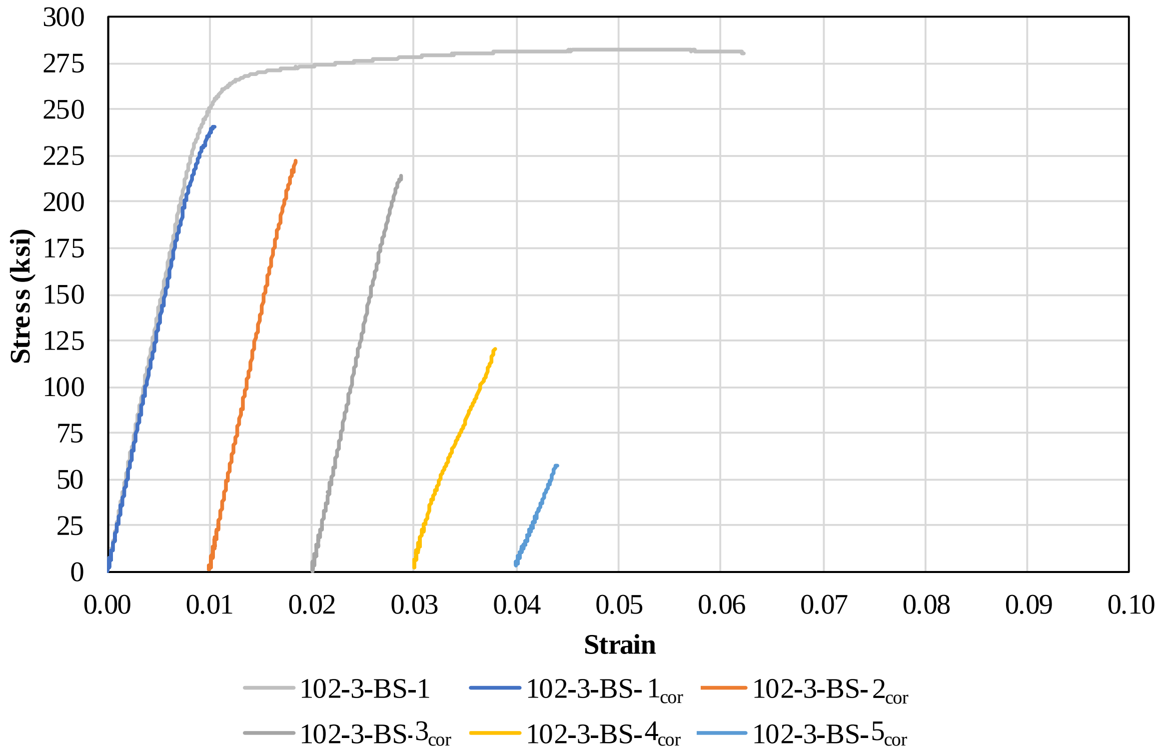

(b) Corroded strand stress-strain curves with 0.01 strain offset

Figure 4.25: Stress vs. Strain for Specimen 102-3-BS Corroded Strand Specimens

4.3.2.2.6 Findings

A summary of the test results is provided in Table 4.13. The strands from Specimens 244-1-LC, K5-1-LC, 79-4-LC and 102-3-BS (Strands 1_{cor} to 3_{cor}) exhibited light corrosion consisting primarily of surface corrosion and minor pitting and were located at longitudinal cracks (Strand 6_{cor} from Specimen 244-1-LC was located at a stained longitudinal crack). These strands were observed to resist over 75% of the average breaking load of the uncorroded strands tested for the same beam specimen. These strands, however, exhibited brittle behavior. Little to no yielding occurred before wire fracture occurred. The strain at fracture was, on average, 0.011.

Strand 13_{cor} of Specimen 56-2-ES was an exposed strand with minor section loss and observed to resist 77% of the average breaking load of the uncorroded strands tested. The strands from Specimen 102-3-BS (Strands 4_{cor} and 5_{cor}) were heavily corroded with significant section loss. Strand 4_{cor} was an exposed strand, and Strand 5_{cor} was located at a longitudinal crack near the edge with rust stains. Both strands were not able to resist more than 50% of the average breaking load of the uncorroded strands.

In general, the corroded strands tested were observed to have residual capacity but did not have any appreciable ductility. Based on the observed behavior, the following recommendations are provided:

1. Assume that strands exhibit no ductility where corrosion is observed and limit strain to 0.01.
2. If surface corrosion and minor pitting are observed, consider 75% of the strand strength and limit the strain to $0.75f_{pu}/E_{ps}$.
3. If severe corrosion or fractured wires are observed, consider 0% of the strand strength.

Table 4.13: Corroded Strand Test Results

Specimen ID (Strand Dia.)	Strand Specimen	Breaking Load (lb)	Percent of full capacity	f_{pu} (ksi)	ε_{pu}	E_{ps} (ksi)
244-1-LC (3/8 in.)	5_{cor}	18,290	83%	228.7	0.012	26,450
	6_{cor}	17,050	78%	213.1	0.009	27,030
K5-1-LC (3/8 in.)	10_{cor}	19,170	88%	239.6	0.014	26,400
	11_{cor}	16,990	78%	212.3	0.008	27,950
79-4-LC (1/2 in.)	1_{cor}	42,960	100%	280.8	0.019	28,910
	2_{cor}	37,720	89%	246.6	0.011	27,810
	3_{cor}	40,110	95%	262.2	0.018	27,770
	4_{cor}	39,510	94%	258.3	0.013	27,590
56-2-ES (1/2 in.)	13_{cor}	32,180	77%	210.3	0.013	20,500
102-3-BS (1/2 in.)	1_{cor}	36,900	85%	241.2	0.010	26,800
	2_{cor}	33,970	79%	222.0	0.008	27,630
	3_{cor}	32,760	76%	214.1	0.009	26,480
	4_{cor}	18,500	43%	120.9	0.008	14,360
	5_{cor}	8,780	20%	57.4	0.004	13,080

4.4 Structural Test Setup

The box beam specimens acquired from the field were designed and constructed as simply supported members. Each beam specimen was tested in four-point bending with simple supports to simulate in-service loading (Figure 4.26(a)). The location of the load points was determined to maximize the applied shear and moment. Load was applied at approximately one third of the span from each support. All beams were tested on bearings without skew. Therefore, the beams that were built with skew were tested on slightly shorter spans. The skew and resulting test span are provided in Table 4.14. The values of L_{cmr} and L_v are also presented in Table 4.14 discussed in the following section.

Table 4.14: Specimen Test Span Dimensions

<table>
<tr><th>Specimen ID</th><th>Source Bridge Beam No.</th><th>Beam Length</th><th>Skew</th><th>Test Span</th><th>L_{cmr}</th><th>L_v</th></tr>
<tr><td>244-1-LC</td><td>6</td><td>44 ft-1 in.</td><td>45°</td><td>39 ft-6 in.</td><td>14 ft</td><td>12 ft-9 in.</td></tr>
<tr><td>409-1-ES</td><td>B9</td><td rowspan="2">50 ft-6 in.</td><td rowspan="2">20°</td><td rowspan="2">47 ft-6 in.</td><td rowspan="2">16 ft</td><td rowspan="2">15 ft-9 in.</td></tr>
<tr><td>409-2-UD</td><td>B8</td></tr>
<tr><td>K5-1-LC</td><td>1</td><td rowspan="2">35 ft-10 in.</td><td rowspan="2">0°</td><td rowspan="2">35 ft</td><td rowspan="2">12 ft</td><td rowspan="2">11 ft-6 in.</td></tr>
<tr><td>K5-2-LC</td><td>7</td></tr>
<tr><td>79-1-UD</td><td>B2</td><td>35 ft-10 in.</td><td rowspan="4">25°</td><td>33 ft-2 in.</td><td>12 ft</td><td>10 ft-7 in.</td></tr>
<tr><td>79-2-UD</td><td>A6</td><td rowspan="3">28 ft-4 in.</td><td rowspan="3">25 ft-7 in.</td><td rowspan="3">8 ft</td><td rowspan="3">8 ft-9.5 in.</td></tr>
<tr><td>79-3-UD</td><td>A1</td></tr>
<tr><td>79-4-LC</td><td>A7</td></tr>
<tr><td>56-1-LC</td><td>A6</td><td>27 ft-8 in.</td><td rowspan="2">0°</td><td>26 ft-5 in.</td><td>8 ft</td><td>9 ft-2.5 in.</td></tr>
<tr><td>56-2-ES</td><td>B1</td><td>35 ft-10in.</td><td>35 ft</td><td>12 ft</td><td>11 ft-6 in.</td></tr>
<tr><td>102-1-BS</td><td>C7</td><td rowspan="4">34 ft-10 in.</td><td rowspan="4">23°</td><td rowspan="4">32 ft-4 in.</td><td rowspan="4">10 ft</td><td rowspan="4">11 ft-2 in.</td></tr>
<tr><td>102-2-BS</td><td>C5</td></tr>
<tr><td>102-3-BS</td><td>B8</td></tr>
<tr><td>102-4-BS</td><td>B7</td></tr>
</table>

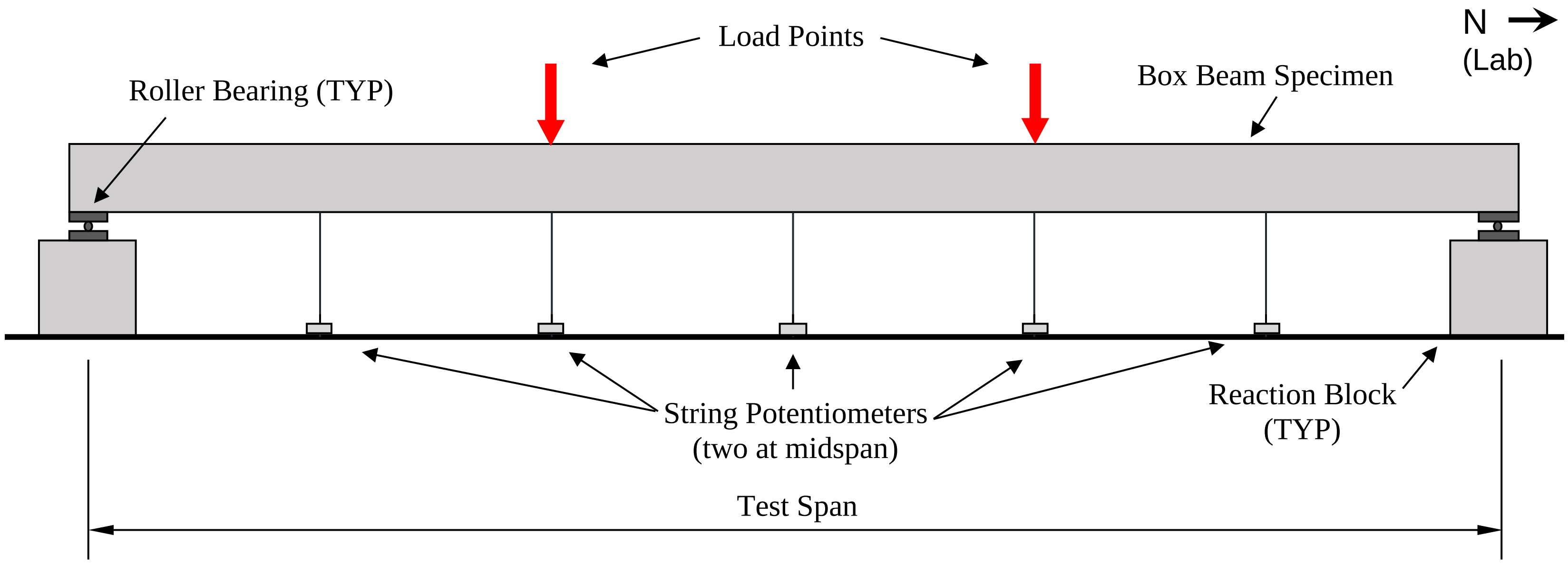

(a) Test setup elevation

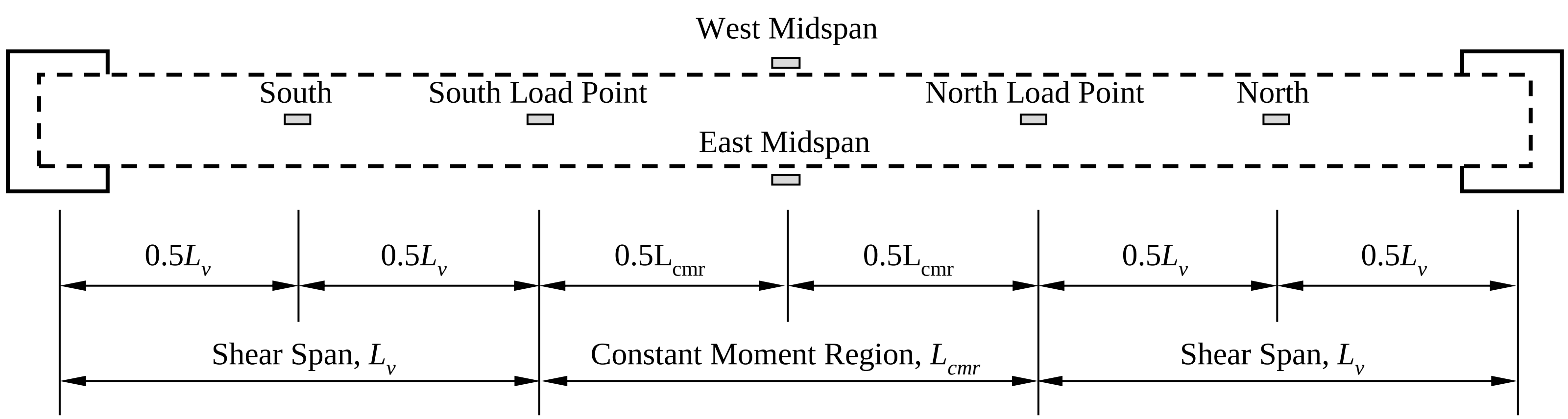

(b) Instrumentation Plan

Figure 4.26: Test Setup

4.4.1 Test Frames and Instrumentation

The strong floor at the Bowen Laboratory has load frame anchor points on a 2 ft grid. Therefore, the length of the constant moment region was constrained to multiples of 2 ft. The length of the constant moment region L_{cmr} and the resulting distance from the support to the load point L_v are provided in Table 4.14. and shown in Figure 4.26(b).

A photo of the test setup is provided in Figure 4.27, and a schematic representation of the load frames used to apply load on either end of the constant moment region is shown in Figure 4.28. Each steel frame consisted of two columns and a crosshead. Two C12x30 channels back to back were used for the columns so that a W14x132 crosshead could fit between the columns and bear on steel bearing blocks (Figure 4.29). The columns were post-tensioned to the strong floor with 1-1/4in. DYWIDAG Bars to anchor the test frame. Load was applied at each load point with a 100-kip hydraulic jack with a stroke of 12 in., and force was measured using 150-kip load cells with an accuracy of ±0.1 kip. The jacks were equipped with spherical bearings to accommodate rotation of the beam during the test (Figure 4.30). Pressure was applied to the jacks using a 10,000 psi pneumatic hydraulic oil pump and was monitored using a 10,000 psi pressure transducer.

The roller bearings at either end of the test span consisted of a 2 in. diameter steel bar sandwiched between two 9.5 in. wide by 2 in. thick steel plates (Figure 4.31(a)). Bolts were used to hold the bearings in place while each beam specimen was placed (Figure 4.31(b)). The bolts were removed from the bearings at the beginning of each test. The bearing assembly was 60 in. wide to allow the widest beam specimen to bear on the full width of the beam. The concrete reaction blocks were approximately 2 ft long, 5 ft wide, and 2 ft tall.

Figure 4.27: Photo of the Test Setup

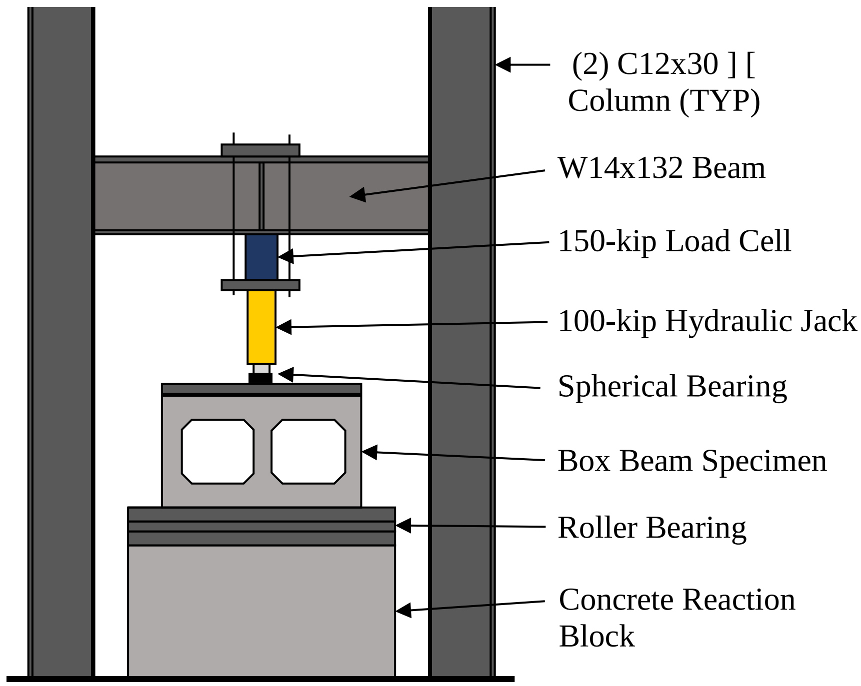

Figure 4.28: Typical Test Frame Schematic

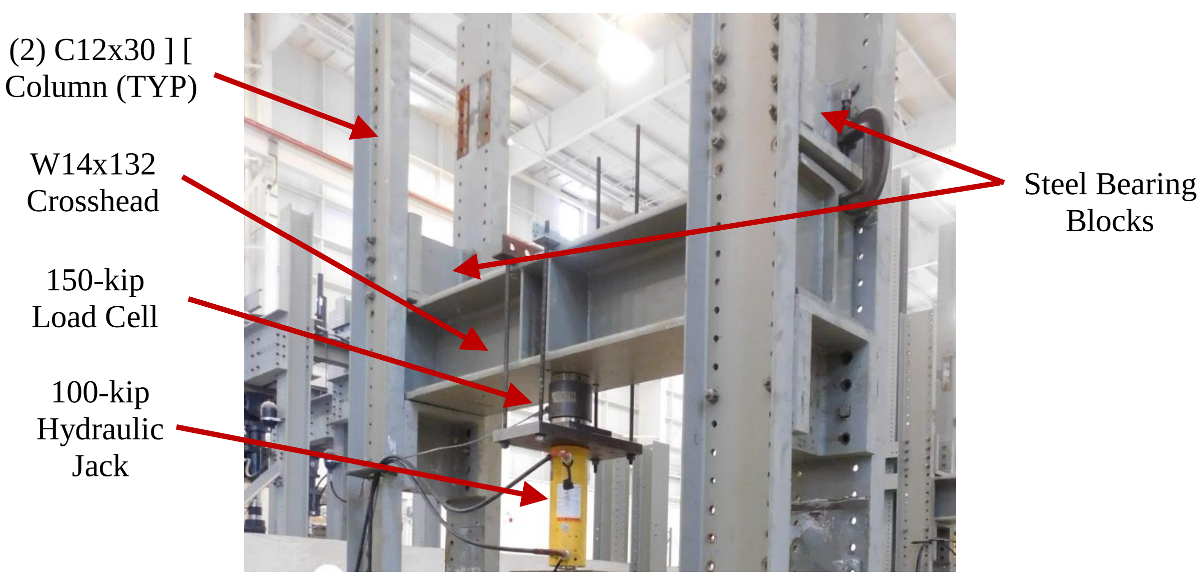

Figure 4.29: Typical Test Frame Crosshead Assembly

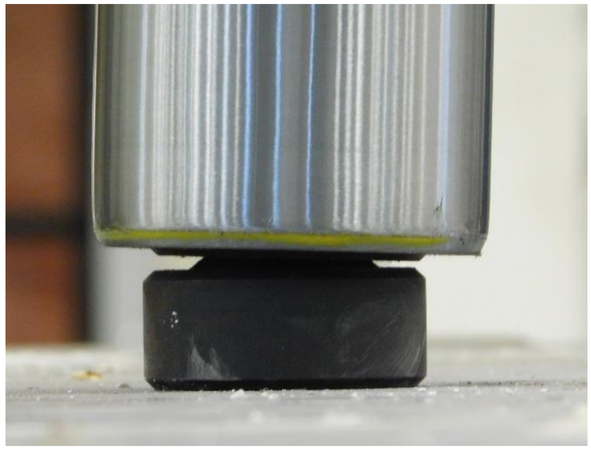

Figure 4.30: Typical Spherical Bearing

(a) Bearing without bolts (test) **(b) Bearing with bolts (setup)**

Figure 4.31: Typical Steel Roller Bearing

Deflection was measured at five points along the test span to determine the deflected shape of each beam specimen (Figure 4.26). Deflection was measured using linear string potentiometers (string pots) with an accuracy of ±0.01 in. As shown in Figure 4.26(b), the deflection at midspan was measured using two string pots, one on each side of the beam, to provide redundancy and determine any torsional rotation.

The string pots were attached to the beam using steel brackets and concrete screws (Figure 4.32). Wooden cribbing was placed around each string pot to protect the sensor from spalling concrete and collapse of the beam specimen at failure (Figure 4.33).

Figure 4.32: String Pot Attachment

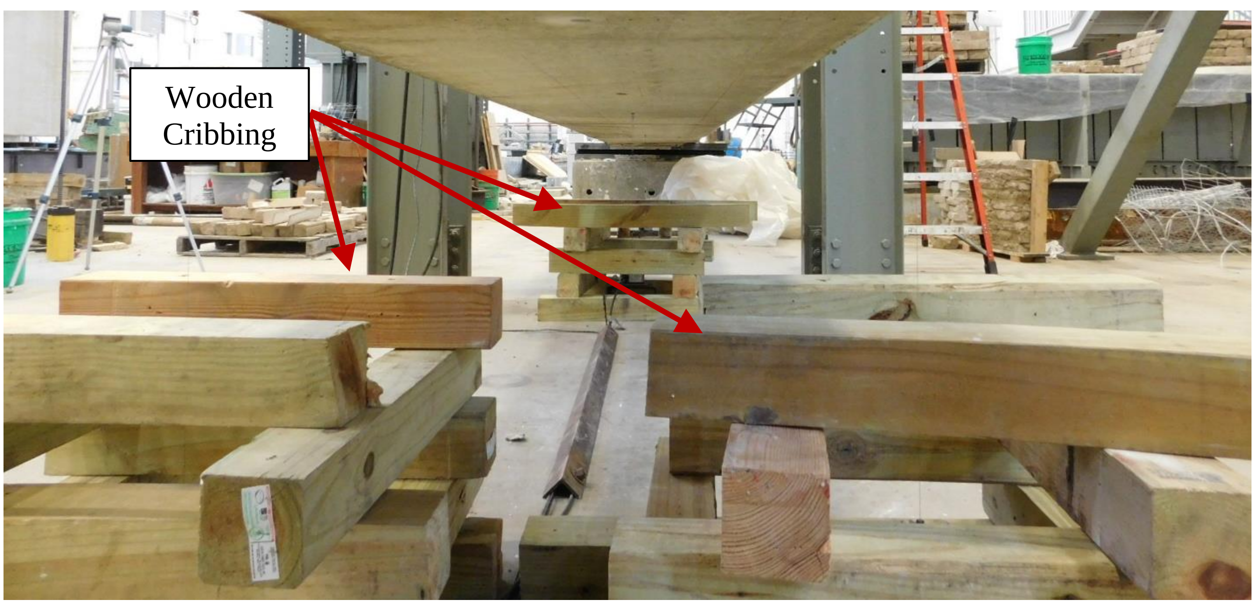

Figure 4.33: String Pot Protection

4.4.2 Loading Procedure

In general, load was applied in three phases. Up to first cracking, load was applied in 5-kip increments. After first cracking was observed, load was applied based on the midspan deflection measurement. Loading was paused at 1/2-in. increments of midspan deflection until a plateau was observed in the load vs. midspan deflection plot. After the load plateaued, loading was paused at 1-in. increments of midspan deflection until the beam specimen collapsed or the test was considered completed and terminated.

At each load step, loading was paused, the specimen was inspected, and photos were taken of any notable distress. After first cracking, cracks were marked on one side of the specimen with black felt-tipped markers at each load step. Cracks were marked until the growth of cracks could no longer be observed, or structural failure was imminent.

The measured force was observed to decrease at each load step during the inspection of the specimens. Decreases in measured force observed in between load steps was commonly due to the formation of new flexural cracks. Special note is made where decreases in force are due to other structural distress or changes in the loading procedure. The decrease in measured force was also caused by a combination of concrete creep and loss of pressure in the hydraulic jacks. The loss of pressure was caused by imperfections in the hydraulic valves that held pressure constant while the hydraulic oil pump was not running. Decreases in measured force are noticed in the experimental load-deflection curves, especially after the cracking moment is exceeded. In some cases, a long period was needed to inspect the specimen between load steps, and the decrease in force was observed to be as large as 4 kips.

A GoPro Hero Black 5 was used to record the failure of each specimen. In many cases, the failure video was able capture information that could not be recorded by still photographs. The video footage was often used to verify the failure mechanism of the beam specimen.

4.5 Experimental Testing

The structural test of each beam specimen was conducted over the course of one working day. For each specimen, a description of the test is provided with the experimental load-deflection curve and photos of the specimen at key points during testing. The flexural crack maps of each beam are provided in Appendix H. In addition, a schematic beam in four-point bending is shown to illustrate the location and type of failure. The type of failure has been abbreviated as CC for concrete crushing, SF for strand fracture, WC for web crushing, and TC for test concluded due to deflection limitations.

4.5.1 Specimen 244-1-LC

As shown in Figure 2.9, Specimen 244-1-LC arrived at the lab with a hole in the top flange at midspan. The loss of section in the compression flange has an obvious effect on the structural capacity of the section. Through the course of this research project, it was observed that top flange deterioration has been repaired using commercial grade concrete available at local hardware stores. Therefore, the opportunity was taken to determine the effectiveness of these types of in-service repairs.

4.5.1.1 Top Flange Repair

To replicate a repair procedure observed in the field, the concrete surrounding the hole was chipped away using a hammer and chisel until removal of concrete became difficult. Existing steel reinforcement exposed by the chipping operation was observed to be corroded. All corrosion product was removed with a wire brush, and after cleaning the reinforcement was observed to have very little section loss. Therefore, no additional steel was added to the repair. Formwork was then installed in the void to prevent concrete from filling the void (Figure 4.34 and Figure 4.35). The formwork and concrete were thoroughly cleaned with a wire brush and vacuum prior placing the patch. The patch concrete consisted of Commercial Grade Quikrete 5000 with an estimated 28-day strength of 5000 psi. The concrete was mixed and placed according the manufacturer’s directions. Formwork was removed following 3-days of wet-curing with burlap covered by a plastic sheet. After formwork was removed, no additional curing time was used to simulate the in-service repair. Figure 4.36 shows the patch after formwork was removed.

Figure 4.34: West Formwork for Specimen 244-1-LC Flange Repair

Figure 4.35: East Formwork for Specimen 244-1-LC Flange Repair

Figure 4.36: Specimen 244-1-LC Patch After Removal of Formwork

Six 4 in. by 8 in. concrete cylinders were prepared in accordance with ASTM C192 (2016) and tested in compression at 28-days and 47-days according to ASTM C39 (2018). Before testing, the ends of each cylinder were ground smooth and parallel using a Marui Co., LTD. Hi-Kenma cylinder end grinder. The compression test results are reported in Table 4.15. The average 28-day strength fell short of the minimum specified strength of 5000 psi. Therefore, curing time was increased by approximately 2-1/2 weeks to allow the concrete to gain strength before conducting the structural test. After 47-days of curing, the cylinder strength exceeded 5000 psi. With the minimum strength achieved, the structural test could begin.

Table 4.15: Specimen 244-1-LC Concrete Patch Compression Test Results

Time (day)	Compressive Strength				Fracture Pattern (ASTM C39)		
	Cylinders			Average	Cylinders		
	1	2	3		1	2	3
28-day	4470	4060	4720	**4420**	6	6	3
47-day	5260	5250	5270	**5260**	3	3	3

4.5.1.2 Structural Test

Specimen 244-1-LC had two longitudinal cracks before the beam was tested. A detailed deterioration map is provided in Figure 3.1. Prior to testing, no flexural cracks were observed along the length of the beam.

At an applied force of 35 kips, a change in stiffness was indicated by the load-deflection curve, and flexural cracking was observed (Figure 4.37). Loading continued after first cracking without any signs of distress in the longitudinal cracks. While crack mapping during the load pause at 3.5 in. of midspan deflection, the first signs of concrete crushing were noticed in the repaired top flange (Figure 4.38). Loading continued, and at an applied force of 49.4 kips (3.7 in of midspan deflection), the top flange concrete crushed. Upon removal of the specimen from the test setup, the specimen was cut in half, and all strands were found intact without any wire fractures.

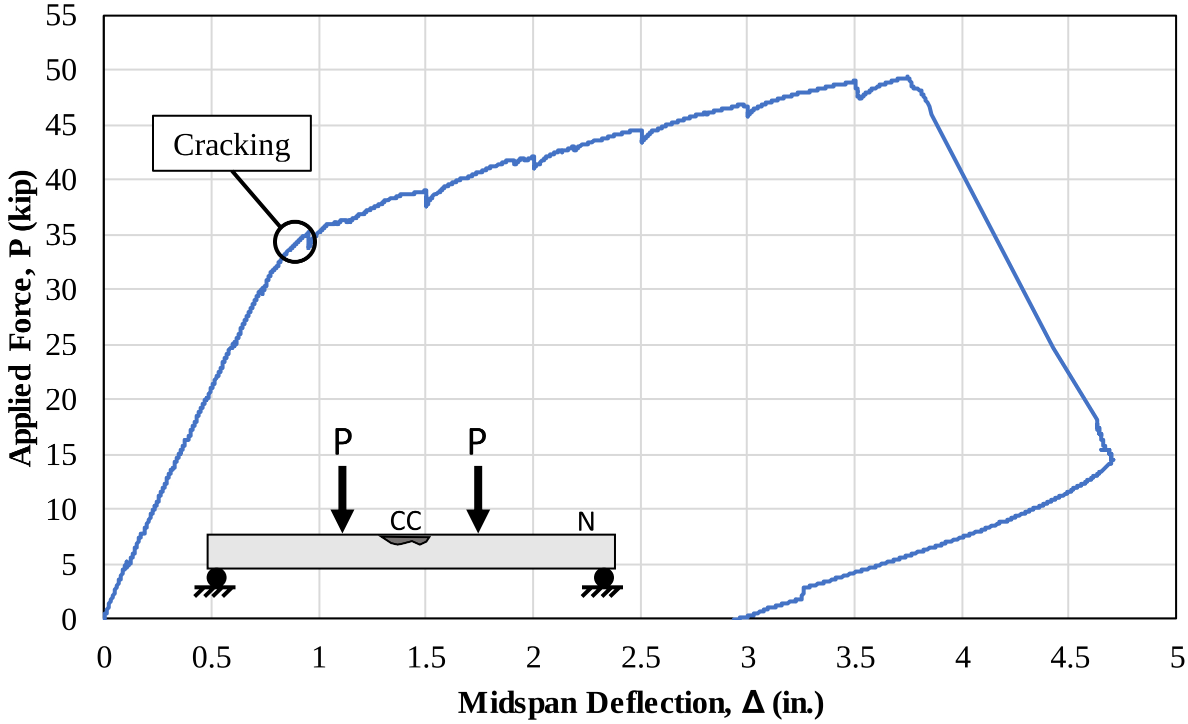

Figure 4.37: Specimen 244-1-LC Experimental Load vs. Deflection

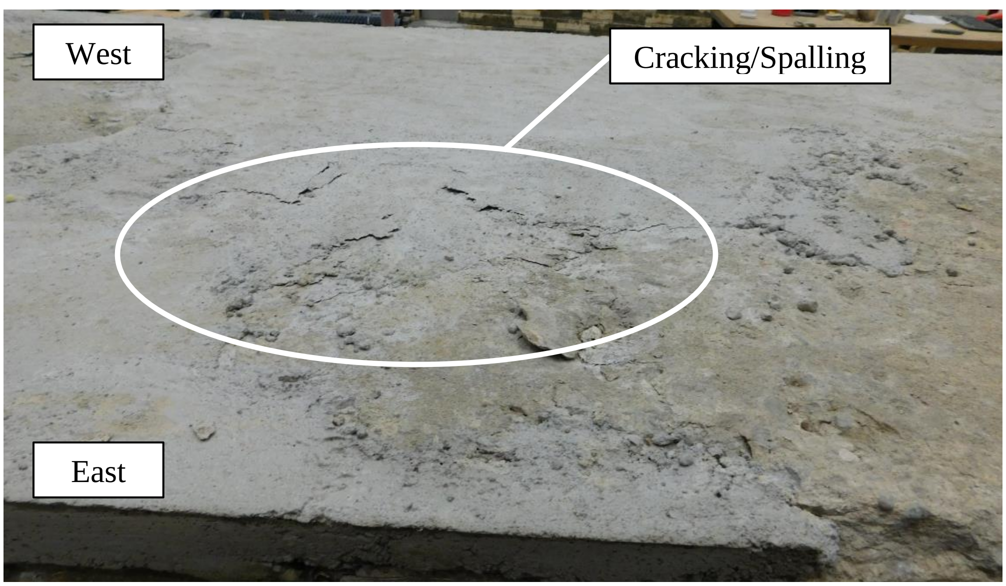

Figure 4.38: First Signs of Concrete Crushing

Investigation of the failure region revealed that concrete crushing extended throughout the width of the top flange. On the west side, where the repair was made, crushed concrete was observed both in the repair and in the existing concrete (Figure 4.39). On the east side, where a shallow spall had been repaired, crushing was observed to extend into the exterior web of the beam (Figure 4.40(a)) and through the entire thickness of the existing flange (Figure 4.40(b)). Cores taken from the top flange after failure indicated that the concrete in the top flange was delaminated (Figure 4.41).

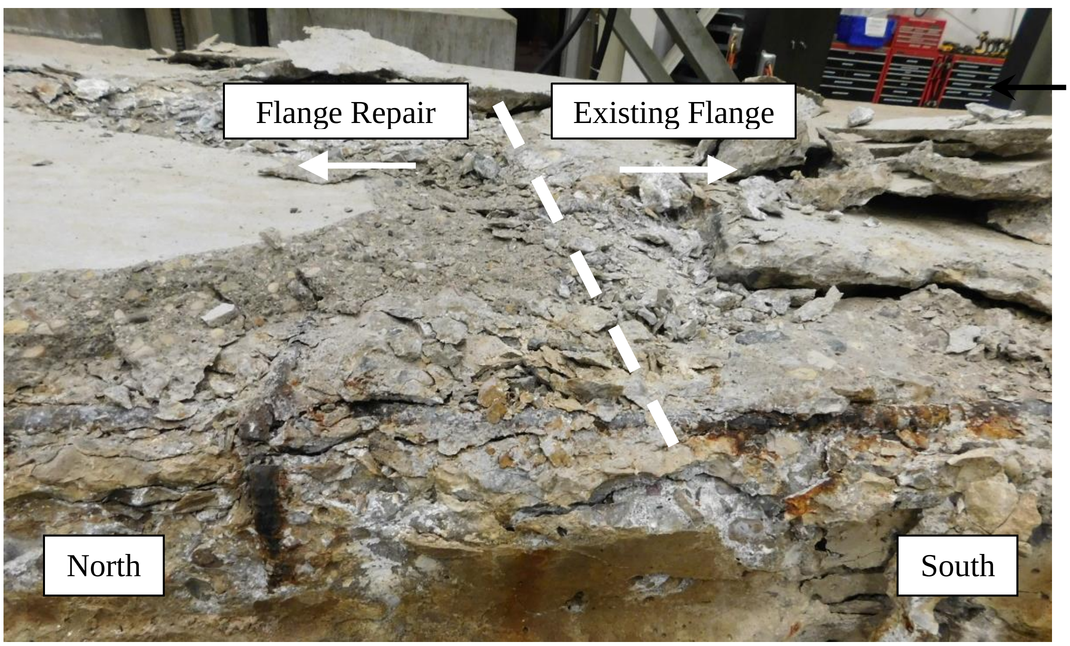

Figure 4.39: Extent of Crushing on West Side of Top Flange

(a) Before concrete spalls removed

(b) After concrete spalls removed

Figure 4.40: Extent of Crushing on East Side of Top Flange

Figure 4.41: Concrete Cores from Specimen 244-1-LC Top Flange

In addition to the extensive crushing, bar buckling was observed on the west side and middle of the failure region (Figure 4.42). The observation was also made that a corroded stirrup fractured on the west side of the beam (Figure 4.43). The stirrup was partially exposed during the repair process and observed with heavy pitting due to corrosion. Small flakes of corrosion product were removed from the stirrup while cleaning with a wire brush. No additional protection measures were taken prior to casting the patch.

The condition of the concrete that crushed around the flange repair was very poor. The extent of deteriorated concrete was not fully removed by a hammer and chisel. A more destructive method would have been required to remove the deteriorated concrete to ensure that sound concrete had been reached before casting a new top flange. However, the process used in this test is consistent with that typically conducted in the field by contractors.

(a) West side of failure region near west edge

(b) West side of failure region near middle

(c) Middle of failure region

Figure 4.42: Bar Buckling

Figure 4.43: Fractured Stirrup

4.5.2 Specimen 409-1-ES

The deterioration of Specimen 409-1-ES consisted of a single concrete spall located 8 ft from the north end of the beam (Figure 3.2) and 7 ft 4 in. from the north test support. The specimen was constructed with a 2-1/2 in. thick concrete topping (Figure D.2). Prior to testing, flexural cracking was observed in the constant moment region (Figure 4.44).

At an applied force of 20 kips, the stiffness of the beam reduced, and the existing cracks were observed to extend, but no new cracks were observed. This load is considered the zero tension point where a stress of 0 occurs at the bottom flange. New cracks were observed at a load of 30 kips, but no change in stiffness was observed. At an applied force of 34.5 kips, a change in stiffness was observed, and many new cracks were observed. Based on the change in stiffness observed in the load-deflection curve (Figure 4.45), the cracking moment was assumed to have been reached at an applied force of 34.5 kips.

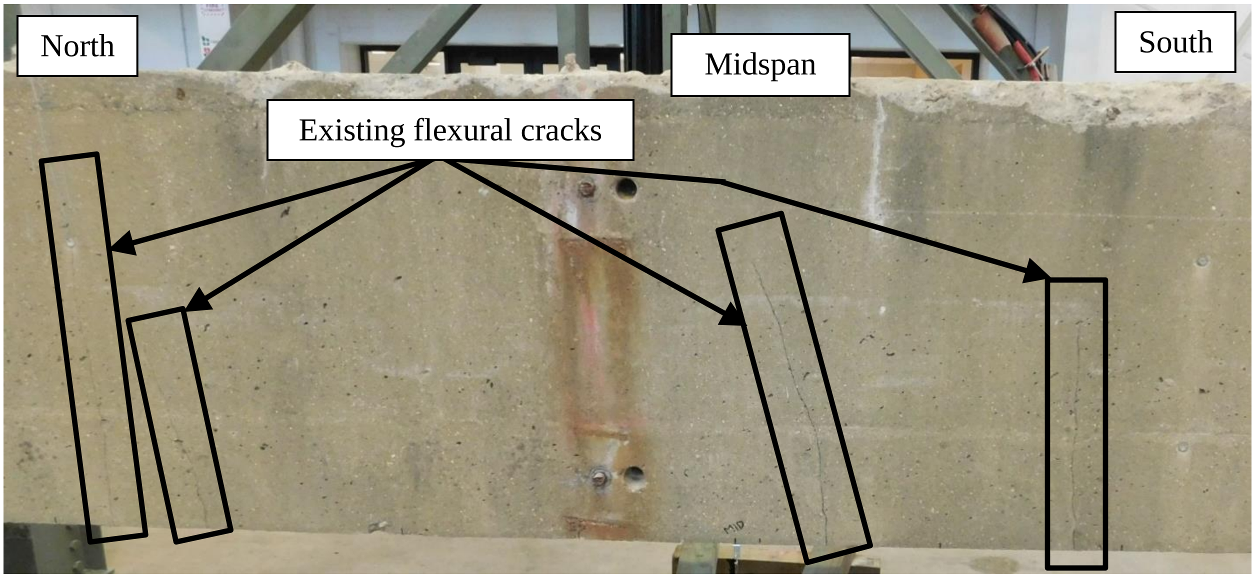

Figure 4.44: Existing Flexural Cracking

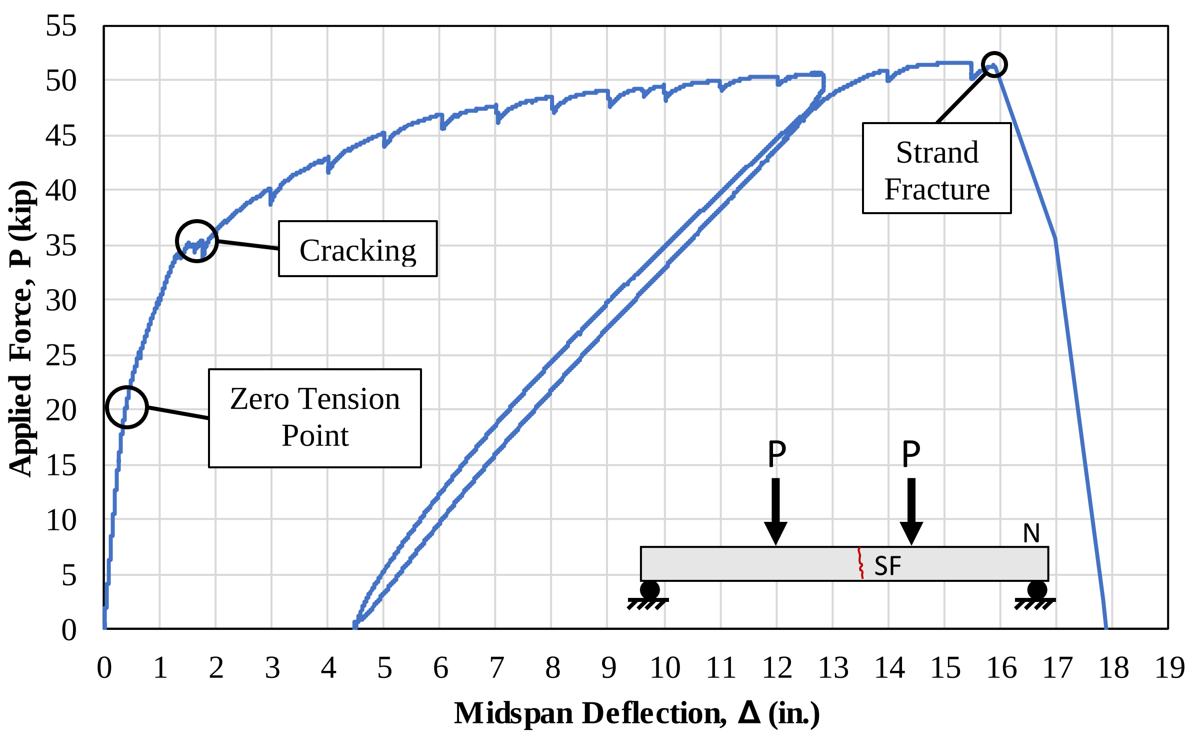

Figure 4.45: Specimen 409-1-ES Experimental Load vs. Deflection

After cracking, loading continued until the stroke limit of the hydraulic jacks was reached at a midspan deflection of 12.85 in (Figure 4.46). The specimen was then completely unloaded, and steel shim-plates were placed between the load plate and the hydraulic jack. The beam was then reloaded to the previous midspan deflection, and the loading procedure was continued. At a load of 51.6 kips, the specimen deflected without an increase in load to a midspan deflection of 15.9 in. At this deflection, a pop was heard, a moment passed, then a louder pop was heard that was followed immediately by collapse of the specimen (Figure 4.47).

Figure 4.46: Specimen 409-1-LC at 12.85 in. of Midspan Deflection

Figure 4.47: Collapse of Specimen 409-1-ES

As shown in Figure 4.47, no concrete crushing was observed in the top flange indicating that failure was controlled by strand fracture. In addition, no slip between the topping slab and top of beam was observed throughout the test. The lack of slip indicates that the topping slab acted compositely with the beam throughout the test.

Visual inspection of the strands revealed that some very light surface rust was present on the strands at the fracture location (Figure 4.48). In addition, the failure section corresponded to one of the existing cracks shown in Figure 4.44. Considering the reduction in ductility observed in the corroded strand tension tests, the cause of failure for Specimen 409-1-ES is likely related to a reduction in the ultimate tensile strain capacity of the strand.

Figure 4.48: Light Surface Rust on Strands

The deterioration located 8 ft from the north support remained unchanged throughout the test. No additional cracking in or around the spall was observed after testing. Considering the location of the spall, the moment demand at the deteriorated section was less than 50% of the demand in the constant moment region. The combination of reduced demand and localized deterioration was considered to have prevented this deterioration from affecting the structural capacity of the beam.

4.5.3 Specimen 409-2-UD

The only deterioration observed in Specimen 409-2-UD was water staining on the west edge from a leaking shear key (Figure 3.3). The specimen was constructed with a 2-1/2 in. thick concrete topping slab (Figure D.3). Existing flexural cracks were also observed and marked before testing began (Figure 4.49).

At an applied force of 18 kip, the stiffness of the beam changed slightly (Figure 4.50) indicating the zero tension load. Although new cracks developed at the zero tension load, the cracking moment corresponded to an applied force of 33 kips based on the significant change in stiffness observed in the load-deflection curve in Figure 4.50.

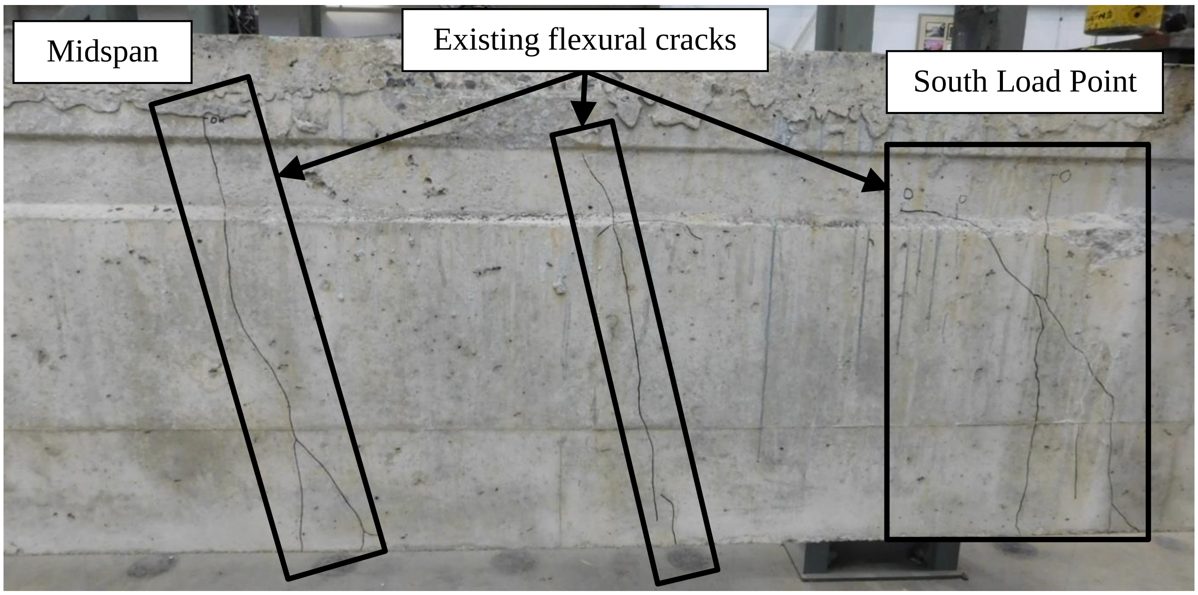

Figure 4.49: Existing Flexural Cracks in Constant Moment Region

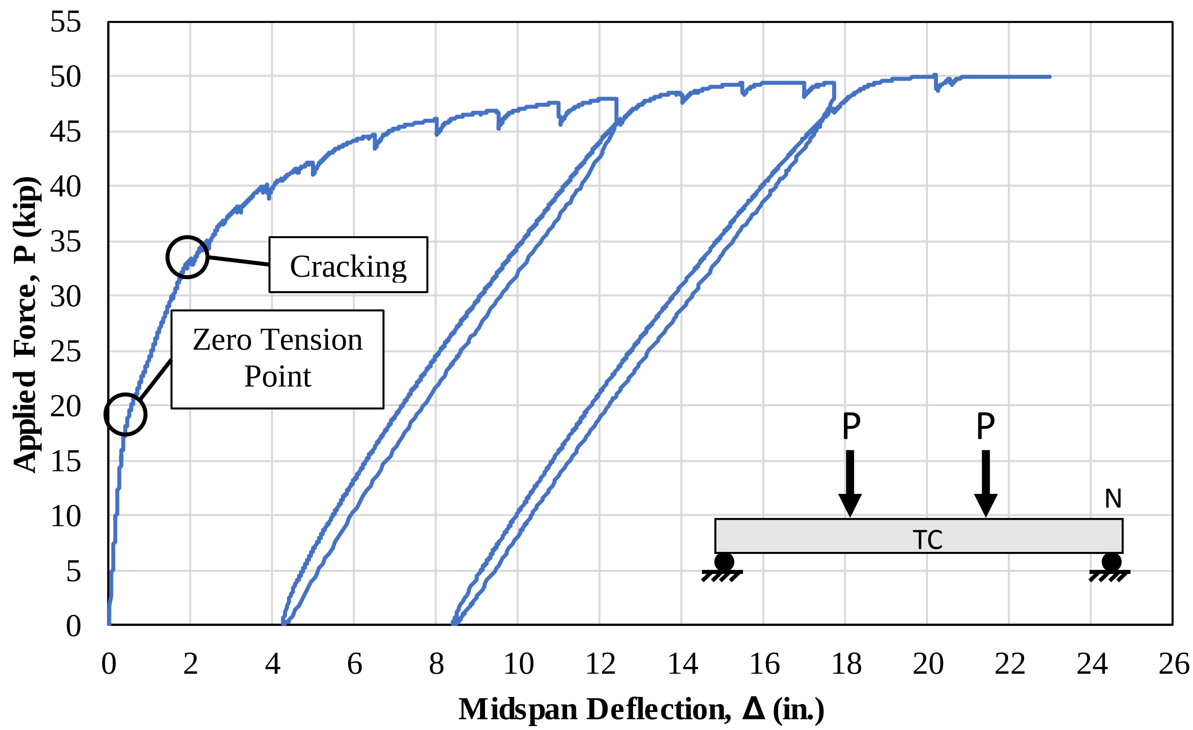

Figure 4.50: Specimen 409-2-UD Experimental Load vs. Deflection

After the cracking moment was exceeded, small decreases in measured force were observed with the formation of new flexural cracks. Flexural cracks continued to form throughout the test until the midspan deflection reached 11 in.

The stroke limit of the hydraulic jacks was reached at a midspan deflection of 12.4 in. and again at 17.7 in. Each time the stroke limit was reached, the beam was completely unloaded, and steel shim-plates were added to continue loading. At 21.1 in. of midspan deflection, the midspan string potentiometers were removed to prevent damage to the sensors. Loading continued using a ruler to record the midspan deflection. At approximately 23 in. of midspan deflection and an applied force of 50.3 kip, the test was discontinued as the limits of the test setup had been reached (Figure 4.51 and Figure 4.52). Although no concrete crushing or strand fracture was observed, the notable plateau in the load-deflection curve indicates that the ultimate capacity of the beam was reached.

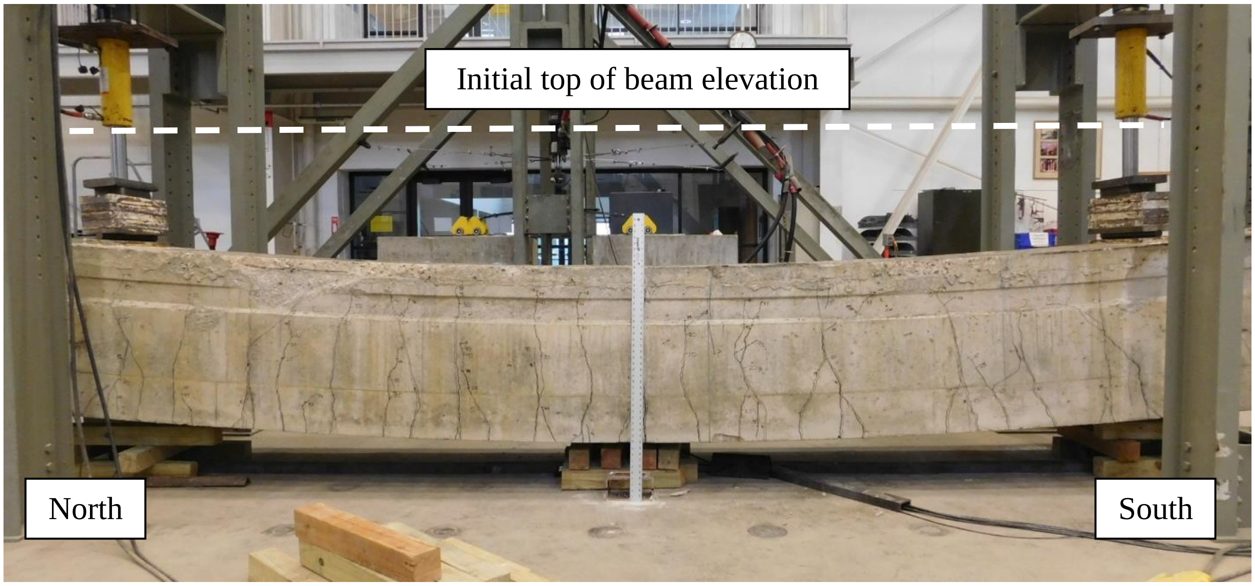

Figure 4.51: Constant Moment Region at End of Test

Figure 4.52: Specimen 409-2-UD at 23 in. of Midspan Deflection

Throughout the test, no distress was observed in the concrete top flange. In addition, no slip was observed between the topping slab and top of beam. The lack of slip between the slab and beam throughout the test indicates that composite action was maintained up to the ultimate capacity of the beam.

4.5.4 Specimen K5-1-LC

The deterioration of Specimen K5-1-LC consisted of two longitudinal cracks (Figure 3.4). The specimen was also constructed with a curb (Figure D.4). Prior to testing, no flexural cracks were observed in the specimen.

At an applied force of 35 kips, the stiffness of the beam changed slightly (Figure 4.53), but no flexural cracks were visible. As loading continued, the stiffness significantly changed at an applied force 39 kip. Based on the change in stiffness observed in the load-deflection curve, the cracking moment was considered to correspond to an applied force of 39 kip (Figure 4.53).

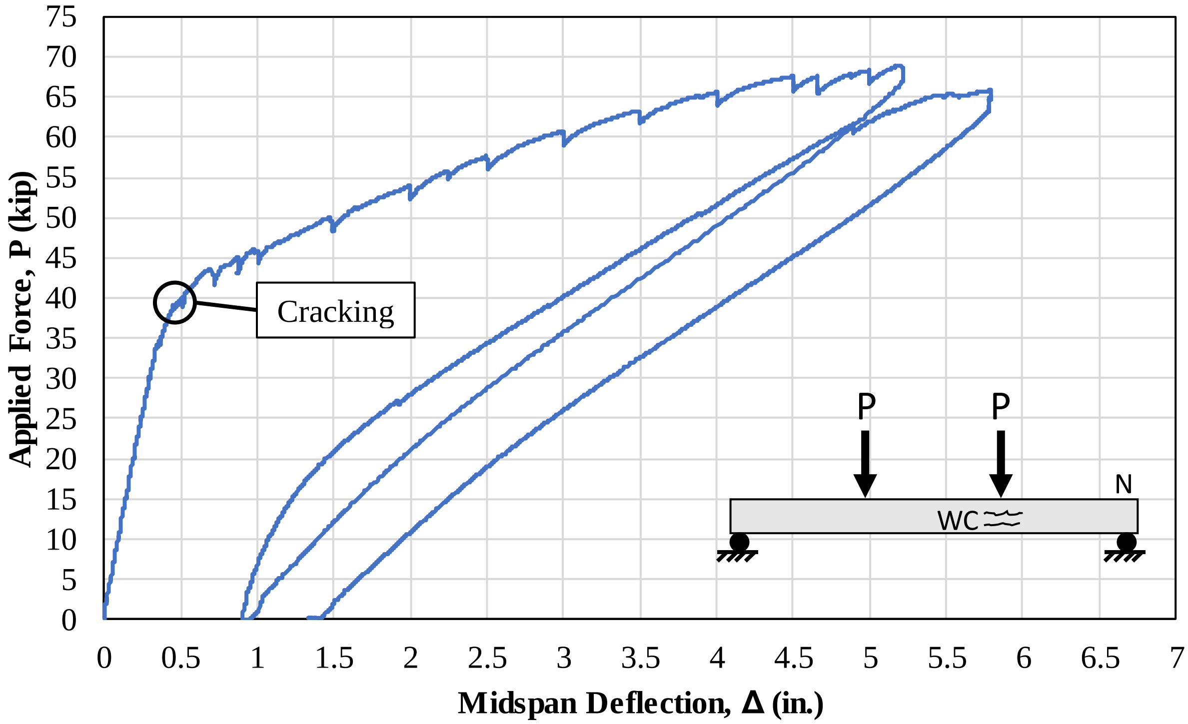

Figure 4.53: Specimen K5-1-LC Experimental Load vs. Deflection

After cracks became visible, the loading procedure was continued until cracking was heard from the north load point at an applied load of 67.5 kip and a midspan deflection of 4.6 in. Loading was paused, and crushing was observed in the top of the curb approximately 1 ft from the north load point within the constant moment region (Figure 4.54). The loading procedure was resumed until the rotation limit of the spherical bearing on the north hydraulic jack was reached (68.9 kips applied load, 5.22 in. midspan deflection). The specimen was completely unloaded, and the bearing plate was tilted using USG Hydro-Stone® to accommodate further rotation. When the specimen was reloaded, cracking in the top flange was observed indicating that the load plate was punching through the top flange (Figure 4.55). The test was discontinued, and the beam was cut apart at the north load point to determine the source of punching.

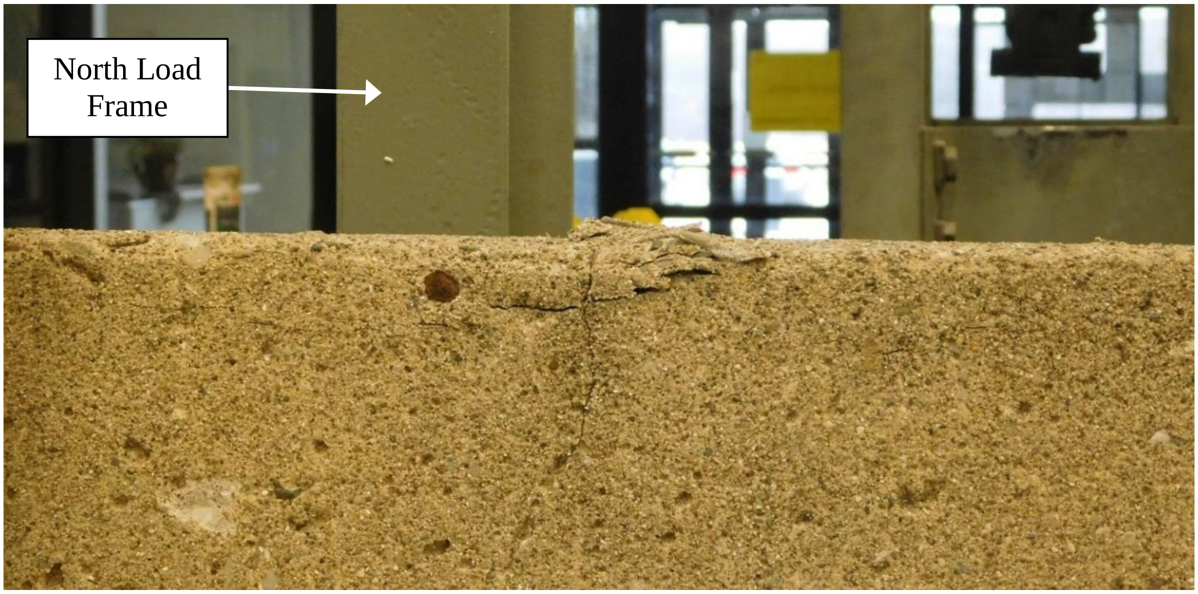

Figure 4.54: Initiation of Concrete Crushing at Top of Curb

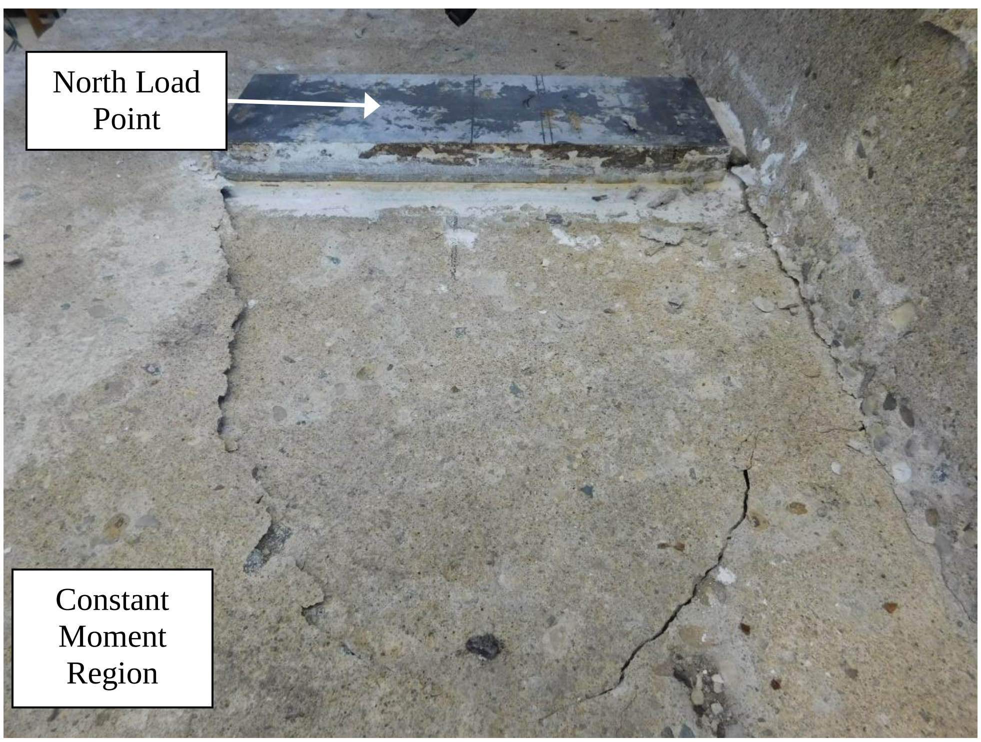

Figure 4.55: Top Flange Cracking

Once the beam was cut apart, the middle web was observed to be crushed for a length of approximately 18 in. (Figure 4.56). In addition, the middle web thickness was measured to be 1 in. For comparison, the standard drawings for Specimen K5-1-LC indicate that the middle web thickness should have been 3.5 in. (Figure D.4(b)). The steel bearing plates used between the hydraulic jacks and the beam were 18 in. wide, 6 in. long and 1 in. thick (plate width oriented across beam width as shown in Figure 4.55). The size of the plate clearly influenced the punching shear failure. If the plate had been wider, the applied force could have been spread to the outer webs. To avoid web crushing in future tests, the size of the bearing plate was increased to 48 in. wide, 12 in. long, and 2 in. thick.

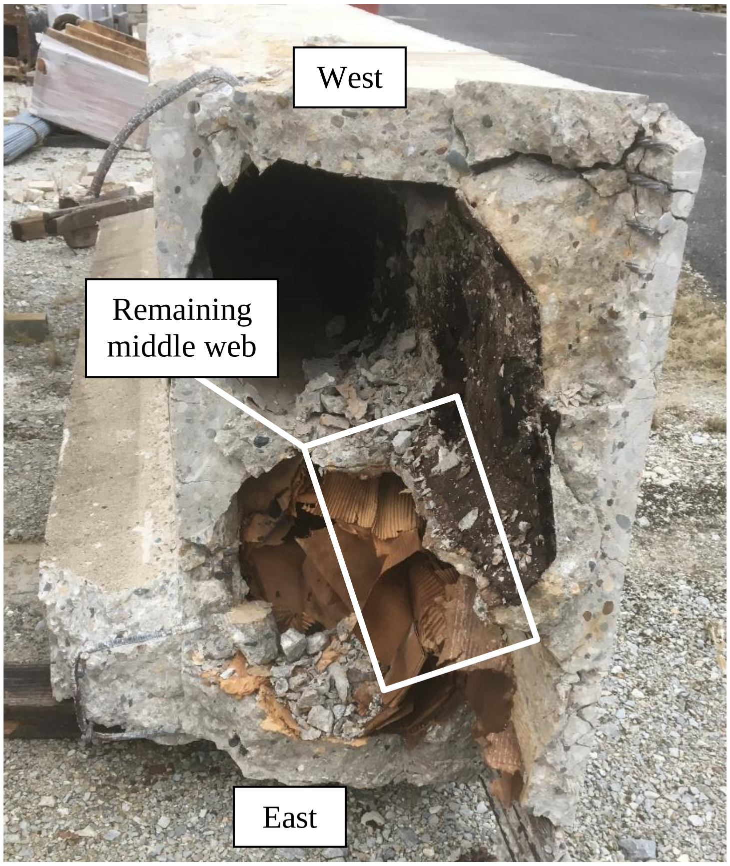

Figure 4.56: Middle Web Crushing

The longitudinal cracks in the bottom flange were investigated after the test was concluded, and similar to Specimen 244-1-LC, further distress of the longitudinal cracks was not observed in Specimen K5-1-LC. In addition, when the beam was cut apart, no fractured strands were found. Failure of the beam was controlled by the crushing of the middle web, which is an unlikely failure mode for realistic load cases. Due to the construction error in the web-width, localized punching failure could have occurred in this bridge for a large concentrated load. Considering the loading required, however, this is unlikely and obviously had not occurred in service.

4.5.5 Specimen K5-2-LC

Deterioration of Specimen K5-2-LC consisted of three longitudinal cracks on the bottom flange and scaling on the top flange (Figure 3.5). Prior to testing, no flexural cracks were observed in the beam.

At an applied force of 30 kips, flexural cracks became visible on the south end of the constant moment region at the location of the longitudinal cracks. A change in stiffness, however, was not observed until an applied force of 35 kips (Figure 4.57). Considering the change in stiffness at 35 kips, the cracking moment was considered to correspond to an applied force of 35 kips.

After the cracking moment was exceeded, cracking and popping were heard throughout the loading periods and during the load pauses. Each noise was associated with a small decrease in measured force. The load procedure was continued up to an applied load of 49.3 kips and a midspan deflection of 3.5 in., when two loud pops were heard. The loud pops were accompanied by a drop in measured force of 4.2 kips, and therefore assumed to correspond to strands fracturing. At the loading pause after the decrease in load, a flexural crack on the east side of the specimen was observed to have increased in width to approximately 1/4 in. (Figure 4.58).

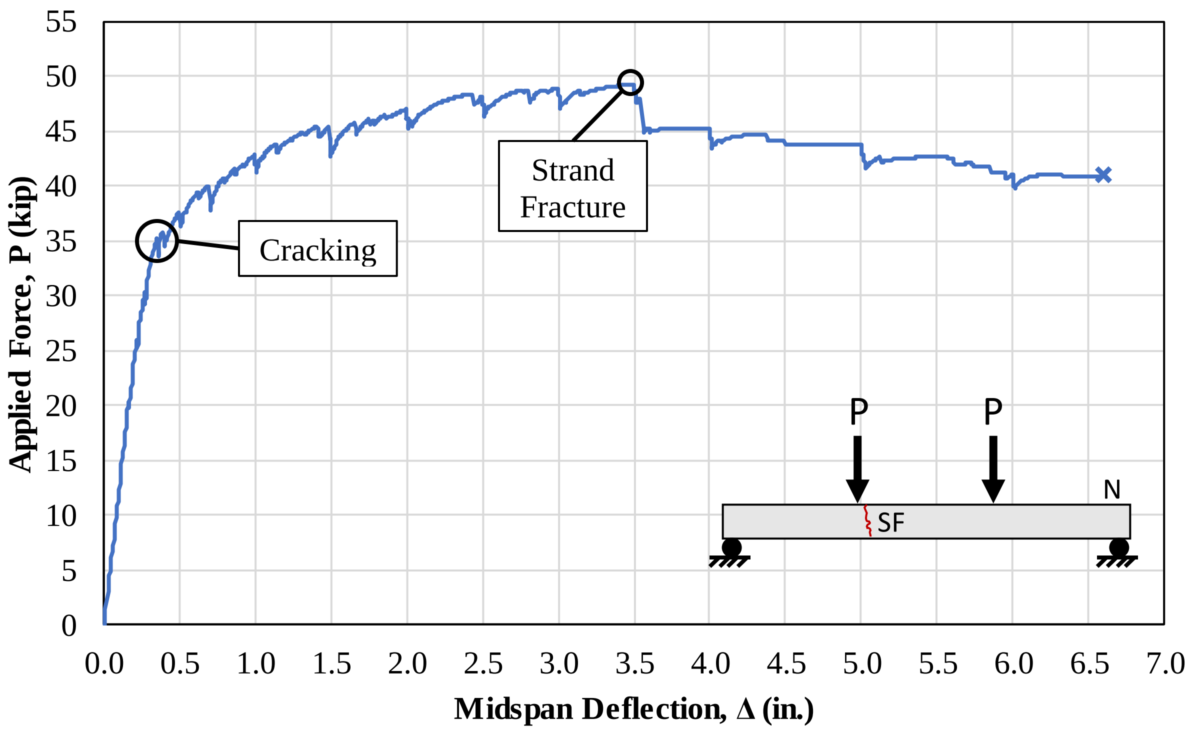

Figure 4.57: Specimen K5-2-LC Experimental Load vs. Deflection

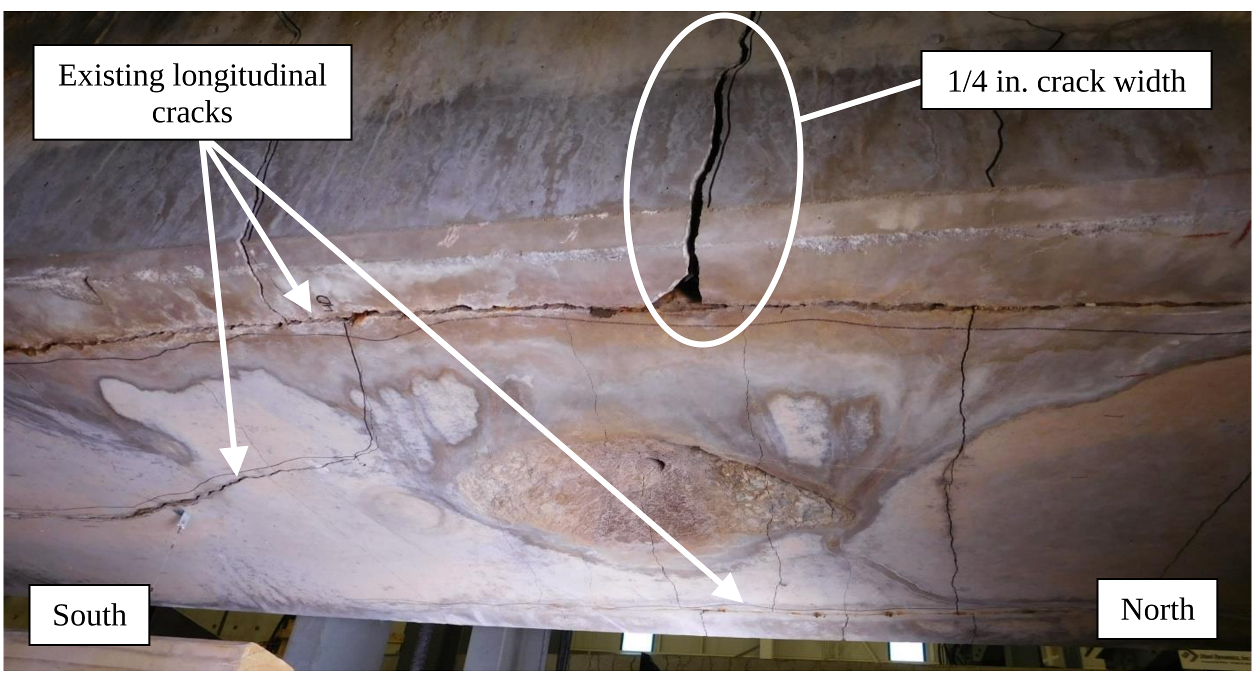

Figure 4.58: Flexural Crack at Existing Deterioration

Loading continued and loud pops were heard again at midspan deflections of 4.0 in. (45.0 kip) and 5.0 in. (43.9 kip). Each pop was accompanied by a drop in measured force of 1 to 2 kips. As loading continued, flexural cracks in the deteriorated region continued to increase in width. At 5.6 in. of midspan deflection (42.5 kip), concrete spalling was observed in the top flange approximately 3 ft from the south load point into the constant moment region. After a load pause at 6.0 in. of midspan deflection, loading continued to a midspan deflection of 6.6 in. when a very loud pop was heard that was immediately followed by total collapse of the beam (Figure 4.59).

The failure section corresponded to the location of the large flexural crack on the west side of the specimen observed after the first two loud pops (Figure 4.60). As shown, the crack exposed the corroded strand at the west longitudinal crack in the bottom flange. On the east side of the beam, the failure region exposed the strand crossed by the east longitudinal crack (Figure 4.61). In addition, minor concrete crushing was observed in the top flange (Figure 4.62) which was evident after failure of the strands.

The east and west longitudinal cracks caused corrosion of two strands at the plane of failure. The loss of these strands created a weak section where deformation was concentrated and drove fracture of additional strands. No further distress of the middle longitudinal crack was observed during the post-failure investigation of the beam. The structural repair of the top flange (Figure D.6) was not in good condition at the end of the test but did not suffer extensive damage until collapse of the beam. Concrete cores taken from the patch after testing revealed significant cracking parallel to the top surface of the beam (Figure 4.1). This indicates that delaminated concrete was present but did not control the failure mode.

Figure 4.59: Failure of Specimen K5-2-LC

Figure 4.60: Large Flexural Crack on West Side After Failure

Figure 4.61: East Side of Failure Section

Figure 4.62: Concrete Crushing in Top Flange

4.5.6 Specimen 79-1-UD

Specimen 79-1-UD was observed with no signs of deterioration (Figure 3.6). Before the start of the test, the specimen was inspected, and no existing flexural cracks were observed.

The first flexural crack became visible at an applied load of 25 kips, but only one crack was observed throughout the length of the beam. At an applied load of 29 kips, multiple cracks became visible and cracking was heard throughout the specimen. Considering the change in stiffness after the load was reached, the cracking moment was considered to correspond to an applied force of 25 kips (Figure 4.63).

After the cracking moment was reached, the loading procedure continued to an applied force of 46.3 kip and a midspan deflection of 11.6 in. At this deflection, the stroke limit of the hydraulic jacks was reached, and the specimen was unloaded to add concrete shim blocks between the bearing plate and beam specimen to extend the stroke of the jacks (Figure 4.64). The loading procedure was resumed, and at a midspan deflection of 13.3 in. (47.4 kips) the rotation limit of the spherical bearing on the north load point was reached. The specimen was unloaded, and the bearing plate was tilted to accommodate more rotation.

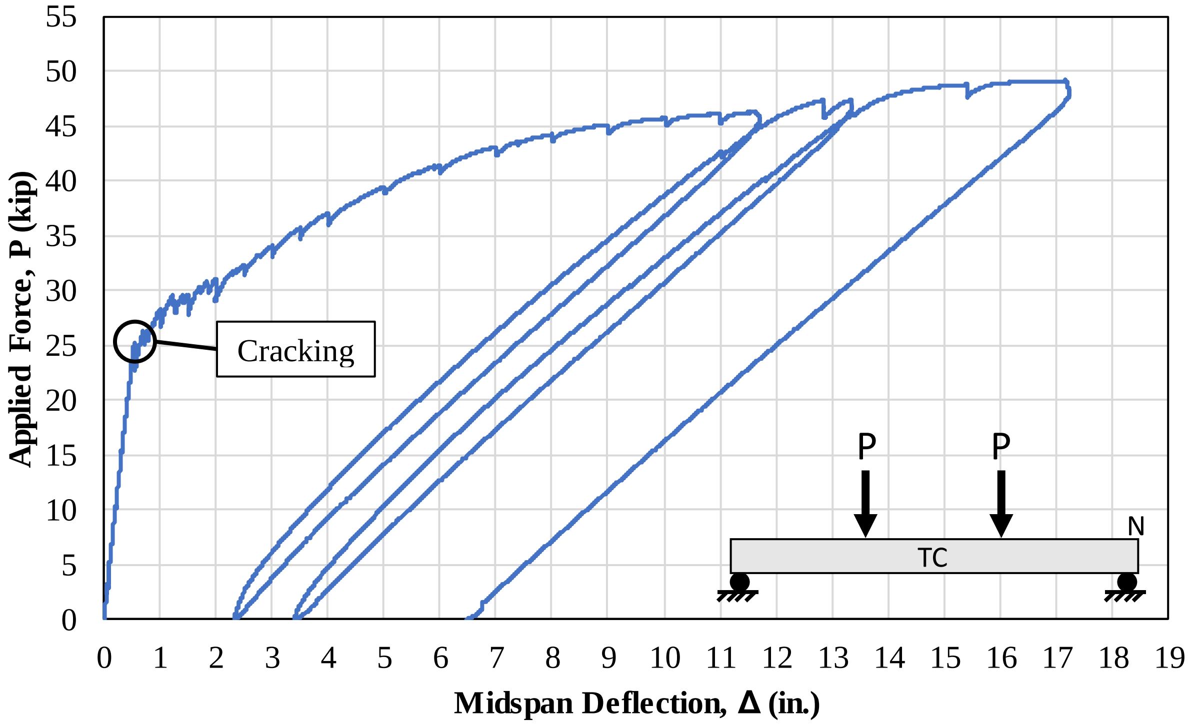

Figure 4.63: Specimen 79-1-UD Experimental Load vs. Deflection

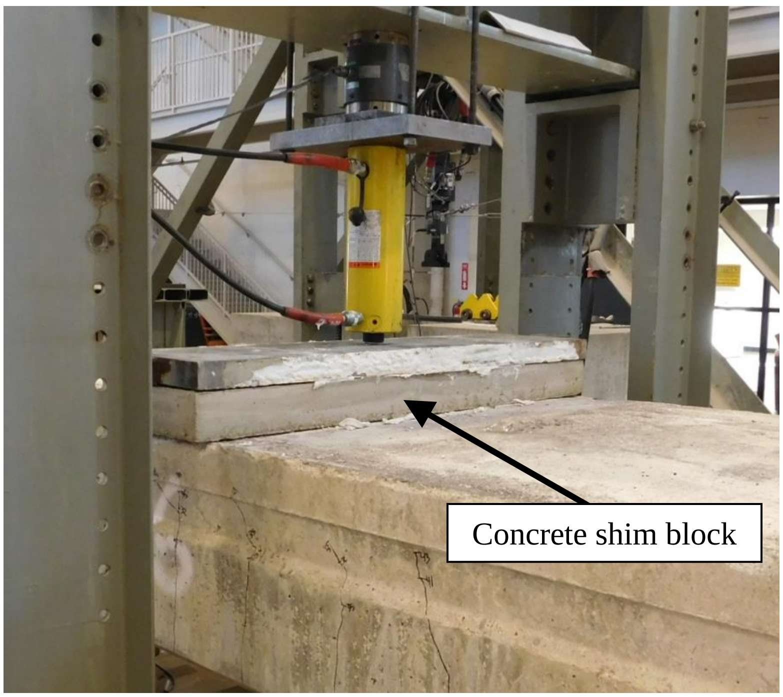

Figure 4.64: Concrete Shim Block

The loading procedure was resumed, and at a midspan deflection of 17.2 in. (49.2 kips) the stroke limit of the hydraulic jacks was reached (Figure 4.65). Considering the excessive deflection of the beam, the test was concluded. Although no strand fracture or concrete crushing was observed (Figure 4.66), the notable plateau in the load-deflection curve indicates that the ultimate capacity of the beam was reached.

Figure 4.65: Specimen 79-1-UD at 17.2 in. of Midspan Deflection

Figure 4.66: Constant Moment Region at Maximum Applied Force and Deflection

4.5.7 Specimen 79-2-UD

The only deterioration in Specimen 79-2-UD was water staining at the longitudinal joint on the south end of the beam (Figure 3.7). Before testing, no existing flexural cracks were observed.

At an applied force of 29 kips, the first flexural cracks became visible, and the stiffness of the beam was observed to change as expected (Figure 4.67). Therefore, the cracking moment was considered to correspond to an applied load of 29 kips.

After first cracking, the load procedure continued until the measured force started to drop at a midspan deflection of 10.9 in. (50.5 kips). As loading continued, the force steadily dropped until loading was paused at 11.0 in (47.7 kips). As the beam was inspected, the concrete suddenly crushed 2 ft from the north load point into the constant moment region, and the measured force reduced to 43.0 kips (Figure 4.68 and Figure 4.69). The stroke limit of the hydraulic jacks had nearly been reached at 11.0 in of midspan deflection. Therefore, considering the 15% reduction in measured force and the evidence of concrete crushing, the test was concluded, and the specimen was unloaded. No strand fracture was observed.

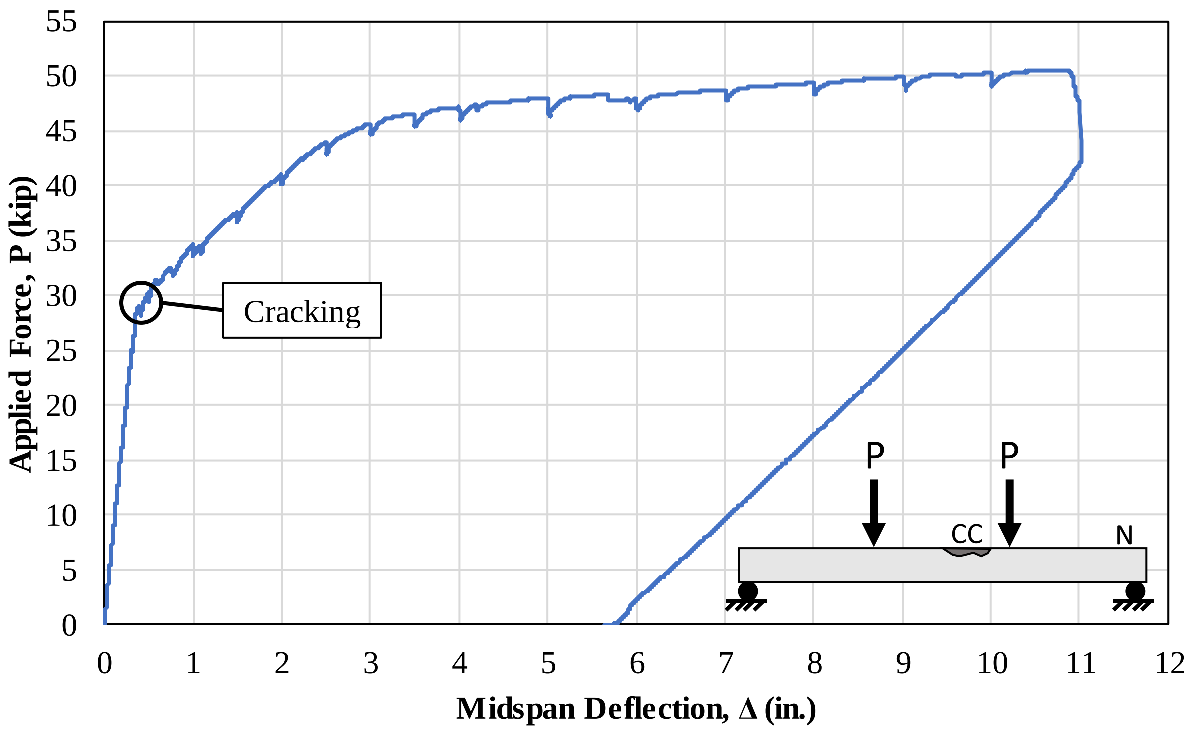

Figure 4.67: Specimen 79-2-UD Experimental Load vs. Deflection

Figure 4.68: Concrete Crushing at 11.0 in. of Midspan Deflection

Figure 4.69: Specimen 79-2-UD at 11 in. of Midspan Deflection (Concrete Crushed)

4.5.8 Specimen 79-3-UD

Specimen 79-3-UD was observed to have no visual signs of deterioration (Figure 3.8). The specimen was constructed with a curb (Figure D.9). To apply load across the entire width of the beam, concrete blocks were placed at the load points so the bearing plates could be placed on top of the curb (Figure 4.70). Prior to testing, no flexural cracks were observed.

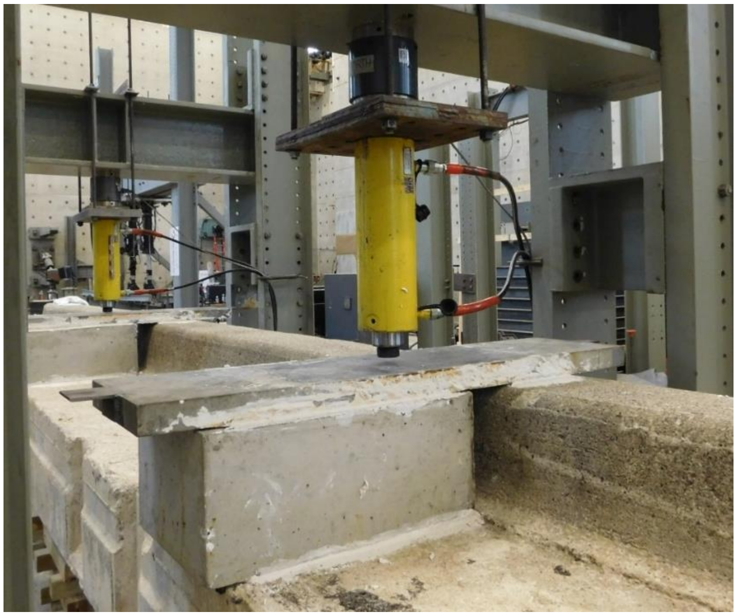

Figure 4.70: Curb Loading Assembly

At an applied force of 28 kips, cracking was heard, and flexural cracks were observed. The formation of each crack was associated with a decrease in measured force and an increase in midspan deflection. The load-deflection curve shows a significant change in stiffness following the first decrease in load at 28 kips (Figure 4.71). Therefore, the cracking moment was considered to correspond to an applied force of 28 kips.

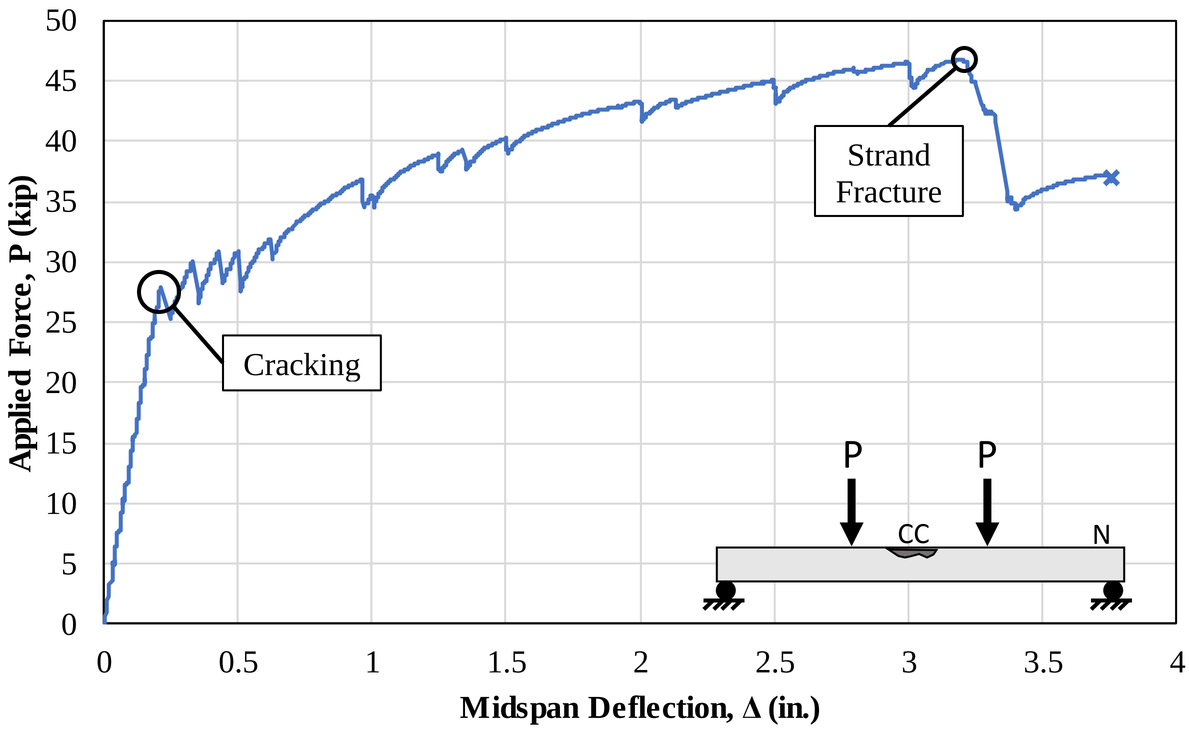

Figure 4.71: Specimen 79-3-UD Experimental Load vs. Deflection

After the cracking moment was exceeded, the loading procedure was continued up to 2.0 in. of midspan deflection (43.3 kips) where the first signs of crushing were observed at the top of the curb at the location of a small piece of wood embedded in the curb (Figure 4.72). As loading continued, concrete crushing around the piece of wood increased. Figure 4.73 shows the region at a midspan deflection of 3.0 in. (46.5 kips).

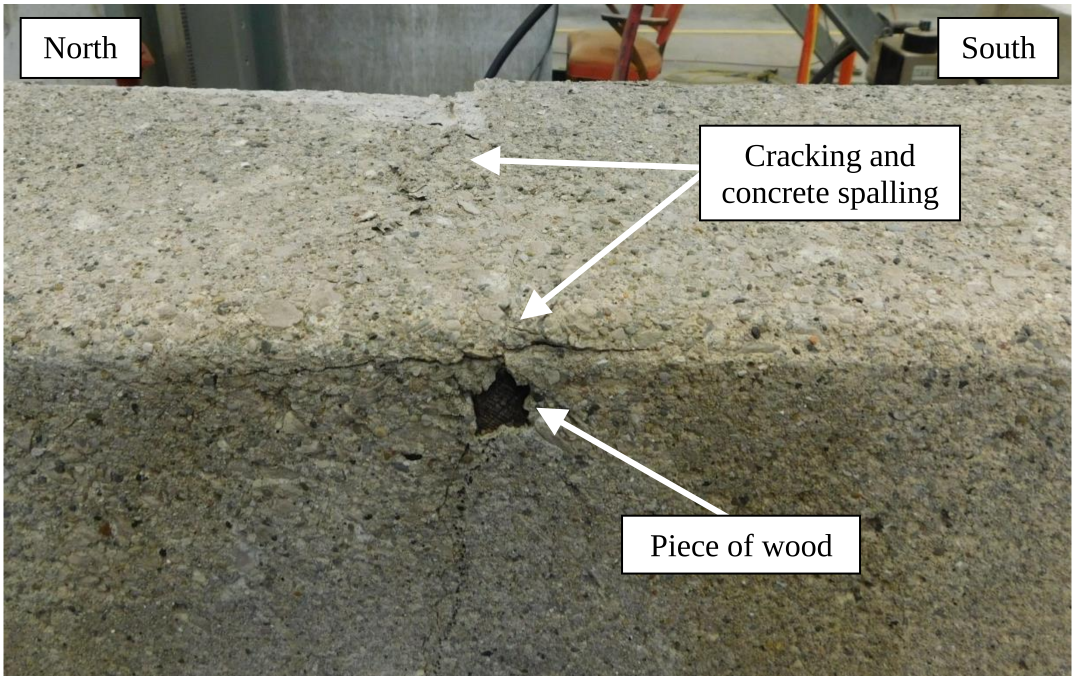

Figure 4.72: Initiation of Concrete Crushing

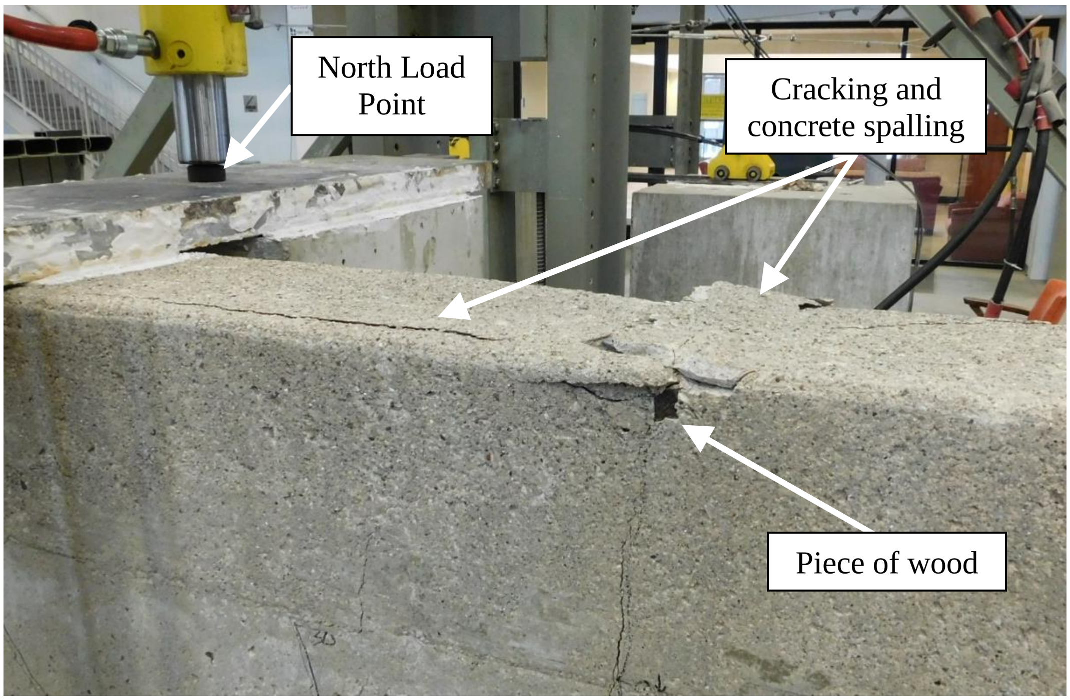

Figure 4.73: Concrete Crushing at 3.0 in. of Midspan Deflection

The loading procedure resumed, and at a midspan deflection of 3.2 in. (46.7 kips), the measured force started to decrease. Three loud pops were heard in succession, and the measured force decreased to 35.1 kips. One of the flexural cracks on the west side (curb side) of the specimen was observed to increase in width to approximately 3/8 in. (Figure 4.74). A similar increase in crack width was not observed on the east side of the specimen. Concrete crushing around the piece of wood increased on the east side of the curb but not on the west side (Figure 4.75).

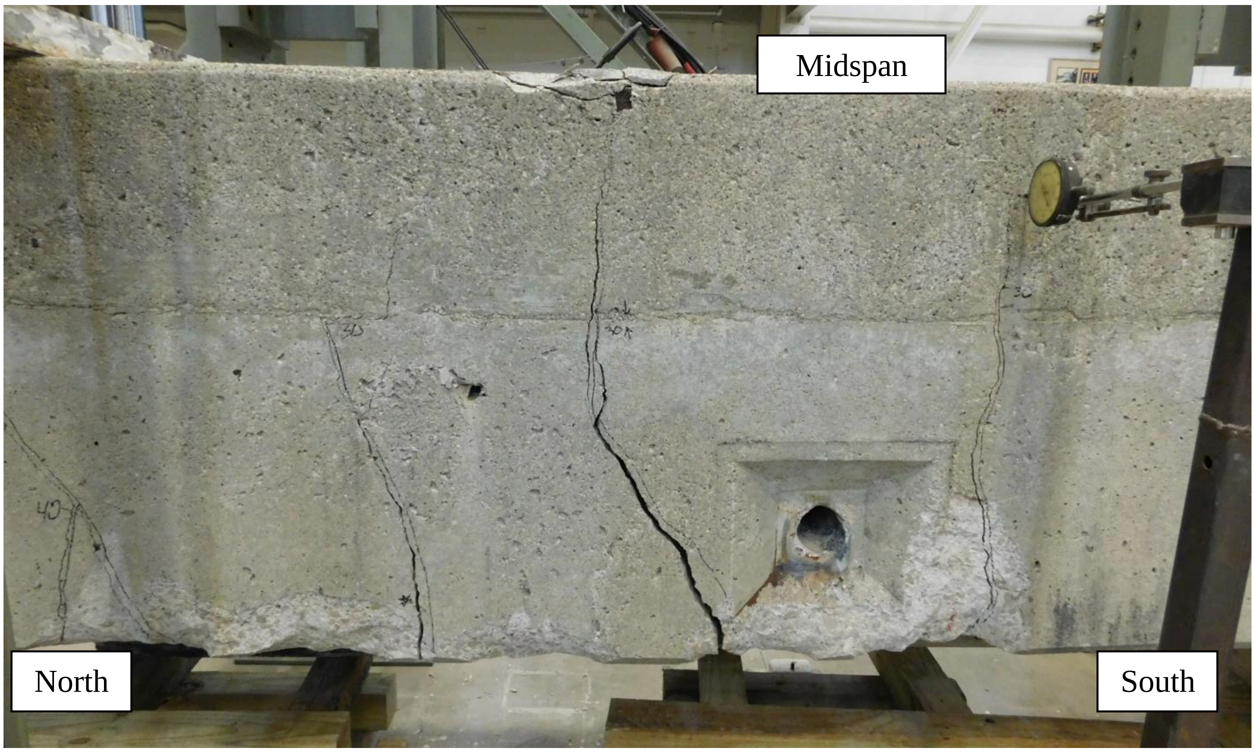

Figure 4.74: Flexural Crack on West Side After Decrease in Measured Force

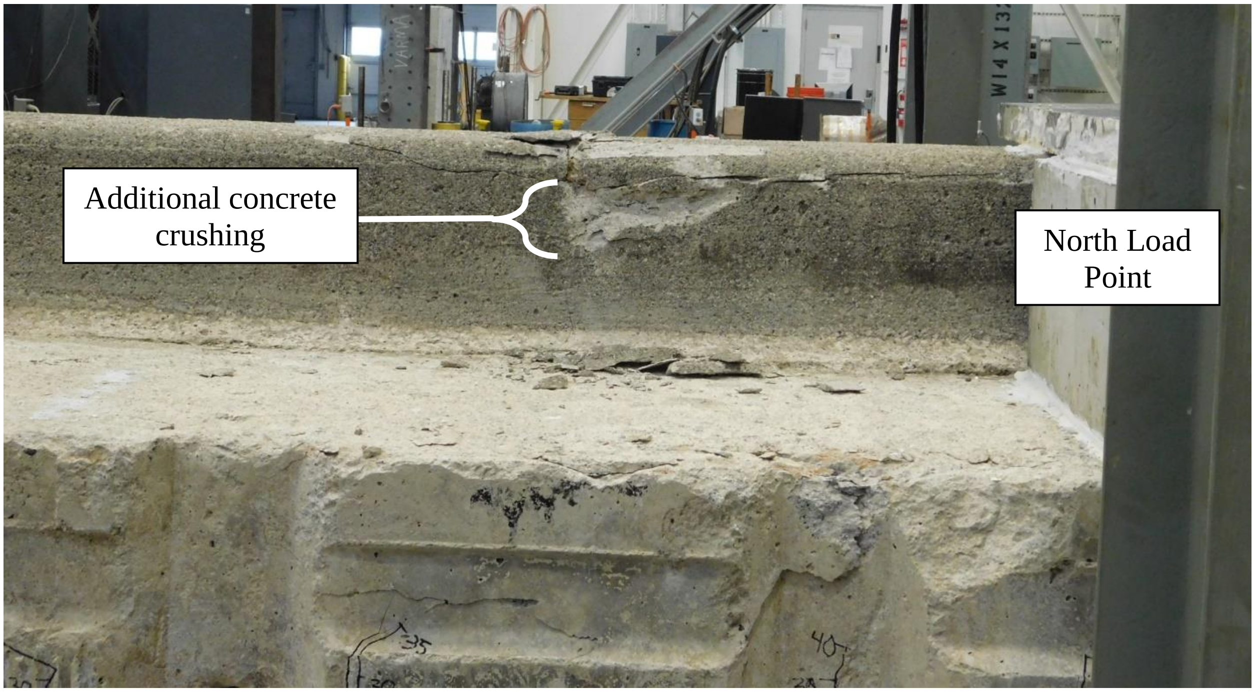

Figure 4.75: Concrete Crushing on East Side of Curb After Decrease in Measured Force

The loading procedure was resumed, and at a midspan deflection of 3.8 in., a loud pop was heard that was immediately followed by total collapse of the beam (Figure 4.76). Figure 4.77 and Figure 4.78 show the extent of crushing observed after collapse. The first strand fracture was heard on the curbside of the beam. The beam was also observed to have swayed toward the curbside after failure.

Figure 4.76: Collapse of Specimen 79-3-UD

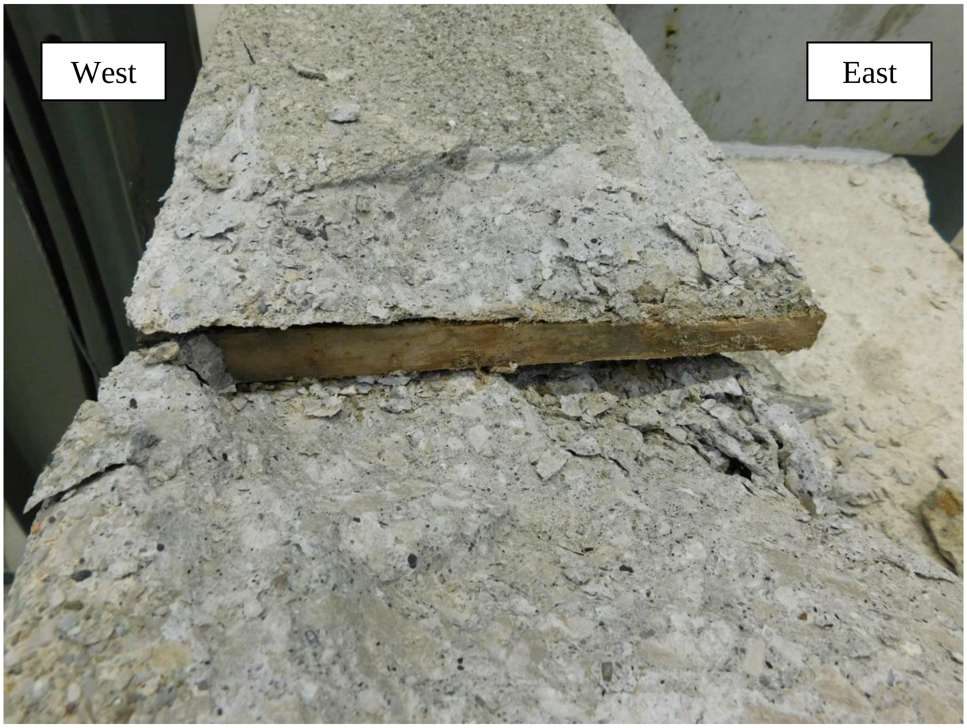

Figure 4.77: Extent of Crushing Around the Piece of Wood

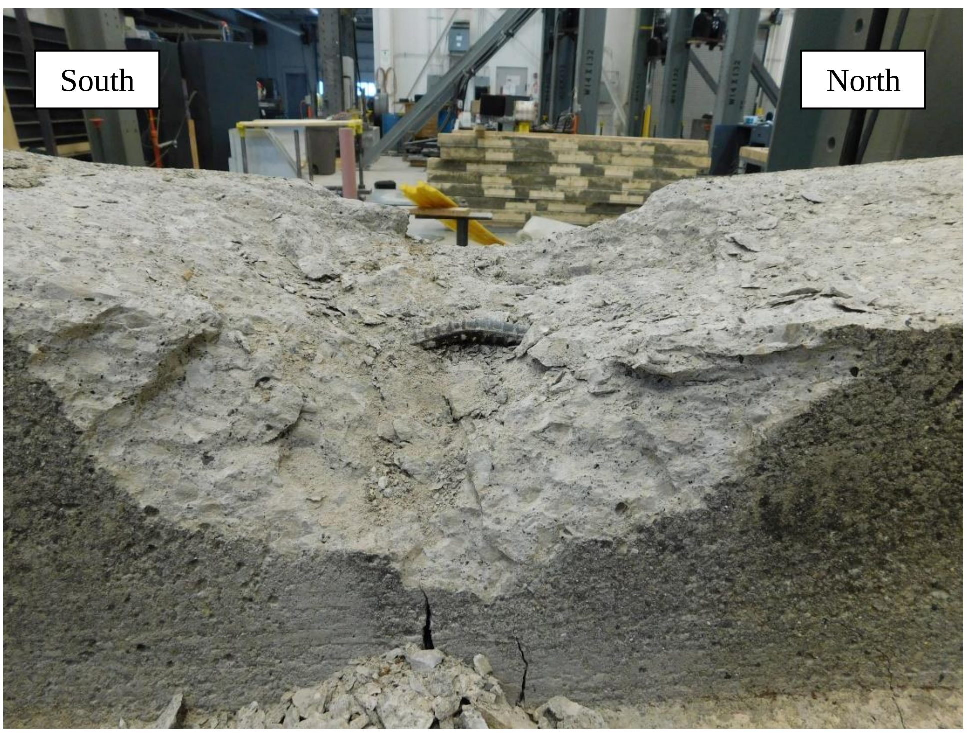

Figure 4.78: Extent of Crushing with Wood Removed

The piece of wood embedded in the top portion of the curb was approximately 1 in. tall by 1/2 in. wide and 11 in. long (length of wood equal to width of curb). This piece of wood caused the cracking and spalling that was observed at 2.0 in. of midspan deflection. After the first signs of crushing were observed, the measured force did not decrease until strand fractures were heard. Therefore, the failure mode of the specimen was assumed to be controlled by strand fracture. No corrosion was observed on the strands during the post-failure review.

4.5.9 Specimen 79-4-LC

The deterioration of Specimen 79-4-LC consisted of longitudinal cracking at the north end of the beam (Figure 3.9). The specimen was constructed with a curb (Figure D.10). Therefore, the curb loading assembly for Specimen 79-3-UD was used (Figure 4.70). Prior to the start of testing, Specimen 79-4-LC was inspected for existing flexural cracks, and no flexural cracks were observed.

First cracking was observed at an applied load of 28.6 kips. At 28.6 kips, flexural cracks were visible in the specimen, and a change in stiffness was observed in the load-deflection curve (Figure 4.79). Therefore, the cracking moment was considered to correspond to an applied load of 28.6 kips.

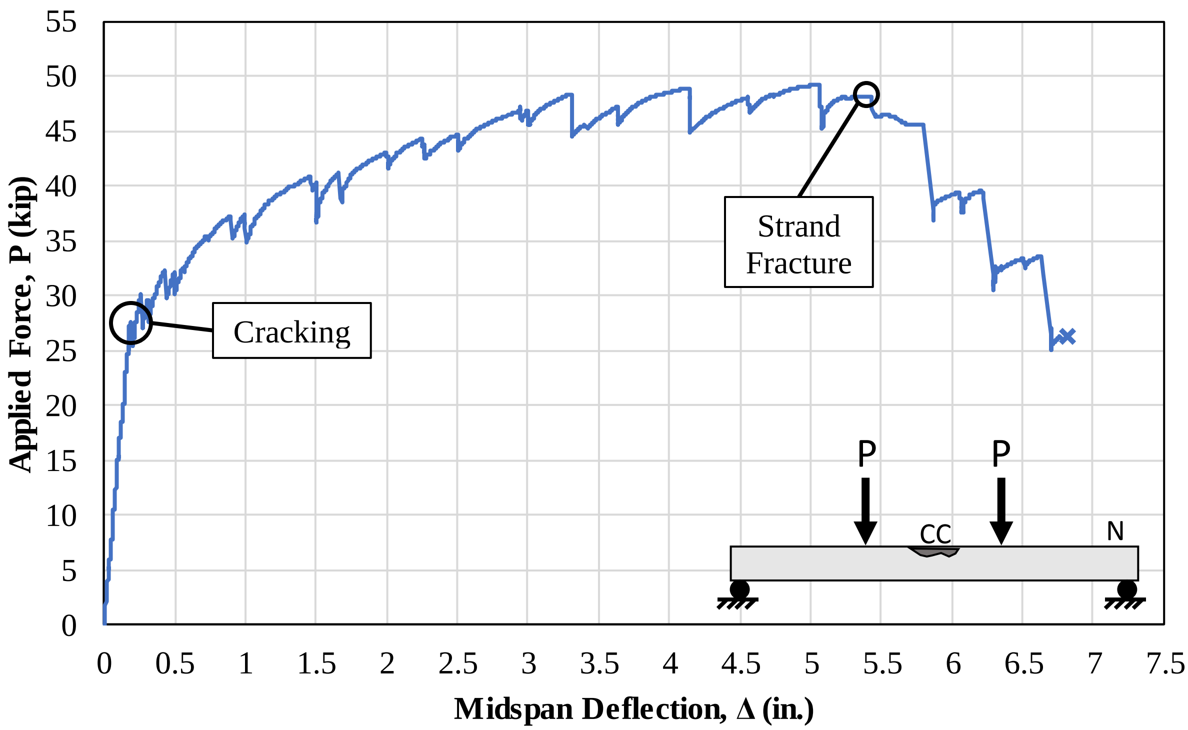

Figure 4.79: Specimen 79-4-LC Experimental Load vs. Deflection

As flexural cracking continued to develop, small decreases in measured force were observed at the formation of each new flexural crack. Flexural cracks continued to develop throughout the test. The large decreases in measured load at midspan deflections of 3.3 in., 3.7 in., 4.2 in., and 5.1 in. occurred at load pauses.

After the cracking moment was exceeded, loading was resumed up to a midspan deflection of 3.3 in. (48.3 kips) where a concrete spall was observed on the west side of the curb (Figure 4.80). As loading continued, the extent of concrete spalling increased along the corner of the west side of the curb until a midspan deflection of 5.1 in. (49.3 kips) was reached. Figure 4.81 shows concrete spalling along the west corner of the curb within the constant moment region. It also appeared that delamination of the concrete in the curb was occurring as evident by the longitudinal cracks over the region.

When loading resumed, concrete crushing intensified (Figure 4.82), and the measured force did not exceed 48.2 kips. At a midspan deflection of 5.4 in. (48.2 kips), a loud pop was heard indicating a strand fracture. As loading continued, the measured force steadily decreased as the midspan deflection increased to 5.8 in. (45.5 kip). A loud series of strand fractures followed until total collapse of the beam was observed (Figure 4.83 and Figure 4.84). No corrosion was observed in the strands in the failure region during the post-failure review.

It should be noted that the first strand fracture was heard from the curbside of the specimen, and the point of failure was observed to be slightly out-of-plane after collapse. In essence, the beam swayed toward the curbside after collapse.

Figure 4.80: Concrete Spall on West Side of Curb at 3.3 in. of Midspan Deflection

(a) Concrete spalling next to north load point

(b) Concrete spalling at midspan

(c) Concrete spalling next to south load point

Figure 4.81: Concrete Spalls at 5.1 in. of Midspan Deflection

(a) Concrete crushing next to north load point

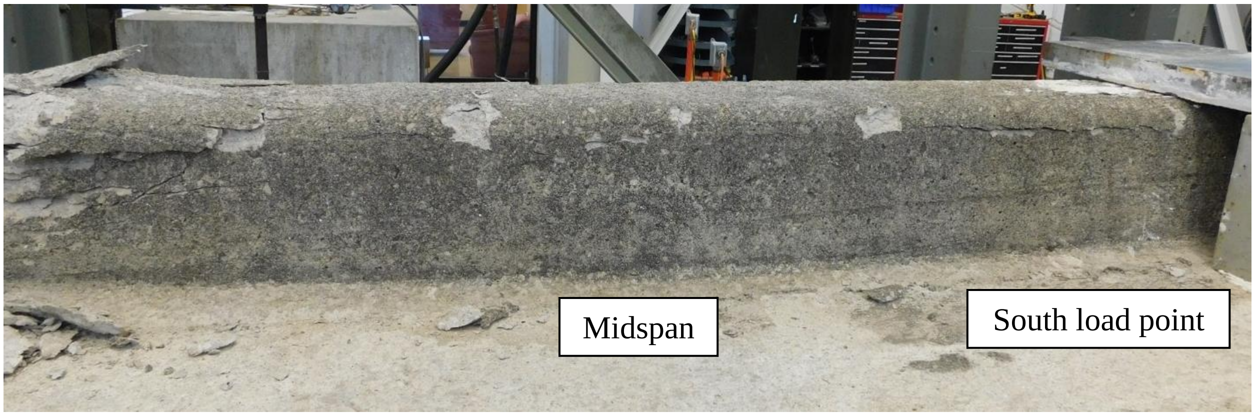

(b) Concrete spalling at midspan and next to south load point

Figure 4.82: Concrete Crushing at 5.4 in. of Midspan Deflection

Figure 4.83: Collapse of Specimen 79-4-LC

(a) West side of failure region

(b) East side of failure region

Figure 4.84: Specimen 79-4-LC Failure Region

The maximum force applied was 49.3 kips and was measured at a midspan deflection of 5.1 in. The loss of moment resistance observed after 5.1 in. of midspan deflection was attributed to concrete crushing. Therefore, the failure mode was controlled by concrete crushing.

Throughout the test, the longitudinal cracks in the north end of the beam were observed to have no change or any sign of distress (Figure 4.85).

Figure 4.85: Longitudinal Cracks After Collapse of Specimen 79-4-LC

4.5.10 Specimen 56-1-LC

The deterioration of Specimen 56-1-LC consisted of a single longitudinal crack in the south end of the beam and water staining along both edges of the bottom flange (Figure 3.10). Before testing, no existing flexural cracks were observed.

The first flexural cracks became visible at an applied load of 24 kips. A large change in stiffness of the beam, however, was not observed until an applied load of 26.5 kips (Figure 4.86). Therefore, the cracking moment was considered to correspond to an applied load of 26.5 kips.

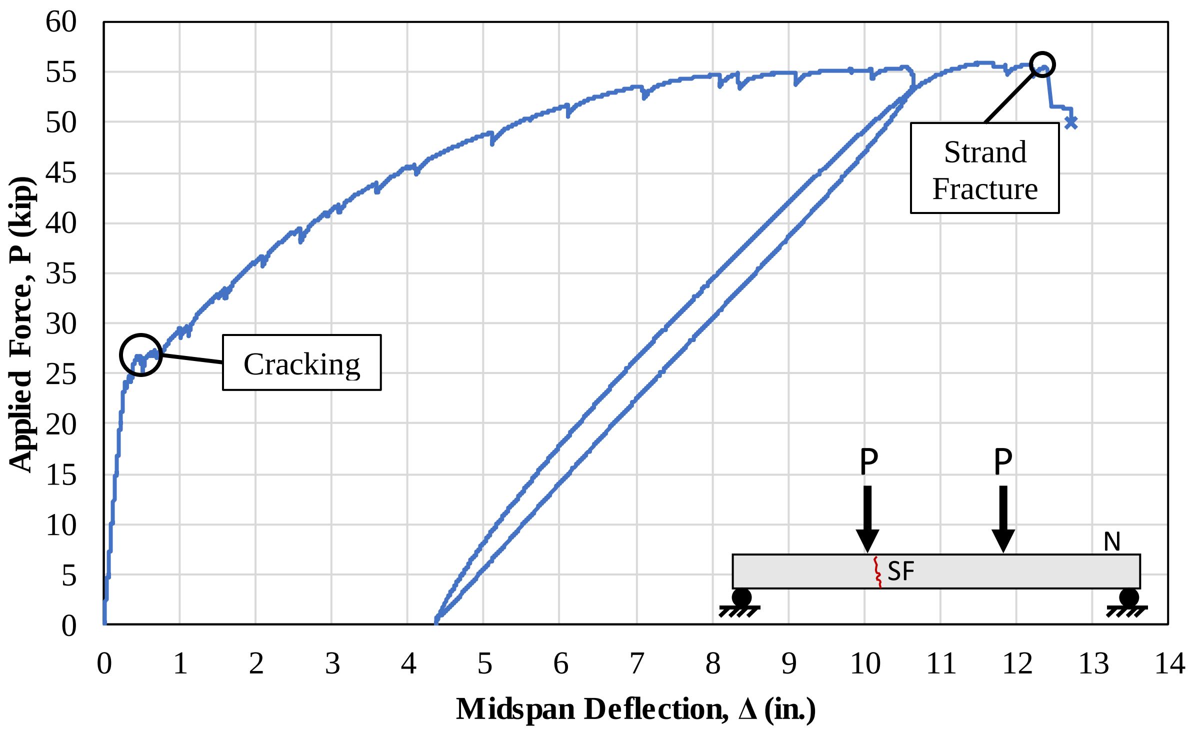

Figure 4.86: Specimen 56-1-LC Experimental Load vs. Deflection

After the cracking moment was exceeded, loading continued. At a midspan deflection of 10.65 in. (54.4 kips) the stroke limit of the hydraulic jacks was reached, and the specimen was unloaded. Concrete blocks were placed between the steel bearing plates and the beam specimen, and the specimen was reloaded. At a midspan deflection of 11.7 in. (56.0 kips), a noise was heard, and the measured force decreased by 0.5 kips. The sound could not be distinguished between concrete cracking or spalling and strand fracture. Inspection of the beam revealed no visual signs of distress likely indicating wire fracture.

At a midspan deflection of 12.4 in. (55.4 kips), a strand fracture was heard, and the measured force decreased by 3.8 kips. As loading continued, concrete crushing was observed at the south load point that was immediately followed by fracture of the remaining strands and complete collapse of the beam (Figure 4.87). Figure 4.88 shows the extent of concrete crushing at failure. After the specimen was removed from the test setup, the beam was examined. Minor pitting was observed on Strand 4 at the failure region (Figure 4.89). Strand 4 was assumed to have fractured at 12.4 in. of midspan deflection.

No change was observed in the hairline longitudinal crack in the south end of the specimen throughout the test.

Figure 4.87: Collapse of Specimen 56-1-LC

Figure 4.88: Concrete Crushing at Failure

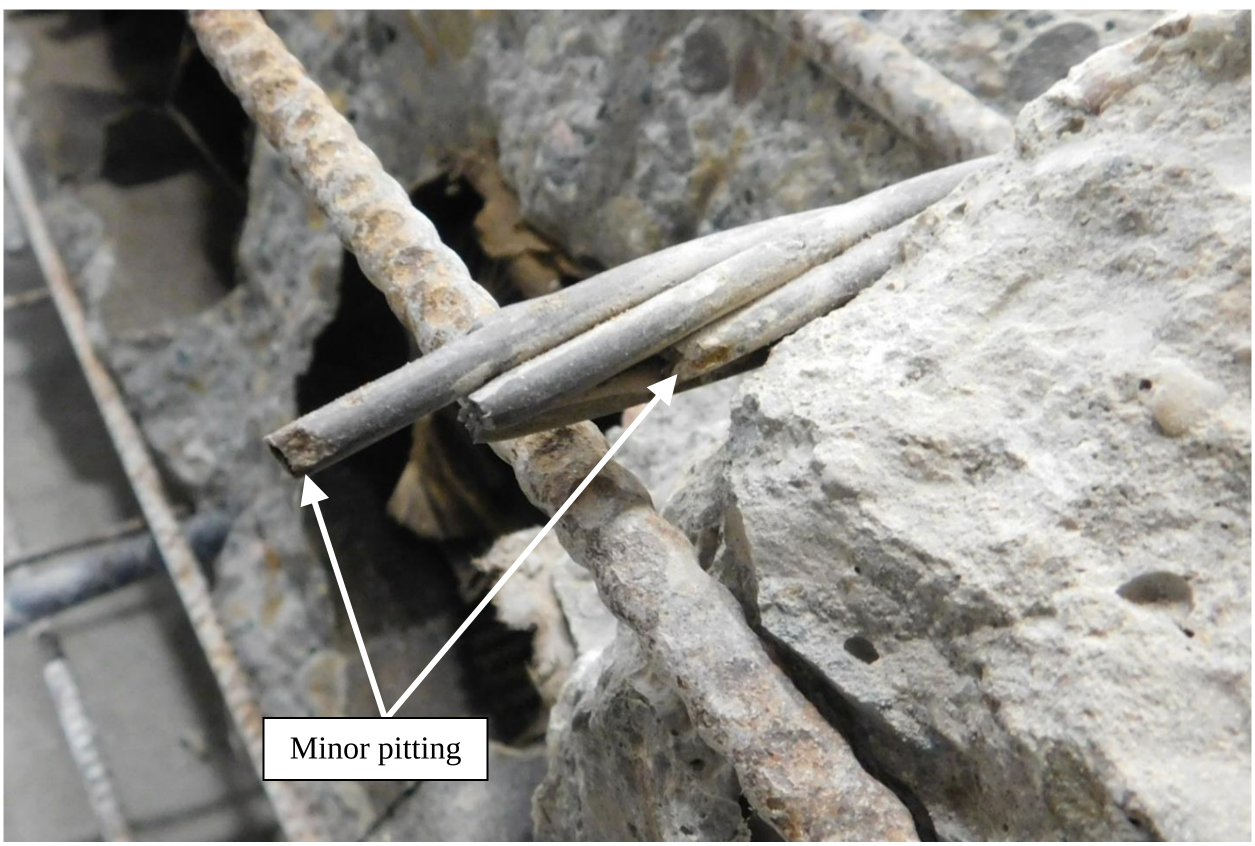

Figure 4.89: Strand 4 of Specimen 56-1-LC After Failure

4.5.11 Specimen 56-2-ES

Specimen 56-2-ES was observed with section loss along the east side of the beam that exposed a single strand for a length of approximately 14 ft (Figure 3.11). Prior to testing, the exposed strand was intact. Dimensions of the deteriorated section are provided in Figure D.12. Prior to testing, the beam was inspected for existing flexural cracks, and no cracks were found. As a safety precaution, three straps were placed around the specimen to catch the exposed strand in case of a fracture (Figure 4.90). The straps were tightened enough to remove slack from the straps, but not enough to put additional force into the exposed strand.

Figure 4.90: Strand Safety Precaution

At an applied load of 20 kips, the first flexural cracks became visible. The stiffness of the beam, however, did not change until the applied force reached 23.5 kips (Figure 4.91).

Considering that a change in stiffness was not observed until 23.5 kips, the cracking moment was considered to correspond to an applied load of 23.5 kips.

After the cracking moment was exceeded, many quiet cracking noises were heard throughout the beam until a midspan deflection of 4 in. (31.7 kips) was reached. Up to 4 in. of midspan deflection, no distress was observed in the top flange. The region anchoring the exposed strand may have been the source of cracking, but the poor condition of the concrete prevented the observation of any flexural cracking or cracks radiating from the corroded strand.

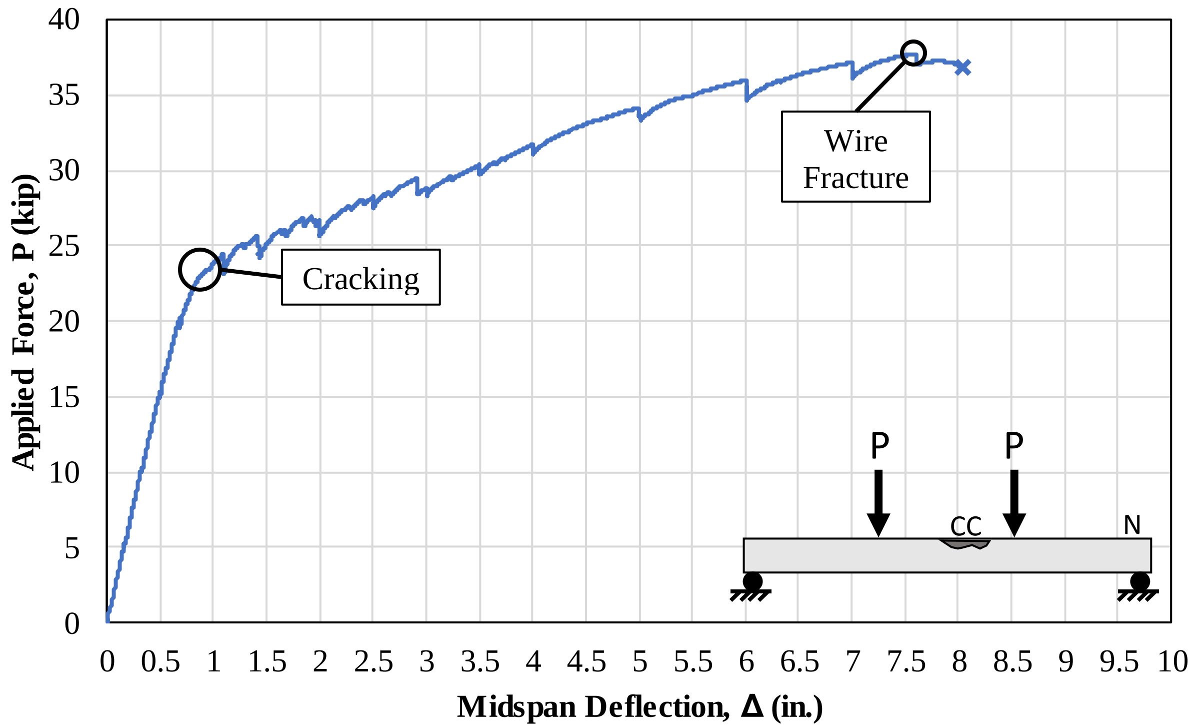

Figure 4.91: Specimen 56-2-ES Experimental Load vs. Deflection

From a midspan deflection of 4 in. up to 7.6 in., no noises were heard, and flexural cracking continued to develop. At 7.6 in. of midspan deflection and an applied force of 37.7 kips, a pop was heard, and the measured force dropped 0.5 kips to 37.2 kips. Loading continued until the concrete in the top flange 4 ft from the north load point suddenly crushed at a midspan deflection of 8.0 in. and an applied force of 37.0 kips (Figure 4.92). Total collapse of the beam was observed with crushing of the concrete top flange (Figure 4.93).

Investigation of the failure region revealed three broken wires on the exposed strand (Figure 4.94). These broken wires may have caused the drop in measured force at 7.6 in. of midspan deflection. The wire fractures in the exposed strand provide evidence that the corroded strand not only contributed to the flexural capacity but had adequate bond within the deteriorated regions on either end of the beam. All other strand at the failure region were intact without any broken wires or corrosion.

Concrete cores extracted from the top flange of the beam for compression testing were noted to contain minor cracks in the top 1/2 in. of each core. In addition, the top flange on either side of the failure was observed to have delaminated concrete by sounding with a hammer.

Figure 4.92: Crushed Concrete at Failure

Figure 4.93: Collapse of Specimen 56-2-ES

Figure 4.94: Exposed Strand Broken Wires

As flexural cracks developed and crack widths began to grow, water was observed dripping from the bottom flange. As the test continued, the amount of water leaking from the beam increased. Water, buckets, and sheets of plastic are visible in many of the figures because of the amount of water that was leaking from the voids. Although the drain holes were cleared before the beginning of the test, the cardboard stiffener panels in the voids acted like dams to prevent the water from reaching the drain holes (Figure 4.95). In future tests, additional drain holes were drilled into the bottom flange to ensure that all water had drained from the void.

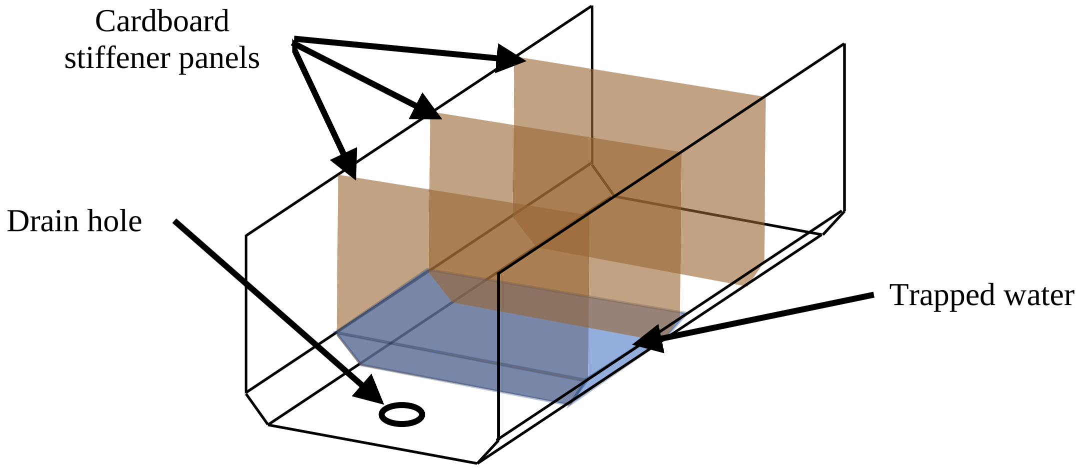

Figure 4.95: Box Beam Void Representation

4.5.12 Specimen 102-1-BS

The deterioration of Specimen 102-1-BS consisted mainly of one broken strand on the east side of the specimen. A detailed map of the deterioration is provided in Figure 3.12. Prior to testing, the beam was inspected for existing flexural cracks, and no cracks were observed.

At an applied force of 15 kips, a change in stiffness was observed in the load-deflection curve (Figure 4.96), but no flexural cracks were visible until the applied force reached 20 kips. The applied force of 15 kips appears to correspond with the zero tension load. This change in stiffness suggests that this specimen likely had existing hairline flexural cracks. Cracking was not audible until the applied load reached 24.1 kips, and a large change in stiffness was observed at this point. Considering the change in stiffness at 24.1 kips, the cracking moment was considered to correspond to an applied load of 24.1 kips.

After the cracking moment was exceeded, many quiet cracking and popping noises were heard in between load steps. In between the load pauses at 3.5 in. and 4.0 in. of midspan deflection, a section of concrete spalled from the east edge of the bottom flange approximately 3 ft south of the south load point (Figure 4.97). The exposed strand at that location was further exposed, and a wire fracture was observed.

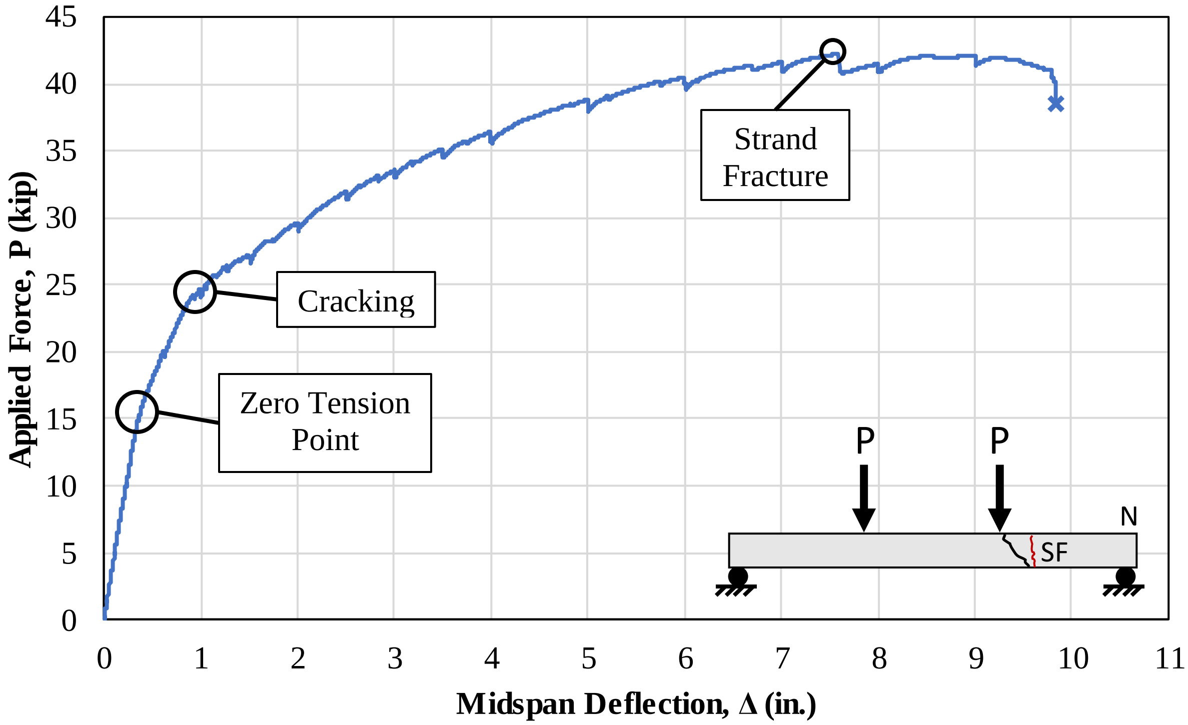

Figure 4.96: Specimen 102-1-BS Experimental Load vs. Deflection

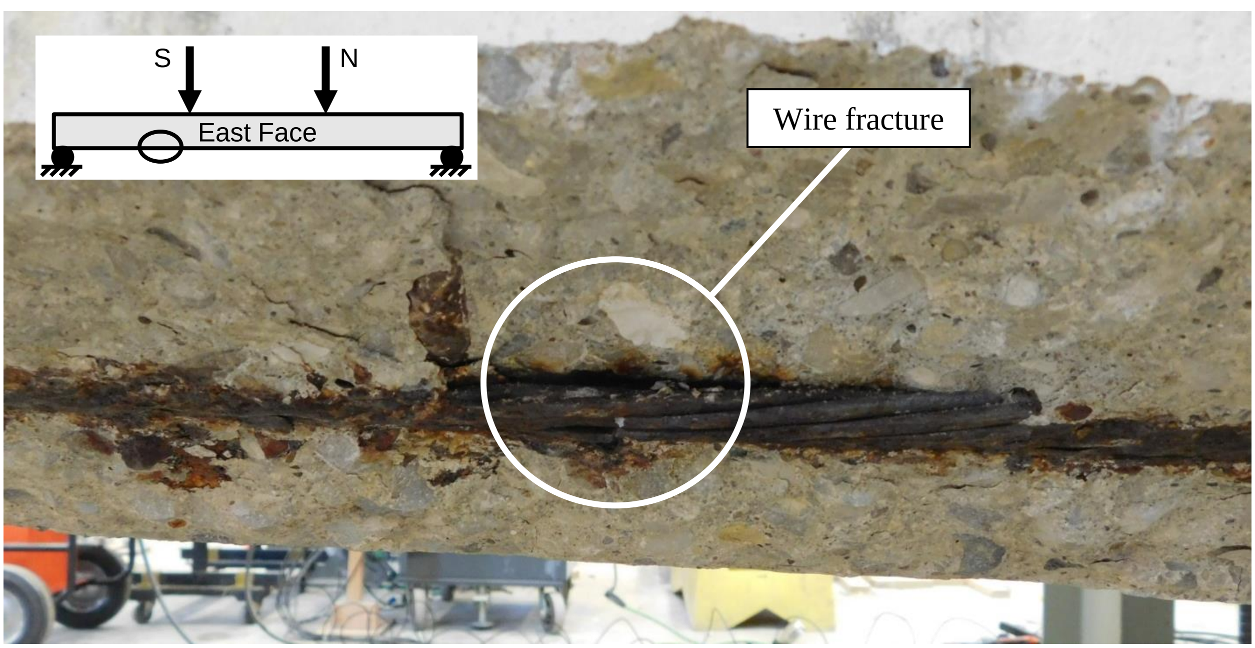

Figure 4.97: Concrete Spall and Wire Fracture

Quiet popping noises were heard in between the loading pauses from 5.0 in. to 7.0 in. of midspan deflection. At a midspan deflection of 7.6 in. and an applied load of 42.3 kips, a strand fracture was heard from the north load point resulting in a measured force decrease of 1.5 kips.

As loading continued, the measured force did not exceed the previous maximum of 42.3 kips. At a midspan deflection of 9.5 in. (41.8 kips), the measured force began to steadily decrease. At a midspan deflection of 9.8 in. and an applied load of 41.0 kips, the beam collapsed (Figure 4.98). Inspection of the failure region revealed that a large shear crack had formed on the north side of the north load point (Figure 4.99). This crack was not noticed prior to failure. As shown, the shear crack propagated in between two halves of the transverse reinforcement. Figure 4.100(a) illustrates how the transverse reinforcement detail was built, while Figure 4.100(b) illustrates the as-designed detail. This poor detailing led to failure of the specimen.

Although collapse of the specimen was caused by shear failure at the north load point. The decrease in the applied load was caused by strand fracture at the maximum applied load of 42.3 kip and 7.6 in. of midspan deflection. The fractured strand was located slightly to the north of the bottom of the shear crack shown in Figure 4.99(b). This strand was by the east face of the specimen adjacent to the strand broken prior to testing. Corrosion of the strand consisted of pitting on one side of the strand (Figure 4.101). All other strands were found intact without any corrosion. Fracture of this strand (along with the previously broken strand) likely led to a decrease in shear capacity which explains the shear failure following strand rupture.

Figure 4.98: Collapse of Specimen 102-1-BS

(a) West side

(b) East side

Figure 4.99: Shear Failure

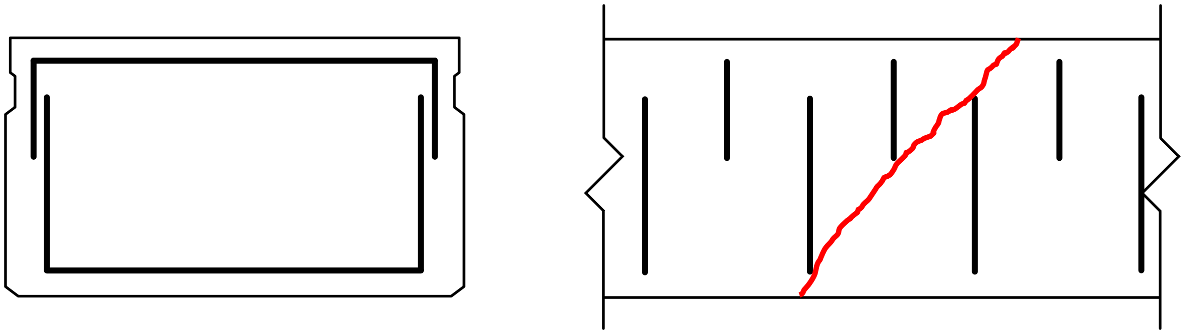

Section

Elevation

(a) As-built detail

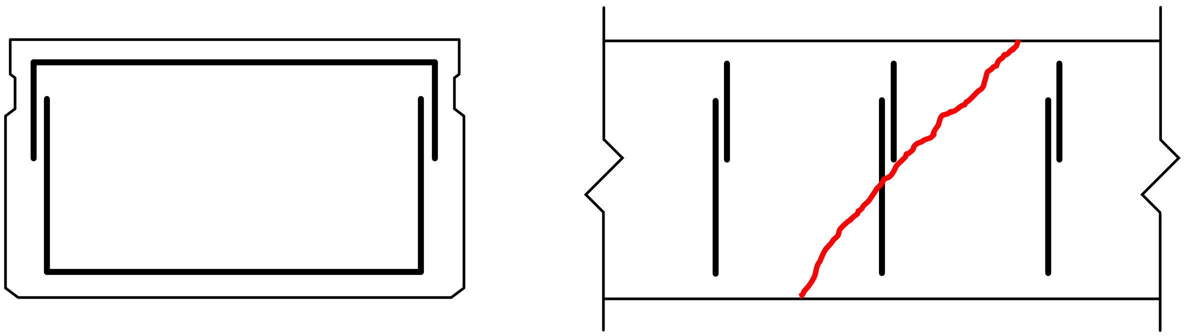

Section

Elevation

(a) As-designed detail

Figure 4.100: Transverse Reinforcement Detailing

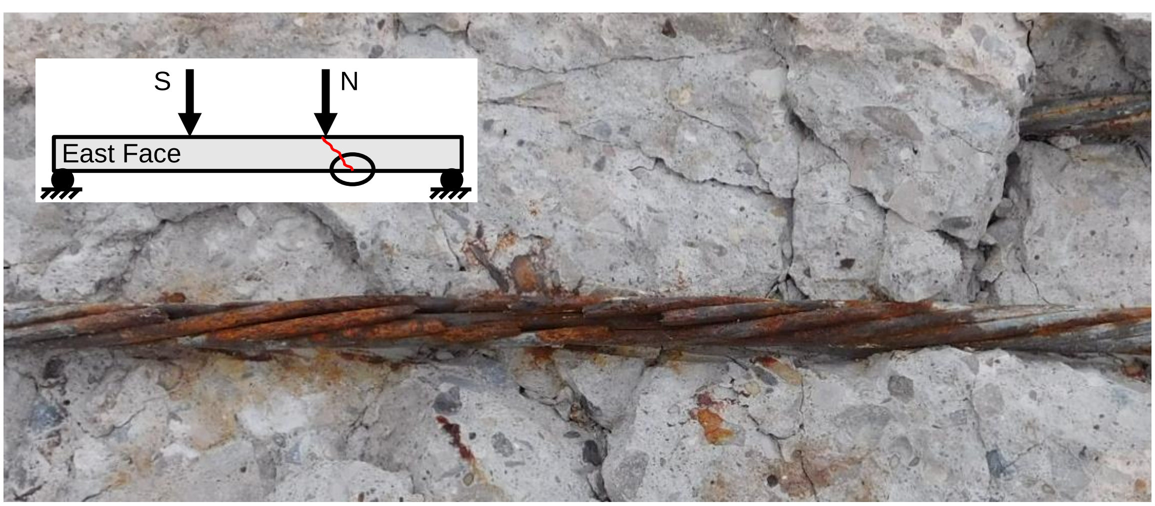

Figure 4.101: Condition of Fractured Strand Adjacent to Existing Broken Strand

4.5.13 Specimen 102-2-BS

The deterioration of Specimen 102-2-BS consisted of a broken strand on the west edge of the bottom flange and a longitudinal crack on the east edge of the bottom flange (Figure 3.13). Prior to testing, no existing flexural cracks were observed.

At an applied force of 22.6 kips, the first flexural cracks became visible, and a change in stiffness was observed in the load-deflection curve (Figure 4.102). Therefore, the cracking moment was considered to correspond to an applied load of 22.6 kips.

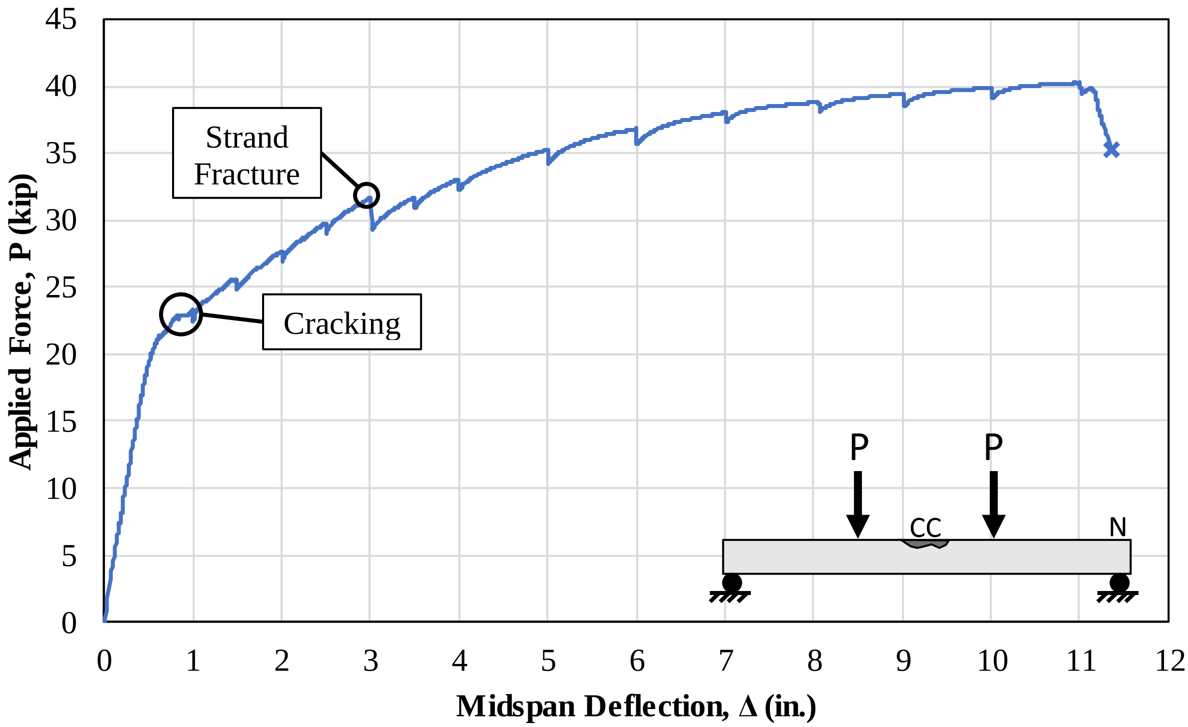

Figure 4.102: Specimen 102-2-BS Experimental Load vs. Deflection

At 3.0 in. of midspan deflection and an applied load of 31.6 kips, a strand fracture was heard, and the measured force decreased by 3 kips. As loading continued, the concrete cover spalled away from the east edge strand between 4 in. and 5 in. of midspan deflection (Figure 4.103). The concrete spall increased in size between 7 in. and 8 in. of midspan deflection (Figure 4.104). The location of the concrete spall corresponded to the location of the north corner crack in the east edge of the bottom flange (Figure 3.13).

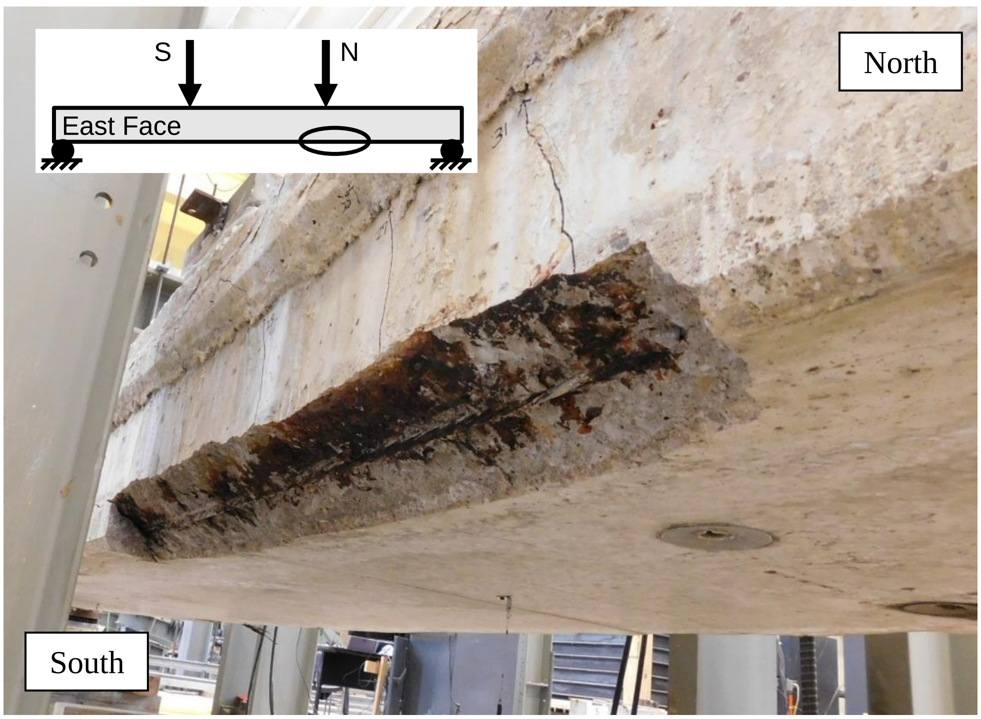

Figure 4.103: Concrete Spall from East Edge Strand

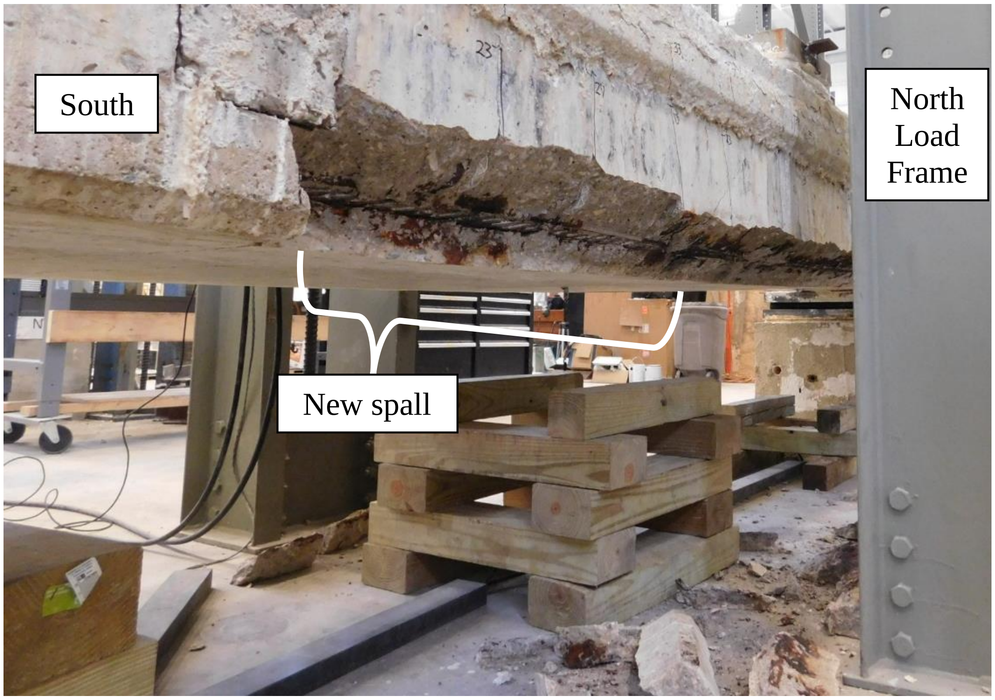

Figure 4.104: Further Concrete Spalling Along East Edge Strand

A maximum applied force of 40.2 kips was measured at 11.0 in. of midspan deflection. As part of the loading procedure, loading was paused, and the specimen was examined. When loading resumed, small chips of concrete were observed popping off of the top flange at midspan indicating the initiation of concrete crushing. At a midspan deflection of 11.2 in. the stroke limit of the hydraulic jacks was reached. Considering that concrete crushing had already initiated, the specimen was allowed to creep to failure. The decrease in measured force observed at the end of the load-deflection curve in Figure 4.102 is a result of the specimen creeping to failure over the course of approximately 2 minutes. At an applied load of 35.3 kips and a midspan deflection of 11.37 in., the specimen collapsed due to concrete crushing of the top flange (Figure 4.105).

Post-failure investigation of the specimen revealed that only the east edge strand fractured during the test. Corrosion on the fractured strand consisted of heavy pitting on one side of the strand (Figure 4.106). All other strands were observed to be intact without any corrosion with the exception of the strand broken prior to testing.

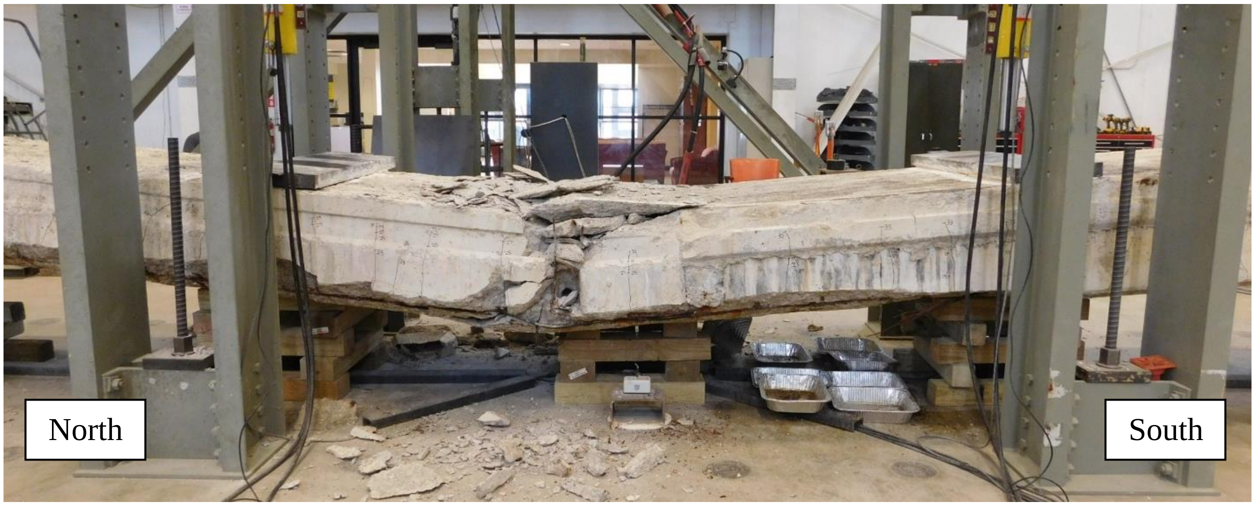

Figure 4.105: Collapse of Specimen 102-2-BS

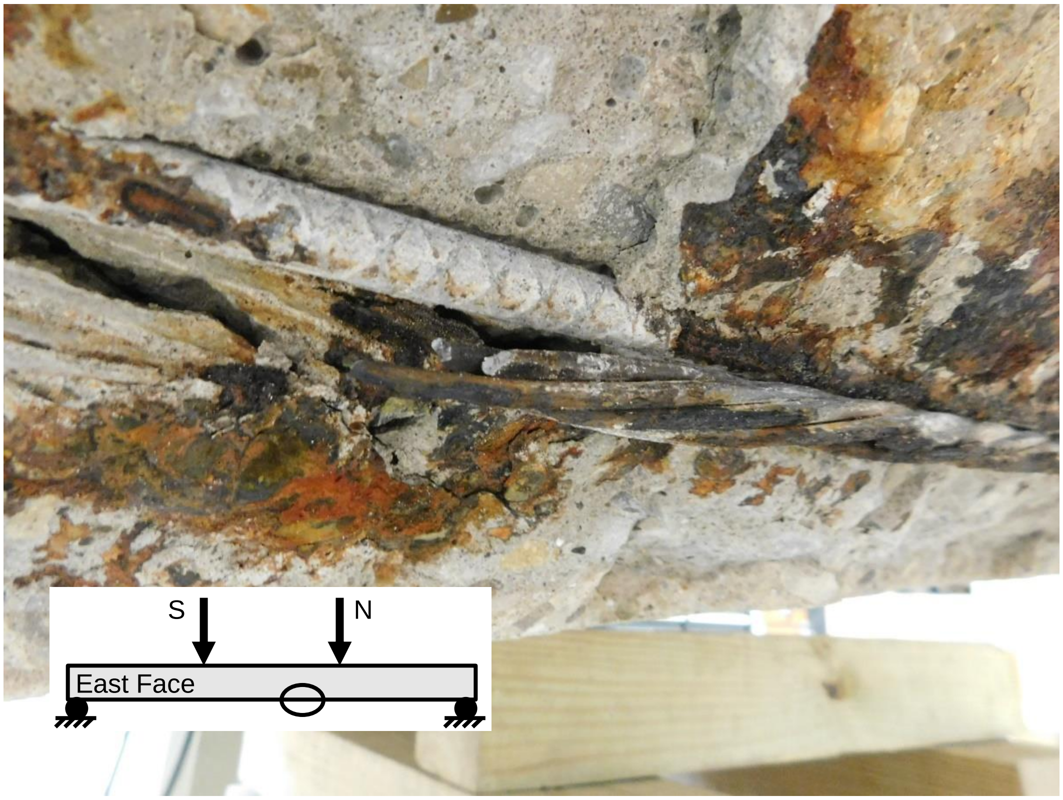

Figure 4.106: Fractured East Edge Stand

4.5.14 Specimen 102-3-BS

The deterioration of Specimen 102-3-BS consisted of a broken and an exposed strand on the west edge of the bottom flange and longitudinal cracks on the east edge of the bottom flange (Figure 3.14). Prior to testing, the specimen was inspected for existing flexural cracks, and no cracks were observed.

At an applied force of 21.9 kips, the first flexural cracks became visible, and a change in stiffness was observed in the load-deflection curve (Figure 4.107). Therefore, the cracking moment was considered to correspond to an applied load of 21.9 kips.

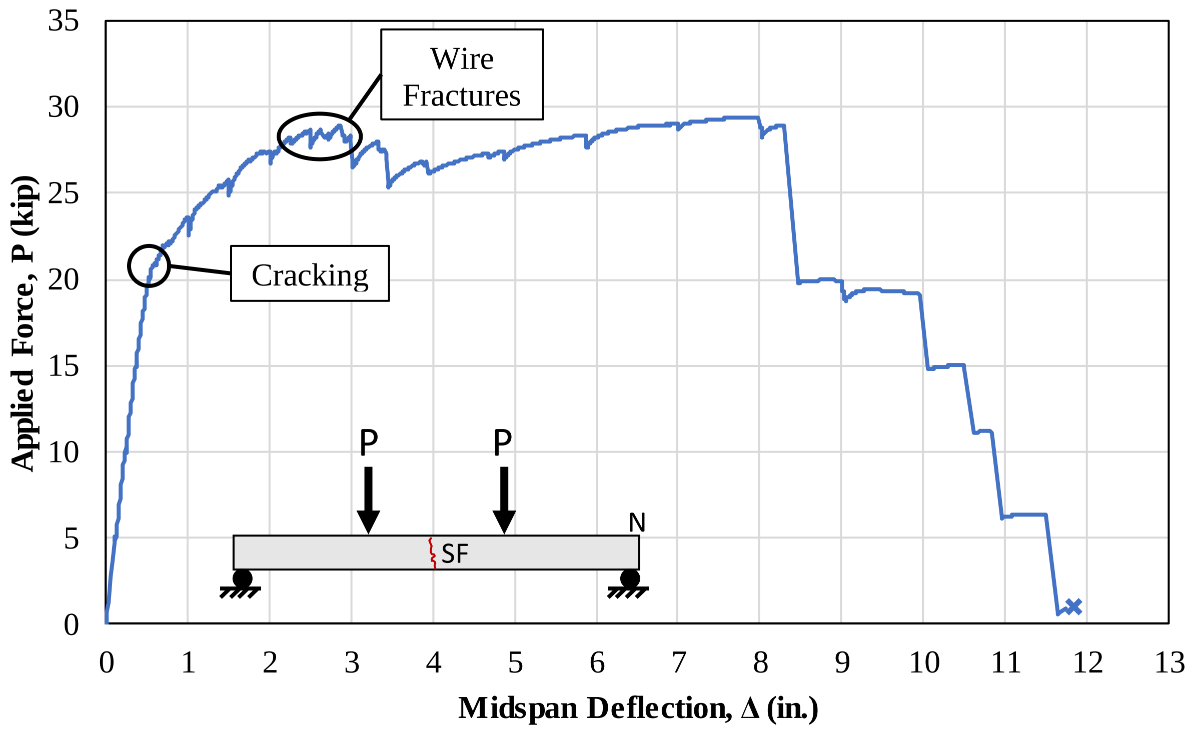

Figure 4.107: Specimen 102-3-BS Experimental Load vs. Deflection

After the cracking moment was exceeded, many quiet cracking and popping noises were heard up to a midspan deflection of 2.25 in. (28.2 kips). At 2.25 in. of midspan deflection, a pop was heard which was assumed to be a wire fracturing, and the measured force decreased by 0.3 kips. Loading continued up to an applied force of 28.9 kips at a midspan deflection of 2.87 in. This was followed by a series of popping sounds accompanied by decreases in measured force between 0.3 kips and 0.5 kips up to a midspan deflection of 4 in. Between 3.5 in. and 4 in. of midspan deflection, the east edge strand was exposed by concrete spalling (Figure 4.108). The strand was observed to have at least two fractured wires.

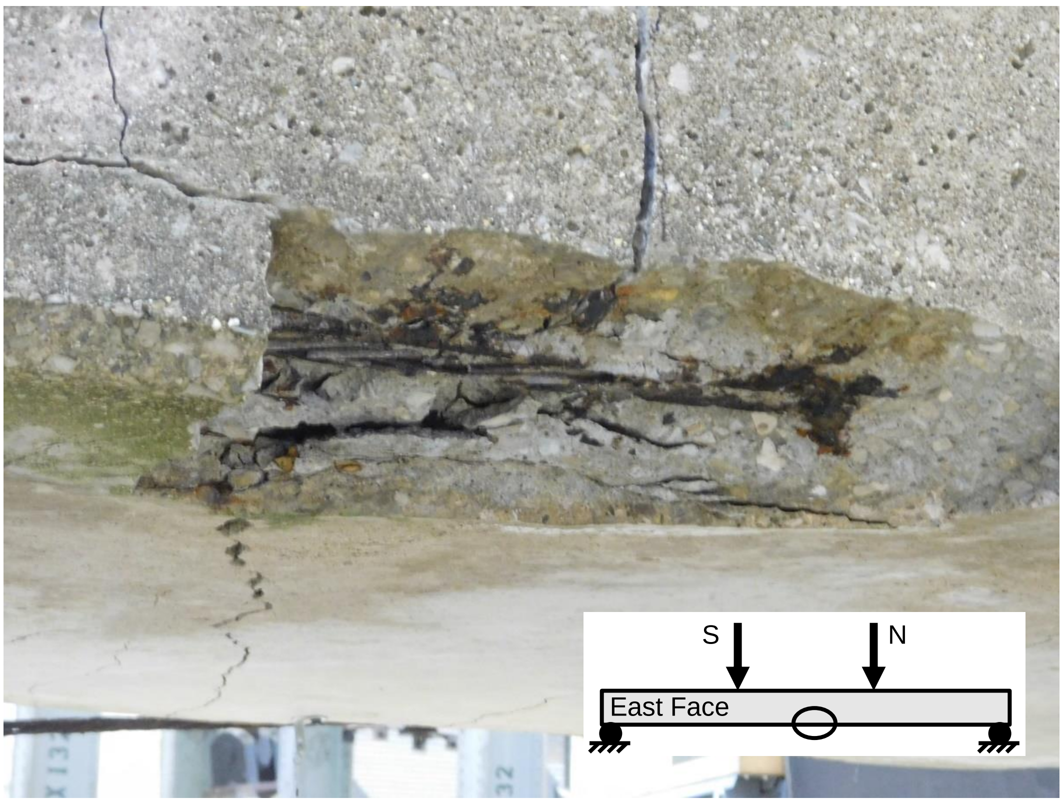

Figure 4.108: Exposed East Edge Strand at 4 in. of Midspan Deflection

From 4 in. to 8 in. of midspan deflection, loading continued without any notable distress in the specimen. At the load pause of 8 in., a maximum applied force of 29.4 kips was measured, and small cracks and concrete spalls were observed in the top flange at midspan (Figure 4.109). When loading resumed, concrete crushing was observed in the top flange, and at 28.9 kips and 8.3

in. of midspan deflection, a strand fracture was heard followed by a decrease in measured load of 9 kips. The specimen was then loaded continuously until collapse was observed due to fracture of the remaining strands (Figure 4.110). Based on the discontinuities in the load-deflection curve between 8.3 in. of midspan deflection and collapse, two strands were assumed to have broken at 8.3 in. of midspan deflection with each of the following jumps assumed to correspond to one strand fracturing.

During the period of continuous loading to collapse, an additional portion of concrete spalled from the east edge of the bottom flange, exposing a total of four strands (Figure 4.111). All four strands were observed to be corroded. The corrosion consisted of heavy pitting with section loss. The location of the corroded strands corresponded with corner cracking, longitudinal cracking, and concrete staining. It should also be noted that the corroded strands were on the exterior side of the beam (an edge beam) when the beam was in-service. A total of 5 strands were observed to be corroded at the failure section, 4 strands on the east side of the specimen and 1 strand that was broken prior to testing.

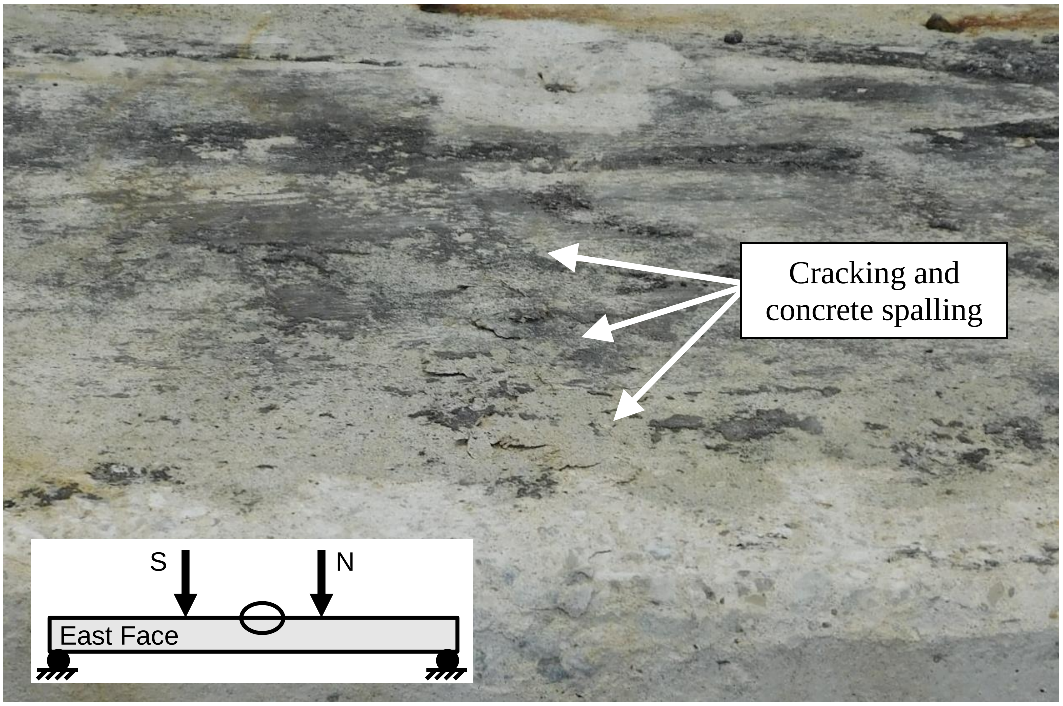

Figure 4.109: Top Flange Cracks and Small Concrete Spalls at 8 in. of Midspan Deflection

Figure 4.110: Collapse of Specimen 102-3-BS

Figure 4.111: Exposed Strands on East Side of Bottom Flange after Collapse

4.5.15 Specimen 102-4-BS

The deterioration of Specimen 102-4-BS consisted of longitudinal cracks and an exposed strand on the west edge of the bottom flange, and a broken and an exposed strand on the east edge of the bottom flange (Figure 3.15). Prior to testing, the specimen was inspected for existing flexural cracks, and no cracks were observed.

At an applied force of 20 kips, the first flexural crack became visible, and a change in stiffness was observed in the load-deflection curve (Figure 4.112). Therefore, the cracking moment was considered to correspond to an applied load of 20 kips.

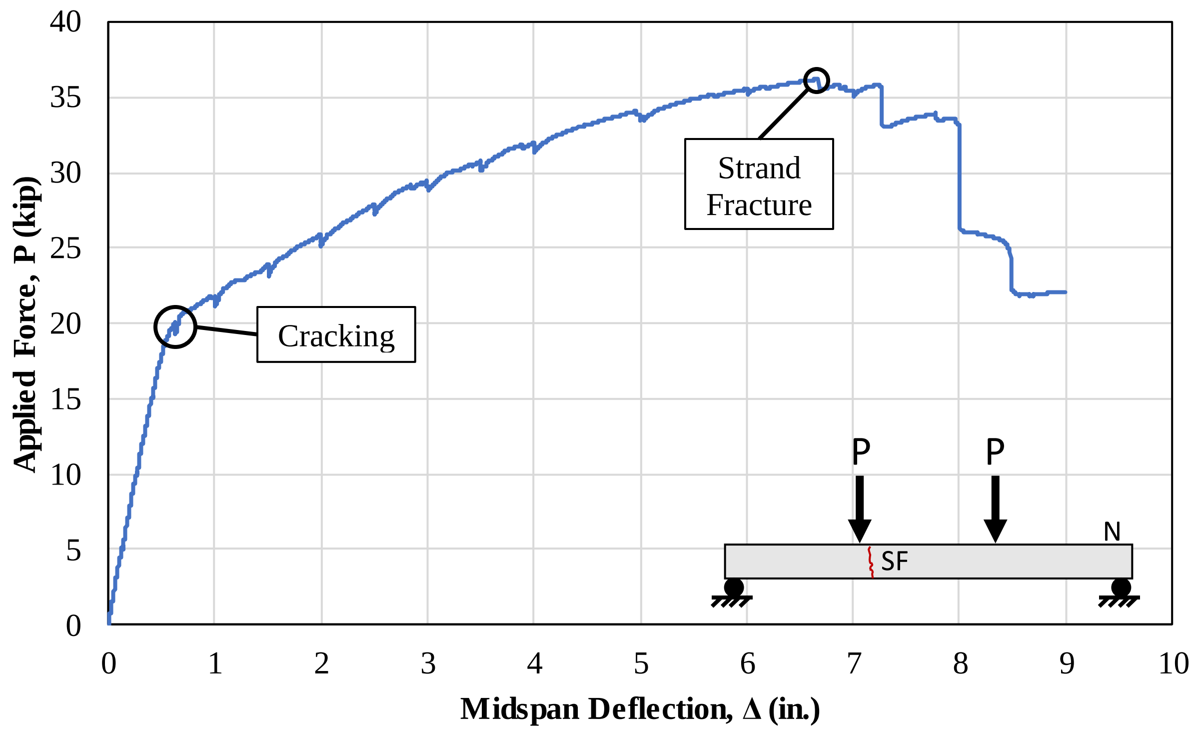

Figure 4.112: Specimen 102-4-BS Experimental Load vs. Deflection

After the cracking moment was exceeded, quiet popping and cracking were heard from around the north load point. At 3 in. of midspan deflection, a portion of concrete spalled from the west side of the bottom flange near the north load point, exposing the edge strand (Figure 4.113). This spall coincided with the location of the corner crack (Segment B, Figure 3.15). Quiet popping and cracking continued up to 5 in. of midspan deflection. From 5 in. to 6 in. of midspan deflection, no further distress was observed in the specimen near the north load point. At 6.7 in. of midspan deflection, the maximum applied load of 36.2 kips was measured and, a loud pop was heard near the south load point. Strand fracture occurred and was accompanied by a decrease in measured force of 0.6 kips. The fracture location coincided with the location of concrete spalling from the east edge strand at the south load point. The spalling further exposed the east edge strand (Figure

4.114). As loading continued, a quiet cracking sound was heard, and the measured force decreased slightly until a pause in loading at 7 in. of midspan deflection.

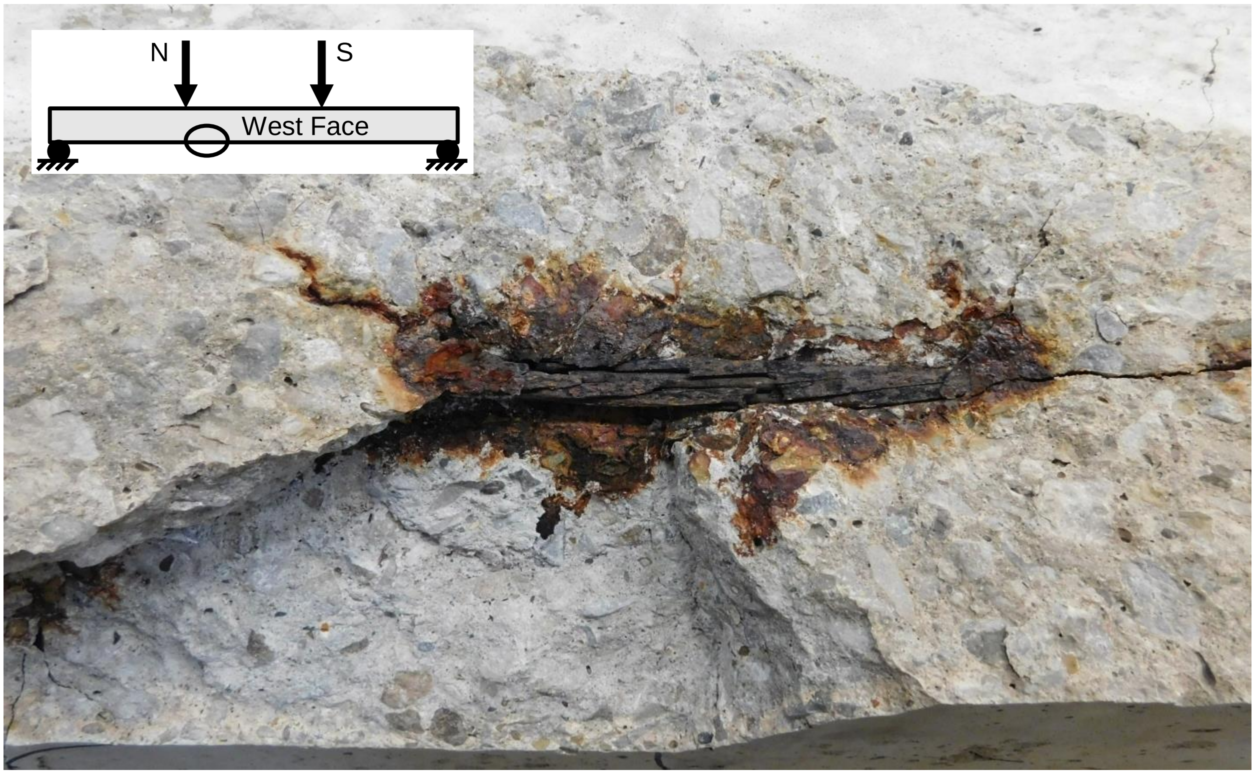

Figure 4.113: Concrete Spall at North Load Point at 3 in. of Midspan Deflection

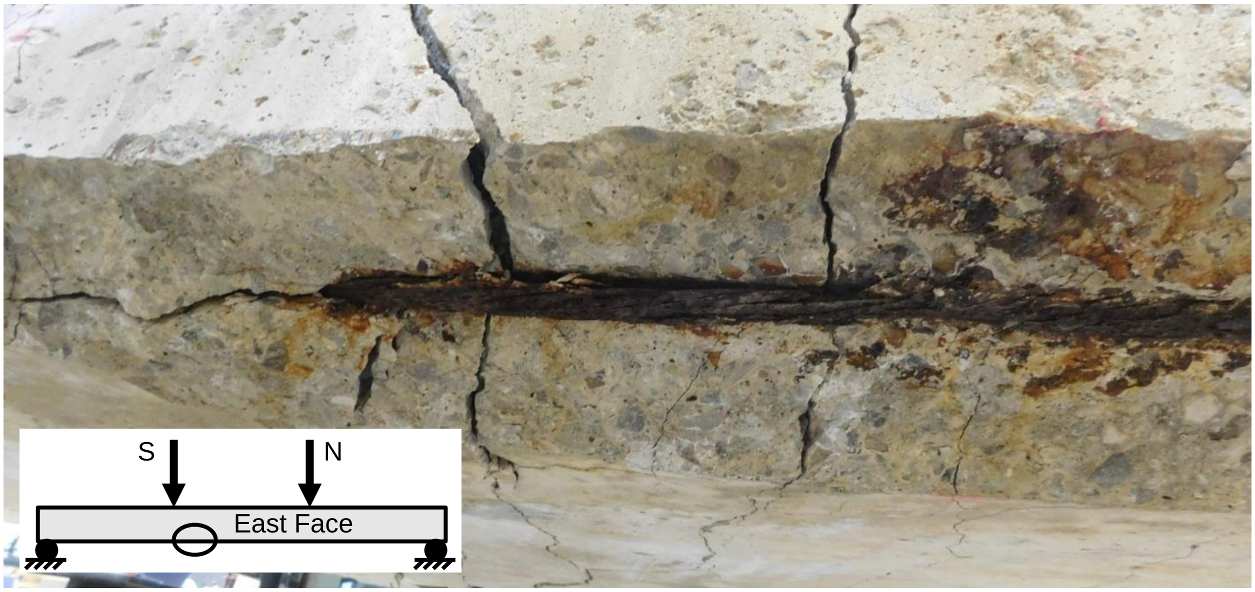

Figure 4.114: Concrete Spall at South Load Point at 6.7 in. of Midspan Deflection

When loading resumed, the measured force increased until, at 7.3 in. of midspan deflection, a loud pop was heard near the south load point, and the measured force decreased by 2.7 kips. As loading continued, the concrete in the top flange at the south load point began to crush (Figure 4.115). At 8.0 in. of midspan deflection, another loud pop was heard near the south load point, and the measured force decreased by 3.8 kips. As loading continued, concrete crushing intensified. At 8.5 in. of midspan deflection, a loud pop was heard, and the measured force decreased by 3 kips. At a midspan deflection of 9.0 in., the stroke limit of the hydraulic jacks was reached, and the test was concluded (Figure 4.116).

Figure 4.115: Concrete Crushing at South Load Point

Figure 4.116: Specimen 102-4-BS at Maximum Deflection of 9.0 in.

After failure, the corroded strands at the north and south load points were inspected. The corroded strands at the north load point were observed with heavy pitting and major section loss. On the east side of the bottom flange, the exposed strand adjacent to the broken strand was observed to have wire fractures along the length of the strand (Figure 4.117). No bright steel was observed at the interface of the wire fractures indicating that the strand was broken prior to testing. The same observation was made during inspection of the strand on the west side of the bottom flange (the strand exposed at a midspan deflection of 3 in. (Figure 4.113)). Based on these observations, three strands near the north load point were assumed to be broken prior to testing.

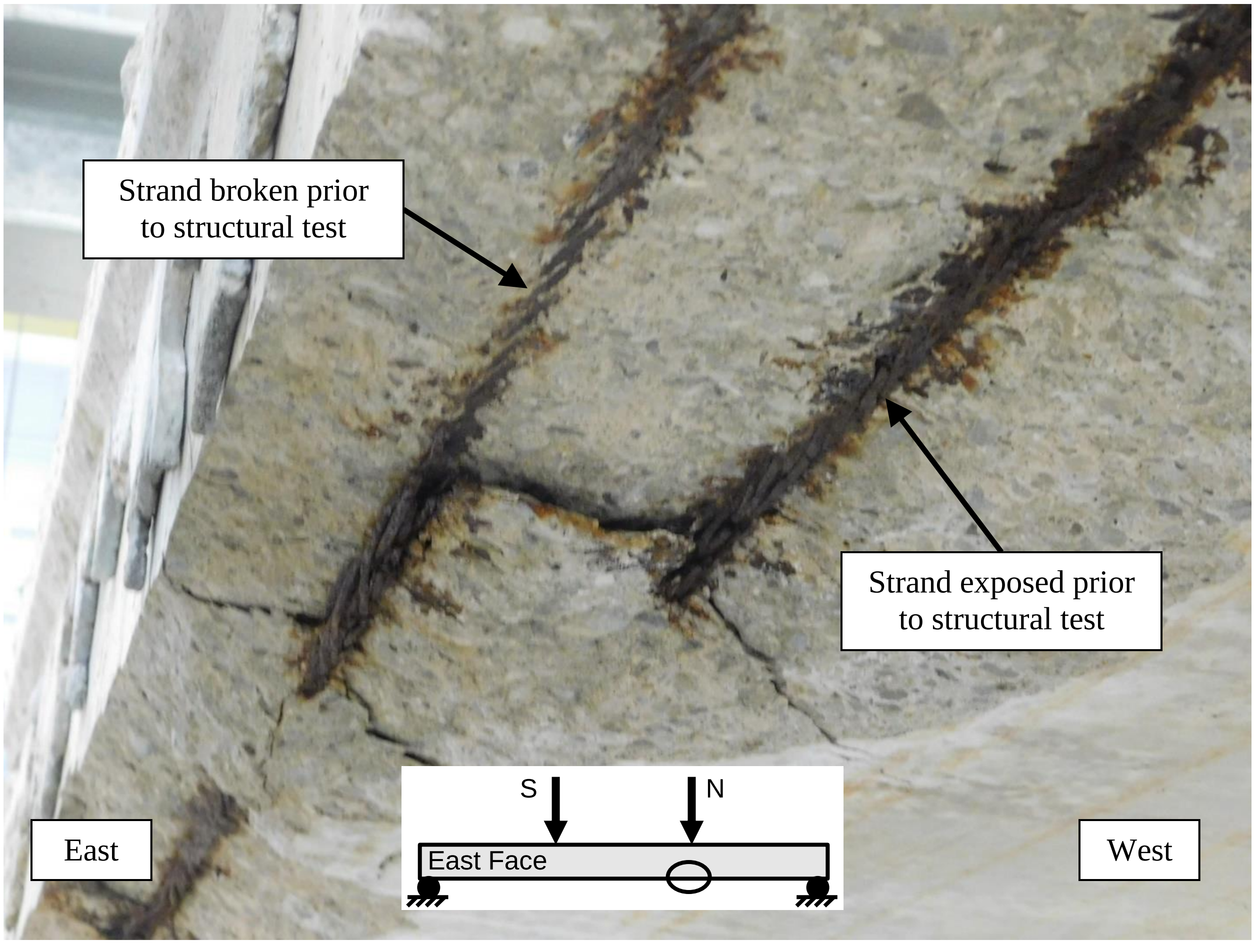

Figure 4.117: Existing Exposed and Broken Strand Near North Load Point After Test

Failure of the specimen, however, occurred at the south load point. Further investigation of the strands near the south load point revealed four strands with pitting corrosion (Section 3.4.1.6). Two strands on the west side (the exposed strand and the adjacent strand (Strands 1 and 2 in Figure 3.46)), and two strands on the east side (the exposed strand and the strand at the longitudinal crack (Strands 9 and 12 in Figure 3.41)). The strands on the west side (Strands 1 and 2) were noted to have bright steel at the fracture interface, as shown in Figure 4.118. The fracture interfaces of the exposed strand on the east side (Strand 12) were observed to be corroded indicating that wire fractures occurred prior to testing. The strand at the longitudinal crack on the east side (Strand 9) was noted to have bright steel at the wire fracture interfaces indicating that the fractures occurred during testing.

The observations of the corroded strands near the north and south load points indicate that three strands near the north load point were ineffective prior to testing. After failure, three of the four strands near the south load point were observed with pitting and indications that wire fractures occurred during testing. Based on these observations, the initial stiffness of the beam was assumed to be controlled by the weak section near the north load point. As testing commenced, the corroded strands near the south load point began to fracture and ultimately controlled the failure mode of the specimen.

Figure 4.118: Example of Bright Steel at Fracture Interface of Corroded Strand

4.5.16 Summary of Test Results

The maximum applied force P_{test}, applied force corresponding to the cracking moment P_{cr}, the cracking moment M_{cr}, midspan deflection at maximum force Δ_{mid}, and failure mode of each beam specimen are summarized in Table 4.16. The cracking moment was calculated by multiplying the value of P_{cr} by L_v (Table 4.14) corresponding to each specimen. The test span is also provided for reference.

Table 4.16: Summary of Structural Test Results

Specimen ID	P_{test} (kip)	P_{cr} (kip)	M_{cr} (kip*in)	Δ_{mid} (in.)	Test Span	Failure mode
244-1-LC	49.4	35.0	5364	3.7	39 ft-6 in.	Concrete Crushing*
409-1-ES	51.6	34.5	6525	15.9	47 ft-6 in.	Strand Fracture
409-2-UD	50.3	33.0	6242	23.0		N/A†
K5-1-LC	68.9	39.0	5392	5.2	35 ft	Web Crushing‡
K5-2-LC	49.3	35.0	4830	3.5		Strand Fracture*
79-1-UD	49.2	25.0	3180	17.2	33 ft-2 in.	N/A†
79-2-UD	50.5	29.0	3063	11.0	25 ft-7 in.	Concrete Crushing
79-3-UD	46.7	28.0	2957	3.2		Concrete Crushing and Strand Fracture
79-4-LC	49.3	28.6	3020	5.1		Concrete Crushing and Strand Fracture
56-1-LC	56.0	26.5	2935	11.7	26 ft-5 in.	Strand Fracture
56-2-ES	37.7	23.5	3243	8.0	35 ft	Concrete Crushing*
102-1-BS	42.3	24.1	3231	7.6	32 ft-4 in.	Strand Fracture
102-2-BS	40.2	22.6	3030	11.0		Concrete Crushing
102-3-BS	29.4	21.9	2936	8.0		Strand Fracture
102-4-BS	36.2	20.0	2681	6.7		Strand Fracture

*Delaminated concrete was present at failure region.
†Test concluded because the deflection limit of the test setup was reached.
‡Concentrated load condition unlikely to occur under actual traffic loading, construction error in web thickness.

4.6 Analysis

A calculation sheet was developed in MathCAD to automate the calculations needed to estimate the load-deflection behavior of prestressed concrete beams. The sheet was used to analyze box beam sections and may also be used to analyze common bridge girder sections such as AASHTO girders, bulb-tees, and hybrid I-beams. The primary outputs of the calculation sheet include the moment-curvature relationship of the user-defined beam section and load-deflection response of the beam in four-point bending.

4.6.1 Material Models

4.6.1.1 Concrete Model

The measured compressive strength of cores taken from the beam specimens ranged from 6,000 psi to 16,000 psi. To approximate the compressive stress-strain relationship of concrete, the Hognestad concrete model (Hognestad 1951) and Thorenfeldt concrete model (Thorenfeldt et al. 1987) were considered. The Hognestad model (Equation 4-3) has been widely used in structural engineering to estimate the flexural capacity of reinforced concrete elements. Wight and MacGregor (2012), however, note that the Hognestad model is only applicable to concrete strengths up to 6,000 psi and recommend the use of the Thorenfeldt model (4-5) for concrete strengths up to 18,000 psi.

$$f_c = f_c^{`}\left[\frac{2\varepsilon_c}{\varepsilon_0} - \left(\frac{\varepsilon_c}{\varepsilon_0}\right)^2\right] \tag{4-3}$$

where:

ε_c	=	strain in concrete
ε_0	=	strain in concrete at peak stress (Eq. 4-4)
f_c	=	stress in concrete (psi)

f_c'	=	concrete compressive strength (psi)

$$\varepsilon_0 = 1.71\left(\frac{f_c'}{E_c}\right) \tag{4-4}$$

It should be noted that the value of ε_0 was determined by assuming Equation 4-3 intersects with the secant modulus (using E_c) at $0.5f_c'$.

$$f_c = 0.9f_c^{`}\left[\frac{n(\varepsilon_c/\varepsilon_0)}{n-1+(\varepsilon_c/\varepsilon_0)^{nk}}\right] \tag{4-5}$$

where:

ε_0	=	strain in concrete at peak stress, Eq. (4-6)
k	=	non-dimensional constant, Eq. (4-7)
n	=	non-dimensional constant, Eq. (4-8)

$$\varepsilon_0 = \frac{f_c'}{E_c}\left(\frac{n}{n-1}\right) \tag{4-6}$$

$$k = \left\{\begin{matrix} 1 & \dfrac{\varepsilon_c}{\varepsilon_0} < 1 \\ 0.67 + \dfrac{f_c'}{9000} & \dfrac{\varepsilon_c}{\varepsilon_0} > 1 \end{matrix}\right\} \tag{4-7}$$

$$n = 0.8 + \left(\frac{f_c'}{2500}\right) \tag{4-8}$$

A comparison between the two models for concrete strengths ranging from 4,000 psi to 16,000 psi is presented in Figure 4.119 with the Hognestad curves noted with an “H” and the Thorenfeldt curves noted with a “T”. As shown, the Thorenfeldt model assumes a stiffer response up to peak stress as compared to the Hognestad model. After peak stress, the Thorenfeldt model assumes a rapid decrease in stress with increasing strain, while the Hognestad model assumes a gradual decrease in stress until concrete crushes.

When the models were compared to the results of the compression tests, the Hognestad model provided the best representation of the results. Therefore, the Hognestad model was used in the analysis of the structural test results for the beam specimens.

The concrete modulus of elasticity, E_c (in psi) was calculated as $57{,}000\sqrt{f_c'}$ (ACI 318-14 Section 19.2.2), and the modulus of rupture, f_r (in psi) was assumed to be $7.5\sqrt{f_c'}$ (ACI 318-14 Section 19.2.4). The value of f_c' is in the units of psi for the calculation of E_c and f_r. The ultimate concrete strain was assumed as 0.003.

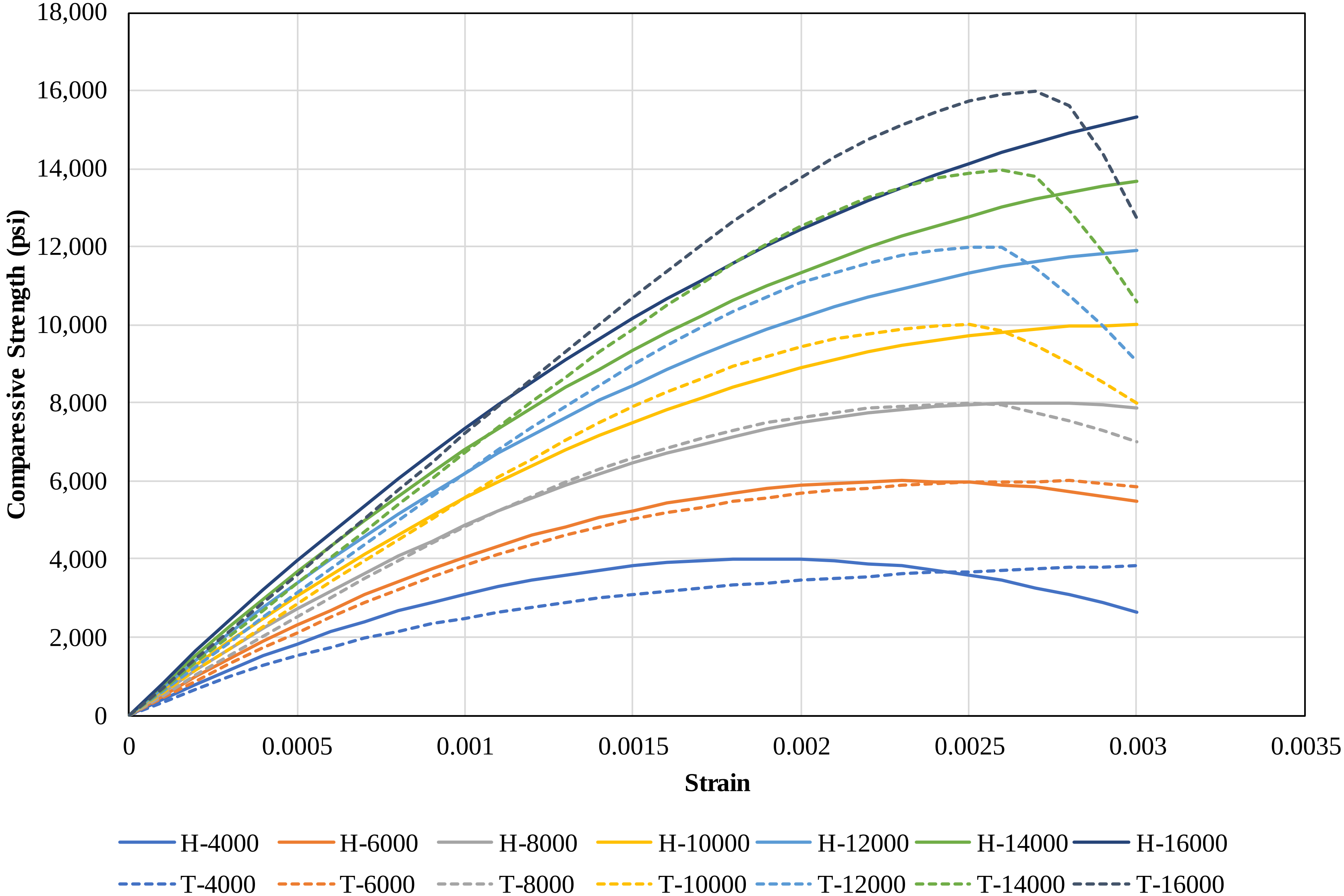

Figure 4.119: Concrete Model Comparison

4.6.1.2 Mild Steel Reinforcement Model

The mild steel reinforcement was modeled considering elastic, perfectly plastic behavior (Equation 4-9). The modulus of elasticity, E_s, was assumed to be 29,000,000 psi, and the fracture strain was assumed to be 0.10.

$$f_s = \begin{Bmatrix} \varepsilon_s E_s & \varepsilon_s \leq \varepsilon_y \\ f_y & \varepsilon_s > \varepsilon_y \end{Bmatrix} \tag{4-9}$$

where:

ε_s	=	strain in mild steel
ε_y	=	yield strain of mild steel, Eq. (4-10)
f_s	=	stress in mild steel (psi)
f_y	=	yield stress of mild steel (psi)

$$\varepsilon_y = \frac{f_y}{E_s} \tag{4-10}$$

4.6.1.3 Prestressing Steel Model

According to Mattock (1979), the tensile stress-strain response of prestressing strand may be approximated by Equation 4-11. This equation depends on two material constants, K and R, which may be determined from tension tests of prestressing strand or by using the assumptions outlined in Mattock (1979). Because strand from each specimen was tested, K and R could be determined from the test data. The values of K and R determined to provide the best representation of the test data are provided in Table 4.17 and illustrated in Appendix F. As shown, values of K = 1.04 and R = 7 provided the best fit of Equation 4-11 to the strand test data from most specimens. Notably, Specimen 79-2-UD, constructed after 1970, is the greatest outlier with K = 1 and R = 15.

Considering the available data, values of K = 1.04 and R = 7 are recommended for use when performing calculations for prestressed concrete structures constructed in or prior to 1970 (older prestressing steel stress-strain response) and values of K = 1 and R = 15 for structures constructed after 1970 (more modern prestressing steel stress-strain response).

$$f_{ps} = \varepsilon_{ps} E_{ps} \left\{ Q + \frac{1 - Q}{\left[1 + \left(\frac{\varepsilon_{ps} E_{ps}}{K f_{py}}\right)^{R}\right]^{1/R}} \right\} \qquad (4\text{-}11)$$

where:

ε_{ps}	=	strain in prestressing steel
E_{ps}	=	modulus of elasticity (psi)
f_{ps}	=	stress in prestressing steel (psi)
f_{py}	=	0.2% offset yield stress of prestressing steel (psi)
K	=	non-dimensional material constant
Q	=	non-dimensional constant (Eq. 4-12)
R	=	non-dimensional material constant

$$Q = \frac{f_{pu} - K f_{py}}{\varepsilon_{pu} E_{ps} - K f_{py}} \qquad (4\text{-}12)$$

where:

ε_{pu}	=	ultimate tensile strain of prestressing steel
f_{pu}	=	ultimate tensile strength of prestressing steel (psi)

Table 4.17: Material Constants for Equation 4-11

Specimen ID	K	R
244-1-LC	1.06	6
409-1-ES	1.04	7
409-2-UD	1.04	7
K5-1-LC	1.02	9
K5-2-LC	1.04	7
79-1-UD	1	7
79-2-UD	1	15
79-3-UD	1.04	7
79-4-LC	1.04	7
56-1-LC	1.04	7
56-2-ES	1.02	9
102-1-BS	1.04	7
102-2-BS	1.04	7
102-3-BS	1.04	7
102-4-BS	1.04	7

The PCI Design Handbook (2017) provides additional equations that are widely used in the design of prestressed concrete using Gr. 250 or Gr. 270 prestressing strand (Equation 4-13 and 4-14). These equations are much better suited to design calculations than Equation 4-11 but are not easily adapted to fit test data. Furthermore, this model is representative of modern stress-strain response of prestressing steel which has a reduced round-house behavior. It should be noted, if f_{pu} = 270,000 psi, K = 1.08, and R = 15, Equation 4-11 is nearly identical to the PCI expression for Gr. 270 strand (Figure 4.120). These constants are consistent with modern steel (produced after 1970 as previously noted and evident for Specimen 79-2-UD). Considering the flexibility of the strand material model presented by Mattock (1979), Equation 4-11 was used in all calculations. This model can be used for both older and modern strand.

Gr. 250 strand:

$$f_{ps}(ksi) = \begin{Bmatrix} 28{,}500\varepsilon_{ps} & \varepsilon_{ps} \leq 0.0076 \\ 250 - \dfrac{0.04}{\varepsilon_{ps} - 0.0064} & \varepsilon_{ps} > 0.0076 \end{Bmatrix} \tag{4-13}$$

Gr. 270 strand

$$f_{ps}(ksi) = \begin{Bmatrix} 28{,}500\varepsilon_{ps} & \varepsilon_{ps} \leq 0.0085 \\ 270 - \dfrac{0.04}{\varepsilon_{ps} - 0.007} & \varepsilon_{ps} > 0.0085 \end{Bmatrix} \tag{4-14}$$

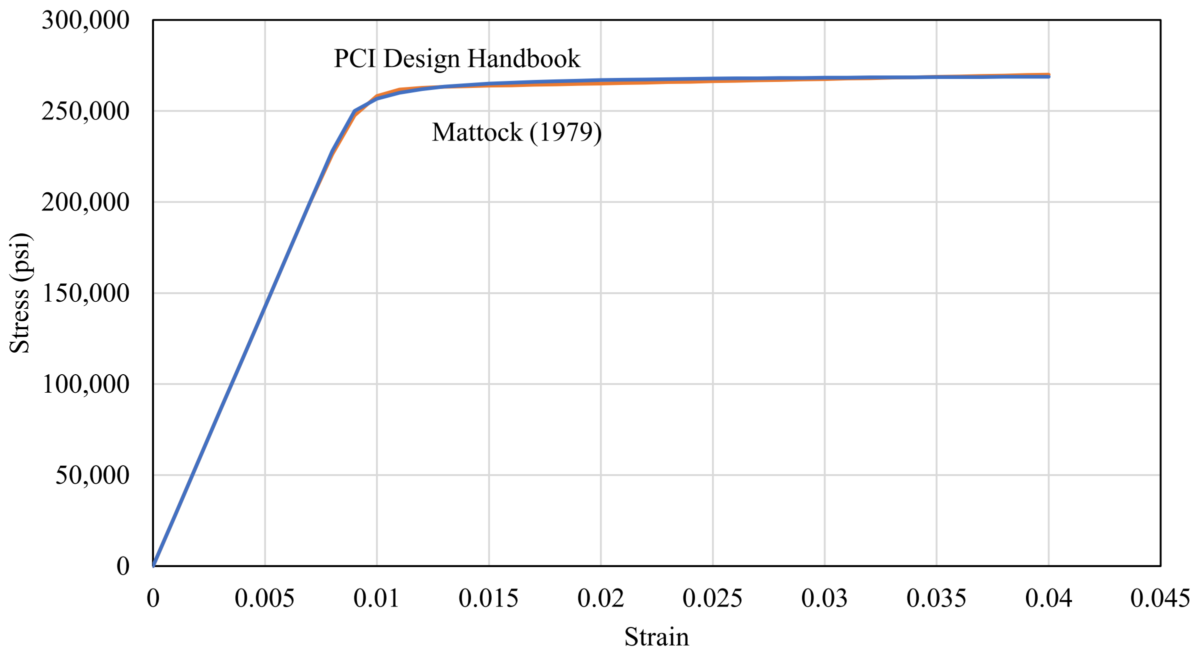

Figure 4.120: Stress-Strain Comparison for Gr. 270 Prestressing Strand

4.6.2 Moment-Curvature

Moment-curvature analysis was conducted in two stages. The first stage considered an uncracked concrete section and calculated moment-curvature assuming elastic behavior of the concrete. For the uncracked section analysis, gross section properties were assumed. The first stage of analysis was carried out from zero applied moment to first cracking. The moment corresponding to first cracking was defined as the moment at which the stress in the extreme fiber in tension was equal to the modulus of rupture, f_r ($7.5\sqrt{f_c'}$).

The second stage of analysis considered a cracked concrete section and nonlinear material response defined by the assumed material models. The cracked section analysis relied on equilibrium of internal forces and the assumption that plane sections remain plane to calculate the moment and curvature associated with a defined extreme fiber compressive strain (Figure 4.121). The calculation procedure began by computing the strain in the extreme fiber in compression at cracking. A trial value of the depth of the neutral axis (N.A.) was then selected. Using the extreme fiber compression strain and trial neutral axis depth, the strain in the reinforcing steel was determined, and the resultant compression and tension forces were calculated. If the resultant forces were in equilibrium within ± 1 kip, the corresponding moment and curvature values were calculated and stored. If the resultant forces were not equilibrium, the depth of the neutral axis was adjusted until equilibrium was satisfied. This calculation procedure was repeated for incremental increases (0.0001) in the extreme fiber compression strain from the strain at cracking to an ultimate strain of 0.003.

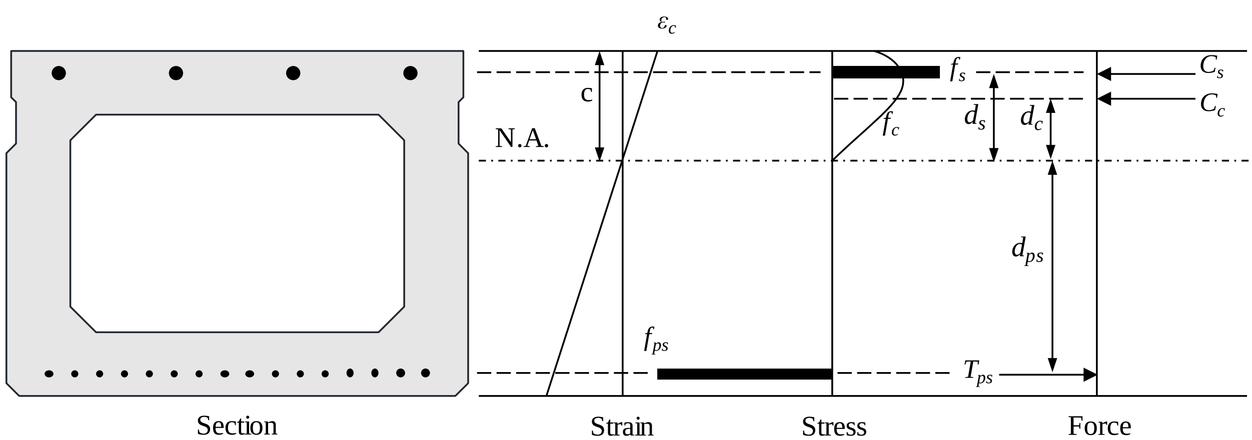

Figure 4.121: Cracked Section Analysis Diagram

To calculate the moment corresponding to a given extreme fiber compressive strain, the internal resultant forces were multiplied by the distance from the internal force to the neutral axis (Equation 4-15). The value of curvature was determined using Equation 4-16.

$$M = C_s(d_s') + C_c(d_c) + T_{ps}\left(d_{ps}\right) + T_s(d_s) \qquad \text{(4-15)}$$

where:

C_c	=	resultant compression force in concrete (kip)
C_s	=	resultant compression force in mild steel (kip)
d_c	=	distance from neutral axis to concrete force (in.)
d_s	=	distance from neutral axis to mild steel in compression (in.)
d_{ps}	=	distance from neutral axis to prestressing steel force (in.)
d_s	=	distance from neutral axis to mild steel in tension (in.)
M	=	moment (kip*in)
T_{ps}	=	resultant tensile force in prestressing steel (kip)
T_s	=	resultant tensile force in mild steel, if any provided (kip)

$$\phi = \frac{\varepsilon_c}{c} \qquad \text{(4-16)}$$

where:

ε_c	=	extreme fiber compressive strain
ϕ	=	curvature (1/in.)
c	=	distance from extreme fiber in compression to neutral axis (in.)

4.6.2.1 Consideration of Concrete Curbs

In some cases, it was necessary to include terms for a concrete curb acting compositely with the box beam section. The curb was located off to one side of the beam creating a section with no lines of symmetry. According to Wight and MacGregor (2012), the lack symmetry causes the neutral axis to be inclined relative to the horizontal in order to keep the location of the resultant internal forces in the plane of loading (Figure 4.122). An experimental study conducted by Kasan and Harries (2013) on a prestressed concrete box beam provided experimental verification of the behavior described by Wight and MacGregor. The result of asymmetry only applied to the beams tested in the laboratory because they were free to deflect vertically and laterally. Box beams in-service are braced by adjacent beams that prevent lateral deflection. Therefore, the following analysis does not apply to in-service beams with curbs.

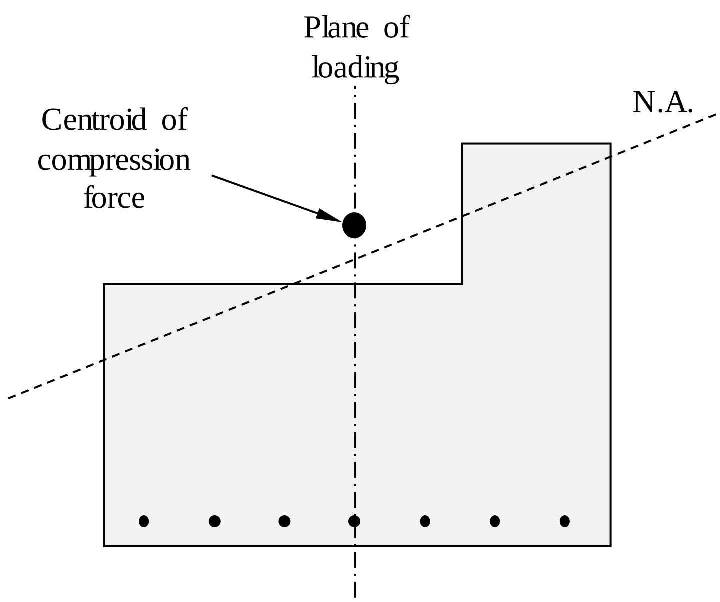

Figure 4.122: Unsymmetrical Beam Section

The analysis used by Kasan and Harries (2013) was carried out using a commercial analysis software. To consider a section bending about an inclined neutral axis using a simple spreadsheet capable of iterative calculations, a series of simplifying assumptions were made. First, a uniform compressive stress equal to $0.85f_c'$ was assumed over the region in compression. Second, the contribution from the steel in the curb and top flange was ignored. Using these two assumptions, the area of concrete in compression, A_c, was calculated for stress in the strands equal to f_{pu} (Equation 4-17).

$$A_c = \frac{A_{ps}f_{pu}}{0.85f_c'} \tag{4-17}$$

where:

A_c = area of concrete in compression (in.^{2})

A_{ps} = area of prestressing steel (in.^{2})

The inclined neutral axis results in an area of compression that is divided into two portions, one at the curb and one at the opposite upper corner of the top flange (Figure 4.123(a)). To determine the location of the resultant compression force, the two areas were proportioned such that the centroid of the total area, A_c, aligns with the plane of loading (Figure 4.123(a)). Once the areas have been proportioned, the distance, c_1, from the top of the curb to the resultant compression force is known.

If the neutral axis is assumed to be horizontal (Figure 4.123(b)), the distance, c_2, from the extreme fiber in compression (top of the curb) to the resultant compression force may be calculated using the cracked section analysis presented previously assuming that the extreme fiber compression strain is 0.003. The distance c_1 will be larger than c_2 due to the inclined neutral axis (Figure 4.123).

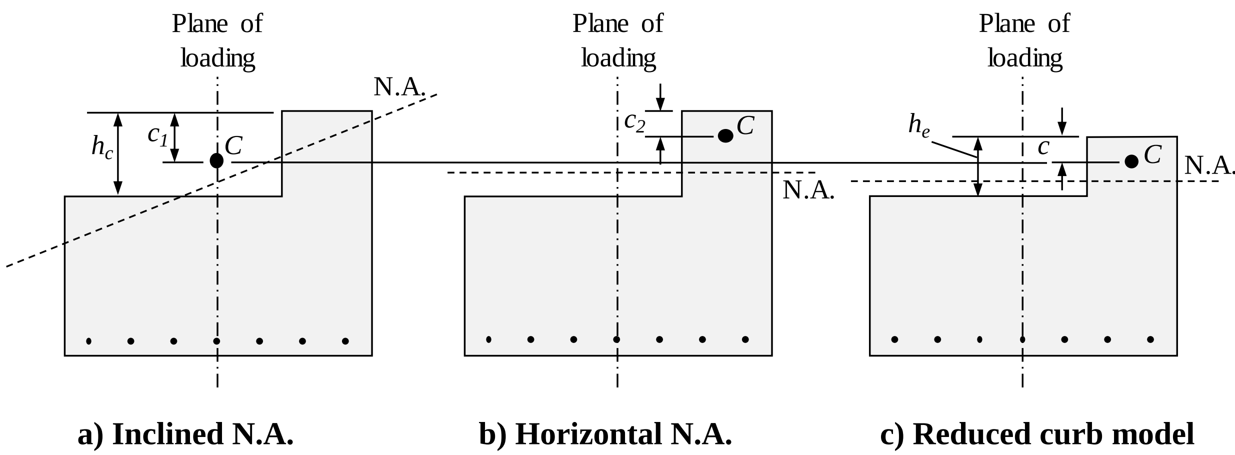

Figure 4.123: Comparison between c_1 and c_2

To analyze the box beam sections with curbs assuming a horizontal neutral axis, the curb height was reduced by the difference between c_1 and c_2 to account for the reduced moment arm resulting from the inclined neutral axis. The effective height of the curb, h_e, was calculated using Equation 4-18.

$$h_e = h_c - (c_1 - c_2) \tag{4-18}$$

One pitfall of this simple analysis is that the strain in the strands is underestimated for strands located on the curbside of the plane of loading and overestimated for strands on the opposite side of the plane of loading (Figure 4.123). This error is due to the assumption of a horizontal neutral axis where the perpendicular distance from the horizontal neutral axis is the same to all strands in a given row of strands. For an inclined neutral axis, the perpendicular distance from the inclined neutral axis to the strand varies for all strands in a given row of strands. For calculation of the ultimate resisting moment of a section, the average of the tensile forces in the strands for the inclined neutral axis is approximately the same as the tensile force in the strands for the horizontal axis. Because the moment arm between the resultant tension and compression forces are approximately equal, the analysis provides a reasonable estimate of the ultimate moment capacity.

4.6.3 Load-Deflection

The load-deflection response of a beam in four-point bending (Figure 4.124) was estimated for comparison with measured forces and deflections. The estimation of midspan deflection, δ_{mid}, for a given load, P, was calculated using the second moment-area theorem (Hibbeler, 2012) (Equation 4-19).

$$\delta_{mid} = \int_0^{L/2} \phi(x) * \bar{x} dx \qquad (4\text{-}19)$$

where:

δ_{mid}	=	midspan deflection (in.)
$\phi(x)$	=	curvature at a distance x from the support (1/in.)
L	=	distance between supports (in.)
x	=	ordinate parallel to the length of the beam (in.)
$\bar{x}$	=	distance from the support to the centroid of the area under the curvature diagram between the support and midspan

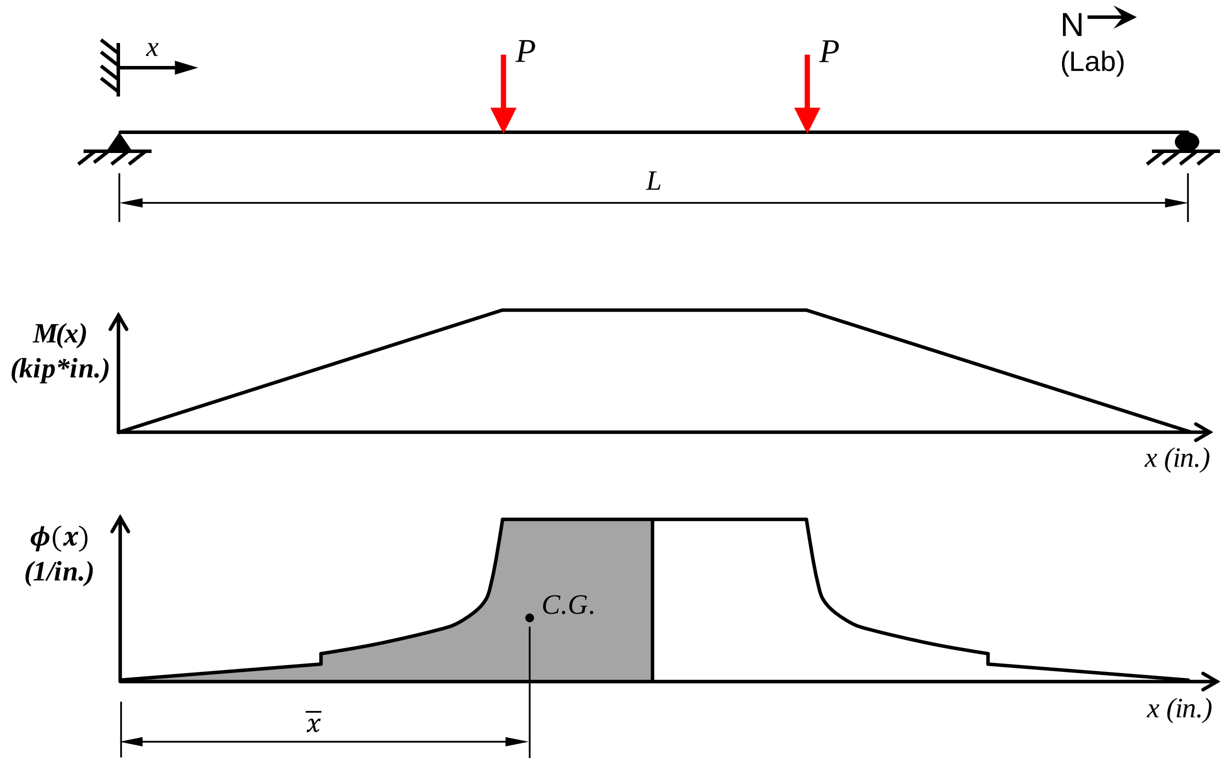

Figure 4.124: Four-Point Bending Loading, Moment, and Curvature Diagrams

4.6.3.1 Accounting for Deterioration

The deflection calculation presented considers a single moment-curvature response based on a constant section. The deteriorated specimens in this study were not observed with uniform deterioration. For instance, a localized section may have a broken strand. While the entire beam could be modeled with this reduced stiffness, the strand is effective and providing stiffness across other regions. Therefore, only in a location of deterioration should a different moment-curvature relationship be used. This analysis considers a non-deteriorated moment-curvature relationship and deteriorated relationship in those regions. The deteriorated regions of each specimen then behave as weak sections which cause concentrated deformation (increased curvature) at the weak section. While exact locations of deterioration can be modeled, this adjustment was made by constructing the curvature diagram assuming the weak section is located at midspan over a length of $2h$, where h is the height of the beam section. The curvature was assumed to concentrate at midspan to simplify the calculation of deflections.

To construct the curvature diagram for a symmetric loading (Figure 4.125), the curvature from x equal zero to ($L/2 - h$) was assumed to correlate with the moment-curvature analysis of the undeteriorated beam section. The curvature from x equal ($L/2 - h$) to $L/2$ was assumed to correlate with the moment-curvature analysis of the deteriorated section. The resulting curvature diagram for a beam in four-point bending will have a jump in curvature for a length of $2h$ at midspan because, for the same value of moment, the deteriorated section will have larger curvature than the undeteriorated section.

Once the deteriorated curvature diagram was constructed, Equation 4-19 was used to estimate the midspan deflection of the deteriorated beam. Please note that for specimens with curbs, the overall height h was assumed to equal the height of the original section less the difference between the original curb height, h_c, and the effective curb height h_e, $h - (h_c - h_e)$.

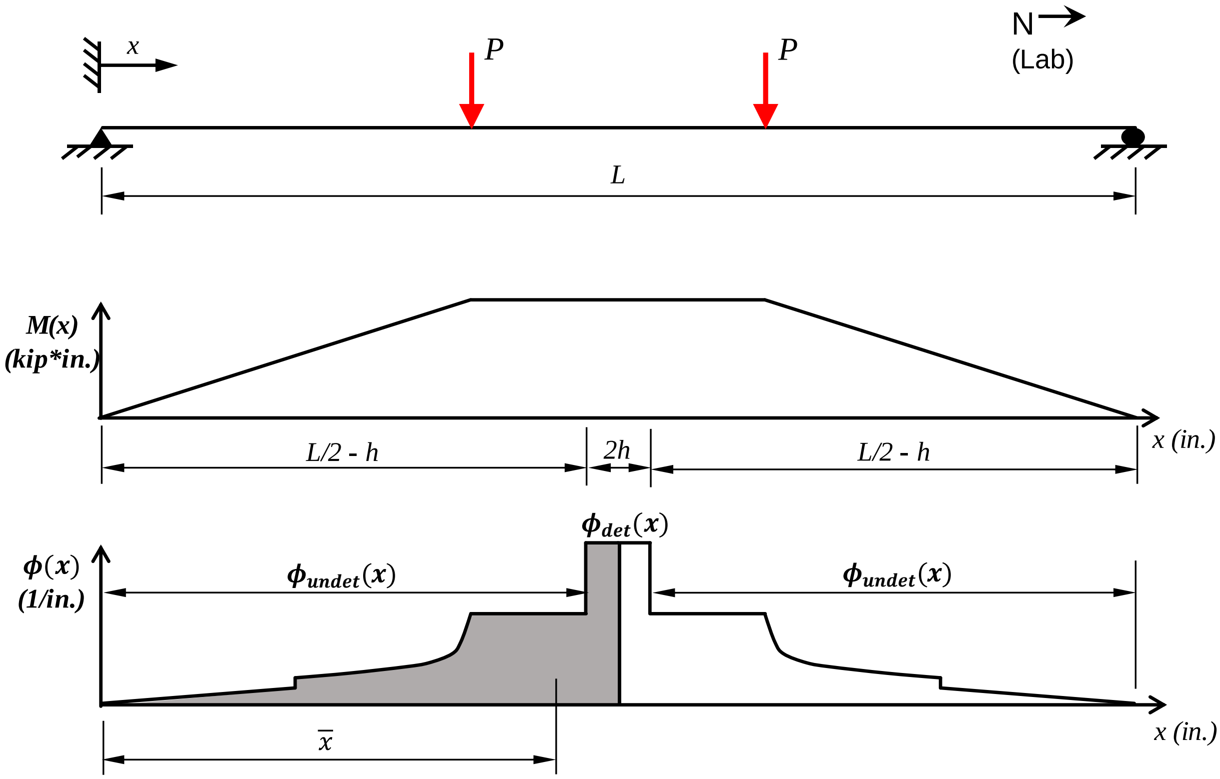

Figure 4.125: Curvature Diagram of a Deteriorated Beam

4.7 Analysis of Test Results

In the following sections, the structural test results of each specimen are compared to the load-deflection estimates made using the analysis discussed in Section 4.6. The load-deflection curves for each specimen include the test results and estimated behavior. The estimated behavior was calculated using two models: an analytical model and a refined model.

Both models use the geometrical properties of each specimen calculated from the as-built dimensions provided in Appendix D. In addition, the concrete strength of each specimen was assumed to be the average compressive strength presented in Table 4.4. For specimens with curbs, the average concrete strength of the curb was used. When cores were taken from the top flange of the beam, the average compressive strength of the flange cores was used (Specimens 244-1-LC and 56-2-ES). Self-weight was accounted for in the analysis assuming the total weight of each specimen to be uniformly distributed over the specimen's length. The weight of each specimen was determined by placing the specimens on three load cells (two on the north end and one on the south end) using an overhead crane and summing the readings of all three load cells (Table 4.18).

The analytical model used Equation 4-11 for the stress-strain response of strand with K = 1.04, R = 7, f_{pu} = 270 ksi, f_{py} = 243 ksi (0.9f_{pu}), E_{ps} = 27,500 ksi, and ε_{pu} = 0.04. The remaining prestress for each member was estimated using the PCI equations for prestress losses (PCI 2017) assuming the initial jacking stress was either 0.7*250 ksi or 0.7*270 ksi. For specimens constructed prior to 1967, the jacking stress was assumed to be 0.7*250 ksi because it was assumed that prior to 1967 all strands were considered Gr. 250. Specimens constructed after 1967 were assumed to have been jacked to 0.7*270 ksi. Table 4.18 provides a summary of the remaining prestress estimated for each specimen assuming either level of initial prestress. Please note that the remaining prestress used in the analytical model is indicated by bold typeface and underline.

The refined approach modeled the prestressing strand using Equation 4-11 with K and R taken from Table 4.17 for each specimen and the values of f_{pu}, f_{py}, E_{ps}, and ε_{pu} from the average values presented for each specimen in Table 4.6. Remaining prestress was calculated from the cracking moment corresponding to P_{cr} in Table 4.16 assuming the modulus of rupture was equal to $7.5\sqrt{f_c'}$. For Specimens 102-1-BS, 102-2-BS, 102-3-BS, and 102-4-BS, the remaining prestress was calculated assuming the broken strands prior to testing did not contribute to the overall prestress force. A single strand was discounted from remaining prestress calculations for Specimens 102-1-BS, 102-2-BS, and 102-3-BS. As discussed for Specimen 102-4-BS, three strands were believed to have been broken prior to testing. Therefore, three strands were discounted for the calculation of remaining prestress. The refined model was also used to estimate a second load-deflection curve for the deteriorated section (“Det”) of Specimens 102-1-BS, 102-2-BS, 102-3-BS and 102-4-BS.

A comparison of the measured and estimated values of remaining prestress shows that, overall, the PCI equations for prestress loss provided reasonable estimates of the remaining prestress. Considering the simplicity of the PCI equations and the resulting estimate of prestress losses, a more refined method, such as the AASHTO approach, was not considered. It should be noted that the lump sum losses suggested by Zia et al. (1979) was 50 ksi for stress-relieved steel. This corresponds to a remaining prestress of 125 ksi and 139 ksi for stress prior to release of 0.7*250 ksi and 0.7*270 ksi. Comparing the lump sum losses with the Table 4.18 values shows that the lump sum losses do not provide a lower bound to losses but do provide reasonable estimates of remaining stress without any calculation.

Table 4.18: Specimen Weight and Remaining Prestress

Specimen ID	Year Built	Total Weight (lb)	Remaining Prestress		
			PCI Estimate (ksi)†		Measured (ksi)
			0.7*250 ksi	0.7*270 ksi	
244-1-LC	1961	23,800	**141**	149	**135**
409-1-ES	1962	31,300	**147**	155	**162**
409-2-UD		31,300	**149**	157	**154**
K5-1-LC	1965	21,100	**141**	149	**113**
K5-2-LC		35,200	**151**	159	**109**
79-1-UD	1966	19,900	**147**	156	**123**
79-2-UD*		16,100	150	**158**	**137**
79-3-UD		14,500	**149**	158	**138**
79-4-LC		14,400	**151**	160	**121**
56-1-LC	1968	16,100	146	**154**	**88**
56-2-ES		16,400	143	**150**	**161**
102-1-BS	1970	20,000	141	**149**	**154**
102-2-BS		19,500	142	**150**	**136**
102-3-BS		19,800	142	**150**	**124**
102-4-BS		19,600	141	**149**	**153**

*Specimen 79-2-UD was a replacement beam. The year of construction is assumed to be after 1967.
†Bold plus underline indicates prestress used in analysis.

The load-deflection curves for each model was plotted up to one of two limiting values of strain. The first limit was 0.003 strain in the extreme fiber in compression which corresponds to concrete crushing failure. The second limit was 0.04 strain in the prestressing strand which corresponds to fracture of the strand. The load-deflection curves also include a hollow black circle that indicates the estimated load and deflection corresponding to the zero-tension stress in the extreme fiber in tension as calculated using the refined analysis.

Please note that the unloading and reloading portions of the experimental load-deflection data have been removed from the plots to facilitate comparison with the results of the analysis. In addition, a schematic beam in four-point bending is shown to illustrate the location and type of failure. The type of failure has been abbreviated as CC for concrete crushing, SF for strand fracture, WC for web crushing, and TC for test concluded due to deflection limitations.

4.7.1 Specimen 244-1-LC

The load-deflection curves for Specimen 244-1-LC are provided in Figure 4.126. As shown, the estimated undeteriorated behavior for the analytical and refined models follow the test data until the test ended at a midspan deflection of 3.7 in. The black dot on the refined curve indicates the load and deflection corresponding to a strain in the extreme fiber in compression of 0.0009 and strain in the prestressing strands of 0.008. Considering that the concrete in the top flange was observed to be delaminated after the test (Figure 4.41), the low strain of 0.0009 suggests that the concrete could not achieve typical strain levels of 0.003. In fact, only one third of that value was obtained for the delaminated concrete.

Corroded strands were observed at the longitudinal cracks in the post-failure investigation, but as shown in the corroded strand tension tests, the strand extracted from midspan (Strand 5_{corr}) fractured at a strain of 0.012 which is greater than 0.008. As observed in the post-failure review, no strands fractured at specimen failure. This indicates that when the concrete crushed, the strain in the strands was not large enough to cause fracture of the corroded strands. If the concrete, however, would have been of better quality with improved strain capacity, fracture of the corroded strands was likely. To achieve the full stress-strain curve, the strand would need to achieve a strain of 0.032 (2.7 times the corroded strand capacity).

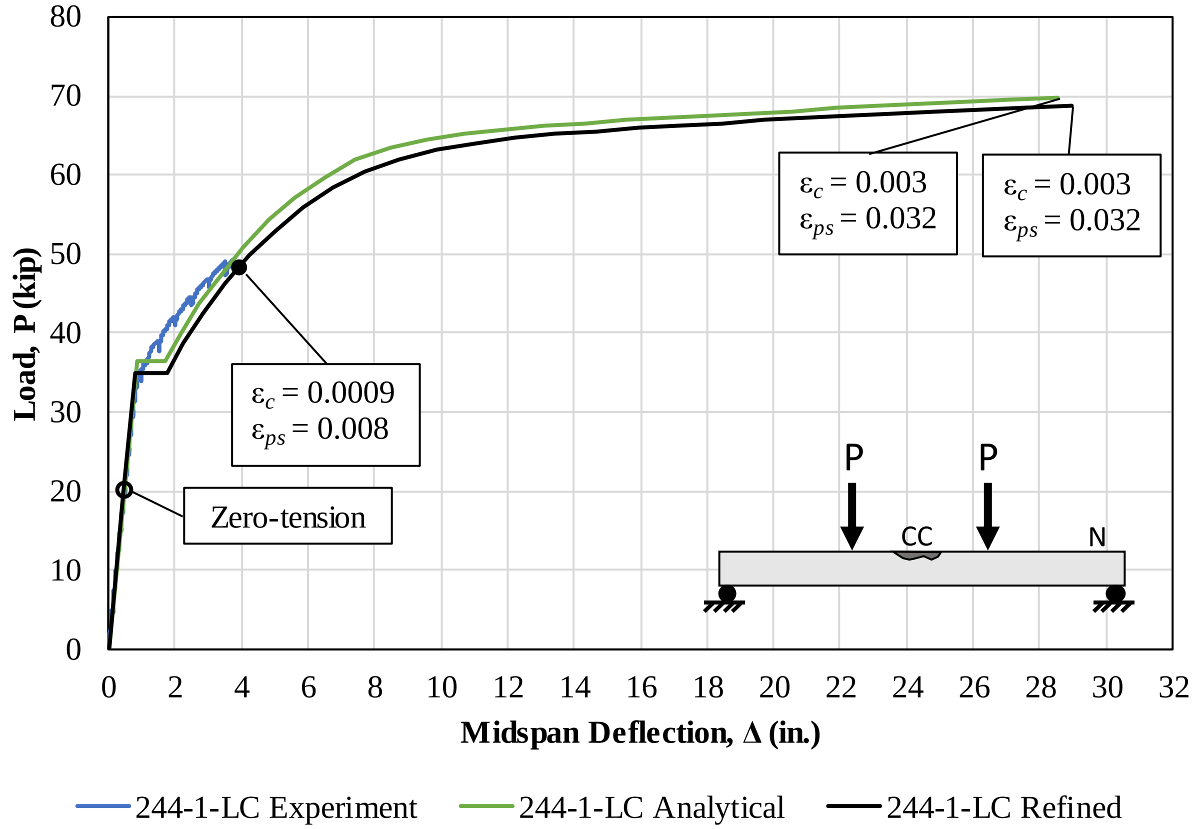

Figure 4.126: Specimen 244-1-LC Load vs. Deflection

4.7.2 Specimen 409-1-ES

The load-deflection curves for Specimen 409-1-ES are provided in Figure 4.127. The analysis was conducted assuming full composite action between the topping slab and beam. As shown in Figure 4.127, the estimated undeteriorated behavior of the analytical and refined models follow the test data until the test ended at a midspan deflection of 15.7 in. The hollow black circle on the refined curve indicates point of zero tension in the extreme fiber in tension at a load of 17.5 kips. The experimental curve does not deviate from initial stiffness until approximately 20 kips. This indicates that the remaining prestress in the section of 162 ksi was slightly underestimated using the cracking load and modulus of rupture of $7.5\sqrt{f_c'}$ (Table 4.18). The remaining stress estimated assuming the zero-tension point corresponds to 20 kips is 168 ksi.

The black dot on the refined curve indicates the load and deflection corresponding to a strain in the prestressing strands of 0.021 and an extreme fiber compressive strain of 0.0017. The low strain in the steel of 0.021 at fracture indicates that the surface corrosion observed during the post-failure review reduced the ductility of the strands. In addition, Strand Specimen 409-1-ES-1 (uncorroded) fractured at a strain of 0.024 (f_{pu} = 276.2 ksi, Table 4.6) and was observed with light surface rust (Figure 4.10). This indicates that very low levels of corrosion, due to the existing flexural cracks, influenced the ductility of the strand and compromised the overall ductility of the beam.

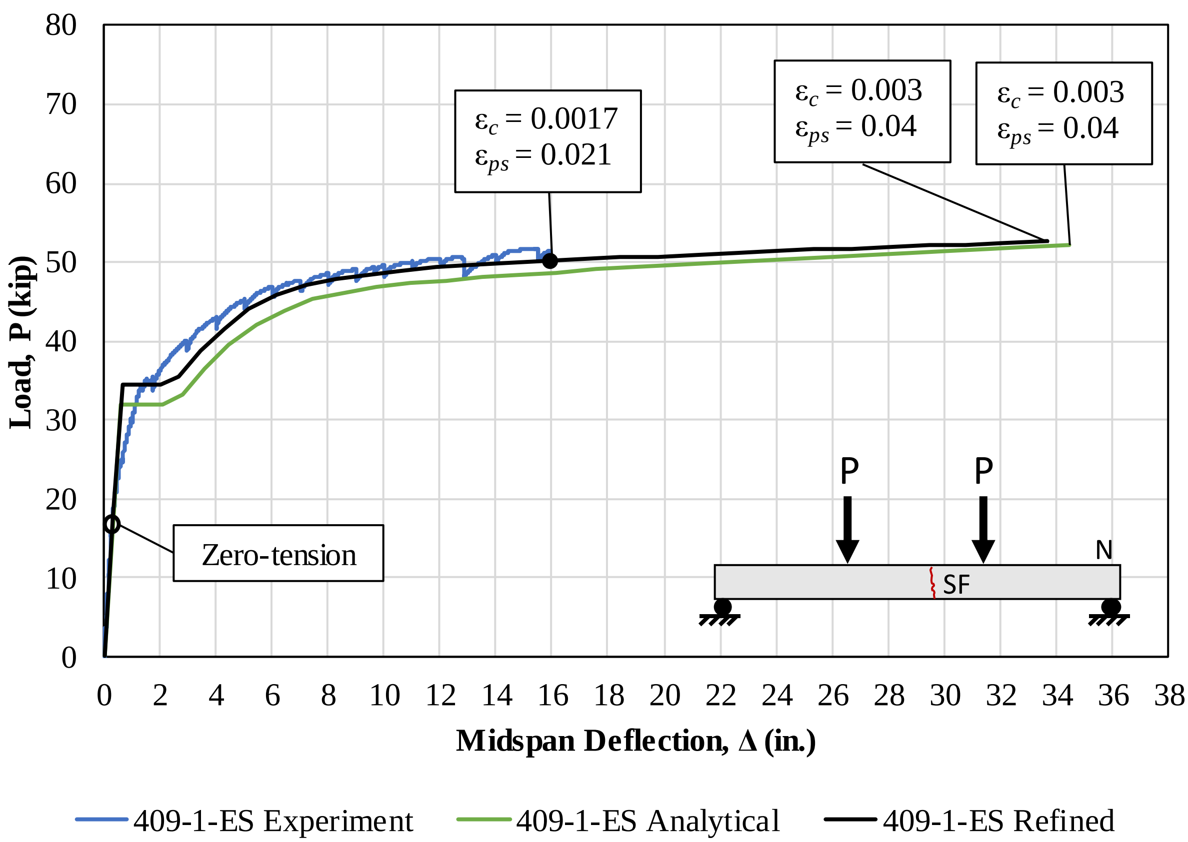

Figure 4.127: Specimen 409-1-ES Load vs. Deflection

4.7.3 Specimen 409-2-UD

The load-deflection curves for Specimen 409-2-UD are provided in Figure 4.128. The analysis was conducted assuming full composite action between the topping slab and beam. As shown in Figure 4.128, the estimated behavior of Specimen 409-2-UD follows the test data well until the test was concluded at a midspan deflection of 23 in. The hollow black circle indicates point of zero tension in the extreme fiber in tension at a load of 15.2 kips. The experimental curve does not deviate from initial stiffness until approximately 17 kips. This indicates that the remaining prestress in the section of 154 ksi was slightly underestimated using the cracking load and modulus of rupture of $7.5\sqrt{f_c'}$ (Table 4.18). The remaining stress estimated assuming the zero-tension point corresponds to 17 kips is 155 ksi.

The end of the calculated curves corresponds to a strain in the extreme compressive fiber of 0.003 and a strain in the strands of 0.04. The strain at peak stress for the cores from Specimen 409-2-UD was measured as high as 0.0032 (Table 4.4), and the average strain at fracture for the strands was 0.058 (Table 4.6). Considering the data, the lack of observed distress in the concrete and strands at 23 in. of midspan deflection is understood. This specimen fully achieved its capacity and was capable of achieving the full assumed concrete and steel strain levels.

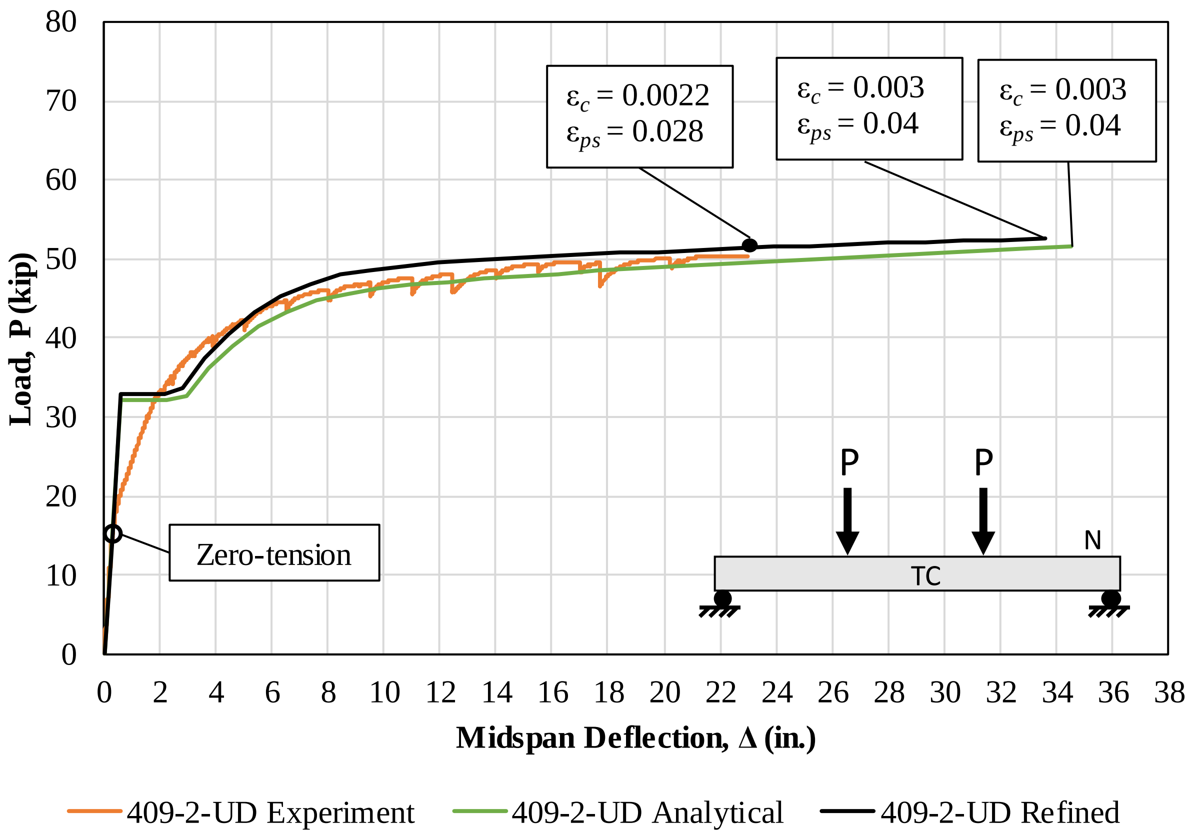

Figure 4.128: Specimen 409-2-UD Load vs. Deflection

Specimens 409-1-ES and 409-2-UD were constructed with the same cross-section and span. For comparison, the load-deflection data for Specimen 409-1-ES is plotted alongside the data for Specimen 409-2-UD in Figure 4.129. As shown, both specimens overall exhibited excellent behavior and achieved approximately the same ultimate load. The only effect of deterioration on Specimen 409-1-ES was that strand fracture was observed prior to the specimen achieving the same midspan deflection as Specimen 409-2-UD. The deterioration of Specimen 409-1-ES was located outside of the maximum moment region. In addition, the extent of strand corrosion did not affect the redevelopment of strand into the maximum moment region.

Considering the location and extent of the deterioration, the effect of the deterioration was minimal and could be neglected in load rating calculations. The presence of flexural cracks, however, did influence the ductility of the strands in Specimen 409-1-ES. Corrosion of these strands at the crack location was observed and likely led to the slight loss of full strain capacity. It should be noted that the presence of flexural cracks in Specimen 409-2-UD had no impact on strain capacity.

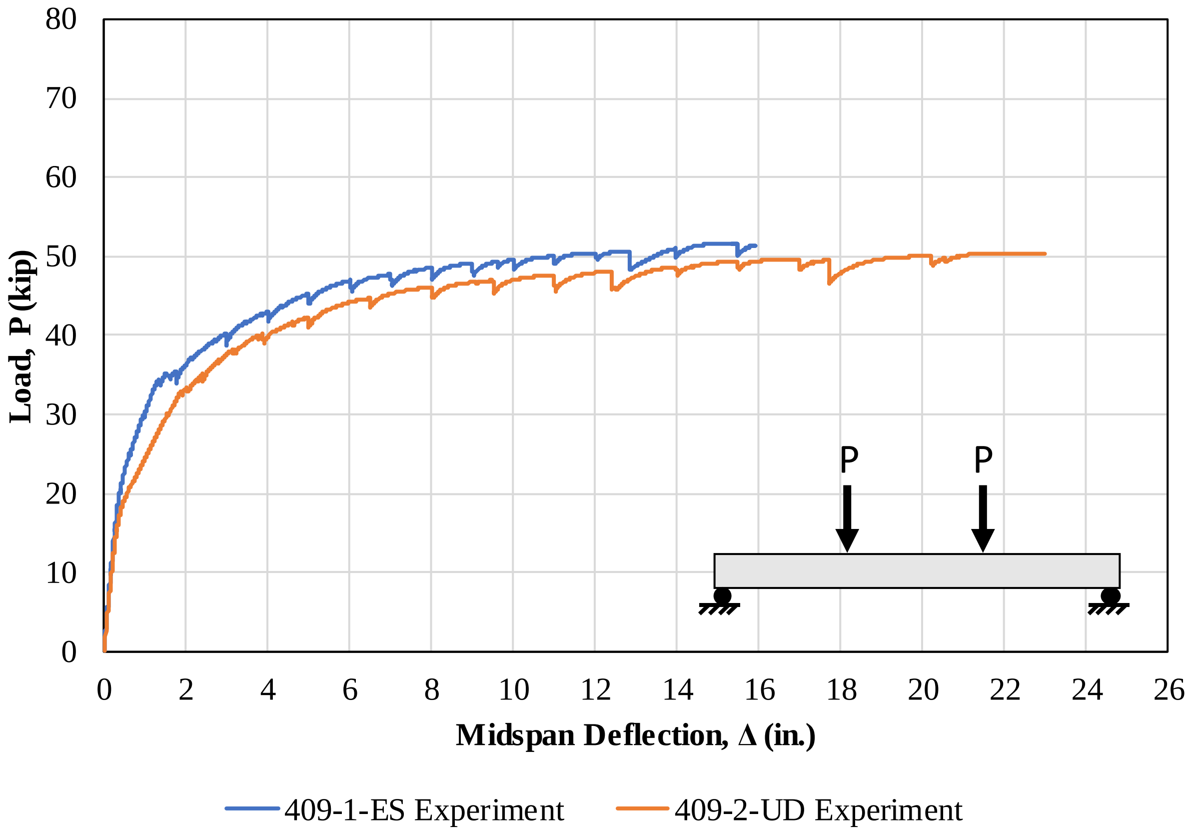

Figure 4.129: Specimen Comparison - 409-1-ES vs. 409-2-UD

4.7.4 Specimen K5-1-LC

The load-deflection curves for Specimen K5-1-LC are provided in Figure 4.130. This specimen included a curb which was modeled with the simplified method. As shown, the simplified curb analysis for undeteriorated behavior trends well with the test data. While the analysis considers flexural failure, this specimen failed due to web crushing. The localized web failure occurred very close to the ultimate capacity. Overall, this specimen can be considered to have achieved its full design capacity (strength). In general, the simplified analysis estimated the general trend of the load-deflection behavior well and the ultimate load (78 kips) within 14% of the load measured at failure.

Typically in design, the curb is not considered. Therefore, an analysis was conducted for the beam without a curb using the analytical model. As shown, the curb significantly increases the strength of the section. In addition, the overall deflection capacity is reduced.

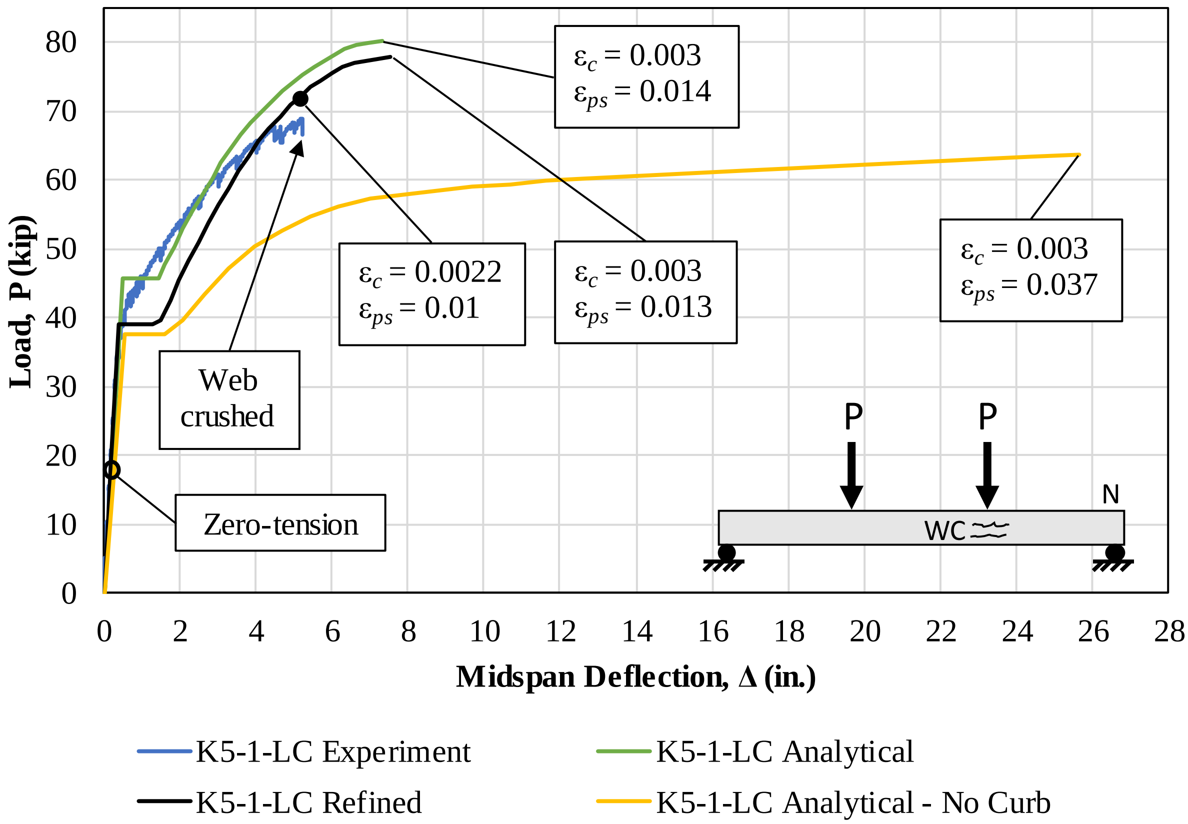

Figure 4.130: Specimen K5-1-LC Load vs. Deflection

4.7.5 Specimen K5-2-LC

The load-deflection curves for Specimen K5-2-LC are provided in Figure 4.131. As shown, the primary difference between the analytical and refined models was the estimated load at cracking. The difference was caused by the estimate of remaining prestress use in the analytical model. The remaining prestress in the beam was actually very low. It was calculated as only 109 ksi.

After cracking, the refined model curve shows a similar post-cracking stiffness as the test data up to a midspan deflection of 3.5 in. where the load decreases due to strand fractures. This indicates that all strands were engaged in resisting the applied moment at the onset of the test. As shown in Figure 4.131, the calculated strain in the steel at peak measured load was 0.01 which is within the range of strain at fracture for the corroded strands tested (Table 4.13). This is consistent with the observation that popping sounds (individual wire fractures) were heard prior to the load decrease at 3.5 in. of midspan deflection. In addition, the concrete strain estimated at peak load (0.0008) corresponds to crushing of the concrete observed just after the decrease in load observed during the test at 3.5 in. of midspan deflection. The estimated concrete strain at peak load (0.0008) is approximately the same as the strain in the concrete at crushing calculated for Specimen 244-1-LC (0.0009). While the concrete strain did not control failure for Specimen K5-2-LC, the repaired flange and delaminated concrete (Figure D.6) indicate that compression failure was likely if the strand would have had more strain capacity.

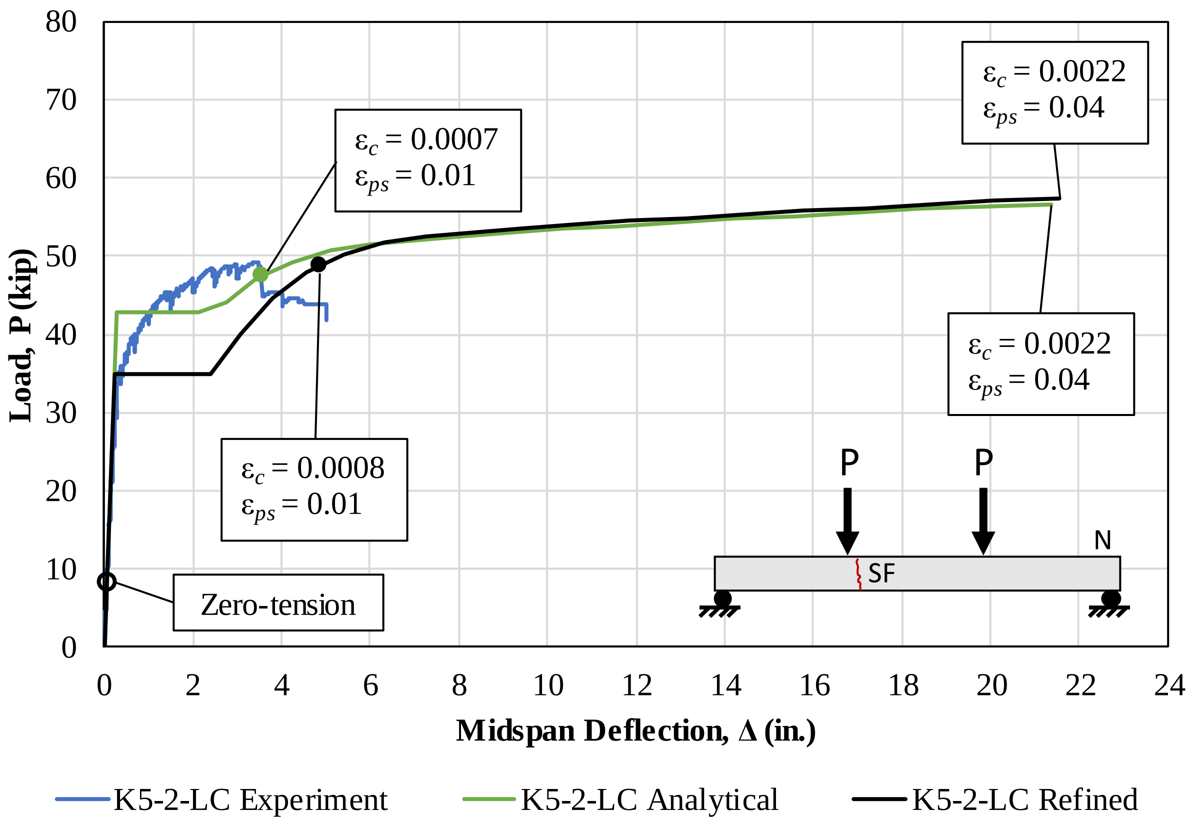

Figure 4.131: Specimen K5-2-LC Load vs. Deflection

Specimen K5-2-LC was observed with three longitudinal cracks meeting at a single section (Figure 3.5). Considering the results of the corroded strand tests, the capacity of the specimen was estimated using the refined model assuming that at a strain in the strands of 0.01, the corroded strands would fracture causing failure of the specimen. These assumptions resulted in an estimated capacity of 48.0 kips which is within 3% of the ultimate measured load of 49.3 kips and shown as a black dot on the refined curve in Figure 4.131. When the same assumptions were used with the analytical model, the estimated capacity was 47.2 kips which is within 5% of the ultimate measure load and shown as the green dot on the analytical curve in Figure 4.131.

4.7.6 Specimen 79-1-UD

The load-displacement curves for Specimen 79-1-UD are provided in Figure 4.132. As shown, the estimated curves for the undeteriorated section follow the test data up to a midspan deflection of 17.2 in. where the test was concluded. The black dot on the refined curve indicates the load and deflection corresponding to an extreme compressive fiber strain of 0.0022 and strain in the strands of 0.021. The last point on the calculated curves corresponds to an extreme compressive fiber strain of 0.003 and a strain in the strands of 0.032 for the analytical model and 0.031 for the refined model.

The compression test results for Specimen 79-1-UD indicated that, on average, the peak compressive stress occurred at a strain of 0.0028 (Table 4.4). Additionally, the average strain at fracture for the tested strands was 0.043 (Table 4.6). Therefore, the lack of concrete crushing and strand fracture at the end of the test is consistent. This specimen was capable of reaching its full capacity both in terms of strength and deformation.

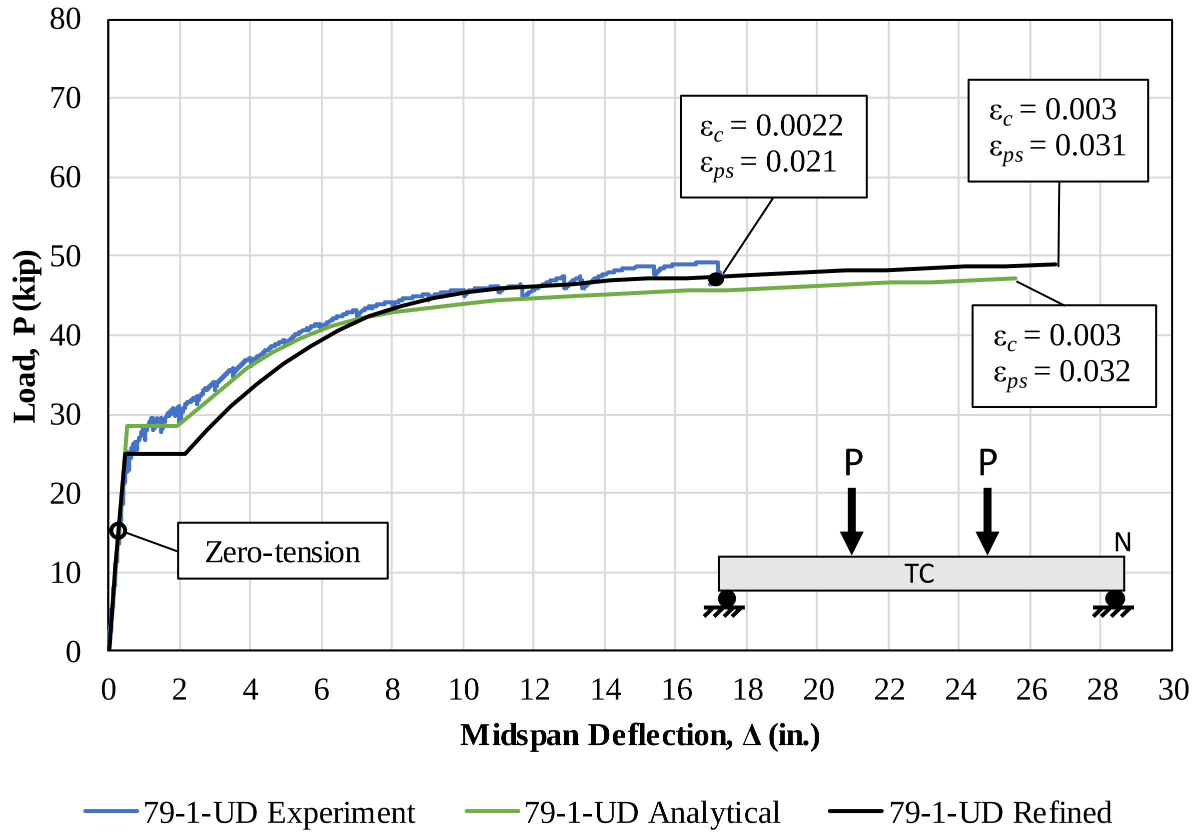

Figure 4.132: Specimen 79-1-UD Load vs. Deflection

4.7.7 Specimen 79-2-UD

The load-deflection curves for Specimen 79-2-UD are provided in Figure 4.133. As shown, the model curves for the undeteriorated section follow the test data up to a midspan deflection of 11.0 in. when the test ended in concrete crushing in the top flange. The black dot on the refined curve indicates the load and deflection corresponding to an extreme fiber compressive strain of 0.0023 and a strain in the strands of 0.025. The last point on the model curves corresponds to an extreme fiber compressive strain of 0.003 and a strain in the strands of 0.032 for the analytical model and 0.034 for the refined model. This specimen is considered to have reached its theoretical capacity.

The compression test results for Specimen 79-2-UD showed that, on average, the strain at peak stress was 0.0024 (Table 4.4), which is very close to the calculated extreme compression fiber strain. In addition, the average strain at fracture for the strands tested from Specimen 79-2-UD was 0.043 (Table 4.6), which is much higher than the estimated strain in the strands when the concrete reached peak stress. Therefore, the analysis matches the observation that the concrete crushed prior to strand fracture. Again, this specimen reached full capacity (strength and deformation).

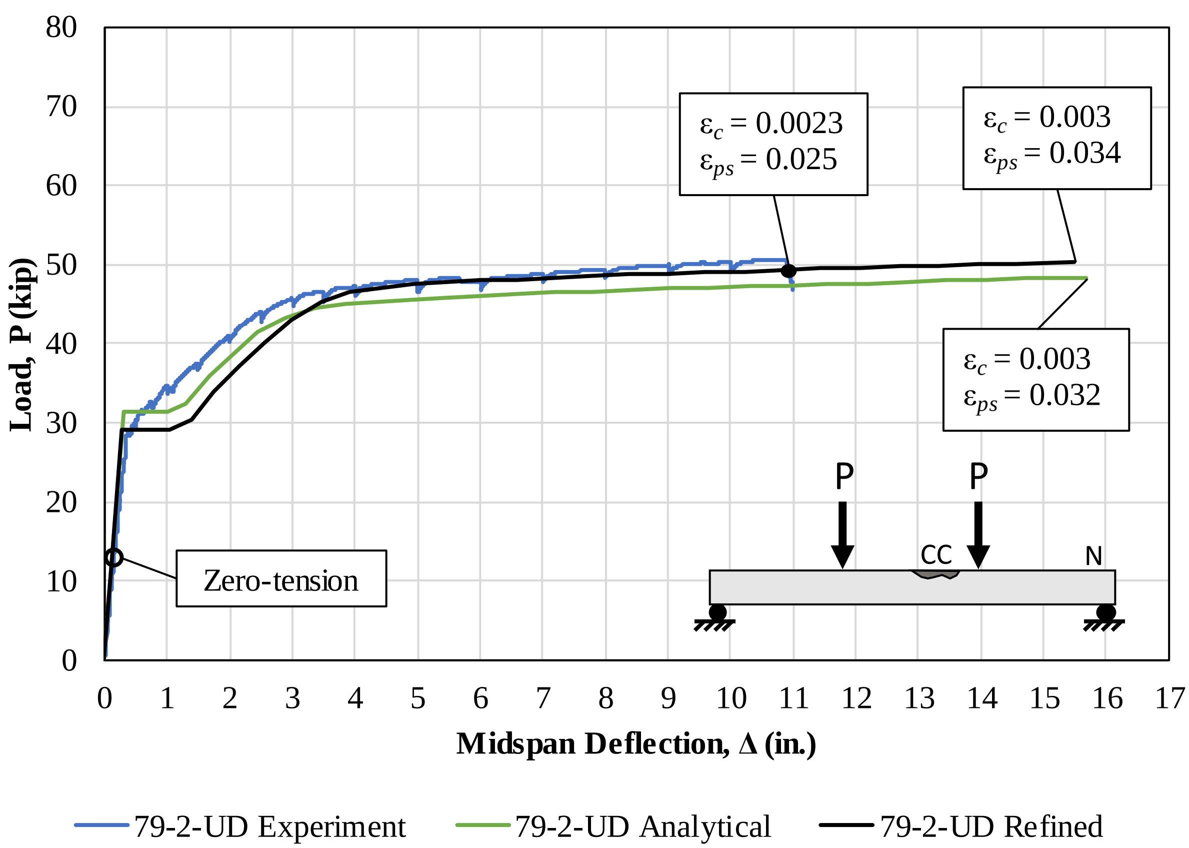

Figure 4.133: Specimen 79-2-UD Load vs. Deflection

4.7.8 Specimen 79-3-UD

The load-deflection curves for Specimen 79-3-UD are provided in Figure 4.134. This specimen included a curb which was modeled with the simplified method. As shown, the simplified curb analysis for both analysis models trends well with the test up to a midspan deflection of 3.2 in. when the concrete in the curb crushed. The black dot on the refined curve indicates the load and deflection corresponding to an extreme fiber compressive strain of 0.0019 and a strain in the strands of 0.011. The last point on the model curves corresponds to an extreme fiber compressive strain of 0.003 and a strain in the strands of 0.019 for the analytical model and 0.018 for the refined model.

The compression test results for the concretes cores from the curb of Specimen 79-3-UD showed that, on average, the strain at peak stress was 0.0027 (Table 4.4) which is higher than the estimated strain of 0.0019. This indicates that the piece of wood embedded in the curb (Figure 4.72) prevented the surrounding concrete from reaching its full strain capacity and caused premature concrete crushing in the curb of the specimen, resulting in reduced ductility of the specimen.

The ultimate load predicted by the simplified analysis was 52.1 kips which is within 12% of the actual peak load of 46.7 kips. The difference between the test result and analysis is assumed to be an effect of the embedded piece of wood.

For consistency with design practices, the capacity of the specimen was estimated using the analytical model assuming no curb. The resulting load-deformation response is shown in Figure 4.134 as the yellow curve (“Analytical - No Curb”). As shown, the curb increased the strength of the specimen by over 40% and significantly reduced the deflection capacity.

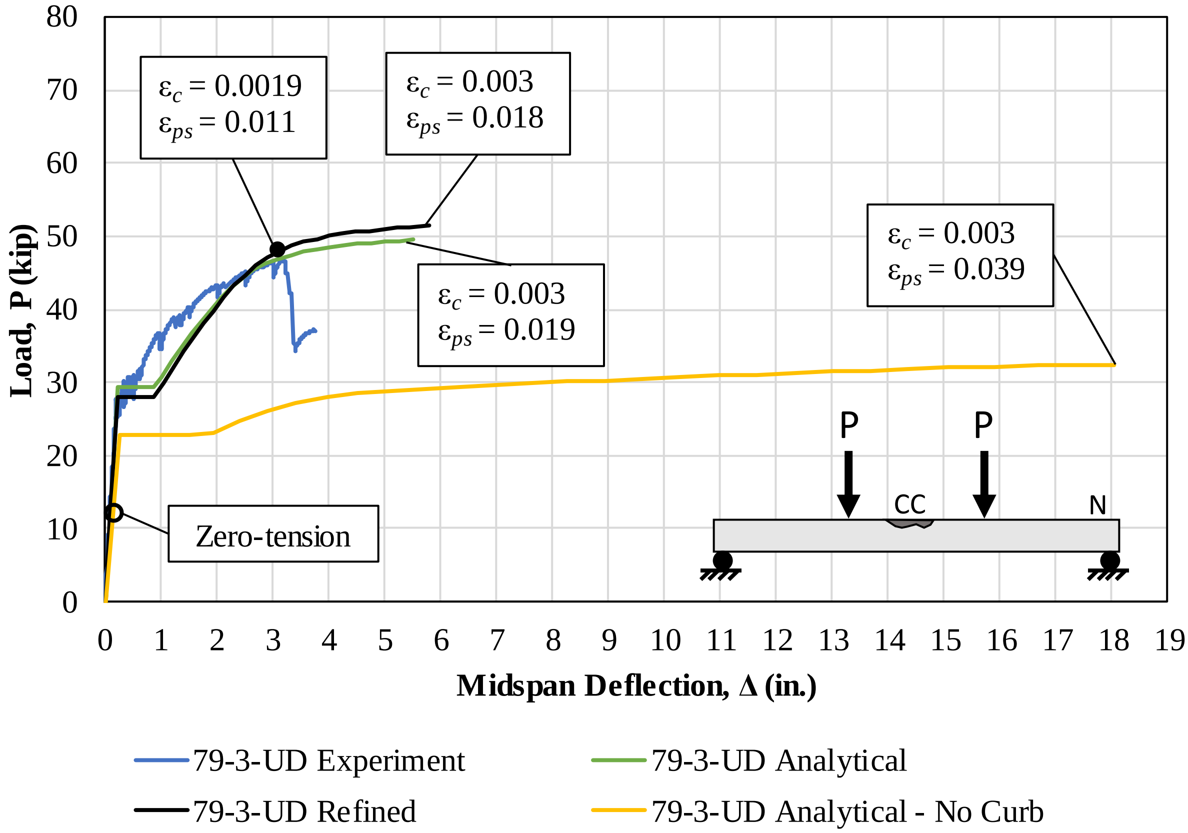

Figure 4.134: Specimen 79-3-UD Load vs. Deflection

4.7.9 Specimen 79-4-LC

The load-deflection curves for Specimen 79-4-LC are provided in Figure 4.136. This specimen included a curb which was modeled with the simplified method. As shown, the simplified curb analysis for both analysis models trends well with the test data up to the peak load measured at 5.1 in. of midspan deflection. The black dot on the refined curve indicates the load and deflection corresponding to an extreme fiber compressive strain of 0.0026 and a strain in the strands of 0.015. The last point on the model curves corresponds to an extreme fiber compressive strain of 0.003 and a strain in the strands of 0.019 for the analytical model and 0.02 for the refined model.

The compression test results for the concretes cores from the curb of Specimen 79-3-UD showed that, on average, the strain at peak stress was 0.0031 (Table 4.4) which is close to the estimated strain of 0.0026. In addition, the average strain at fracture for the strands tested from Specimen 79-4-LC was 0.058 (Table 4.6), which is much higher than the estimated strain in the strands of 0.019 when the concrete reached a strain of 0.0026. This indicates that the observed failure mode of concrete crushing is consistent with the analysis models.

The ultimate load estimated by the simplified analysis was 50.8 kips which agrees very well with the peak measured load of 49.3 kips (within 3%).

For consistency with design practices, the capacity of the specimen was also estimated using the analytical model assuming no curb. The resulting load-deformation response is shown in Figure 4.135 as the yellow curve ("Analytical - No Curb"). As shown, the curb increased the strength of the specimen by over 50% and significantly reduced the deflection capacity.

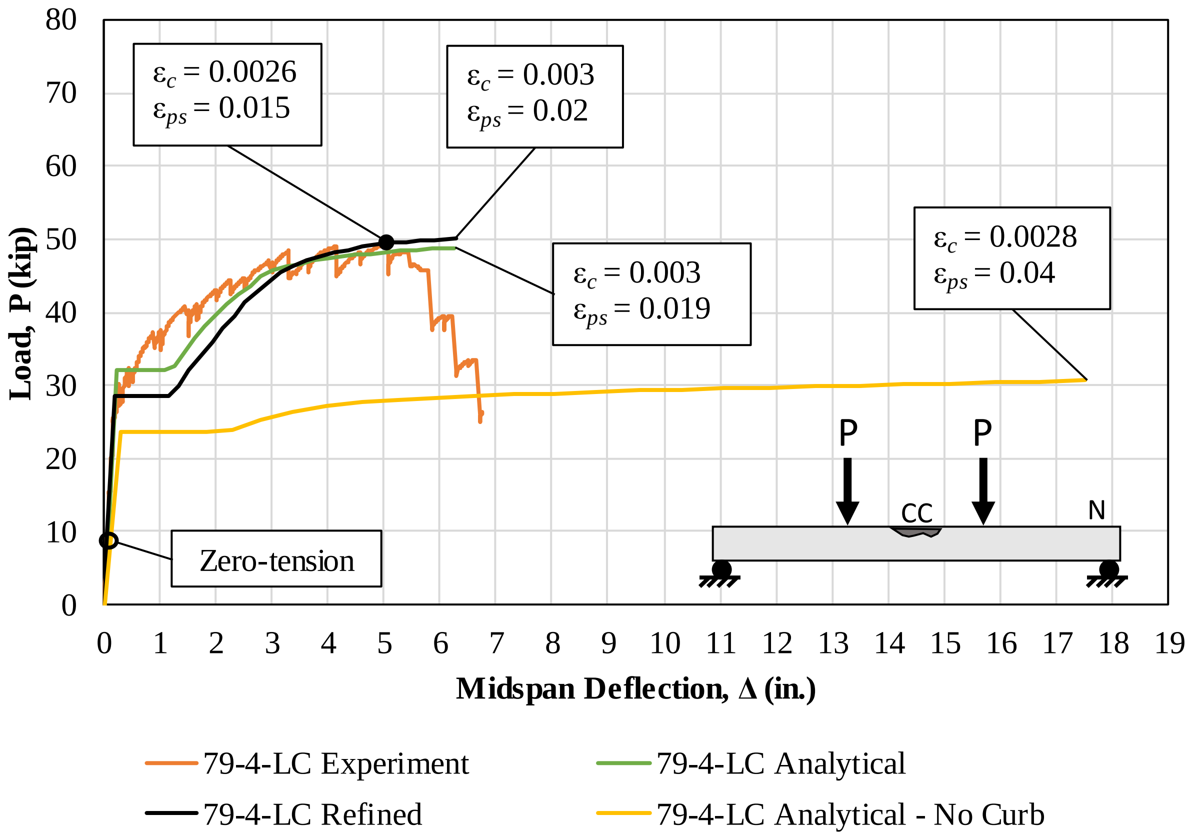

Figure 4.135: Specimen 79-4-LC Load vs. Deflection

Specimens 79-3-UD and 79-4-LC have identical cross-sections and span lengths. Furthermore, Specimen 79-3-UD did not have any deterioration while only limited deterioration of longitudinal cracking at the north end existed in Specimen 79-4-LC. Therefore, the test data for Specimen 79-3-UD is plotted in Figure 4.136 to evaluate the effect of deterioration in Specimen 79-4-LC. As, shown, the load-displacement curves for both specimens are identical up to the failure of Specimen 79-3-UD which was initiated by the wood embedded in the curb. The longitudinal cracks observed in the end of Specimen 79-4-LC caused minimal strand corrosion and had no effect on the structural capacity of the specimen. As shown, there was no impact of the end corrosion on Specimen 79-4-LC. In fact, the wood embedded in the curb during construction was shown to have a greater impact on structural capacity of Specimen 79-3-UD than the bottom flange deterioration of Specimen 79-4-LC.

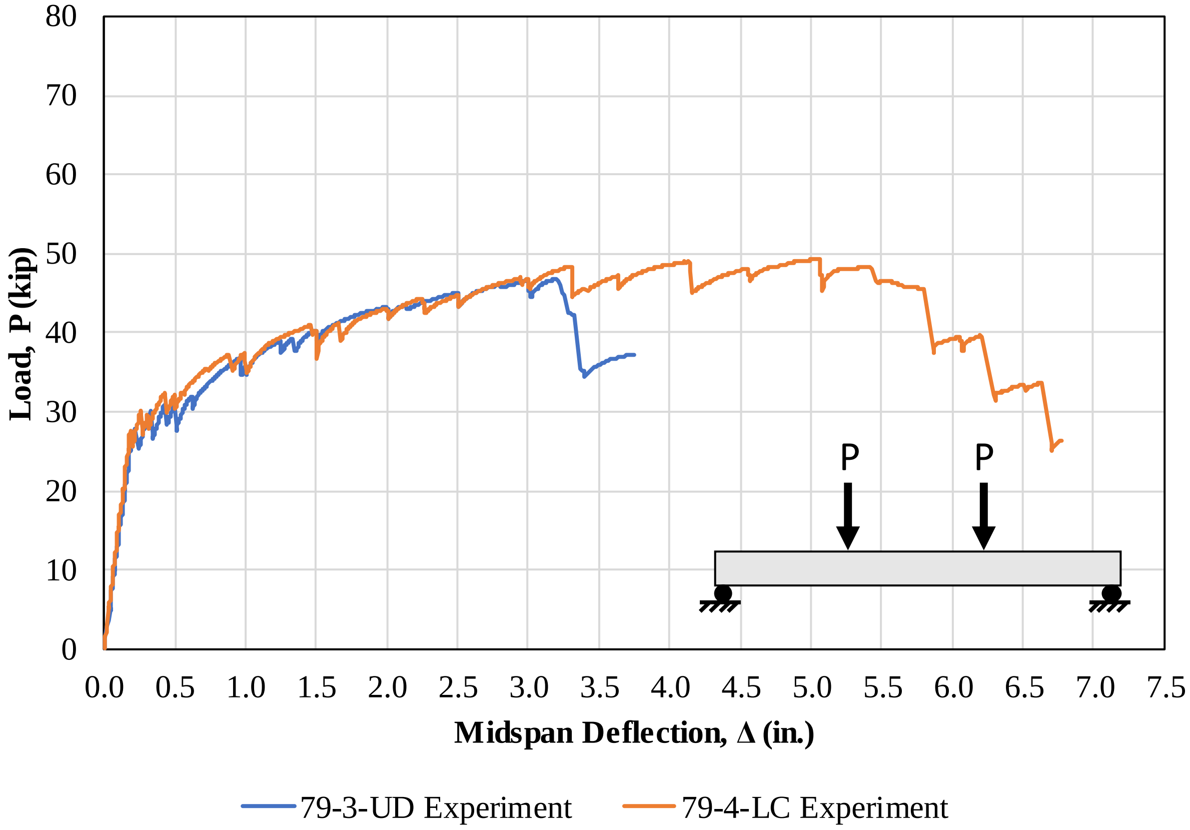

Figure 4.136: Specimen Comparison - 79-3-UD vs. 79-4-LC

4.7.10 Specimen 56-1-LC

The load-deflection curves for Specimen 56-1-LC are provided in Figure 4.137. As shown, the cracking load was overestimated by the analytical model. The remaining prestress calculated from the measured cracking load, 88 ksi, was considerably lower than the remaining prestress calculated for all other specimens. In addition, the remaining prestress from 56-2-ES was calculated as 161 ksi indicating that the low value of remaining prestress for Specimen 56-1-LC is not likely due to a lower value of specified prestress during design. It is not clear why this specimen had such a low prestress level other than the possibility of a construction error.

The refined curve for the undeteriorated section follows the test data up to a midspan deflection of 11.7 in. when strand fracture was observed (Figure 4.137). The black dot on the refined curve indicates the load and deflection that corresponds to an extreme fiber compressive strain of 0.0023 and a strain in the strands of 0.025. The end of the estimated curves corresponds to an extreme fiber compressive strain of 0.003 and a strain in the strands of 0.037 for the analytical model and 0.035 for the refined model.

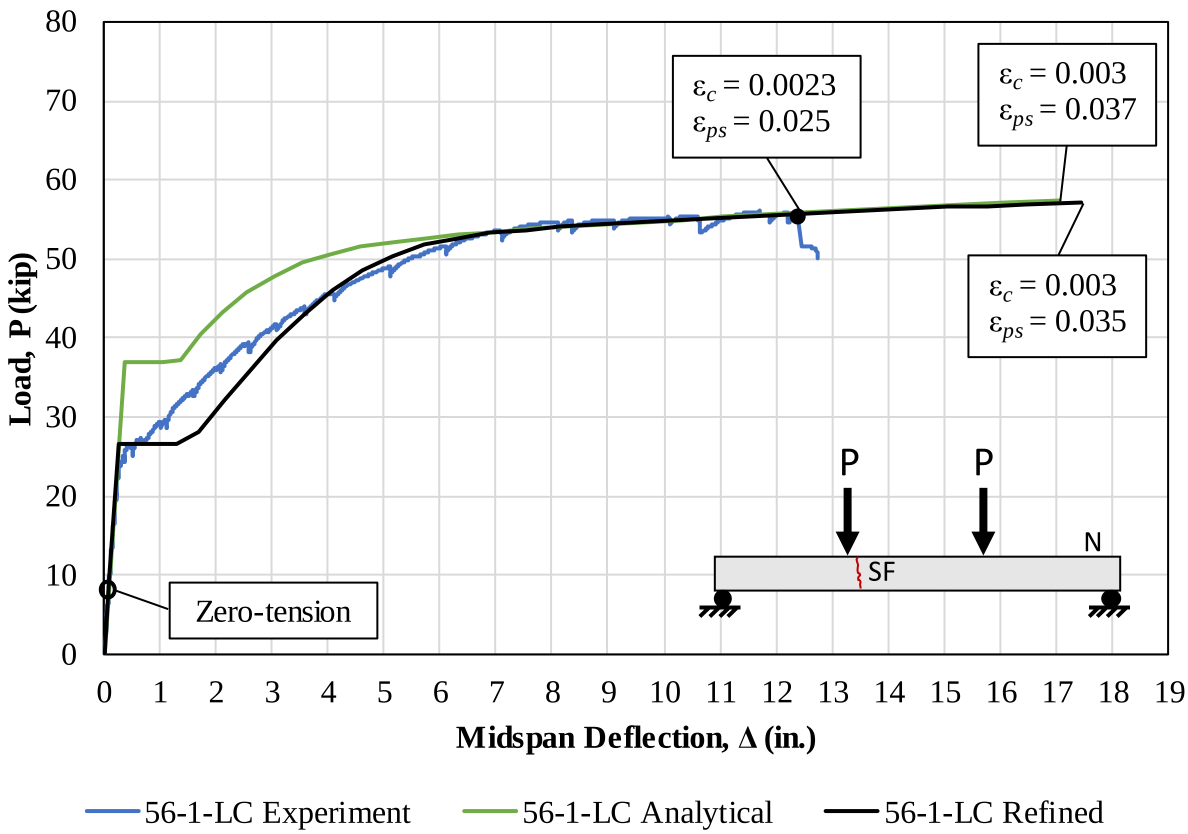

Figure 4.137: Specimen 56-1-LC Load vs. Deflection

The results from the compression tests indicated that peak concrete stress occurred, on average, at a strain of 0.0032 which accounts for the lack of crushing prior to the first strand fracture observed during the test. The first fracture was attributed to minor pitting observed during the post-failure review. The calculated strain at fracture of 0.025 is close to the strain at fracture measured for Strand Specimen 79-4-LC-1_{cor} (0.019, Table 4.13) which had slightly more corrosion (Figure 4.17(a)) and achieved 100% of the average breaking strength of the uncorroded strands. This again illustrates the loss of ductility in the strand and overall beam behavior caused by corrosion. The remaining strands in the section were observed to have exhibited ductile type fractures consistent with those observed during tensile testing (Figure 4.9 and Figure 4.138). The fracture of these strands was assumed to be caused by the increase in strain caused by the increase in neutral axis depth when the concrete began crushing after the first strand facture. While the full strain capacity was not achieved, the specimen exhibited excellent ductility and achieved 98% of the ultimate capacity. This specimen can be considered as achieving design strength.


(a) Strand 1 **(b) Strand 9**


(c) Strand 10 **(d) Strand 11**

Figure 4.138: Strand Fractures in Specimen 56-1-LC

4.7.11 Specimen 56-2-ES

The load-deflection curves for Specimen 56-2-ES are provided in Figure 4.139. As shown, the analysis model curves follow the test data up to a midspan deflection of 8.0 in. where concrete crushing of the top flange was observed. The analysis for Specimen 56-2-ES assumed the reduced geometrical properties of the section provided in Appendix D but does not discount the exposed strand on the east side of the specimen. The black dot on the refined curve indicates the load and deflection that corresponds to an extreme fiber strain of 0.0014 and a strain in the steel of 0.012. The end of the estimated curves corresponds to an extreme fiber compressive strain of 0.003 and a strain in the strands of 0.029 for both analysis models.

The low strain of 0.0014 corresponding to concrete crushing of the delaminated concrete in the top flange is consistent with the strains calculated at concrete crushing for Specimens 244-1-LC and K5-2-LC (0.0009 and 0.0008). The slightly higher concrete strain at crushing may be due to the difference in condition of the concrete between the specimens. The cores taken from Specimens 244-1-LC and K5-2-LC showed large cracks through the top flange indicating advanced concrete delamination, while the cores extracted from Specimen 56-2-ES were observed to have only minor cracks in the top 1/2 in. of the top flange. Delaminated concrete was also indicated in Specimen 56-2-ES by sounding the top flange. In all cases, delaminated concrete prevented the development of the full strain capacity of the concrete and resulted in loss of strength and ductility.

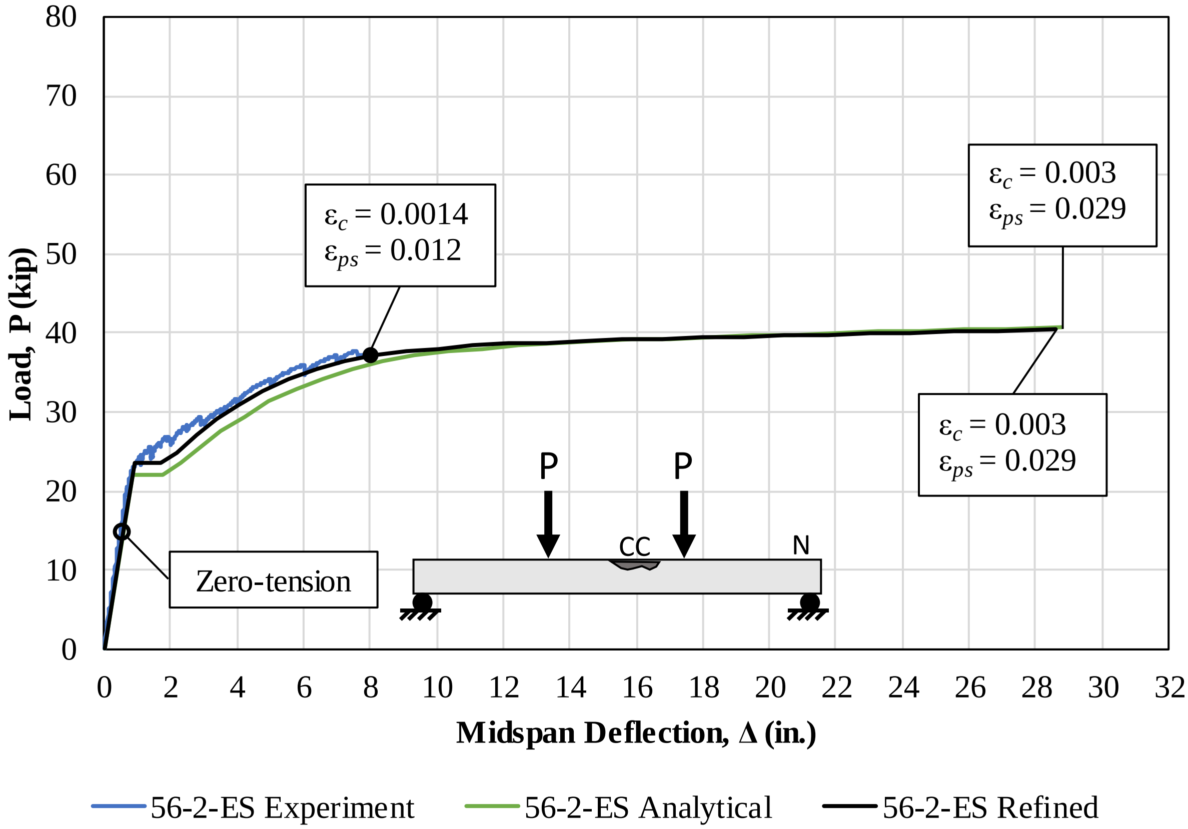

Figure 4.139: Specimen 56-2-ES Load vs. Deflection

The agreement between the test results and the analysis model curves indicate that the exposed strand was effective in resisting the applied demand on the specimen. It should be noted that a pop was heard at 7.6 in. of midspan deflection, and after failure, the exposed strand was observed with multiple wire fractures (Figure 4.94). After crushing, redistribution of forces decreased the moment arm resulting in higher steel strains. The fracture of these wires in a brittle mode, however, indicates that the strand would not have remained effective if larger concrete strains could have been achieved.

4.7.12 Specimen 102-1-BS

The load-deflection curves for Specimen 102-1-BS are provided in Figure 4.140. The load-deflection curves calculated using the analytical and refined models assumed that the broken strand observed prior to testing was ineffective. The refined model with the simplified deteriorated deflection model was used to compute the deteriorated curve ("Det"), which was calculated assuming the broken strand and one additional strand was ineffective. The hollow black circle in Figure 4.140 indicates the point of zero tension in the extreme fiber in tension at a load of 14 kips. The experimental curve deviates from the initial stiffness at approximately the same point indicated by the hollow black circle. This indicates that the remaining prestress in the section of 154 ksi was estimated well using the cracking load in Table 4.18 and a modulus of rupture of $7.5\sqrt{f_c'}$ (Table 4.18).

As shown in Figure 4.140, the analysis model curves for the undeteriorated section follow the data up to a midspan displacement of 7.2 in. The black dot on the refined curve indicates the load and deflection that corresponds to an extreme fiber strain of 0.0017 and a strain in the steel of 0.013. The last point on both the analytical and refined curves corresponds to an extreme compressive fiber strain of 0.003 and a strain in the strands of 0.024. The last point on the deteriorated curve corresponds to an extreme compressive fiber strain of 0.003 and a strain in the strands of 0.026

The strain in the strands of 0.013 indicated at strand fracture by the black dot is consistent with the measured fracture strain of the corroded 1/2 in. diameter strands tested from Specimens 56-2-ES and 102-3-BS (Table 4.13). After fracture, the specimen behavior follows the deteriorated curve until, at applied load of 41.9 kips and a midspan deflection of 9.2 in., a large shear crack formed at the north load point which ultimately caused collapse.

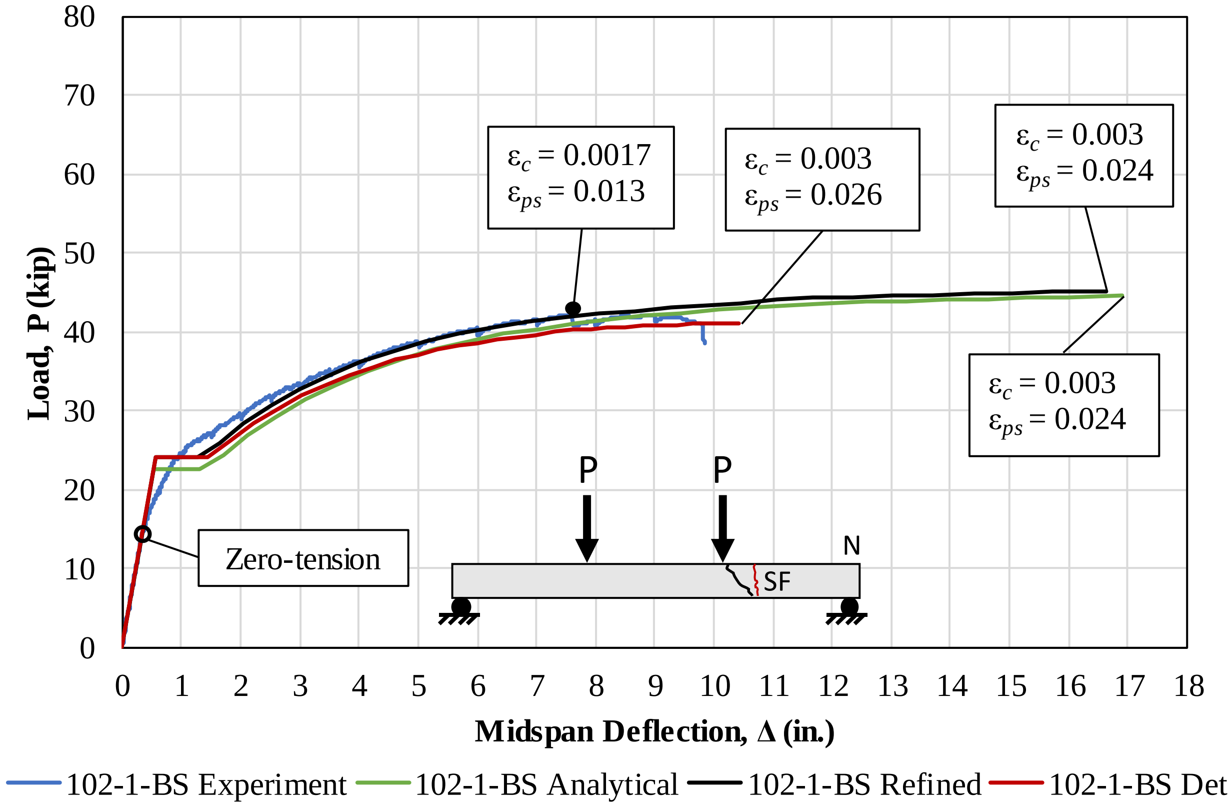

Figure 4.140: Specimen 102-1-BS Load vs. Deflection

The concrete shear resistance calculated using $5\sqrt{f_c'}b_w c$ (Frosch et al. 2017) was equal to 42.5 kips at the north load point, where b_w is the width of the section in shear (48 in.) and c is the depth of the neutral axis (2.0 in.) estimated using the refined model assuming two ineffective strands. The shear resistance calculated assuming one strand was ineffective was 46.5 kips (b_w = 48 in., c = 2.2 in.). This indicates that the shear failure was a direct result of the strand fracture that occurred at 7.6 in. of midspan deflection.

The deterioration of Specimen 102-1-BS primarily consisted of a broken strand adjacent to a rust stained concrete spall. Behavior up to strand fracture was modeled well using one broken strand and considering a corroded strand fracture strain of 0.013. As shown, fracture of one strand may not directly limit the final capacity of a beam. Therefore, to consider the limiting capacity, the deteriorated model can be used. Considering the results of the corroded strands, the capacity was estimated assuming two ineffective strands. The estimated capacity using the deteriorated model was 41.1 kip which is within 3% of the ultimate measured load of 42.3 kip. The two ineffective strands correspond to the broken strand and corroded strand observed adjacent to the broken strand during the strand extraction (Figure 3.32). In addition, the simplified deteriorated deflection model estimated the deflection at ultimate within 6% (10.4 in. estimated, 9.8 in. measured).

4.7.13 Specimen 102-2-BS

The load-displacement curves for Specimen 102-2-BS are provided in Figure 4.141. The load-deflection curves calculated using the analytical and refined models assumed that the broken strand observed prior to testing was ineffective. The refined model with the simplified deteriorated deflection model was used to compute the deteriorated curve ("Det"), which was calculated assuming the broken strand the west side of the bottom flange and the corroded strand at the longitudinal crack on the east side of the bottom flange were ineffective.

As shown in Figure 4.141, the analysis model curves for the undeteriorated section follow the test data up to a midspan deflection of 3.0 in. The black dot on the refined curve indicates the load and deflection that corresponds to an extreme fiber strain of 0.0008 and a strain in the steel of 0.009. The last point on the analytical and refined curves corresponds to an extreme compressive fiber strain of 0.003 and a strain in the strands of 0.027 for the analytical model and 0.025 for the refined model. The last point on the deteriorated curve corresponds to an extreme compressive fiber strain of 0.003 and a strain in the strands of 0.027.

The strain in the strands of 0.009 indicated at strand fracture by the black dot is consistent with the measured fracture strain of the corroded strands tested from Specimen 102-3-BS (Strands

2_{cor} to 5_{cor}, Table 4.13). After fracture, the specimen behavior follows the deteriorated curve until a midspan deflection of 11.0 in. where concrete strain is estimated to be 0.003 and concrete crushing was observed in the specimen.

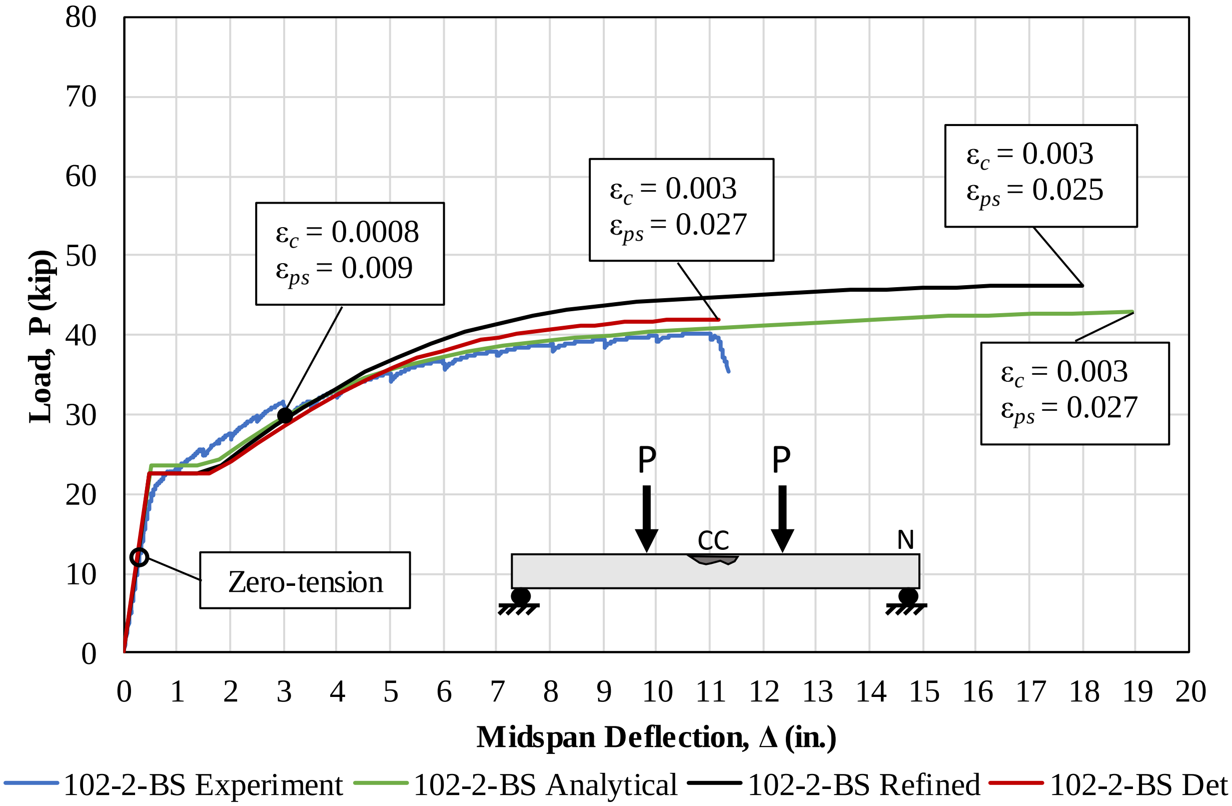

Figure 4.141: Specimen 102-2-BS Load vs. Deflection

The deterioration of Specimen 102-2-BS primarily consisted of a broken strand on the edge of the bottom flange and a rust stained longitudinal crack on the opposite edge of the bottom flange. Considering the results of the corroded strand tests, the capacity of the specimen was estimated using the deteriorated model assuming the strand at the longitudinal crack and the broken strand were completely ineffective. The estimated capacity using the deteriorated model, assuming two ineffective strands, was 41.9 kips, which is within 4% of the peak measured load of 40.2 kips at

11.0 in. of midspan deflection. The two ineffective strands correspond to the broken strand on the west edge of the bottom flange (Strand 1 in Figure 3.34) and the corroded strand at the longitudinal crack on the east edge of the bottom flange (Figure 4.106). In addition, the simplified deflection calculation accounting for deterioration estimated the midspan deflection within 2% (11.2 in.). This shows that the deteriorated model assuming two ineffective strands was in agreement with the experimental test data.

4.7.14 Specimen 102-3-BS

The load-deflection curves for Specimen 102-3-BS are presented in Figure 4.142. The load-deflection curves calculated using the analytical and refined models assumed that the broken strand observed prior to testing was ineffective. The refined model with the simplified deteriorated deflection model was used to compute the deteriorated curve ("Det"), which was calculated assuming a total of five strands at midspan were ineffective. The five strands include the existing broken strand on the west side of the bottom flange and the four corroded strands at the longitudinal cracks on the east side of the bottom flange (Figure 4.111).

As shown in Figure 4.142, the analysis model curves for the undeteriorated section follow the test data up to a midspan deflection of 2.9 in. The black dot on the refined curve indicates the load and deflection that corresponds to an extreme fiber strain of 0.0007 and a strain in the steel of 0.007. The last point on the analytical and refined curves corresponds to an extreme compressive fiber strain of 0.003 and a strain in the strands of 0.029 for the analytical model and 0.027 for the refined model. The last point on the deteriorated curve corresponds to an extreme compressive fiber strain of 0.003 and a strain in the strands of 0.037.

The strain in the strands of 0.007 indicated at strand fracture by the black dot is very close to the measured fracture strain of 0.008 for the corroded strands tested from Specimen 102-3-BS

(Strands 2_{cor} and 4_{cor}, Table 4.13). After fracture, the deteriorated curve follows the experimental behavior until a midspan deflection of 8.0 in. where concrete crushing was observed in the specimen followed by strand fracture and total collapse. The black "X" on the deteriorated curve indicates the load and deflection that correspond to an extreme fiber compressive strain of 0.0026 and strain in the strands of 0.033.

The compression test results for Specimen 102-3-BS showed that, on average, the strain at peak stress was 0.0029 (Table 4.4), which is close to the calculated extreme compression fiber strain of 0.0026. This indicates that the concrete reached its full strain capacity. After crushing, redistribution of forces decreased the moment arm resulting in higher steel strains and strand fracture.

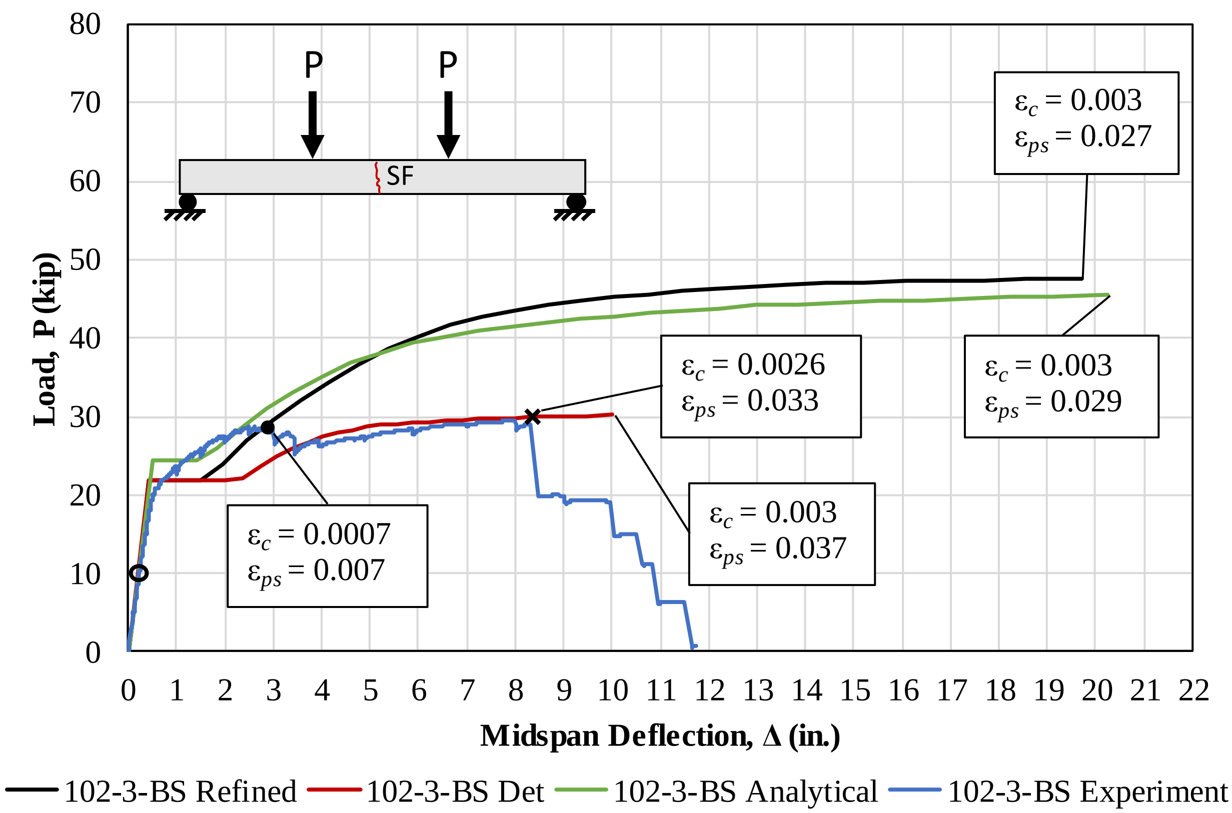

Figure 4.142: Specimen 102-3-BS Load vs. Deflection

The deterioration of Specimen 102-3-BS consisted primarily of a broken strand on the edge of the bottom flange and longitudinal cracking at four strands on the opposite edge of the bottom flange. Considering the results of the corroded strand tests, all five strands were assumed to be ineffective for the deteriorated analysis. The ultimate load estimated assuming five ineffective strands was 30.2 kips which is within 3% of the peak measured load of 29.4 kips at 8.0 in. of midspan deflection. In addition, the simplified deflection calculation overestimated the midspan deflection at ultimate by 2.0 in., a 25% difference. Overall, the analysis models agreed with the experimental data. The analytical model can be used up to fracture of the strands with the deteriorated model being used post-fracture up to final failure of the specimen.

4.7.15 Specimen 102-4-BS

The load-deflection curves for Specimen 102-4-BS are presented in Figure 4.143. The load-deflection curves calculated using the analytical and refined models assumed three strands at the north load point were ineffective prior to testing as discussed in Section 4.5.15. The refined model with the simplified deteriorated deflection model was used to compute the deteriorated curve (“Det”), which was calculated assuming a total of four strands at midspan were ineffective. The four strands correspond to the corroded strands observed at the south load point as discussed in Section 4.5.15.

As shown in Figure 4.143, the analysis model curves for the undeteriorated section follow the test data up to a midspan deflection of 6.7 in. The black dot on the refined curve indicates the load and deflection that corresponds to an extreme fiber strain of 0.0014 and a strain in the steel of 0.012. The last point on the analytical and refined curves corresponds to an extreme compressive fiber strain of 0.003 and a strain in the strands of 0.024 for both analysis models. The last point on the deteriorated curve corresponds to an extreme compressive fiber strain of 0.003 and a strain in the strands of 0.026.

The strain in the strands of 0.012 indicated at strand fracture by the black dot is consistent with the measured fracture strain of the corroded strands tested from Specimens 79-4-LC and 56-2-ES (Strands 4_{cor} and 13_{cor}, Table 4.13). After fracture, the deteriorated curve follows the experimental behavior until a midspan deflection of 7.8 in. where concrete crushing was observed in the specimen followed by strand fracture and total collapse. The black "X" on the deteriorated curve indicates the load and deflection that correspond to an extreme fiber compressive strain of 0.0024 and strain in the strands of 0.021.

The compression test results for Specimen 102-4-BS showed that, on average, the strain at peak stress was 0.0024 (Table 4.4), which is consistent with the calculated extreme compression fiber strain of 0.0024. This indicates that the concrete reached its full strain capacity. After crushing, redistribution of forces decreased the moment arm resulting in higher steel strains and strand fracture.

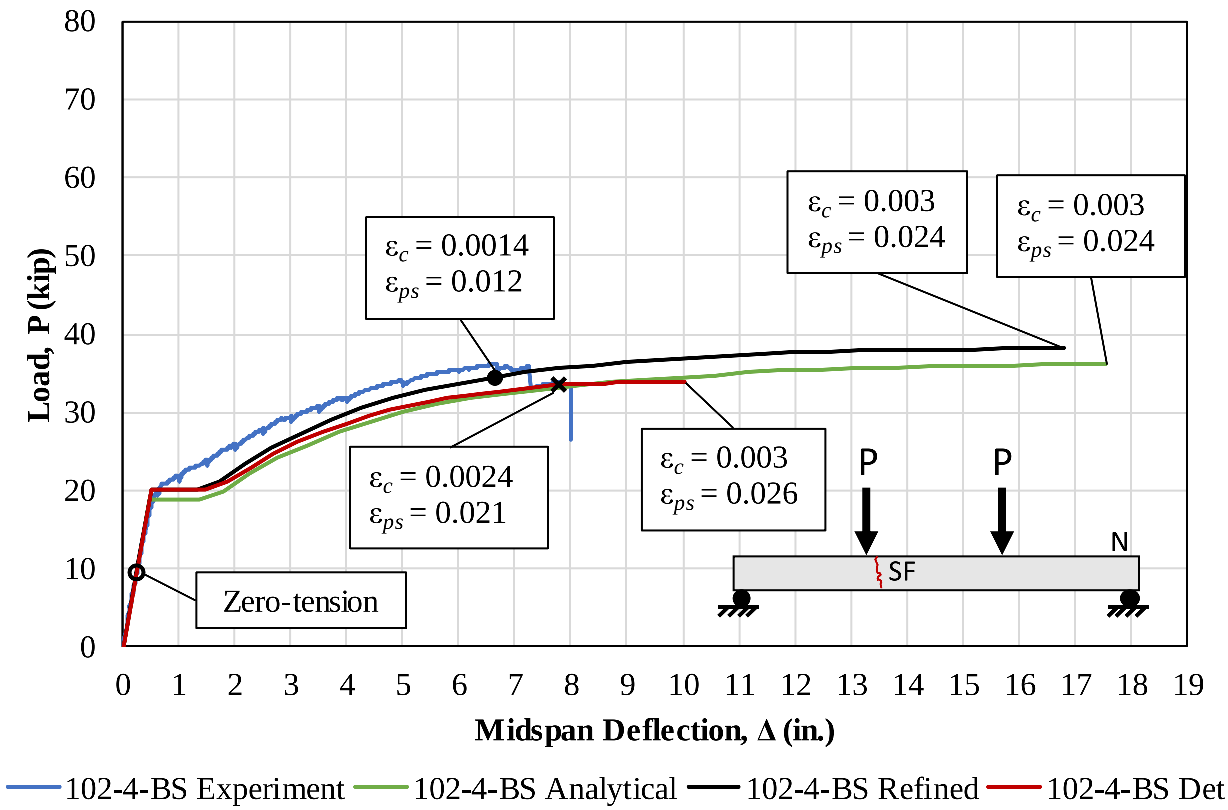

Figure 4.143: Specimen 102-4-BS Load vs. Deflection

The assumption of three ineffective strands, for calculation of the analytical and refined curves, provided an accurate estimation of the load-deformation behavior up to strand fracture at the peak load of 36.2 kips. Considering the results of the corroded strand tests, the capacity of the specimen was estimated at a strain in the strands of 0.01 assuming three ineffective strands. Using the refined model, the estimated capacity was 32.8 kips (within 9% of the peak load), while using the analytical model resulted in a capacity of 30.3 kips (within 16% of the peak load).

The behavior of the specimen after strand fracture was approximated well by the deteriorated model assuming four ineffective strands. The load at ultimate estimated by the deteriorated model was 33.9 kips which is within 6% of the peak measured load. The simplified deflection calculation overestimated the midspan deflection at ultimate by 2.0 in., a 25% difference. Overall, the analysis models were in excellent agreement with the experimental data.

4.8 Discussion of Analysis Results

4.8.1 Modeling

In general, the analytical and refined models provided accurate estimates of the observed structural behavior of each specimen. It should be noted that the analytical model provided essentially the same ultimate load estimates as the refined model without the use of strand test data or structural test data. The analytical model used only the results from the compression tests, which could be obtained by extracting and testing concrete core samples from a bridge beam.

For beams without significant deterioration, the analytical load-deflection response matched the measured behavior using typical values of ultimate concrete strains (ε_{cu} = 0.003) and prestressing steel strains (ε_{pu} =0.04). Structural behavior of deteriorated concrete beams could also be calculated using the analytical model through the use of a limiting value of strain for either the concrete compressive strain for the case of deteriorated concrete or prestressing steel strain for the case of corroded strand. Failure is considered once the limiting strain is reached. For cases of strand failure, there may be reserve capacity. Reserve capacity can be estimated using the analytical model where corroded strand are considered ineffective.

4.8.1.1 Concrete Model

Based on the agreement between the analysis and compression test results, the Hognestad concrete model assuming $E_c = 57{,}000\sqrt{f_c'}$ is recommended for estimating the flexural behavior of both undeteriorated and deteriorated concrete beams. The value of f_c' determined from cores extracted from the specimens provided excellent results. Where core extraction is not possible, the use of a rebound hammer to estimate the concrete strength will provide conservative values of f_c'.

4.8.1.2 Prestressing Steel Model

The prestressing strand model by Mattock is recommended to model the behavior of prestressing strand with a minimum tensile strength of 270 ksi produced before or after 1970. For strand produced in or prior to 1970, the values of K = 1.04 and R = 7 are recommended. For strand produced after 1970, the values of K = 1 and R = 15 are recommended. It should be noted that the ratio of yield strength to minimum tensile strength was assumed to be 0.9, regardless of the year produced.

4.8.2 Cross-Section

4.8.2.1 Composite Action

Specimens 409-1-ES and 409-2-UD were observed with 2.5 in. topping slabs. The analysis of both specimens was conducted assuming full-composite action between the slab and beam. The agreement between the test results and analysis indicate that full composite action was exhibited throughout the structural tests of Specimens 409-1-ES and 409-2-UD. Therefore, composite action can be assumed for concrete overlays.

4.8.2.2 Concrete Curb

Specimens K5-1-LC, 79-3-UD, and 79-4-LC were tested with typical concrete curbs (10 in. tall and 11 in. wide) cast flush with one side of the box beam section. The observed behavior of the specimens indicated that the curbs acted compositely with the beam section. Composite action significantly increased the strength and reduced the overall deflection capacity of the specimens.

4.8.3 Concrete Deterioration

4.8.3.1 Delaminated Concrete

The analysis of Specimens 244-1-LC, K5-2-LC, and 56-2-ES indicate that delaminated concrete cannot achieve the typical full strain capacity of 0.003. In fact, the strain at concrete crushing was observed to be as low as 0.0008 (Specimen K5-1-LC) which corresponds to a concrete stress of $0.45f_c'$ using the Hognestad concrete model. It is generally considered that concrete exhibits linear-elastic behavior up to approximately $0.4f_c'$ to $0.5f_c'$. This indicates that delaminated concrete in flexure exhibits extremely brittle behavior and modeling should only consider the linear-elastic response of concrete in compression (strains up to $0.5f_c'/E_c$).

4.8.4 Prestressing Steel Deterioration

4.8.4.1 Strand Corrosion

Tests of corroded strand, discussed in Section 4.3.2.2, demonstrate that corrosion significantly impairs the ductility of prestressing strand. The lack of ductility of corroded strands translates to reduced ductility of beams containing corroded strands. This loss of ductility was exhibited in the analysis of Specimens 409-1-ES, K5-2-LC, 102-1-BS, 102-2-BS, 102-3-BS, and 102-4-BS. The estimated strain in the strands at fracture among all the specimens was between 0.007 to 0.021. For specimens with longitudinal cracks or exposed strands within the constant moment region, the estimated strand in the strands at first fracture of corroded strand was between 0.007 and 0.013 with an average value of 0.010. In addition, the average strain at fracture measured for the corroded strand tests was 0.011. Considering the test data, exposed strands with minor corrosion or corroded strands at longitudinal cracks may be assumed on average to be effective up to a strain of 0.01. If pitting is observed, it is recommended that the maximum strain be considered as $0.75f_{pu}/E_{ps}$ (0.0074 for f_{pu} = 270 ksi and E_{ps} = 27,500 ksi) which is consistent with the earlier recommendation of considering 75% of the tensile strength of corroded strand.

Specimen 409-1-ES was observed to have existing flexural cracks prior to testing. The estimated strain in the strands at fracture was 0.021. This indicates that beams with existing flexural cracks may achieve the design load but will not exhibit the same level of ductility as uncracked sections. For pre-existing flexural cracks, a reduced strain capacity of $0.75f_{pu}/E_{ps}$ is also recommended.

4.8.4.2 Effective Prestress

The remaining prestress for each member was estimated using the PCI equations for prestress losses (PCI 2017) assuming the initial jacking stress was 0.7*250 ksi for specimens constructed prior to 1967 and 0.7*270 ksi for specimens constructed after 1967. A comparison of the measured and estimated values of remaining prestress in Table 4.18 shows that, overall, the PCI equations for prestress loss provided reasonable estimates of the remaining prestress. As demonstrated by the structural analysis, the exact value of effective prestress did not significantly affect the calculated strength. Therefore, use of PCI estimated prestress values are appropriate. To simplify analysis, an effective prestress of 150 ksi can be simply assumed.

4.8.4.3 Location of Deterioration

The redevelopment of strands away from deterioration at ultimate strength has not been previously verified in structural tests of deteriorated box beams. The development length equation provided in ACI 318 (2014) (Equation 4-20) was used to conservatively estimate the development length of the strand reinforcement in the beam specimens as $170d_b$ (f_{se} = 150 ksi, f_{ps} = 270 ksi). A development length of $170d_b$ corresponds to 63.75 in. for 3/8 in. diameter strand and 85 in. for 1/2 in. diameter strands. The exposed 3/8 in. diameter strands in Specimen 409-1-ES (Figure 3.67) were located 94 in. from the constant moment region and the intersection of the longitudinal cracks, and the 1/2 in. diameter strands in Specimen 79-4-LC (Figure 3.74) were located approximately 78 in. from the constant moment region. This indicates that the deterioration of either specimen was located outside or approximately the same as the distance required to properly develop the strand at maximum moment. It should be noted that the ACI 318 equation for development length was designed to be a conservative estimate of the length required to develop 7-wire strand.

$$l_d = \left(\frac{f_{se}}{3000}\right) d_b + \left(\frac{f_{ps} - f_{se}}{1000}\right) d_b \qquad (4\text{-}20)$$

where:

l_d	=	transfer length of the effective prestress in strands (in.)
d_b	=	7-wire strand diameter (in.)
f_{ps}	=	stress in the strands at nominal flexural strength (psi)
f_{se}	=	effective prestress in strands (psi)

The analysis of Specimens 409-1-ES and 79-4-LC showed that both specimens achieved the design capacity for the constructed cross-section and span during the structural test. This suggests that the ACI equation for development length may be used to approximate the length required to redevelop strands for flexural capacity calculations. It should be noted that the equation provided in AASHTO is the same as the ACI equation.

In addition, study of a precast, prestressed concrete box beam by Kasan and Harries (2011) showed that severing of a pretensioned strand causes localized loss of prestress. The study determined that, when a strand is intentionally cut, the prestress force is redeveloped to either side of the cut. The transfer length of the severed strands was found to be approximated well by the equation provided in ACI 318-08 (Equation 4-21). It should be noted that the equation for transfer length has not changed in ACI 318-14.

$$l_{tr} = \left(\frac{f_{se}}{3000}\right) d_b \tag{4-21}$$

where:

l_{tr} = transfer length of the effective prestress in strands (in.)

d_b = 7-wire strand diameter (in.)

f_{se} = effective prestress in strands (psi)

The transfer length for Specimens 409-1-ES and 79-4-LC was 20.25 in. and 20.2 in. based on the remaining prestress in Table 4.18. If the remaining prestress is assumed to be 150 ksi, the transfer length for Specimen 409-1-ES is 18.75 in. (3/8 in. diameter strand) and 25 in. for Specimen 79-4-LC (1/2 in. diameter strand). This indicates that the full remaining prestress force should have been active over the constant moment region for both specimens.

A comparison of the calculated remaining prestress for specimens with the same cross-section and span, Specimens 409-1-ES (162 ksi) and 409-2-UD (154 ksi) which are comparison specimens (with and without deterioration) and Specimens 79-3-UD (138 ksi) and 79-4-LC (121 ksi) (Table 4.18) which are also comparison specimens, suggests that the level of prestress was unaffected by the deterioration located outside of the constant moment region.

The existing strand fractures in Specimens 102-1-BS, 102-2-BS, 102-3-BS, and 102-4-BS were located within the maximum moment region. Therefore, the overall prestress force at the section of maximum moment was reduced because there was zero force in the fractured strands. The loss of prestress at a section of maximum moment leads to a reduced cracking moment that may lead to flexural cracking under service loads which may result in strand corrosion. Corrosion was observed at existing flexural cracks in Specimens 409-1-ES (Figure 4.48) and 102-4-BS (Figure 3.41).

4.9 Summary and Findings

4.9.1 As-Built Section vs. INDOT Standard Section

A comparison between the as-built and INDOT standard section geometry was conducted to determine any differences between what was built and what was specified. The comparison revealed that the overall height and width of the beam sections matched the standard sections. The flange and web thicknesses, however, varied largely due to the void shifting while concrete was cast. For specimens with two or more voids, the void was found to have shifted toward the middle of the section and up. Middle web thicknesses and top flange thicknesses were observed to be less than the standard thicknesses by up to 3 in.

A similar comparison was conducted between the reinforcement provided in the as-built section and the reinforcement specified on the INDOT standard drawings. For every specimen, the number of strands provided in the specimen as constructed was greater than or equal to the number of strands specified on the standard drawing. Differences between the as-built and standard section reinforcement were observed to be negligible.

4.9.2 Material Testing

In general, the corroded strands tested were observed to have residual capacity but did not have any appreciable ductility. Based on the observed behavior, it is recommended to assume that strands exhibit no ductility where corrosion of any kind is observed. In addition, if surface corrosion and minor pitting are observed, only 75% of the strand strength should be considered along with limiting strain to 0.01. If severe corrosion or fractured wires are observed, 0% of the strand strength should be considered.

4.9.3 Structural Testing

The deteriorated capacity of each specimen was determined through structural testing. The results of each structural test were compared to an analytical model used to estimate the behavior of each specimen. The findings of these comparisons may be summarized as follows.

1. Structural repair of a concrete top flange must remove all deteriorated concrete prior to placing a structural concrete patch. A jack hammer or other suitable tool is recommended for removal of deteriorated concrete.
2. Delaminated concrete exhibits brittle behavior. Structural capacity calculations considering delaminated concrete in compression should limit the compressive strain to $0.5f_c'/E_c$.
3. Only strand corrosion located within the development length from the point of maximum moment needs to be considered as reducing the flexural capacity. Strands with corrosion and fractured strand outside of the maximum moment region can redevelop capacity and maintain prestress force.
4. Reduced ductility of corroded strand led to reduced overall ductility of the beam specimens. The strain in the strand at fracture in the beam specimen correlated with the strain at fracture measured during tensile testing of the corroded strand. Based on the presented analysis, the strain in corroded strains should be limited to 0.01 for structural capacity calculations. If minor pitting is observed, the strain should be further limited to $0.75f_{pu}/E_{ps}$ consistent with the recommendation of 75% of the strand strength.

CHAPTER 5. LIVE-LOAD DISTRIBUTION

5.1 Introduction

Evidence of a leaking shear key or presence of a reflective crack calls into question the condition of a shear key and the capacity of a shear key to transfer load between beams (Figure 5.1). The position of a shear key within an adjacent box beam bridge makes visual inspection impossible, and there is no standard non-destructive inspection method to evaluate the condition of the shear key. The lack of dependable inspection may lead load rating engineers to assume that there is no load distribution where signs of shear key deterioration are observed.

For adjacent box beam bridges with reinforced concrete decks, the deck provides an additional mechanism for load distribution. The load distribution of this mechanism acting without shear keys, however, is not currently considered by current bridge design specifications.

Figure 5.1: Leaking Shear Key (Bridge 35-00013, Pond Creek)

The AASTHO LRFD Bridge Design Specifications (2017) provide equations for two load distribution cases for adjacent box beam bridge systems, Cases (f) and (g). Case (f) considers adjacent beams with shear keys and a concrete deck. Case (g) considers adjacent beams with shear keys and transverse post-tensioning to provide compression of the longitudinal joint. When evaluating a Case (f) bridge with shear keys exhibiting signs of deterioration, the amount of load distribution offered by the concrete deck alone is needed. The AASHTO Manual for Bridge Evaluation (2018) and AASHTO LRFD (2017) provide no guidance on the live-load distribution of an adjacent beam bridge with a concrete deck and no shear keys. In addition, research regarding the load distribution of a concrete deck over adjacent beams without shear keys is not available.

Considering the lack of test data and general uncertainty in analyzing deteriorated concrete structures, a series of load tests were conducted to determine the load distribution of an adjacent concrete box beam bridge with a non-composite reinforced concrete deck. The load tests were conducted on Tippecanoe 115 (79-00115), a 40 ft long adjacent precast, prestressed concrete box beam bridge in Tippecanoe County, Indiana. The bridge was loaded with a typical triaxle truck, while deflections and strains were measured for each of the seven beams. The bridge was tested in four conditions: (i) as-built, (ii) after removal of the bituminous wearing surface, (iii) after the shear keys were disabled, and (iv) with a reinforced concrete deck installed. The results of this study can serve as the basis for which a concrete deck could be used as a retrofit strategy to restore load distribution or serve as the primary load distribution mechanism in an adjacent beam bridge.

5.2 Bridge Description

The adjacent box beam bridge used for the load tests was constructed in Tippecanoe County in 1957 and designed using the 1957 AASHO Standard Specifications for Highway Bridges. The single-span bridge consists of seven adjacent precast, prestressed concrete box beams 45 in. wide and 21 in. deep. The total length of the bridge is 40 ft, and the beams span approximately 39 ft from centerline of bearing to centerline of bearing. The section properties were assumed to be similar to the 1961 INDOT standard box beam Section B-21-3-9 (Figure 5.2). The complete original design drawings were not available, and standard drawings prior to 1961 do not exist. The portion of the remaining original drawings specified 3/8-in. diameter seven-wire stress relieved strand with a minimum tensile strength of 250 ksi. In 1993, the north exterior box beam (Beam 7) was replaced with a precast, prestressed concrete box beam of the same overall dimensions (Figure 5.3 provides beam labeling). The number of strands in each beam was determined using ground penetrating radar (GPR). The 1957 beams were found to have 21 strands, and the 1993 beam was found to have 12 strands. The difference in the number of strands led to the conclusion that the 1993 replacement beam was reinforced with 1/2-in. diameter strand (drawings were not available for the 1993 beam).

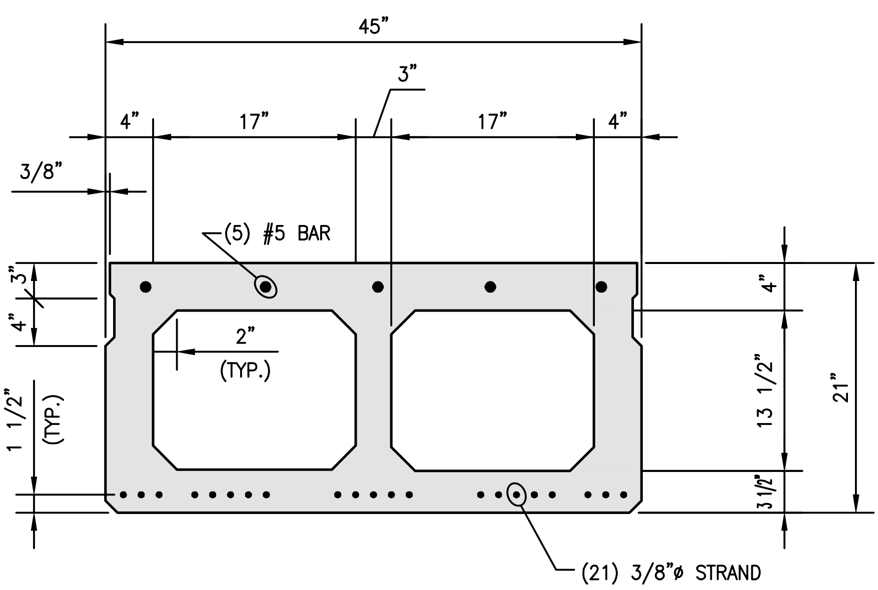

Figure 5.2: 1961 INDOT Standard Section B-21-3-9

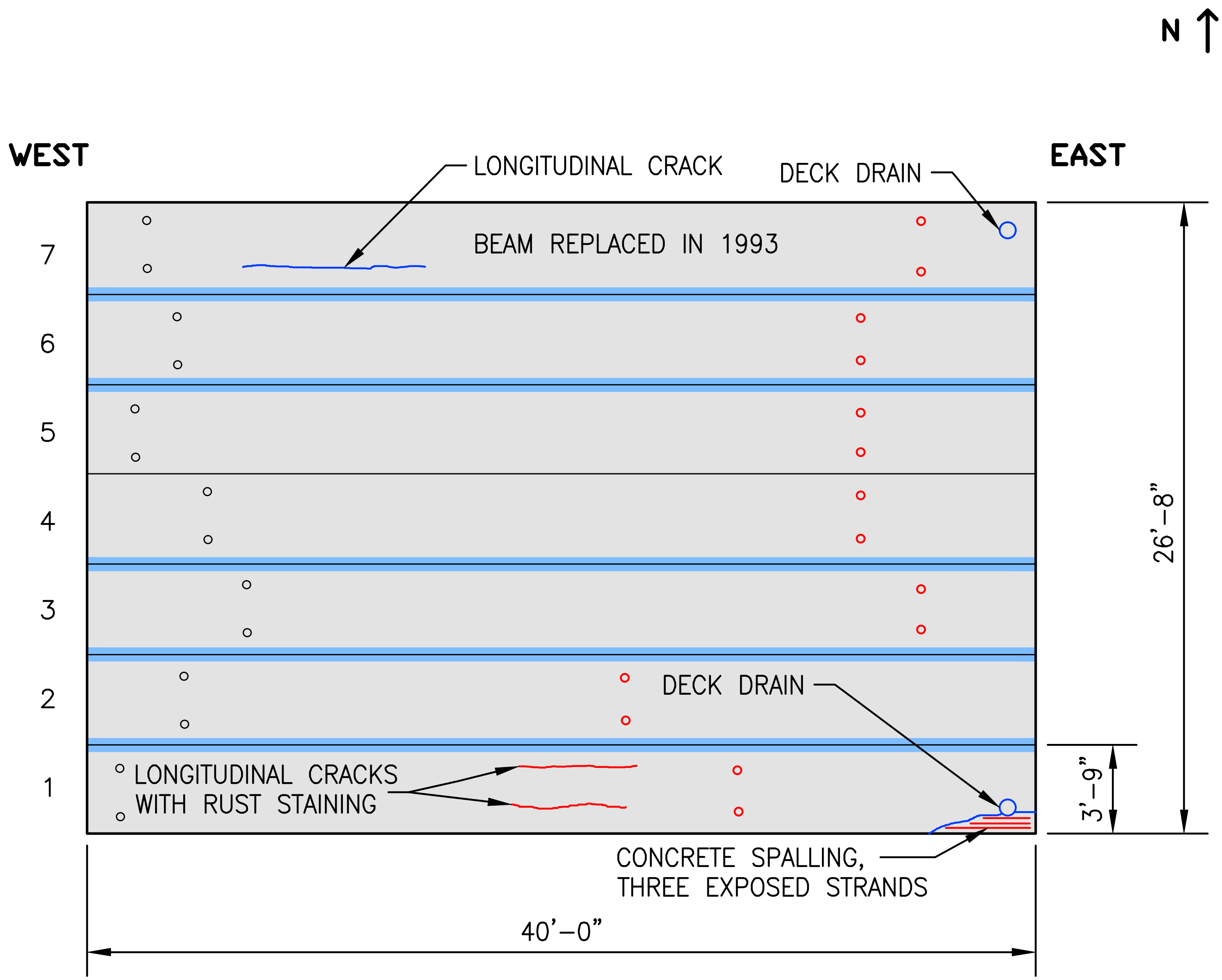

Figure 5.3: Tippecanoe 115 Bottom Flange Deterioration

5.2.1 Bridge Deterioration

A supplementary bridge inspection was performed by an INDOT bridge inspector before testing began to determine the condition of the bridge (Figure 5.3). The investigation revealed deterioration on Beam 1 and Beam 7 (Figure 5.4). Minor longitudinal cracking was observed on the west end of Beam 7 (Figure 5.4(a)). The cracking in Beam 7 was considered minimal and assumed to have a negligible effect on the flexural strength of the beam. Beam 1 was observed to have three exposed strands at the east support (Figure 5.4(d)) and two rust-stained longitudinal cracks approximately 5-ft long located at midspan (Figure 5.4(b) and (c)). Concern regarding the deterioration of Beam 1 prevented direct loading until the concrete deck was placed. Evidence of water leaking through the shear keys was also observed between every beam with exception to the joint between Beams 4 and 5 (Figure 5.3). In addition to the observed deterioration, the thickness of the bituminous wearing surface was estimated to be 5 in. based on a survey using GPR. The supplementary inspection report is provided in Appendix I.

5.2.2 Bridge Deck Design

The concrete deck cast on Bridge 115 was designed using the Indiana Design Manual (IDM) (2013) and AASHTO LRFD (2017). The provided reinforcement was determined based on the temperature and shrinkage reinforcement requirements of AASHTO LRFD (2017). The area of reinforcement required was calculated to be 0.11 in.^{2}/ft. The IDM (2013) also specifies an 8 in. maximum spacing for bridge deck reinforcement. The light reinforcement requirement could have been satisfied using #3 bars or even welded wire fabric. The use of small diameter bars or welded wire fabric in bridge decks is not recommended due to flexibility as this reinforcement can be easily bent upon walking on it leading to difficulties maintaining minimum cover requirements and controlling effective depth of the reinforcement. Therefore, #4 bars were selected (0.3 in.^{2}/ft) to prevent constructability issues. To conform with bridge deck reinforcement requirements of the IDM, Gr. 60 epoxy coated bars were specified.

The thickness of the concrete deck was determined based on the minimum cover requirements of the IDM. The minimum required top cover was 2.5 in. plus 0.5 in. for a sacrificial wearing surface. The minimum required bottom cover was 1 in. A single mat of #4 bars in both directions is 1 in. thick. The total minimum thickness of the deck was consequently determined to be 5 in.

(a) Longitudinal cracking in Beam 7

(b) Rust stained longitudinal crack on south side of Beam 1

(c) Rust stained longitudinal crack on north side of Beam 1

(d) Three exposed strands at east support of Beam 1

Figure 5.4: Tippecanoe 115 Deterioration

5.3 Instrumentation Plan

The bridge was instrumented such that the deflection of each beam at the quarter points was recorded. A total of 21 linear string potentiometers (seven beams, three on each beam) were used to record deflections. The potentiometers were mounted on a wooden frame erected on top of steel scaffolding under the bridge. By mounting the potentiometers to a frame, absolute deflections could be recorded. The scaffolding was rented from Midwest Rentals in Lafayette, IN. The instrumentation frame was constructed similar to a two-girder bridge with stringer beams. Aluminum planks, 20 ft long, were placed between two scaffolding towers to span across the creek (Figure 5.5). Wood 2x6 in. boards spanned between the planks (Figure 5.6). Potentiometers were attached to the wooden boards using metal brackets and clamps (Figure 5.7). In addition to the potentiometers, concrete strain gauges (90 mm gage length) were also installed on the bottom flange of each beam at midspan as a redundant measurement in the event a potentiometer failed. A plan view of the bridge indicating the location of each sensor is shown in Figure 5.8.

Figure 5.5: Instrumentation Frame - Aluminum planks spanning between scaffolding towers

(a) Wooden boards bearing on aluminum planks (looking North)

(b) Wooden boards spanning between aluminum planks (looking Southwest)

Figure 5.6: Instrumentation Frame

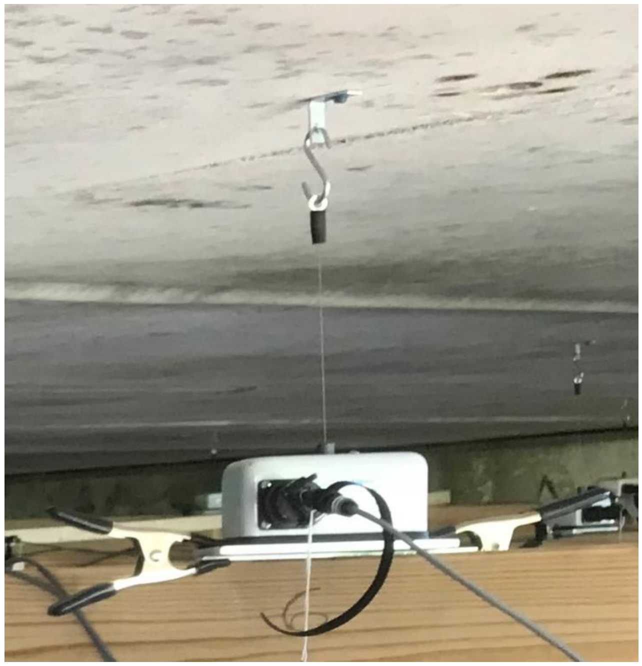

Figure 5.7: Linear String Potentiometer

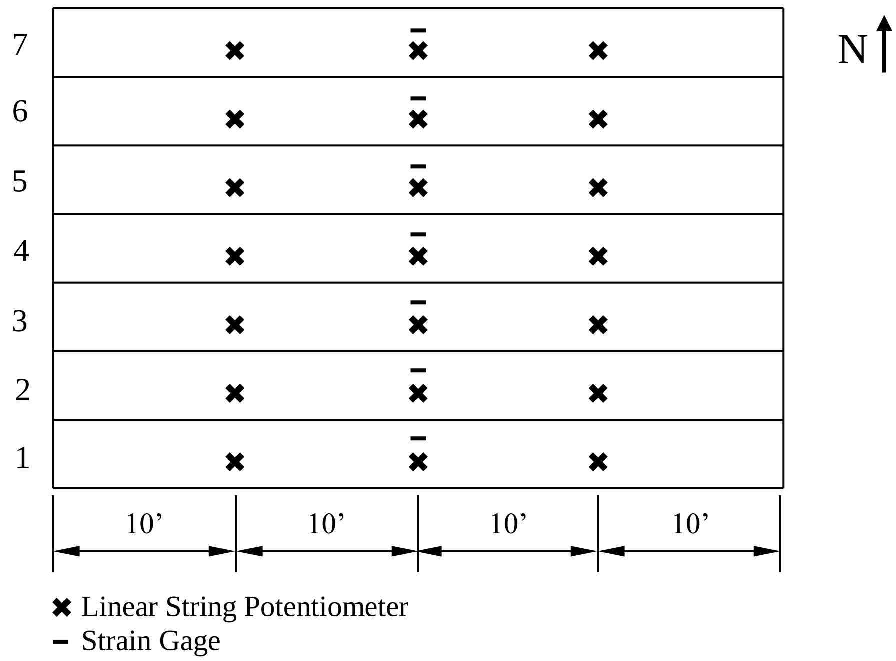

Figure 5.8: Instrumentation Plan

5.4 Load Tests

The bridge was load tested in four conditions to capture the live-load distribution contribution of each superstructure element. A visual summary of the conditions is provided in Figure 5.9.

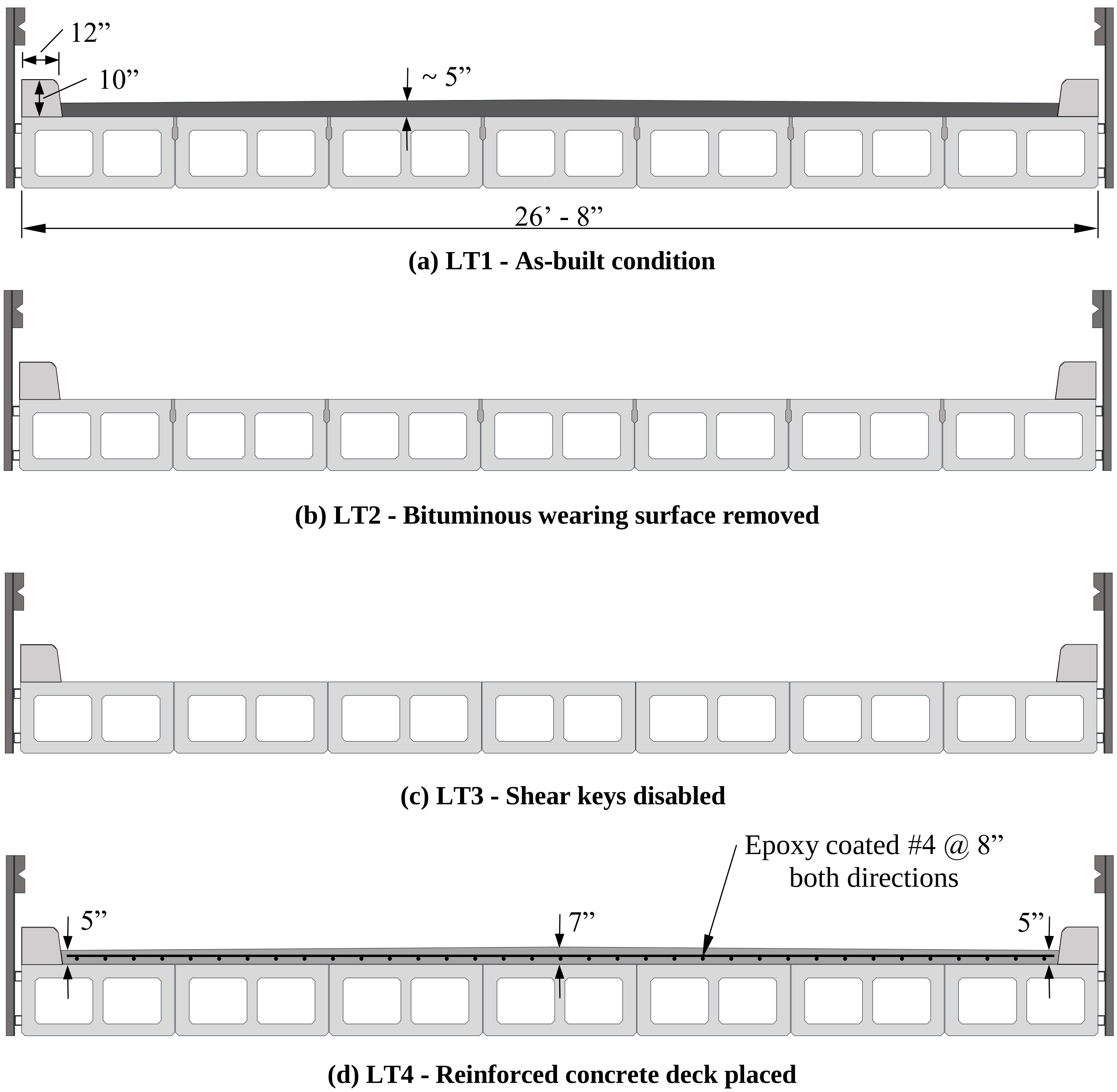

(a) LT1 - As-built condition

(b) LT2 - Bituminous wearing surface removed

(c) LT3 - Shear keys disabled

(d) LT4 - Reinforced concrete deck placed

Figure 5.9: Load Test Conditions

5.4.1 Load Test One (LT2) - As-Built Condition

The first load test (LT1) was performed on the bridge as-built, without any modifications.

5.4.2 Load Test Two (LT2) - Wearing Surface Removed

After LT1 was completed, the bridge was closed on 2 July 2018 to all traffic to allow bridge modifications to be completed safely. Yates Construction, a bridge contractor, was hired to remove the bituminous wearing surface (Figure 5.10). During removal of the wearing surface, the milling machine removed a portion of the top flange of each beam and exposed regions of deterioration in Beam 1 (Figure 5.11(a)) and Beam 3 (Figure 5.11(b)). The hole in Beam 1 was approximately 10 in. by 10 in., and the concrete around the hole had been reduced to rubble. Both holes in Beam 3 were approximately 30 in. long and 10 in. wide after removing the deteriorated concrete.

Figure 5.12 shows the location of the top flange deterioration exposed by the milling machine. The holes in each beam were prepared for repair by removing any deteriorated concrete and cleaning the surface around each hole. The top flange was then repaired with Quikrete mixed in a wheelbarrow by the contractor (Figure 5.13).

Once the repairs to the top flange of Beams 1 and 3 were completed, a second load test (LT2) was performed. As a consequence of the damage to the top flanges, Beams 1, 2, and 3 were not directly loaded during the second and third load tests.

Figure 5.10: Wearing Surface Milling Operation

(a) Hole in Beam 1

(b) Holes in Beam 3 before deterioration was removed

Figure 5.11: Exposed Top Flange Deterioration

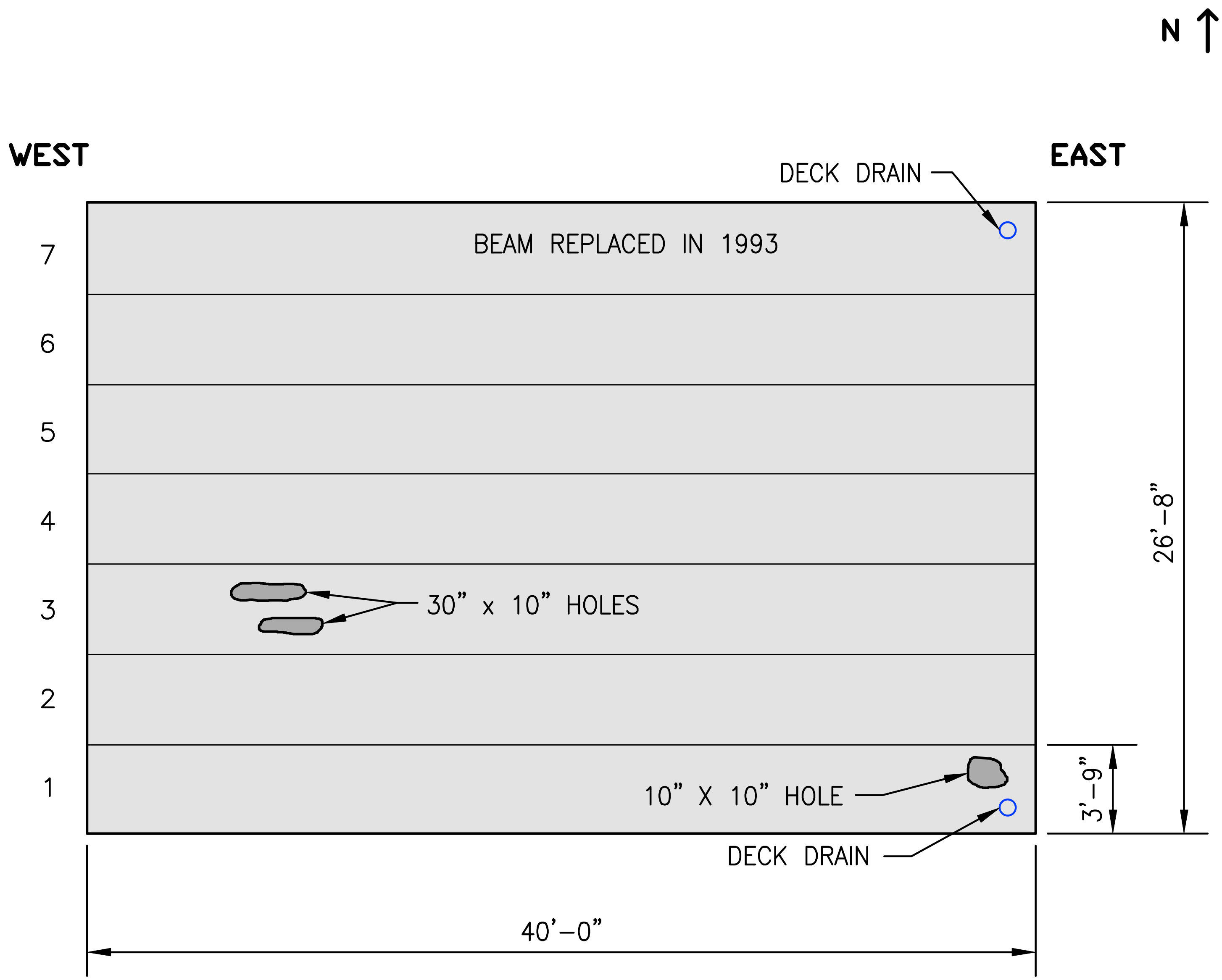

Figure 5.12: Bridge 79-00115 Plan of Top Flange Deterioration

(a) Beam 1 repair patch

(b) Beam 3 repair patches

Figure 5.13: Top Flange Repairs

5.4.3 Load Test Three (LT3) - Shear Keys Disabled

A concrete cutting contractor, ABC Cutting Contractors Inc., was hired by the research project to disable the shear keys. A pavement saw, cutting to depth of 12 in., was used to fully cut through the shear keys (Figure 5.14 and Figure 5.15). The third load test (LT3) was performed to verify that the shear keys were disabled and that each beam was acting independently.

Figure 5.14: Pavement Saw

Figure 5.15: Shear Key Cutting Operation

5.4.4 Load Test Four (LT4) - Concrete Deck Placed

The fourth and final load test (LT4) was completed after the reinforced concrete deck had been placed. The surface of each box beam was prepared by sandblasting (Figure 5.16) to ensure adequate bond between the beams and the deck could be achieved. The deck concrete mix design (Table 5.1) followed the INDOT Class C specifications as specified in Section 702 of the Standard Specifications (INDOT 2018). The deck was reinforced with Gr. 60 #4 epoxy coated bars, supplied by Gerdau, spaced at 8 in. on-center in both the longitudinal and transverse directions with a minimum top cover of 3 in. and 1 in. minimum bottom cover. The yield and ultimate tensile strength of the bars reported on the mill certification was 88 ksi and 104 ksi. The steel mill certification and concrete information are provided in Appendix J.

Figure 5.16: Sandblasted Box Beam Surface

Table 5.1: Concrete Mix Design

Material	Type	Mix Design
Cement	ASTM C150 – Type I (lb/ft^3)	658
Coarse Aggregate	#8 Limestone (lb/ft^3)	1725
Fine Aggregate	#23 Natural Sand (lb/ft^3)	1225
Air-Entrainment	ASTM C260 - Micro Air (oz/yd^3)	3.3
Water-Reducer and Retarder	ASTM C494 - MasterSet Delvo (oz/yd^3)	19.7
Water (lb/yd^3)		249
Water/Cement Ratio		0.38
Slump (in.)		4

The deck was tapered from the bridge centerline to the curb for water drainage. The thickness of the deck was 7 in. at centerline and 5 in. at each curb-line of the transverse section (1.3% cross slope). The cross slope was achieved by using tapered formwork at the bridge ends and finishing the bridge along the span and across the width using a mechanical screed (Figure 5.17). For the final surface finish, the deck was tined after the concrete set (Figure 5.18)

Figure 5.17: Screed Machine

Figure 5.18: Tined Surface Finish

5.4.4.1 Concrete Deck Cast

The concrete deck was cast on 23 July 2018. Equipment and manpower for the cast were provided by Yates Construction, and the concrete was supplied by Irving Materials, Inc. The deck was placed in four sections, each requiring one concrete truck. After the surface finish was applied, the deck was covered with wet burlap and plastic for a 3-day wet cure.

5.4.4.2 Concrete Material Testing

Concrete cylinders (6 in. x 12 in.) were cast for compression testing from the four trucks needed for the deck cast (13 cylinders from each truck). Cylinders from each truck were tested at 3, 5, 7, 14, 21, and 28-days to monitor the strength gain of the concrete deck. According to Tippecanoe County's construction guidelines, the deck needed to reach a minimum compressive strength of 4000 psi before the bridge was opened to traffic. All cylinders were made and stored at the bridge site, in accordance with ASTM C31 (2018), until the cylinders were transported from the site for testing.

Each concrete cylinder was tested in a Forney compression machine with a 600-kip capacity. Before testing, the ends of the cylinders were ground smooth and parallel using a Marui Co., LTD. Hi-Kenma cylinder end grinder. A total of eight cylinders (two from each truck) was tested on each test day in accordance with ASTM C39 (2018). The test results are reported in Table 5.2 and Table 5.3. The average strength of the cylinders is plotted with time in Figure 5.19. An extra cylinder was made from each truck in the event a cylinder could not be tested due to oblong shape or other damage. If available, the extra cylinder was tested at 28-days.

As shown in Figure 5.19, at three days, the concrete met the minimum requirements to be opened to traffic. The bridge was opened on 2 August 2018 10 days after casting (1 week was required for paving the bridge approaches). Total bridge closure time was one month (July 2 to August 2).

Table 5.2: Cylinder Compression Strength for Truck 1- Truck 4

Time (days)	Cylinder Compressive Strength, $f`_c$ (psi)												
	Truck 1			**Truck 2**			**Truck 3**			**Truck 4**			**Avg.**
	A	**B**	**C**	**A**	**B**	**C**	**A**	**B**	**C**	**A**	**B**	**C**	
3	4850	5180	-	4260	4710	-	3370	4460	-	4630	4700	-	**4520**
5	5610	5310	-	5050	5030	-	5020	4440	-	5490	5260	-	**5150**
7	5410	5990	-	5170	5050	-	5150	5020	-	5270	5190	-	**5280**
14	6290	5680	-	5530	5420	-	5650	5560	-	5600	5400	-	**5640**
21	6170	6330	-	5630	5880	-	5790	5050	-	5850	5810	-	**5810**
28	5020	6220	-	5930	5940	5490	5800	5740	5990	6120	5910	5980	**5830**

Table 5.3: Fracture Pattern for Truck 1 - Truck 4

Time (days)	Fracture Pattern (ASTM C39)											
	Truck 1			**Truck 2**			**Truck 3**			**Truck 4**		
	A	**B**	**C**	**A**	**B**	**C**	**A**	**B**	**C**	**A**	**B**	**C**
3	2	2	-	3	2	-	3	2	-	2	2	-
5	2	2	-	2	2	-	2	3	-	3	3	-
7	3	2	-	2	2	-	3	2	-	2	2	-
14	4	2	-	3	2	-	2	2	-	4	4	-
21	1	4	-	3	4	-	3	3	-	2	3	-
28	3	3	-	2	4	2	4	2	1	3	3	3

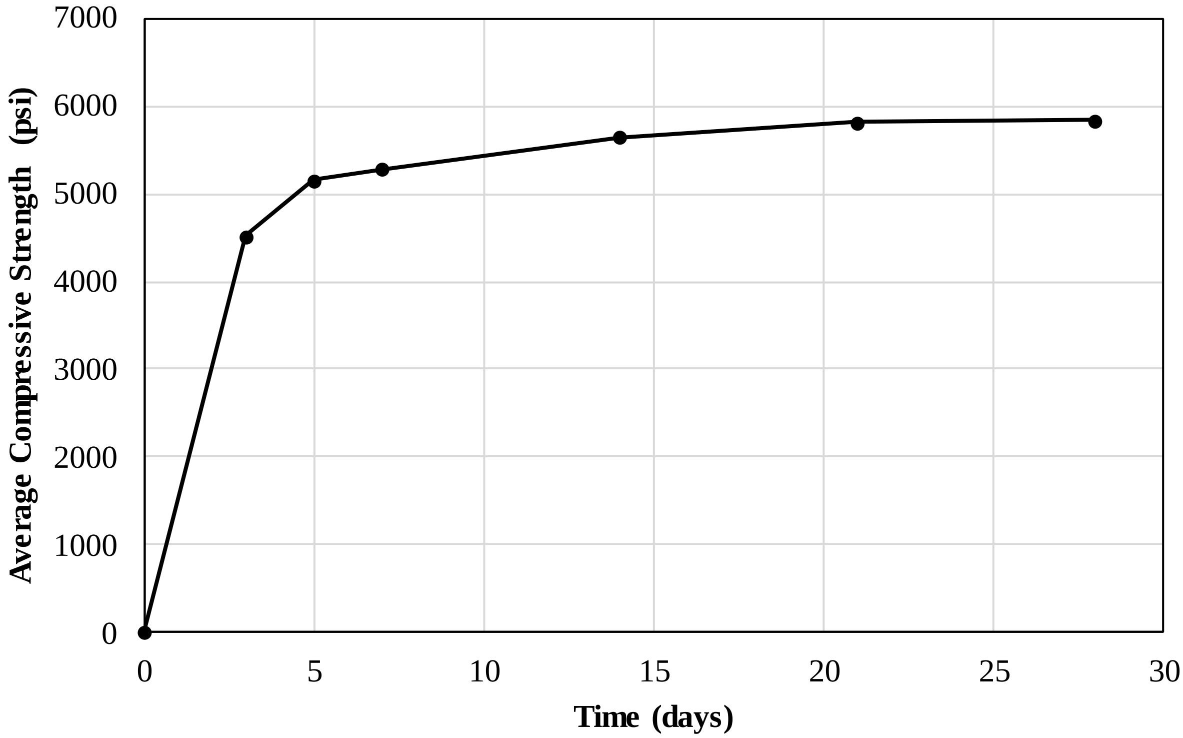

Figure 5.19: Cylinder Compressive Strength Over Time

5.5 Loading Procedure

Each of the four load tests were conducted with the same triaxle truck loaded with gravel (Figure 5.20). The weight of the truck was measured using portable truck weigh scales from the Indiana State Police Division of Commercial Vehicles. The wheelbase dimensions and axle labels are provided in Figure 5.21, and the axle weights for each load test are provided in Table 5.4. A reduced load was used for LT3 because the shear keys were disabled.

Figure 5.20: Tri-Axle Truck

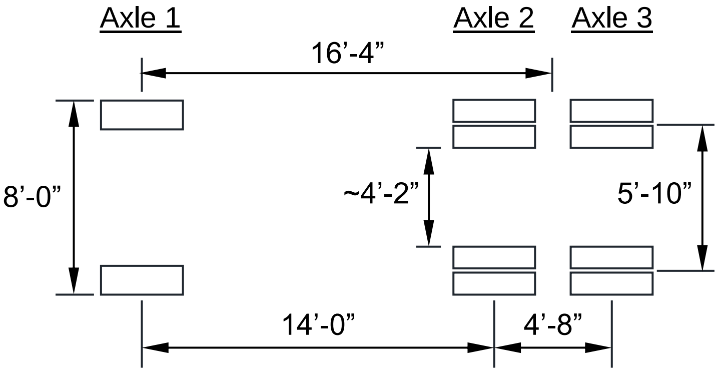

Figure 5.21: Truck Wheelbase Dimensions and Axle Labels

Table 5.4: Truck Weights

Load Test	Axle 1	Axle 2	Axle 3	Total
	lb	lb	lb	lb
LT1	16,450	21,100	20,050	57,600
LT2	15,650	22,300	21,350	59,300
LT3	14,800	15,450	14,450	44,700
LT4	16,450	21,000	21,300	58,750

A total of 50 load positions were defined for the bridge, five longitudinal locations along ten transverse paths. The five positions along the span were selected to approximate the progression of a vehicle crossing the bridge (Figure 5.22). The ten transverse paths traveled by the truck were split into five eastbound paths and five westbound paths. The transverse positions of the truck for the ten paths are given in Figure 5.23 and Table 5.5. The deterioration observed in the site survey and after removal of the bituminous wearing surface prevented some paths from being used for LT1, LT2, and LT3. A summary of the paths used for each load test is provided in Table 5.6.

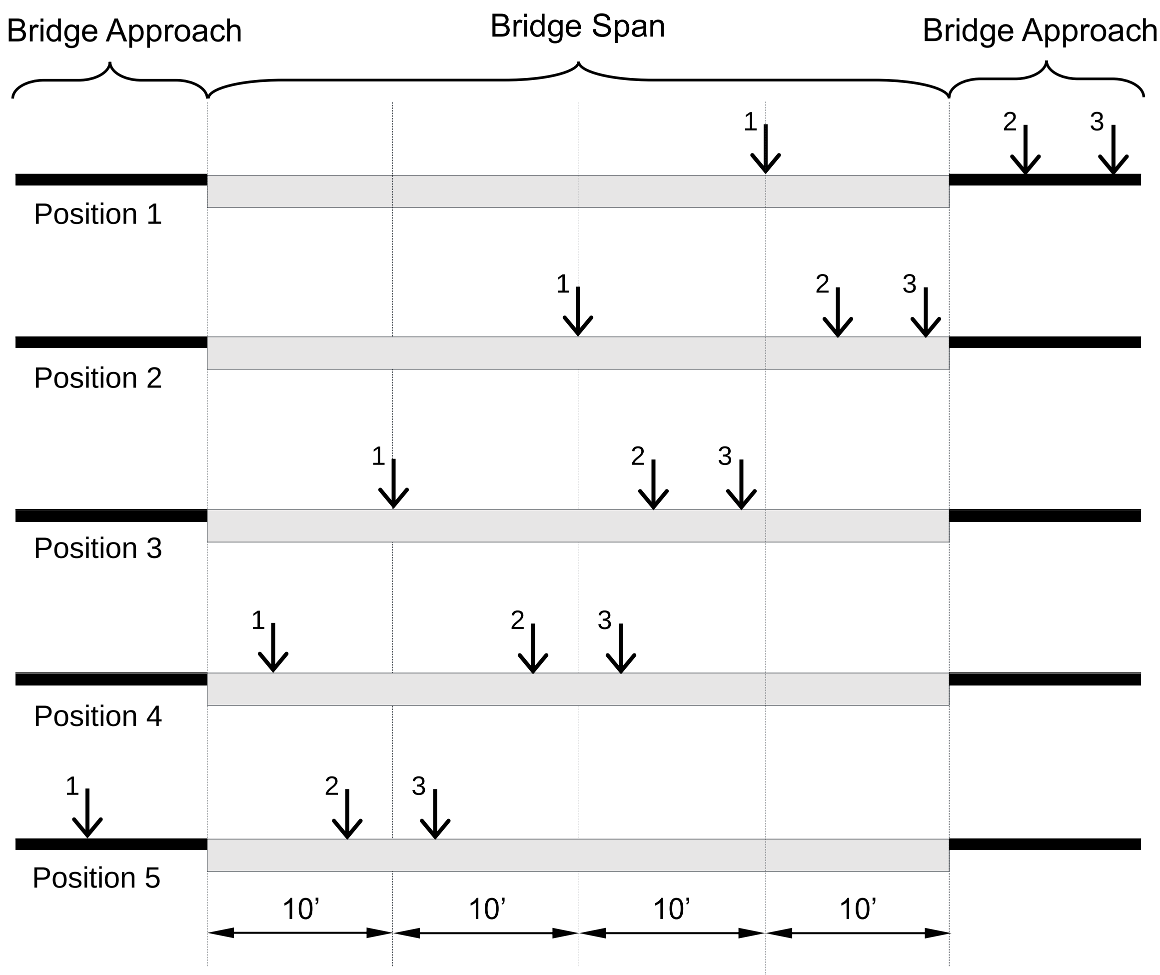

Figure 5.22: Longitudinal Truck Positions

South North

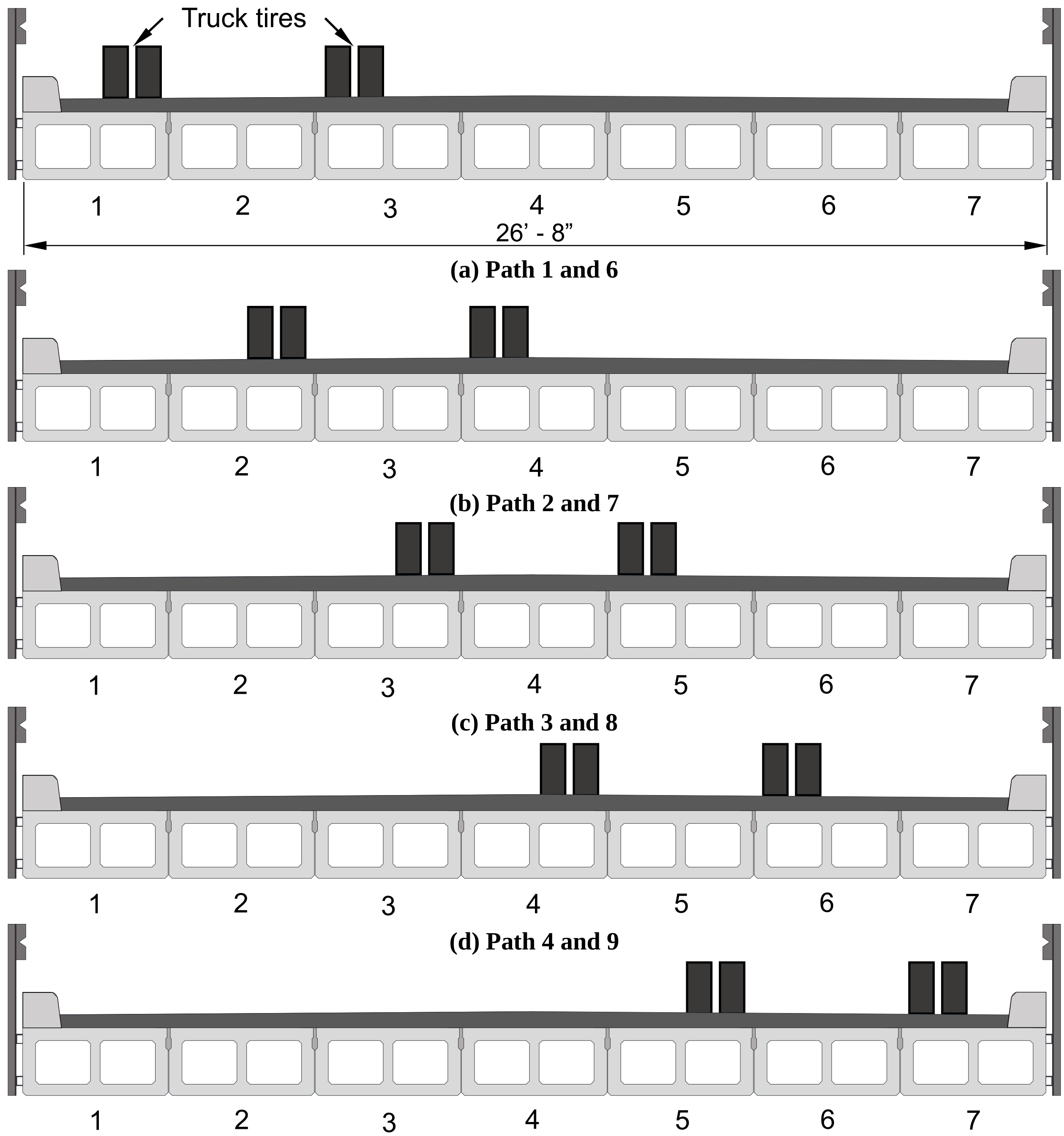

(a) Path 1 and 6

(b) Path 2 and 7

(c) Path 3 and 8

(d) Path 4 and 9

(e) Path 5 and 10

Figure 5.23: Transverse Truck Positions

Table 5.5: Truck Wheel Paths

Path	Wheel Path		Direction of Travel
	Left Wheel	Right Wheel	
1	Beam 3	Beam 1	West to East
2	Beam 4	Beam 2	
3	Beam 5	Beam 3	
4	Beam 6	Beam 4	
5	Beam 7	Beam 5	
6	Beam 1	Beam 3	East to West
7	Beam 2	Beam 4	
8	Beam 3	Beam 5	
9	Beam 4	Beam 6	
10	Beam 5	Beam 7	

Table 5.6: Summary of Loaded Wheel Paths

Load Test	Paths Used
1	2 - 5, 7 - 10
2	4, 5, 9, 10
3	4, 5, 9, 10
4	1 - 10

5.6 Load Test Results

A summary of the load test results is provided in Figure 5.24. At the top of the figure, the illustration shows the longitudinal position of the truck (Position 4) and the direction of travel shown as eastbound for (a) and (b) and westbound for (c) and (d). Position 4 is provided because the maximum midspan deflections were recorded when the truck was in this position. A representation of the bridge cross section is illustrated above each deflection plot, and a set of truck tires is shown on top of each cross section to illustrate the transverse position of the truck as summarized in Table 5.5. Midspan deflections of each beam are shown for the truck in Position 4 traveling through Paths 4, 5, 9, and 10. Paths 4, 5, 9, and 10 are shown because these paths are the only paths loaded for all four load tests (Table 5.6). A comparison between the results from the eastbound and westbound paths shows the results for either traveling direction were very similar.

5.6.1 LT1 - As-Built Condition

Deflections recorded during LT1 from Paths 2 to 5 (eastbound) and Paths 7 to 10 (westbound) are presented in Figure 5.25 and Figure 5.26, respectively. Similar to Figure 5.24, the illustrations provide a guide to the location of the truck on the bridge that corresponds to the plotted deflections. The deflected shape of the transverse section of each path shows that a non-zero value of deflection was recorded for every beam. This indicates that every beam was engaged to carry the truck for each path. Although the longitudinal joints exhibited signs of water leaking through the shear keys, load was distributed to all seven beams for each transverse position. This clearly shows that a leaking shear key is not an indication that load transfer has been eliminated or that the shear key has failed.

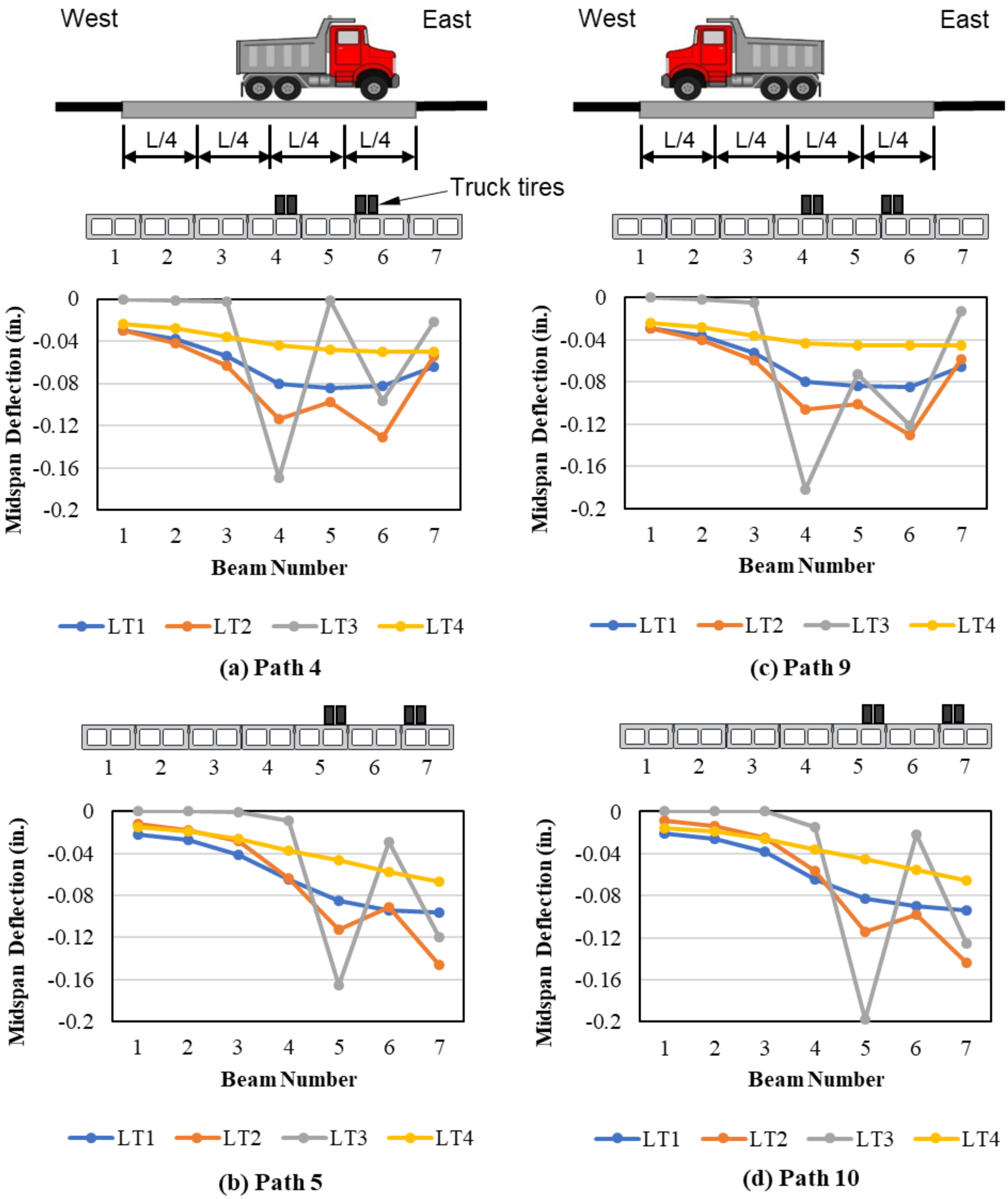

Figure 5.24: Summary of Load Test Results

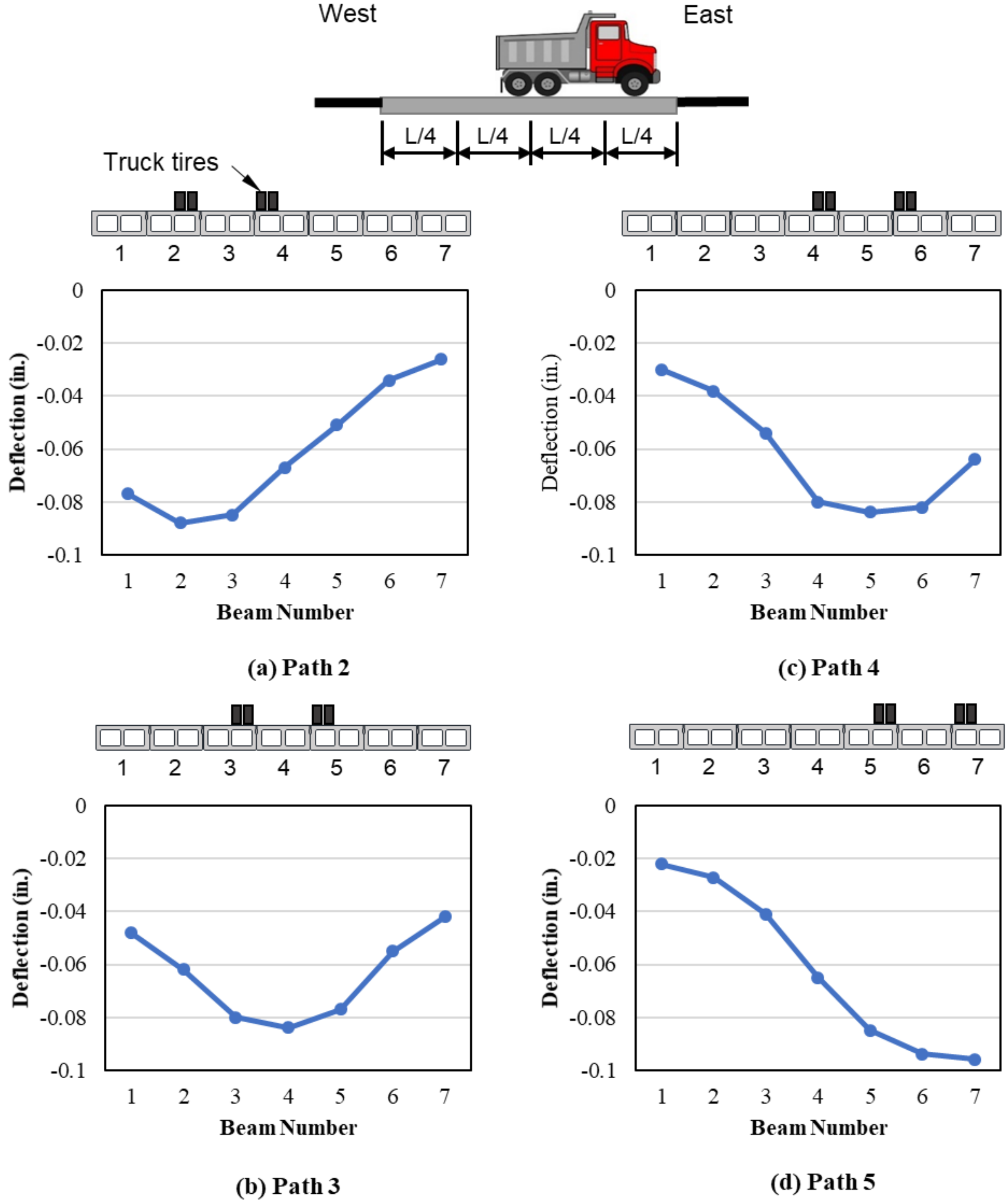

Figure 5.25: As-Built (LT1) Midspan Deflected Shapes – Eastbound

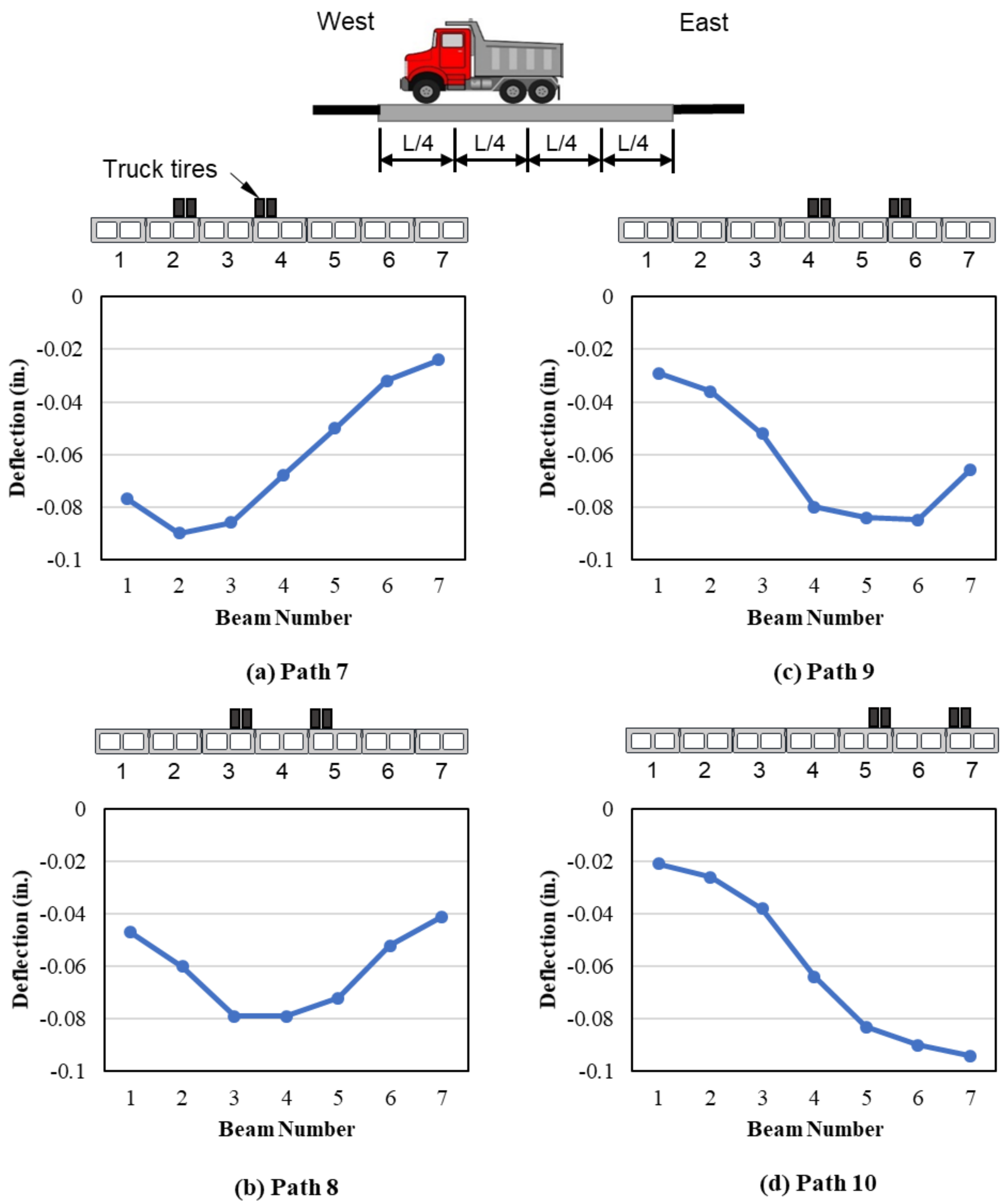

Figure 5.26: As-Built (LT1) Midspan Deflected Shapes - Westbound

5.6.2 LT2 - Wearing Surface Removed

In evaluating the influence of the wearing surface, a comparison between LT1 and LT2 Figure 5.27) shows that larger deflections were generally measured for the directly loaded beams during LT2. In addition, the discontinuities in the transverse deflected shape appear for the directly loaded beams. The increase in measured deflections was caused by two factors.

First, the milling operation that was conducted between LT1 and LT2 removed a small portion of each beam top flange, approximately 0.5 in. to 2 in. The exact reduction in depth could not be accurately measured, but a GPR survey was conducted which estimated the depth to the box beam void. The depth to the void was then compared to the top flange thickness noted on the 1961 INDOT Standard Drawing B-21-3-9 (Figure 5.2) to estimate the amount of section lost during the milling operation. Beams 1, 2, and 3 suffered the greatest reduction, while Beams 4, 5, 6, and 7 were reduced by 0.5 in. to 1 in. The reduction in depth caused a small change in the moment of inertia, decreasing the flexural stiffness.

Second, removal of the wearing surface and a portion of the top flange (and resulting part of the grout between beams) may have allowed slip to occur at each shear key. The loss of shear key thickness caused higher shear stresses in the keyway that may have resulted in cracking of the shear key (Figure 5.28). In addition, the loss of material reduced the shear stiffness of the shear key. The combination of these factors would account for the increased deflections and discontinuities in the deflected shape.

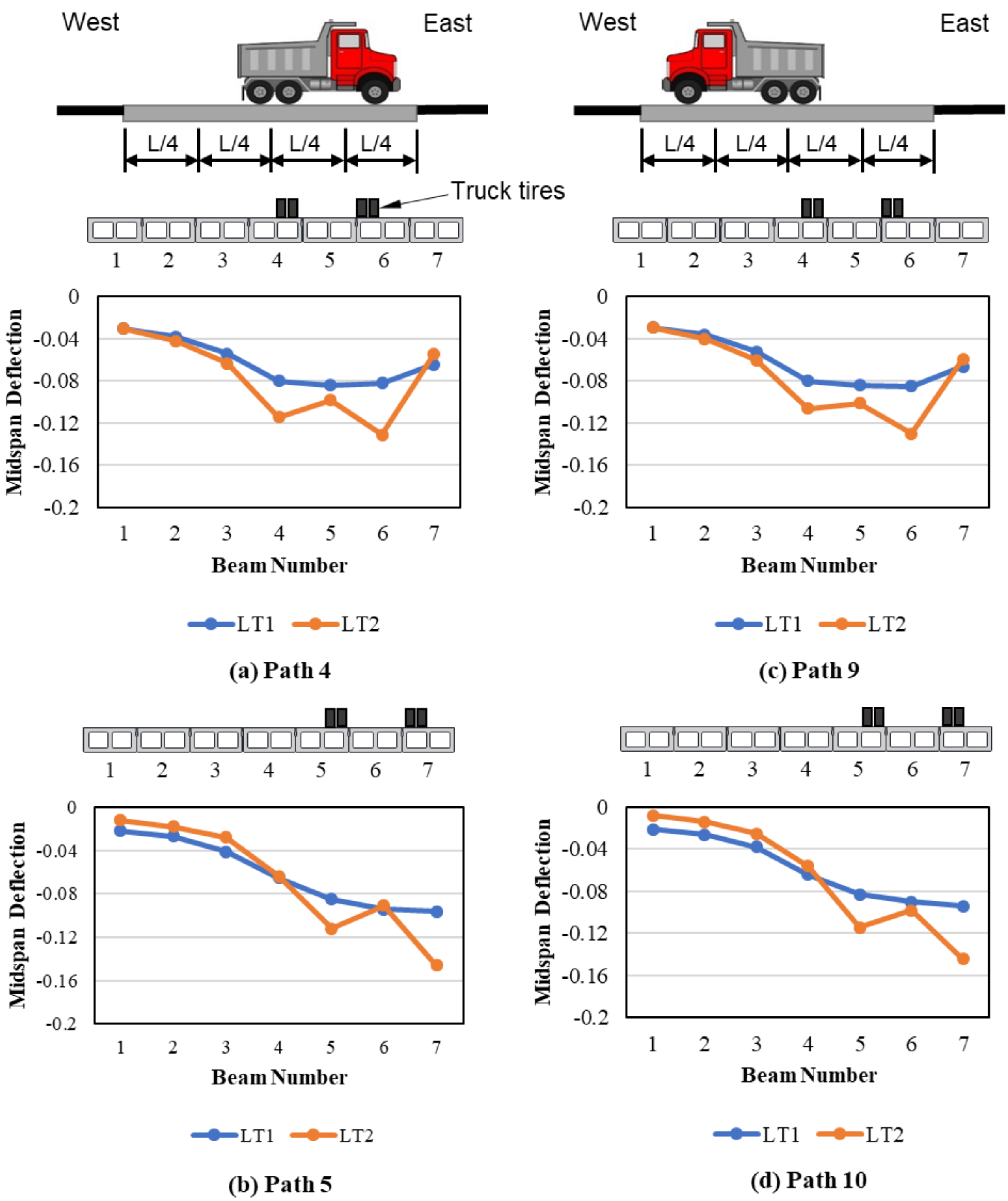

Figure 5.27: As-Built (LT1) vs. Wearing Surface Removed (LT2)

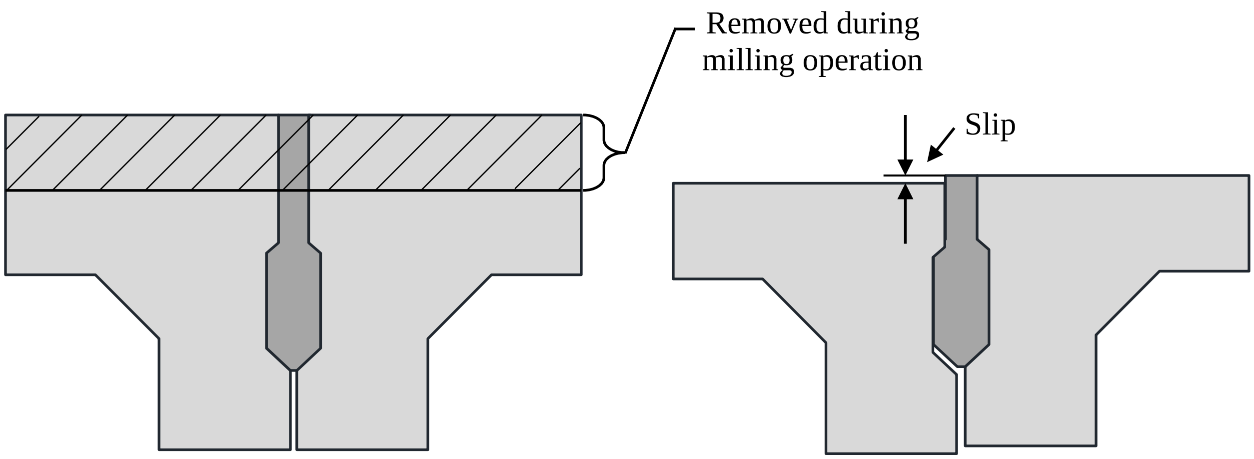

(a) As-Built **(b) After milling**

Figure 5.28: Shear Key Slip

5.6.3 LT3 - Shear Keys Disabled

LT3 was conducted to verify that the shear key cutting operation had been successful in disabling the shear keys. Figure 5.29 shows the comparison between LT1 and LT3. As shown, the deflected shape for LT3 has large discontinuities at the directly loaded beams indicating the shear keys were disabled. The deflections measured on the beams between the truck tires is attributable to the proximity of the tires to the shear key joint. The distance between the rear axle tires of the truck was approximately 50 in., while the width of one box beam was 45 in. Consequently, positioning the truck so that both rear tires were straddling a beam proved difficult. As shown in Figure 5.29, however, Beams 3 and 7 in Path 4 and 9 were clearly not transferring load. Path 4 also shows that Beam 5 was disengaged. In considering Paths 5 and 10, Beam 4 is noted to also be disengaged. While there is some transfer in Beam 6, the large jump indicates that the key was disengaged, but some load was applied through the tires. Observation of the lack of load transferred supports the conclusion that the shear keys were disabled.

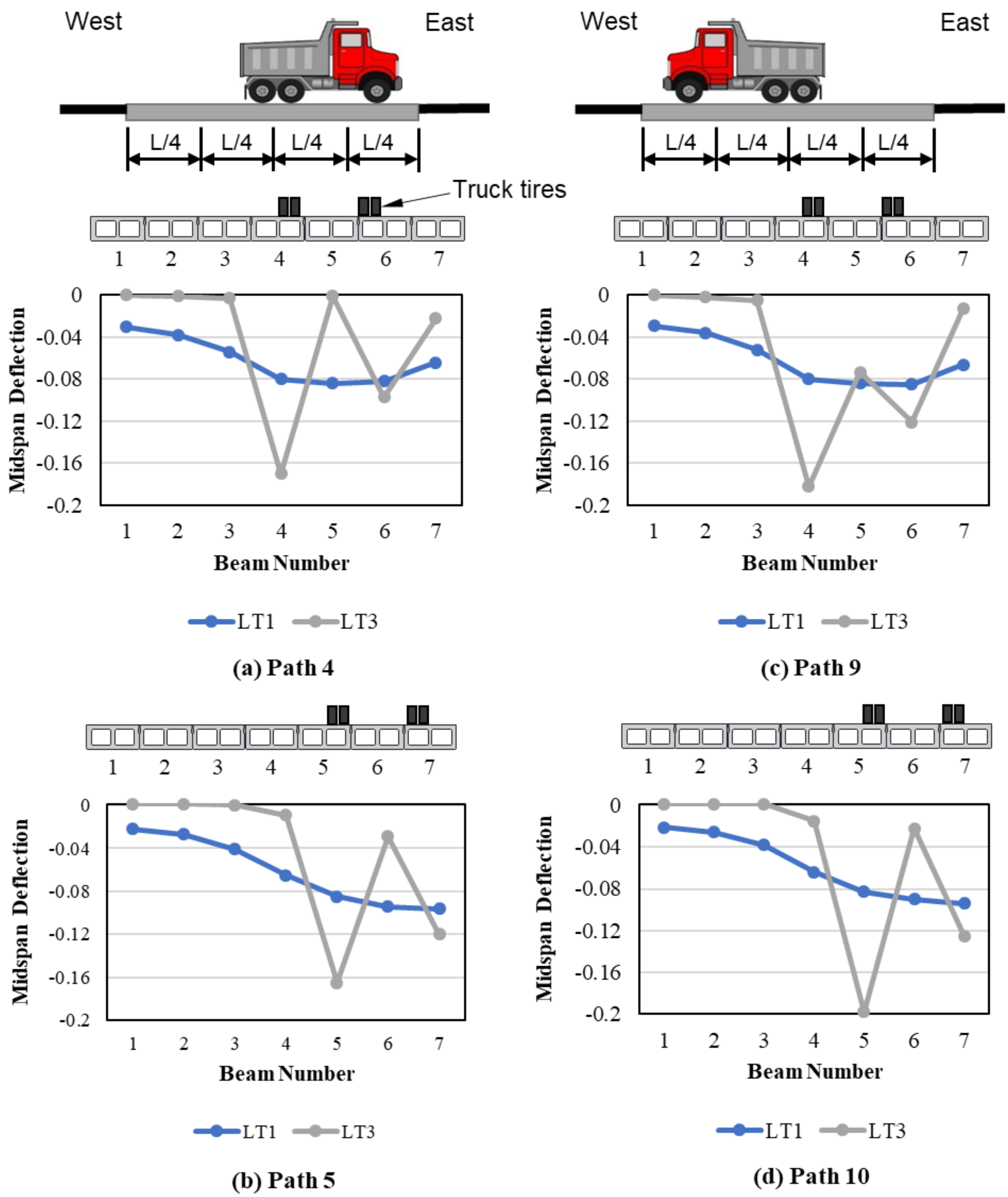

Figure 5.29: As-Built (LT1) vs. Shear Keys Disabled (LT3)

5.6.4 LT4 - Concrete Deck Placed

LT4 was conducted on 14 August 2018, 22 days after the deck was cast. The concrete cylinder strength was approximated as 5,800 psi at the time of testing. The results from LT4 are presented in Figure 5.30 to Figure 5.32 and compared to results of LT1 in Figure 5.31 and Figure 5.32. The data from Paths 1 and 6 in LT4 could not be compared to data from LT1 but are presented in Figure 5.30 to provide complete results. The comparison most notably shows that the load distribution was restored by the concrete deck after the shear keys had been completely disabled. A smooth deflected shape is observed. In addition, the deflections measured during LT4 were on average 37% lower than the deflections measured during LT1.

The reduction in deflection provides evidence that the concrete deck was acting compositely with the beams. A simple calculation based on Article 5.7.4.3 of AASHTO LRFD (2017) estimates the adhesion between the concrete deck and concrete box beams for a width of 45 in. results in a factored resistance of 150 kip/ft. The shear flow generated by the fully factored HL-93 loading on the bridge was calculated as 30 kip/ft. Therefore, adhesion between the deck and the beams is adequate to transfer the horizontal shear required for composite action under the truck loading.

To further investigate the amount of composite action between the box beams and the concrete deck, the midspan deflection of each beam was estimated for LT1 (no concrete deck, $\delta_{est.,LT1}$) and LT4 (full composite action, $\delta_{est.,LT4}$) for the truck in Position 4 (Figure 5.22) for each load path in LT1 (Table 5.6). Midspan deflection of each beam was estimated assuming simple support conditions and elastic beam behavior. The load on each beam was distributed using the midspan deflection data for each load path. A discussion on load distribution is provided in section 5.7. Deflections for LT1 were calculated using a moment of inertia of 30,100 in.^{4} as calculated for the beam without a concrete deck. Deflections for LT4 were calculated using a moment of inertia of 53,100 in.^{4} as calculated for the composite beam and deck.

The reduction in midspan deflection between LT1 and LT4 was calculated as 1-($\delta_{est.,LT1}/\delta_{est.,LT4}$) for all load cases (Table 5.7). The calculated average reduction in midspan deflection was 39%. The average reduction in measured midspan deflection between LT1 and LT4 was measured as 37% (Table 5.8). This comparison shows that the concrete deck and concrete box beams exhibited full composite behavior without traditional composite-action detailing.

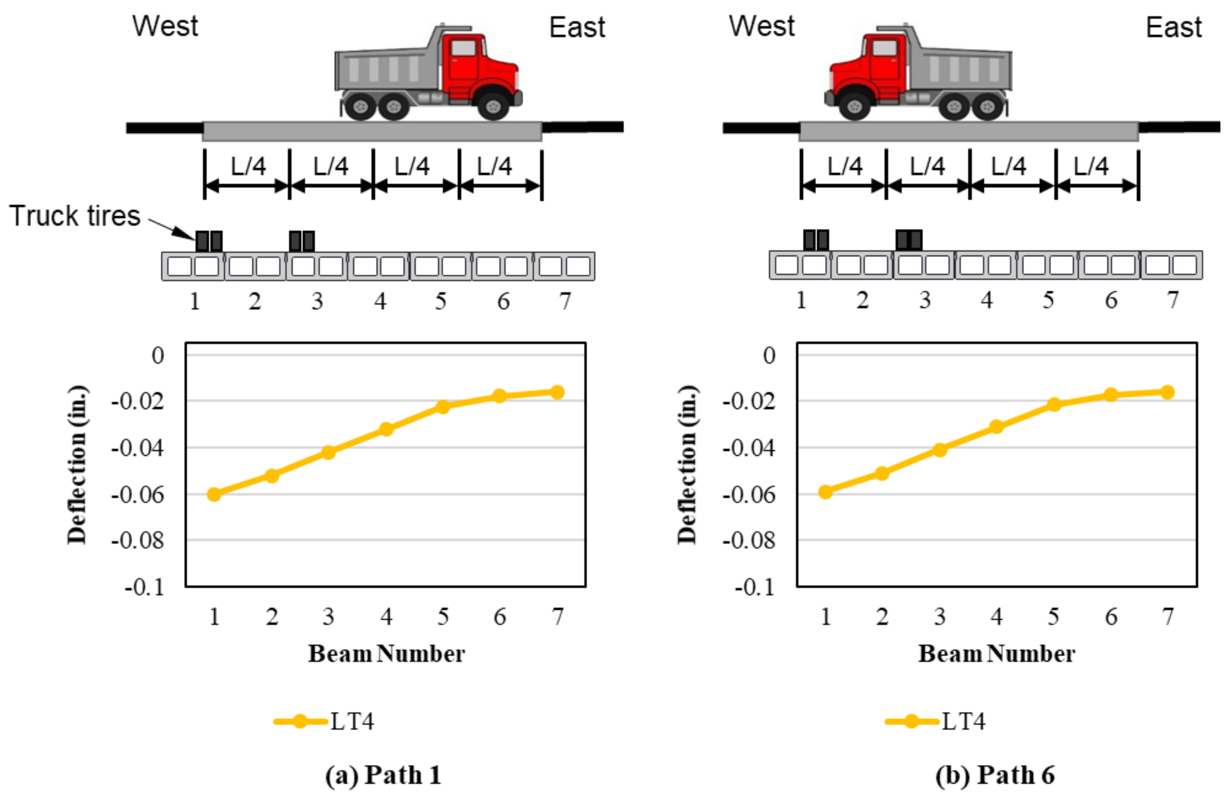

Figure 5.30: Midspan Deflection Data - Concrete Deck Installed (LT4)

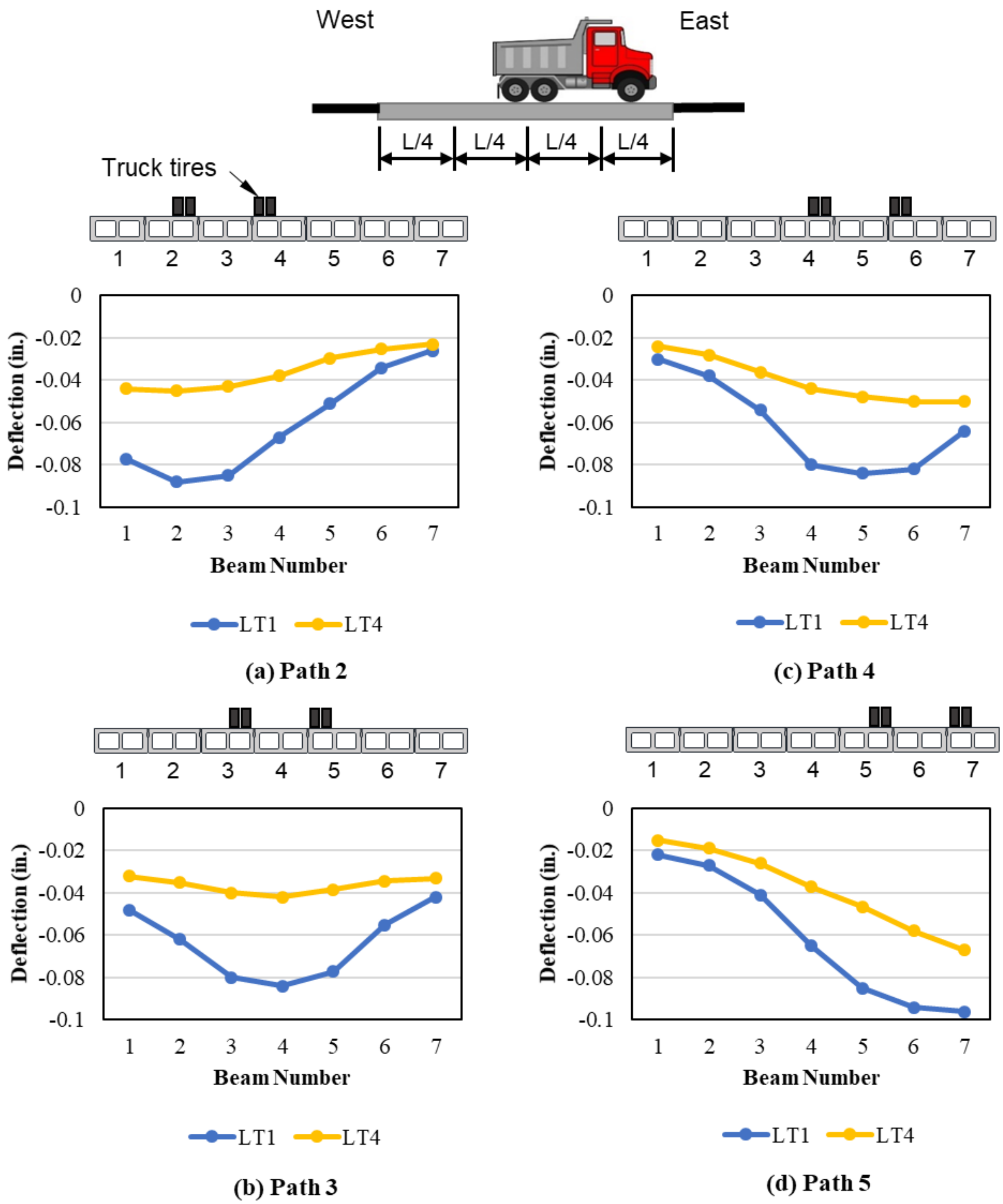

Figure 5.31: As-Built (LT1) vs. Concrete Deck Installed (LT4) -Eastbound

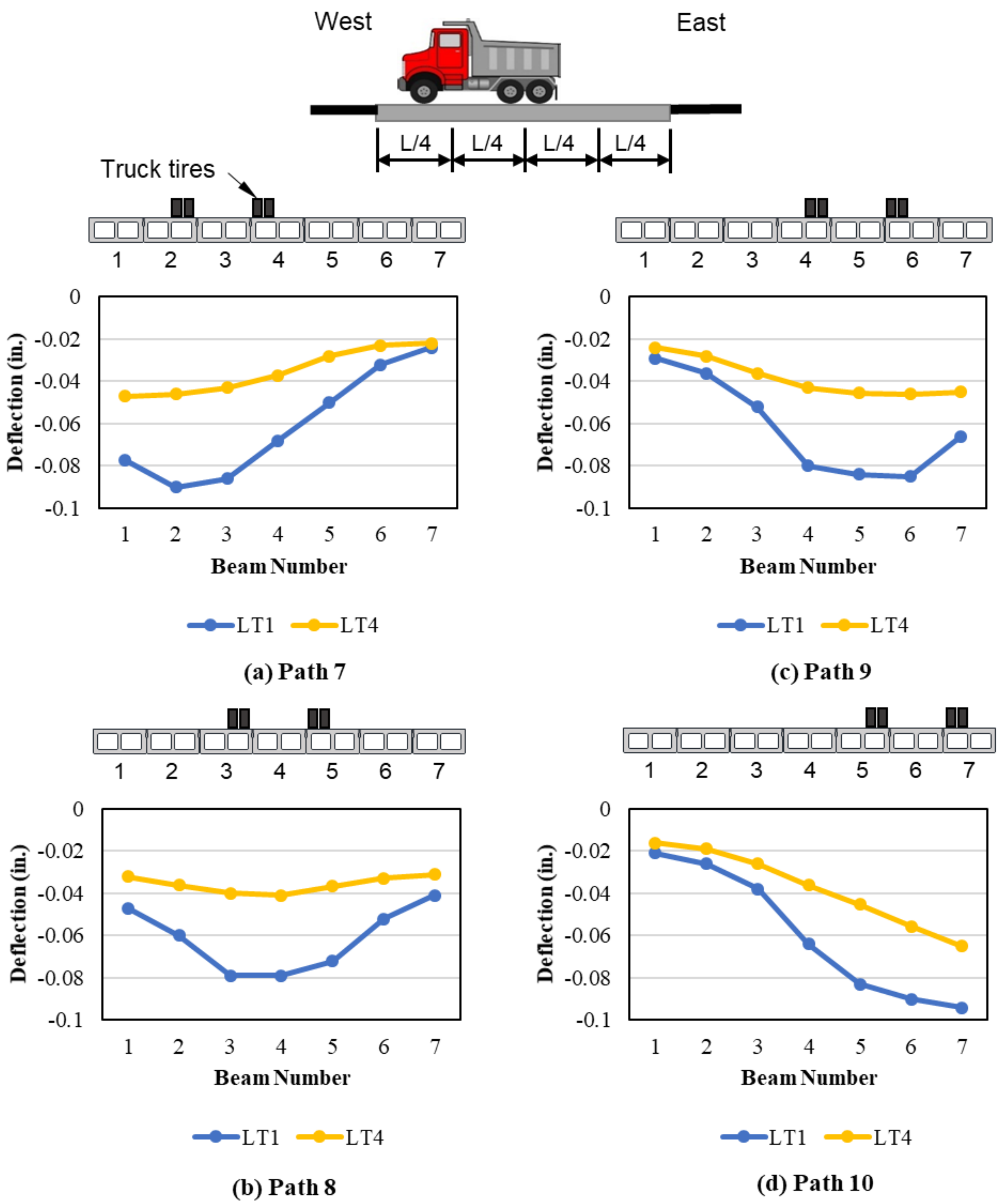

Figure 5.32: As-Built (LT1) vs. Concrete Deck Installed (LT4) - Westbound

Table 5.7: Reduction in Estimated Deflection (1-($\delta_{est.,LT1}/\delta_{est.,LT4}$)

Path	Beam 1	Beam 2	Beam 3	Beam 4	Beam 5	Beam 6	Beam 7
2	0.43	0.49	0.49	0.43	0.42	0.25	0.11
3	0.32	0.42	0.49	0.49	0.49	0.36	0.20
4	0.28	0.34	0.40	0.51	0.49	0.45	0.30
5	0.37	0.34	0.41	0.47	0.49	0.43	0.35
7	0.38	0.48	0.50	0.45	0.44	0.28	0.07
8	0.32	0.40	0.49	0.48	0.49	0.37	0.24
9	0.22	0.27	0.35	0.50	0.49	0.49	0.36
10	0.30	0.33	0.37	0.48	0.50	0.43	0.36
						Average	**0.39**

Table 5.8: Reduction in Measured Deflection (1-($\Delta_{LT1}/\Delta_{LT4}$))

Path	Beam 1	Beam 2	Beam 3	Beam 4	Beam 5	Beam 6	Beam 7
2	0.43	0.49	0.49	0.43	0.42	0.25	0.11
3	0.32	0.42	0.49	0.49	0.49	0.36	0.20
4	0.28	0.34	0.40	0.51	0.49	0.45	0.30
5	0.37	0.34	0.41	0.47	0.49	0.43	0.35
7	0.38	0.48	0.50	0.45	0.44	0.28	0.07
8	0.32	0.40	0.49	0.48	0.49	0.37	0.24
9	0.22	0.27	0.35	0.50	0.49	0.49	0.36
10	0.30	0.33	0.37	0.48	0.50	0.43	0.36
						Average	**0.37**

5.7 Live-Load Distribution

Four load tests were conducted on the bridge to determine the live-load distribution in four conditions: as-built, wearing surface removed, shear keys disabled, and concrete deck placed. The results of each load test are presented in this section to evaluate the influence of each superstructure component on the live-load distribution and determine the live-load distribution of a reinforced concrete deck over adjacent box beams that are not connected with shear keys.

5.7.1 Experimental Live-Load Distribution

The proportion of the truck carried by each beam, hereby referred to as live-load distribution, was determined by dividing the midspan deflection of a single beam by the sum of midspan deflection for every beam in the span, as shown in Equation 5-22. By expressing the live-load distribution of each beam as a ratio of the midspan deflection to the sum of midspan deflection, the results from each load test can be compared independent of the flexural stiffness of the superstructure and variance in the weight of the truck.

$$LLD_i = \frac{\Delta_{mid_i}}{\sum \Delta_{mid_{1\ to\ 7}}} \tag{5-22}$$

where:

LLD_i	=	proportion of load carried by beam i
Δ_{mid_i}	=	midspan deflection of beam i (in.)
i	=	beam number

In the following sections, the results from LT1, LT2, and LT4 are compared. In these comparisons, zero slope in the distribution curve is considered perfect load distribution (all beams carrying equal load). In addition, LT3 was omitted from these comparisons because the shear keys were disabled, and all load was carried by the directly load beams (zero load distribution).

5.7.1.1 Live-Load Distribution - Wearing Surface Removed (LT1 and LT2)

A comparison of the live-load distribution from LT1 and LT2 is provided in Figure 5.33. As shown, the live-load distribution of the bridge after the wearing surface was removed (LT2) was reduced compared to the live-load distribution of the original condition (LT1). The live-load distribution decreased because deflections of the directly loaded beams relative to the indirectly loaded beams increased. The increase in relative deflections was caused in part by the reduction in flexural stiffness of the bridge and the increase in slip between beams that occurred after the milling operation. It appears that loss of stiffness of the shear keys occurred due to the reduction in the grouted region plus removal of the wearing surface.

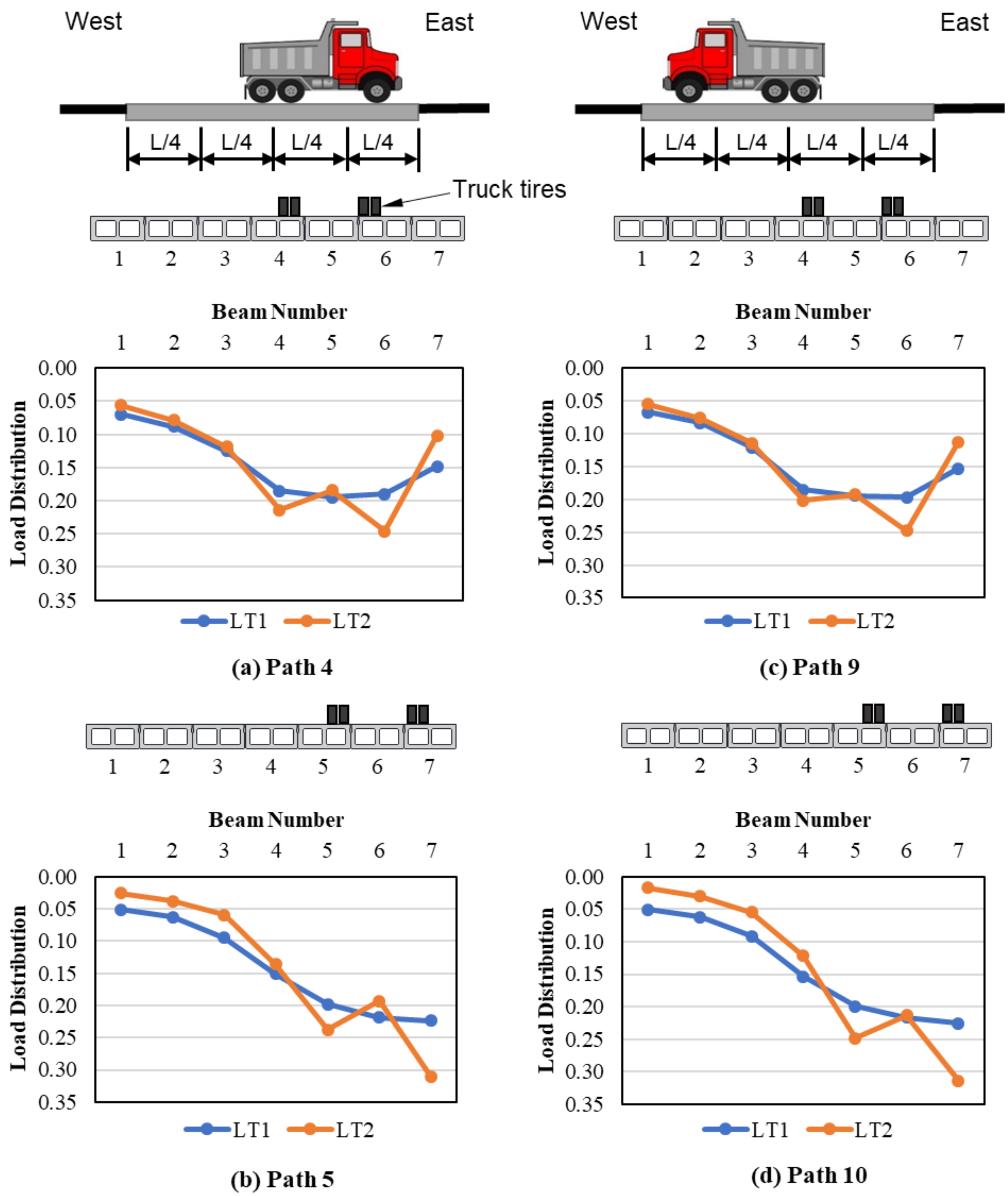

Figure 5.33: Live-Load Distribution As-Built (LT1) vs. Wearing Surface Removed (LT2)

5.7.1.2 Live-Load Distribution - Concrete Deck Addition (LT1 and LT4)

A comparison of the live-load distribution from LT1 and LT4 is provided in Figure 5.34 and Figure 5.35. As shown, the addition of a concrete deck to the bridge without shear keys restored the live-load distribution to a level similar to or greater than that of the bridge in the original condition. For Paths 5 and 10 (exterior beams loaded), the live-load distribution was restored to a similar level as the original condition (LT1) by the addition of a concrete deck. For Paths 2 to 4 and 7 to 9 (interior beams loaded), the live-load distribution was improved compared to the original condition.

Further comparison between the two load tests was made by determining the standard deviation of each load distribution curve. The standard deviation provided a metric to describe the difference between the experimental results and perfect load distribution. A standard deviation of zero indicates that all values in a data set are the same. Therefore, if the standard deviation of the load distribution values is zero, all beams would be carrying equal load which is considered perfect load distribution. The population standard deviation was calculated using the load distribution value of Beams 1-7 for each loaded path. The standard deviation of each load distribution curve for all paths loaded in LT1 and LT4 is reported in Table 5.9. Comparison of the values in Table 5.9 show that for all cases, the concrete deck was superior or the same as the original condition in regard to load distribution.

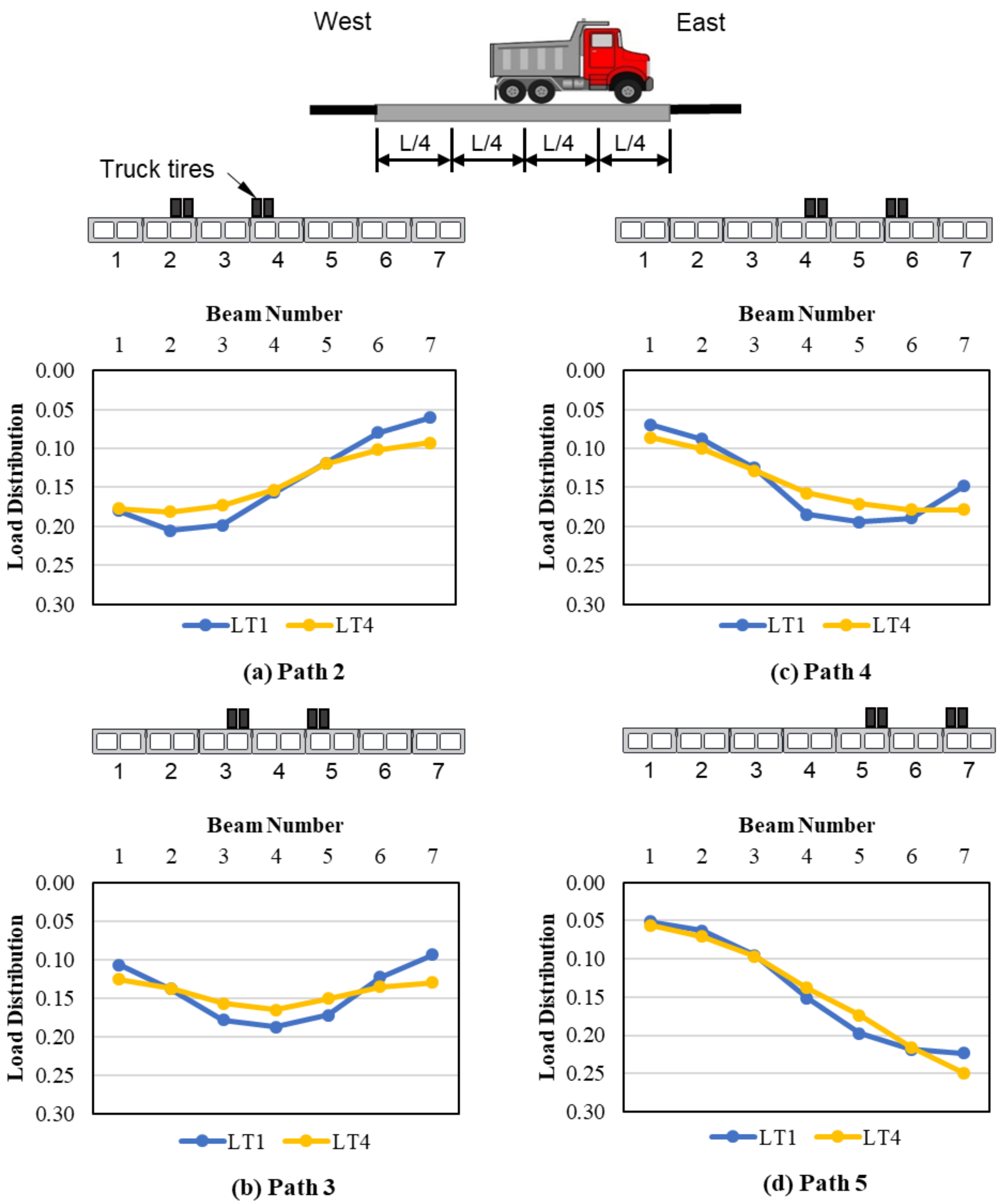

Figure 5.34: Live-Load Distribution As-Built (LT1) vs Concrete Deck Installed (LT4) Eastbound

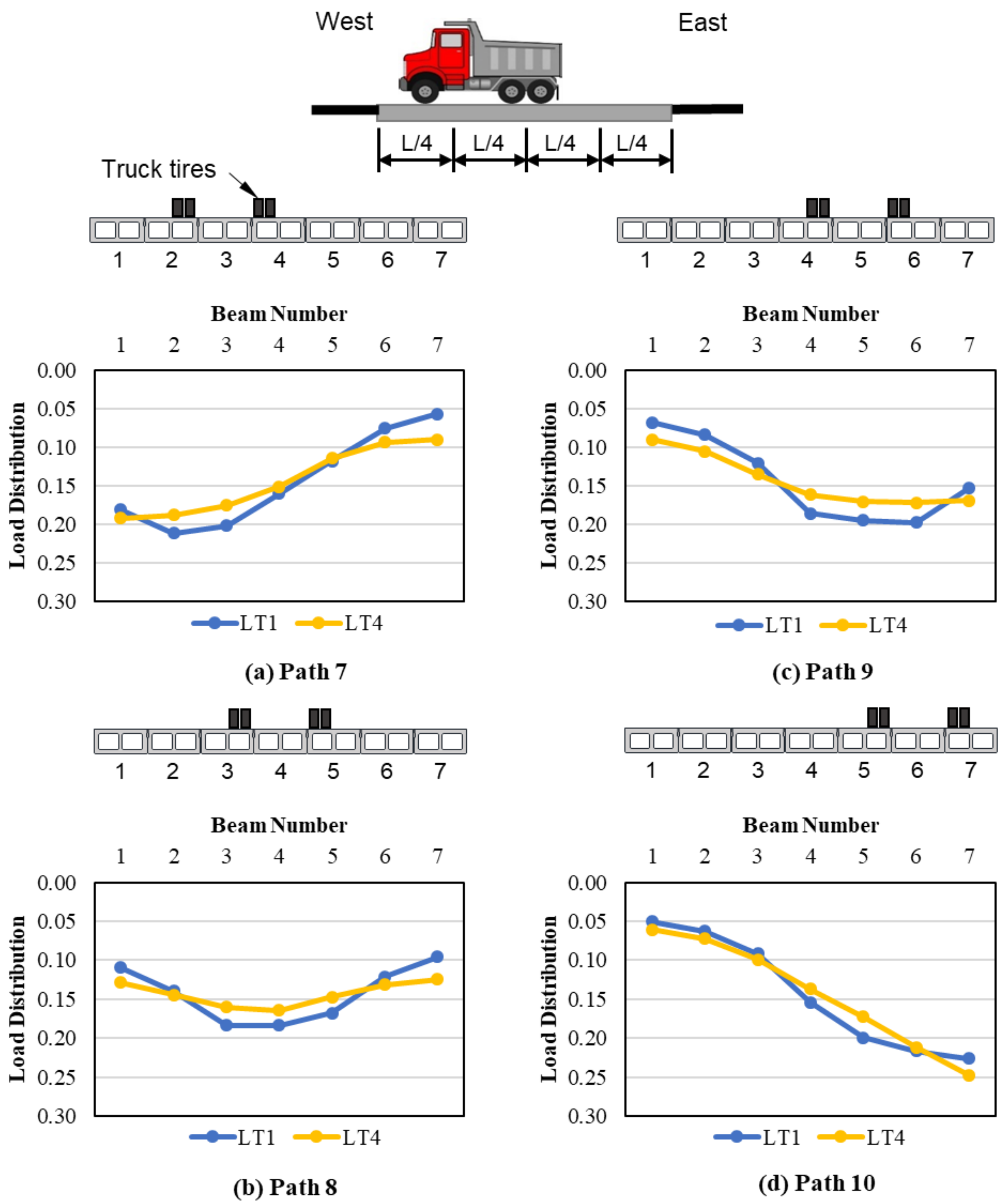

Figure 5.35: Live-Load Distribution As-Built (LT1) vs. Concrete Deck Installed (LT4) Westbound

Table 5.9: Standard Deviation of Load Distribution

Path	Load Test		Difference
	LT1	LT4	
1		0.07	
2	0.05	0.03	-0.02
3	0.03	0.01	-0.02
4	0.05	0.04	-0.01
5	0.07	0.07	0
6		0.07	
7	0.06	0.04	-0.02
8	0.03	0.01	-0.02
9	0.05	0.03	-0.02
10	0.07	0.07	0

*Deterioration prevented the use of Paths 1 and 6 during LT1

5.7.2 Measured Live-Load Distribution Factor

When a simplified beam-line analysis is used to determine the force effects for bridge design, a live-load distribution factor is required to assign a proportion of the force effects to each beam in the bridge (Barker and Puckett 1997). Using the deflection data, the measured live-load distribution factors for the bridge in the original condition and after the concrete deck had been placed were determined. The distribution factors for the interior and exterior beam cases were determined by finding the maximum distribution of load to the interior beams and the exterior beams considering the results from all the loaded paths for both LT1 and LT4 (Figure 5.34 and Figure 5.35) while the truck was in Position 4 (Figure 5.22). Table 5.10 provides the maximum distribution factors that were measured.

Table 5.10: Measured Live-Load Distribution Factors

Live-Load Distribution Factor	Load Test	
	LT1	LT4
Interior	0.22	0.23
Exterior	0.23	0.25

Although the distribution factor for LT4 is higher than that of LT1, the difference is very small (0.01 to 0.02). In addition, the overall behavior of the bridge system was improved by increasing the flexural stiffness of the bridge resulting in decreased deflections and a reduction in the service stresses of the box beams.

5.7.3 Design Live-Load Distribution Factors

5.7.3.1 1957 AASHO Live-Load Distribution Factor

The AASHO Standard Specifications for Highway Bridges (1957) do not include specific design expressions to calculate distribution factors for adjacent beam bridges. The specifications only include an equation for concrete stringers. The AASHO specifications at the time Tippecanoe 115 was constructed provided for load distribution based on the following:

$$\text{Load Fraction} = \frac{S}{5.0} \tag{5-23}$$

where:

Load Fraction	=	live-load distribution factor
S	=	width of the section (ft)

The width of the beams in Tippecanoe 115 were 3.75 ft resulting in a “Load Fraction” value of 0.75.

5.7.3.2 2002 AASHTO Live-Load Distribution Factor

The AASHTO Standard Specification (2002) equation (Article 3.23.4) for live-load distribution of moment is expressed as:

$$\text{Load Fraction} = \frac{S}{D} \tag{5-24}$$

where:

D = $(5.75 - 0.5N_L) + 0.7N_L(1 - 0.2C)^2$

N_L = number of traffic lanes

C = $\begin{Bmatrix} K(W/L)\ if\ W/L < 1 \\ K\ for\ W/L \geq 1 \end{Bmatrix}$

W = overall width of the bridge

L = span length of the beams (ft)

K = $\left[(1+\mu)\left(\frac{I}{J}\right)\right]^{0.5}$

μ = Poisson's ratio

I = moment of inertia (in.^{4})

J = torsion constant (in.^{4})

The torsion constant, J, is approximated using the following expression:

$$J = \frac{2tt_f(b-t)^2\left(d-t_f\right)^2}{bt + dt_f - t^2 - t_f^2} \tag{5-25}$$

where:

d = depth of the section (in.)

b = width of the section (in.)

t = web thickness (in.) (use single web for multiple web beam)

t_f = thickness of the flange (in.)

For the calculation of the load distribution for Tippecanoe 115, the section properties were taken from the 1961 INDOT standard drawing (Figure 5.2), Poisson's ratio was assumed to be 0.2 as recommended by AASHTO (2002), and the number of lanes was 2. The resulting value of the "Load Fraction" using Equation 5-235-24 is 0.64.

5.7.3.3 2017 AASHTO LRFD Live-Load Distribution Factors

AASHTO LRFD (2017) provides a similar empirical equation for live-load distribution which was developed by Zokaie et al. (1991). To determine the live-load distribution using the AASHTO LRFD (2017), the bridge was assumed to be a Type (f) typical cross-section (Table 4.6.2.2.1-1, Article 4.6.2.2.1). The live-load distribution for moment in an interior girder, $g_{int,m}$, was estimated using the following expression:

$$g_{int,m} = k\left(\frac{b}{33.3L}\right)^{0.35}\left(\frac{I}{J}\right)^{0.25} \tag{5-26}$$

where:

k = $2.5(N_b)^{-0.2}$

N_b = number of beams in the bridge

The live-load distribution factor for moment in an exterior girder, $g_{ext,m}$, was estimated using Equation 5-27:

$$g_{ext,m} = g_{int,m}\left(1.125 + \frac{d_e}{30}\right) \tag{5-27}$$

where:

d_e = distance from the centerline of the exterior web to the curb edge (ft)

The curbs of Tippecanoe 115 sit on top of the exterior beam's web. Therefore, $d_e = 0$ was used for the calculation of $g_{ext,m}$. Using section properties taken from the 1961 INDOT standard drawings (Figure 5.2) and Equations 5-26 and 5-27, the moment distribution factors were estimated to be 0.25 for the interior beams and 0.29 for the exterior beams.

To compare the moment distribution factors calculated using the AASHTO LRFD (2017) equations to the measured distribution factors, the calculated interior and exterior distribution factors were divided by a multiple presence factor of 1.2 in consideration of the single lane loading of the load tests. The resulting distribution factors were calculated as 0.21 for the interior beams and 0.24 for the exterior beams.

5.7.4 Discussion

Both the 1957 AASHO and 2002 AASHTO Standard Specifications equations for “Load Fraction” are intended to be applied to the wheel load of the standard truck loading, which is half the axle load of the design truck. However, the live-load distribution factors measured in the test conducted in this study and the live-load distribution factors calculated using the AASHTO LRFD (2017) equations are intended to be applied to the load effect of the entire design truck over the full design lane. To compare the measured and AASHTO LRFD (2017) distribution factors to the 1957 AASHO and 2002 AASHTO Standard Specifications “Load Fraction”, the results of Equations 5-23 and 5-24 must be adjusted. As shown in Figure 5.36, the axle load of the full design truck is applied over two wheels (Figure 5.36(a)), and the wheel load is half the axle load (Figure 5.36(b)). The measured and AASHTO LRFD (2017) distribution factors were calculated based on the application of the full design truck being applied over two wheels. The “Load Fraction” is calculated based on the application of only the wheel load (therefore twice the distribution factor). Therefore, if the full design truck is applied as a single wheel load (Figure 5.36(c)) for use with the “Load Fraction”, the result must be divided by 2.

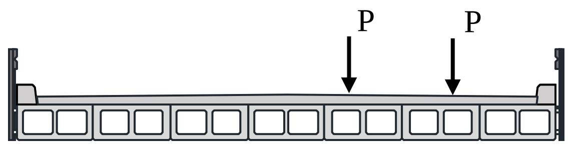

(a) Application of the full design truck

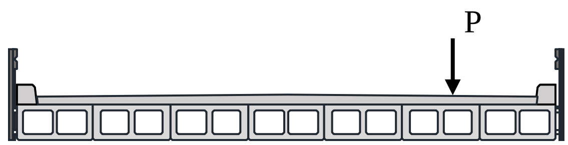

(b) Application of a single wheel load

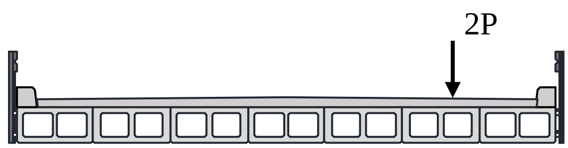

(c) Application of design truck as a wheel load

Figure 5.36: Live-Load Distribution

A summary of the measured and design load distribution factors is presented in Table 5.11. The values of the "Load Fraction" calculated for the Standard Specifications (1957 and 2002) is greater than the maximum distribution factor of Tippecanoe 115 for both LT1 and LT4. The greater value of the Standard Specifications (1957 and 2002) "Load Fraction" shows that load ratings performed using the older specification are conservative. In addition, the load distribution factor computed using the older specifications significantly overestimate the demand on the box beams. The interior load distribution factor calculated using the AASHTO LRFD (2017) equations was in excellent agreement with the experimental results (0.01 difference). Similar results are evident for the exterior load distribution factor. The results indicate that the AASHTO LRFD (2017) Case (f) equations for live-load distribution factors may be used for a bridge with a concrete deck on adjacent box beams without shear keys.

Table 5.11: Summary of Live-Load Distribution Factors

Distribution Factor	Load Test		1957 AASHO Standard Spec.	2002 AASHTO Standard Spec.	2017 AASHTO LRFD
	Original	After			
Interior	0.22	0.23	0.38	0.32	0.21
Exterior	0.23	0.25			0.24

5.8 Summary and Conclusions

An experimental investigation was conducted on a full-scale adjacent precast, prestressed concrete box beam bridge while in service. The study included four load tests of the bridge under four conditions: (1) as-built, (2) bituminous wearing surface removed, (3) shear keys disabled, and (4) reinforced concrete deck installed. Load was applied using a triaxle truck, and deflections of each beam at each quarter-point were measured. Load distribution was calculated based on the midspan deflections of each beam when the truck was in the load position where maximum deflection was recorded. The load distribution was compared between all load tests. In addition, the load distribution factor for each load test was determined and compared to the "Load Fraction" calculated from the 1957 AASHO and the 2002 AASHTO Standard Specification as well as the interior and exterior moment distribution factors calculated using the equations from the 2017 AASHTO LRFD Bridge Design Specifications. The primary findings of the investigation can be summarized as follows:

1. Shear keys showing evidence of leaking may have no impact on live-load distribution. The test results show that even though the shear keys were leaking, live-load distribution was maintained.
2. The results of the load tests indicate that a 5 in. thick concrete deck reinforced with #4 bars at an 8 in. spacing in both the longitudinal and transverse directions can restore load distribution after the primary load distribution mechanism (shear keys) were disabled.

3. A concrete deck placed on concrete beams can achieve full composite action through adhesion of the deck concrete to the concrete beams. The surface should be properly cleaned and roughened prior to placement of the concrete deck.
4. The "Load Fraction" computed from both the 1957 AASHO and the 2002 AASHTO Standard Specification was found to be conservative for load rating 1950s-era adjacent box beam bridges. Similar results are provided by both expressions and both significantly overestimate the demand on the box beams.
5. The AASHTO LRFD (2017) equations for live-load distribution factors for moment are suitable for estimating the live-load distribution factors for a reinforced concrete deck on adjacent concrete beams without shear keys. The test results indicate that these expressions provide extremely accurate estimates of the load distribution.

CHAPTER 6. LOAD RATING

6.1 Capacity of Deteriorated Box Beams

One of the objectives of this research was to develop recommendations for the load rating of adjacent box beam bridges. The analysis model presented in Section 4.6 was used to compute the full load-deflection behavior of each specimen and shown to provide an accurate estimation of structural behavior. In this chapter, the ultimate load of each specimen is calculated following the common load rating practice of adjacent box beam bridges and compared to the structural test results. In addition, the results and findings of visual and NDT inspection, material tests, and structural tests are used to develop an improved calculation procedure for estimating the capacity of deteriorated box beams.

6.2 Common Load Rating Practice

A common assumption used when load rating prestressed concrete box beams is as follows: for every longitudinal crack, concrete spall, and exposed or broken strand, the strand at the deterioration and the immediately adjacent strands are discounted (considered ineffective) from calculation of the structural capacity. In practice, this assumption leads to discounting two or more strands for each type of deterioration (Figure 6.1). The location of the crack or concrete spall is not addressed because the longitudinal extent of corrosion is considered uncertain. Therefore, discounted strands are considered ineffective for the entire length of the beam for conservative strength calculations.

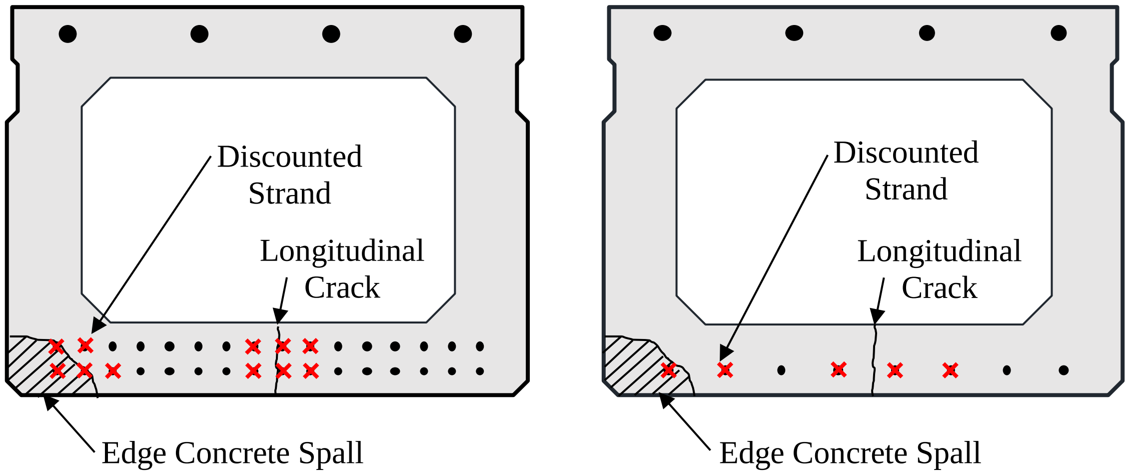

(a) Heavily reinforced beam **(b) Lightly reinforced beam**

Figure 6.1: Discounted Strands Based on Common Load Rating Assumptions

This common practice assumption was applied to each of the beam specimens tested in this study to determine the load rating capacity, P_{LR}. Calculations were performed using the analytical model discussed in Section 4.7 to provide a consistent comparison to the test results and the proposed calculation procedure. For this analysis, the full concrete capacity (ε_{cu} = 0.003) is assumed along with the strain capacity (ε_{pu} = 0.04) of the effective strands. The calculation results are provided in Table 6.1. The number of discounted strands were determined for each specimen based on the deterioration shown in Figure 3.1 to Figure 3.15. The application of the load rating assumption is summarized for each specimen in Table 6.2.

Table 6.1: Summary of Load Rating Analysis Results

Specimen ID	P_{test} (kip)	P_{LR} (kip)	P_{test}/P_{LR}	Strands Discounted
244-1-LC	49.4	55.8	0.88	6
409-1-ES	51.6	37.2	1.39	5
409-2-UD	50.3	51.6	0.98	0
K5-1-LC	68.9	62.3	1.11	6
K5-2-LC	49.3	28.5	1.73	9
79-1-UD	49.2	47.4	1.04	0
79-2-UD	50.5	48.3	1.05	0
79-3-UD	46.7	49.7	0.94	0
79-4-LC	49.3	20.4	2.42	4
56-1-LC	56.0	41.4	1.35	3
56-2-ES	37.7	34.1	1.11	2
102-1-BS	42.3	40.7	1.04	2
102-2-BS	40.2	31.0	1.30	4
102-3-BS	29.4	20.3	1.45	7
102-4-BS	36.2	28.3	1.28	5
		Average:	**1.27**	
		Standard Deviation:	**0.38**	
		Coefficient of Variation:	**0.30**	

Table 6.2: Summary of Load Rating Assumption Application

Specimen ID	Deterioration	Strands Discounted	Number of Discounted Strands
244-1-LC	Both longitudinal cracks located within the constant moment region.	Discount strand at crack and both adjacent strands for each crack.	6
409-1-ES	Spall exposed 3 strands.	Discount adjacent strands on either side of spall.	5
409-2-UD	No visible deterioration.	Discount zero strands.	0
K5-1-LC	Two longitudinal cracks.	Discount strand at each crack and both adjacent strands for each crack.	6
K5-2-LC	Three longitudinal cracks meet 12 ft from south support.	Discount 3 strands for each crack.	9
79-1-UD 79-2-UD 79-3-UD	No visible deterioration.	Discount zero strands.	0
79-4-LC	Two longitudinal cracks. Only 6 strands in the section.	Discount strand at each crack and adjacent the strand.	4
56-1-LC	Hairline longitudinal crack at south support.	Discount strand at crack and both adjacent strands.	3
56-2-ES	Exposed edge strand.	Discount exposed strand and the adjacent strand.	2
102-1-BS	Broken edge strand.	Discount broken strand and the adjacent strand.	2
102-2-BS	Broken strand on west edge, longitudinal cracking on east edge.	Discount broken strand, strand at longitudinal crack, and strands adjacent to each edge strand.	4
102-3-BS	Broken edge strand next to exposed strand on west edge. Longitudinal cracking on east edge.	Discount broken and exposed strand plus one adjacent strand. Also, discount strand at each crack and one adjacent strand.	7
102-4-BS	Broken strand next to exposed strand on east edge. Longitudinal cracking on west edge.	Discount broken and exposed strand plus one adjacent strand. Also, discount strand at edge crack and one adjacent strand.	5

A review of Table 6.1 shows that the load rating assumption was conservative for all deteriorated specimens except Specimen 244-1-LC (P_{test}/P_{LR} = 0.88). The ratio of P_{test}/P_{LR} ranged from 0.88 (Specimen 244-1-LC) to 2.42 (Specimen 79-4-LC). The undeteriorated specimens (Specimens 409-2-UD, 79-1-UD, 79-2-UD, and 79-3-UD) were assumed to have zero strands discounted in the analysis. Therefore, the estimated strength is equivalent to the analytical values calculated for these specimens in Chapter 4.

The common practice assumption was most conservative for beams with deterioration localized at the end of the specimen, or, in the case of Specimen K5-2-LC, where the deterioration was caused by water ingress into the void. This indicates that the assumption could be modified such that only strands aligned with or intersected by a longitudinal crack are discounted from the analysis for cases where the crack is located away from the edge of the bottom flange.

The capacity of Specimen 244-1-LC was underestimated because concrete deterioration is not considered in the analysis. Deterioration of the concrete in the top flange of this specimen limited the strain capacity of the concrete and resulted in premature compressive failure of the flange. Deteriorated concrete in the top flange of box beams has not been considered in common practice as the focus has been on loss of strand capacity. The capacities of Specimens K5-2-LC and 56-2-ES, which also had concrete deterioration of the top flange, were not underestimated because the conservatism of the common practice assumption paired with the severity of bottom flange deterioration was enough to compensate for deterioration of the top flange.

Specimen 244-1-LC makes clear that concrete delamination in the top flange concrete is important and should be considered. One difficulty lies in identifying top flange concrete delamination as many bridges include a bituminous wearing surface that obscures visual inspection of the top flange concrete. GPR is one NDT method that provides the potential for detecting concrete delamination where bituminous wearing surfaces are in place.

6.3 Proposed Analysis Procedure

Based on the results of tensile tests of corroded strands and structural tests of undeteriorated and deteriorated box beams, the following analysis procedure is proposed to estimate the capacity of box beams exhibiting signs of deterioration.

Initial Capacity

For this analysis, all strands, unless broken or severely pitted, are considered effective.

1. If delaminated concrete is observed in concrete in the compression flange, the capacity P_{dc} is calculated by limiting the strain in the extreme fiber in compression to $0.5f_c'/E_c$.
2. Exposed strands and strands at rust stained longitudinal cracks are assumed to be limited in capacity. The capacity P_{ds} is calculated by limiting the strain in the prestressing strand to $0.75f_{pu}/E_{ps}$.

Residual Capacity

For this analysis, all corroded strands are assumed to be ineffective.

1. If delaminated concrete is observed in the compression flange, the reserve capacity P_{rdc} is calculated by limiting the strain in the extreme fiber in compression to $0.5f_c'/E_c$. Full strain capacity of the remaining effective strands (ε_{pu} = 0.04) is assumed.
2. The reserve capacity P_{rds} is calculated considering the remaining effective strand to have full strain capacity (ε_{pu} = 0.04). Full concrete strain capacity (ε_{cu} = 0.003) is also considered.

The capacity P_{dc} represents the load corresponding to crushing of the deteriorated concrete with all strands effective. The value of P_{ds} represents the load corresponding to fracture of the corroded strands in the beam. The reserve capacity of a beam with deteriorated concrete corresponds to P_{rdc}. Finally, P_{rds} represents the load corresponding to the reserve capacity of the section with only non-corroded strands effective. Considering the behavior observed in structural tests, the controlling capacity P_d is determined by comparing the minimum values of the initial deteriorated capacities to the minimum reserve capacity. As shown in Figure 6.2, the minimum of the initial deteriorated capacities P_{dc} and P_{ds} will control the initial failure load with all strands effective. The beam may have reserve capacity which is controlled by the minimum of P_{rdc} and P_{rds}. The value of P_d is then equal to the maximum value between the controlling initial capacity and reserve capacity. Depending on the number of corroded strands, the reserve capacity can be less than or greater than the initial capacity.

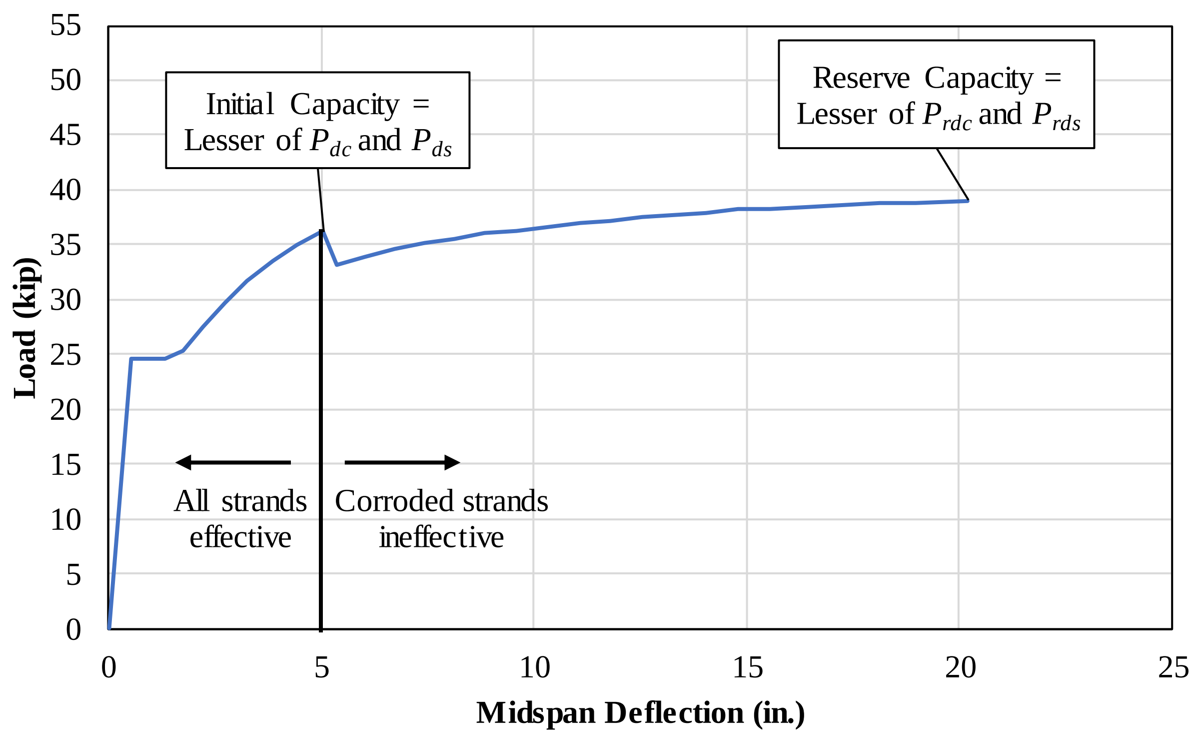

Figure 6.2: Load-Deflection Response of a Beam with Corroded and Uncorroded Strands

Using the proposed calculation procedure, the capacity P_d was computed for each specimen using the analytical model presented in Section 4.6, and the results are provided in Appendix K and summarized in Table 6.3. The calculation of P_{dc} was performed only for the specimens that exhibited top flange deterioration (Specimens 244-1-LC, K5-2-LC, and 56-2-ES). The calculation of P_{ds} considered all strands effective except in the case of Specimens 102-1-BS, 102-2-BS, 102-3-BS, and 102-4-BS where the strands broken prior to testing were considered ineffective. The number of corroded strands discounted from the computation of P_{db} is reported in Table 6.3 and is based on the correlation between visual deterioration and strand corrosion discussed in Chapter 3. In addition, strand corrosion located more than one development length (as estimated by Equation 4-19) from the section of maximum moment was considered to have no effect on structural capacity. The number of discounted strands for each specimen is explained in Table 6.4.

A review of Table 6.3 shows that the proposed analysis procedure provides accurate estimates of the deteriorated capacity. The average value of P_{test}/P_d is 1.04 for all specimens and ranged from 0.94 (Specimen 79-3-UD) to 1.29 (Specimen 56-2-ES). The low value for Specimen 79-3-UD is due to the piece of wood that was embedded in the curb. It should be noted that the concrete curbs on Specimens K5-1-LC, 79-3-UD, and 79-4-LC were considered in this analysis. As discussed previously, the curbs increase the strength of the cross section. If the proposed analysis procedure is performed without considering the curb, the ratio of P_{test}/P_d is conservative for each specimen (Specimen K5-1-LC (1.08), Specimen 79-3-UD (1.44), and Specimen 79-4-LC (1.60)).

The average value of P_{test}/P_d is 1.06 for specimens with visual signs of deterioration and ranged from 0.96 (Specimen K5-1-LC) to 1.29 (Specimen 56-2-ES). The low value of P_{test}/P_d for Specimen K5-1-LC is due to the reduced middle web thickness caused by a construction error.

The high value of 1.29 for Specimen 56-2-ES is due to the greater strain capacity of the corroded strand and deteriorated concrete. Overall, the propose analysis procedure provided accurate estimates of the deteriorated capacity.

Table 6.3: Proposed Analysis Procedure Results

Specimen	P_{test} kip	Failure Mode Capacity				Deteriorated Capacity		Strands Discounted
		Initial Capacity		Reserve Capacity				
		Concrete	Steel	Concrete	Steel			
		P_{dc} kip	P_{ds} kip	P_{rdc} kip	P_{rds} kip	P_d kip	P_{test}/P_d	
244-1-LC	49.4	50.9	47.4	46.4	60.5	47.4	1.04	4
409-1-ES	51.6				52.1	52.1	0.99	0
409-2-UD	50.3				51.6	51.6	0.98	0
K5-1-LC*	68.9		55.6		71.5	71.5	0.96	3
K5-2-LC	49.3	52.1	42.8	41.8	45.5	42.8	1.15	3
79-1-UD	49.2				47.4	47.4	1.04	0
79-2-UD	50.5				48.3	48.3	1.05	0
79-3-UD*	46.7				49.7	49.7	0.94	0
79-4-LC*	49.3				48.9	48.9	1.01	0
56-1-LC	56.0				57.4	57.4	0.98	0
56-2-ES	37.7	31.3	27.5	29.2	37.4	29.2	1.29	1
102-1-BS	42.3		30.5		40.7	40.7	1.04	2
102-2-BS	40.2		27.5		39.0	39.0	1.03	2
102-3-BS	29.4		29.3		29.1	29.3	1.00	5
102-4-BS	36.2		22.8		32.3	32.3	1.12	4

*Constructed with a concrete curb.

Overall Average: 1.04
Deteriorated Specimen Average: 1.06
Overall Standard Deviation: 0.09
Overall Coefficient of Variation: 0.08

Table 6.4: Summary of NDT Result Application

Specimen ID	Deterioration	Corroded Strand	Number of Ineffective Strands
244-1-LC	GPR indicated that 4 strands intersected two longitudinal cracks. The intersection locations were within one development length of the section at 17 ft from the south support which is within the constant moment region.	Discount 4 strands	4
409-1-ES	The edge of the concrete spall was located more than one development length from the constant moment region.	Discount zero strands	0
409-2-UD	No visible signs of deterioration	Discount zero strands	0
K5-1-LC	GPR indicated that 3 strands intersected the south longitudinal crack within one development length of the constant moment region.	Discount 3 strands	3
K5-2-LC	GPR indicated that 3 strands intersected the longitudinal cracks at approximately 15 ft from the south support which is within the constant moment region.	Discount 3 strands	3
79-1-UD 79-2-UD 79-3-UD	No visible signs of deterioration	Discount zero strands	0
79-4-LC	GPR indicated that 4 strands intersected the longitudinal cracking in the north end of the specimen. The locations of intersection were all located more than one development length from the constant moment region.	Discount zero strands	0
56-1-LC	The end of the longitudinal crack in the south end of the specimen was located more than one development length from the constant moment region.	Discount zero strands	0
56-2-ES	Spalling exposed a single strand and did not extend to the adjacent strand.	Discount 1 strand	1

Table 6.4: Continued

Specimen ID	Deterioration	Corroded Strand	Number of Ineffective Strands
102-1-BS	Spalling exposed one broken strand and extended to the adjacent strand.	Discount the broken strand and the strand at the concrete spall.	2
102-2-BS	Spalling exposed one broken strand on the west edge. Longitudinal cracking on east edge caused by corrosion of edge strand.	Discount the broken strand and the strand at the longitudinal crack.	2
102-3-BS	Spalling exposed one broken strand on west edge within one development length of the constant moment region and did not extend to the adjacent strand. Longitudinal cracking on east edge aligned with four strands within the constant moment region.	Discount the broken strand and each of the four strands at the longitudinal cracking.	5
102-4-BS	Spalling exposed 2 strands on the east side of the beam and 1 strand on the west side of the beam within the constant moment region. The spall on the west side extended to the adjacent strand.	Discount the three exposed strands and the unexposed strand at the concrete spall.	4

6.4 Load Rating Comparison

The calculation results using the common practice assumption (P_{LR}) and proposed calculation procedure (P_d) are compared in Table 6.5. As shown, the average value of P_{test}/P_{LR} is 1.27 (ranging from 0.88 to 2.42) while the average value of P_{test}/P_d is 1.04 (ranging from 0.94 to 1.29). For deteriorated specimens, the average value of P_{test}/P_{LR} is 1.37 (ranging from 0.88 to 2.42) and 1.06 for P_{test}/P_d (ranging from 0.96 to 1.29). As discussed, the low value of P_{test}/P_{LR} = 0.88 for Specimen 244-1-LC is due to concrete deterioration that was not considered by common practice. Using the proposed analysis procedure, however, the strength is conservatively calculated with P_{test}/P_d = 1.04. In addition, the conservative value of P_{test}/P_{LR} = 2.42 for Specimen

79-4-LC is reduced to P_{test}/P_d = 1.01 using the proposed analysis. By considering the strain capacity of deteriorated concrete (if applicable) and corroded strand, the proposed analysis provides more accurate estimates of the deteriorated capacity.

Table 6.5: Calculation Procedure Comparison

Specimen ID	P_{test} kip	Common Practice P_{LR} kip	Proposed Analysis P_d kip	P_{test}/P_{LR}	P_{test}/P_d
244-1-LC	49.4	55.8	47.4	0.88	1.04
409-1-ES	51.6	37.2	52.1	1.39	0.99
409-2-UD	50.3	51.6	51.6	0.98	0.98
K5-1-LC	68.9	62.3	71.5	1.11	0.96
K5-2-LC	49.3	28.5	42.8	1.73	1.15
79-1-UD	49.2	47.4	47.4	1.04	1.04
79-2-UD	50.5	48.3	48.3	1.05	1.05
79-3-UD	46.7	49.7	49.7	0.94	0.94
79-4-LC	49.3	20.4	48.9	2.42	1.01
56-1-LC	56.0	41.4	57.4	1.35	0.98
56-2-ES	37.7	34.1	29.2	1.11	1.29
102-1-BS	42.3	40.7	40.7	1.04	1.04
102-2-BS	40.2	31.0	39.0	1.30	1.03
102-3-BS	29.4	20.3	29.1	1.45	1.01
102-4-BS	36.2	28.3	32.3	1.28	1.12
			Overall Average:	**1.27**	**1.04**
			Deteriorated Average:	**1.37**	**1.06**

6.5 Recommendation

Based on the comparison of the common practice procedure and the proposed analysis, the proposed analysis is recommended for estimating the capacity of deteriorated box beams for use in load rating. The proposed procedure utilizes the improved understanding of the extent and effect of deterioration on the assessment of strength. By incorporating the capacity of the deteriorated prestressing strand and deteriorated concrete (if applicable), an accurate estimation of the deteriorated capacity can be made. This procedure also has the benefit of allowing for load-deflection response of the deteriorated beam to also be estimated.

CHAPTER 7. NEW DESIGN

7.1 Introduction

The information gathered through inspection of deteriorated box beam bridges and investigation of the extent of strand corrosion have provided an understanding of the mechanisms that contribute to the poor performance of adjacent box beam bridges. The goal of this chapter is to recommend improvements for this type of construction.

7.2 Cross Section

7.2.1 Standard Box Beam Section Improvement

Bridge inspections presented in Chapter 2 frequently observed longitudinal cracking, and exposed and broken strands in the edges of the bottom flange at the longitudinal joint or bridge exterior. The deterioration was caused by chloride-laden water leaking or draining onto the sides of the box beams and curling onto the bottom flange. A 3/4-in. half-round drip bead is recommended to be added to the edges of the bottom flange to prevent water from curling onto the bottom flange and is shown in Figure 7.1.

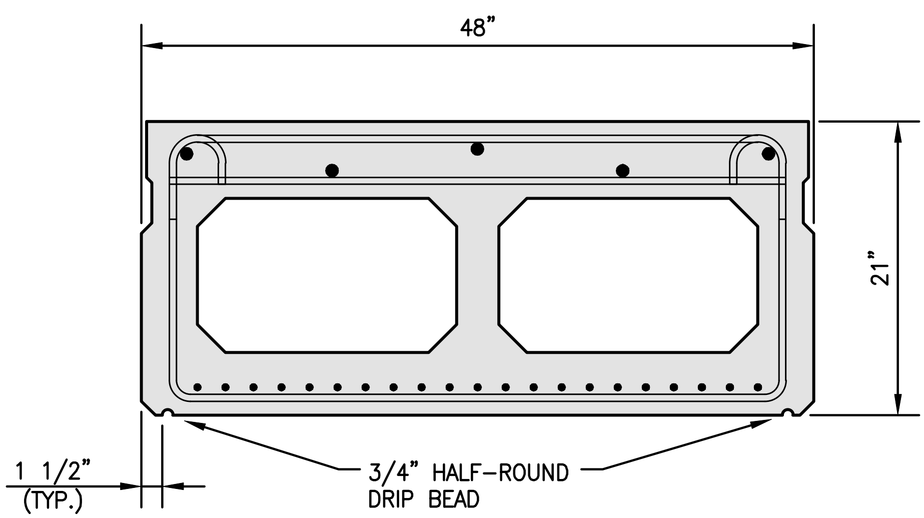

Figure 7.1: Example Improved INDOT Standard Box Beam Sections

It is recommended that the drip bead be located between the edge of the bottom flange and the first strand from the edge of the bottom flange. A beam tested by Miller and Parekh (1994) included a drip bead (noted as a drip groove by Miller and Parekh) on the exterior side of an exterior beam. The drip bead was located under the second strand from the edge of the beam (Figure 7.2). The strands between the drip bead and the edge of the beam were observed to be corroded and broken. Considering the 4-in. side cover required for edge strands in all box beam standard sections (IDM 2013), the location of the drip bead 1-1/2 in. from the beam edge is considered to be adequate to prevent the deterioration observed in the beam tested by Miller and Parekh.

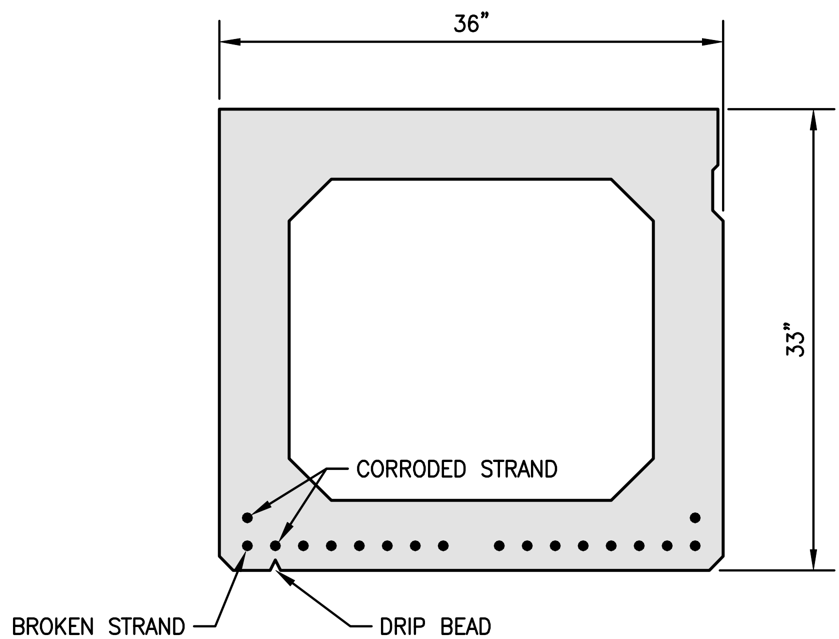

Figure 7.2: Box Beam Section Tested by Miller and Parekh

The addition of a drip bead to the edge of the bottom flange of the standard sections provides a simple solution to the issue of joint leakage and water draining onto the sides and bottom flange of the exterior beam. These details also allow the continued use of standard forms used by precast concrete producers. This small addition to the current standard section, however, does not address the issues regarding the inspection of the sides of box beams.

7.2.2 Proposed Winged Beam Section

Inspection of the sides of box beams is inherently impeded by the side-by-side placement of each beam. To allow the inspection of the sides of the box beams as well as prevent leakage from flowing down the sides of the box, a winged beam section is proposed (Figure 7.3). By adding 6 in. extensions to either side of the top flange, a space is created between beams that allows inspection. To prevent potential leakage from the longitudinal joint from draining down the side of the beam, two 3/4 in. half-round drip beads are provided on the wings of the section.

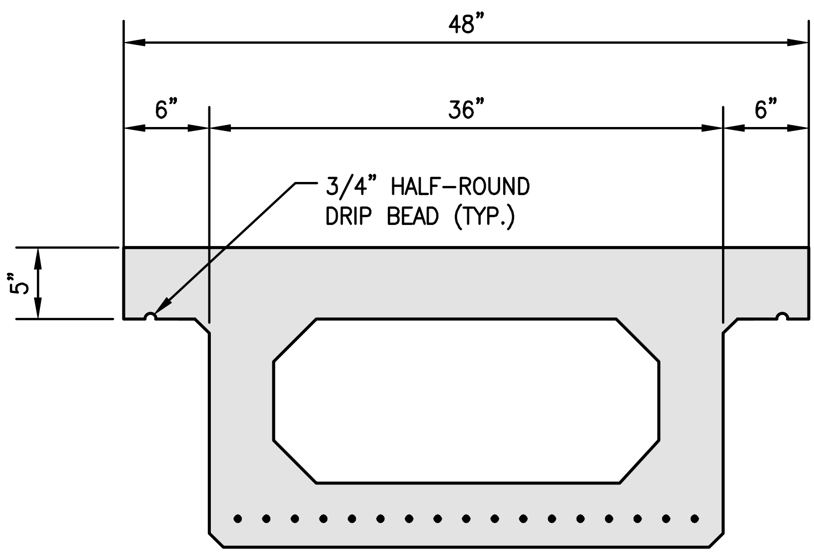

Figure 7.3: Proposed Wing Beam Section

While new overall cross-sectional widths can be developed, existing 48 in. wide forms used for current standard box beam sections can be used. The void between the web and edge of the wing may be created by block-outs set into the existing forms. In addition, the internal void is formed following the current practice of using closed-cell foam. Drain holes at each end of the internal void must also be provided to prevent water retention in the internal void.

The proposed section has been developed considering the installation of a concrete deck over the adjacent beams. Through composite action, the concrete deck connects the adjacent beams so that load may be resisted by the combined action of the beams and deck acting as a unit. Therefore, shear keys and transverse tie-rods are not needed to connect the adjacent beams (Figure 7.4). The elimination of shear keys and transverse tie-rods simplify construction leading to overall reduced construction costs.

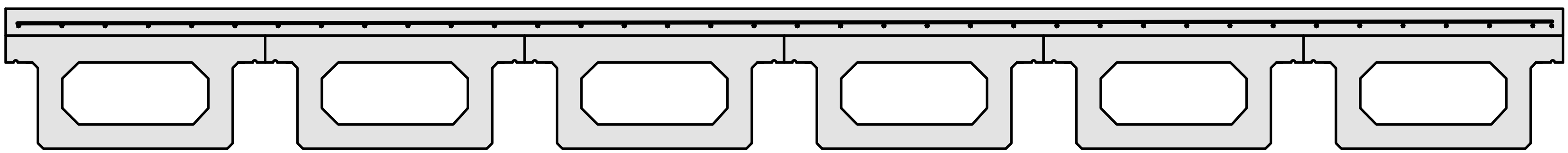

Figure 7.4: Example Bridge Section with Winged Beams

7.3 Composite Section

Composite action between a concrete deck and adjacent box beams may be developed by intentionally roughening the top surface of the beam. The surface prior to casting the deck should be clean and free of laitance. By relying on shear friction at the concrete deck/beam interface to resist horizontal shear demands, there is no need to extend steel reinforcement into the deck. Without reinforcement extending from the beam into the deck, deck replacement is greatly simplified reducing rehabilitation costs and allowing for increased service life of the bridge.

7.4 Interior Joints

To prevent leakage of the longitudinal joint, installing a flexible sealant at the top of the joint is recommended. Installation of the joint sealant may be improved by tooling a small radius into the edge of the top flange to provide a small recess for the application of the sealant.

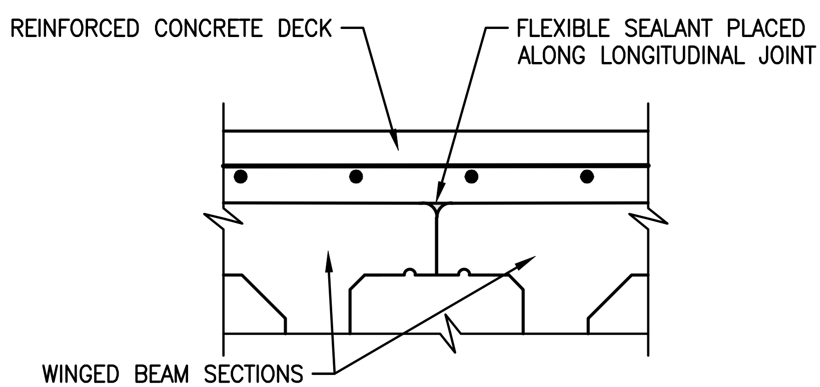

Figure 7.5: Location of Flexible Joint Sealant

7.5 Bridge Deck

The use of bituminous wearing surfaces should be discontinued. Bridge inspections conducted through the course of this study have shown that bituminous wearing surfaces do not contribute to the durability of adjacent box beams. Concrete decks are recommended with a minimum thickness of 5 in. and minimum reinforcement consisting of a single mat of #4 bars at 8 in. spacing in the longitudinal and transverse directions. Corrosion resistant bars are recommended. In addition, to improve existing box beam bridges, a drip edge should be provided at the edge of the bridge deck to prevent water from draining down the side of the exterior beam. An example of the recommended edge of slab detail with a drip bead is shown in Figure 7.6.

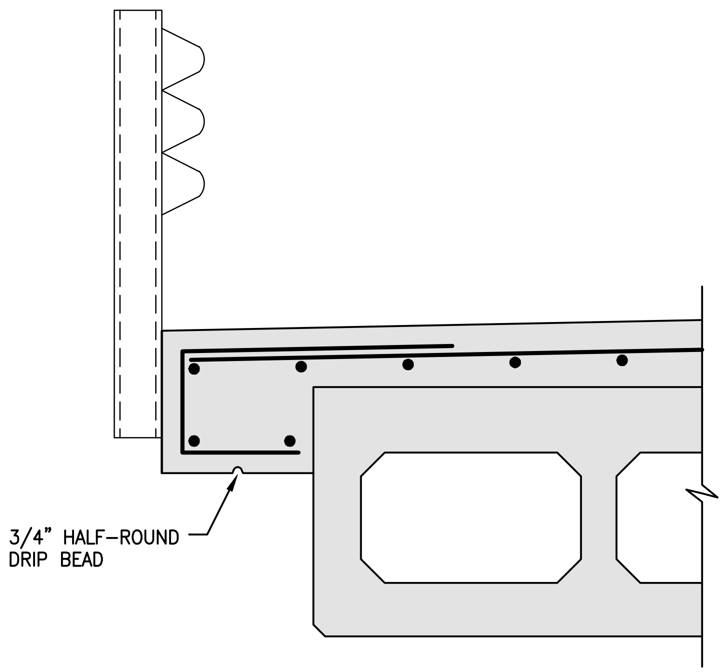

Figure 7.6: Edge of Slab Detail with Drip Bead

7.6 Curbs and Concrete Barriers

The use of curbs or concrete barriers is recommended as they prevent water drainage down the sides of box beams and reduce the potential of road spray wetting the exterior beams. The use of deck drains through the deck and beam should be avoided to protect the superstructure. Where deck drains must be placed through the deck and exterior box beam, it is recommended that non-metallic drain pipes are installed and extended past the face of the bottom flange (Figure 7.7). By extending the drain pipe, water is prevented from curling on to the bottom flange of the box beam. Deck drains placed horizontally through curbs or concrete barriers should be avoided unless the potential for water washing down the side of the exterior beam is prevented.

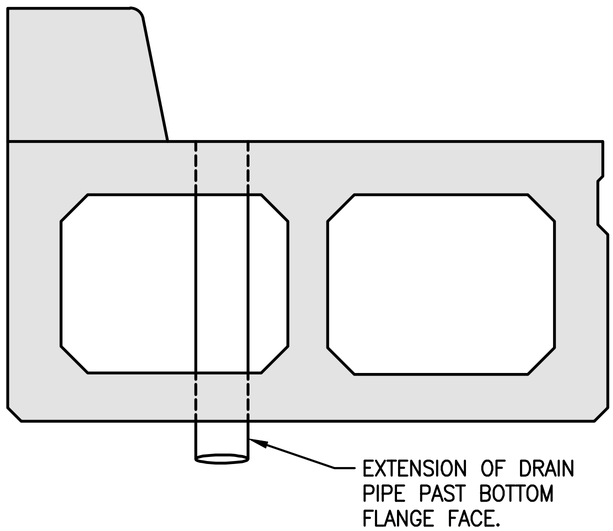

Figure 7.7: Extension of Non-Metallic Drain Pipe

CHAPTER 8. SUMMARY AND CONCLUSIONS

8.1 Summary

Accurate assessment of deteriorated adjacent box beam bridges is imperative for maintaining a safe and operable bridge infrastructure. Furthermore, the new design of adjacent box beam bridges must provide a durable, as well as efficient and economical, bridge solution. Therefore, the objective of this research is to develop improved recommendations for the inspection, load rating, and design of adjacent box beam bridges. Research focused on the following:

- Inspection of bridges to observe common types of deterioration and identify deteriorated box beams for experimental study.
- Investigation of the extent of deterioration through visual inspection, non-destructive evaluation, and destructive evaluation.
- Determining the capacity of deteriorated beams.
- Development of a rehabilitation procedure to restore load transfer.
- Development of an analysis procedure to calculate the capacity of deteriorated box beams.
- Development of the next generation of adjacent box beam bridges.

8.2 Bridge Inspections

A total of 18 bridges were inspected through the course of the research study. Six of the 18 bridges inspected were identified as source bridges for 15 prestressed, precast box beam specimens. In addition to finding and acquiring specimens for experimental study, understanding of the deterioration of adjacent box beam bridges gained through field observation of in-service bridges informed the following conclusions:

1. Deck systems need to prevent moisture migration through the joint and prevent saturation of the top flange of the beam. Based on this investigation, concrete decks demonstrated greater durability of the box beam system than bituminous wearing surfaces.
2. Deicing salts are the primary cause of deterioration at longitudinal joints due to leakage and on exterior beams due to water drainage over the side of the exterior beam. The initiation of reflective cracking and seepage of water through the longitudinal joint needs to be prevented through improvement of the connection between adjacent box beams.
3. The current practice of using expanded polystyrene to form the void in tandem with drain holes prevents water from filling the void. Eliminating the potential of retained water prevents longitudinal cracking of the bottom flange through either corrosion of the saturated bottom flange or freezing of the retained water.
4. Top flange deterioration is caused by (1) saturation of the concrete due to saturation of the wearing surface as provided by bituminous wearing surfaces, and (2) chloride-induced corrosion of the reinforcement in the top flange. This deterioration can be prevented by using either wearing surfaces with low permeability, such as concrete, or through the use of waterproofing membranes. Regular bridge deck maintenance using deck sealers and crack sealers should also be provided to maintain water resistance of the deck.

8.3 Extent of Deterioration

The visual deterioration of 15 box beam specimens acquired from decommissioned bridges was documented. Each specimen was tested using three NDT methods: connectionless electrical pulse response analysis (CEPRA), ground penetrating radar (GPR), and half-cell potentials. After completion of the nondestructive evaluation, strands in the location of visual signs of deterioration, as well as several "hot spots" detected by NDT, were removed to determine the actual extent of deterioration. The NDT results were then compared to the strand corrosion observed. The extent of deterioration and the comparison between the NDT results and strand corrosion is summarized as follows:

8.3.1 Visual Inspection

1. Visible inspection provided an excellent means of identifying the locations of corroded strand. Corrosion was limited to regions exhibiting visual distress such as cracking, spalling, and delamination.
2. Longitudinal cracks near the edge of the beam were observed to correspond with strand corrosion along the length of the crack. Corrosion only extended a few inches beyond the end of the visible crack.
3. Longitudinal cracks in the middle of the box were caused by water freezing in the void and do not generally align with the strand. The crack was often observed to meander and not be completely longitudinally aligned with the axis of the beam. Corrosion in this case was observed to be localized to the intersection of strands with the crack and any locations where the strand aligned with the crack.
4. Flexural cracking was observed in several beams. Strands intersecting flexural cracks were observed to be corroded only at the intersection with the flexural crack.

5. Strands at concrete spalls and delamination (exposed or not exposed) were observed to be corroded.
6. Corner cracks which are only visible for exterior girders were observed to correspond with strand corrosion over the length of the crack. For interior joints, this crack would not be visible; the only potential visible indicator would be rust staining at the joint.

8.3.2 NDT Inspection

8.3.2.1 CEPRA

1. CEPRA was capable of determining corrosion where visual inspection would not have observed deterioration.
2. CEPRA did not demonstrate an ability to accurately assess the condition of strands adjacent to corrosion. Often, heavily corroded strands influenced the readings of adjacent strands causing overestimations of the indicated corrosion which may be a halo effect of the adjacent corroded strand. This effect was primarily observed for specimens exhibiting deterioration related to leaking longitudinal joints or water draining over the side of the exterior beam. Considering the progression of corrosion for this type of deterioration, the observed halo effect may also be an indication of future corrosion.
3. Correlation between corrosion rate measurements and severity of corrosion as noted in the literature did not correspond well with the test results. For the strand in the box beam specimens (3/8 in. and 1/2 in.), modifying the thresholds by a factor of 2.3 (the ratio of surface area of strand to bar reinforcement) resulted in significantly improved correlation. Further research is needed to verify the appropriate CEPRA modification

factor for use on structures reinforced with strands with a nominal diameter other than 3/8 in. or 1/2 in.

4. Using a threshold of 23 μm/year, where strands are considered corroded if measurements are above the threshold, provided adequate correlation between corrosion rate measurements and corroding strand. This "hot spot" analysis may be useful to inspectors, but information regarding regions of distress may be lost.
5. CEPRA provides a simple tool to augment visual inspection. The system is lightweight and easy to operate with minimal training.

8.3.2.2 GPR

1. GPR provides an accurate method to locate strand embedded in concrete and is recommended for this purpose.
2. GPR is not recommended for general deterioration mapping of the bottom flange of box beams. GPR can locate areas of delaminated concrete which are likely locations of corrosion. This system can be helpful in locating corrosion due to corner cracking or other regions where delaminated concrete is suspected. Outside of these regions, corrosion could not be detected.
3. The 8 dB threshold provided poor correlation to delaminated areas of concrete, whereas the 6 dB threshold provided good correlation. Therefore, the 6 dB threshold is recommended for delamination detection.

8.3.2.3 Half-Cell Potentials

1. Good correlation was observed between indicated strand corrosion and actual strand corrosion of strands adjacent to visual signs of deterioration. Measurements were not possible directly over longitudinal cracks or on the rough surfaces at concrete spalls.

2. Similar to the CEPRA method, the half-cell potential readings were observed to be influenced by heavily corroded strand. This halo effect was observed for specimens exhibiting deterioration related to leaking longitudinal joints or water draining over the side of the exterior beam but to less extent than was observed for the CEPRA method. Considering that corrosion propagates from strand to strand for this type of deterioration, the observed halo effect may also be an indication of future corrosion.
3. The ASTM C879 correlation between voltage potential and corrosion corresponded well with the test results, but strand corrosion was only observed where corrosion was indicated. Therefore, a condensed scale using a threshold of -0.35 V, where corrosion is indicated for voltage potentials less than the threshold, also provided adequate correlation to the observed corrosion and simplified data interpretation.
4. While half-cell potentials require access to select locations of the reinforcement and is not fully non-destructive, it provided the best results related to identifying the corrosion of strands adjacent to visual signs of deterioration.

8.3.3 Overall Inspection Findings

1. The ingress of salt-water to the bottom flange of box beams from leaking joints or drainage over the side of the bridge results in corrosion of the strands at the edge of the box section. Where longitudinal cracks or spalls exist, strands at the longitudinal cracks or concrete spalls were corroded. Where staining was present in addition to transverse cracks, the strands at the cracks were also corroded.
2. Longitudinal cracks located away from the edge of the bottom flange of box beams were caused by water freezing in the void. Cracks were observed in many cases away from reinforcement. Furthermore, corrosion was not observed on the longitudinal

strand except at localized locations where the longitudinal crack traversed the strand. These findings indicate that corrosion was not the cause of longitudinal cracking. Evidence of corrosion in strands adjacent to the strands at longitudinal cracks was not found.

3. Based on the findings of the visual inspections and NDT method evaluation, visual inspection of bottom flange deterioration proved to provide the most reliable method for determining the extent of deterioration. The NDT methods may be used to augment visual inspection. For example, GPR may be used to locate reinforcement such that the number of strands intersecting or aligning with a crack may be determined. Also, CEPRA and GPR may be used to identify corrosion at the edge of a bottom flange where delamination may be suspected.
4. GPR is extremely useful to identify the number strands actually provided in the section especially when construction drawings are not available.

8.4 Capacity of Deteriorated Box Beams

Load tests were conducted to evaluate the deteriorated capacity of each specimen. Following the load tests, the cross-sectional geometry of each specimen was documented, and concrete and strand samples were extracted for materials testing. The findings and conclusions based on these tests and documentation are summarized in the following sections.

8.4.1 As-Built Section vs. INDOT Standard Section

A comparison between the as-built and INDOT standard section geometry was conducted to determine any differences between what was built and what was specified. The comparison revealed that the overall height and width of the beam sections matched the standard sections. The flange and web thicknesses, however, varied largely due to the void shifting while concrete was cast. For specimens with two or more voids, the void was found to have shifted toward the middle of the section and up. Middle web thicknesses and top flange thicknesses were observed to be less than the standard thicknesses by up to 3 in.

A similar comparison was conducted between the reinforcement provided in the as-built section and the reinforcement specified on the INDOT standard drawings. For every specimen, the number of strands provided in the specimen as constructed was greater than or equal to the number of strands specified on the standard drawing. Differences between the as-built and standard section reinforcement were observed to be negligible.

8.4.2 Material Testing

In general, the corroded strands tested were observed to have residual capacity but did not have any appreciable ductility. Based on the observed behavior, it is recommended to assume that strands exhibit no ductility where corrosion of any kind is observed. In addition, if surface corrosion and minor pitting are observed, only 75% of the strand strength should be considered along with limiting strain to $0.75f_{pu}/E_{ps}$. If severe corrosion or fractured wires are observed, 0% of the strand strength should be considered.

8.4.3 Structural Testing

The deteriorated capacity of each specimen was determined through structural testing. The results of each structural test were compared to an analytical model used to estimate the behavior of each specimen. The findings of these comparisons may be summarized as follows.

1. Delaminated concrete exhibits brittle behavior. Structural capacity calculations considering delaminated concrete in compression should limit the compressive strain to $0.5f_c'/E_c$.

2. Only strand corrosion located within the development length from the point of maximum moment needs to be considered as reducing the flexural capacity. Strands with corrosion and fractured strand outside of the maximum moment region can redevelop capacity and maintain prestress force.
3. Reduced ductility of corroded strand led to reduced overall ductility of the beam specimens. The strain in the strand at fracture in the beam specimen correlated with the strain at fracture measured during tensile testing of the corroded strand. Based on the presented analysis, the strain in corroded strains should be limited to 0.01 for structural capacity calculations. If minor pitting is observed, the strain should be further limited to $0.75f_{pu}/E_{ps}$ consistent with the recommendation of 75% of the strand strength. If severe corrosion or fractured wires are observed, the strand should not be considered.

8.5 Live-Load Distribution

An experimental investigation was conducted on a full-scale adjacent precast, prestressed concrete box beam bridge while in service. The study included four load tests of the bridge under four conditions: (1) as-built, (2) bituminous wearing surface removed, (3) shear keys disabled, and (4) reinforced concrete deck installed. Load was applied using a triaxle truck, and deflections of each beam at each quarter-point were measured. Load distribution was calculated based on the midspan deflections of each beam when the truck was in the load position where maximum deflection was recorded. The load distribution was compared between all load tests. In addition, the load distribution factor for each load test was determined and compared to the "Load Fraction" calculated from the 1957 AASHO and the 2002 AASHTO Standard Specification as well as the interior and exterior moment distribution factors calculated using the equations from the 2017

AASHTO LRFD Bridge Design Specifications. The primary findings of the investigation can be summarized as follows:

1. Shear keys showing evidence of leaking may have no impact on live-load distribution. The test results show that even though the shear keys were leaking, live-load distribution was maintained.
2. The results of the load tests indicate that a 5 in. thick concrete deck reinforced with a single mat of #4 bars spaced at 8 in. in both the longitudinal and transverse direction can restore load distribution after the primary load distribution mechanism (shear keys) were disabled.
3. A concrete deck placed on concrete beams can achieve full composite action through adhesion of the deck concrete to the concrete beams. The surface should be properly cleaned and roughened prior to placement of the concrete deck.
4. The "Load Fraction" computed from both the 1957 AASHO and the 2002 AASHTO Standard Specification was found to be conservative for load rating 1950s-era adjacent box beam bridges. Similar results are provided by both expressions and both significantly overestimate the demand on the box beams.
5. The AASHTO LRFD (2017) equations for live-load distribution factors for moment are suitable for estimating the live-load distribution factors for a reinforced concrete deck on adjacent concrete beams without shear keys. The test results indicate that these expressions provide extremely accurate estimates of the load distribution.

8.6 Recommendations

Based on the observations made during bridge inspections of distressed adjacent box beam bridges and the findings of NDT, material tests, structural tests of decommissioned box beams, and load testing of an existing adjacent box beam bridge, a series of recommendations for the improved inspection, load rating, and design of box beams is provided. These recommendations may be summarized as follows.

8.6.1 Inspection

A correlation between visual signs of deterioration and strand corrosion has been identified through investigation of the extent of corrosion associated with common types of deterioration. These types included longitudinal cracking at the edge of the bottom flange, longitudinal cracking located away from the edge of the bottom flange, flexural cracking, and concrete spalling. In each case, strand corrosion was limited to the location of deterioration.

Longitudinal cracks in the bottom edge of the box section accompanied by signs of leaking shear keys or water draining over the side of the exterior beam correspond to corrosion of the strand along the length of the crack with corrosion extending only a few inches past each end of the crack. Corner cracks in the bottom edge of the beam section cause delamination of concrete cover. These corner cracks may be obscured from view by the adjacent beam. Where heavy concrete staining from joint leakage is observed or delaminated concrete is suspected, CEPRA and GPR can be used to identify corrosion of the edge strand.

Longitudinal cracks located away from the edge of the bottom flange are caused by water freezing in the void. These cracks cause localized corrosion of strands that intersect or align with the crack. The extent of corrosion is limited to the length of the strand intersecting or aligning with the crack. No corrosion occurs in the strands adjacent to the crack. GPR is especially useful in determining the location and number of strands intersecting the crack. It should be noted that this type of longitudinal cracking is possible in for older beams constructed with cardboard voids or other formwork that voids the beam. Closed-cell foam forms are not capable of holding water.

Flexural cracks also cause localized corrosion of strands intersecting the crack. Strand corrosion at the crack may consist of mainly surface rust but could cause premature strand fracture. The use of GPR provides an accurate number of strands intersecting the crack and removes uncertainty regarding the number of strands in the beam if construction drawings are unavailable.

The corrosion of strands exposed by concrete spalling extends a few inches past the end of the concrete spall. If a strand is located at concrete spall but has not been exposed, the length of strand at the spall is considered corroded.

8.6.2 Load Rating

Based on the results of material testing and structural tests of decommissioned box beams, an analysis procedure was developed to estimate the capacity of box beams with visual signs of deterioration. The analysis procedure considers both the initial failure capacity and the residual capacity.

Initial Capacity

For this analysis, all strands, unless broken or severely pitted, are considered effective.

1. If delaminated concrete is observed in concrete in the compression flange, the capacity P_{dc} is calculated by limiting the strain in the extreme fiber in compression to $0.5f_c'/E_c$.
2. Exposed strands and strands at rust stained longitudinal cracks are assumed to be limited in capacity. The capacity P_{ds} is calculated by limiting the strain in the prestressing strand to $0.75f_{pu}/E_{ps}$.

Residual Capacity

For this analysis, all corroded strands are assumed to be ineffective.

1. If delaminated concrete is observed in the compression flange, the reserve capacity P_{rdc} is calculated by limiting the strain in the extreme fiber in compression to $0.5f_c'/E_c$. Full strain capacity of the remaining effective strands (ε_{pu} = 0.04) is assumed.
2. The reserve capacity P_{rds} is calculated considering the remaining effective strand to have full strain capacity (ε_{pu} = 0.04). Full concrete strain capacity (ε_{cu} = 0.003) is also considered.

The initial capacity considers the behavior of delaminated concrete and corroded strands prior to crushing of deteriorated concrete (P_{dc}) or fracture of corroded strands (P_{ds}). The residual capacity P_{rdc} considers the potential of deteriorated concrete crushing after fracture of corroded strands. If there is no concrete deterioration, the reserve strength available after corroded strands fracture is calculated as P_{rds}. The controlling capacity P_d is determined by comparing the minimum values of the initial deteriorated capacity (P_{dc} or P_{ds}) to the minimum reserve capacity (P_{rdc} or P_{rds}). The value of P_d is then equal to the maximum value between the controlling initial capacity and reserve capacity.

The proposed analysis procedure was compared to common load rating practice and found to provide more accurate estimates of deteriorated capacity. The proposed procedure utilizes the improved understanding of the extent and effect of deterioration on the assessment of strength. By incorporating the capacity of deteriorated prestressing strand and deteriorated concrete (if applicable), an accurate estimation of the deteriorated capacity can be made.

8.6.3 Restoring Live-Load Distribution

Leaking longitudinal joints are commonly observed in adjacent box beam bridges and are often associated with a loss of load distribution over the leaking joint. The restoration of load distribution may be achieved by casting a reinforced concrete deck over the existing box beams.

Based on load tests of an in-service adjacent box beam bridge, the live-load distribution of a bridge rehabilitated with the addition of a reinforced concrete deck may be estimated using AASHTO LRFD (2017) equations for load distribution. In addition, with proper surface preparation, the concrete deck may be assumed to act compositely with the existing box beams. The procedure and details for performing a concrete deck rehabilitation on an adjacent box beam bridge are as follows.

1. Remove the existing wearing surface to expose the top flange of the box beams and inspect the top flange for any signs of delamination or other concrete deterioration.
2. If needed, remove all deteriorated concrete from the existing box beams using a jack hammer or other suitable tool and restore the top flange using a structural concrete repair.
3. Sandblast the surface of the box beams in preparation for casting the reinforced concrete deck.
4. Minimum reinforcement of the concrete deck shall be #4 bars spaced at 8 in. in the longitudinal and transverse directions. Corrosion resistant reinforcement is recommended. Minimum thickness of the concrete deck shall be greater of 5 in. or the thickness required to meet minimum concrete cover requirements.

8.6.4 Design of Adjacent Box Beam Bridges

Based on the information gathered through study of deteriorated box beams, a series of recommendations were developed for the improved construction of adjacent box beam bridges.

General Recommendations

1. A drip bead is recommended to be added to the current INDOT standard box beam sections. A drip bead should be located on each edge of the bottom flange between the

side of the box section and the edge strand. The drip bead provides a simple solution to the issue of joint leakage and allows for continued use of standard box beam forms.

2. Flexible sealant is recommended to be placed at the top of the longitudinal joint between beams to prevent leakage.
3. Concrete decks are recommended with a minimum thickness of 5 in. and a single mat of corrosion resistant #4 bars at 8 in. spacing in the longitudinal and transverse directions. Where curbs or concrete barriers are not used at the exterior edges of the bridge deck, a drip edge should be provided to prevent water from draining down the sides of the box beams.
4. The use of concrete curbs or barriers is recommended to prevent water from flowing down the sides of exterior box beams. If deck drains through the deck and beam may not be avoided, a non-metallic drain pipe should be specified to extend past the face of the bottom flange to prevent water from curling onto the bottom flange.
5. The use of bituminous wearing surfaces should be discontinued.

New Box Beam Section

1. To facilitate the inspection of the sides of box beams, a winged beam section is recommended. As shown in Figure 8.1, the proposed section includes drip beads on either side of the longitudinal joint to prevent water from draining down the side of the beam.

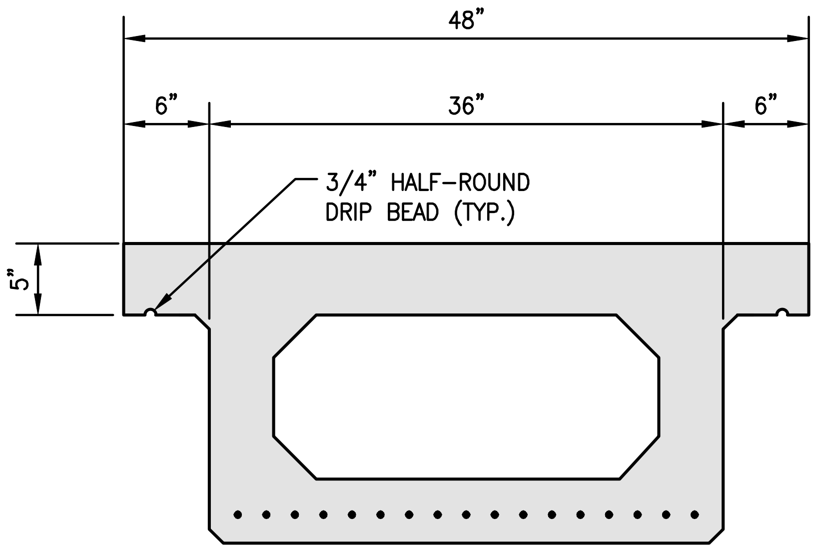

Figure 8.1: Proposed Wing Beam Section

2. The proposed section considered the use of a composite concrete deck. Composite action between the deck and beams can be developed by intentionally roughening the top surface of the beam. Adhesion developed across the width of the top flange provides resistance to horizontal shear demands and eliminates the need for extending steel reinforcement into the bridge deck to develop composite action. This system allows for ease of deck replacement to provide future bridge rehabilitations.

8.7 Future Research

To improve the inspection, load rating, and new design of adjacent box beam bridges, it is suggested that further research be conducted with a focus on the following topics:

1. Non-Destructive Testing: Further application of the CEPRA device may be improved by verifying the modification factor of 2.3 for 7 wire strands with nominal diameters other than 3/8 in. or 1/2 in. In addition, further research should investigate the effect of surface moisture or internal moisture of the concrete on corrosion rate measurements

with the goal of determining if there is an optimum moisture content for corrosion measurement.

2. Load Rating: To confirm the findings of this research, a case study is recommended in which the proposed inspection techniques and analysis are used to load rate an existing bridge. Following rating, load testing of the bridge or testing of individual beams would be useful to evaluate the performance of the recommendations.
3. New Design: As a proof of concept of the winged beam section, it is recommended that a bridge using the proposed section be constructed. Live-load testing would also be useful to evaluate accuracy of current live-load distribution calculations.

REFERENCES

AASHO, 1957, *Standard Specifications for Highway Bridges*, Seventeenth Edition, American Association of State Highway Officials, Washington, D.C., 286 pp.

AASHTO, 2002, *Standard Specifications for Highway Bridges*, Seventeenth Edition, American Association of State Highway and Transportation Officials, Washington, D.C., 1071 pp.

AASHTO, 2018, *Manual for Bridge Evaluation*, American Association of State Highway and Transportation Officials, Washington, D.C., 674 pp.

AASHTO LRFD, 2017, Bridge Design Specifications, Eighth Edition, American Association of State Highway and Transportation Officials, Washington, D.C., 1781 pp.

ACI Committee 222, 2001, *Corrosion of Prestressing Steels*, ACI 222.2R-01, American Concrete Institute, Farmington Hills, MI, 43 pp.

ACI Committee 318, 2014, *Building Code Requirements for Structural Concrete and Commentary*, ACI 318-14, American Concrete Institute, Farmington Hills, MI, 519 pp.

Alonso,C.; Andrade, C.; and González, J.A., 1988, "Relation between Resistivity and Corrosion Rate of Reinforcements in Carbonated Mortar made with Several Cement Types," *Cement and Concrete Research*, V. 8, pp. 687-698.

Andrade, C., and Alonso, C., 1996, "Corrosion Rate Monitoring in the Laboratory and On-site," *Construction and Building Materials*, V. 10, No. 5, pp. 315-328.

ASTM A1061, 2016, *Standard Test Methods for Testing Multi-Wire Steel Prestressing Strand*, American Society of Testing and Materials International, West Conshohocken, PA, 4 pp.

ASTM C31, 2018, *Standard Practice for Making and Curing Concrete Test Specimens in the Field*, American Society of Testing and Materials International, West Conshohocken, PA, 6 pp.

ASTM C39, 2018, *Standard Test Method for Compressive Strength of Cylindrical Concrete Specimens*, American Society of Testing and Materials International, West Conshohocken, PA, 8 pp.

ASTM C42, 2018, *Standard Test Method for Obtaining and Testing Drilled Cores and Sawed Beams of Concrete*, American Society of Testing and Materials International, West Conshohocken, PA, 7 pp.

ASTM C150, 2018, *Standard Specification for Portland Cement*, American Society of Testing and Materials International, West Conshohocken, PA, 9 pp.

ASTM C192, 2018, *Standard Practice for Making and Curing Concrete Test Specimens in the Laboratory*, American Society of Testing and Materials International, West Conshohocken, PA, 8 pp.

ASTM C260, 2016, *Standard Specification for Air-Entraining Admixtures for Concrete*, American Society of Testing and Materials International, West Conshohocken, PA, 4 pp.

ASTM C494, 2017, *Standard Specification for Chemical Admixtures for Concrete*, American Society of Testing and Materials International, West Conshohocken, PA, 10 pp.

ASTM C805, 2013, *Standard Test Method for Rebound Number of Hardened Concrete*, American Society of Testing and Materials International, West Conshohocken, PA, 4 pp.

ASTM C876, 2015, *Standard Test Method for Corrosion Potentials of Uncoated Reinforcing Steel in Concrete*, American Society of Testing and Materials International, West Conshohocken, PA, 8 pp.

ASTM D6087, 2015, *Standard Test Method for Evaluating Asphalt-Covered Concrete Bridge Decks Using Ground Penetrating Radar*, American Society of Testing and Materials International, West Conshohocken, PA, 6 pp.

Attanayake, U., and Aktan, H., 2011, “Capacity Evaluation of a Severely Distressed and Deteriorated 50-Year-Old Box Beam with Limited Data,” *Journal of Performance of Constructed Facilities*, American Society of Civil Engineers, July/August, pp. 299-308

Barker, R.M, and Puckett, J.A, 1997, *Design of Highway Bridges*, John Wiley & Sons, Inc., New York, NY, 1169 pp.

Carino, N.J., 1998, “Nondestructive Techniques to Investigate Corrosion Status in Concrete Structures,” ASCE Journal of Performance of Constructed Facilities, Vol. 13, No. 4, August, pp. 96-106.

Dong, X., 2002, “Traffic Forces and Temperature Effects on Shear Key Connections for Adjacent Box Girder Bridge,” Ph.D. Dissertation, Department of Civil and Environmental Engineering, University of Cincinnati, 208 pp.

Fahim, A.; Ghods, P.; Alizadeh, A.; Salehi, M.; and Decarufel, S., 2019a, “CEPRA-A New Test Method for Rebar Corrosion Rate Measurement,” *ASTM International STP: Selected Technical Papers*, pp. 59-80.

Fahim, A.; Ghods, P.; Alizadeh, A.; and Decarufel, S., 2019b, “Assessing Corrosion of Reinforcing Steel” *Concrete International*, V.41, No. 2, pp. 37-43.

Fernandes, B., Titus, M., Nims, D.K., Ghorbanpoor, A., and Devabhaktuni, V.K., 2013, “Practical Assessment of Magnetic Methods for Corrosion Detection in an Adjacent Precast, Prestressed Concrete Box-Beam Bridge,” *Nondestructive Testing and Evaluation*, Vol. 28, No. 2, pp. 99-118.

FHWA, 1995, “Recording and Coding Guide for the Structure Inventory and Appraisal of the Nation’s Bridges,” U.S. Department of Transportation: Federal Highway Administration, Washington, D.C.,124 pp.

FHWA, *LTBP InfoBridge*, online database, https://infobridge.fhwa.dot.gov/Data (accessed 15 September 2019)

Frosch, R.J., Yu, Q., Cusatis, G., and Bažant, Z.P., 2017, "A Unified Approach to Shear Design," *Concrete International*, Vol. 39, No. 9, September, pp. 47-52

Ghods, P.; Alizadeh, A.; and Salehi, M., 2017, "Electrical Methods and Systems for Concrete Testing," U.S. Patent Application No. 20170227481A1, U.S. Patent and Trademark Office, Washington, DC.

GSSI, photo of extension pole, accessed 4 September 2019, https://www.geophysical.com/accessories

Halbe, K.R., 2014, "New Approach to Connections between Members of Adjacent Box Beam Bridges," Ph.D. Dissertation, Virginia Polytechnic Institute and State University, 356 pp.

Harries, K.A., Gostautas, R., Earls, C.J., and Stull, C., 2006, "Full-scale Testing Program on De-commissioned Girders from the Lake View Drive Bridge,", University of Pittsburgh, FHWA-PA-2006-008-EMG001, 159 pp.

Hawkins, N.M., and Fuentes, J.B., 2003, "Test to Failure of a 54 ft Deteriorated Pretensioned Precast Concrete Deck Beam," Department of Civil and Environmental Engineering, University of Illinois, FHWA-IL-UD-281, 105 pp.

Hibbeler, R.C., 2012, *Structural Analysis, Eighth Edition*, Pearson Prentice Hall, Pearson Education Inc., Upper Saddle River, NJ.

Hognestad, E., 1951, *A Study of Combined Bending and Axial Load in Reinforced Concrete Members*, Bulletin 399, University of Illinois Engineering Experiment Station, Urbana, IL, November, 128 pp.

Huckelbridge, A.A., and El-Esnawi, H.H., 1997, "Evaluation of Improved Shear Key Designs for Multi-Beam Box Girder Bridges," Ohio Department of Transportation, Report No. FHWA/OH-97/009, 70 pp.

iCOR User Manual V5.0, Giatec Scientific, accessed 1 August 2019, https://www.giatecscientific.com/wp-content/uploads/2019/05/Giatec-iCOR-User-Manual-V5-new-app.pdf.

INDOT, 2013, Indiana Design Manual, accessed 1 August 2019, https://www.in.gov/indot/design_manual/design_manual_2013.htm

INDOT, 2017, INDOT Bridge Inspection Manual, accessed 1 August 2019, https://www.in.gov/dot/div/contracts/standards/bridge/inspector_manual/

INDOT, 2018, *Standard Specifications*, Indiana Department of Transportation, Indianapolis, IN.

Jones, L., Pessiki, S., Naito, C., and Hodgson, I., 2010, "Inspection Methods and Techniques to Determine Non Visible Corrosion of Prestressing Strands in Concrete Bridge Components Task 2 - Assessment of Candidate NDT Methods," ATLSS Report No. 09-09, Lehigh University, 176 pp.

Kasan, J., and Harries, K.A., 2011, "Redevelopment of Prestressing Force in Severed Prestressed Strands," *Journal of Bridge Engineering*, Vol. 16, No. 3, May, pp. 431-437

Kasan J., and Harries, K., 2013, "Analysis of Eccentrically Loaded Adjacent Box Girders," *Journal of Bridge Engineering*, Vol. 18, No. 1, January 1, pp. 15-25

Kassner, B.L., and Balakumaran, S.S.G., 2016, "Live-Load Test of a 54-Year Old Prestressed Concrete Voided Slab Bridge," *PCI Convention and National Bridge Conference, February 28 - March 4, 2017*, Huntington Convention Center, Cleveland, OH, 25 pp.

Millard, S.G., and Gowers, K.R., 1992, "Resistivity Assessment of In-situ Concrete: The Influence of Conductive and Resistive Surface Layers," Proceedings Institution of Civil Engineers Structures and Buildings, V. 94, November, pp. 389-396.

Miller, R., and Parekh, K., 1994, "Destructive Testing of Deteriorated Prestressed Box Bridge Beam," *Transportation Research Record 1460*, pp. 37-44

Miller, R.A.; Hlavacs, G.M.; Long, T.; and Greuel, A., 1999, "Full-Scale Testing of Shear Keys for Adjacent Box Girder Bridges," *PCI Journal*, V.44, No.6, November-December, pp. 80-90

Molley, R.T., 2017, "Evolution and Performance of Box Beam Bridges in Indiana," Master's Thesis, Lyles School of Civil Engineering, Purdue University, West Lafayette, IN, 332 pp.

Naito, C., Sause, R., Hodgson, I., Pessiki, S., and Macioce, T., 2010, "Forensic Examination of a Noncomposite Adjacent Precast Prestressed Concrete Box Beam Bridge," *Journal of Bridge Engineering*, Vol. 15, No. 4. July, pp. 408-418

Naito, C., Jones, L., and Hodgson, I., 2011, "Development of Flexural Strength Rating Procedures for Adjacent Prestressed Concrete Box Girder Bridges," *Journal of Bridge Engineering*, Vol. 16, No. 5, September, pp. 662-670

NCHRP, 2009, Adjacent Precast Concrete Box Beam Bridges: Connection Details, NCHRP Synthesis 393, National Cooperative Highway Research Program, Transportation Research Board.

Precast/Prestress Concrete Institute - PCI, 2017, "PCI Design Handbook: Precast and Prestressed Concrete," *MNL-120*, Eighth Edition, Industry Handbook Committee, Precast/Prestressed Concrete Institute, Chicago, IL, 885 pp.

Shenoy, C.V., and Frantz, G.C., 1991, "Structural Tests of 27-Year-Old Prestressed Concrete Bridge Beams," *PCI Journal*, Vol. 36, Issue. 5, September-October, pp. 80-90

Steinburg, E., Miller, R., Nims, D., Sargand, S., 2011, "*Structural Evaluation of LIC-310-0396 and FAY-35-17-6.82 Box Beams with Advanced Strand Deterioration*," Ohio Department of Transportation, Office of Research and Development.

Thorenfeldt, E.; Tomaszewicz, A.; and Jensen, J.J., 1987, "Mechanical Properties of High Strength Concrete and Application to Design," *Proceedings of the Symposium: Utilization of High-Strength Concrete*, Stavanger, Norway, Jun. 1987, Tapir, Trondheim, pp. 149-159.

Wight, J.K., and MacGregor, J.G., 2012, *Reinforced Concrete Mechanics and Design, 6th Edition*, Pearson Education Inc., Upper Saddle River, NJ.

Yuan, J., and Graybeal, B., 2016, "Full-Scale Testing of Shear Key Details for Precast Concrete Box-Beam Bridges," ASCE Journal of Bridge Engineering, V.21, No. 9, September, 14 pp.

Zia, P., Preston, H.K., Scott, N.L., and Workman, E.B., 1979, "Estimating Prestress Losses," *Concrete International*, Vol. 1, No. 6, June, pp. 32-38.

Zokaie, T.; Osterkamp T.A.; and Imbsen, R.A., 1991. "Distribution of Wheel Loads on Highway Bridges," NCHRP 12-26 Final Report Volume 1, Transportation Research Board, Washington, D.C. 710 pp.

APPENDIX A. BRIDGE INSPECTION REPORTS

Inspection reports available from INDOT by request

Table A.1: Inspection Reports

Inspector	Asset Name	Date of Routine Inspection
Olson, J.	14-00095	27 June 2017
Scott, M. D.	14-00160	20 June 2017
Hankins, S.	20-00102	24 August 2016
May, S.	20-00385	14 August 2018
Magers, S. R.	20-00404	22 August 2018
Magers, S. R.	20-00406	22 August 2018
Hankins, S.	20-00409	24 August 2016
Minnich, S. G.	20-00410	8 August 2018
Gould, J.	28-00008	25 July 2018
Coop, R. M.	43-00018	22 March 2018
Trana, P. A.	45-00061	8 August 2016
Vereb, M.	45-00264	20 August 2018
Swor, S. M.	56-000K5	20 September 2016
Wessling, A. V.	56-00056	19 September 2018
Lankford, M. D.	79-00244	26 September 2017
Lankford, M. D.	79-00504	26 September 2017
Arnold, B. M.	90-00079	25 October, 2016

APPENDIX B. EXAMPLES OF LEAKING SHEAR KEY DETERIORATION

Figure B.1 to Figure B.17 provide examples of deterioration caused by leaking shear keys or water draining over the side of the bridge. Photos courtesy of Beam, Longest, and Neff LLC.

Figure B.1: Leaking Shear Key Deterioration

Figure B.2: Leaking Shear Key Deterioration

Figure B.3: Water Draining Over the Side of the Bridge Deterioration

Figure B.4: Leaking Shear Key Deterioration

Figure B.5: Leaking Shear Key Deterioration

Figure B.6: Leaking Shear Key Deterioration

Figure B.7: Leaking Shear Key Deterioration

Figure B.8: Leaking Shear Key Deterioration

Figure B.9: Leaking Shear Key Deterioration

Figure B.10: Leaking Shear Key Deterioration

Figure B.11: Leaking Shear Key Deterioration

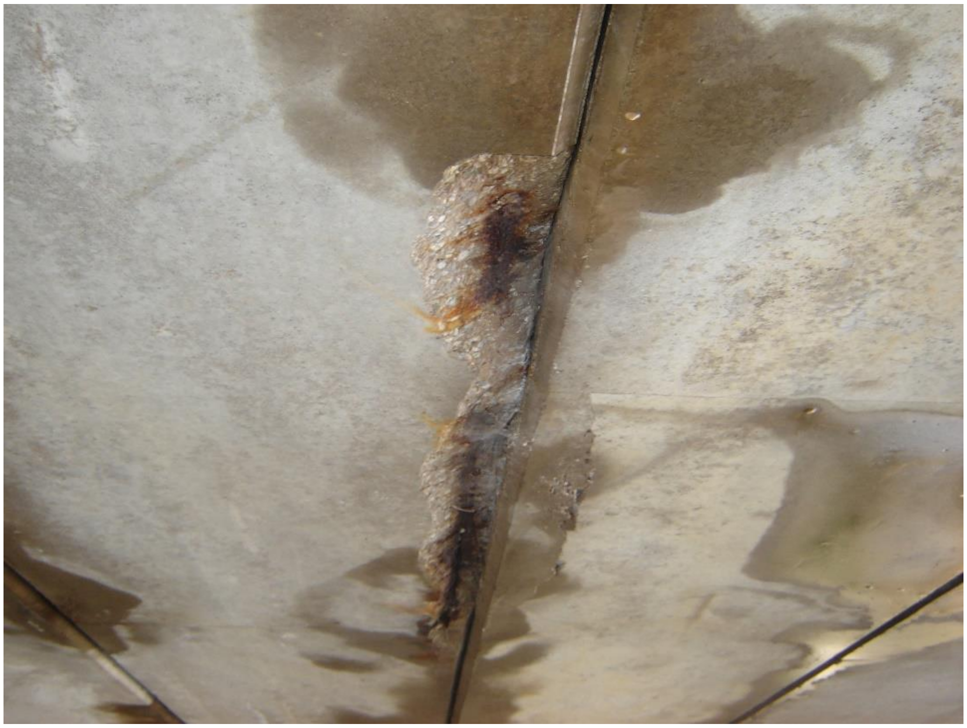

Figure B.12: Leaking Shear Key Deterioration

Figure B.13: Leaking Shear Key Deterioration

Figure B.14: Leaking Shear Key Deterioration

Figure B.15: Leaking Shear Key Deterioration

Figure B.16: Leaking Shear Key Deterioration

Figure B.17: Leaking Shear Key Deterioration

APPENDIX C. EXAMPLES OF WATER INGRESS INTO BOX BEAM VOID DETERIORATION

Figure C.1 to Figure C.17 provide examples of deterioration caused by water ingress into the box beam void. Photos courtesy of Beam, Longest, and Neff LLC.

Figure C.1: Water Ingress into the Box Beam Void Deterioration

Figure C.2: Water Ingress into the Box Beam Void Deterioration

Figure C.3: Water Ingress into the Box Beam Void Deterioration

Figure C.4: Water Ingress into the Box Beam Void Deterioration

Figure C.5: Water Ingress into the Box Beam Void Deterioration

Figure C.6: Water Ingress into the Box Beam Void Deterioration

Figure C.7: Water Ingress into the Box Beam Void Deterioration

Figure C.8: Water Ingress into the Box Beam Void Deterioration

Figure C.9: Water Ingress into the Box Beam Void Deterioration

Figure C.10: Water Ingress into the Box Beam Void Deterioration

Figure C.11: Water Ingress into the Box Beam Void Deterioration

Figure C.12: Water Ingress into the Box Beam Void Deterioration

Figure C.13: Water Ingress into the Box Beam Void Deterioration

Figure C.14: Water Ingress into the Box Beam Void Deterioration

Figure C.15: Water Ingress into the Box Beam Void Deterioration

Figure C.16: Water Ingress into the Box Beam Void Deterioration

Figure C.17: Water Ingress into the Box Beam Void Deterioration

APPENDIX D. SPECIMEN CROSS-SECTION GEOMETRY

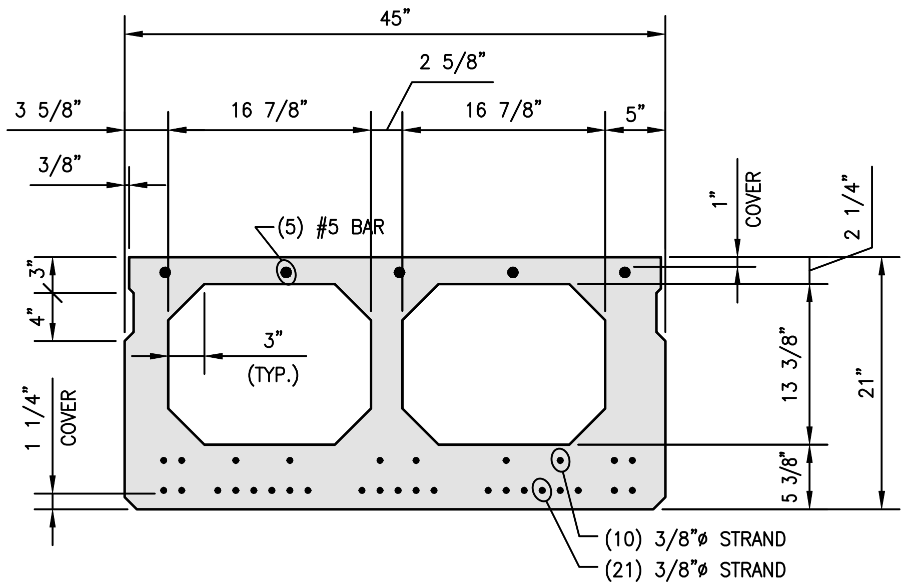

(a) As-built cross-section

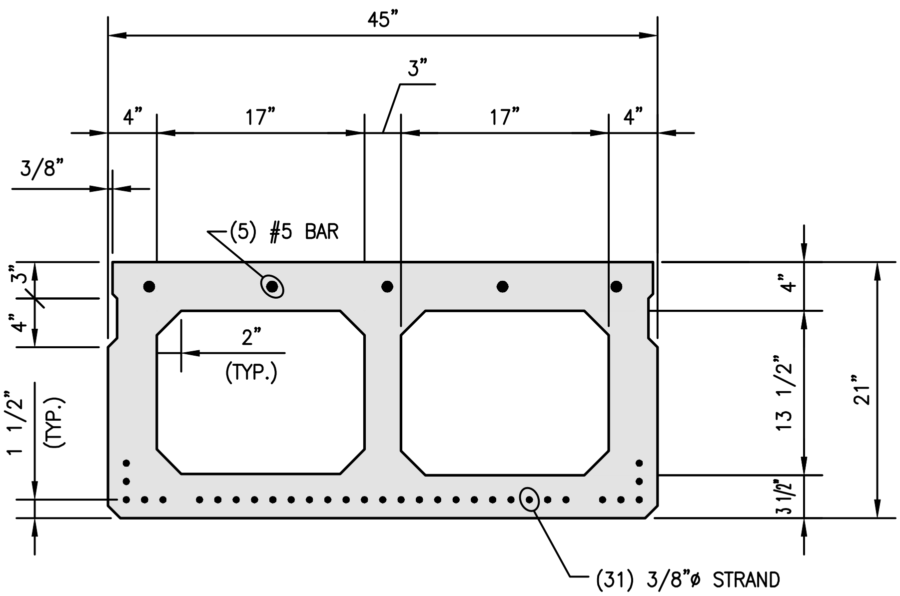

(b) 1961 INDOT standard section B-21-3-9

Figure D.1: Specimen 244-1-LC Cross-Section Geometry

(c) Cross-section photo

Figure D.1: Continued

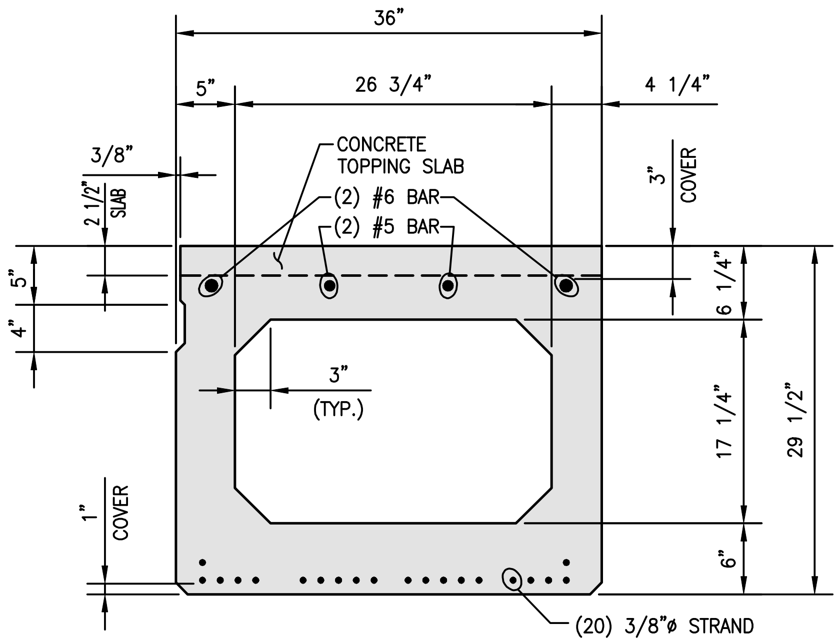

(a) As-built cross-section

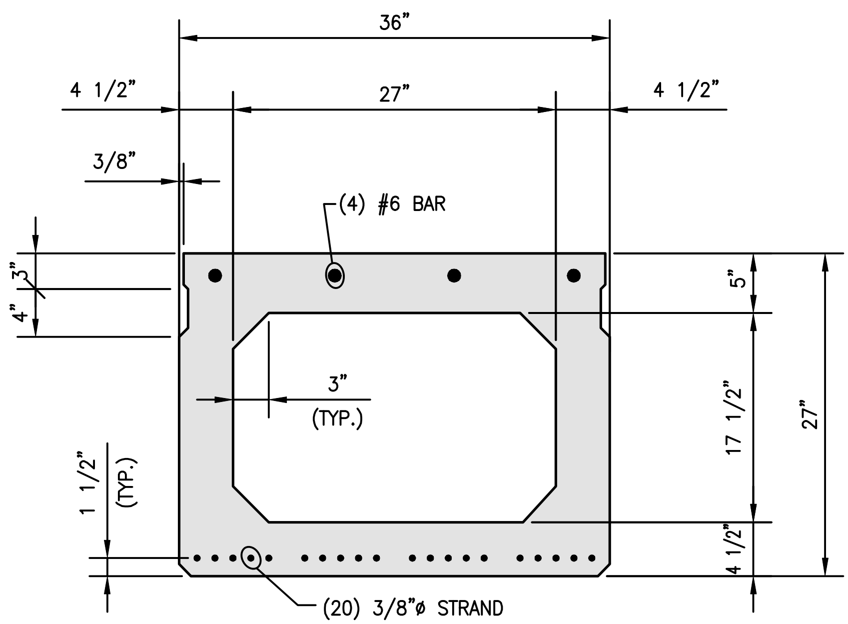

(b) 1961 INDOT standard section B-27

Figure D.2: Specimen 409-1-ES Cross-Section Geometry

(c) Cross-section photo

Figure D.2: Continued

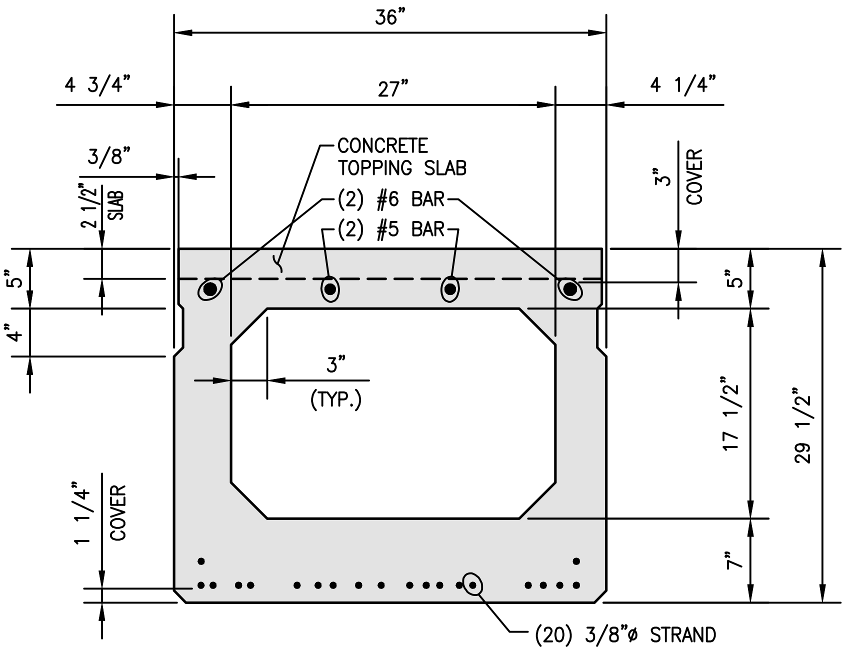

(a) As-built cross-section

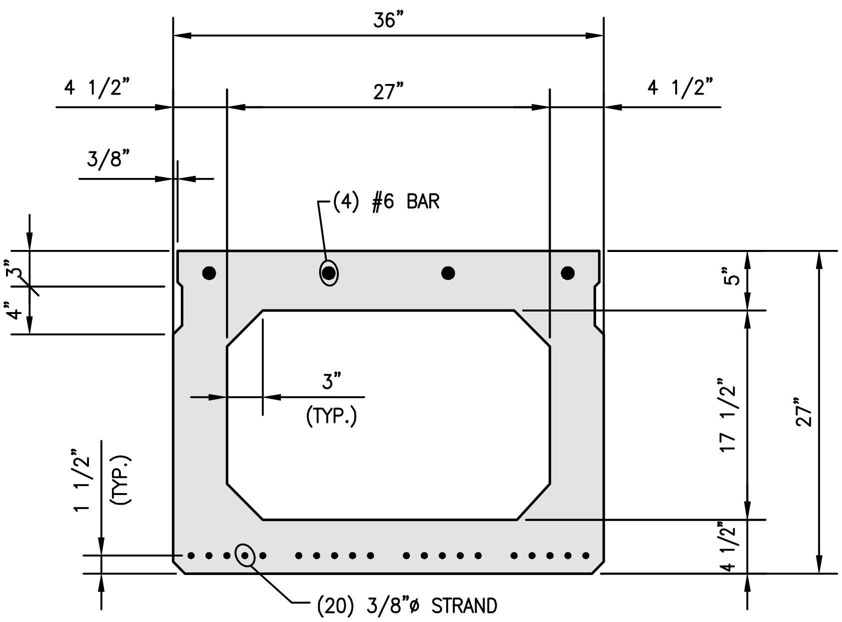

(b) 1961 INDOT standard section B-27

Figure D.3: Specimen 409-2-UD Cross-Section Geometry

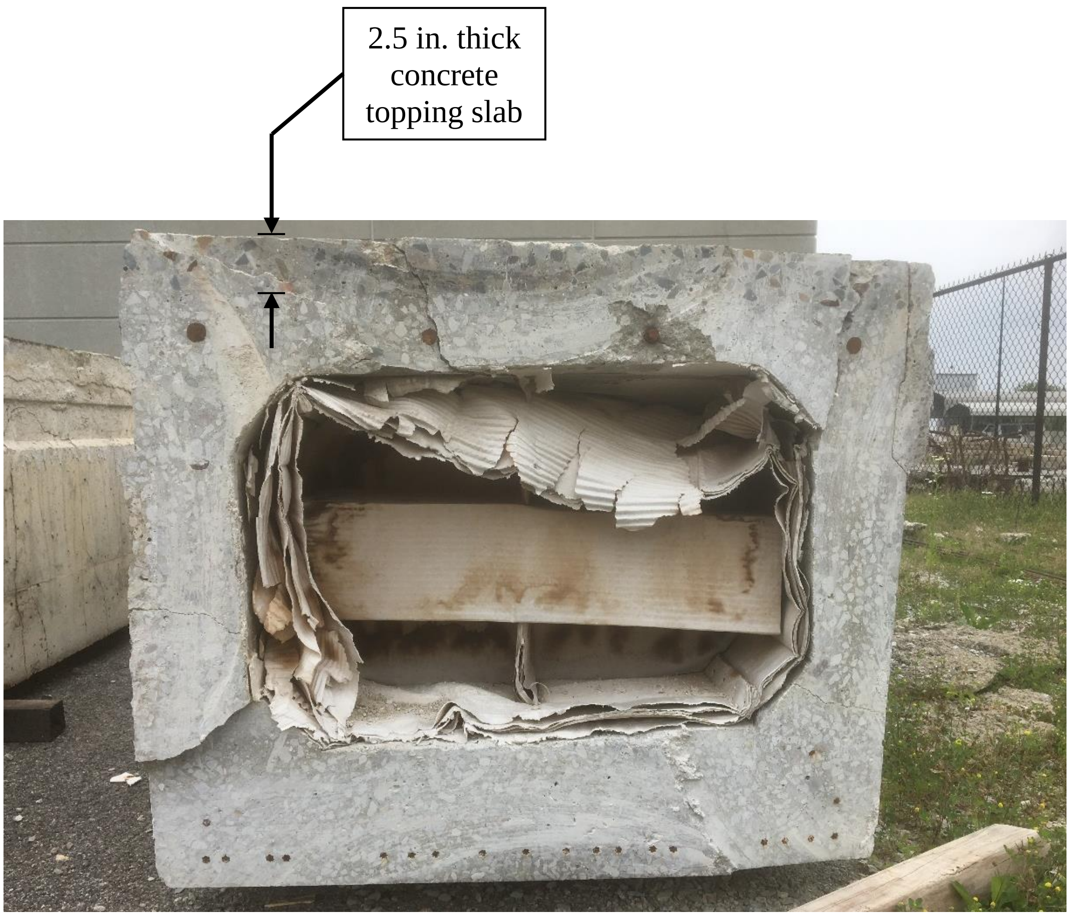

(c) Cross-section photo

Figure D.3: Continued

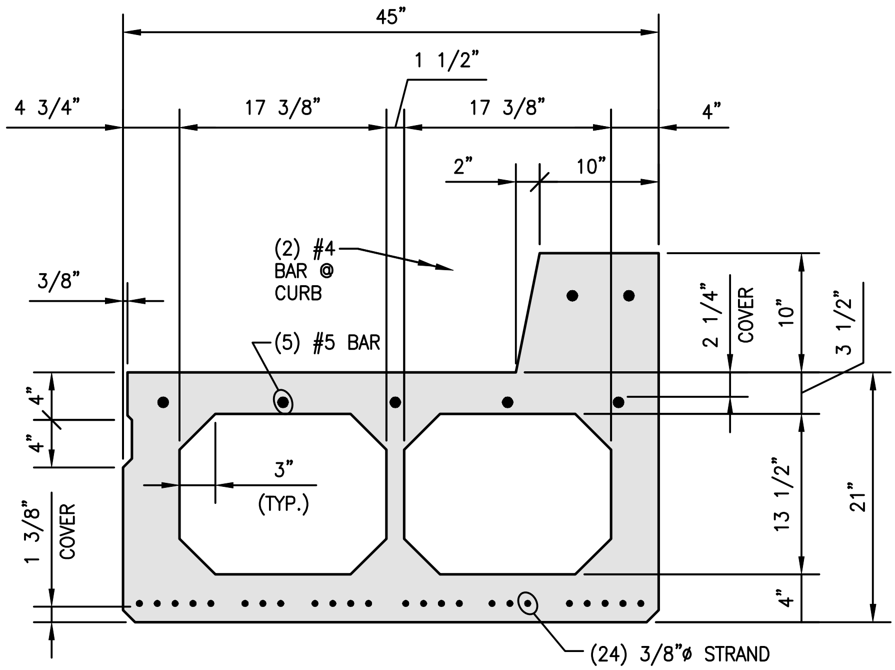

(a) As-built cross-section

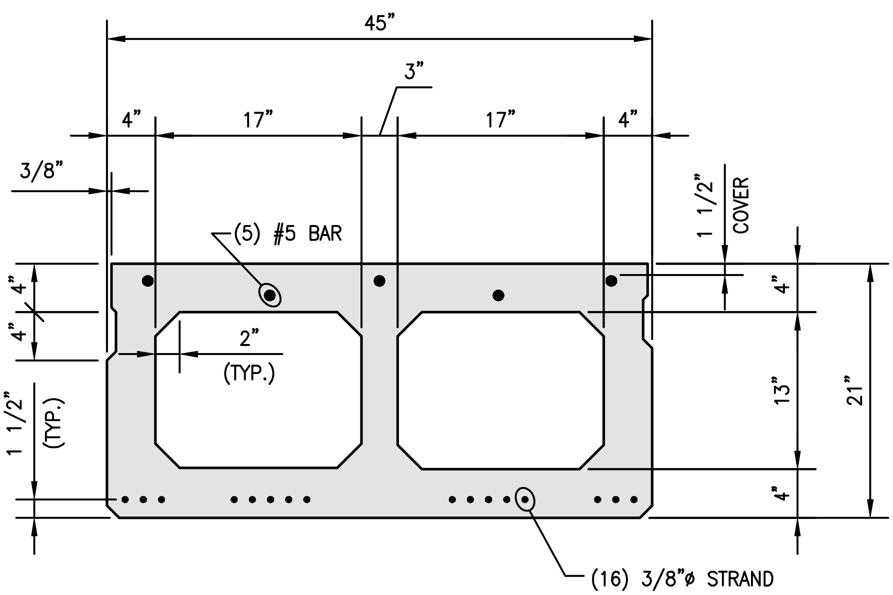

(b) 1965 INDOT standard section B-21-3-9

Figure D.4: Specimen K5-1-LC Cross-Section Geometry

(c) Cross-section photo

Figure D.4: Continued

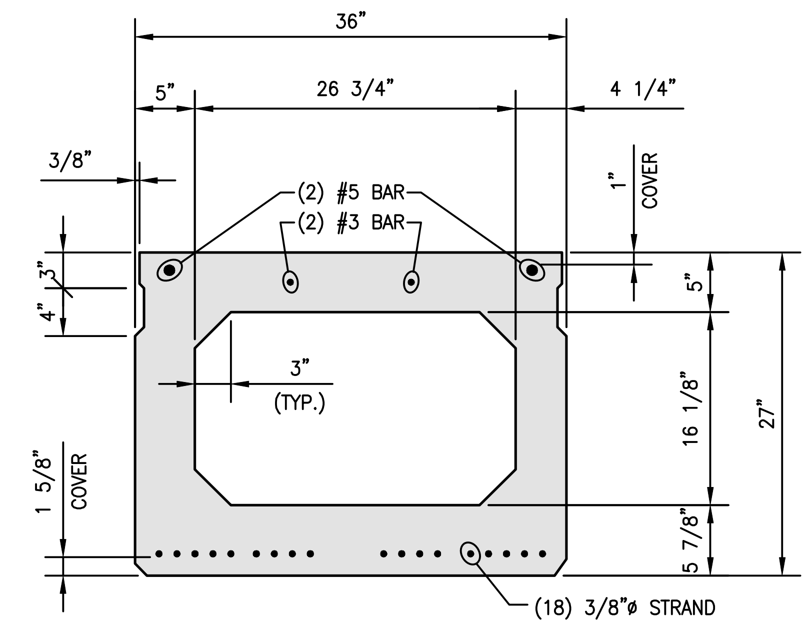

(a) As-built cross-section (original section)

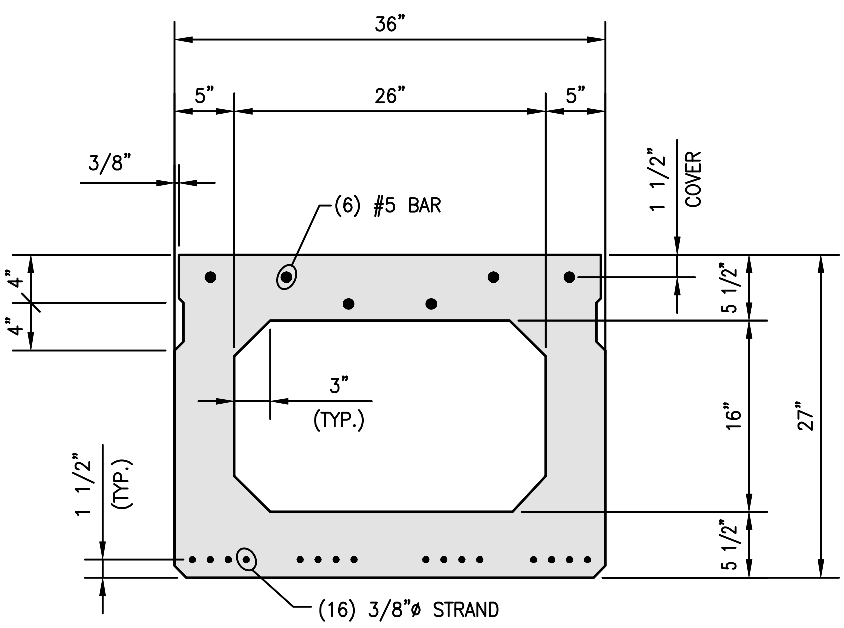

(b) 1965 INDOT standard section B-27

Figure D.5: Specimen K5-2-LC Cross-Section Geometry

(c) Cross-section photo

Figure D.5: Continued

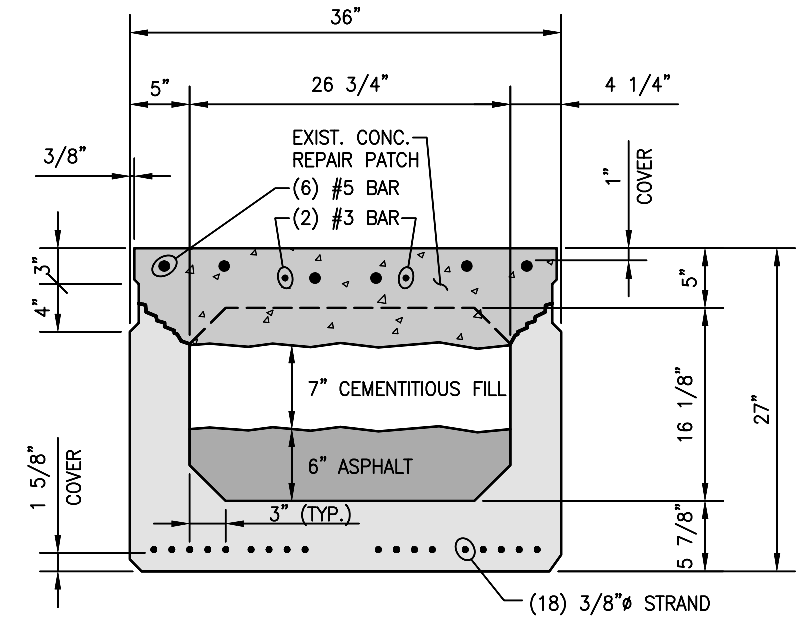

(a) As-built cross-section (repaired section)

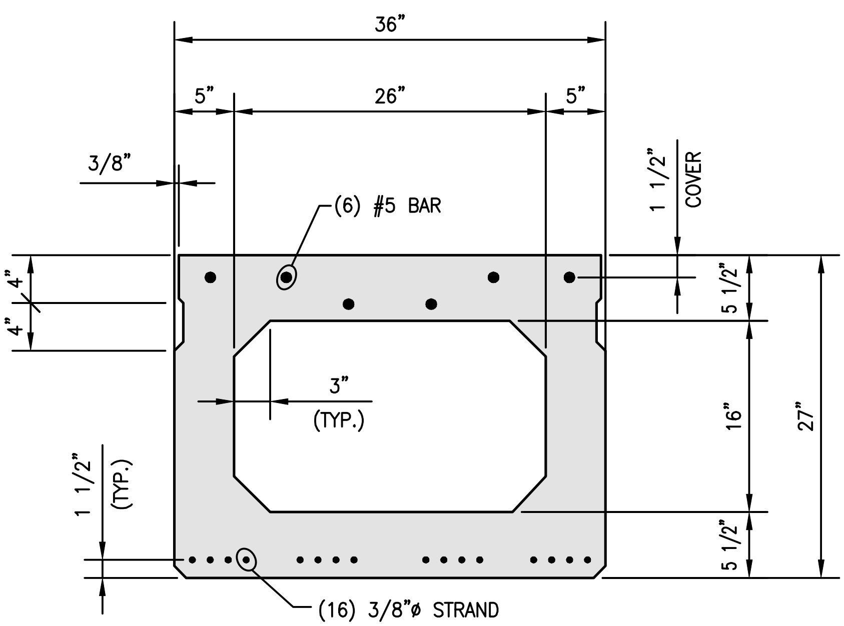

(b) 1961 INDOT standard section B-21-3-9

Figure D.6: Specimen K5-2-LC (Repair) Cross-Section Geometry

(c) Cross-section photo

Figure D.6: Continued

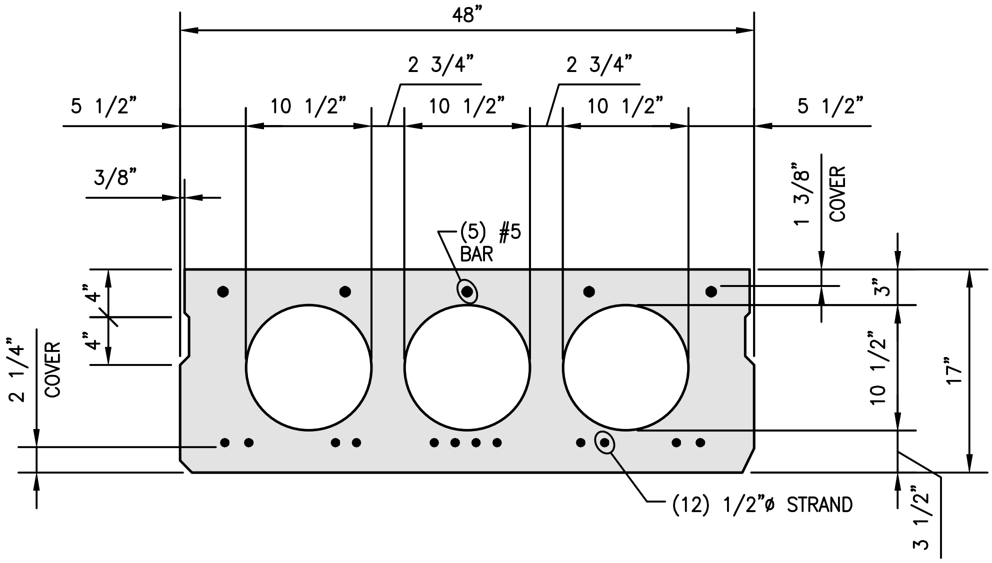

(a) As-built cross-section

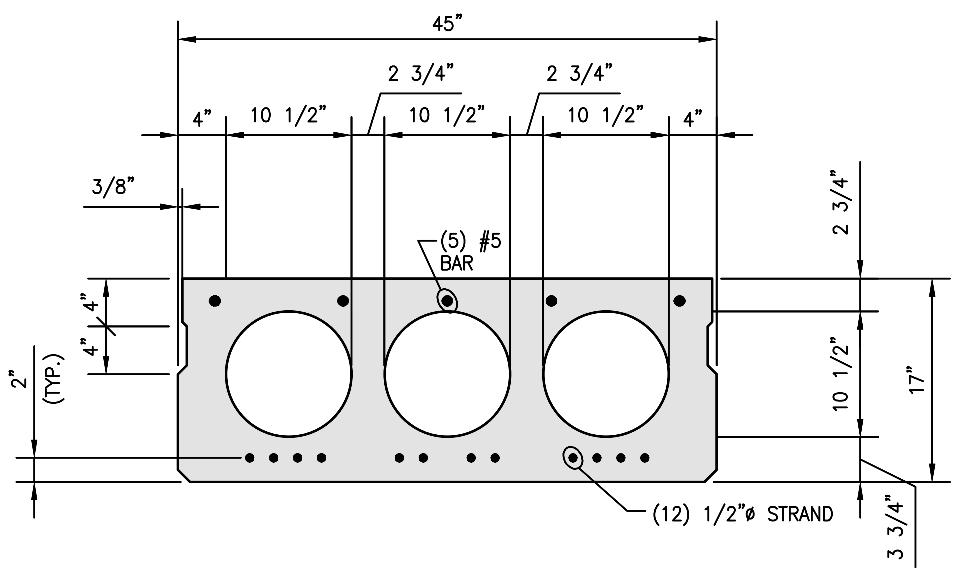

(b) 1961 INDOT standard section B-17-3-9

Figure D.7: Specimen 79-1-UD Cross-Section Geometry

(c) Cross-section photo

Figure D.7: Continued

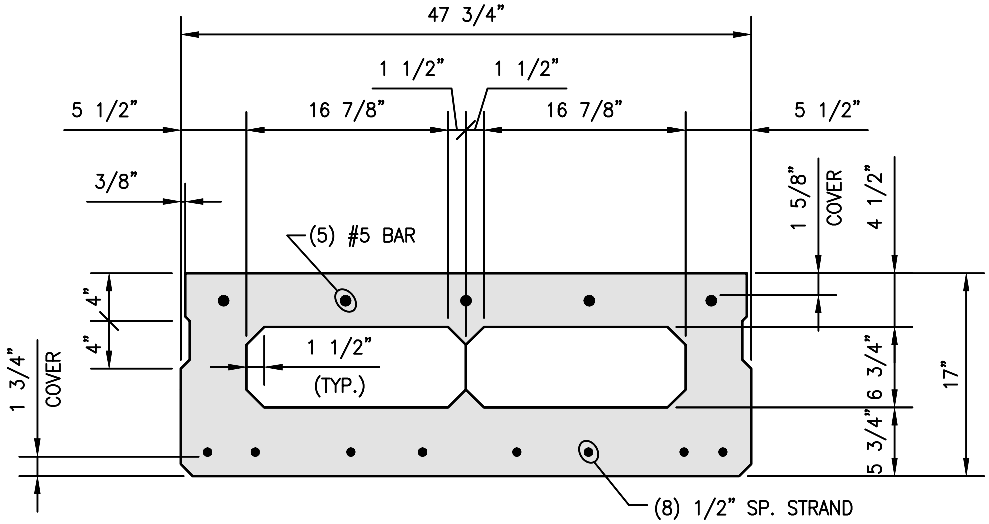

(a) As-built cross-section

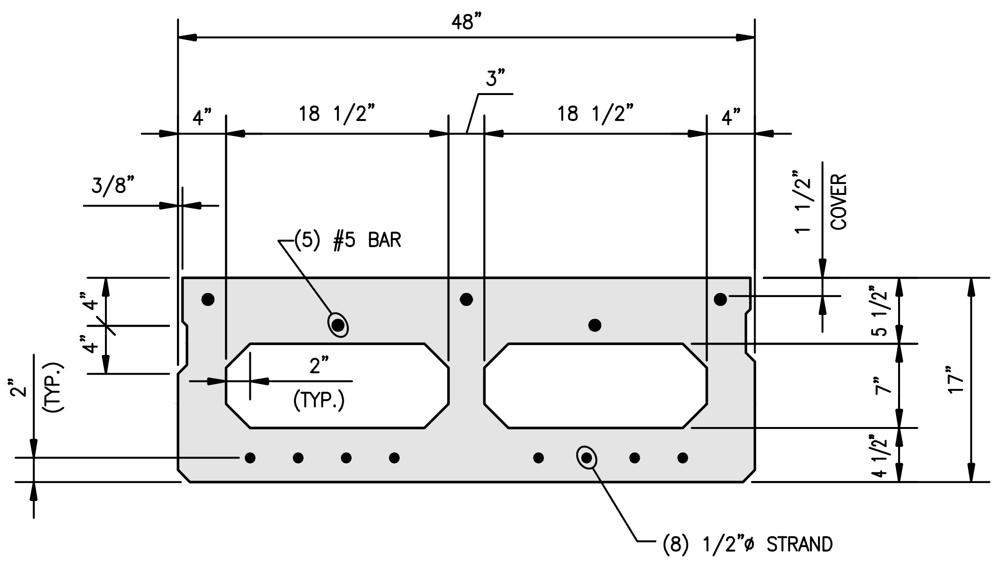

(b) 1971 INDOT standard section WS-17

Figure D.8: Specimen 79-2-UD Cross-Section Geometry

(c) Cross-section photo

Figure D.8: Continued

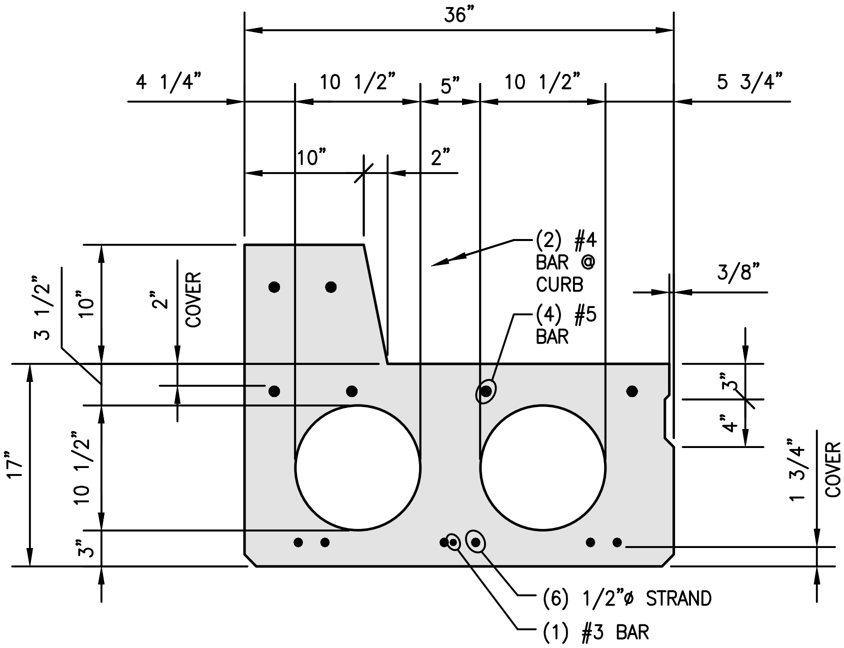

(a) As-built cross-section

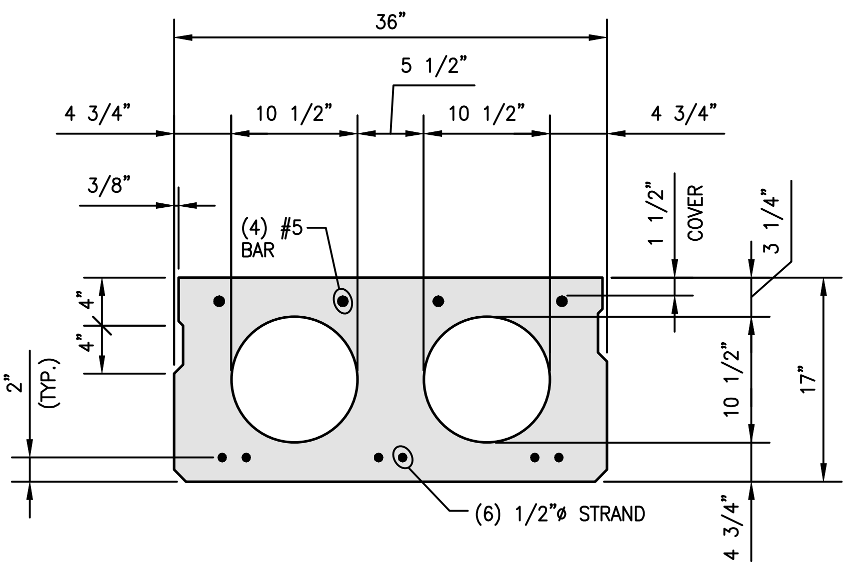

(b) 1961 INDOT standard section B-17

Figure D.9: Specimen 79-3-UD Cross-Section Geometry

(c) Cross-section photo

Figure D.9: Continued

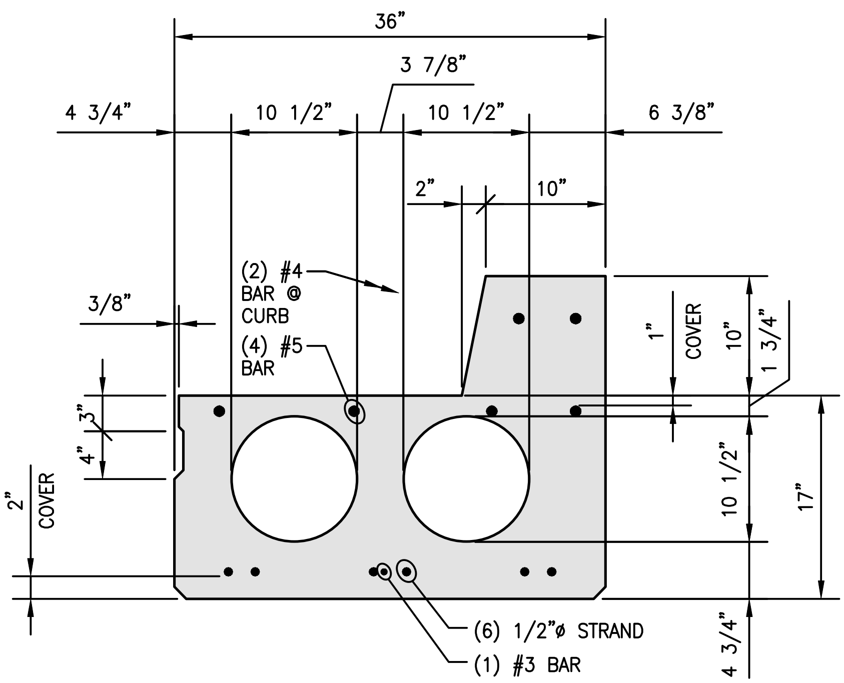

(a) As-built cross-section

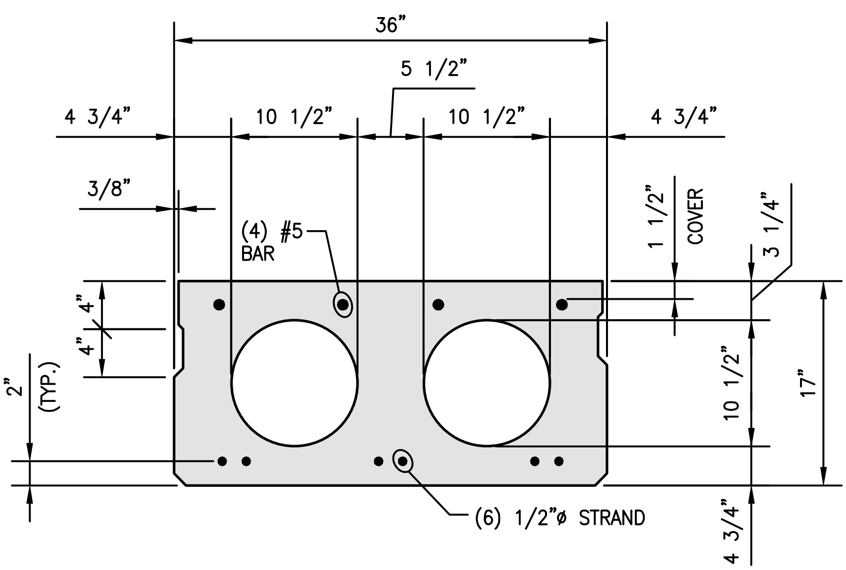

(b) 1961 INDOT standard section B-17

Figure D.10: Specimen 79-4-LC Cross-Section Geometry

(c) Cross-section photo

Figure D.10: Continued

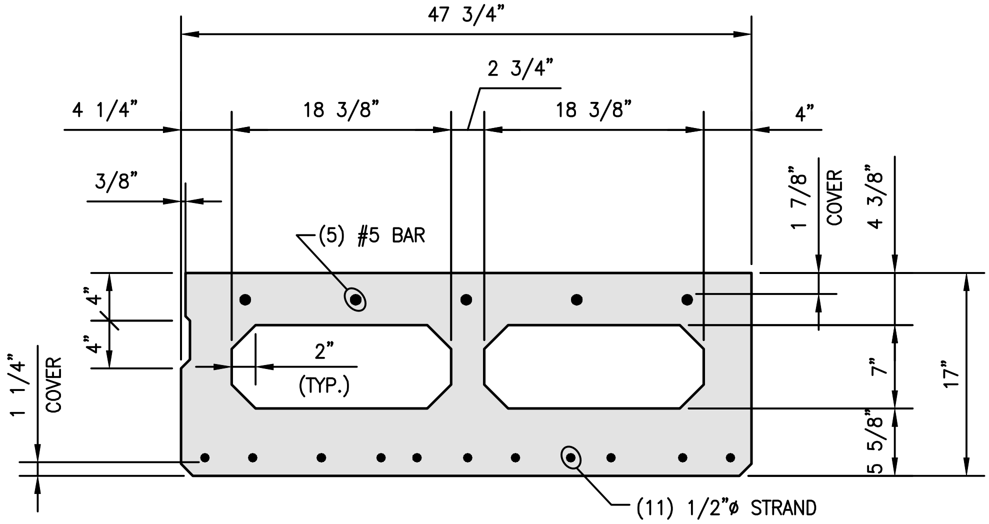

(a) As-built cross-section

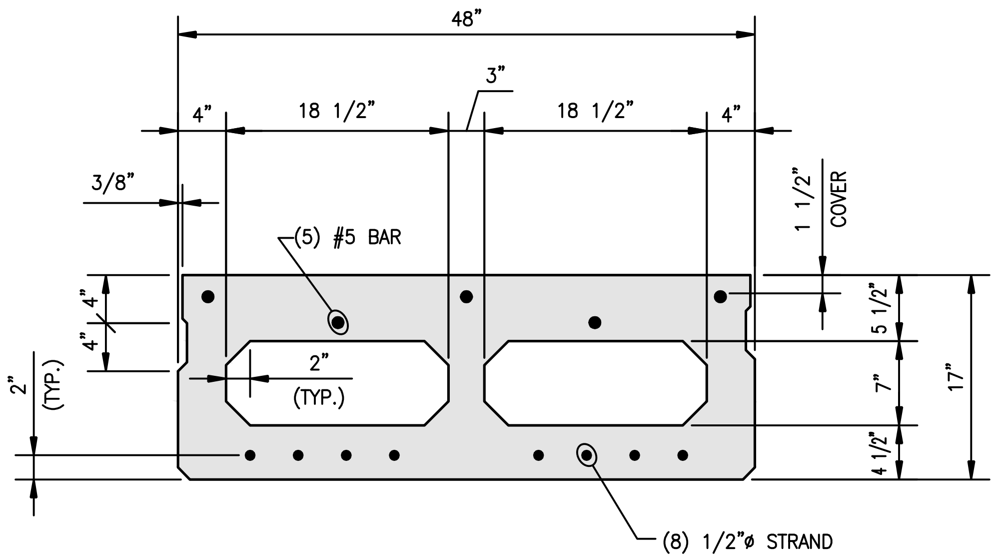

(b) 1965 INDOT standard section WS-17

Figure D.11: Specimen 56-1-LC Cross-Section Geometry

(c) Cross-section photo

Figure D.11: Continued

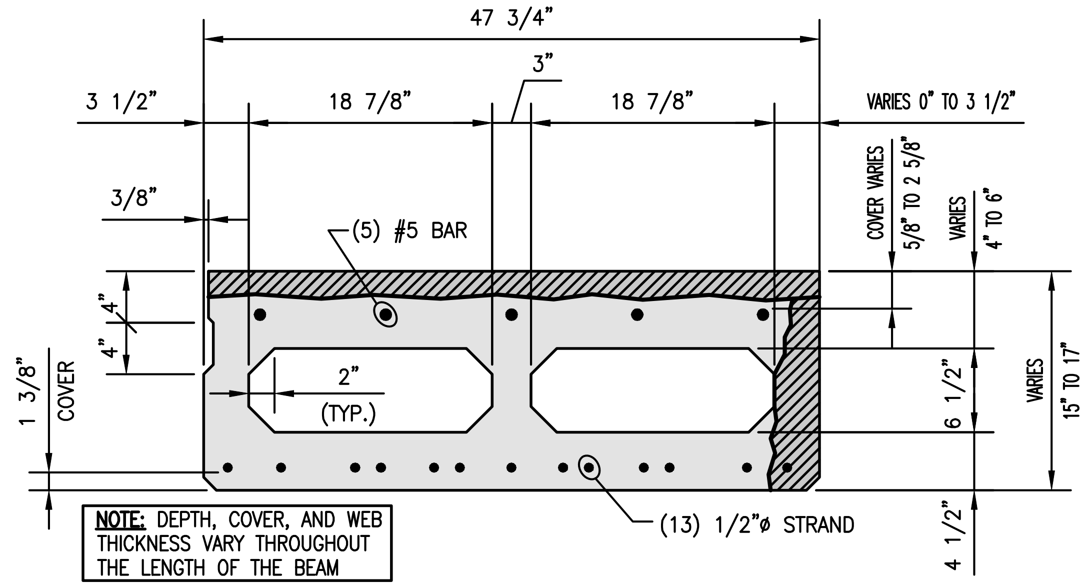

(a) As-built cross-section

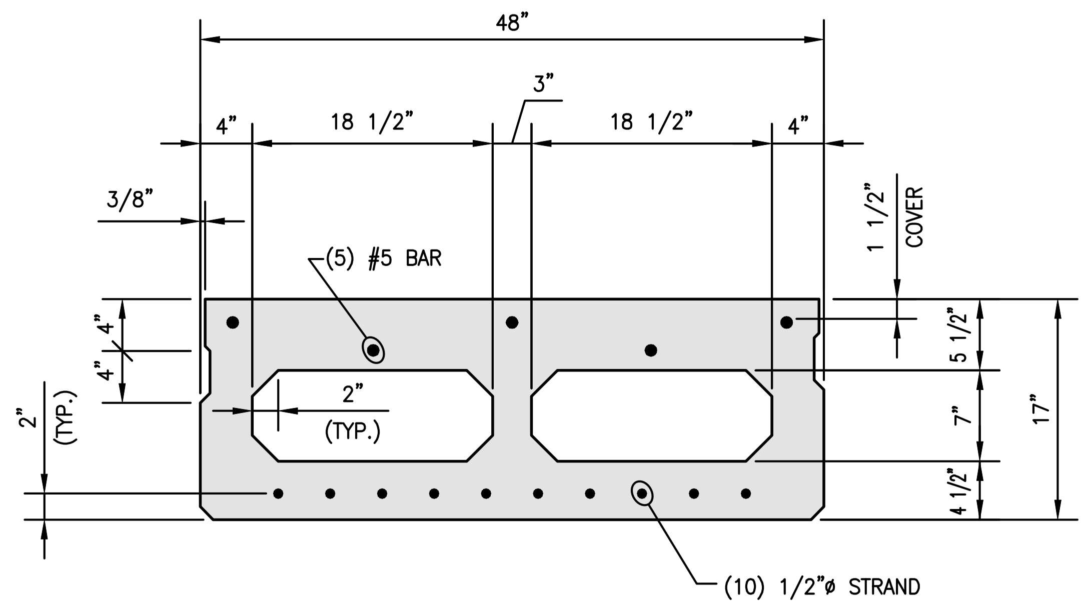

(b) 1965 INDOT standard section WS-17

Figure D.12: Specimen 56-2-LC Cross-Section Geometry

(c) Cross-section photo

Figure D.12: Continued

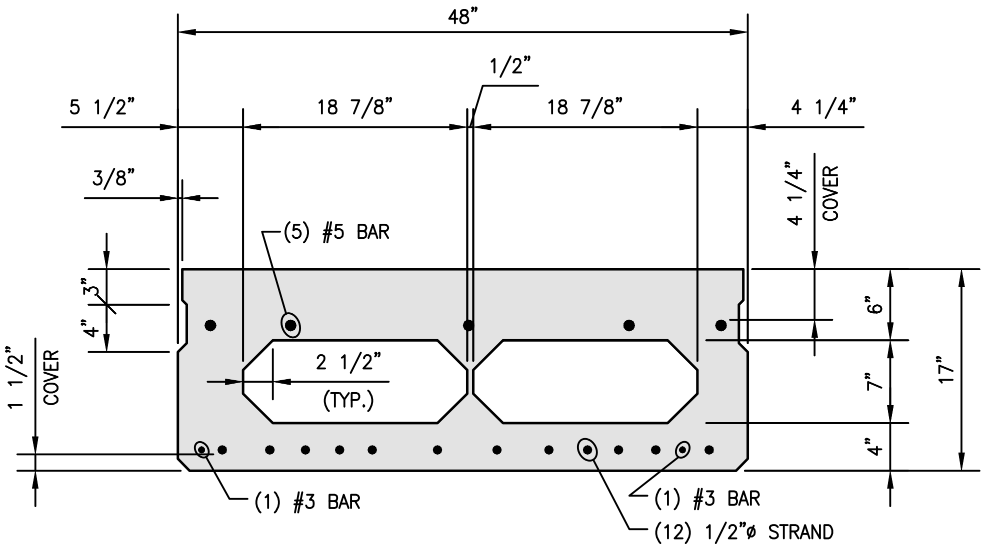

(a) As-built cross-section

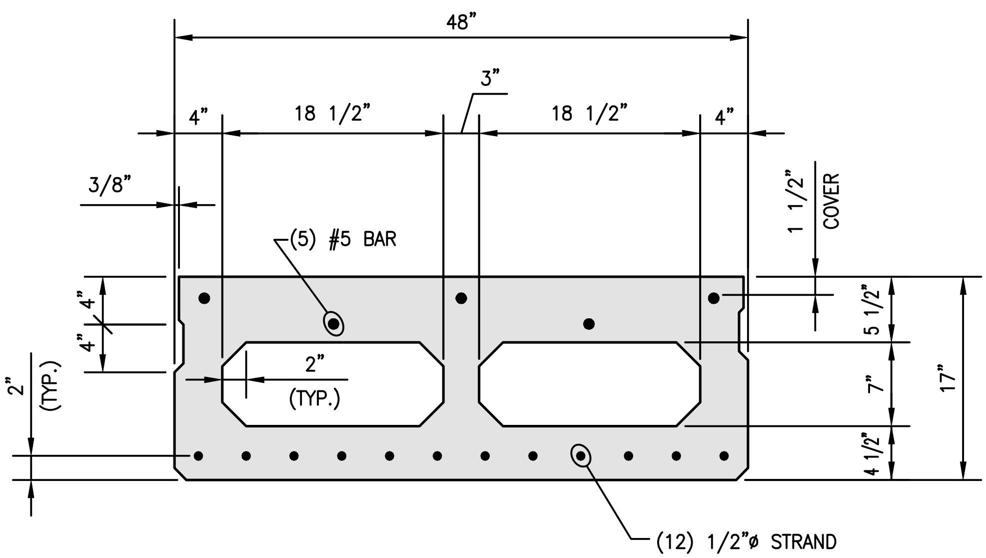

(b) 1970 INDOT standard section WS-17

Figure D.13: Specimen 102-1-BS Cross-Section Geometry

(c) Cross-section photo

Figure D.13: Continued

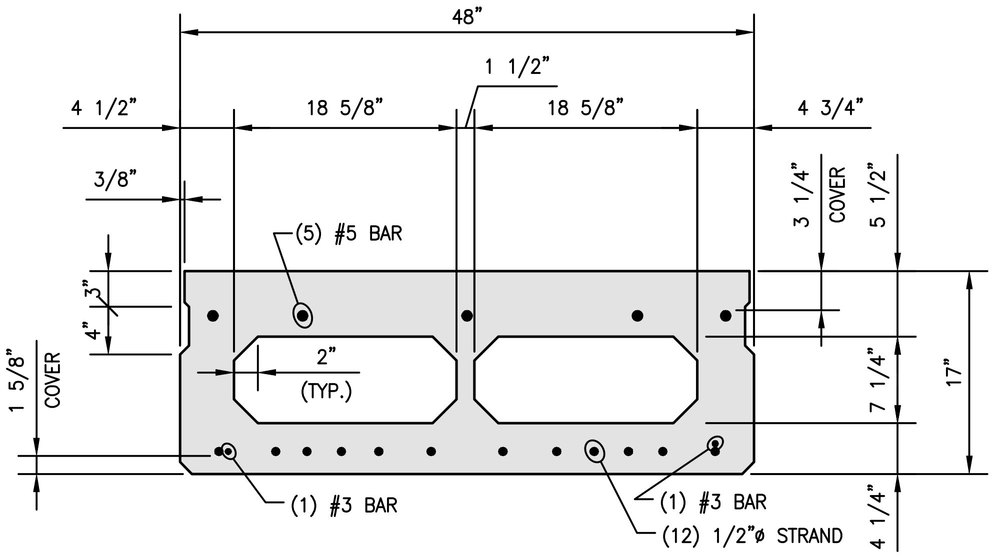

(a) As-built cross-section

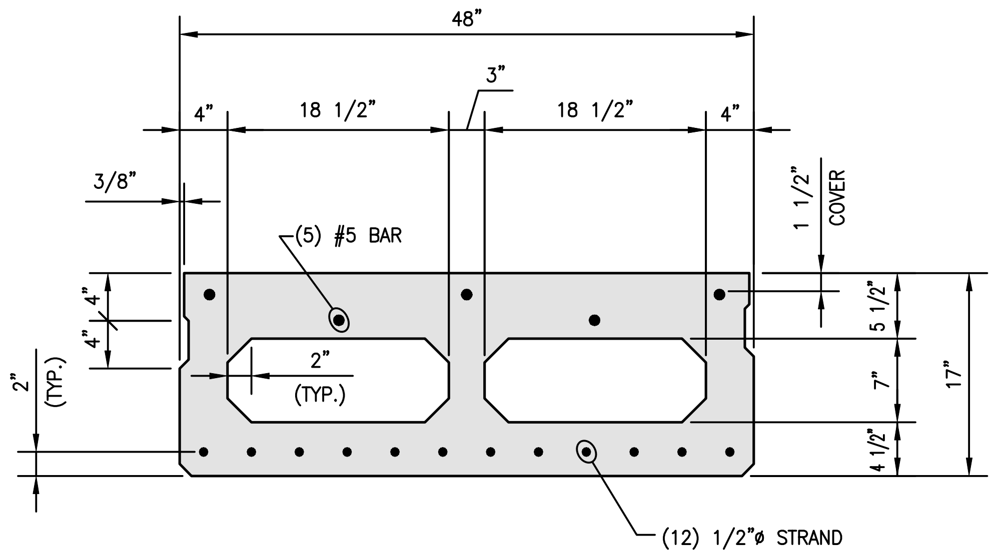

(b) 1970 INDOT standard section WS-17

Figure D.14: Specimen 102-2-BS Cross-Section Geometry

(c) Cross-section photo

Figure D.14: Continued

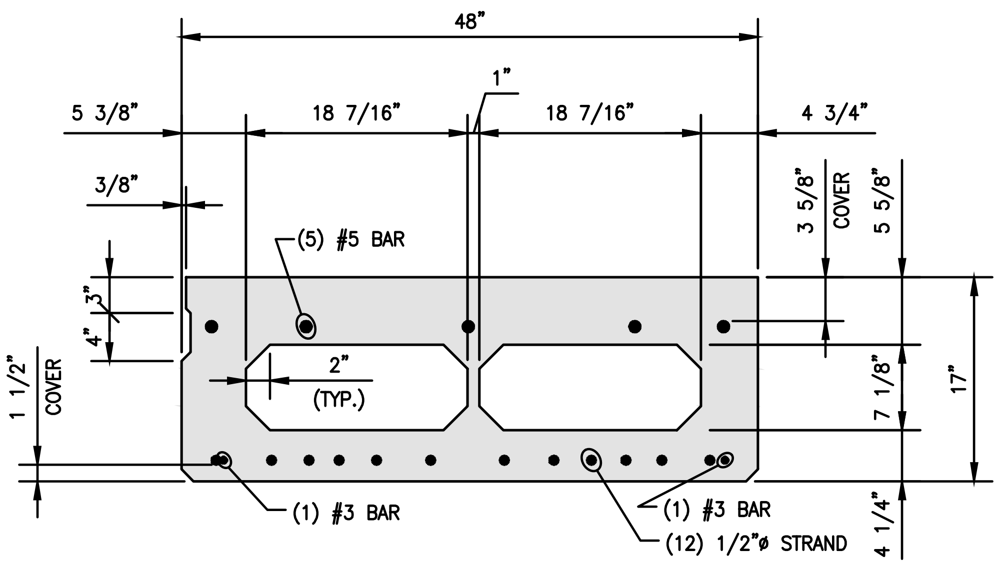

(a) As-built cross-section

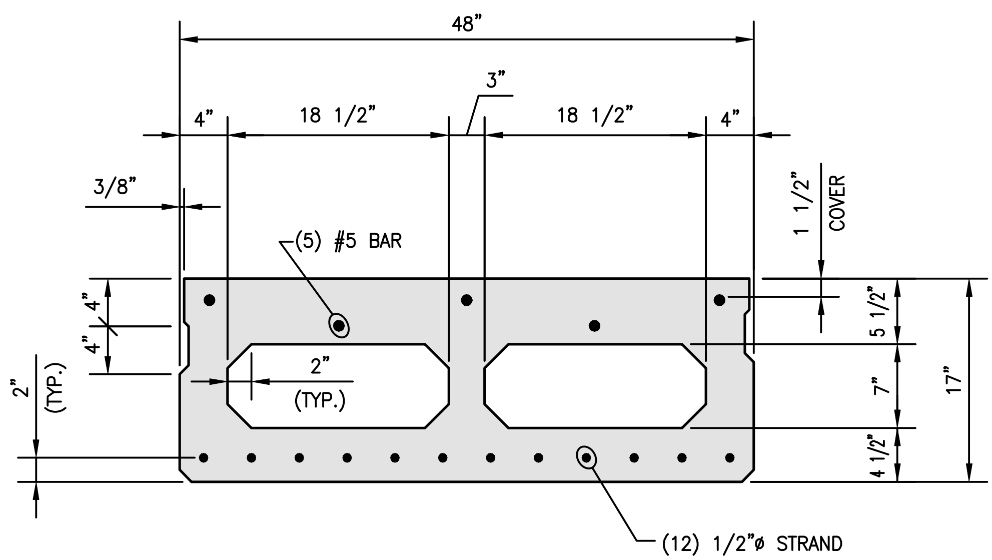

(b) 1970 INDOT standard section WS-17

Figure D.15: Specimen 102-3-BS Cross-Section Geometry

(c) Cross-section photo

Figure D.15: Continued

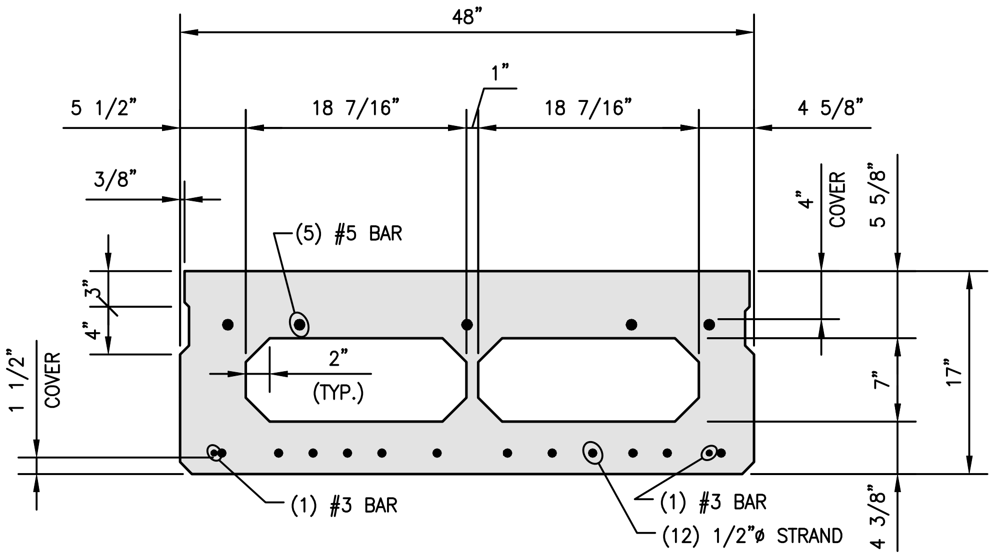

(a) As-built cross-section

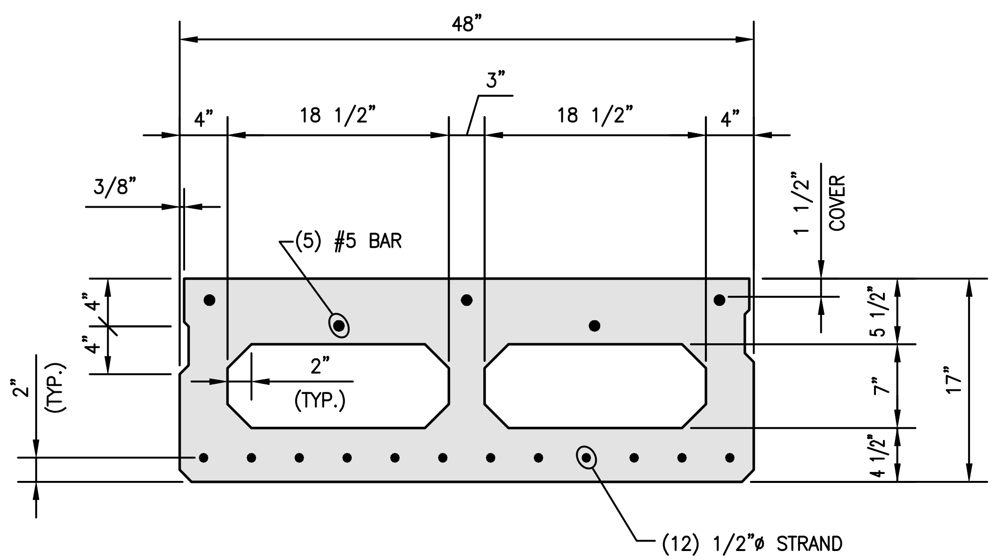

(b) 1970 INDOT standard section WS-17

Figure D.16: Specimen 102-4-BS Cross-Section Geometry

(c) Cross-section photo

Figure D.16: Continued

APPENDIX E. CONCRETE STRESS VS. STRAIN CURVES

The Hognestad and Thorenfeldt concrete models are presented in comparison with the compression test data of the concrete cores extracted from each specimen. Please note that the results for Specimen 56-2-ES (Core 1 to 3 taken from the flange) are in error due to the short height of the concrete cores.

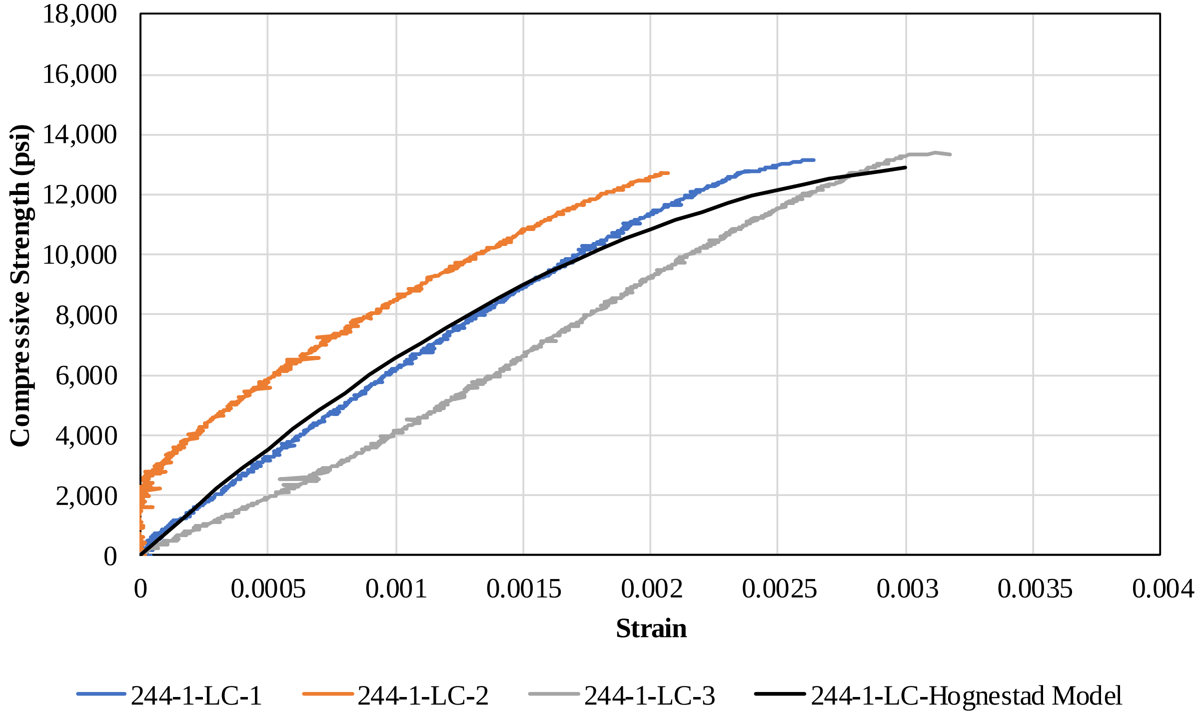

(a) Hognestad

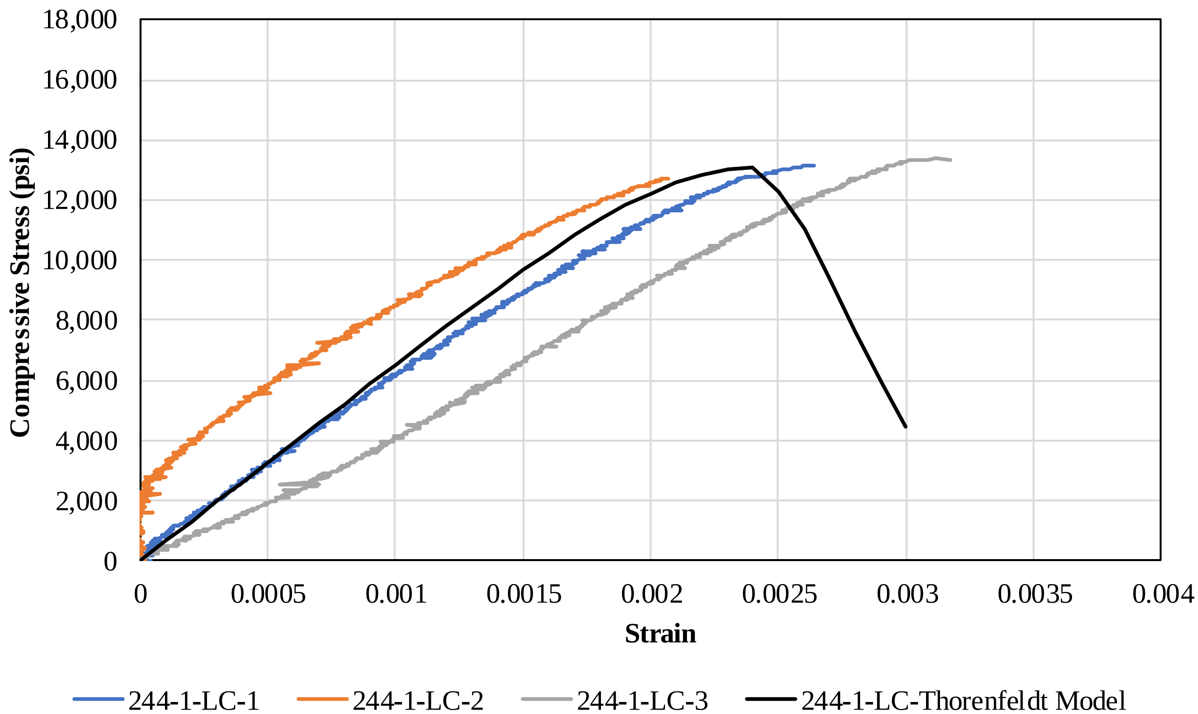

(b) Thorenfeldt

Figure E.1: Specimen 244-1-LC Compressive Stress vs. Strain

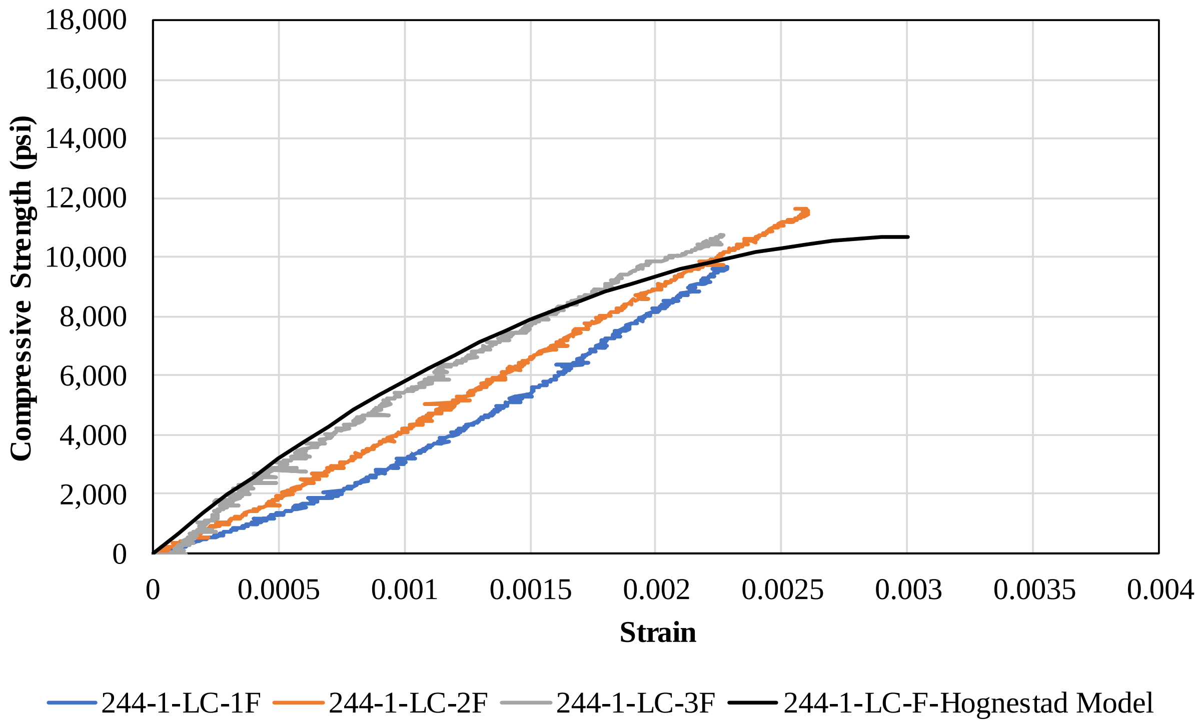

(a) Hognestad

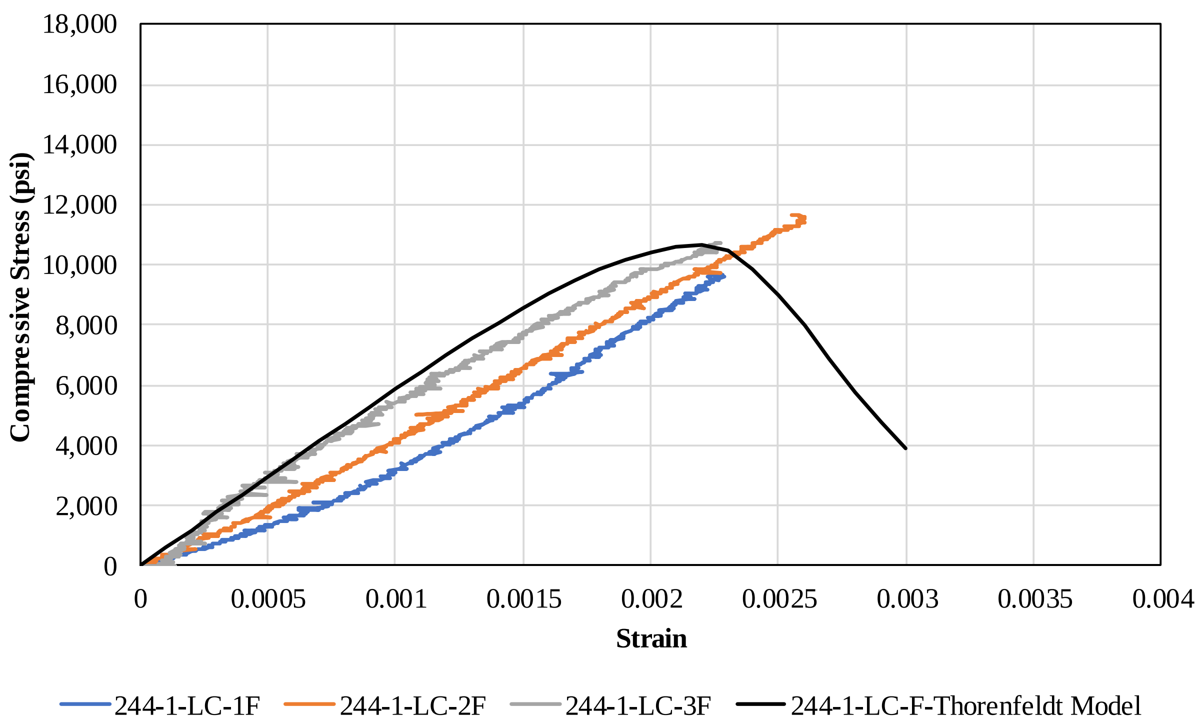

(b) Thorenfeldt

Figure E.2: Specimen 244-1-LC (Flange) Compressive Stress vs. Strain

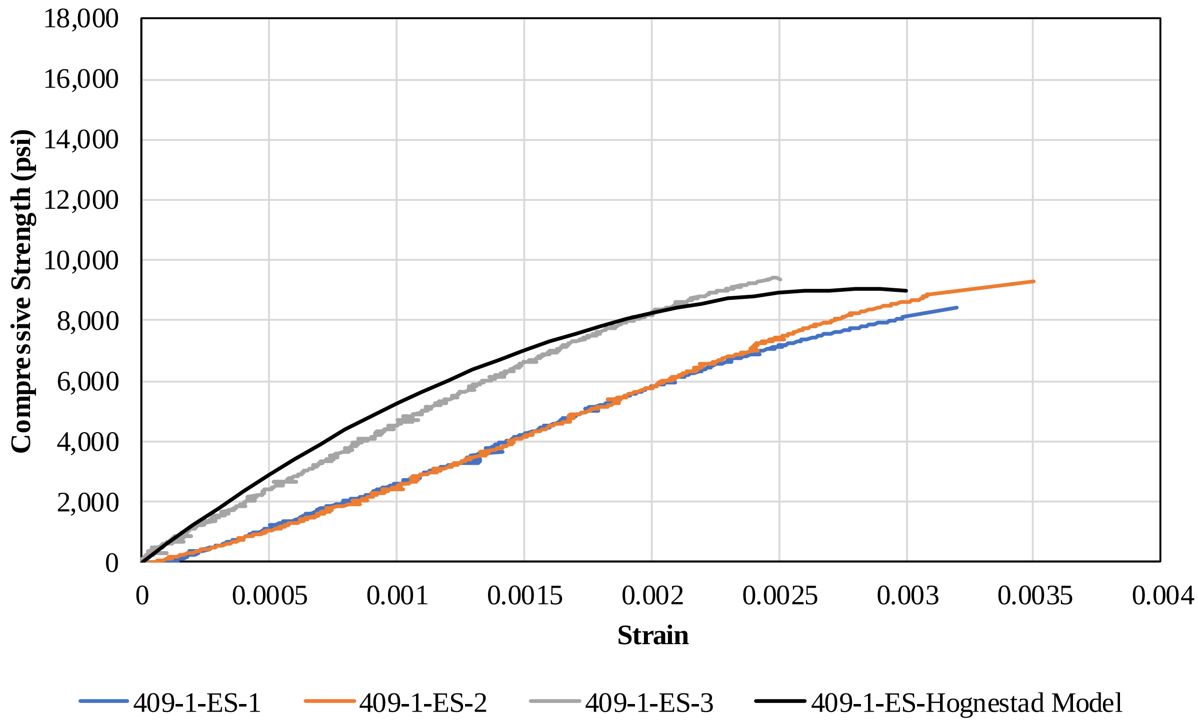

(a) Hognestad

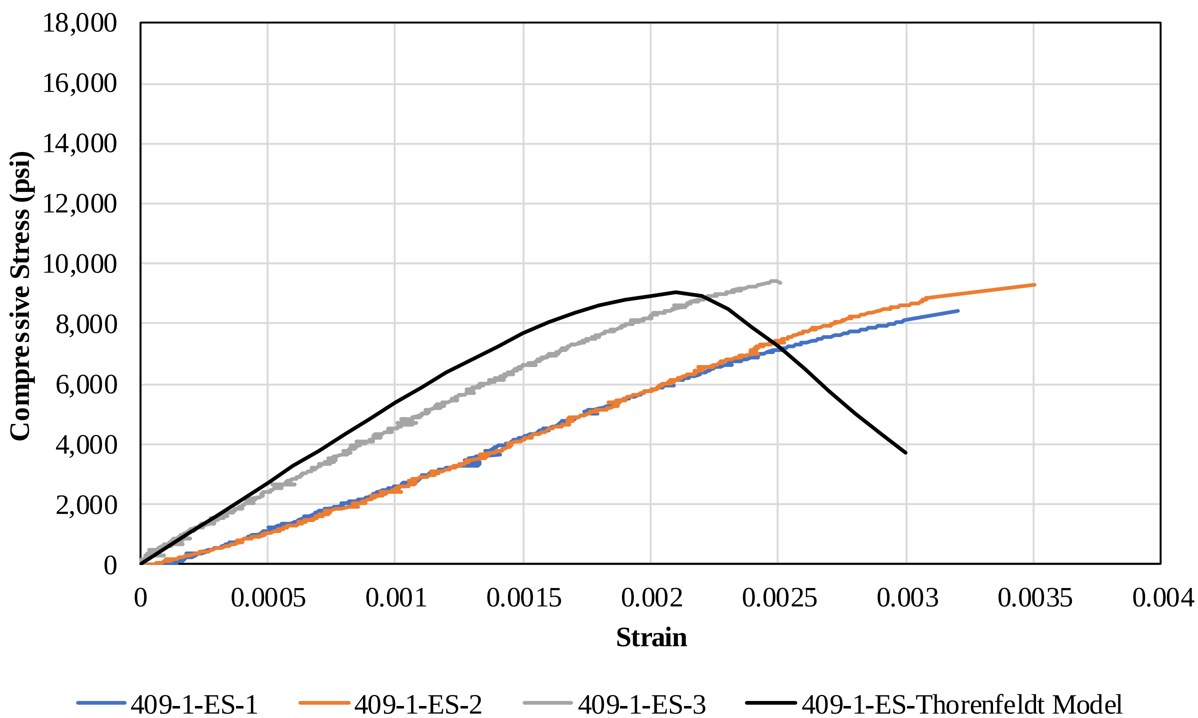

(b) Thorenfeldt

Figure E.3: Specimen 409-1-ES Compressive Stress vs. Strain

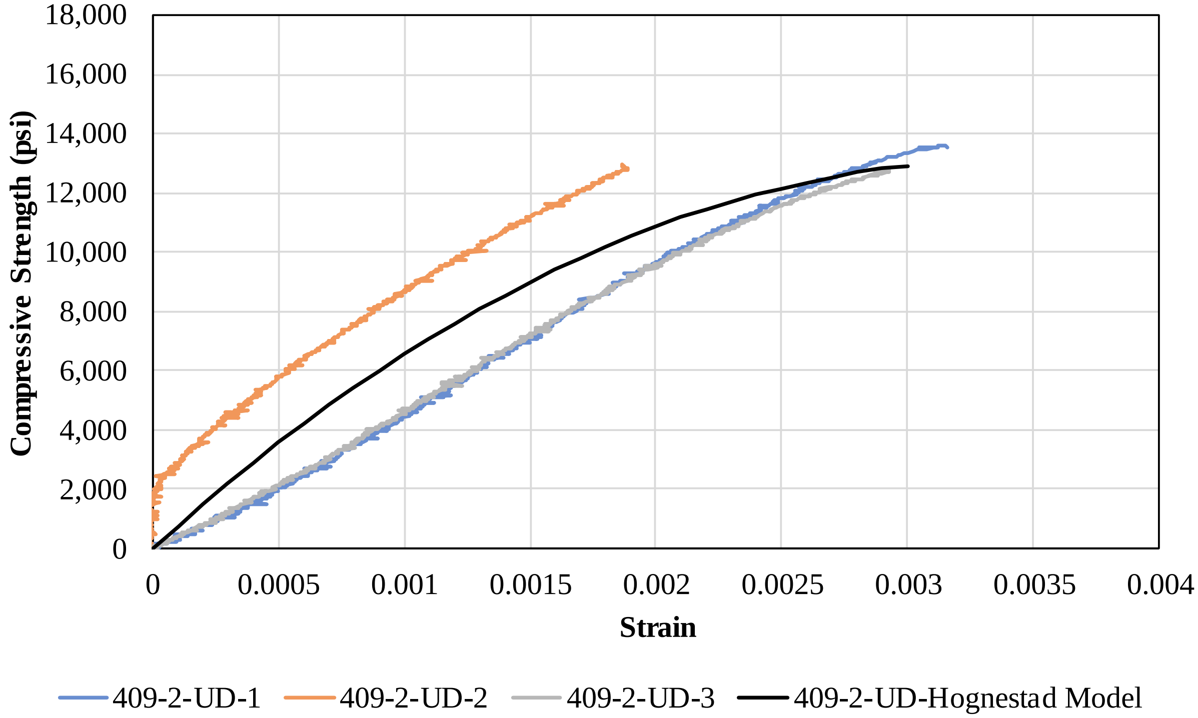

(a) Hognestad

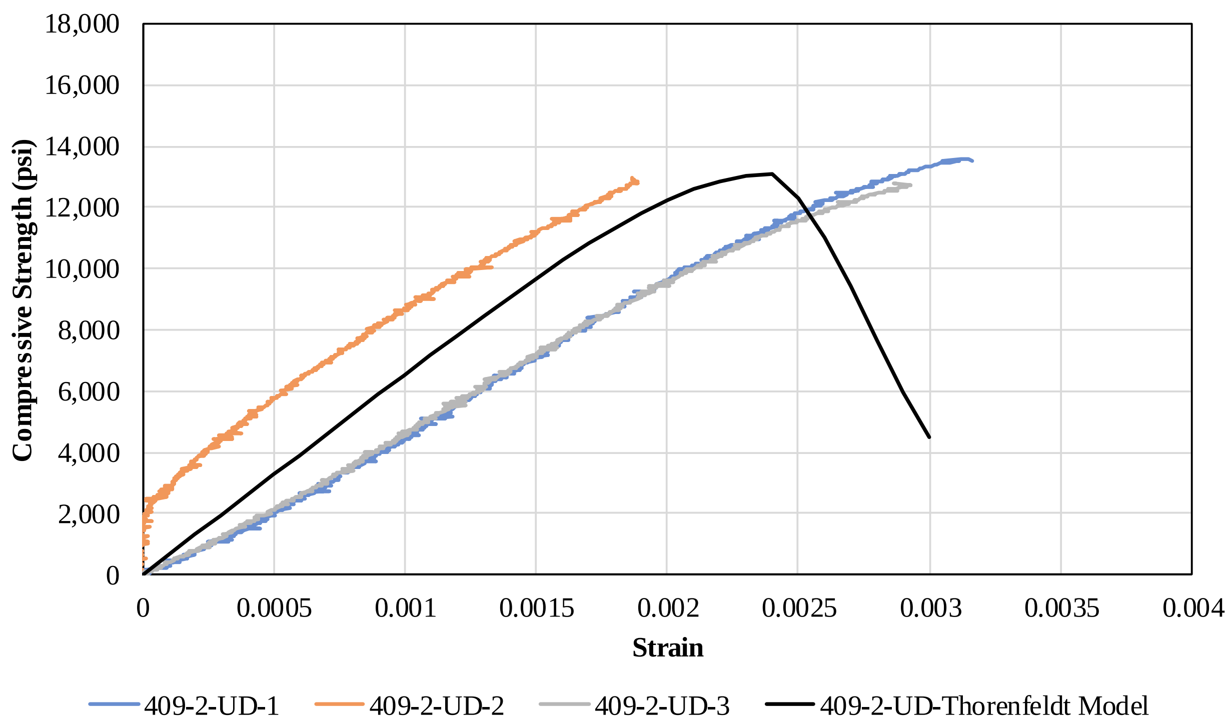

(b) Thorenfeldt

Figure E.4: Specimen 409-2-UD Compressive Stress vs. Strain

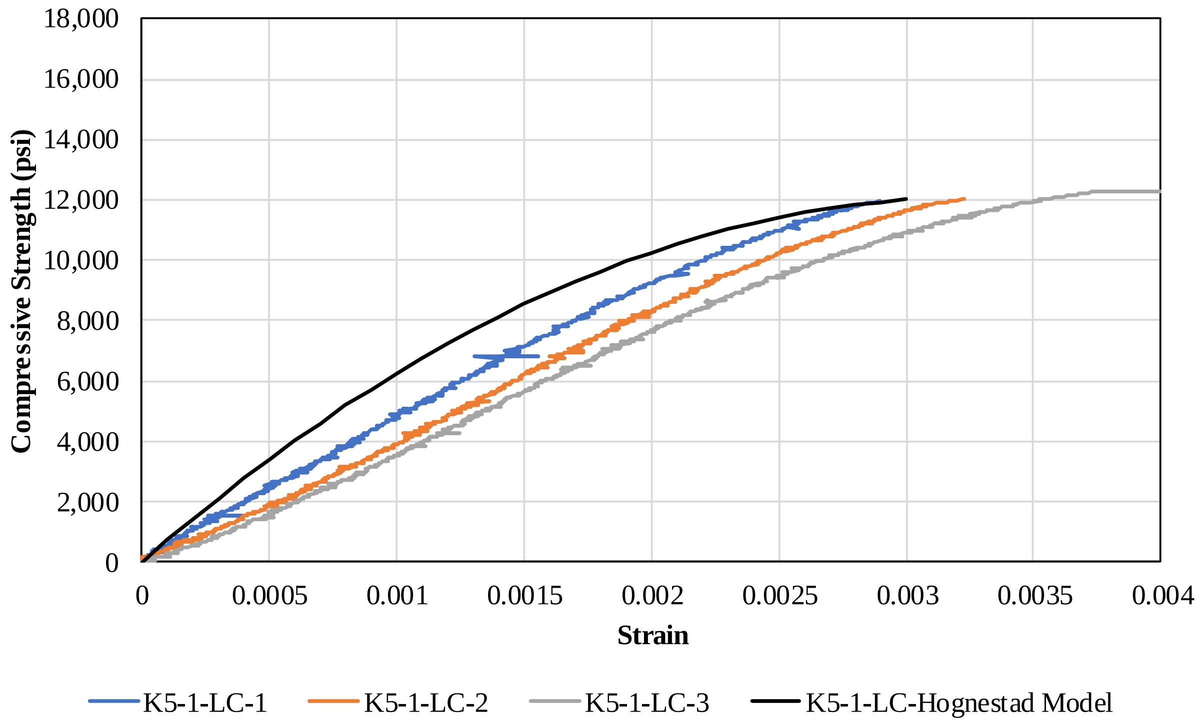

(a) Hognestad

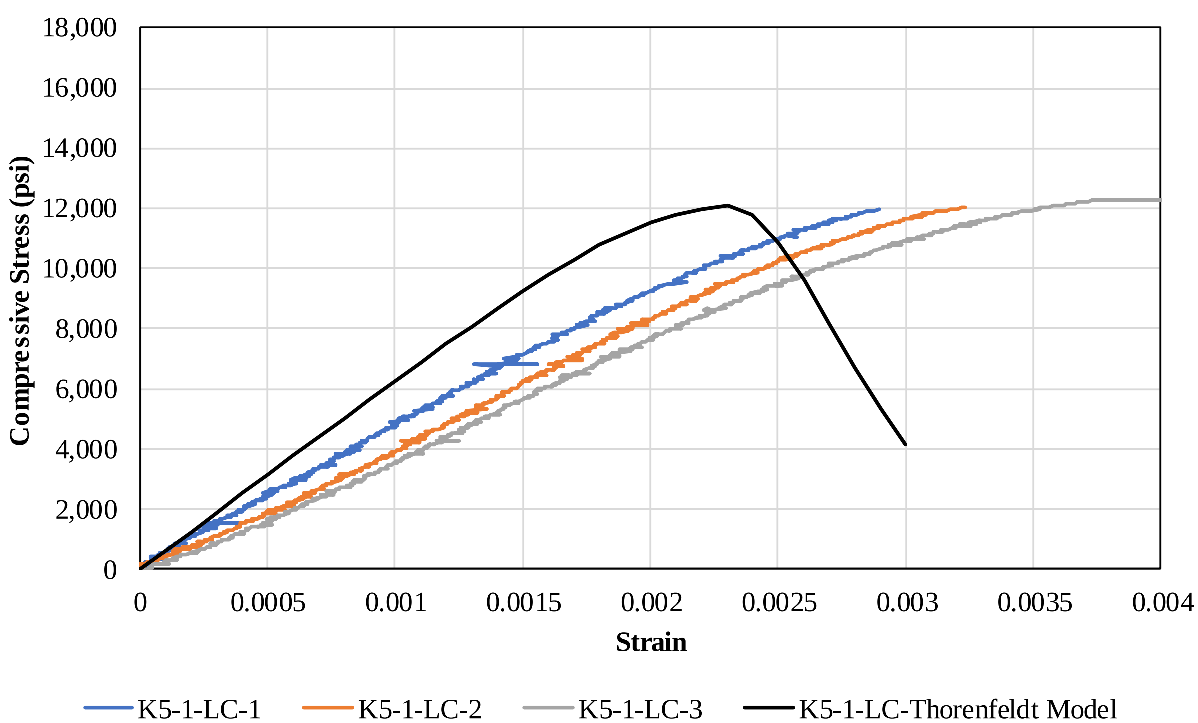

(b) Thorenfeldt

Figure E.5: Specimen K5-1-LC Compressive Stress vs. Strain

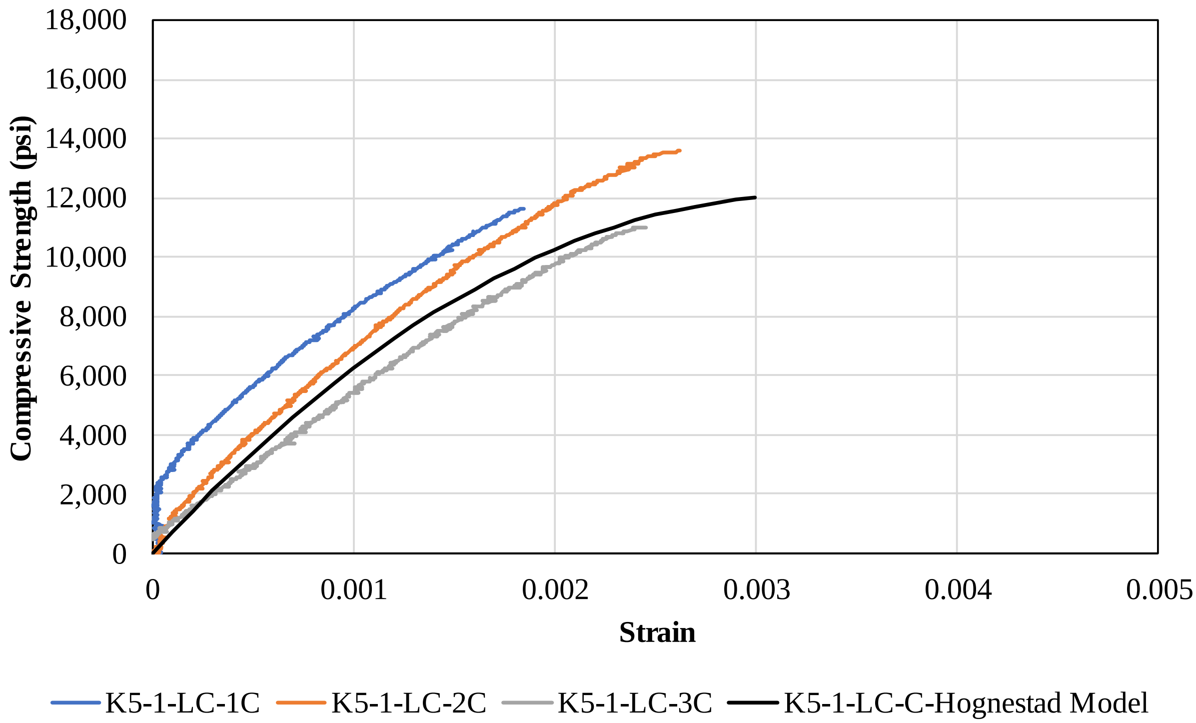

(a) Hognestad

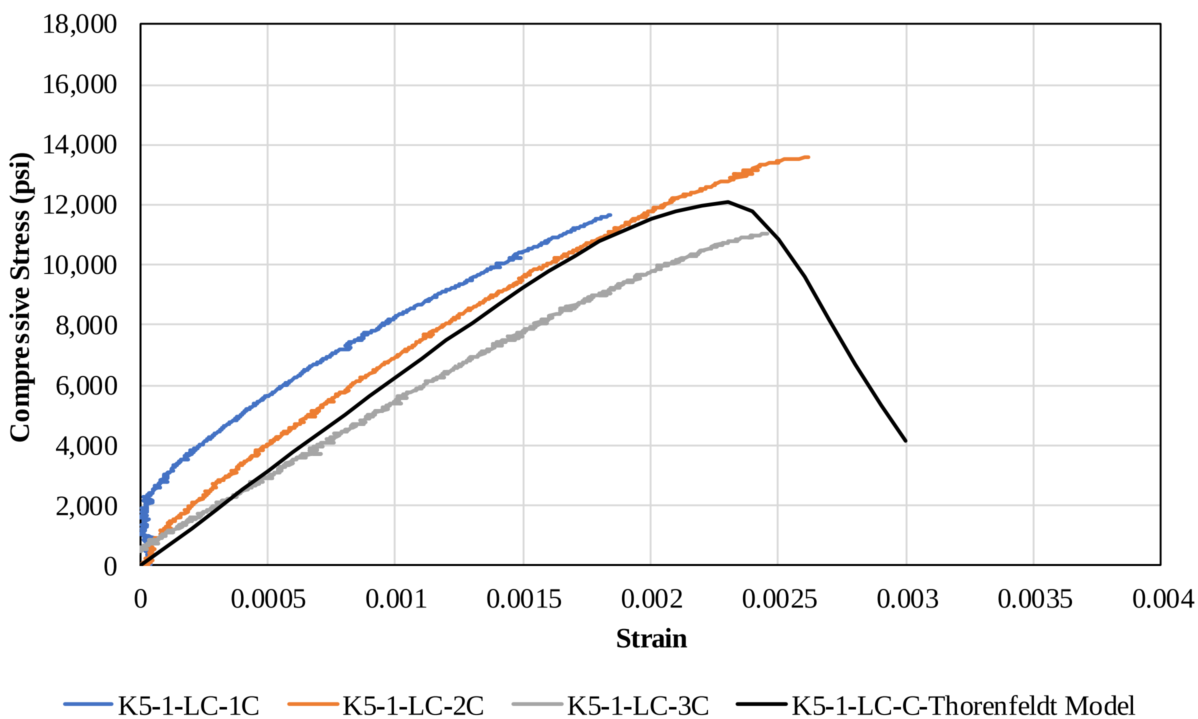

(b) Thorenfeldt

Figure E.6: Specimen K5-1-LC (Curb) Compressive Stress vs. Strain

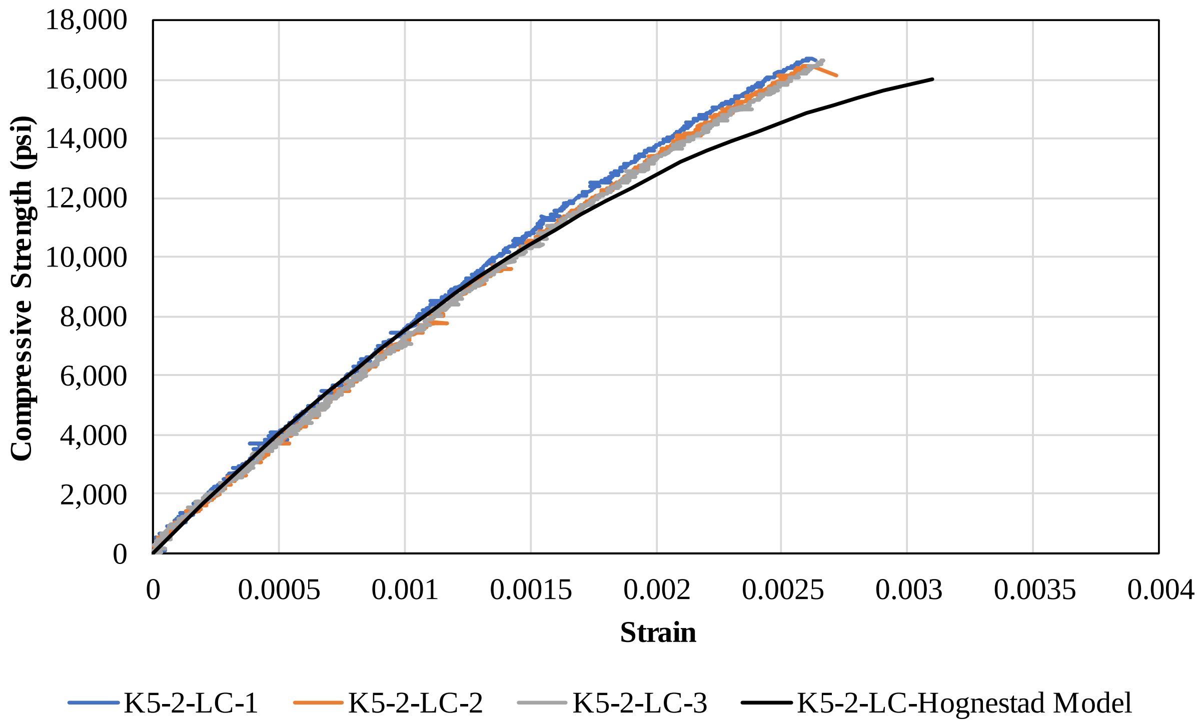

(a) Hognestad

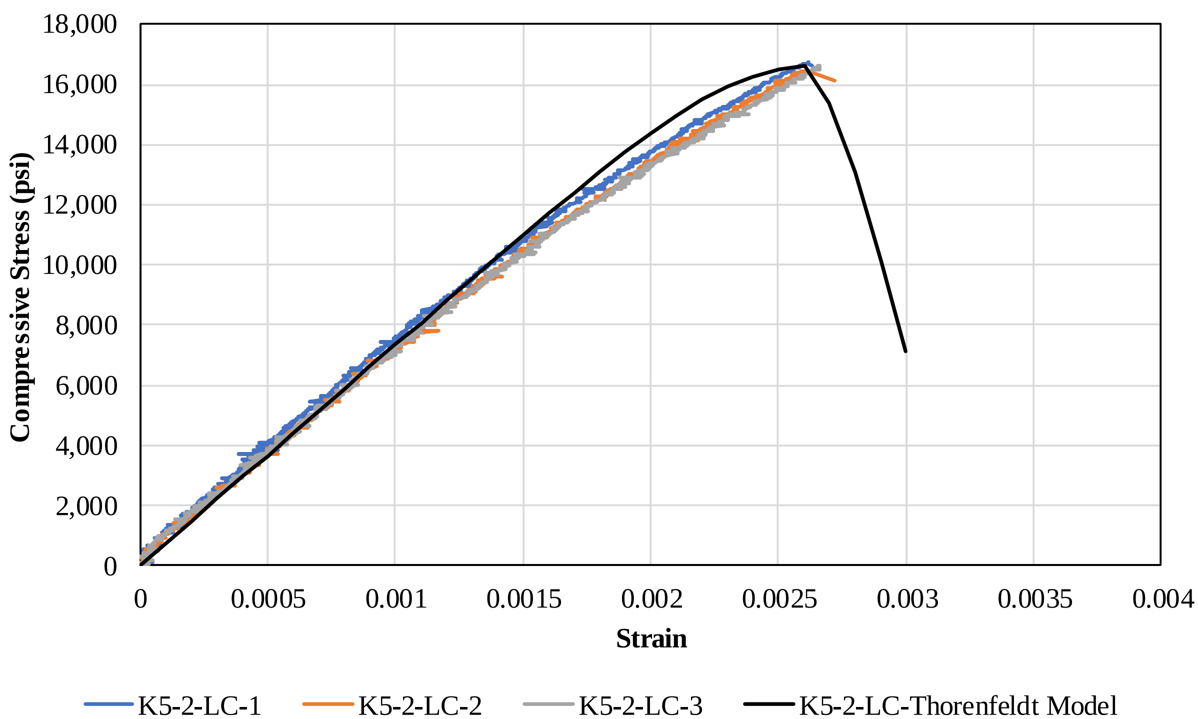

(b) Thorenfeldt

Figure E.7: Specimen K5-2-LC Compressive Stress vs. Strain

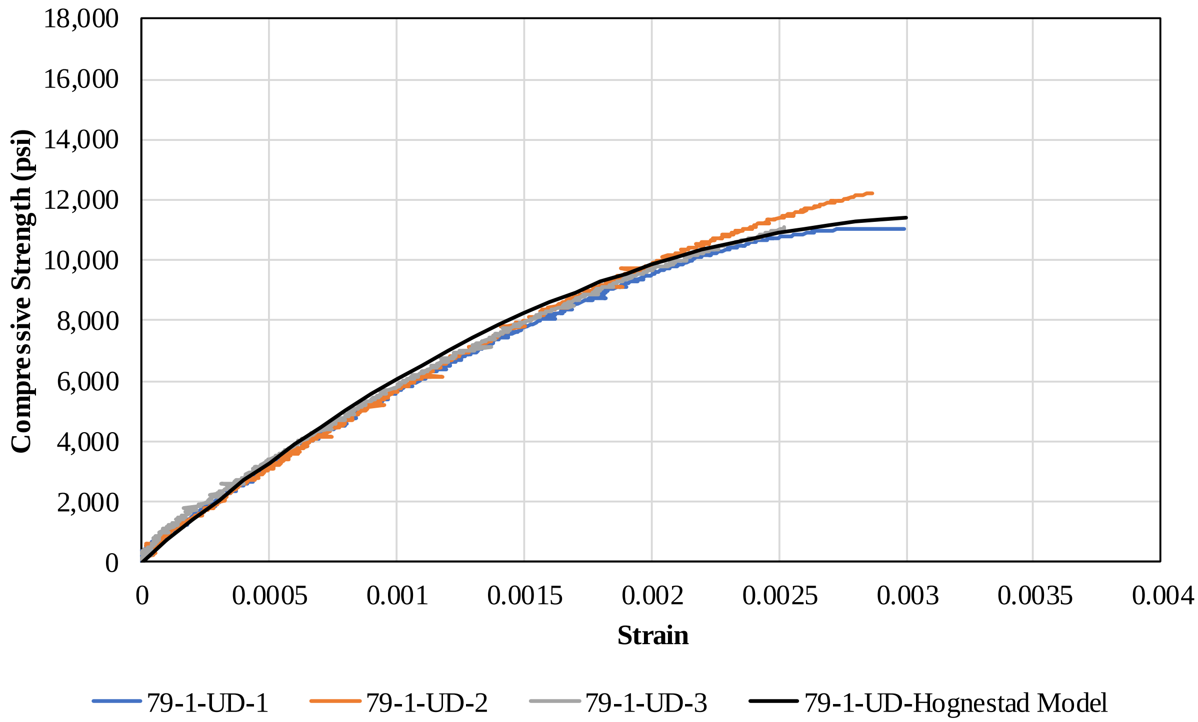

(a) Hognestad

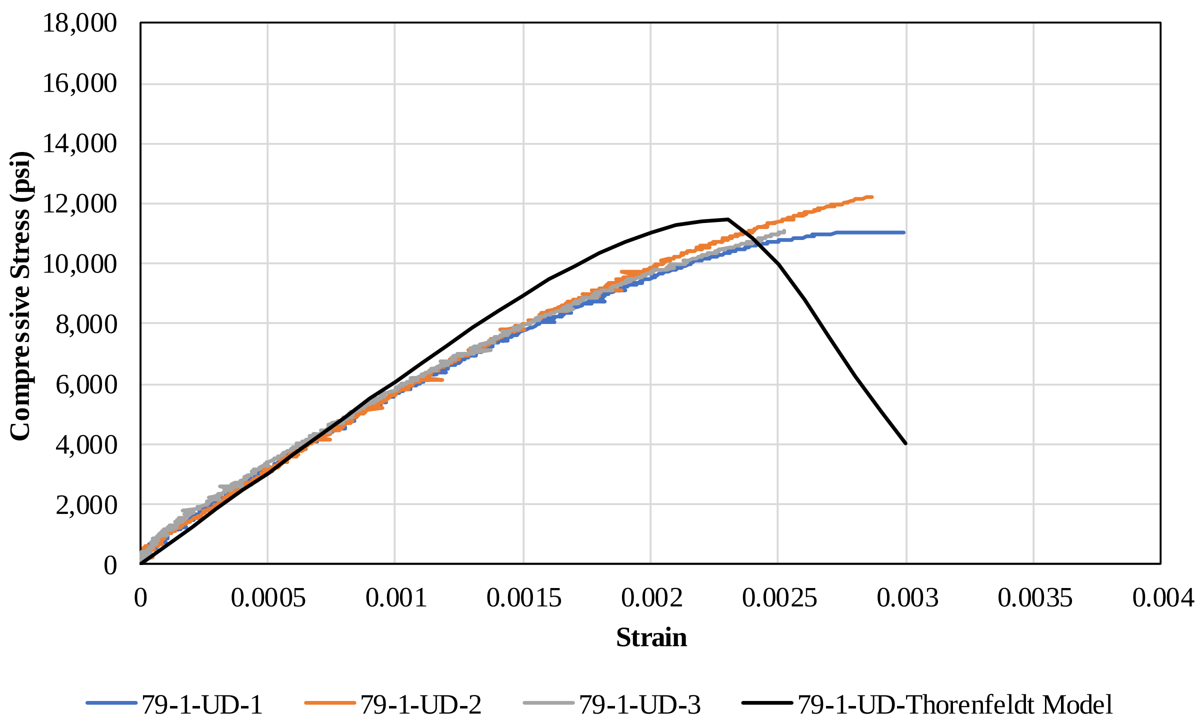

(b) Thorenfeldt

Figure E.8: Specimen 79-1-UD Compressive Stress vs. Strain

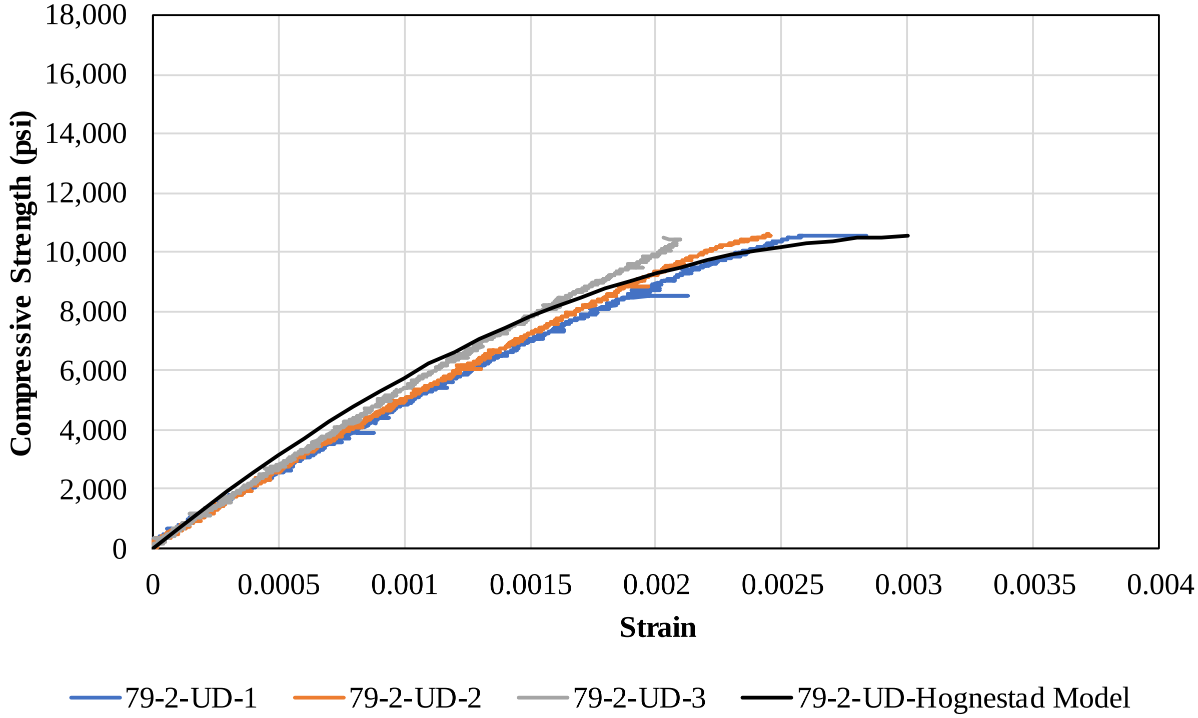

(a) Hognestad

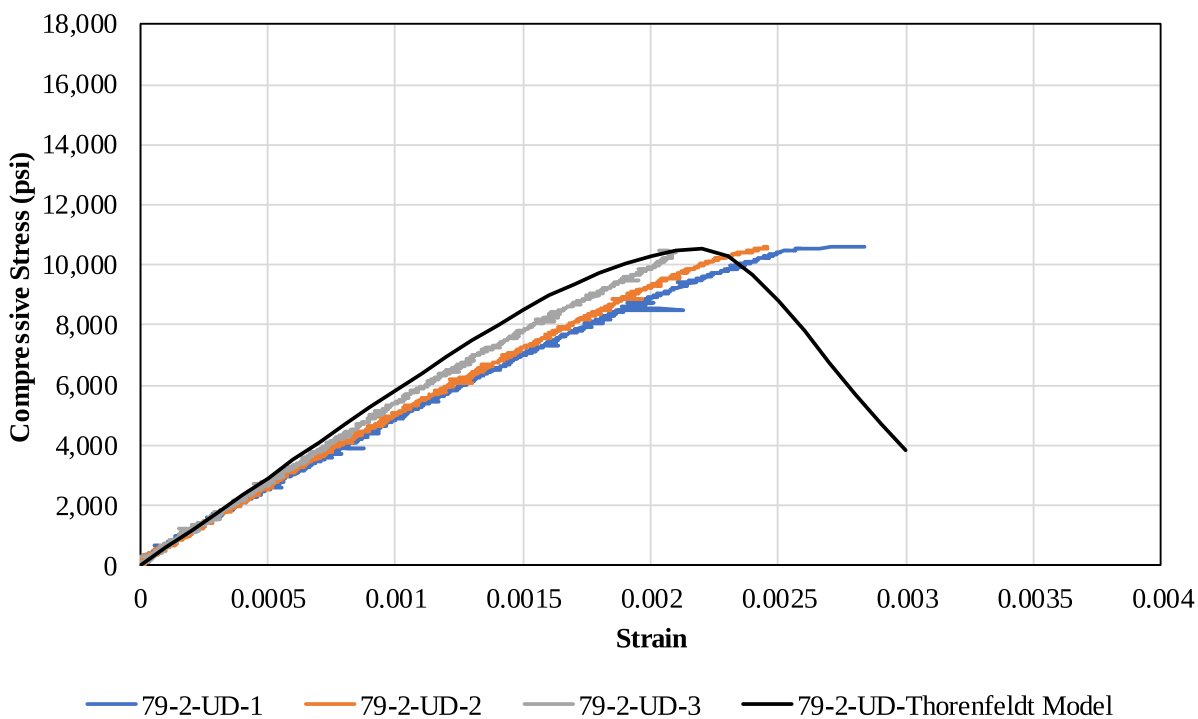

(b) Thorenfeldt

Figure E.9: Specimen 79-2-UD Compressive Stress vs. Strain

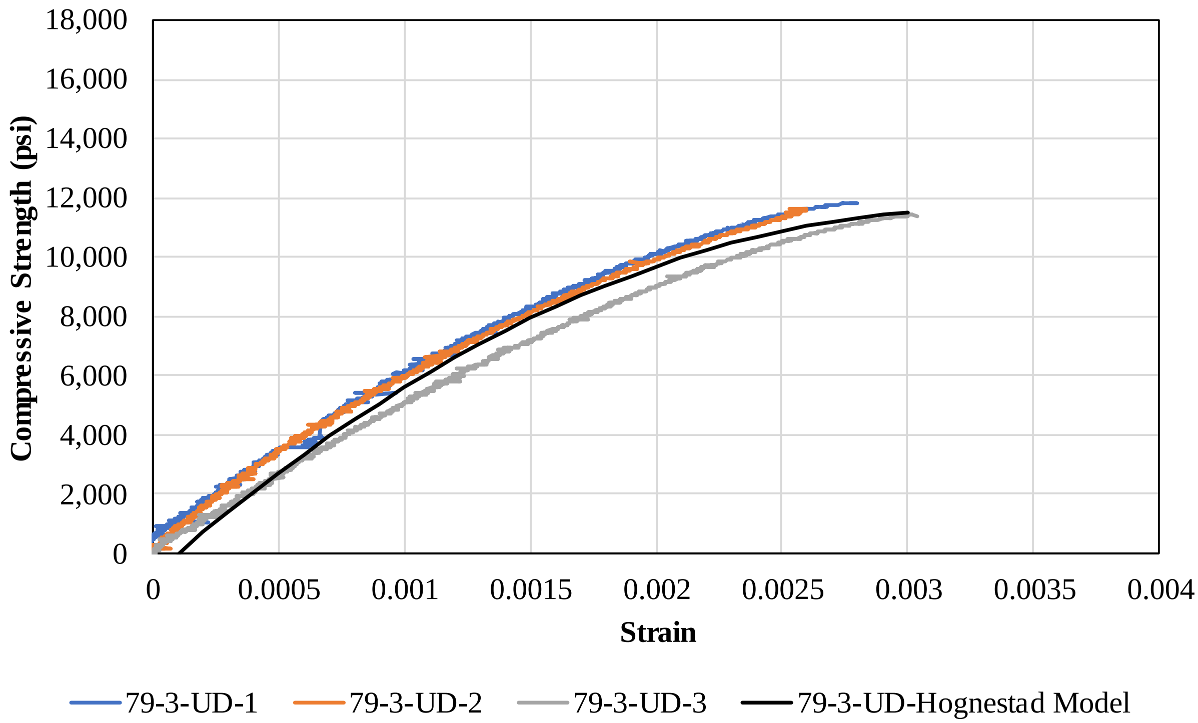

(a) Hognestad

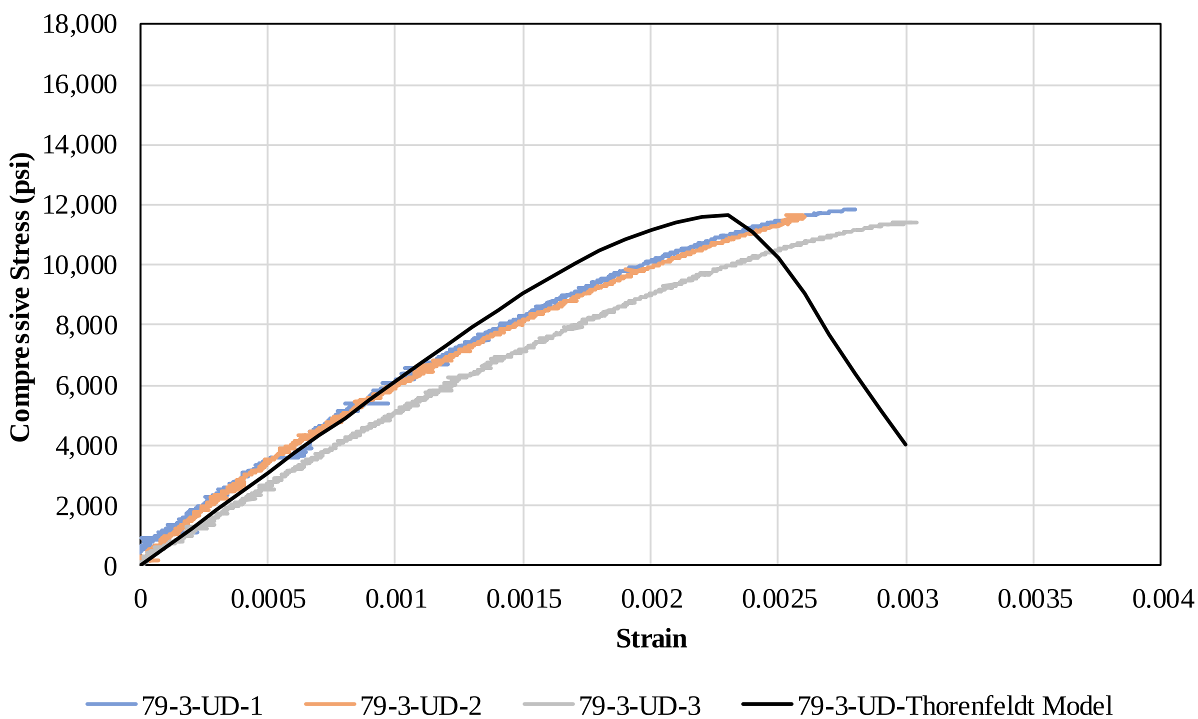

(b) Thorenfeldt

Figure E.10: Specimen 79-3-UD Compressive Stress vs. Strain

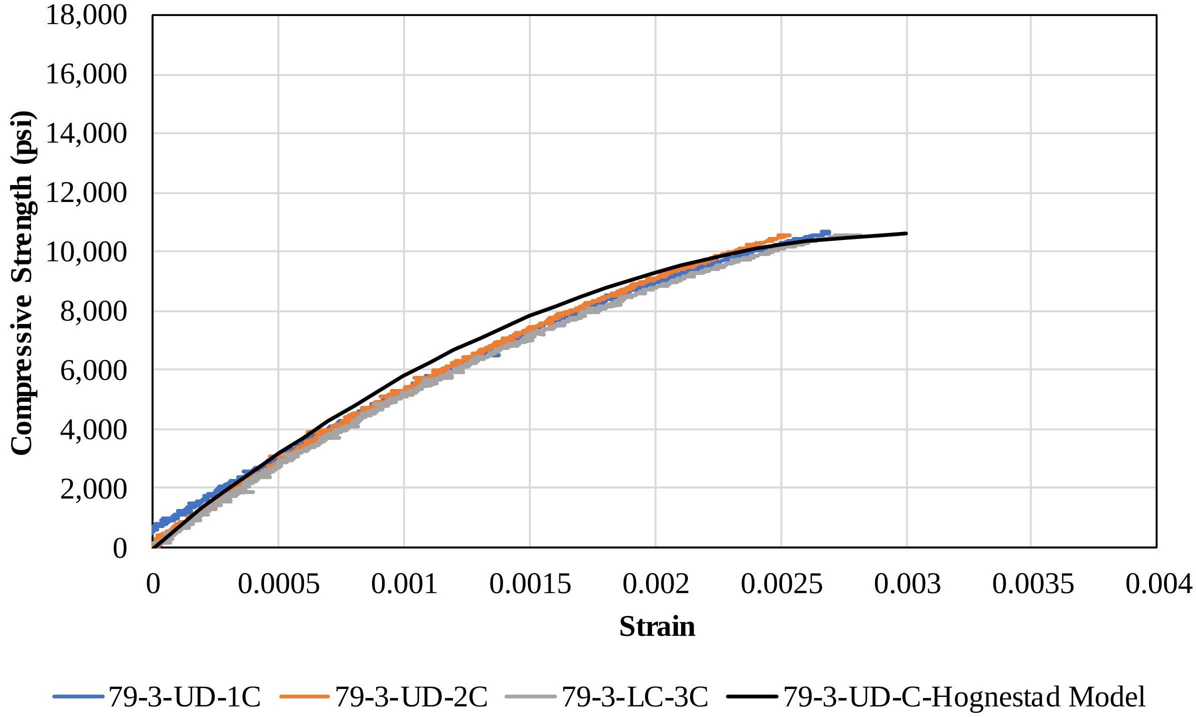

(a) Hognestad

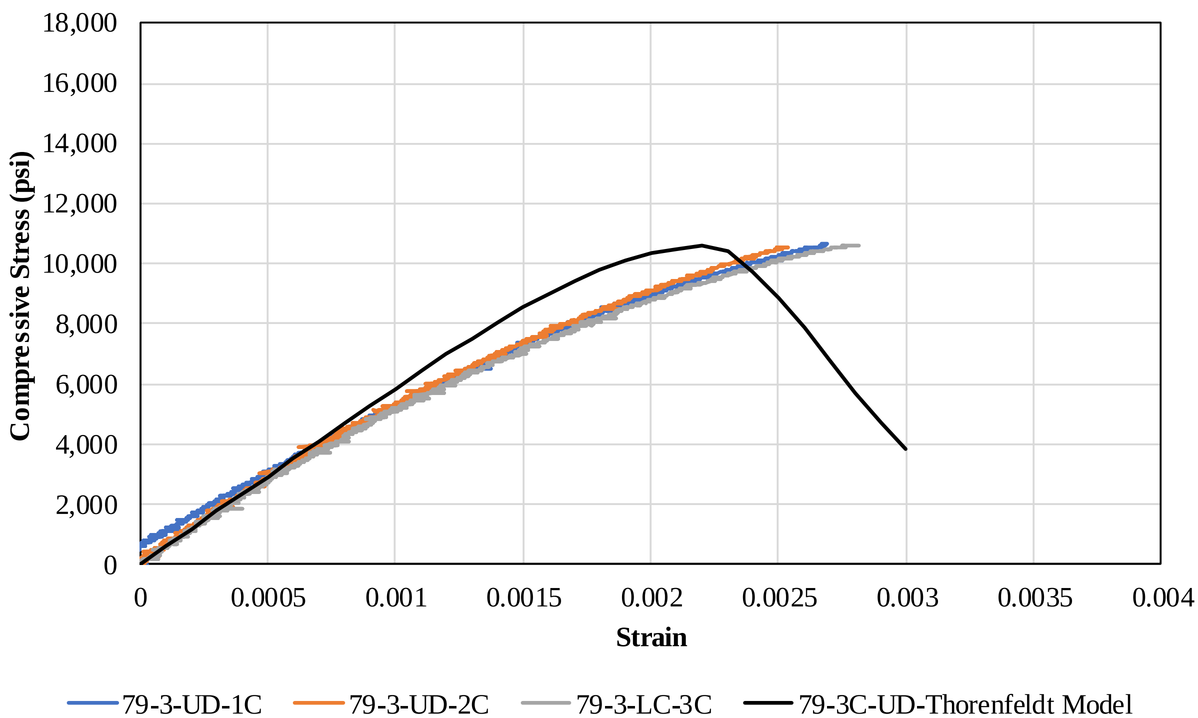

(b) Thorenfeldt

Figure E.11: Specimen 79-3-UD (Curb) Compressive Stress vs. Strain

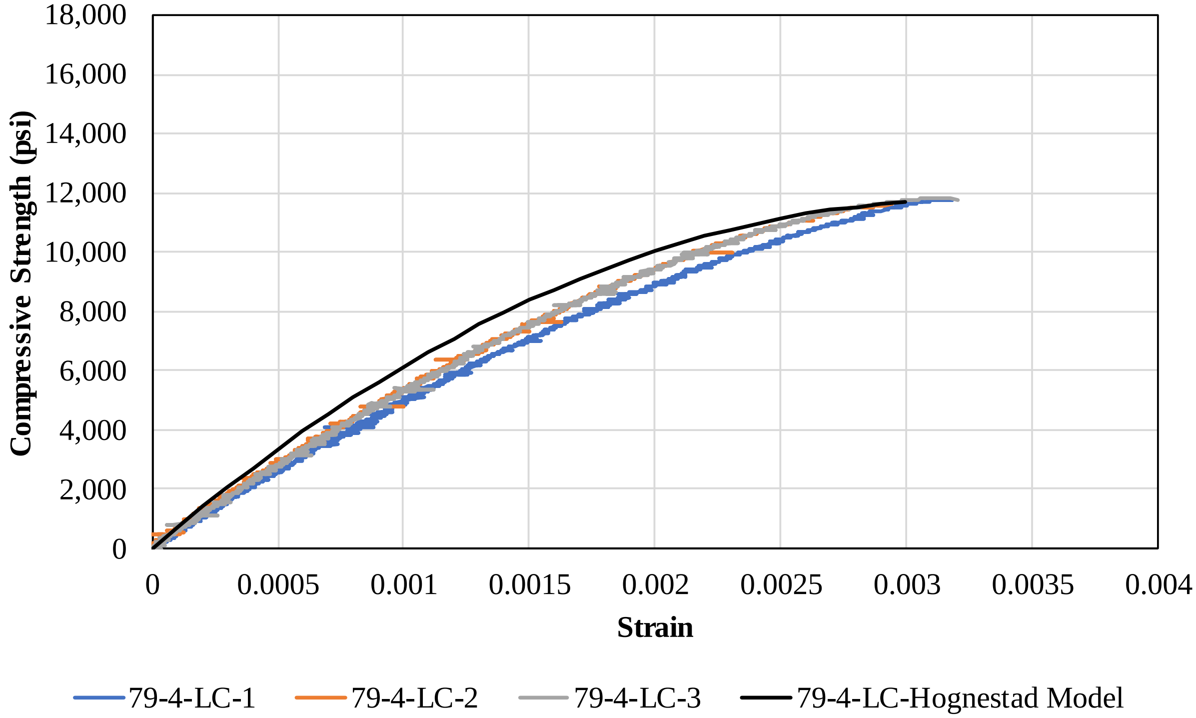

(a) Hognestad

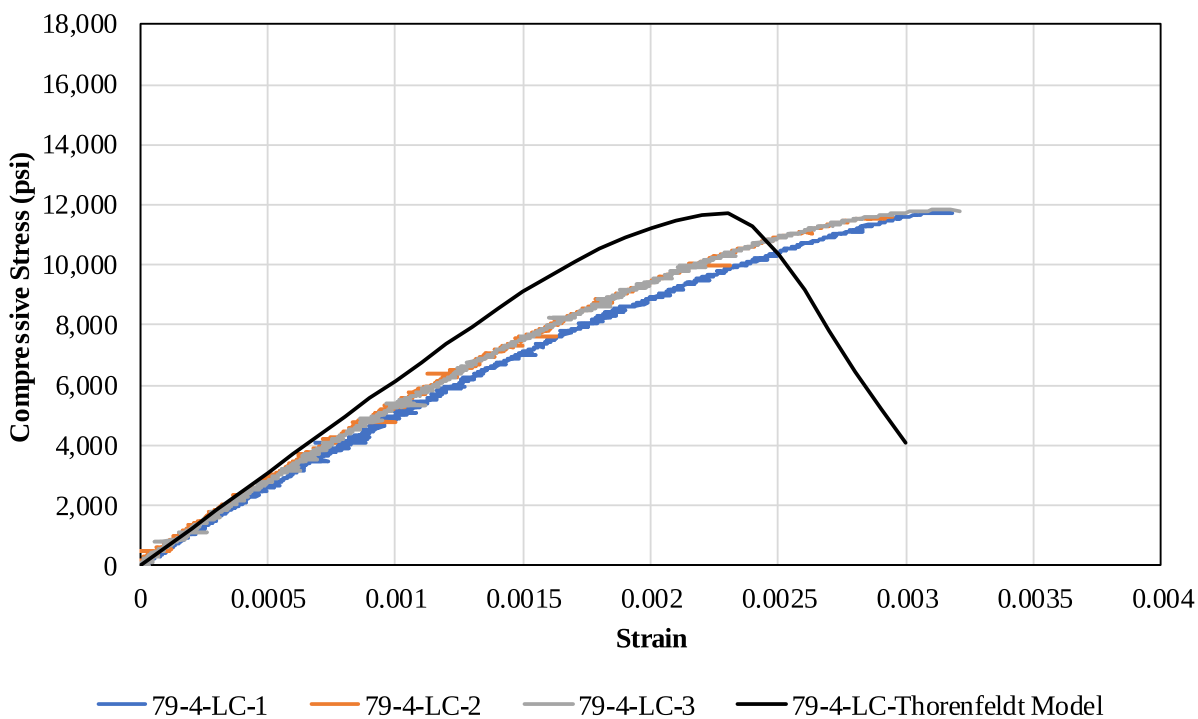

(b) Thorenfeldt

Figure E.12: Specimen 79-4-LC Compressive Stress vs. Strain

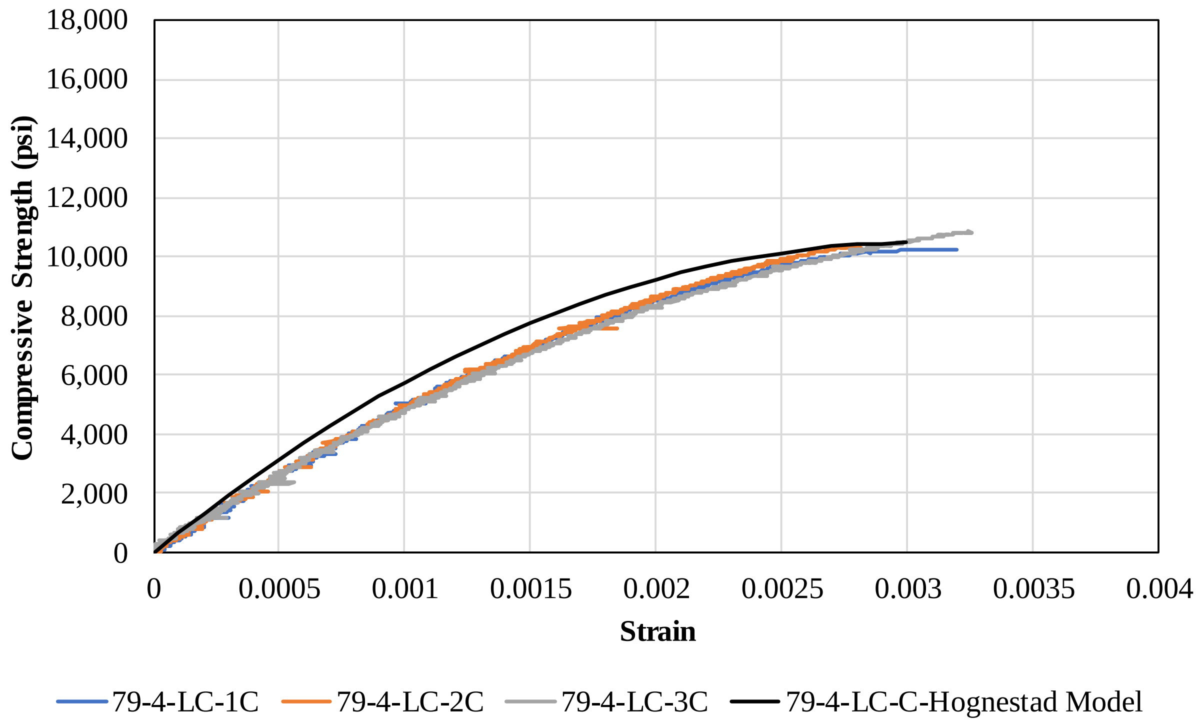

(a) Hognestad

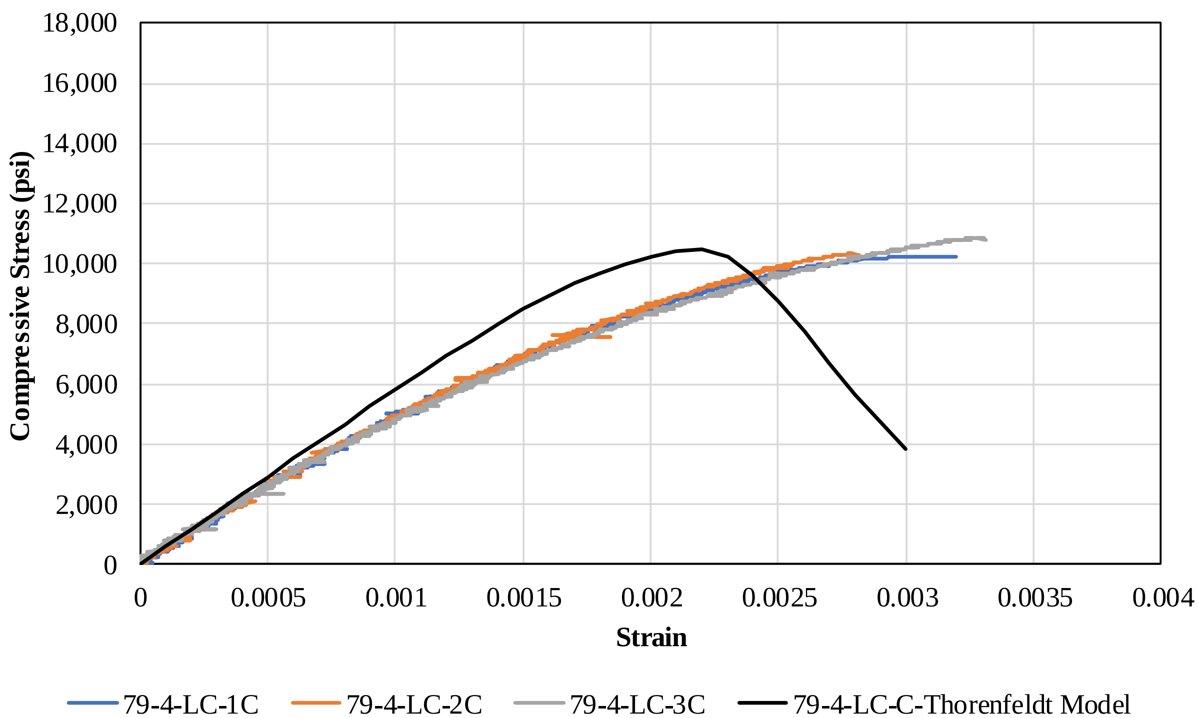

(b) Thorenfeldt

Figure E.13: Specimen 79-4-LC (Curb) Compressive Stress vs. Strain

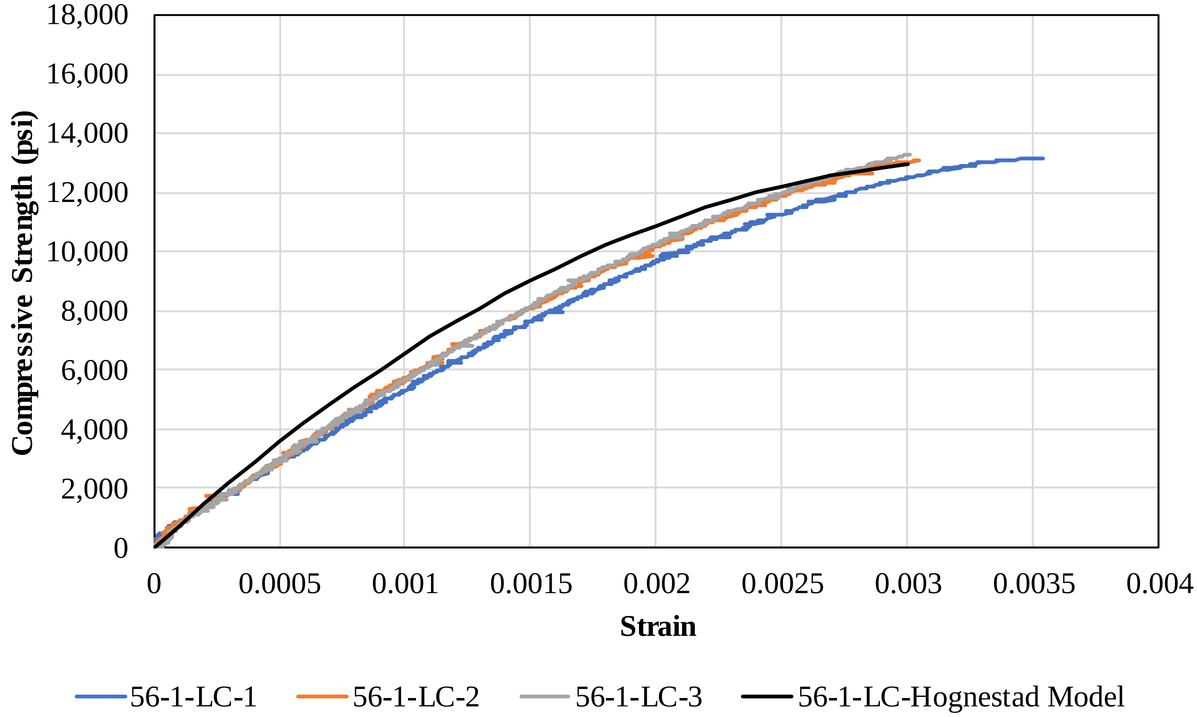

(a) Hognestad

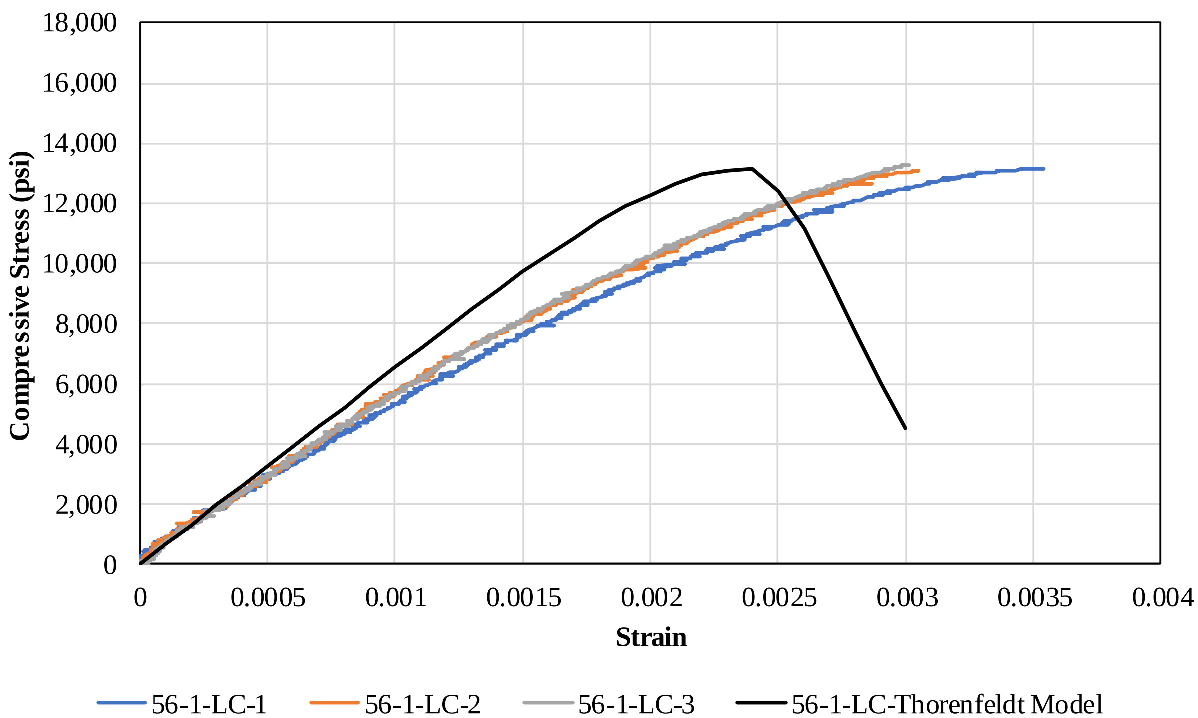

(b) Thorenfeldt

Figure E.14: Specimen 56-1-LC Compressive Stress vs. Strain

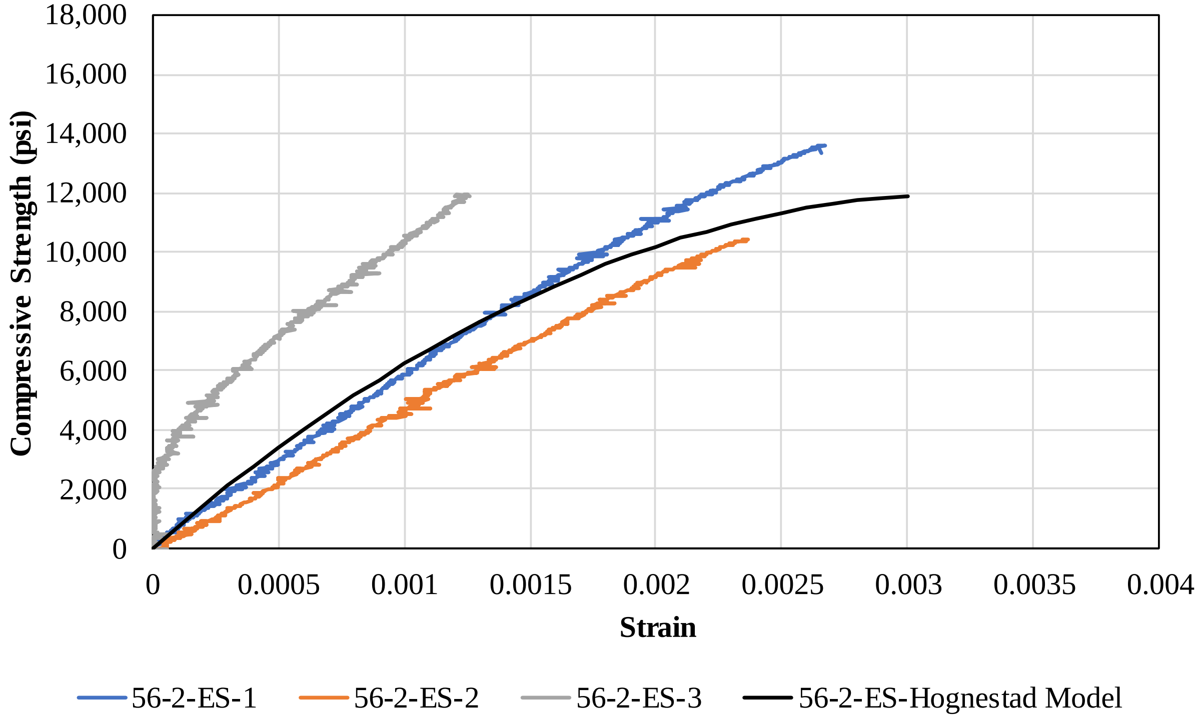

(a) Hognestad

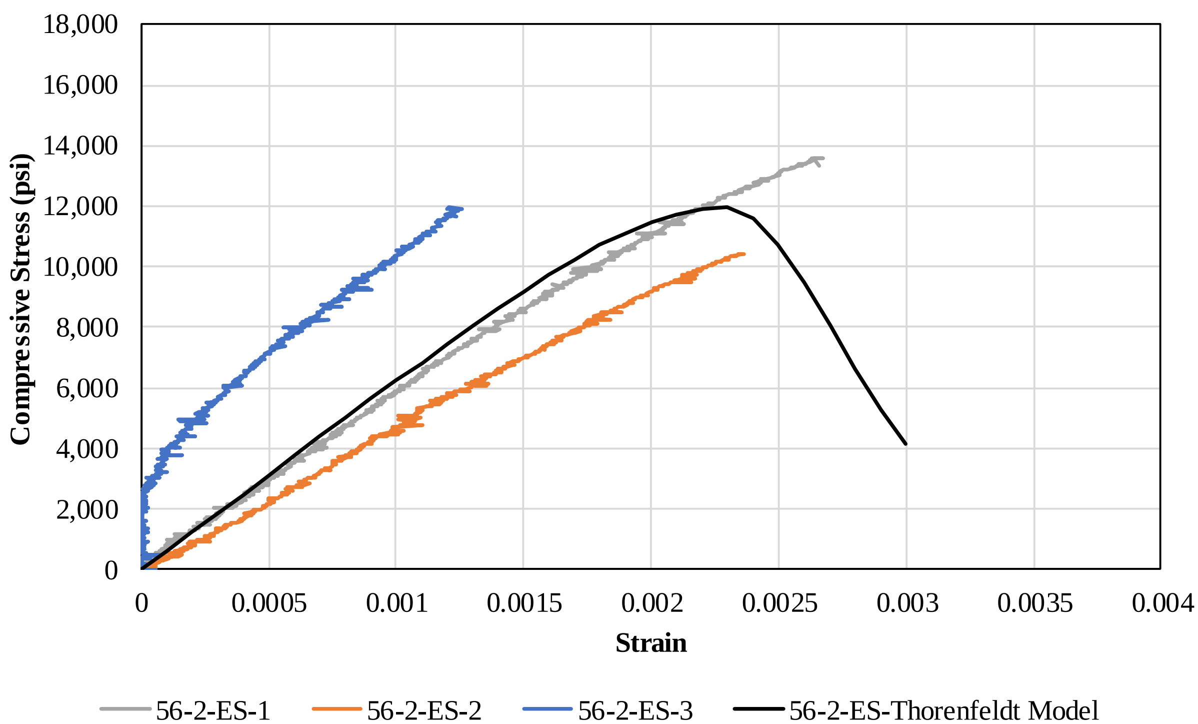

(b) Thorenfeldt

Figure E.15: Specimen 56-2-ES Compressive Stress vs. Strain

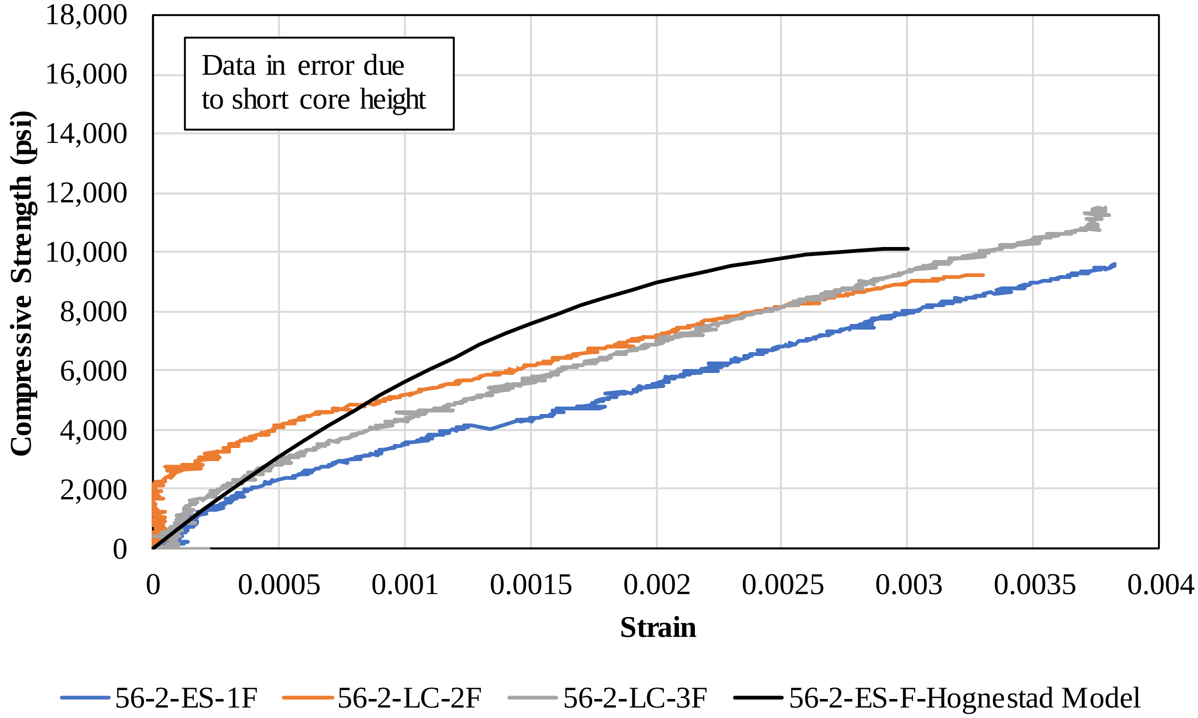

(a) Hognestad

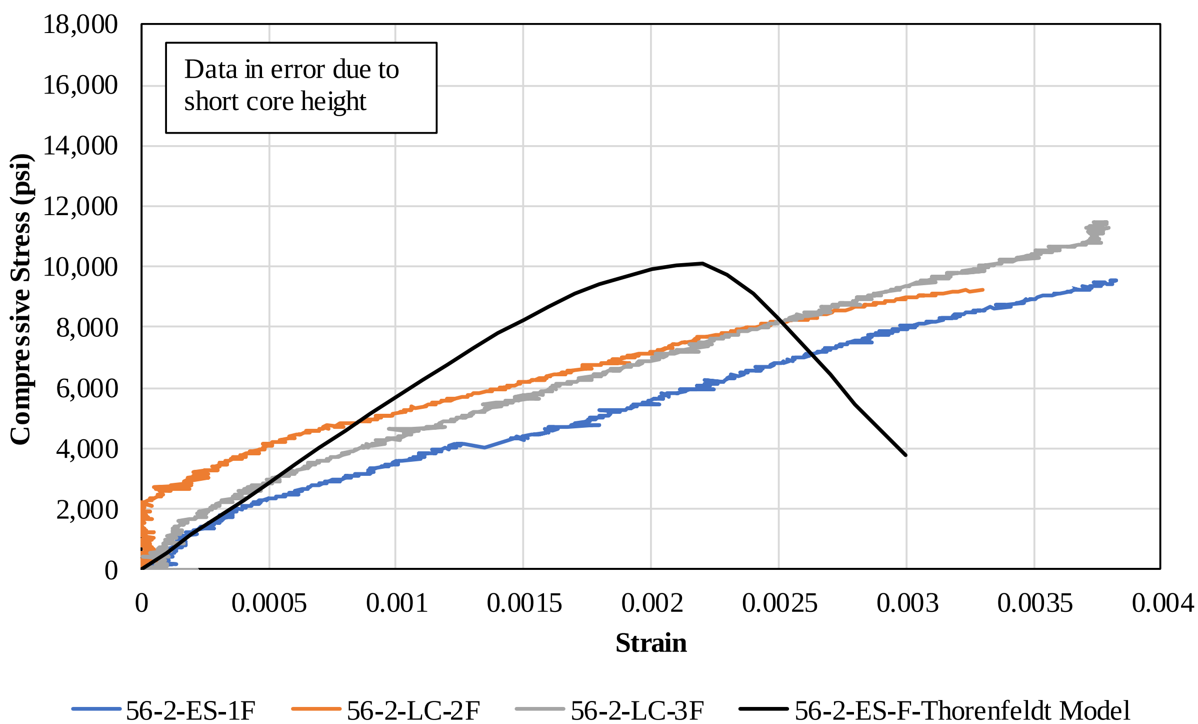

(b) Thorenfeldt

Figure E.16: Specimen 56-2-ES (Flange) Compressive Stress vs. Strain

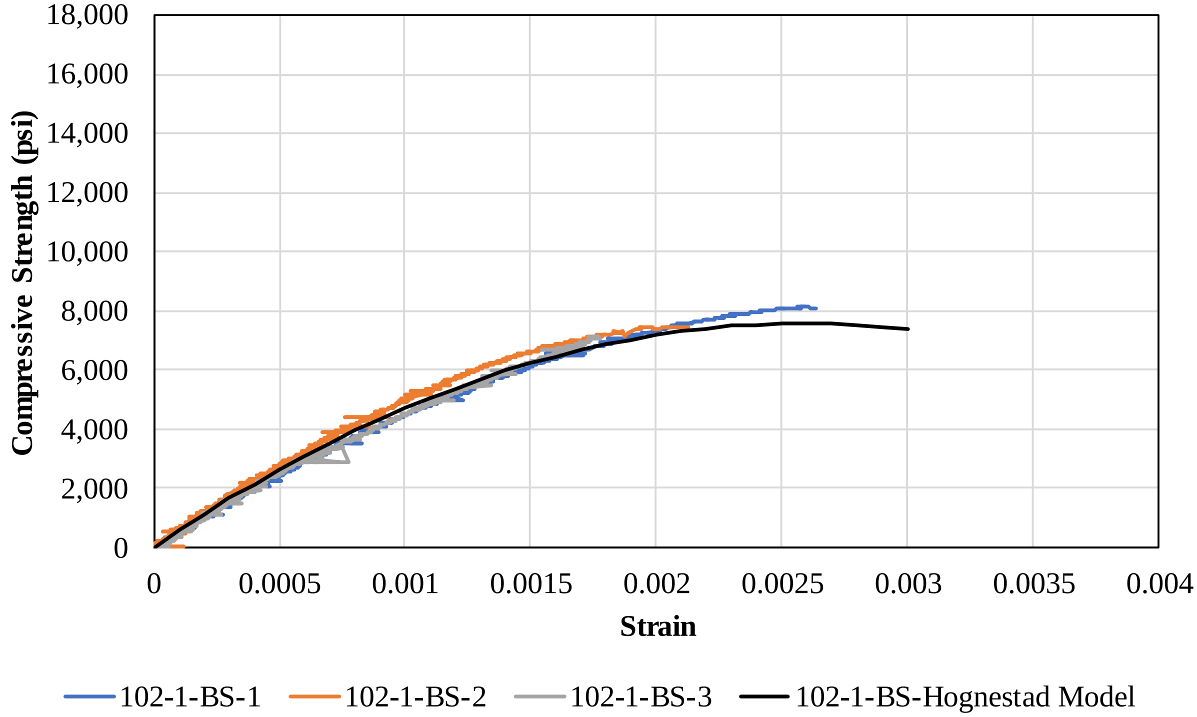

(a) Hognestad

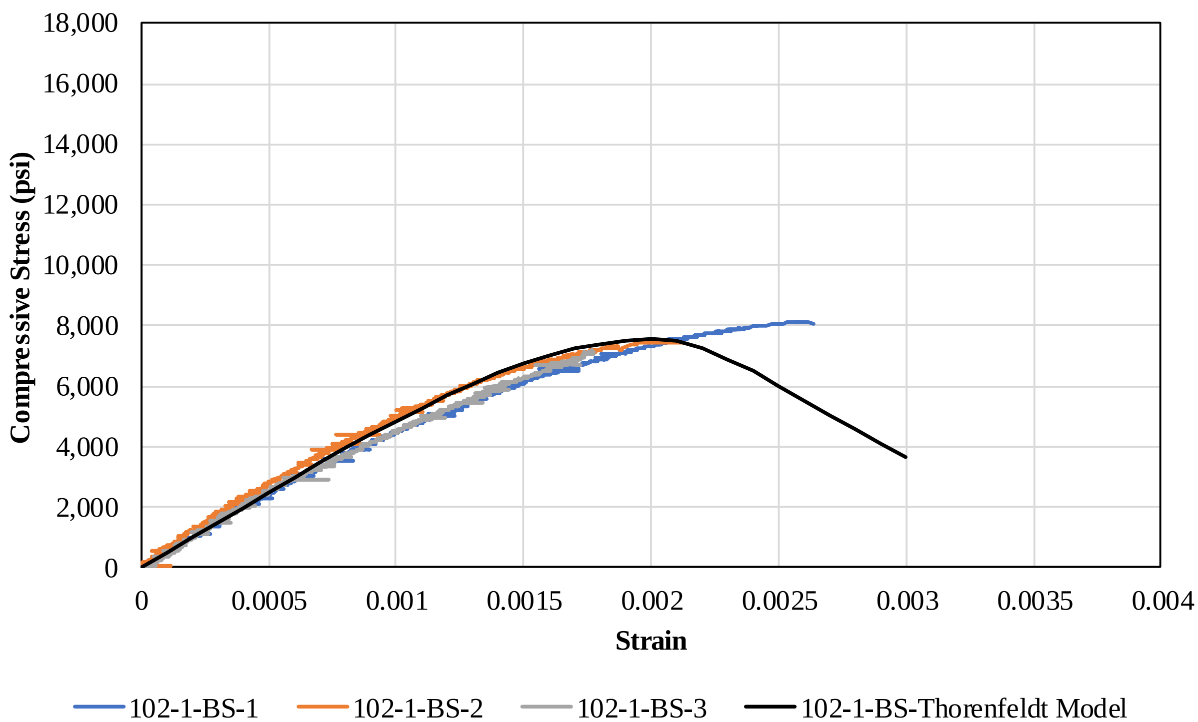

(b) Thorenfeldt

Figure E.17: Specimen 102-1-BS Compressive Stress vs. Strain

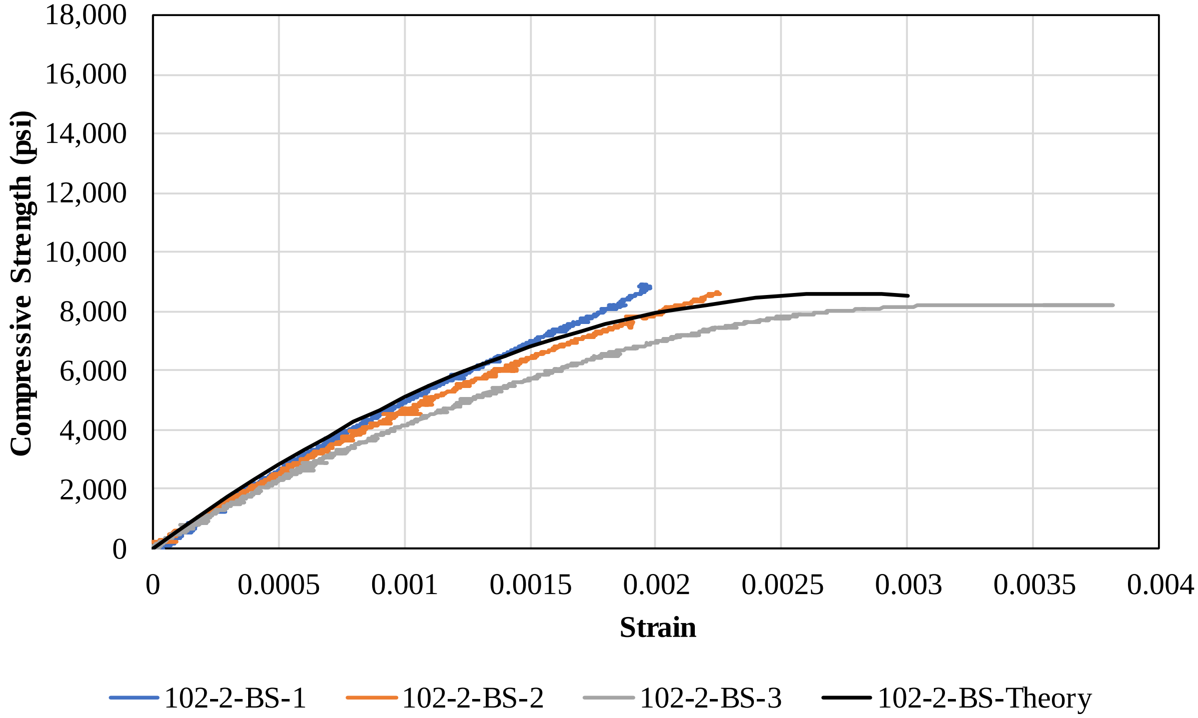

(a) Hognestad

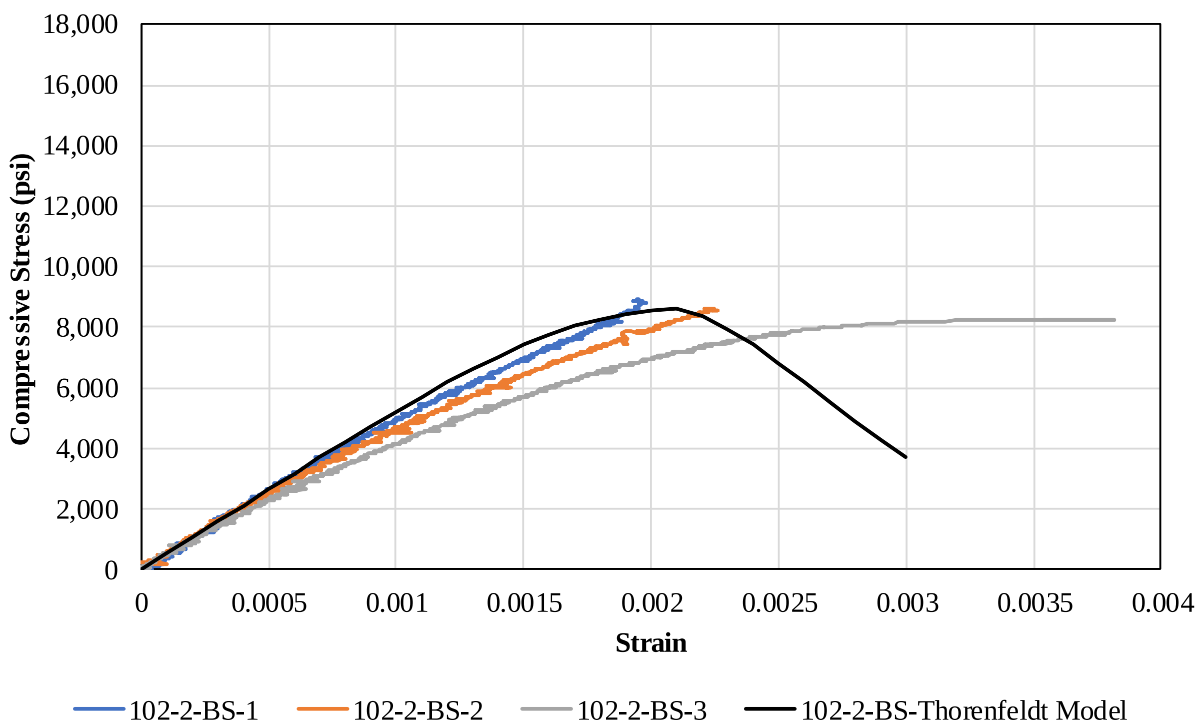

(b) Thorenfeldt

Figure E.18: Specimen 102-2-BS Compressive Stress vs. Strain

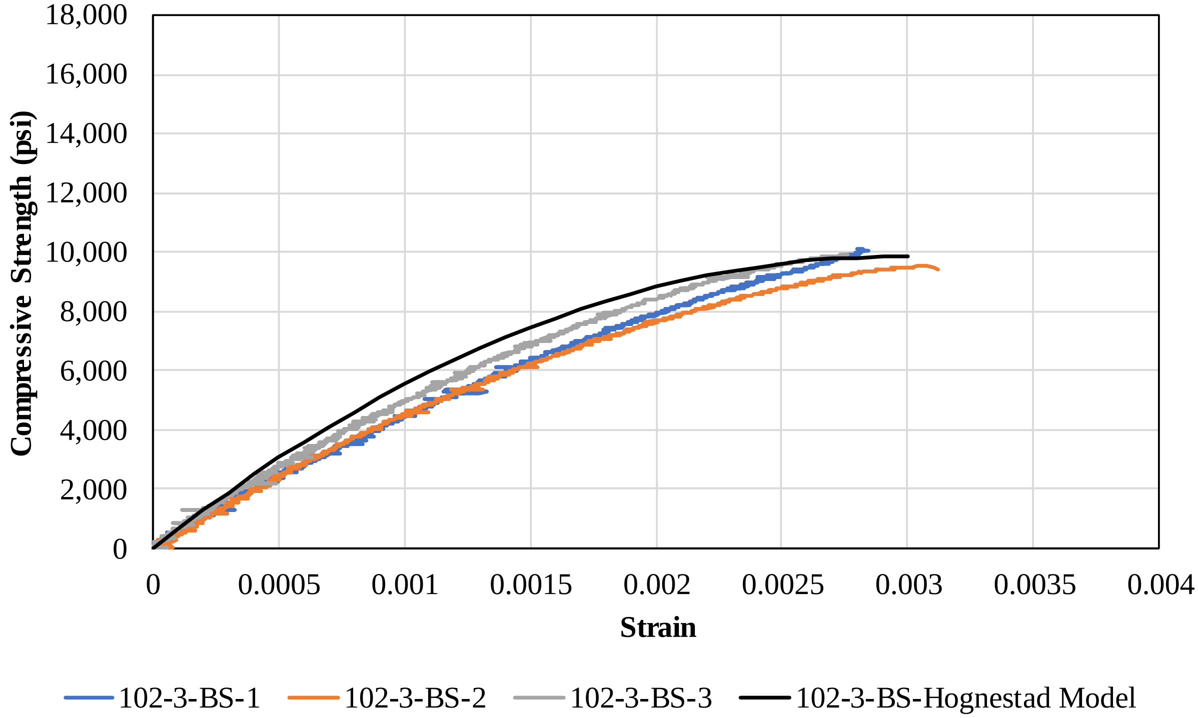

(a) Hognestad

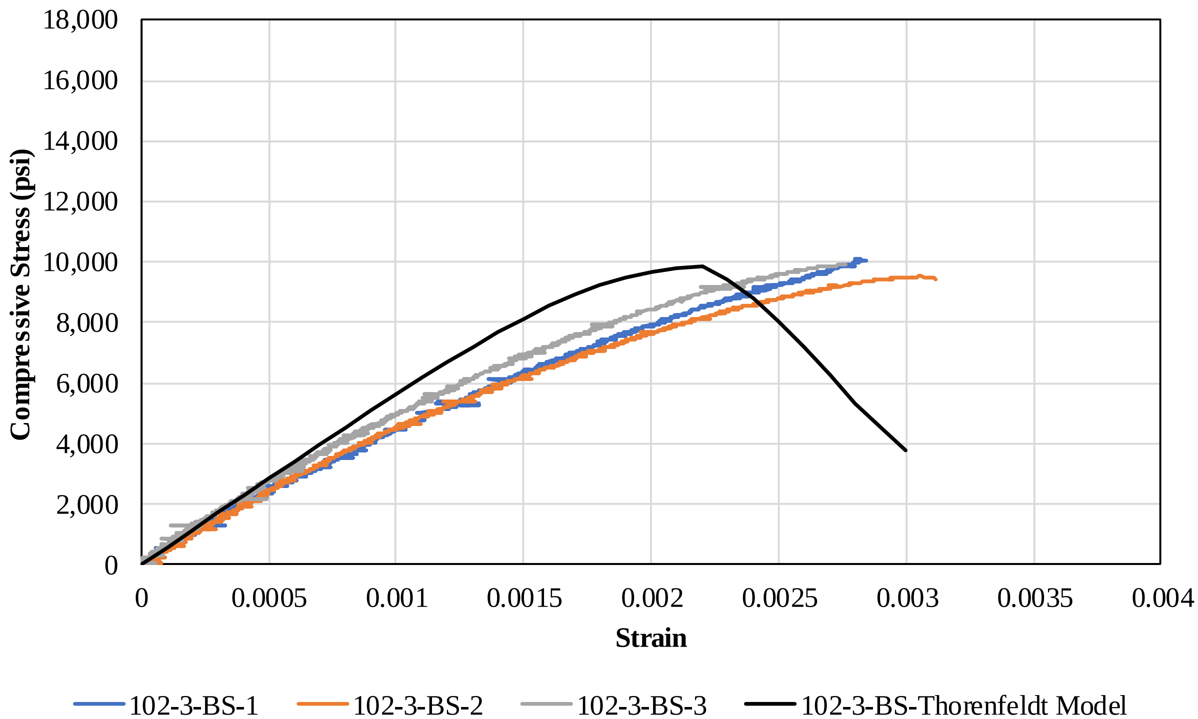

(b) Thorenfeldt

Figure E.19: Specimen 102-3-BS Compressive Stress vs. Strain

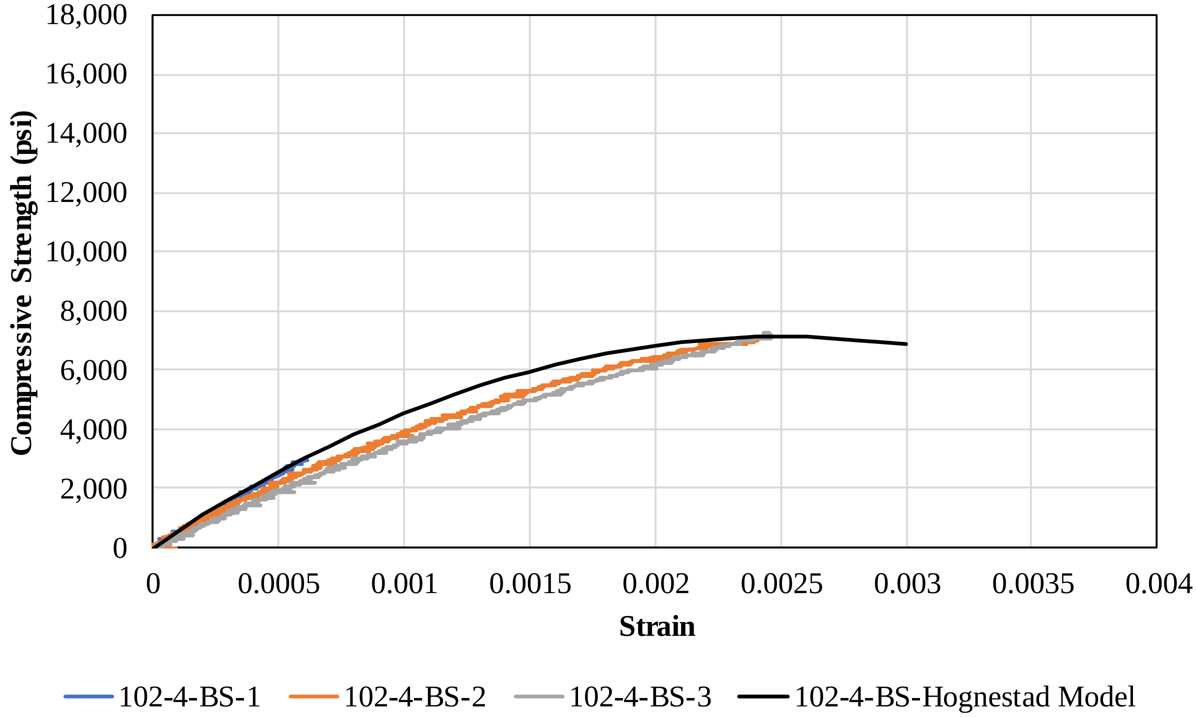

(a) Hognestad

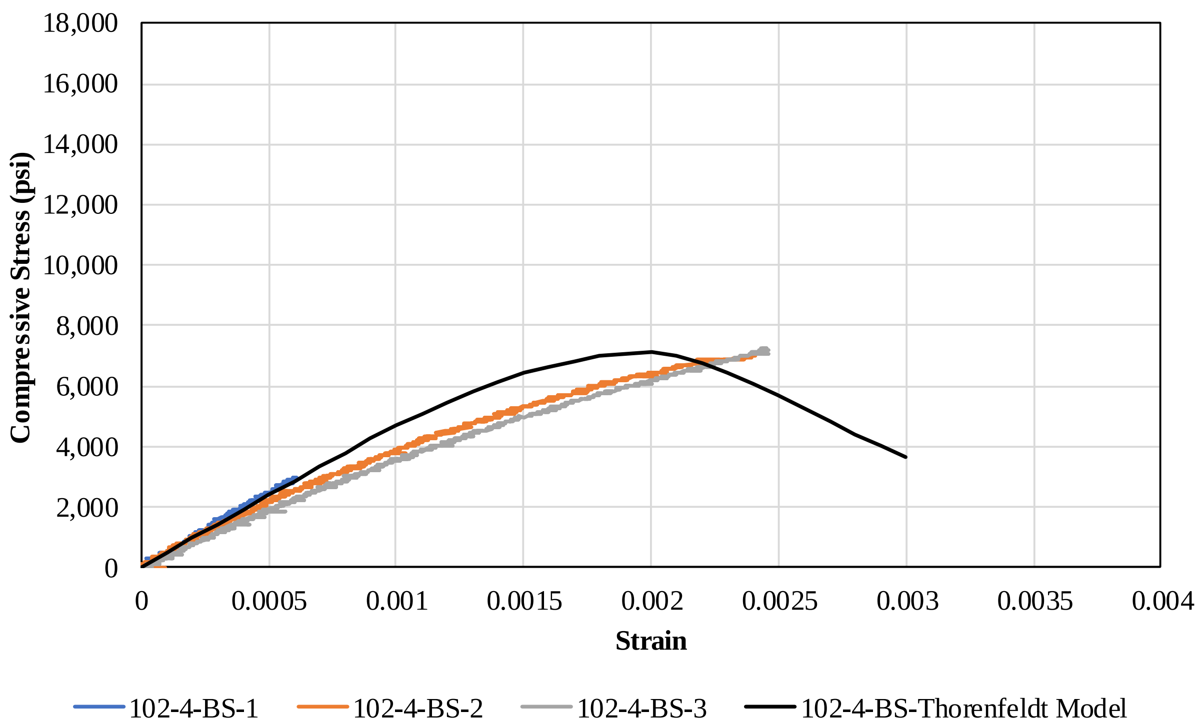

(b) Thorenfeldt

Figure E. 20: Specimen 102-4-BS Compressive Stress vs. Strain

APPENDIX F. STRAND STRESS VS. STRAIN CURVES

Figure F.1 to Figure F.15 presents the test data from the tensile tests of the uncorroded strand extracted from the beam specimens. The stress-strain curves in part (a) of each figure are offset by 0.01 strain to display the initial portion of each curve. The stress-strain curves in part (b) of each figure includes the Mattock (1979) stress-strain model curve. The constants used to plot the Mattock curves is provided in each plot. A consistent set of constants is used for the vintage of strands (prior to 1970 and after 1970).

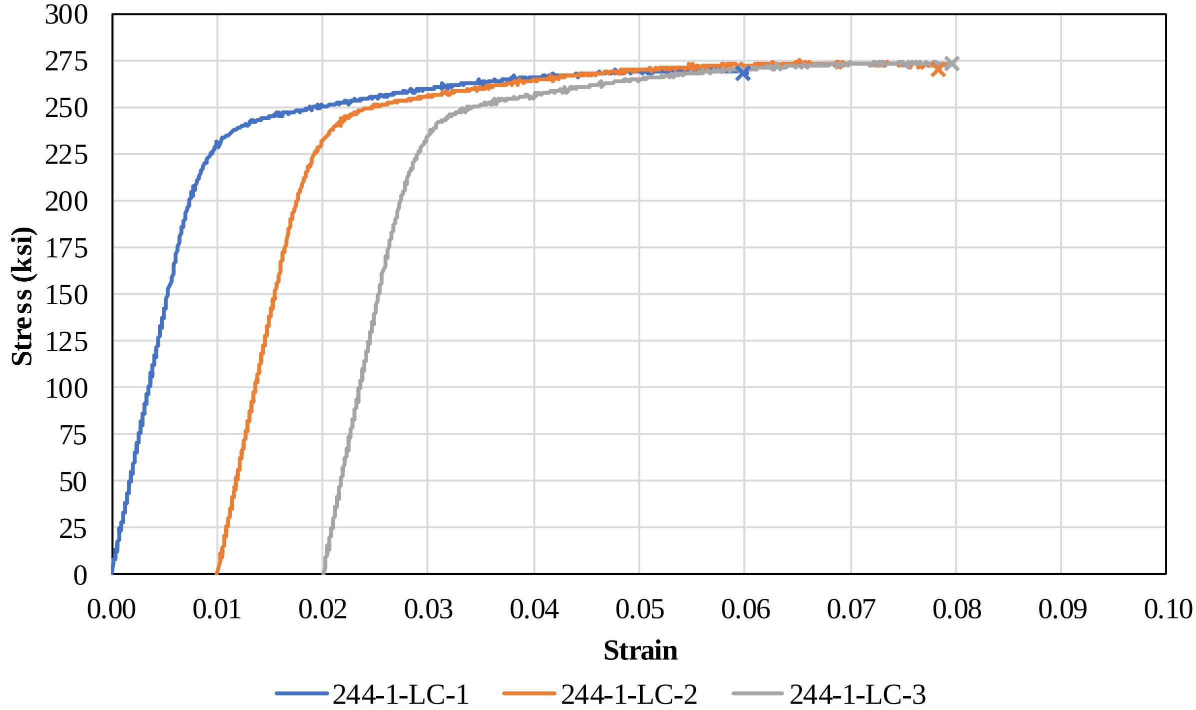

(a) Stress vs. strain curves offset by 0.01

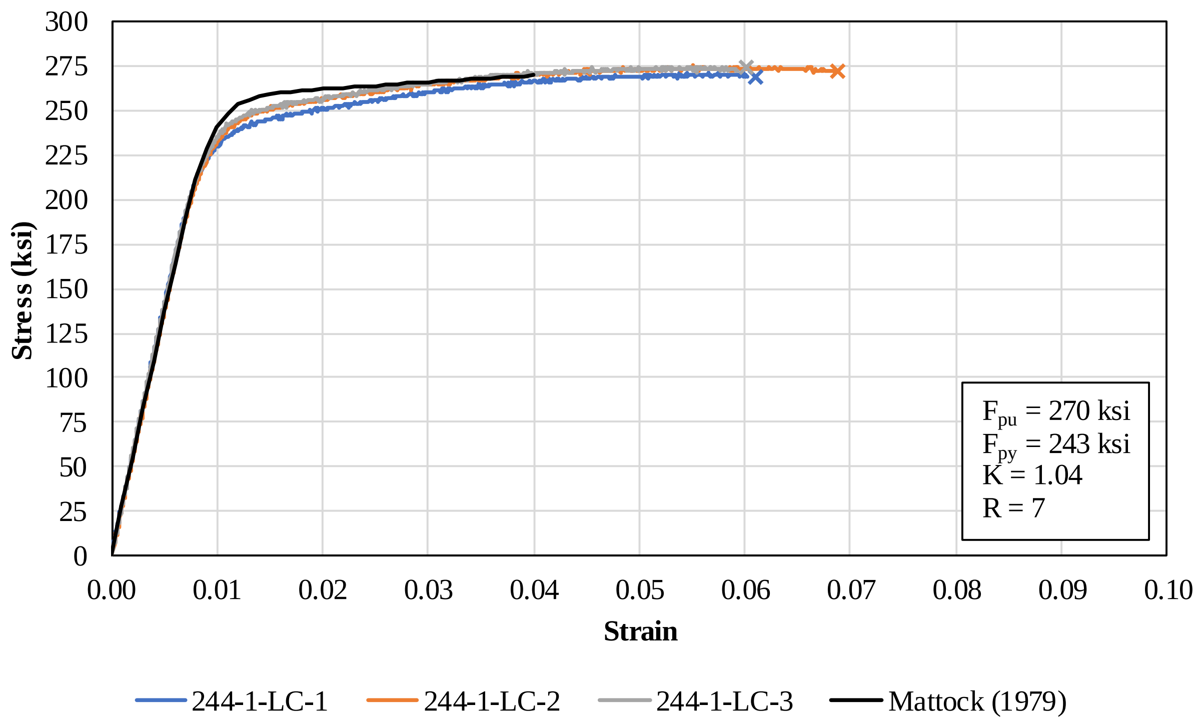

(b) Stress vs. strain curves without offset

Figure F.1: Specimen 244-1-LC Strand Stress vs. Strain

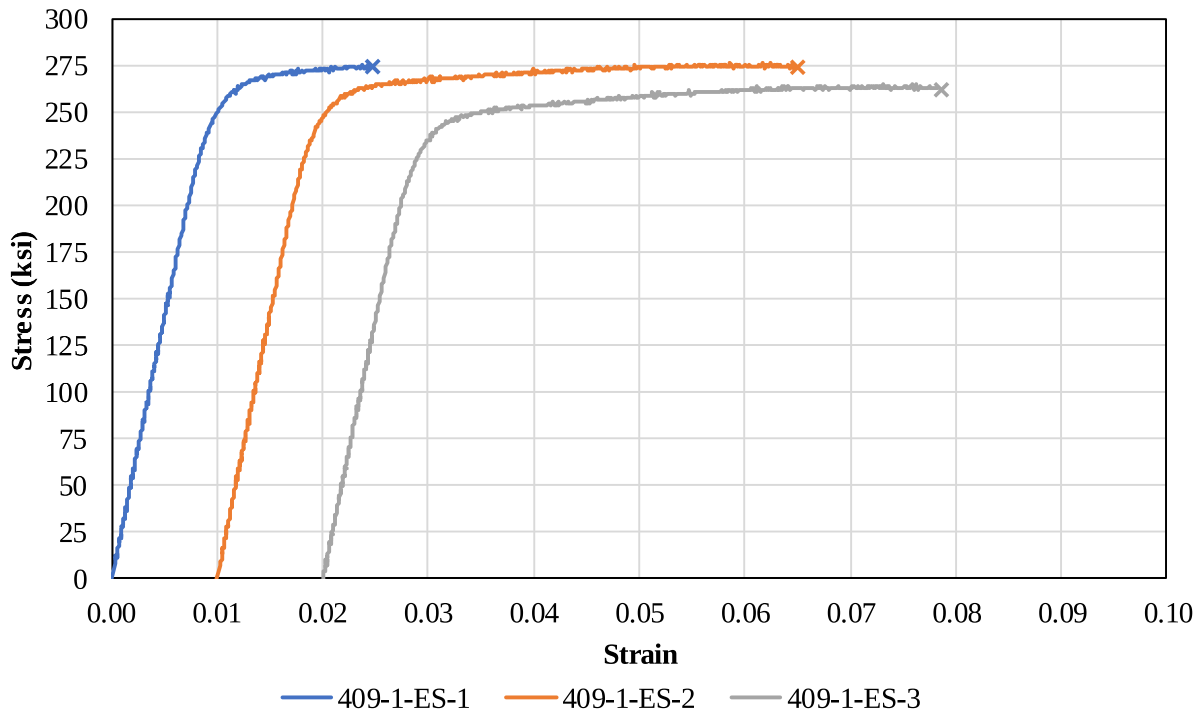

(a) Stress vs. strain curves offset by 0.01

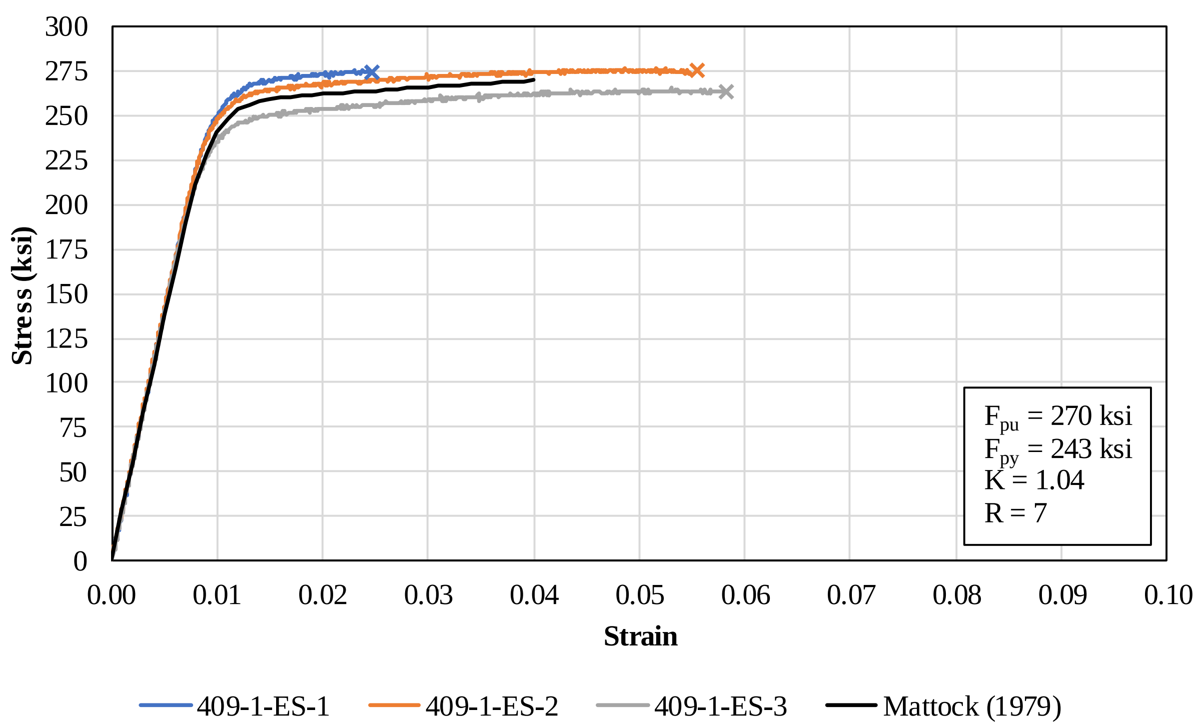

(b) Stress vs. strain curves without offset

Figure F.2: Specimen 409-1-ES Strand Stress vs. Strain

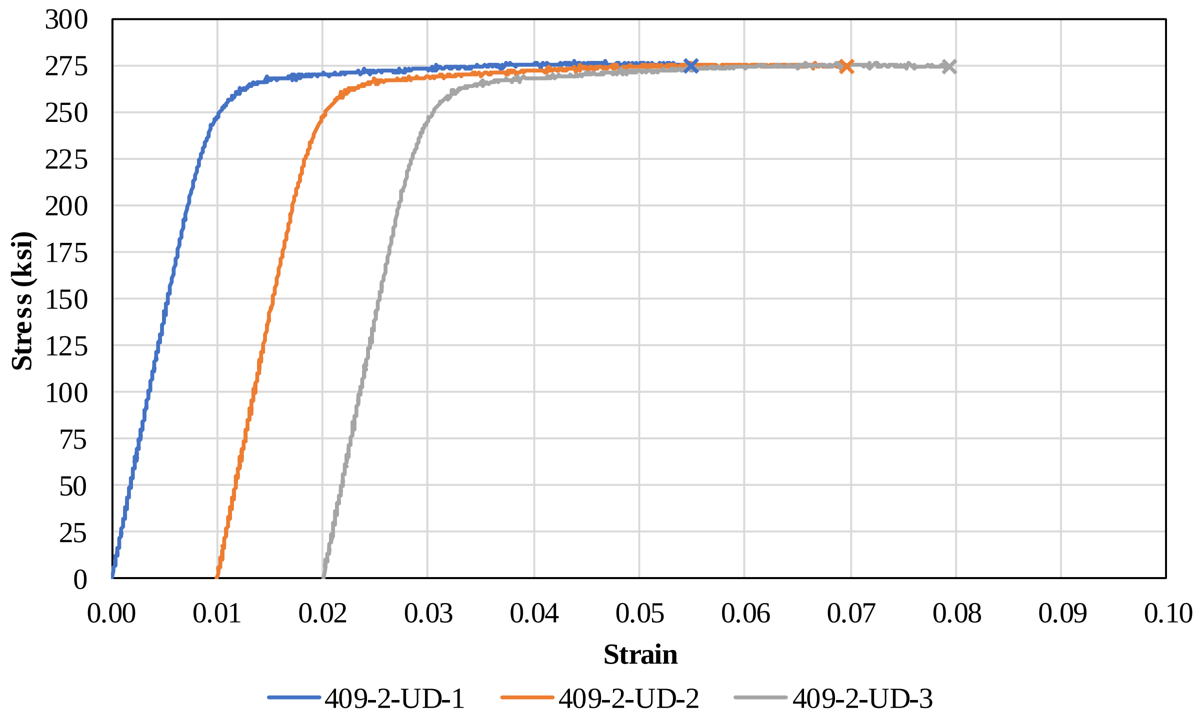

(a) Stress vs. strain curves offset by 0.01

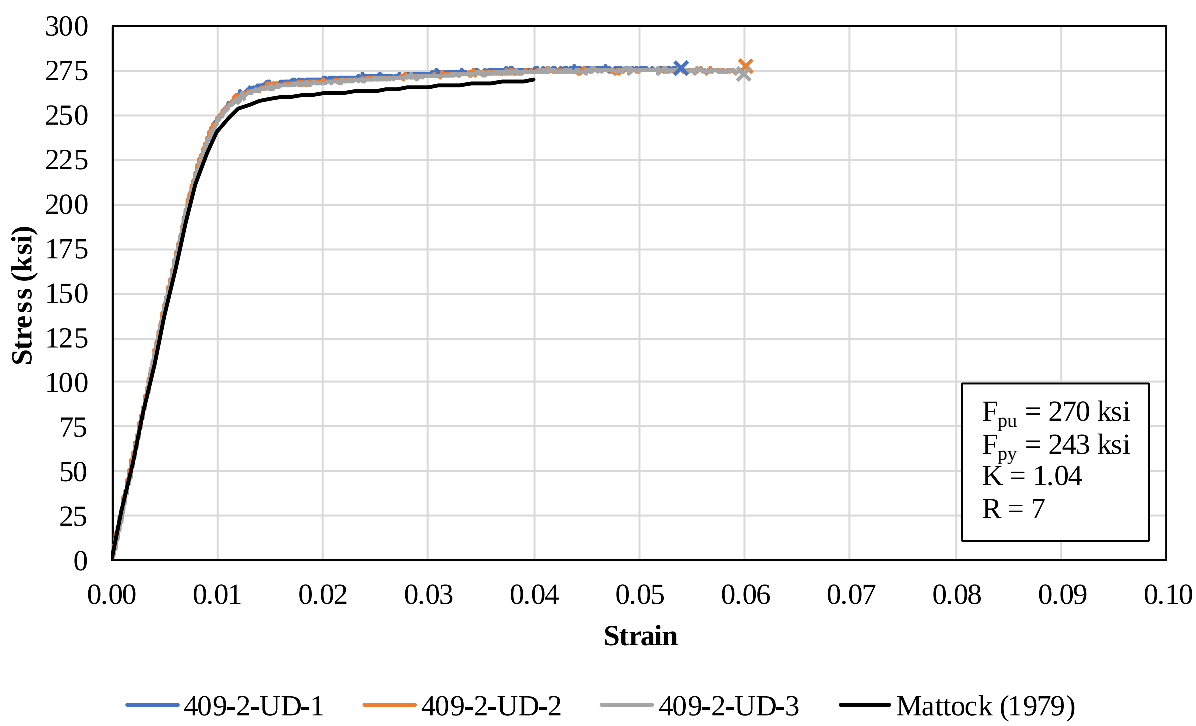

(b) Stress vs. strain curves without offset

Figure F.3: Specimen 409-2-UD Strand Stress vs. Strain

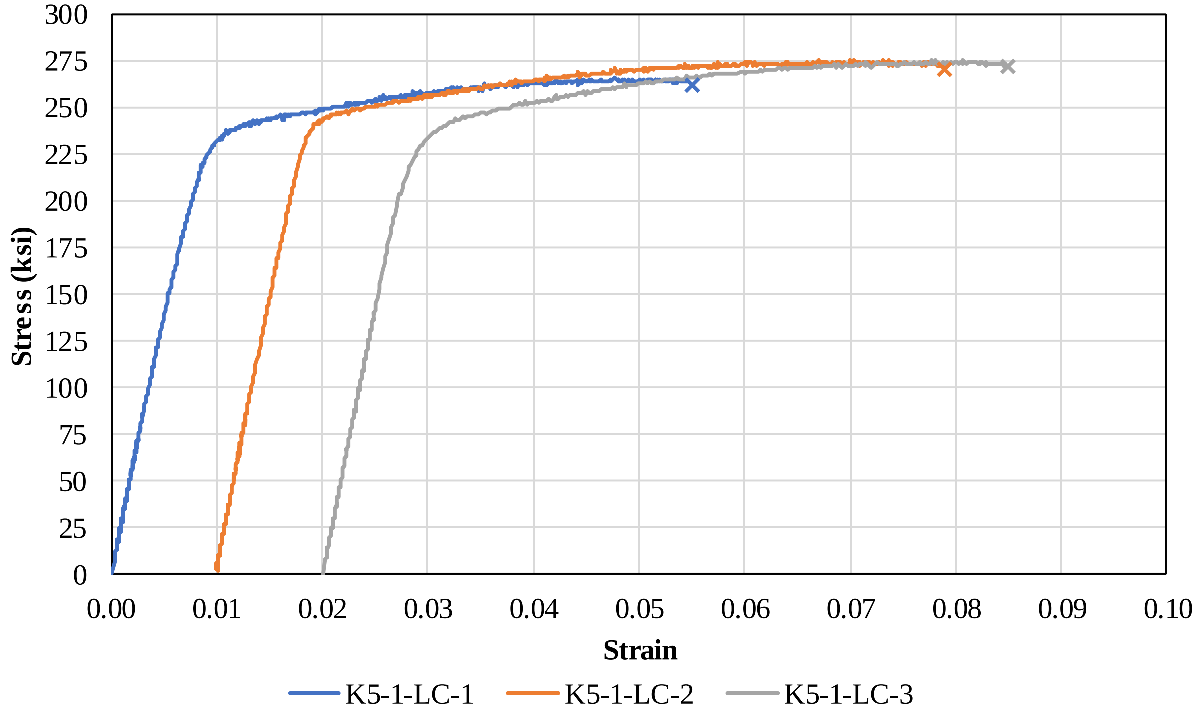

(a) Stress vs. strain curves offset by 0.01

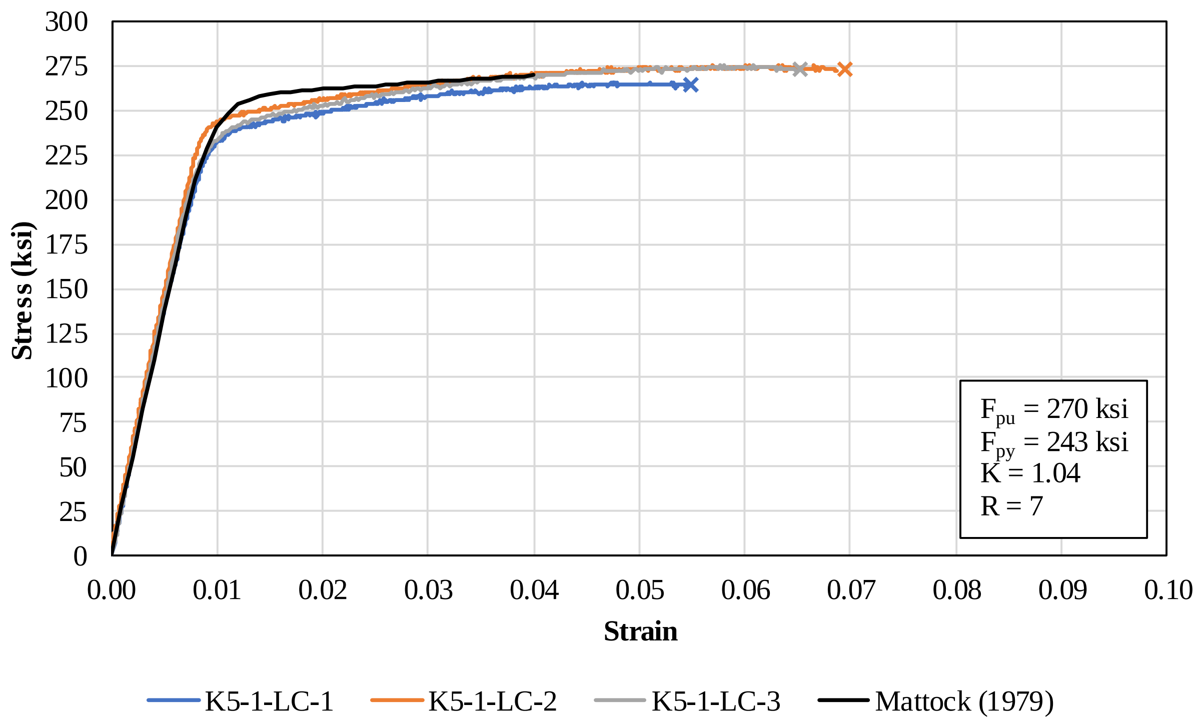

(b) Stress vs. strain curves without offset

Figure F.4: Specimen K5-1-LC Strand Stress vs. Strain

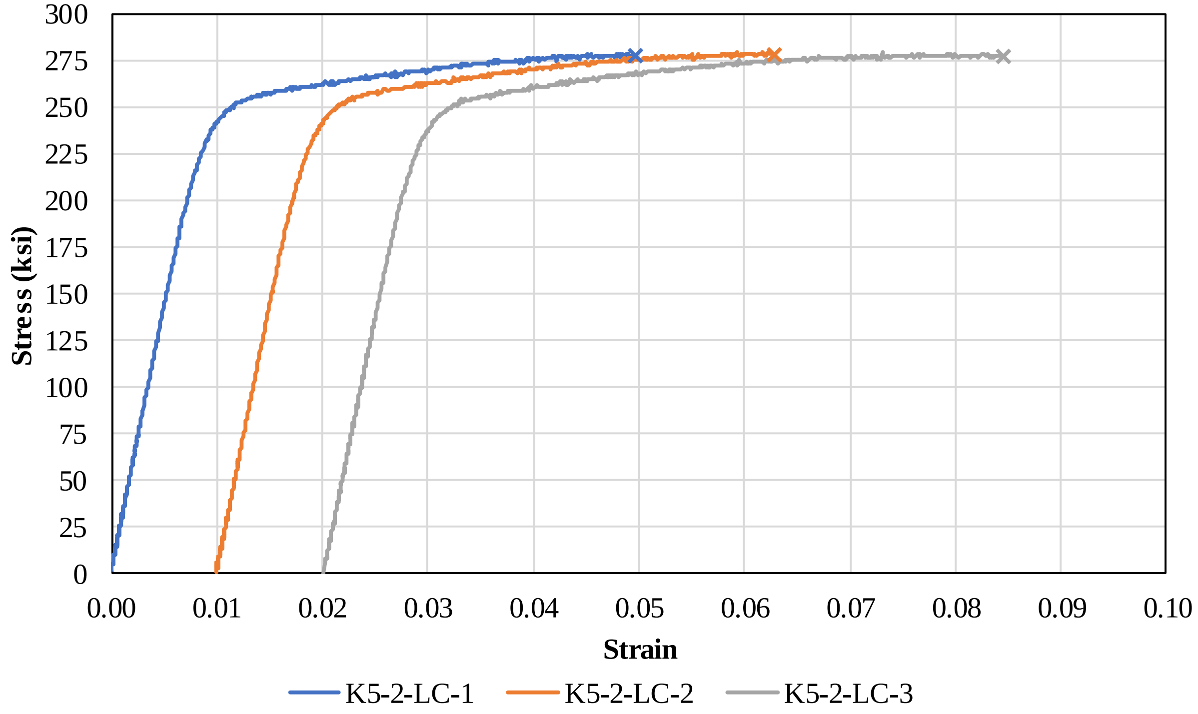

(a) Stress vs. strain curves offset by 0.01

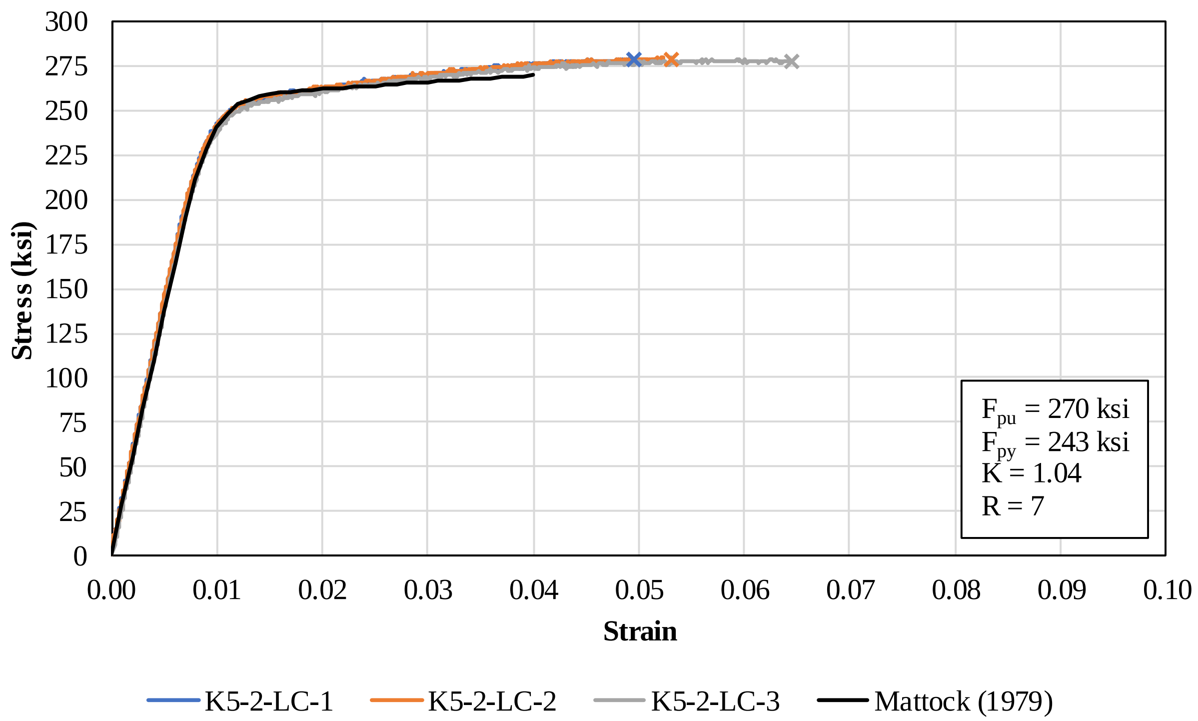

(b) Stress vs. strain curves without offset

Figure F.5: Specimen K5-2-LC Strand Stress vs. Strain

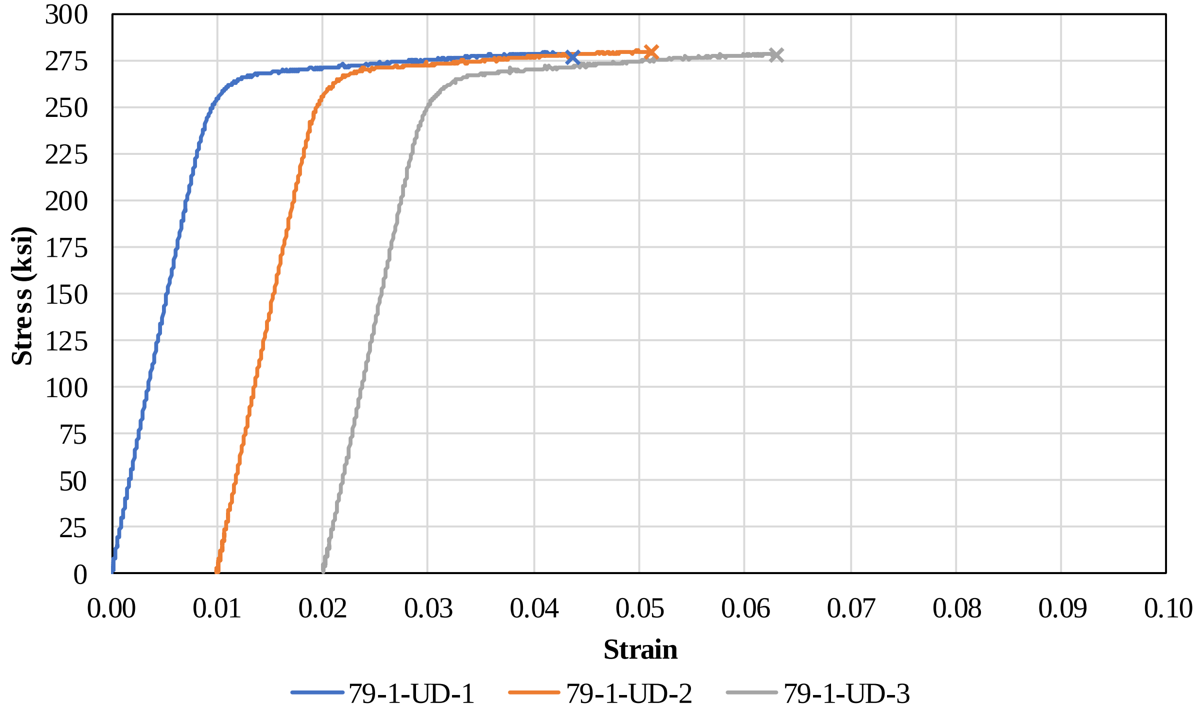

(a) Stress vs. strain curves offset by 0.01

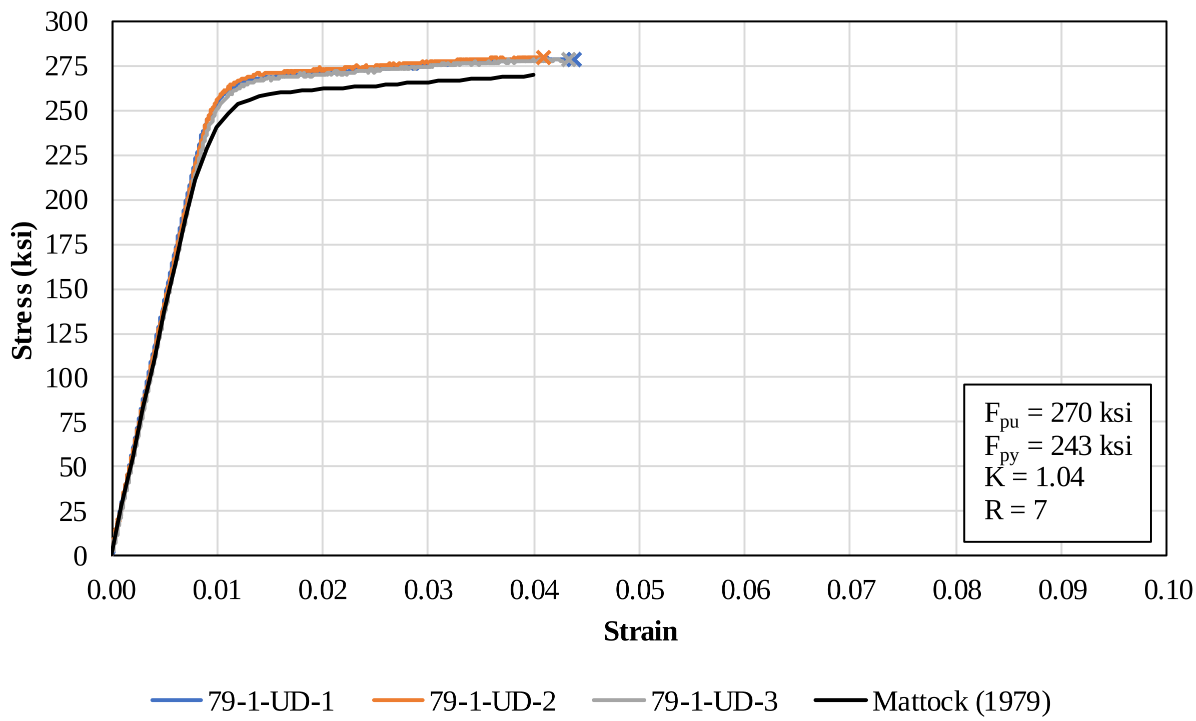

(b) Stress vs. strain curves without offset

Figure F.6: Specimen 79-1-UD Strand Stress vs. Strain

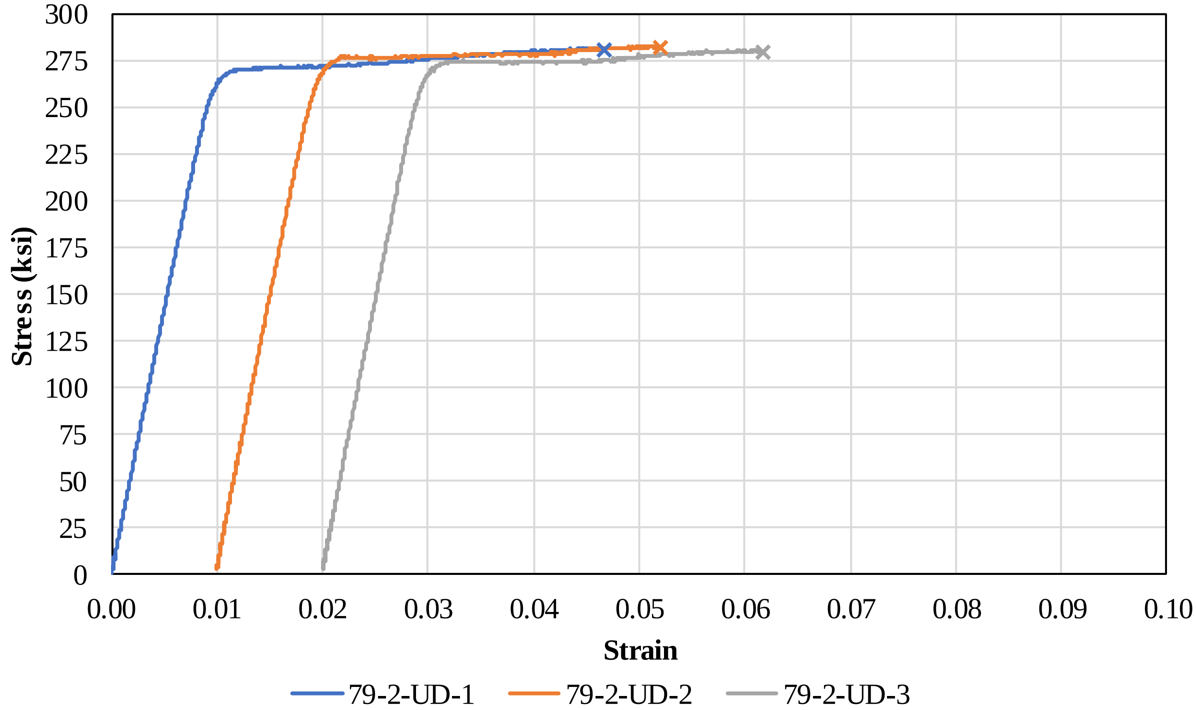

(a) Stress vs. strain curves offset by 0.01

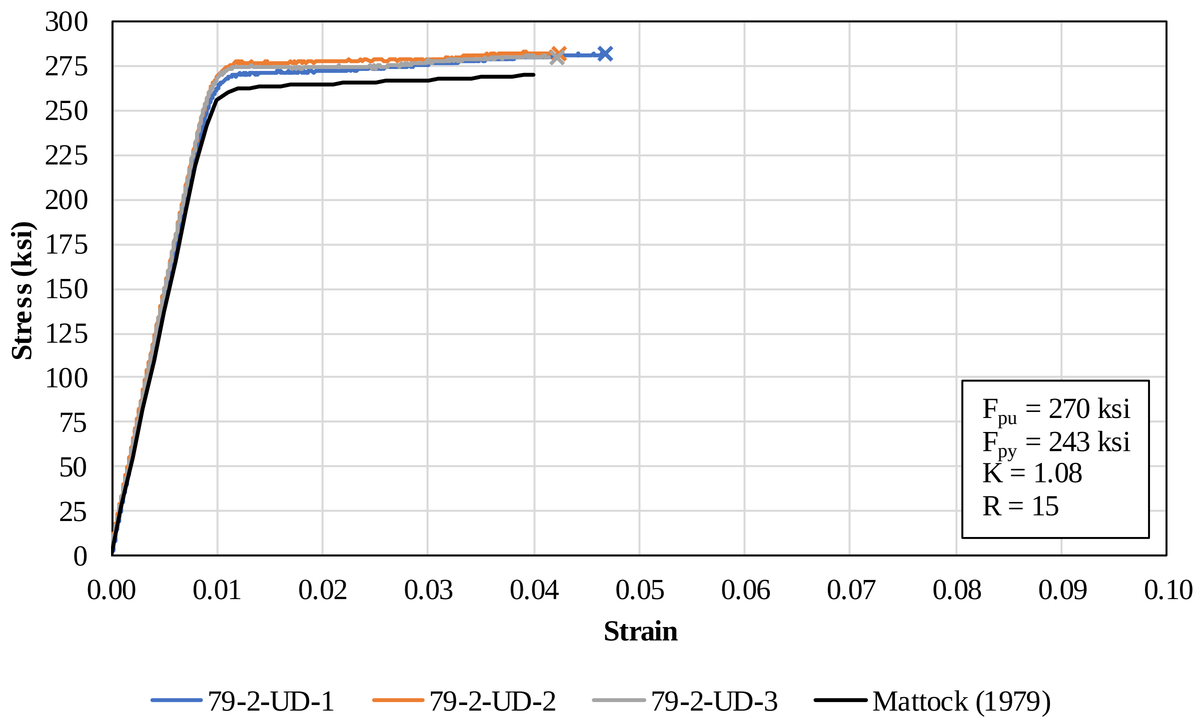

(b) Stress vs. strain curves without offset

Figure F.7: Specimen 79-2-UD Strand Stress vs. Strain

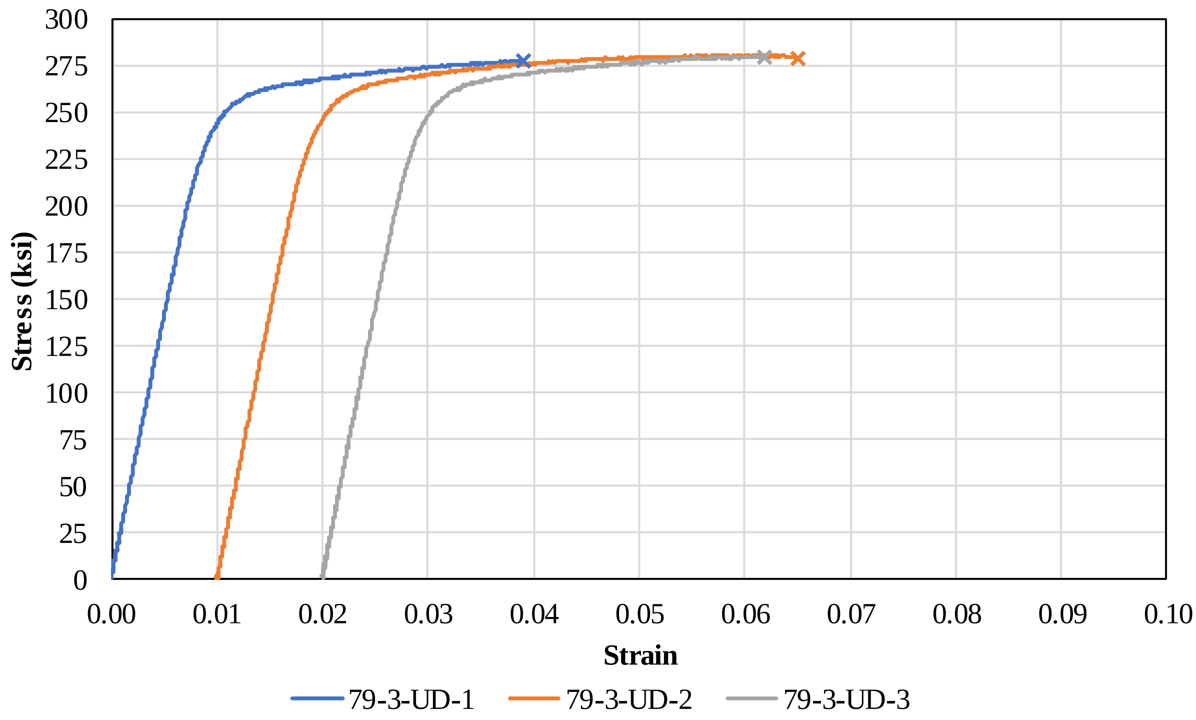

(a) Stress vs. strain curves offset by 0.01

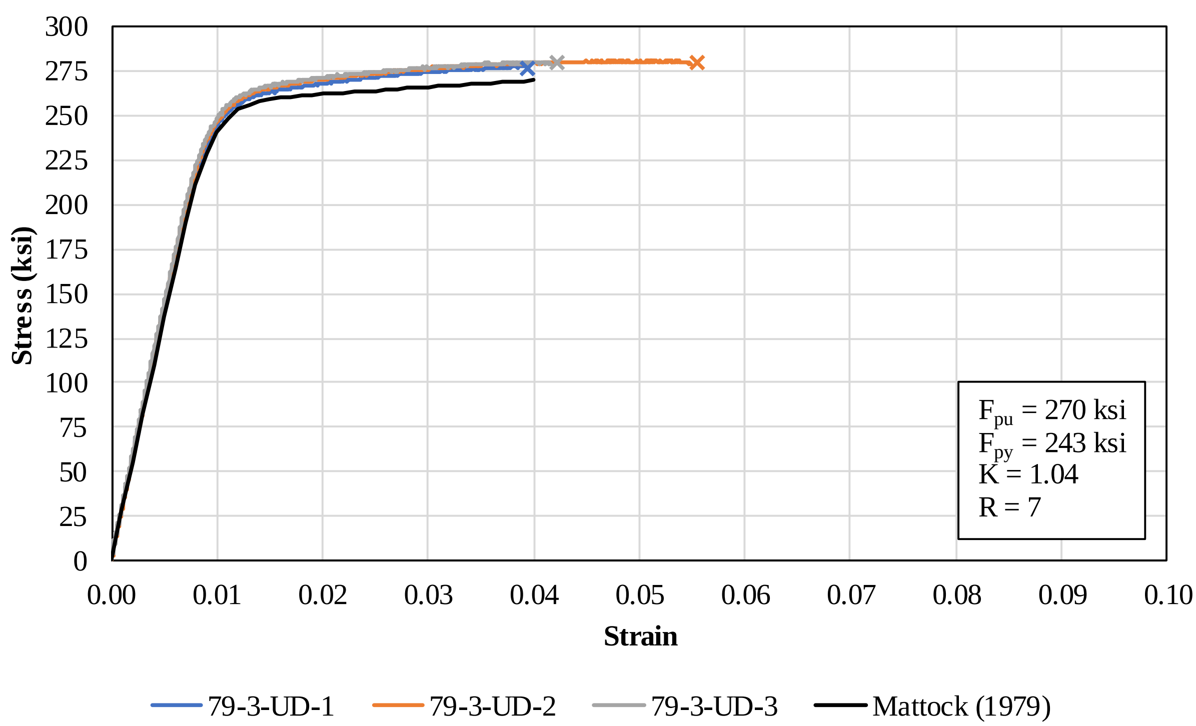

(b) Stress vs. strain curves without offset

Figure F.8: Specimen 79-3-UD Strand Stress vs. Strain

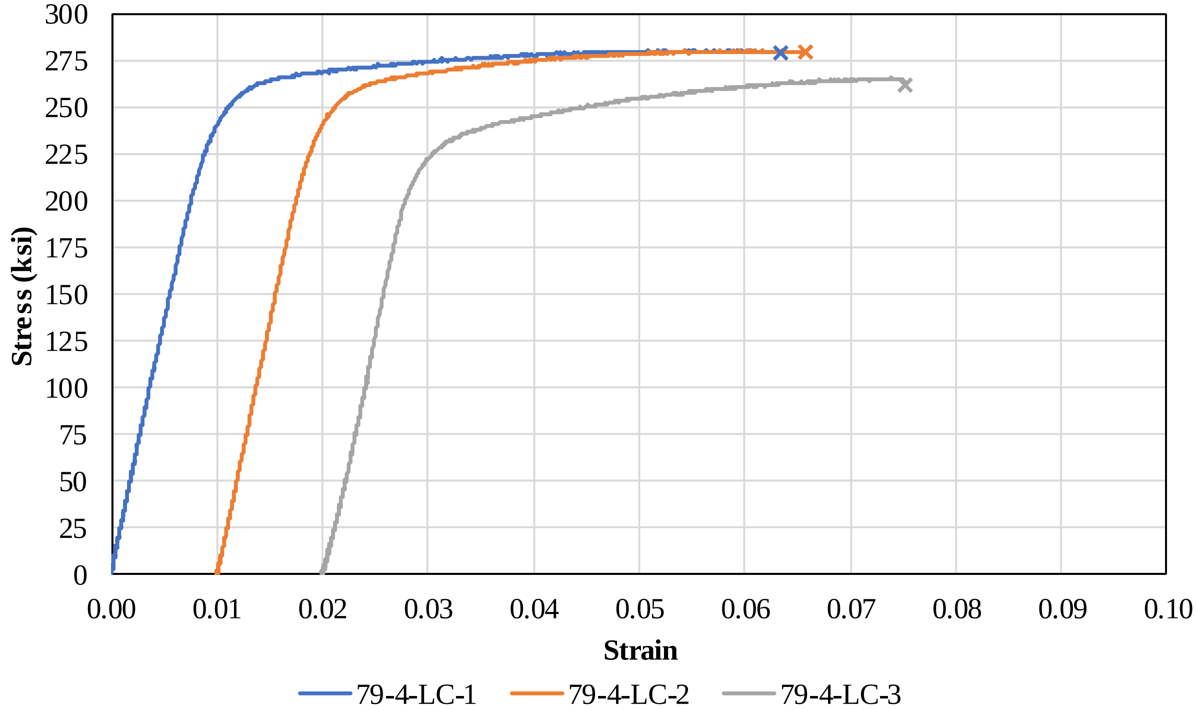

(a) Stress vs. strain curves offset by 0.01

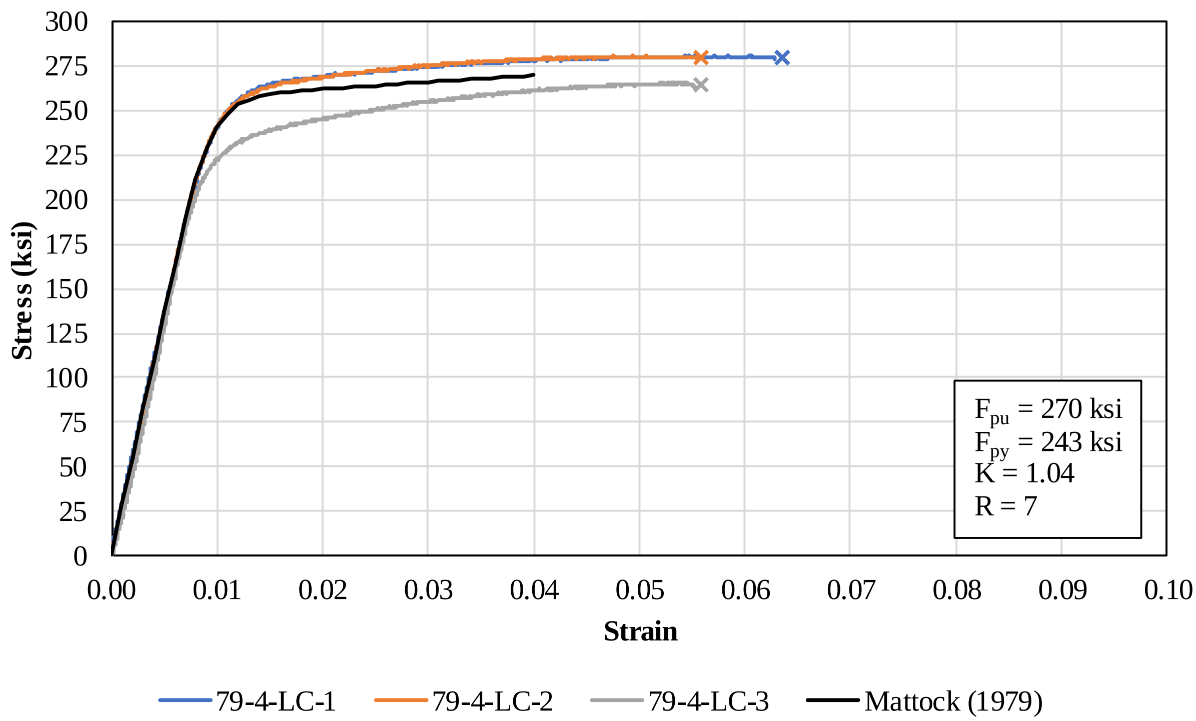

(b) Stress vs. strain curves without offset

Figure F.9: Specimen 79-4-LC Strand Stress vs. Strain

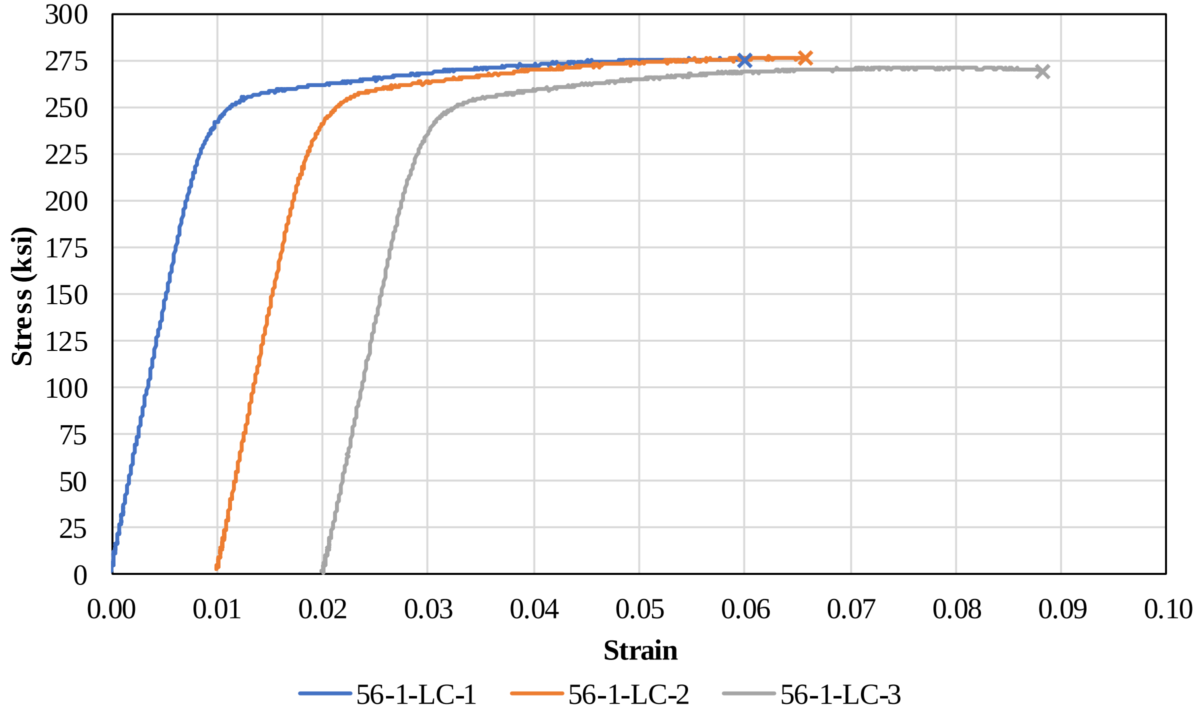

(a) Stress vs. strain curves offset by 0.01

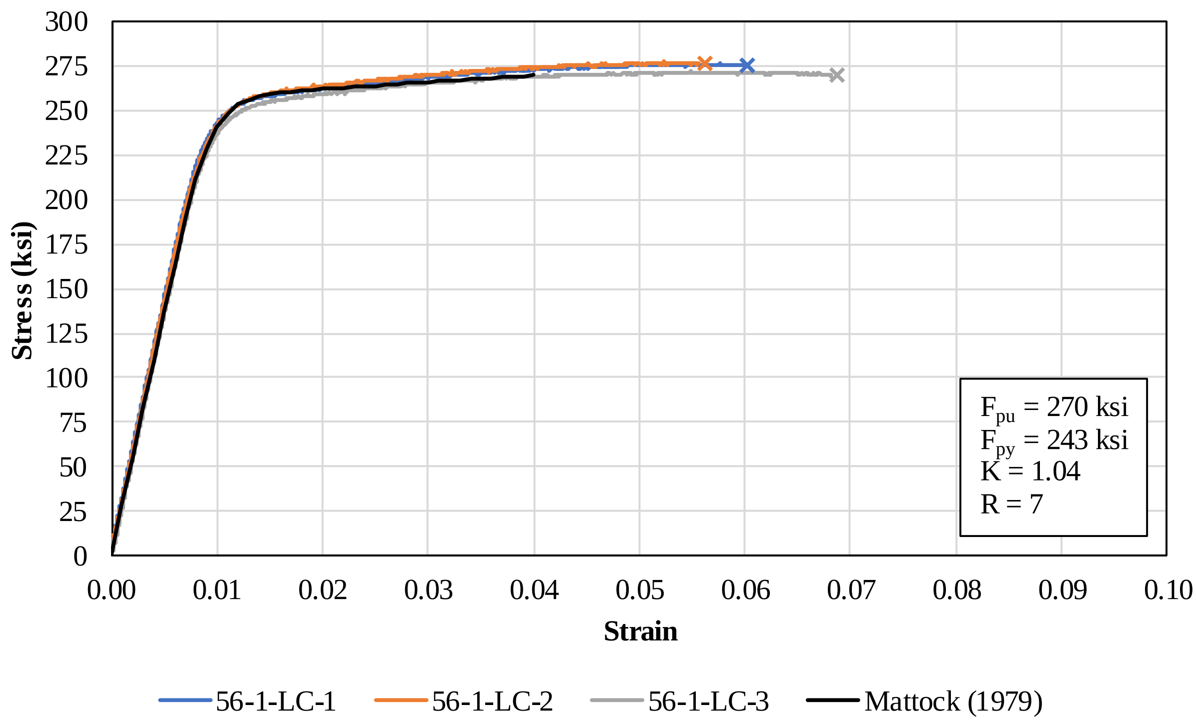

(b) Stress vs. strain curves without offset

Figure F.10: Specimen 56-1-LC Strand Stress vs. Strain

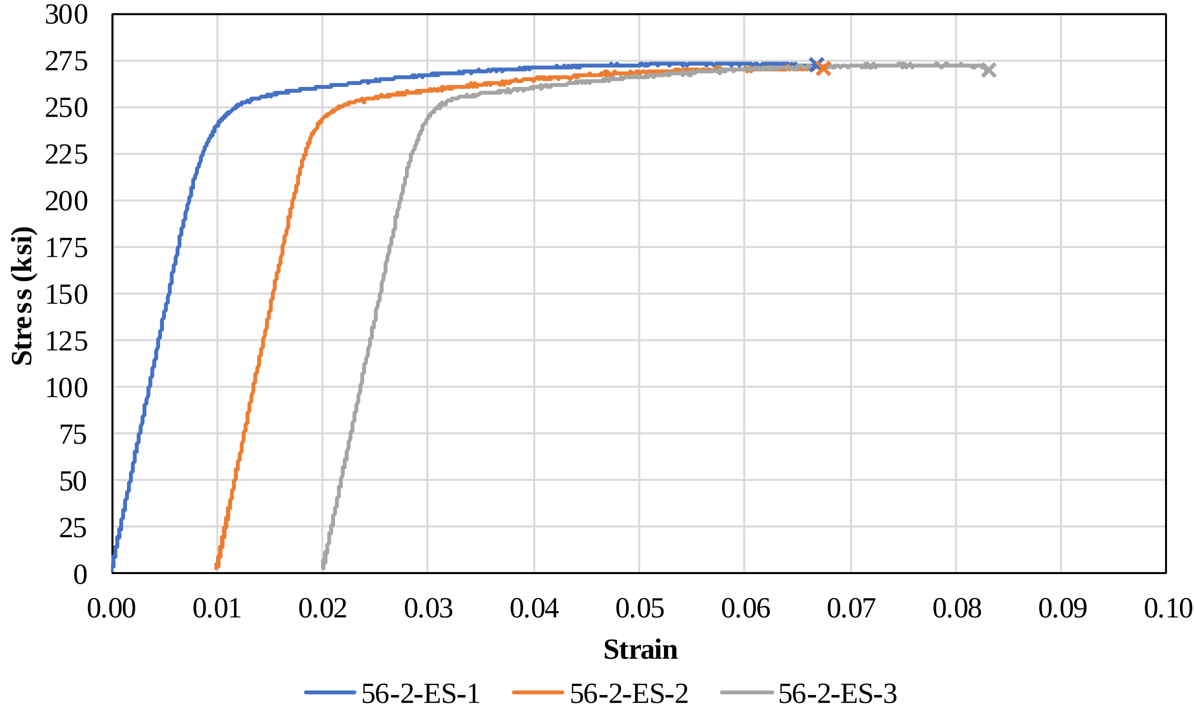

(a) Stress vs. strain curves offset by 0.01

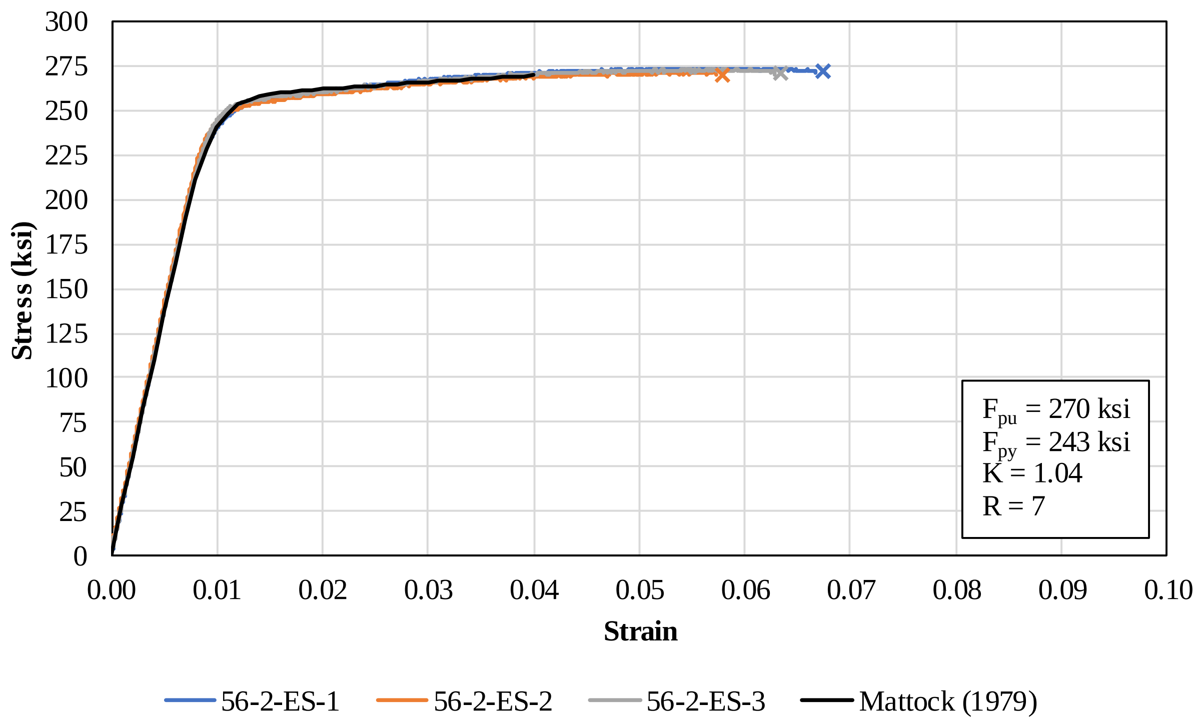

(b) Stress vs. strain curves without offset

Figure F.11: Specimen 56-2-ES Strand Stress vs. Strain

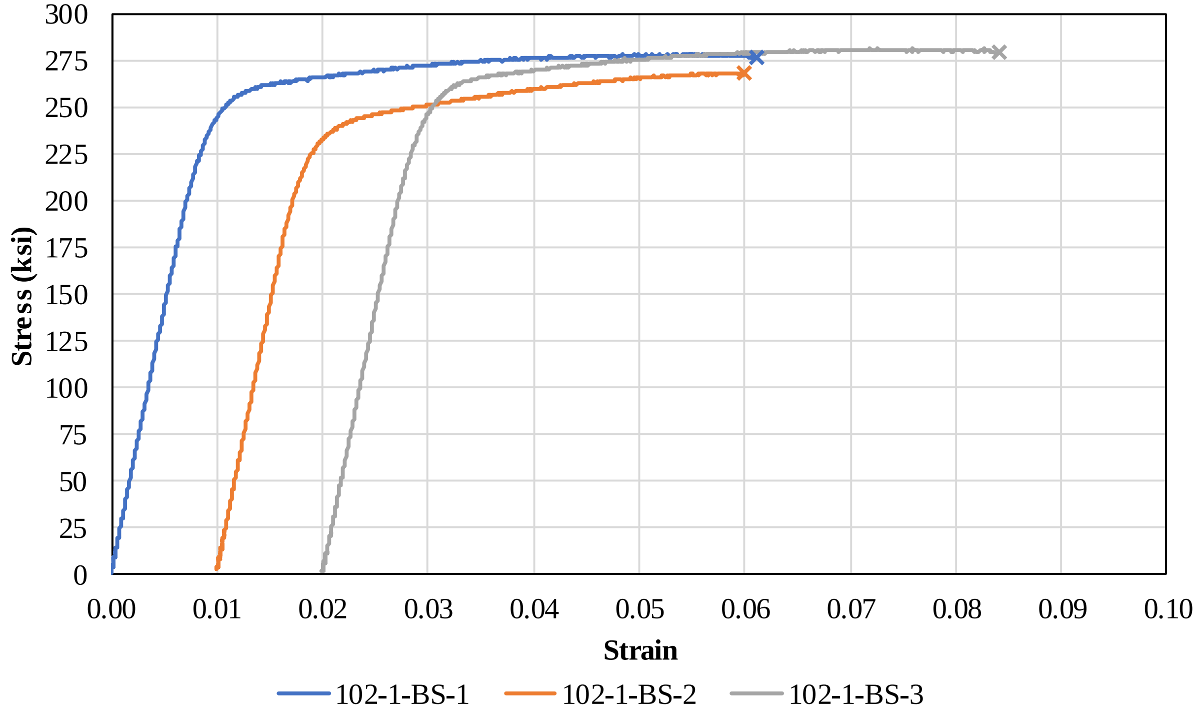

(a) Stress vs. strain curves offset by 0.01

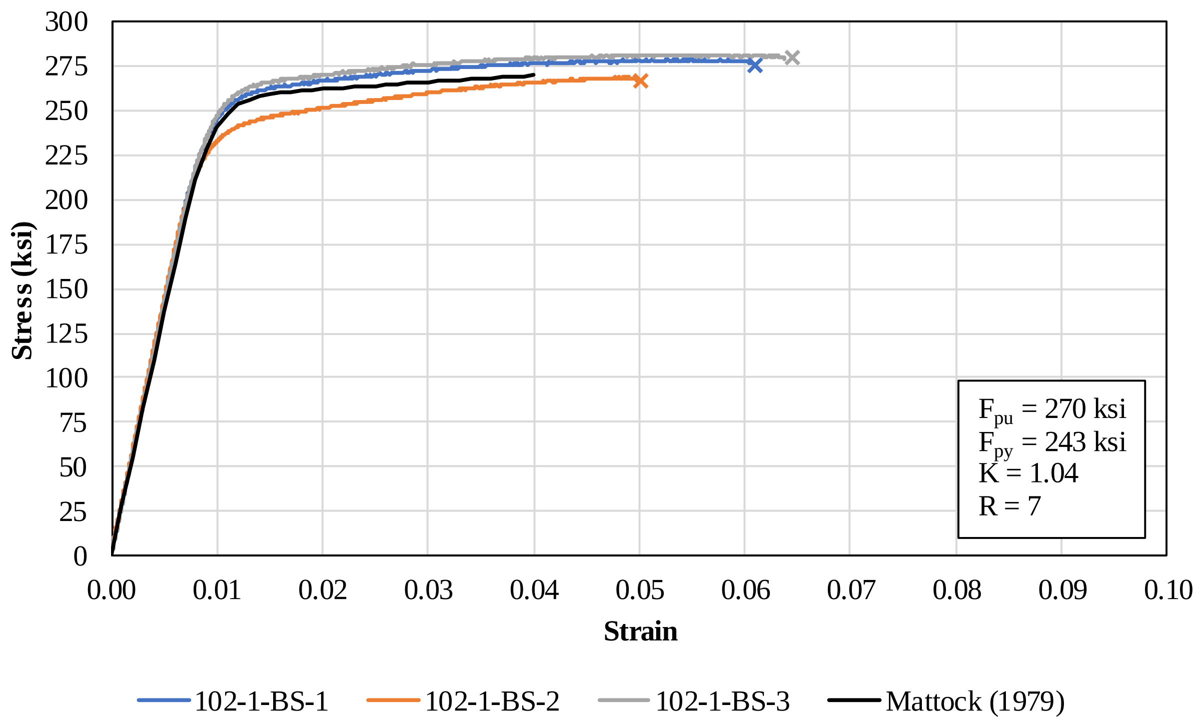

(b) Stress vs. strain curves without offset

Figure F.12: Specimen 102-1-BS Strand Stress vs. Strain

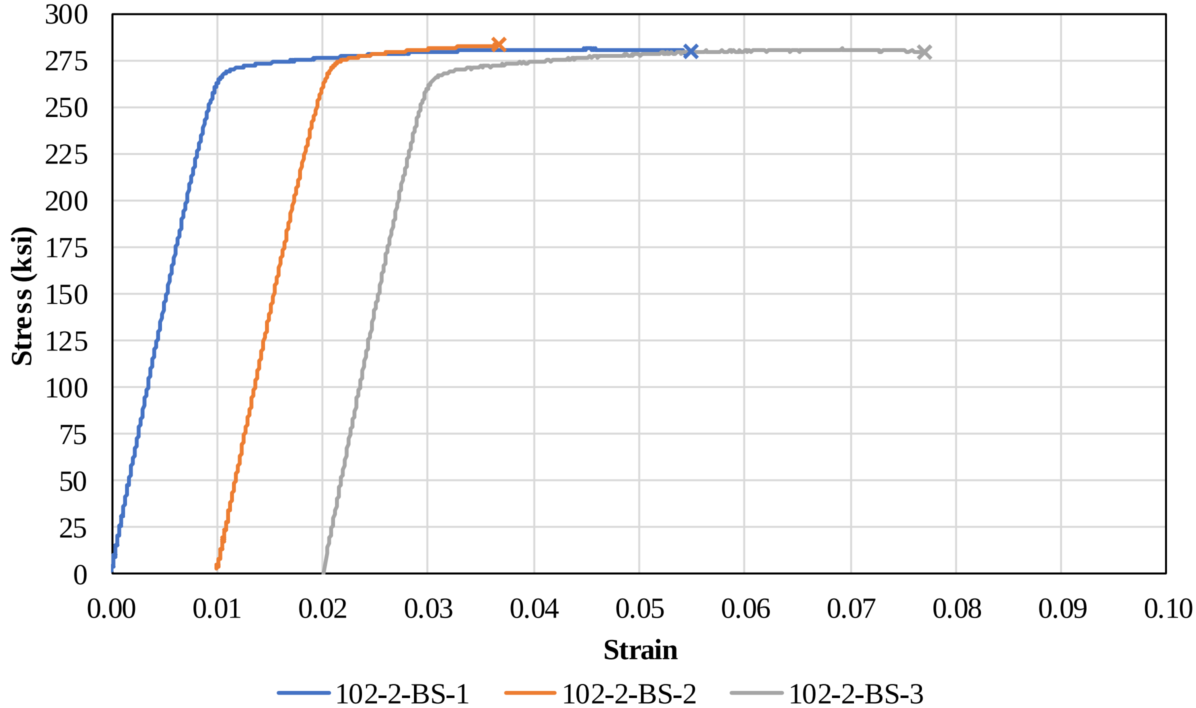

(a) Stress vs. strain curves offset by 0.01

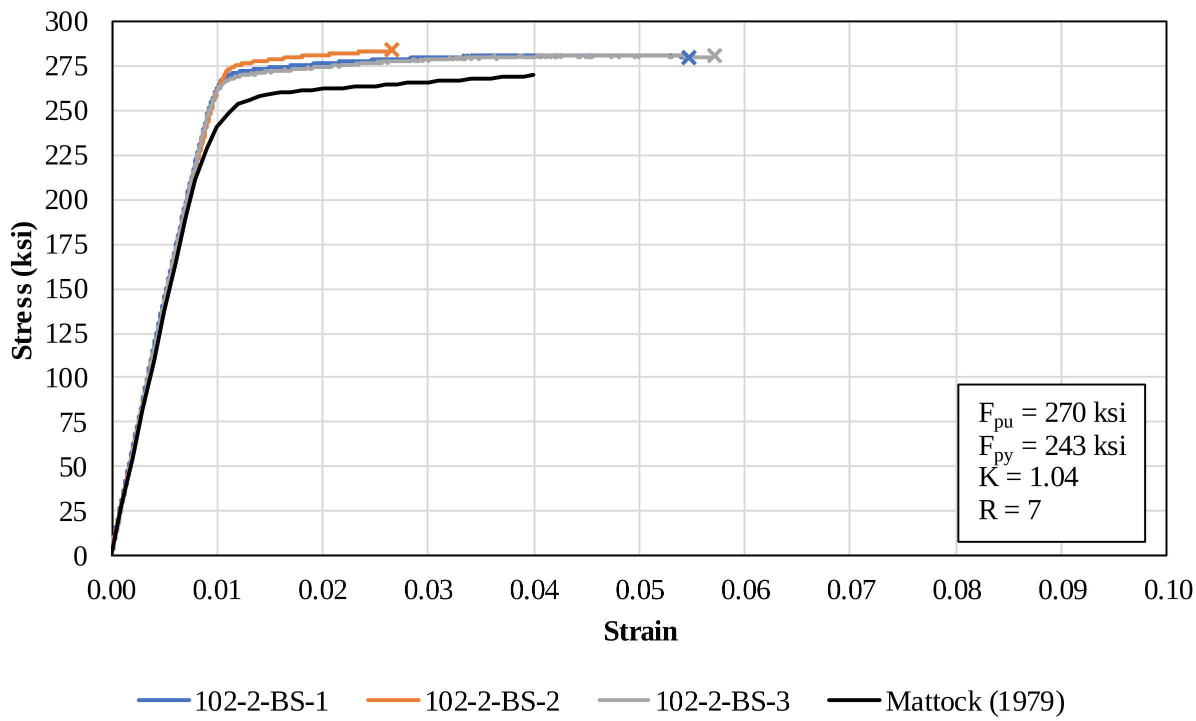

(b) Stress vs. strain curves without offset

Figure F.13: Specimen 102-2-BS Strand Stress vs. Strain

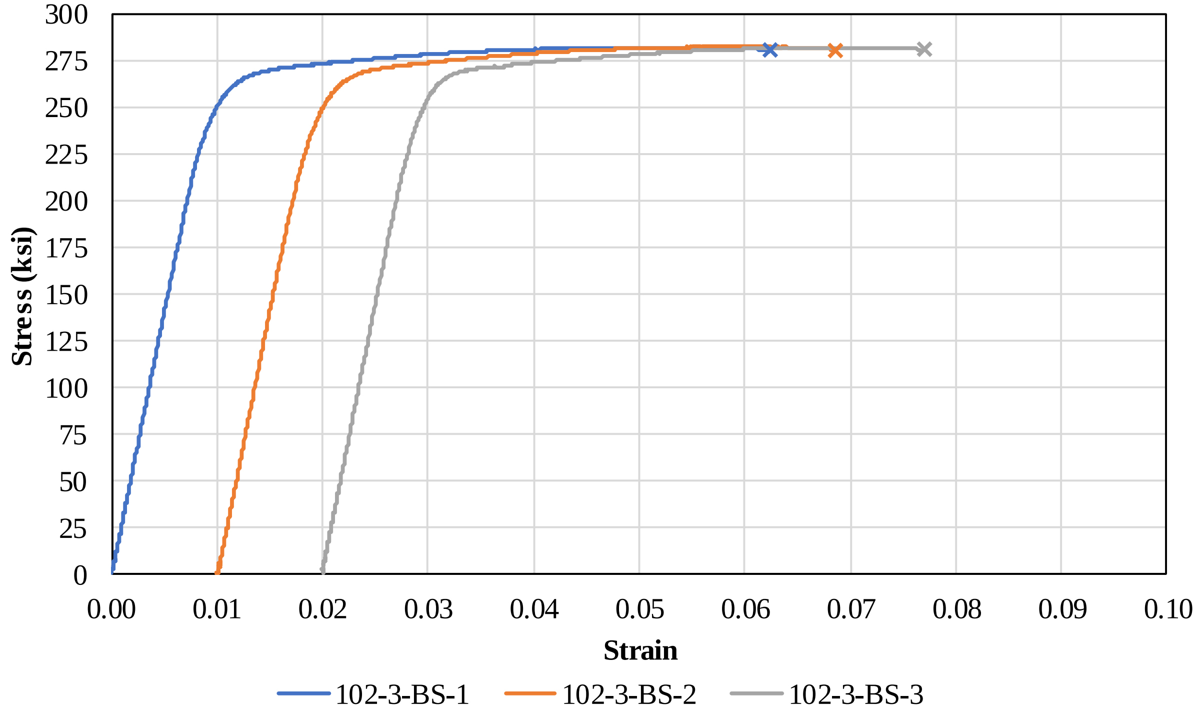

(a) Stress vs. strain curves offset by 0.01

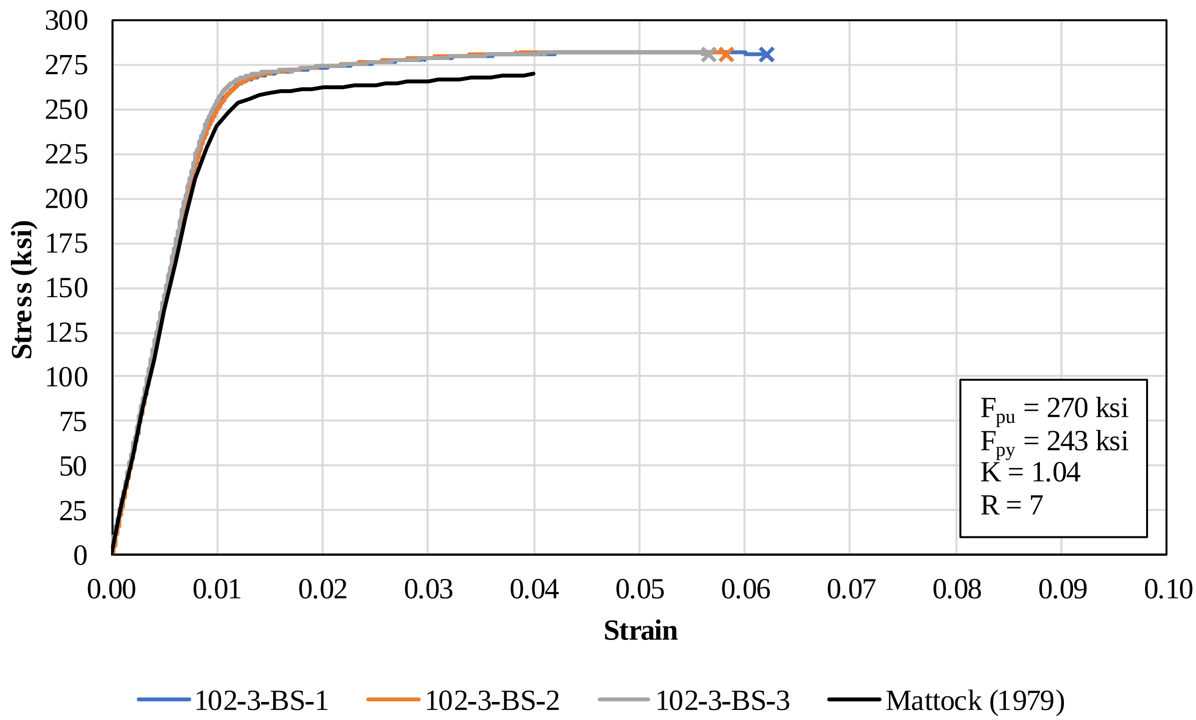

(b) Stress vs. strain curves without offset

Figure F.14: Specimen 102-3-BS Strand Stress vs. Strain

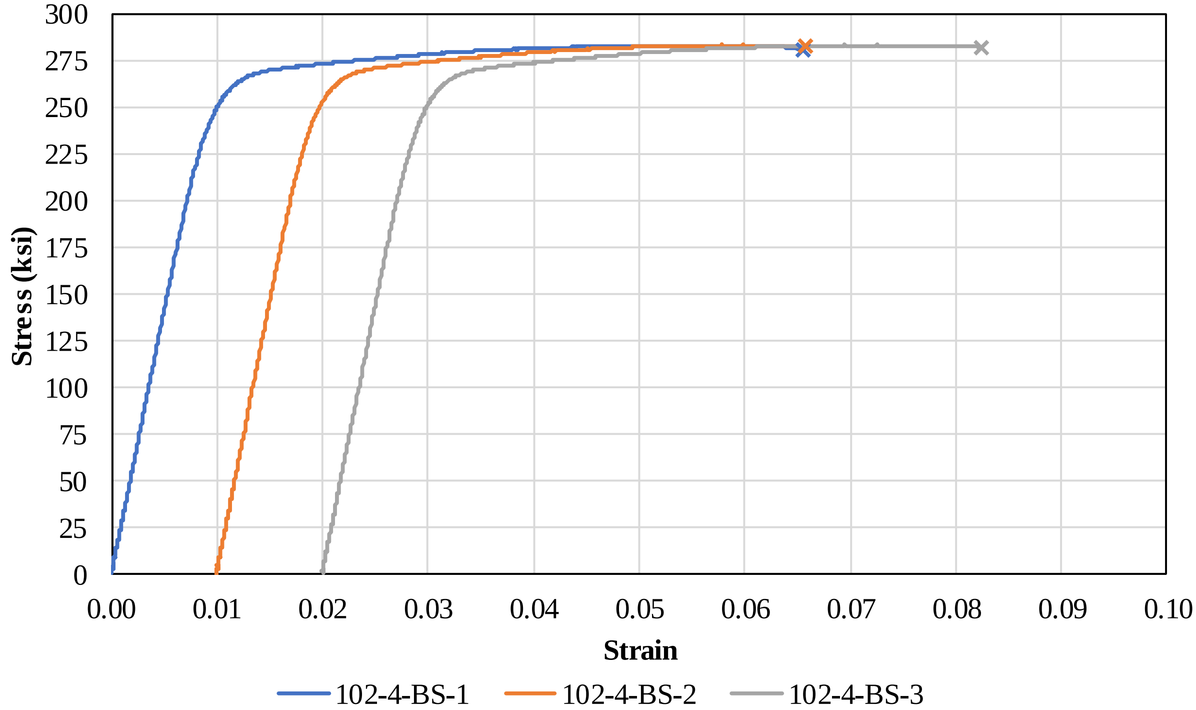

(a) Stress vs. strain curves offset by 0.01

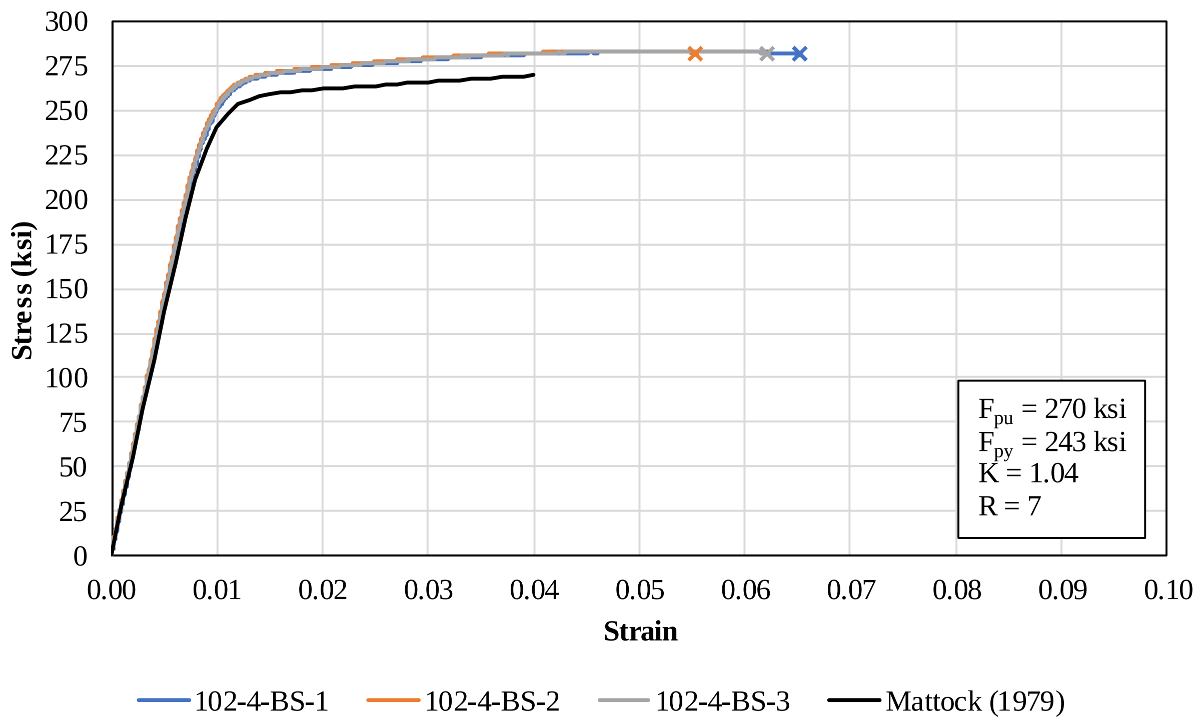

(b) Stress vs. strain curves without offset

Figure F.15: Specimen 102-4-BS Strand Stress vs. Strain

APPENDIX G. CORRODED STRAND TEST SPECIMEN LOCATIONS

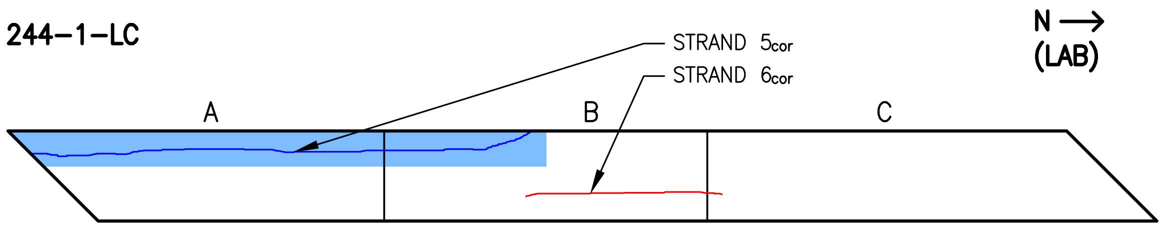

Figure G.1: Corroded Strand Test Specimen Location - Specimen 244-1-LC

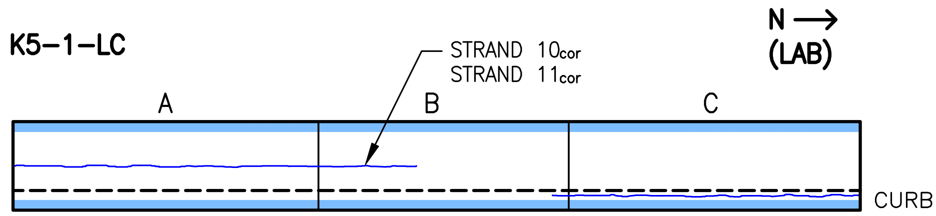

Figure G.2: Corroded Strand Test Specimen Location - Specimen K5-1-LC

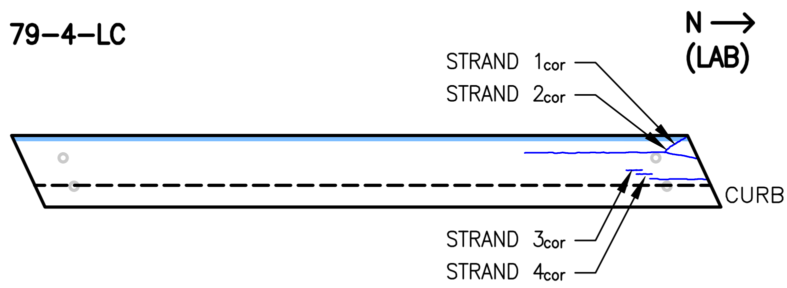

Figure G.3: Corroded Strand Test Specimen Location - Specimen 79-4-LC

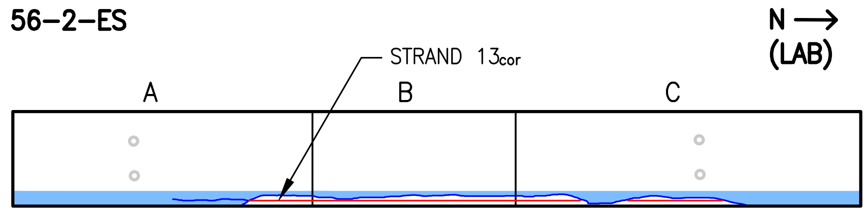

Figure G.4: Corroded Strand Test Specimen Location - Specimen 56-2-ES

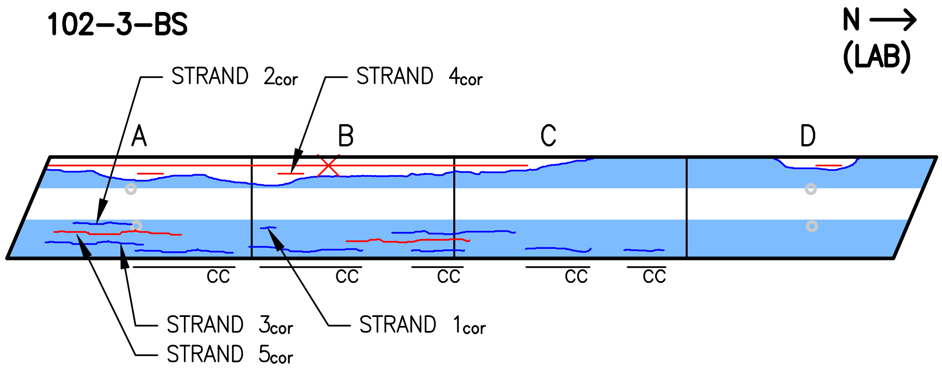

Figure G.5: Corroded Strand Test Specimen Location - Specimen 102-3-BS

APPENDIX H. FLEXURAL CRACK MAPS

Note: Red cracks indicate the location of strand fracture at collapse.

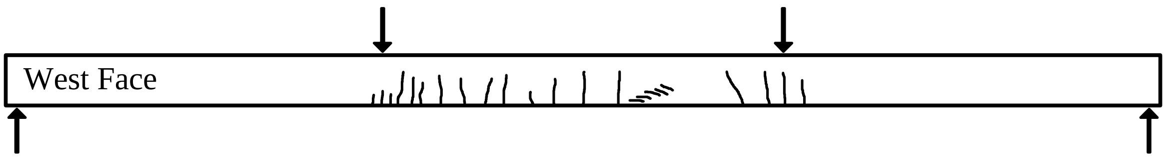

Figure H.1: Specimen 244-1-LC Crack Map

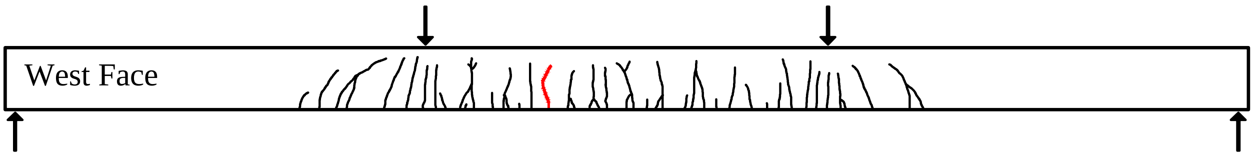

Figure H.2: Specimen 409-1-ES Crack Map

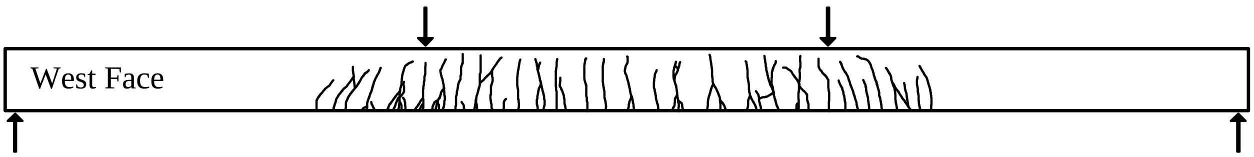

Figure H.3: Specimen 409-2-ES Crack Map

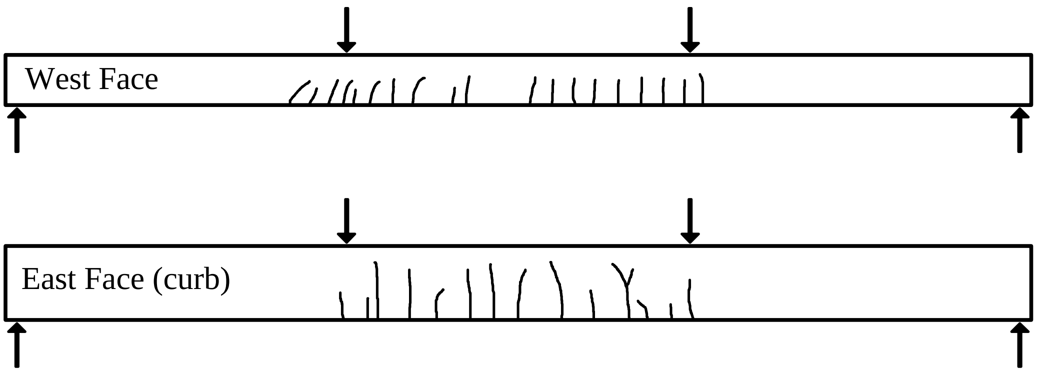

Figure H.4: Specimen K5-1-LC Crack Map

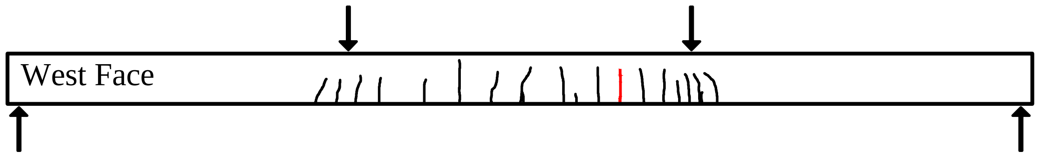

Figure H.5: Specimen K5-2-LC Crack Map

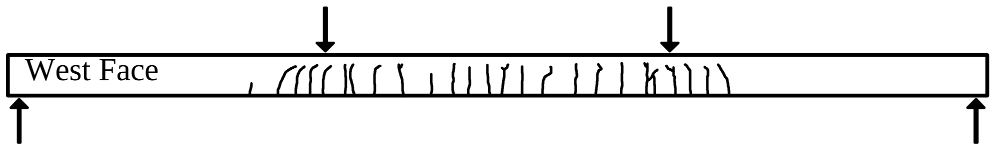

Figure H.6: Specimen 79-1-UD Crack Map

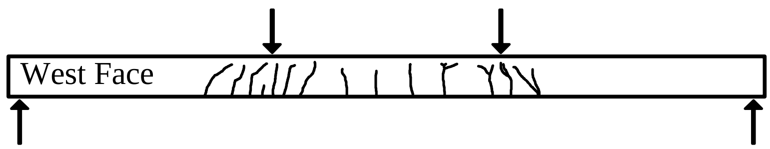

Figure H.7: Specimen 79-2-UD Crack Map

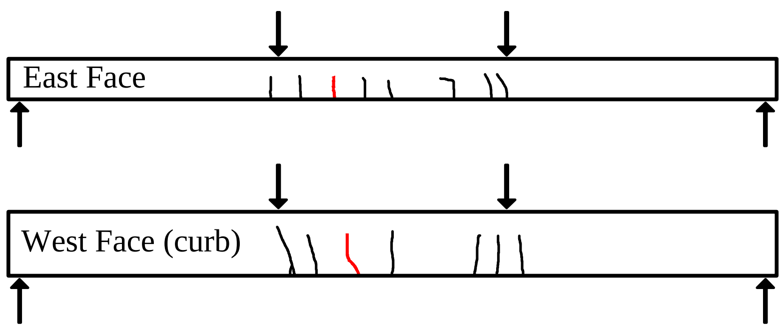

Figure H.8: Specimen 79-3-UD Crack Map

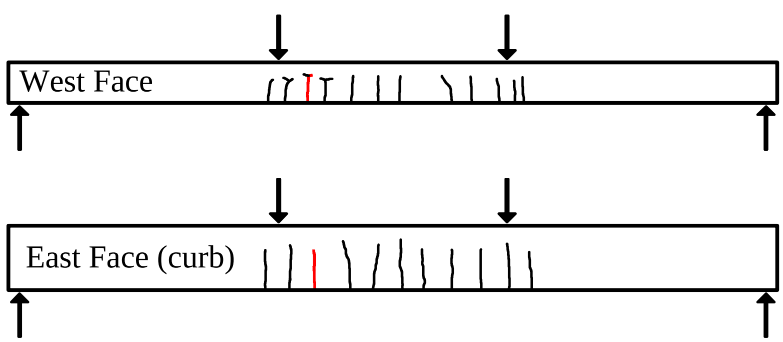

Figure H.9: Specimen 79-4-LC Crack Map

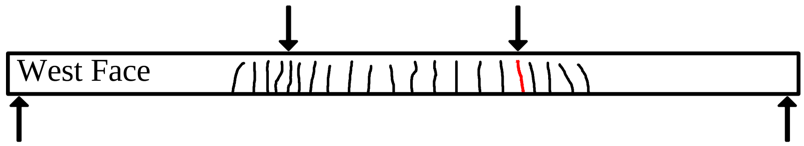

Figure H.10: Specimen 56-1-LC Crack Map

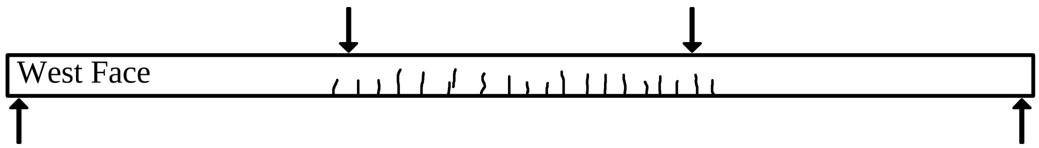

Figure H.11: Specimen 56-2-ES Crack Map

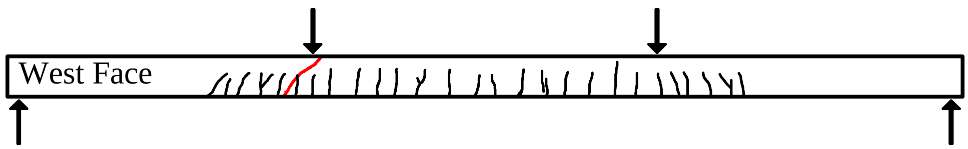

Figure H.12: Specimen 102-1-BS Crack Map

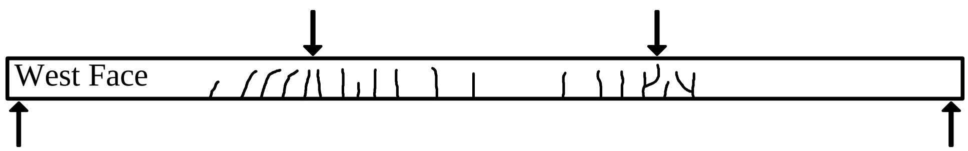

Figure H.13: Specimen 102-2-BS Crack Map

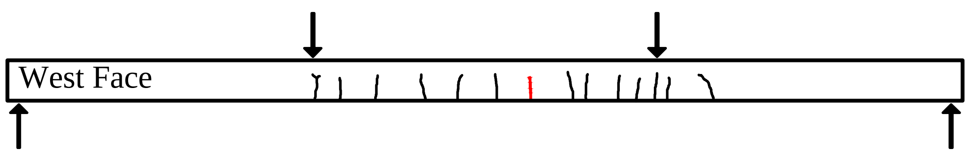

Figure H.14: Specimen 102-3-BS Crack Map

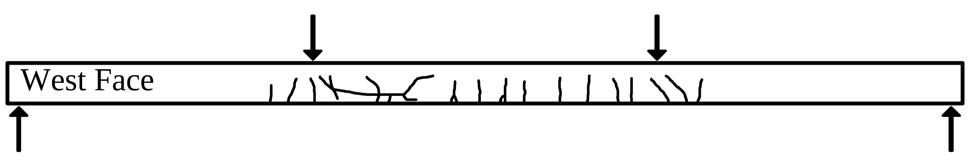

Figure H.15: Specimen 102-4-BS Crack Map

APPENDIX I. SUPPLEMENTAL BRIDGE INSPECTION OF BRIDGE 115

Bridge Inspection Report

Copy of 79-00115

CR 750 N
over
BURNETT CREEK

Inspection Date: 06/01/2018

Inspected By: Nathaniel Pfeiffer

Inspection Type(s): Routine

TABLE OF CONTENTS

Inspector: Nathaniel Pfeiffer

Inspection Date: 06/01/2018

Asset Name: Copy of 79-00115

Facility Carried: CR 750 N

Bridge Inspection Report

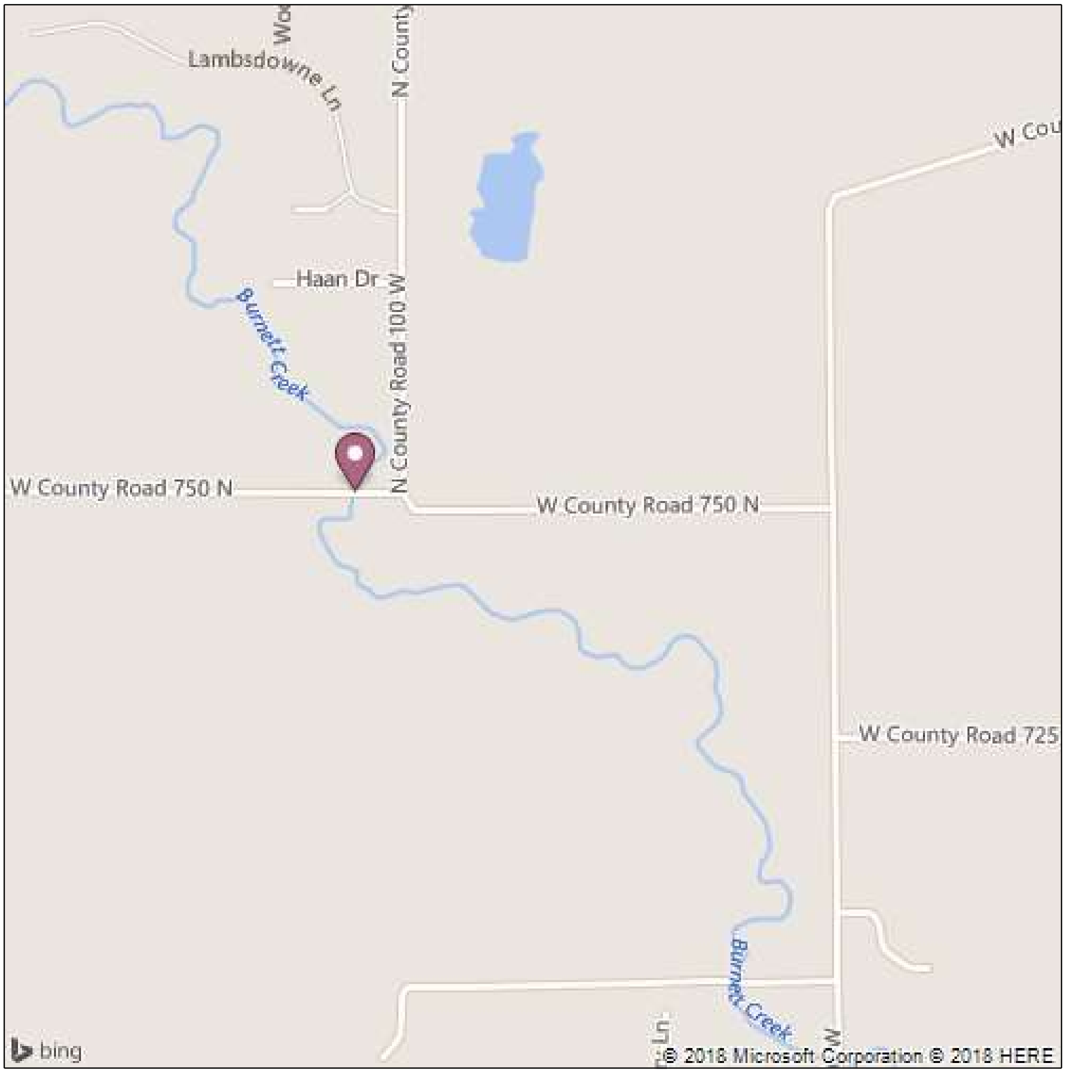

Latitude: 40.52615

Longitude: -86.926064

Inspector: Nathaniel Pfeiffer

Inspection Date: 06/01/2018

Asset Name: Copy of 79-00115

Facility Carried: CR 750 N

Bridge Inspection Report

This inspection was performed to support Study Advisory Committee SPR-4009 activities. To avoid over-writing the official inspection, this is a copy of bridge 79-00115. As such, the load rating information is not populated. Original plans (not dated, but assumed to be 1957) indicate 7 prestressed concrete box beams surfaced with 1"-2" of asphalt surface. Rehab plans (1993) indicate that the north facia beam was replaced and there was a waterproofing membrane placed over the beams with an asphalt overlay. (NP 6/1/2018)

Previous notes:

<u>Describing Item 75 Proposed Improvements:</u>

Replace Bridge.

Inspector: Nathaniel Pfeiffer
Inspection Date: 06/01/2018
Asset Name: Copy of 79-00115
Facility Carried: CR 750 N

Bridge Inspection Report

IDENTIFICATION

(1) STATE CODE:	**185 - Indiana**
(8) STRUCTURE:	**copy of 7900080**
(5 A-B-C-D-E) INV. ROUTE:	**1 - 4 - 1 - 00070 - 0**
(2) HIGHWAY AGENCY DISTRICT:	**01 - Crawfordsville**
(3) COUNTY CODE:	**079 - TIPPECANOE**
(4) PLACE CODE:	**00000 - N/A**
(6) FEATURES INTERSECTED:	**BURNETT CREEK**
(7) FACILITY CARRIED:	**CR 750 N**
(9) LOCATION:	**00.05 W CR 100 W**
(11) MILEPOINT:	**0000.000**

(12) BASE HIGHWAY NETWORK:	**0**
(13A) INVENTORY ROUTE:	
(13B) SUBROUTE NUMBER:	
(16) LATITUDE:	**40.52615**
(17) LONGITUDE:	**-86.926064**
(98) BORDER	
A) STATE NAME:	
B) PERCENT	**%**
(99) BORDER BRIDGE STRUCT. NO:	

STRUCTURE TYPE AND MATERIAL

(43) STRUCTURE TYPE, MAIN:	
A) KIND OF MATERIAL/DESIGN:	**5 - Prestressed concrete**
B) TYPE OF DESIGN/CONSTR:	**05 - Box Beam or Girders - Multiple**
(44) STRUCTURE TYPE, APPROACH SPANS:	
A) KIND OF MATERIAL/DESIGN:	**0 - Other**
B) TYPE OF DESIGN/CONSTR:	**00 - Other**

(45) NUMBER OF SPANS IN MAIN UNIT:	**001**
(46) NUMBER OF APPROACH SPANS:	**0**
(107) DECK STRUCTURE TYPE:	**N - Not Applicable**
(108) WEARING SURFACE/PROT SYS:	
A) WEARING SURFACE:	**N - NA**
B) DECK MEMBRANE:	**N - NA**
C) DECK PROTECTION:	**N - NA**

AGE OF SERVICE

(27) YEAR BUILT:	**1957**
(106) YEAR RECONSTRUCTED:	**1994**
(42) TYPE OF SERVICE:	
A) ON BRIDGE:	**1 - Highway**
B) UNDER BRIDGE:	**5 - Waterway**

(28) LANES:		
A) ON BRIDGE:	**02**	
B) UNDER BRIDGE:	**00**	
(29) AVERAGE DAILY TRAFFIC:	**000177**	
(30) YEAR OF AVERAGE DAILY TRAFFIC:	**2005**	
(109) AVERAGE DAILY TRUCK TRAFFIC:	**05**	**%**
(19) BYPASS DETOUR LENGTH:	**004**	**MI**

Inspector: Nathaniel Pfeiffer **Asset Name:** Copy of 79-00115
Inspection Date: 06/01/2018 **Facility Carried:** CR 750 N

Bridge Inspection Report

GEOMETRIC DATA

(48) LENGTH OF MAX SPAN:	**0039.0**	**FT**
(49) STRUCTURE LENGTH:	**00040.0**	**FT**
(50) CURB/SIDEWALK WIDTHS:		
A) LEFT	**00.7**	**FT**
B) RIGHT:	**00.7**	**FT**
(51) BRDG RDWY WIDTH CURB-TO-CURB:	**024.7**	**FT**
(52) DECK WIDTH, OUT-TO-OUT:	**026.7**	**FT**
(32) APPROACH ROADWAY	**018.0**	**FT**
(33) BRIDGE MEDIAN:	**0 - No median**	
(34) SKEW:	**00**	**DEG**

(35) STRUCTURE FLARED:	**0 - No flare**	
(10) INV RTE, MIN VERT CLEARANCE:	**99.99**	**FT**
(47) TOT HORIZ CLEARANCE:	**024.7**	**FT**
(53) VERT CLEAR OVER BR RDWY:	**99.99**	**FT**
(54) MIN VERTICAL UNDERCLEARANCE:		
A) REFERENCE FEATURE:	**N**	
B) MIN VERT UNDERCLEAR:	**0**	**FT**
(55) LATERAL UNDERCLEARANCE RIGHT:		
A) REFERENCE FEATURE:	**N**	
B) MIN LATERAL UNDERCLEAR:	**000.0**	**FT**
(56) MIN LATERAL UNDERCLEAR ON LEFT:	**000.0**	**FT**

INSPECTIONS

(90) INSPECTION DATE:	**06/01/2018**
(92) CRITICAL FEATURE INSPECTION:	
A) FRACTURE CRITICAL REQUIRED/FREQUENCY:	**N**
B) UNDERWATER INSPECTION REQUIRED/FREQUENCY:	**N**
C) OTHER SPECIAL INSPECTION REQUIRED/FREQUENCY:	**N**

(91) DESIGNATED INSPECTION FREQUENCY:	**12 MONTHS**
(93) CRITICAL FEATURE INSPECTION DATE:	
A) FRACTURE CRITICAL DATE:	
B) UNDERWATER INSP DATE:	
C) OTHER SPECIAL INSP DATE:	

CONDITION

(58) DECK:	**N - Not Applicable**
(58.01) WEARING SURFACE:	**N - Not Applicable**
(59) SUPERSTRUCTURE:	**4 - Poor Condition (advanced deterioration)**
(60) SUBSTRUCTURE:	**6 - Satisfactory Condition (minor deterioration)**
(61) CHANNEL/CHANNEL PROTECTION:	**6 - Bank slump. widespread minor damage**
(62) CULVERTS:	**N - Not Applicable**

CONDITION COMMENTS

(58) DECK: **N - Not Applicable**

Comments:
Currently no deck. Prestressed concrete box beams were overlayed with asphalt when the road was paved. (NP 6/1/2018)

(58.01) WEARING SURFACE: **N - Not Applicable**

Comments:
See deck comments (NP 6/1/2018).

Previous notes:
Asphalt w/ Membrane
5.50 Inches

Inspector: Nathaniel Pfeiffer | **Asset Name:** Copy of 79-00115
Inspection Date: 06/01/2018 | **Facility Carried:** CR 750 N

Bridge Inspection Report

(59) SUPERSTRUCTURE: **4 - Poor Condition (advanced deterioration)**

Comments:
North faica beam is newer than the rest of the beams (replaced in 1994 per design documents). There is hairline crack at the west end of this beam with some delamination present. The south facia beam has a spall with 2 broken & 2 exposed strands at the east end. Additionally, this beam has two medium-width cracks with rust staining just east of midspan. (NP 6/1/2018)

Previous notes:
Crack, Delam., 4 Strands Exposed (19% of Total Individual Beam Strands) in SE Beam
Material:
Adjacent PC Box Beams

(60) SUBSTRUCTURE: **6 - Satisfactory Condition (minor deterioration)**

Comments:
Abutments have minor cracking and efflorescence. West abutment has exposed timber piling with voids below the bent cap. Gabion baskets are present in front of piles and some have been cut open. East abutment has had flowable grout placed in front of bent cap. (NP 6/1/2018)

Previous notes:
Minor Cracks & Spalls
Material:
Concrete Caps on Piles

(61) CHANNEL/CHANNEL PROTECTION **6 - Bank slump. widespread minor damage**

Comments:
Channel migrating towards west. Gabion baskets protect west abutment. Banks are beginning to slump. East abutment protected by grouted riprap. (NP 6/1/2018)

Some Gabions Cut Open
Material:
Gabions/Riprap Slopes

(62) CULVERTS: **N - Not Applicable**

Comments:

LOAD RATING AND POSTING

(31) DESIGN LOAD:		(66) INVENTORY RATING:
(70) BRIDGE POSTING		(65) INVENTORY RATING METHOD:
		(66B) INVENTORY RATING (H):
(41) STRUCTURE OPEN/POSTED/CLOSED:	**A - Open**	(66C) TONS POSTED :
(64) OPERATING RATING:		(66D) DATE POSTED/CLOSED:
(63) OPERATING RATING METHOD:		

Inspector: Nathaniel Pfeiffer | **Asset Name:** Copy of 79-00115
Inspection Date: 06/01/2018 | **Facility Carried:** CR 750 N

Bridge Inspection Report

APPRAISAL

SUFFICIENCY RATING:	**66.9**	(36) TRAFFIC SAFETY FEATURE:	
STATUS:	**1**	36A) BRIDGE RAILINGS:	**0**
(67) STRUCTURAL EVALUATION:	**4**	36B) TRANSITIONS:	**0**
(68) DECK GEOMETRY:	**5**	36C) APPROACH GUARDRAIL:	**1**
(69) UNDERCLEARANCES, VERTICAL & HORIZONTAL:	**N**	36D) APPROACH GUARDRAIL ENDS:	**0**

(71) WATERWAY ADEQUACY: **9 - Bridge Above Flood Water Elevations**

Comments:
Plans show a high water elevation of 79.0 and a roadway crown elevation of 84.0. Bridge is at the low point of the sag curve. (NP 6/1/2018)

Previous notes:
Bridge Above Flood Water Elevations

(72) APPROACH ROADWAY ALIGNMENT: **8 - Equal to present desirable criteria**

Comments:
No substantial reduction in speed is necessary for traffic to safely cross the bridge (NP 6/1/2018).

Previous notes:
Minor Cracks
Material: Asphalt
72: No Speed Reduction Required

(113) SCOUR CRITICAL BRIDGES: **8 - Stable for scour conditions**

Comments:

CLASSIFICATION

(20) TOLL:	**3 - On Free Road**	(21) MAINT. RESPONSIBILITY:	**02 - County Highway Agency**
(22) OWNER:	**02 - County Highway Agency**	(26) FUNCTIONAL CLASS OF INVENTORY RTE:	**09 - Rural - Local**
(37) HISTORICAL SIGNIFICANCE:	**5 - Not eligible**	(100) STRAHNET HIGHWAY:	**Not a STRAHNET route**
(101) PARALLEL STRUCTURE:	**N - No parallel structure**	(102) DIRECTION OF TRAFFIC:	**2-way traffic**
(103) TEMPORARY STRUCTURE:		(104) HIGHWAY SYSTEM OF INVENTORY ROUTE:	**0 - Structure/Route is NOT on NHS**
(105) FEDERAL LANDS HIGHWAYS:	**0-Not Applicable**	(110) DESIGNATED NATIONAL NETWORK:	**Inventory route not on network**
(112) NBIS BRIDGE LENGTH:	**Yes**		

NAVIGATION DATA

(38) NAVIGATION CONTROL:	**0 - No navigation control on waterway (bridge permit not required)**	(39) NAVIGATION VERTICAL CLEAR:	**000.0**	**FT**
		(116) MINIMUM NAVIGATION VERT. CLEARANCE, VERT. LIFT BRIDGE:		**FT**
(111) PIER OR ABUTMENT PROTECTION:		(40) NAV HORIZONTAL CLEARANCE:	**0000.0**	**FT**

Inspector: Nathaniel Pfeiffer **Asset Name:** Copy of 79-00115
Inspection Date: 06/01/2018 **Facility Carried:** CR 750 N

Bridge Inspection Report

PROPOSED IMPROVEMENTS

(75A) TYPE OF WORK:	**31 - Replacement - Load/Geometry**	(95) ROADWAY IMPROVEMENT COST:	**$ 000067**
(75B) WORK DONE BY:	**1 - Work to be done by contract**	(96) TOTAL PROJECT COST:	**$ 000322**
		(97) YR OF IMPROVEMENT COST EST:	**2012**
(76) LENGTH OF IMPROVEMENT:	**000054 FT**	(114) FUTURE AVG DAILY TRAFFIC:	**00239**
(94) BRIDGE IMPROVEMENT COST:	**$ 000170**	(115) YR OF FUTURE ADT:	**2030**

Inspector: Nathaniel Pfeiffer
Inspection Date: 06/01/2018

Asset Name: Copy of 79-00115
Facility Carried: CR 750 N

Bridge Inspection Report

PHOTO 1

Description 6-1-2018 str 79-00115 - W abutment looking W

PHOTO 2

Description 6-1-2018 str 79-00115 - Alignment looking E

Inspector: Nathaniel Pfeiffer
Inspection Date: 06/01/2018

Asset Name: Copy of 79-00115
Facility Carried: CR 750 N

Bridge Inspection Report

PHOTO 3

Description 6-1-2018 str 79-00115 - Alignment looking W

PHOTO 4

Description 6-1-2018 str 79-00115 - Downstream channel looking S

Inspector: Nathaniel Pfeiffer **Asset Name:** Copy of 79-00115

Inspection Date: 06/01/2018 **Facility Carried:** CR 750 N

Bridge Inspection Report

PHOTO 5

Description 6-1-2018 str 79-00115 - N half E abutment looking E

PHOTO 6

Description 6-1-2018 str 79-00115 - N half W abutment looking W

Inspector: Nathaniel Pfeiffer
Inspection Date: 06/01/2018

Asset Name: Copy of 79-00115
Facility Carried: CR 750 N

Bridge Inspection Report

PHOTO 7

Description 6-1-2018 str 79-00115 - Profile looking SE

PHOTO 8

Description 6-1-2018 str 79-00115 - S coping looking E

Inspector: Nathaniel Pfeiffer
Inspection Date: 06/01/2018

Asset Name: Copy of 79-00115
Facility Carried: CR 750 N

Bridge Inspection Report

PHOTO 9

Description 6-1-2018 str 79-00115 - S half E abutment looking SE

PHOTO 10

Description 6-1-2018 str 79-00115 - S half W abutment looking W

Inspector: Nathaniel Pfeiffer
Inspection Date: 06/01/2018

Asset Name: Copy of 79-00115
Facility Carried: CR 750 N

Bridge Inspection Report

PHOTO 11

Description 6-1-2018 str 79-00115 - Top side condition looking SW

PHOTO 12

Description 6-1-2018 str 79-00115 - Upstream channel looking N

Inspector: Nathaniel Pfeiffer **Asset Name:** Copy of 79-00115
Inspection Date: 06/01/2018 **Facility Carried:** CR 750 N

Bridge Inspection Report

PHOTO 13

Description 6-1-2018 str 79-00115 - W abutment exposed piles looking N

PHOTO 14

Description 6-7-2018 str 79-00115 - S facia beam crack with rust staining looking W

Inspector: Nathaniel Pfeiffer
Inspection Date: 06/01/2018

Asset Name: Copy of 79-00115
Facility Carried: CR 750 N

Bridge Inspection Report

PHOTO 15

Description 6-7-2018 str 79-00115 - E end S facia beam looking E

PHOTO 16

Description 6-7-2018 str 79-00115 - N facia beam cracking looking W

Inspector: Nathaniel Pfeiffer
Inspection Date: 06/01/2018

Asset Name: Copy of 79-00115
Facility Carried: CR 750 N

Bridge Inspection Report

PHOTO 17

Description 6-7-2018 str 79-00115 - N facia beam spalling delamination looking W

PHOTO 18

Description 6-7-2018 str 79-00115 - S facia beam crack along S side with rust staining looking W

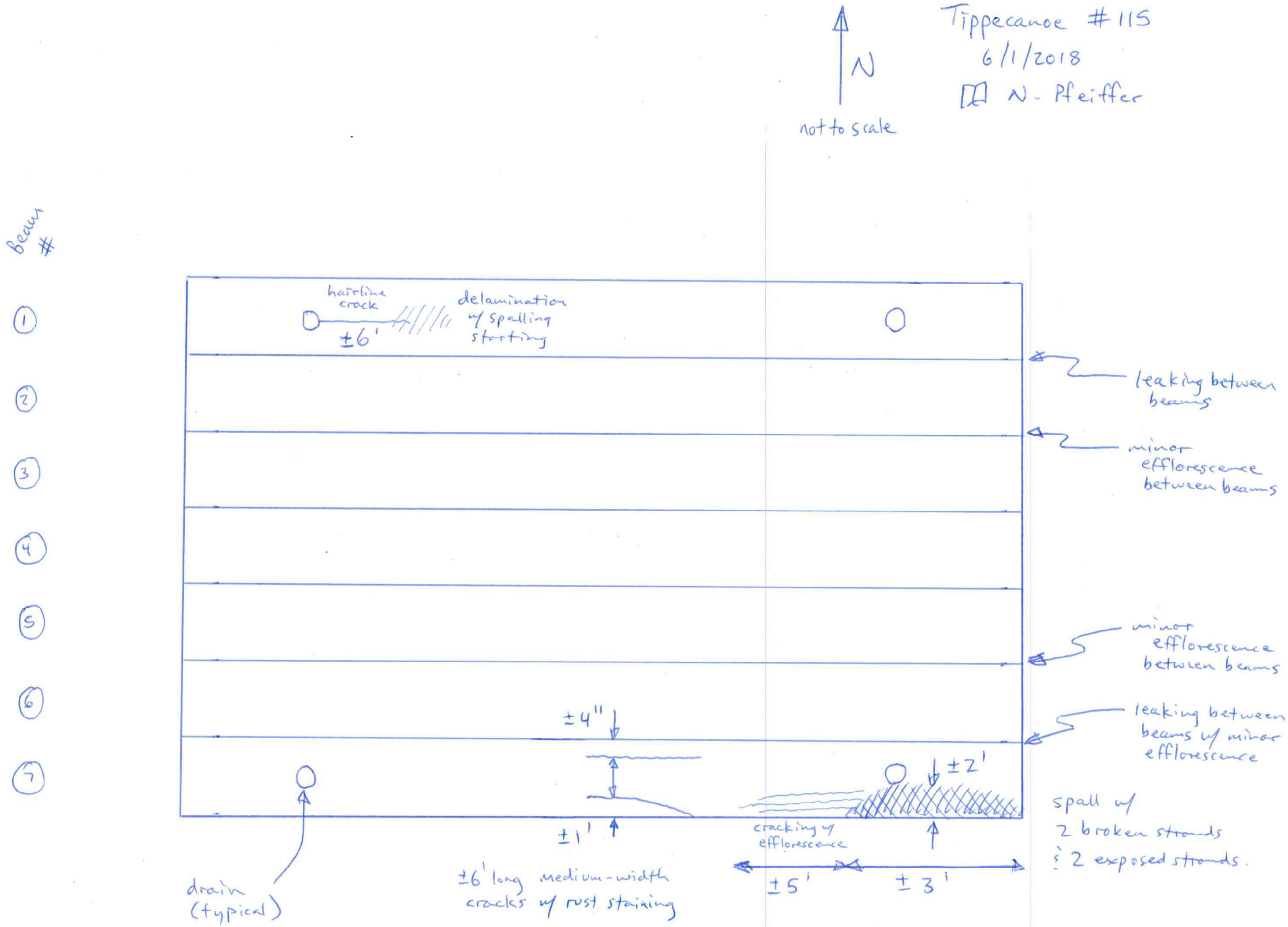

Tippecanoe #115
6/1/2018
N. Pfeiffer
N
not to scale
Beam #
1
2
3
4
5
6
7
hairline crack
±6'
delamination w/ spalling starting
leaking between beams
minor efflorescence between beams
minor efflorescence between beams
leaking between, beams w/ minor efflorescence
±4"
±1'
±2'
spall w/ 2 broken strands & 2 exposed strands.
cracking w/ efflorescence
±5'
±3'
drain (typical)
±6' long medium-width cracks w/ rust staining

Miscellaneous Asset Data

Copy of 7900080

Asset Management

Inv Type: **Inv #:** **RP:** **Offset**

Original RP Data Source **MAD_GIS_RP:**

17_LRS_ROUTE_ID: **17_LRS_ROUTE_MEASURE:**

Load Rating 2:

Has the dead load or the structural condition of the primary load carrying members changed since the last inspection? No

---

Extended Frequency: Submittal Date:

Inspector:

INDOT Reviewer:

This bridge has been accepted into the Extended Frequency Program.

Joints:

** Indicate location, type, and rating of lowest rated joint.*

No Joints Present

Comments:

Bearings:

** Indicate type, and rating of lowest rated bearing.*

N - No Bearing(s)

Comments:

Approach Slabs:

** Indicate if present & condition rating.*

N - No Approach Sla

Comments:

Paint

** Indicate if paint present , year painted & condition rating.*

N - No Paint Not Rated

Comments:

☐ Asset Type Has Changed

Scour POA? N

Comment:

Endangered Species

Bats: seen or heard under structure? * N

Birds/swallows/nests seen? Empty nests present? * N

** If yes, add one photo to the dropdown field*

BRIDGE Culvert Geometry

Barrel Length

Height

Width

Inspector: Nathaniel Pfeiffer

Inspection Date: 06/01/2018

Asset Name: Copy of 79-00115

Facility Carried: CR 750 N

Bridge Inspection Report

Date Reported: 06/08/2018

Priority: Green - 3

Work Code: Substructure Repair

Deficiency Description:

West abutment has exposed timber piles and voids below the bent cap.

Work Description:

Date Repairs Completed:

Maintenance Comments:

Stage: Open

PHOTO 1 Description 6-1-2018 str 79-00115 - N half W abutment looking W

Stage: Open

PHOTO 2 Description 6-1-2018 str 79-00115 - S half W abutment looking W

Inspector: Nathaniel Pfeiffer
Inspection Date: 06/01/2018

Asset Name: Copy of 79-00115
Facility Carried: CR 750 N

Bridge Inspection Report

Stage: Open

PHOTO 3 Description 6-1-2018 str 79-00115 - W abutment exposed piles looking N

Inspector: Nathaniel Pfeiffer

Inspection Date: 06/01/2018

Asset Name: Copy of 79-00115

Facility Carried: CR 750 N

Bridge Inspection Report

Date Reported: 06/08/2018

Priority: Green - 3

Work Code: Superstructure Repair

Deficiency Description:

North facia beam is cracked with delamination. South facia beam is cracked with rust staining and spalled with broken & exposed strands.

Work Description:

Date Repairs Completed:

Maintenance Comments:

Stage: Open

PHOTO 1 Description 6-7-2018 str 79-00115 - S facia beam crack with rust staining looking W

Stage: Open

PHOTO 2 Description 6-7-2018 str 79-00115 - E end S facia beam looking E

Inspector: Nathaniel Pfeiffer
Inspection Date: 06/01/2018

Asset Name: Copy of 79-00115
Facility Carried: CR 750 N

Bridge Inspection Report

Stage: Open

PHOTO 3 Description 6-7-2018 str 79-00115 - N facia beam cracking looking W

Stage: Open

PHOTO 5 Description 6-7-2018 str 79-00115 - S facia beam crack along S side with rust staining looking W

Stage: Open

PHOTO 4 Description 6-7-2018 str 79-00115 - N facia beam spalling delamination looking W

APPENDIX J. STEEL AND CONCRETE MATERIAL INFORMATION

GERDAU MUNCIE

REBAR COATING PLANT
1810 S MACEDONIA AVE.
MUNICE, IN 47302

IMPORTANT CERTIFICATION DOCUMENTS ATTACHED

GIVE TO SITE SUPERVISOR

XQNY :00 Scott   Ryan 5-643-3344   Mun 13688

GERDAU

Straight Bill of Lading

S. MACEDONIA AVE. MUNCIE, IN 47302 US

BOL No. 2819-0000018788

Shipment Doc. No. 9466461

Project: BOWEN LAB RESEARCH

RECEIVED, subject to the classification and tariffs in effect on the date of the issue of this Bill of Lading.

CONSIGNED TO
PURDUE UNIVERSITY
JOB IN PURDUE UNIV RESEARCH PROJECT
1040 SOUTH RIVER RD
WEST LAFAYETTE, IN, 47907

INVOICE TO
PURDUE UNIVERSITY
JOB IN PURDUE UNIV RESEARCH PROJECT
401 S GRANT ST
WEST LAFAYETTE, IN, 47907

SHIP DATE
14-JUN-18

CUST.ACCOUNT NO
100708896

APPROVAL CODE
EXMKNOTT

CONTRACT
40071166

CARRIER: 2819 GERDAU AMERISTEEL US INC
DESTINATION: SEE CONSIGNED TO
ROUTE: T-2819-IN-WEST LAFAYETTE
SPECIAL INSTRUCTIONS: MATL CERTS REQUIRED, SHARON NEMETH 765-494-2162, snemeth@purdue.edu

CAR / VEHICLE INITIALS: 48M9
DELIVERY ADDRESS: SEE CONSIGNED TO
DELIVERY CARRIER: 2819 GERDAU AMERISTEEL US INC

Freight Charges are to be PREPAID, unless marked Collect. Check Box if Collect. [ ]

CTRL CODE	PRODUCT	DESCRIPTION	GRADE BUNDLE ID	MILL	LENGTH	CUST PO # HEAT / BATCH	SALES ORDER # WEIGHT (LB)	ITEM # WEIGHT (KG)	DELIVERY # PCS	ITEM #
BLXQNX	BLXQNX	FABRICATION EPOXY Per Release 0006 Control Code XQNX #4 EPOXY	60 (420)		0	JOB#33	6600687	70	8112307572	10
				2819		XQNX0000/01	2,133 LB	968 KG	2133	
			TOTAL				2,133 LB	968 KG		

Received by (Consignee): ____________________ Date: ______________

Print Name : ____________________

Shippers Total Net Weight (LB)	2,133	AGENT
Shippers Total Net Weight (KG)	968	DATE

Gerdau Corporation Shipper, per ....
Permanent post office address of shipper
S. MACEDONIA AVE. MUNCIE IN 47302 US
Time of Day 06/14/2018 13:51:25

Subject to Section 7 of the conditions, if this shipment is to be delivered to the consignee without recourse on the consigner, the consignor shall sign the following statement. The carrier shall not make delivery of this shipment without payment of freight and all other lawful charges.

GERDAU
(SIGNATURE OF CONSIGNOR)

NOTE : To obtain allowance for shortage or damage, customer must advise shipper within 5 days of receipt of material. Customer has absolutely nopermission to refabricate material which will result in a back charge toshipper without writt consent of shipper.
Gerdau warrants the performance of the FIBC bags only to the point of initial removal from the delivery trailer by Customer. Thereafter, Customer fully releases and discharges Gerdau, its officers, agents and employees from any liability or any loss, cost, damage, expense, injury or death arising from or in any manner connected with Customer's receipt and use of the FIBC bags.

Left Gerdau	Arrived on Jobsite	Departed Jobsite	Driver / Date
Time ____ : ____ AM / PM	____ : ____ AM / PM	____ : ____ AM / PM	____________

9466461

Gerdau

Muncie Reinforcing

FABRICATOR'S HEAT NUMBER IDENTIFICATION
OF REINFORCING BARS

County ______

Project Number__BOWEN LAB RESEARCH MATERIAL___

Supplier ____ GERDAU

Number _____40071166_____

Fabricator____ GERDAU

Bar List Number(s)___ XQNX___

Drawing Number ____#4 EPOXY____

Contractor___PURDUE UNIVERSITY ___

The following table lists heat numbers and mill marks so that each heat number involved may be positively identified and separated, if necessary, at destination.

BAR LIST OR ORDER NO.	BAR TYPE OR MARK	BAR SIZE	GRADE	WEIGHT (Lbs.)	MANUFACTURER (Mill Mark)	HEAT NO.	Powder MFR	Powder Lot Number
XQNX	EPOXY	13	420	1069	AKS	5717327202	3M SCOTCHKOTE	000008D19B
	EPOXY	13	420	1064	AKS	5717442602	3M SCOTCHKOTE	000008D18C

Date 6/14/18

Misty Dusinger

Signature of Authorized Representative

Daily Report

SPC - Daily Report - 05/24/2018

Work Center	Start Date	Shift	Quality Control Inspector
54000002	05/23/2018 03:30:00 pm	2nd Shift	Ryan Webb/Eric Rutherford
54000002	05/24/2018 01:00:00 am	3rd Shift	None
54000002	05/24/2018 05:00:00 am	1st Shift	Jade Byrne/Josh Brown
54000002	05/24/2018 03:30:00 pm	2nd Shift	Ryan Webb/Eric Rutherford

Manufacturer	Batch Number
EPOXY POWDER 3M SCOTCHKOTE 413 1500LB.	000008D19C
EPOXY POWDER 3M SCOTCHKOTE 413 1500LB.	000008D19B

Produced Batches	
5614097812	5717065914
5717264714	5717324112
5717327212	

Mill Batches			
5614097802	5717065904	5717119002	5717267702
5717321404	5717324102	5717327202	5717356802
5717370002	5717374702	5717375502	5717383902

Batch Number	Inspection Lot

Actual Calibration (high)	Actual Calibration (low)	Bend Test	Cure Time	Gel Time	Hand Held Holidays	Inline Holidays	Temperature
9.78	4.97	PASS	33.25	5.39	1	3	450
9.80	4.84	PASS	35.13	5.47	2	6	450
9.78	4.97	PASS	35.44	5.94	1.5	3.25	450
9.80	4.81	PASS	35.26	5.41	1.66	5.66	450
9.80	4.82	PASS	34.57	5.35	0.5	2	450

This letter is to certify that the epoxy-coated material listed above has been coated per the powder manufacturer's recommendations and conforms to ASTM D3963, ASTM A775, AASHTO M-284, and the Gerdau Amersiteel coating division's quality assurance program. The supporting data for coating thickness, continuity, flexibility and material composition are attached.

Measurement Distribution

Note: The measurement distribution and statistics are for the entire production on 05/24/2018

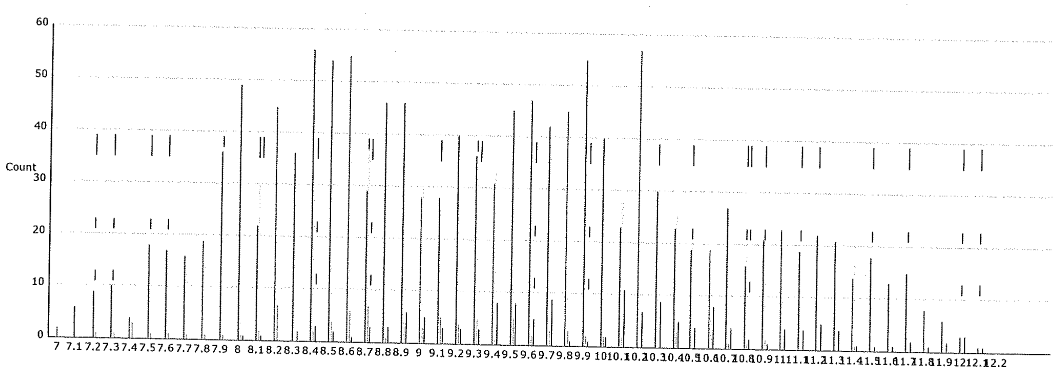

Readings Size	Count	Average	Min	Max	Standard Deviation SD	-2 SD	+2 SD
16MM	1,410.00	9.38	7.00	12.10	1.14	7.10	11.66
13MM	1,020.00	9.40	7.00	12.20	1.09	7.21	11.59
10MM	90.00	9.03	7.20	11.40	0.92	7.20	10.87
32MM	150.00	10.03	8.00	12.10	0.95	8.13	11.92
	2670	9.41	7	12.2	1.12	7.18	11.65

Epoxy Coating
Applied At
Muncie, Indiana

Misty Drsinger

3M

Certificate of Analysis

3M Angleton

1508 East Cedar St.
Angleton, TX 77515

Customer:	GERDAU
3M Invoice Number:	YF62602
Customer PO Number:	4509285298
Date certificate prepared:	7-May-18

The 3M product listed below was produced in accordance with standard manufacturing processes for the product in effect at the time of manufacture. This is to certify that the lot(s) of SCOTCHKOTE 413 Fusion Bonded Epoxy Coating manufactured by 3M at Angleton, Texas, meets the requirements of the following standards. ASTM A 775/A 775M-07b (2014), ASTM A 884/A884M-14, ASTM A1078/A1078M-12 Type 1, AASHTO M284-09 and AASHTO M254-06 (2010). This coating, when applied to steel or iron in the U.S., meets the Buy America provision as set forth in FHWA 23 CFR 635.410 Section 1041(a) of the ISTEA. The Lot(s) of Scotchkote™413 is (are) chemically the same Material that was tested and certified by the third party lab.

3M Stock Number:	Catalog Number:	Quantity:	
80-6116-1551-1	413 SCOTCHKOTE RESIN 1800 LB. SACK	39,600	LB
UPC Number:			
00051128612231			
Shelf Life ³ months from date of ɪanufacture	Storage Condition for this Product: General Warehouse Storage (≤+27°C/80°F)		

Test Property:	Test Method Number	Min Spec.	Max Spec	Units
Gel Time Average 380°F (193°C) ± 3°	TM-001	5.0	9.0	SECONDS
Passed Through 325 Screen (45 Micron)	TM-003	32	42	%
Moisture Content-Computrac Max 4000 XL	TM-004		0.5	%

Lot Number:	Date of Manufacture:	Expiration Date:	Batch Size In Lb.	Gel Time Average 380° F (193° C)+/- 3°	Passed Through 325 Screen (45 Micron) (Avge)	Moisture Content-Computrac Max 4000 XL (Avge)
8D18C	18-Apr-18	18-Oct-18		7.3	39	0.1
8D19A	19-Apr-18	19-Oct-18		6.8	35	0.2
8D19B	19-Apr-18	19-Oct-18		7.0	39	0.1
8D19C	19-Apr-18	19-Oct-18		7.1	40	0.0
⁰D20A	20-Apr-18	20-Oct-18		7.3	37	0.2

Authorized By:	Title :	Date Signed:	
Lisa Skinner	Quality Control	7-May-18	
Lisa J Skinner			
Please contact your 3M Customer Service Representative if you have any questions.			

Warranty and Limited Remedy: Unless stated otherwise in 3M's product literature, packaging inserts or product packaging for individual products, 3M warrants that each 3M product meets the applicable 3M specifications at the time 3M ships the product. Individual products may have additional or different warranties as stated on product literature, package inserts or product packages. **3M MAKES NO OTHER WARRANTIES OR CONDITIONS, EXPRESS OR IMPLIED, INCLUDING, BUT NOT LIMITED TO, ANY IMPLIED WARRANTY OR CONDITION OF MERCHANTABILITY OR FITNESS FOR A PARTICULAR PURPOSE OR ANY IMPLIED WARRANTY OR CONDITION ARISING OUT OF A COURSE OF DEALING, CUSTOM OR USAGE OF TRADE.** User is responsible for determining whether the 3M product is fit for a particular purpose and suitable for user's application. If the 3M product is shown to be nonconforming within the warranty period, your exclusive remedy and 3M's sole obligation will be, at 3M's option, to replace the nonconforming 3M product or refund the purchase price.

Limitation of Liability: Except where prohibited by law, 3M will not be liable for any loss or damage arising from the 3M product, whether direct, indirect, special, incidental or consequential, regardless of the legal theory asserted, including warranty, contract, negligence or strict liability.

NOTARY PUBLIC STATE OF TEXAS
KAREN J. OBENHAUS
Notary Public, State of Texas
Comm. Expires 03-26-2022
Notary ID 129760105

The foregoing document was acknowledged before me this 7th day of May 2018

Notary Public

GERDAU

US-ML-KNOXVILLE
1919 TENNESSEE AVENUE N. W.
KNOXVILLE, TN 37921
USA

CERTIFIED M RIAL TEST REPORT

Page 1/1

CUSTOMER SHIP TO	CUSTOMER BILL TO	GRADE	SHAPE / SIZE	DOCUMEN
GERDAU AMERISTEEL US INC 1810 S MACEDONIA AVENUE MUNCIE,IN 47302 USA		60 (420) TMX	Rebar / #4 (13MM)	0000020422

LENGTH	WEIGHT	HEAT / BATCH
40'00"	48,096 LB	57173272/02

SALES ORDER	CUSTOMER MATERIAL N°	SPECIFICATION / DATE or REVISION
4509288485/000110		ASTM A615/A615M-16

CUSTOMER PURCHASE ORDER NUMBER	BILL OF LADING	DATE
	1326-0000082660	05/04/2018

CHEMICAL COMPOSITION

C %	Mn %	P %	S %	Si %	Cu %	Ni %	Cr %	Mo %	Sn %	V %	CEqyA706 %
0.29	0.61	0.001	0.051	0.18	0.32	0.13	0.11	0.022	0.005	0.003	0.42

MECHANICAL PROPERTIES

YS PSI	YS MPa	UTS PSI	UTS MPa	G/L Inch	G/L mm
88300	609	103770	716	8.000	200.0

MECHANICAL PROPERTIES

Elong. %	BendTest
10.00	OK

GEOMETRIC CHARACTERISTICS

%Light %	Def Hgt Inch	Def Gap Inch	DefSpace Inch
4.50	0.030	0.099	0.311

COMMENTS / NOTES

The above figures are certified chemical and physical test records as contained in the permanent records of company. We certify that these data are correct and in compliance with specified requirements. This material, including the billets, was melted and manufactured in the USA. CMTR complies with EN 10204 3.1.

Bhaskay
BHASKAR YALAMANCHILI
QUALITY DIRECTOR
Phone: (409) 769-1014 Email: Bhaskar.Yalamanchili@gerdau.com

Jim Hall
JIM HALL
QUALITY ASSURANCE MGR.
Phone: 865-202-5972 Email: Jim.hall@gerdau.com

GERDAU

US-ML-KNOXVILLE
1919 TENNESSEE AVENUE N. W.
KNOXVILLE, TN 37921
USA

CERTIFIED MATERIAL TEST REPORT

Page 1/1

CUSTOMER SHIP TO	CUSTOMER BIL	GRADE	SHAPE / SIZE	DOCUMENT ID:
GERDAU AMERISTEEL US INC 1810 S MACEDONIA AVENUE MUNCIE,IN 47302 USA		60 (420) TMX	Rebar / #4 (13MM)	0000022349

LENGTH	WEIGHT	HEAT / BATCH
60'00"	13,466 LB	57174426/02

SALES ORDER	CUSTOMER MATERIAL N°
4509439682/000160	

SPECIFICATION / DATE or REVISION
ASTM A615/A615M-16

CUSTOMER PURCHASE ORDER NUMBER	BILL OF LADING	DATE
	1326-0000084282	06/05/2018

CHEMICAL COMPOSITION

C %	Mn %	P %	S %	Si %	Cu %	Ni %	Cr %	Mo %	Sn %	V %	CEqyA706 %
0.26	0.56	0.006	0.040	0.21	0.34	0.12	0.14	0.024	0.009	0.004	0.38

MECHANICAL PROPERTIES

YS PSI	YS MPa	UTS PSI	UTS MPa	G/L Inch	G/L mm
81470	562	97280	671	8.000	200.0

MECHANICAL PROPERTIES

Elong. %	BendTest
11.30	OK

GEOMETRIC CHARACTERISTICS

%Light %	Def Hgt Inch	Def Gap Inch	DefSpace Inch
4.79	0.032	0.125	0.330

COMMENTS / NOTES

The above figures are certified chemical and physical test records as contained in the permanent records of company. We certify that these data are correct and in compliance with specified requirements. This material, including the billets, was melted and manufactured in the USA. CMTR complies with EN 10204 3.1.

Bhaskar

BHASKAR YALAMANCHILI
QUALITY DIRECTOR
Phone: (409) 267-1071 Email: Bhaskar.Yalamanchili@gerdau.com

Jim Hall

JIM HALL
QUALITY ASSURANCE MGR.
Phone: 865-202-5972 Email: Jim.hall@gerdau.com

Muncie Reinforcing & Coating
1810 S. Macedonia Ave
Muncie, IN 47302-
Phone: (765)286-5472 FAX: (765)288-1631

JOB NUMBER	RELEASE NUMBER	REQ. DELIVERY DATE	PAGE
40071166	0006		1C

JOB NAME: BOWEN LAB RESEARCH MATERIAL	CC: XQNX
CUSTOMER: PURDUE UNIVERSITY	BY: RSW

MATERIAL TYPE	REFERENCE	DRAWING ID	DESCRIPTION
Rebar, Grade 60, Epoxy			#4 EPOXY

COMMENT PAGE

Requested Date: 06/15/18 Sales Rep: Credit APP'L:

Billing Information

S/O	Item	Final (I=Item / J=Job)
60	RE	P

Ticket #
Bar Support PO # 6/15
Wire Mesh PO #
Accessory PO # MUN 613689
Invoice #

Estimate Segment: 40071166.SP / Simple
Reason Code: 0 Part of Contract (Default)

XQNX

Contact Information

Contact Name: SHARON NEMETH
Jobsite Phone:
Mobile Phone:
Office Phone: (765) 494-2162
Jobsite Fax:
Office Fax:
Email Address:

Routing

ENGR MGR LOAD 0070 39
SHOP
SALES
DIV MGR
BILLING

Delivery Address

~~1040 SOUTH RIVER RD~~
7508 NORTH 100 WEST
West Lafayette In
47906
West Lafayette, IN 47907

Delivery Instructions

Call Ryan for further info

Ordered By: RYAN
If Shop Shortage/Error:
Orig. Rel/CC: / XQNX
If Change Order:
Change Order #:

Shipped Date:
Engr HR: 0

Ref. Item:
Ship Location:
Delivery Charge:

Epoxy

Detailer Comments

Muncie Reinforcing & Coating
1810 S. Macedonia Ave
Muncie, IN 47302-
Phone: (765)286-5472 FAX: (765)288-1631

JOB NUMBER	RELEASE NUMBER	REQ. DELIVERY DATE	PAGE
40071166	0006		2C

JOB NAME	CC
BOWEN LAB RESEARCH MATERIAL	XQNX

CUSTOMER	BY
PURDUE UNIVERSITY	RSW

MATERIAL TYPE	REFERENCE	DRAWING ID	DESCRIPTION
Rebar, Grade 60, Epoxy			#4 EPOXY

COMMENT PAGE

Manning Details - FAB Loc: MUN

Shear	Crew
16	25

TB(1)	TB(2)	TB(3)	TB(4)	Total	Crew
0	0	0	0	0	0

RB(1)	RB(2)	RB(3)	RB(4)	Total	Crew
0	0	0	0	0	0

Auto	Crew
0	0

Misc	Crew
0	0

DB(1)	DB(2)	DB(3)	DB(4)	Total	Crew
0	0	0	0	0	0

Bar List Weight: 2,133 This Release Contains: RE

Muncie Reinforcing & Coating
1810 S. Macedonia Ave
Muncie, IN 47302-
Phone: (765)286-5472 FAX: (765)288-1631

JOB NUMBER	RELEASE NUMBER	REQ. DELIVERY DATE	PAGE
40071166	0006		1 of 1

JOB NAME: BOWEN LAB RESEARCH MATERIAL
CC: XQNX
CUSTOMER: PURDUE UNIVERSITY
BY: RSW

TERIAL TYPE	REFERENCE	DRAWING ID	DESCRIPTION
bar, Grade 60, Epoxy			#4 EPOXY

Itm	Qty	Size	Length	Mark	Shape	LB	A	B	C	D	E	F/R	G	H	J	K	O	BC
1	40	4	40-00			1069												01
2	65	4	24-06			1064												00
	105.					2133.												

Total Weight: 2,133 LB

Longest Length: 40-00

WEIGHT SUMMARY

Rebar, Grade 60, Epoxy

SIZE	TOTAL ITEMS	TOTAL PIECES	TOTAL LB	STRAIGHT ITEMS	STRAIGHT PIECES	STRAIGHT LB	LIGHT BENDING ITEMS	LIGHT BENDING PIECES	LIGHT BENDING LB	HEAVY BENDING ITEMS	HEAVY BENDING PIECES	HEAVY BENDING LB
4	2	105	2,133 ✓	2	105	2,133	0	0	0	0	0	0
	2	105	2,133	2	105	2,133	0	0	0	0	0	0

Total Weight: 2,133 LB

Longest Length: 40-00

Ctrl Code	Bar Size	Grade	Ctg.	Item Tag #	Quantity	BL Weight	Mill Tag ID	Mill Batch	ORIGINAL BATCH	POWDER BATCH	POWDER MANUFACTURER
XQNX	13	420	E	3978890001	20	535	12819540000020028668	5717327212	5717327202	000008D19B	EPOXY POWDER 3M SCOTCHKOTE 413 1500LB.
XQNX	13	420	E	3978890001	20	534	12819540000020028670	5717327212	5717327202	000008D19B	EPOXY POWDER 3M SCOTCHKOTE 413 1500LB.
XQNX	13	420	E	3978890002	65	1064	12819540000020028965	5717442612	5717442602	000008D18C	EPOXY POWDER 3M SCOTCHKOTE 413 1500LB.

Gerdau

Master Bundle Check List

Session: 284361 Fab Shop: Muncie Fab Date: 6/7/2018 Muncie
Run: 397889 Shift: Shift 1 Caption:

XQNX

Job Name: BOWEN LAB RESEARCH MATERIAL Job: 40071166 Description: #4 EPOXY
Customer: PURDUE UNIVERSITY Release: 0006 Ship Date: 6/15/2018 XQNX

Master Bundle	Load	Color / Shape	Size	Grade	Coating	Bend Class	No. Of Tags	Pieces	LB	Longest Length
1K	________		4	60	Epx	1	1	40	1,069	40-00
2K	________		4	60	Epx	00	1	65	1,064	24-06
				Control Code: XQNX		Total:	2	105	2,133	40-00

Remit To: P.O. Box 7048, Group #2
Indianapolis, IN 46207-7048

Concrete Delivery Ticket

imi
Irving Materials, Inc.

Plant #	Ticket Number	Truck	Load Size	Mix	Slump	Use	Date	Customer
118	11849590	2322	6.25cy	9080IN	4.00	BRIDGE DECK	07/23/18	92914

Sold To	Tax Code	Driver	Project No.	Order No.
PURDUE UNIVERSITY	7	GREG JOHNS	0	1380

Delivery Address	P.O. Number
1040 W 750 N 2 TRUCKS ON EACH SIDE 1ST & 3RD TRUCKS PAST HARRISON THRU CURVE ON LEFT 2ND & 4TH TRUCKS 50 TO 600 T/L TO 225 T/R TO 750 T/R	4500612039

Job No.
GLORIA MULLI

Time Printed 07:00

Load Quantity	Total	Ordered Quantity	Product Code	Product Description	Unit Price	Amount
6.25	6.25cy	25.00cy	9080IN	CLASS C STONE		
6.25		1.00/y	18401	RETARDER 1		
				ENVIRONMENTAL FEE		

imi
www.irvmat.com

Water Added At Customer's Request					Total No. Gallons	Slump Meter Reading				

On Job Time	Finish Pour Time

Subtotal
Tax
Total

PROPERTY DAMAGE RELEASE / WARNING - Irritating To The Skin and Eyes

Dear Customer - The Seller is not responsible for slumps, strength or quality of concrete to which water or any other material has been added by the purchaser or at his request.

The undersigned hereby authorizes Irving Materials, Inc. to use private property for making the delivery shown here on and assumes full responsibility for any damage or injury due to the premises.

The undersigned agrees to reimburse said Company for loss of time and equipment by reason of such delivery and also to identify and save harmless said Company from any and all claims, demands and suits for or on account of or in any manner caused by or arising from private property delivery.

The undersigned assumes responsibility for a suitable roadway from public highway to point of delivery and is responsible for any needed wrecker service charges as a result.

SAFETY WARNING: Keep away from children. Contains Portland Cement. Irritating to the skin and eyes. Wear rubber boots, gloves and eye protection. Prolonged contact may cause burns. In case of contact with skin or eyes, flush thoroughly with water. If irritation persists, get medical attention. For additional information regarding the HAZARDS OF READY MIX CONCRETE, consult the Material Data Safety Sheet (MSDS) available upon request.

PRODUCT NOTICE: Seller will not be held responsible for the final appearance of exposed aggregate, integral coloring, stamped and decorative surfacing, and all other forms of architectural and design concrete.

DELIVERY NOTICE: Seller assumes no responsibility for deliveries beyond the public right of way. Buyer assumes responsibility for damages including but not limited to curb, sidewalk, driveway, or any property of the contractor or property owner or agents.

NOTICE: MY SIGNATURE BELOW INDICATES THAT I HAVE READ THE SAFETY AND HEALTH WARNING NOTICE AND ACCEPTANCE OF THE LOAD.

Release, Load and Terms Accepted By:
X

4000367

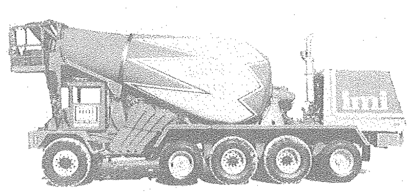

11849590

Concrete - Sand - Gravel - Stone "We're Proud Of Our Work" General Office (317) 326-3101

CUSTOMER COPY

Remit To: P.O. Box 7048, Group #2
Indianapolis, IN 46207-7048

Concrete Delivery Ticket

imi
Irving Materials, Inc.

Plant #	Ticket Number	Truck	Load Size	Mix	Slump	Use	Date	Customer
118	11849590	2322	6.25cy	9000IN	4.00	BRIDGE DECK	07/23/18	92914

Sold To	Tax Code	Driver	Project No.	Order No.
PURDUE UNIVERSITY	Z	GREG JOHNS	0	1300

Delivery Address	P.O. Number
1048 W 750 N 2 TRUCKS ON EACH SIDE 1ST & 3RD TRUCKS PAST HARRISON THRU CURVE ON LEFT 2ND & 4TH TRUCKS 50 TO 600 T/L TO 225 T/R TO 750 T/R	4500612039

Job No.
GLORIA MULLI

Time Printed 07:00

Load Quantity	Total	Ordered Quantity	Product Code	Product Description	Unit Price	Amount
6.25	6.25cy	25.00cy	9000IN	CLASS C STONE		
6.25		1.00/y	10401	RETARDER 1		
				ENVIRONMENTAL FEE		

imi
www.irvmat.com

Water Added At Customer's Request					Total No. Gallons	Slump Meter Reading				

On Job Time	Finish Pour Time

Subtotal
Tax
Total

PROPERTY DAMAGE RELEASE / WARNING - Irritating To The Skin and Eyes

Dear Customer - The Seller is not responsible for slumps, strength or quality of concrete to which water or any other material has been added by the purchaser or at his request.

The undersigned hereby authorizes Irving Materials, Inc. to use private property for making the delivery shown here on and assumes full responsibility for any damage or injury due to the premises.

The undersigned agrees to reimburse said Company for loss of time and equipment by reason of such delivery and also to identify and save harmless said Company from any and all claims, demands and suits for or on account of or in any manner caused by or arising from private property delivery.

The undersigned assumes responsibility for a suitable roadway from public highway to point of delivery and is responsible for any needed wrecker service charges as a result.

SAFETY WARNING: Keep away from children. Contains Portland Cement. Irritating to the skin and eyes. Wear rubber boots, gloves and eye protection. Prolonged contact may cause burns. In case of contact with skin or eyes, flush thoroughly with water. If irritation persists, get medical attention. For additional information regarding the HAZARDS OF READY MIX CONCRETE, consult the Material Data Safety Sheet (MSDS) available upon request.

PRODUCT NOTICE: Seller will not be held responsible for the final appearance of exposed aggregate, integral coloring, stamped and decorative surfacing, and all other forms of architectural and design concrete.

DELIVERY NOTICE: Seller assumes no responsibility for deliveries beyond the public right of way. Buyer assumes responsibility for damages including but not limited to curb, sidewalk, driveway, or any property of the contractor or property owner or agents.

NOTICE: MY SIGNATURE BELOW INDICATES THAT I HAVE READ THE SAFETY AND HEALTH WARNING NOTICE AND ACCEPTANCE OF THE LOAD.

Release, Load and Terms Accepted By:
X

4000367

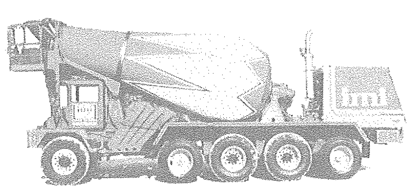

11849590

Concrete - Sand - Gravel - Stone "We're Proud Of Our Work" General Office (317) 326-3101

DRIVER COPY

Truck	Driver	User	Disp Ticket Num	Ticket ID	Time	Date
2322	2315	user	11849590	0	7:14	7/23/18

Load Size	Mix Code	Returned	Qty	Mix Age	Seq	Load ID
6.25 CYDS	9080IN				D	60430

Description	Design Qty	Adj.T	Required	Batched	Actual Wat
Batch: 1 -----	Start: 7:14:43		End:	------- Time (hh:mm:ss):	: : -----
STONE-8	1725 lb		10835 lb	10740 lb	6 gl
SAND-23	1225 lb		7924 lb	7920 lb	32 gl
Buzzi	658 lb		4113 lb	4120 lb	
WATER	249.0 lb	#	1234.4 lb	1224.0 lb	146.7 gl
MICROAIR	.50 /C		20.56 oz	20.50 oz	
DELVO	3.00 /C	#	123.38 oz	124.00 oz	

Actual Num Batches: 1

Load 24013 lb Design W/C: 0.378 Water/Cement: 0.375 A Design 186.5 gl Actual 185.2 gl To Add: 1.3 gl

Slump: 4.00 in Water in Truck: 0.0 lb Adjust Water: 0.0 lb / Load Trim Water: 0.0 lb / CYD

Remit To: P.O. Box 7048, Group #2
Indianapolis, IN 46207-7048

Concrete Delivery Ticket

imi
Irving Materials, Inc.

Plant #	Ticket Number	Truck	Load Size	Mix	Slump	Use	Date	Customer
118	11849595	2336	6.25cy	9080IN	4.00	BRIDGE DECK	07/23/18	92914

Sold To	Tax Code	Driver	Project No.	Order No.
PURDUE UNIVERSITY	Z	DAN WRIGHT	0	1380

Delivery Address	P.O. Number
1040 W 750 N 2 TRUCKS ON EACH SIDE 1ST & 3RD TRUCKS PAST HARRISON THRU CURVE ON LEFT 2ND & 4TH TRUCKS 50 TO 600 T/L TO 225 T/R TO 750 T/R	4500612039

Job No. GLORIA MULLI

Time Printed 07:30

Load Quantity	Total	Ordered Quantity	Product Code	Product Description	Unit Price	Amount
6.25	12.50cy	25.00cy	9080IN	CLASS C STONE		
6.25		1.00/y	18401	RETARDER 1		
				ENVIRONMENTAL FEE		

2

www.irvmat.com

Water Added At Customer's Request					Total No. Gallons	Slump Meter Reading				

On Job Time	Finish Pour Time

Subtotal
Tax
Total

PROPERTY DAMAGE RELEASE / WARNING - Irritating To The Skin and Eyes

Dear Customer - The Seller is not responsible for slumps, strength or quality of concrete to which water or any other material has been added by the purchaser or at his request.

The undersigned hereby authorizes Irving Materials, Inc. to use private property for making the delivery shown here on and assumes full responsibility for any damage or injury due to the premises.

The undersigned agrees to reimburse said Company for loss of time and equipment by reason of such delivery and also to identify and save harmless said Company from any and all claims, demands and suits for or on account of or in any manner caused by or arising from private property delivery.

The undersigned assumes responsibility for a suitable roadway from public highway to point of delivery and is responsible for any needed wrecker service charges as a result.

SAFETY WARNING: Keep away from children. Contains Portland Cement. Irritating to the skin and eyes. Wear rubber boots, gloves and eye protection. Prolonged contact may cause burns. In case of contact with skin or eyes, flush thoroughly with water. If irritation persists, get medical attention. For additional information regarding the HAZARDS OF READY MIX CONCRETE, consult the Material Data Safety Sheet (MSDS) available upon request.

PRODUCT NOTICE: Seller will not be held responsible for the final appearance of exposed aggregate, integral coloring, stamped and decorative surfacing, and all other forms of architectural and design concrete.

DELIVERY NOTICE: Seller assumes no responsibility for deliveries beyond the public right of way. Buyer assumes responsibility for damages including but not limited to curb, sidewalk, driveway, or any property of the contractor or property owner or agents.

NOTICE: MY SIGNATURE BELOW INDICATES THAT I HAVE READ THE SAFETY AND HEALTH WARNING NOTICE AND ACCEPTANCE OF THE LOAD.

Release, Load and Terms Accepted By:
X

4000372

11849595

Concrete - Sand - Gravel - Stone "We're Proud Of Our Work" General Office (317) 326-3101

CUSTOMER COPY

Remit To: P.O. Box 7048, Group #2
Indianapolis, IN 46207-7048

Concrete Delivery Ticket

imi
Irving Materials, Inc.

Plant #	Ticket Number	Truck	Load Size	Mix	Slump	Use	Date	Customer
118	11849595	2236	6.25cy	90A0IN	4.00	BRIDGE DECK	07/23/18	92914

Sold To	Tax Code	Driver	Project No.	Order No.
PURDUE UNIVERSITY	Z	DAN WRIGHT	0	1380

Delivery Address	P.O. Number
1048 W 750 N 2 TRUCKS ON EACH SIDE 1ST & 3RD TRUCKS PAST HARRISON THRU CURVE ON LEFT 2ND & 4TH TRUCKS 50 TO 600 T/L TO 225 T/R TO 750 T/R	4500612039

Job No. GLORIA MULLI

Time Printed 07:30

Load Quantity	Total	Ordered Quantity	Product Code	Product Description	Unit Price	Amount
6.25	12.50cy	25.00cy	90A0IN	CLASS C STONE		
6.25		1.00/y	18401	RETARDER 1		
				ENVIRONMENTAL FEE		

imi
www.irvmat.com

Water Added At Customer's Request					Total No. Gallons	Slump Meter Reading				

On Job Time	Finish Pour Time

Subtotal
Tax
Total

PROPERTY DAMAGE RELEASE / WARNING - Irritating To The Skin and Eyes

Dear Customer - The Seller is not responsible for slumps, strength or quality of concrete to which water or any other material has been added by the purchaser or at his request.

The undersigned hereby authorizes Irving Materials, Inc. to use private property for making the delivery shown here on and assumes full responsibility for any damage or injury due to the premises.

The undersigned agrees to reimburse said Company for loss of time and equipment by reason of such delivery and also to identify and save harmless said Company from any and all claims, demands and suits for or on account of or in any manner caused by or arising from private property delivery.

The undersigned assumes responsibility for a suitable roadway from public highway to point of delivery and is responsible for any needed wrecker service charges as a result.

SAFETY WARNING: Keep away from children. Contains Portland Cement. Irritating to the skin and eyes. Wear rubber boots, gloves and eye protection. Prolonged contact may cause burns. In case of contact with skin or eyes, flush thoroughly with water. If irritation persists, get medical attention. For additional information regarding the HAZARDS OF READY MIX CONCRETE, consult the Material Data Safety Sheet (MSDS) available upon request.

PRODUCT NOTICE: Seller will not be held responsible for the final appearance of exposed aggregate, integral coloring, stamped and decorative surfacing, and all other forms of architectural and design concrete.

DELIVERY NOTICE: Seller assumes no responsibility for deliveries beyond the public right of way. Buyer assumes responsibility for damages including but not limited to curb, sidewalk, driveway, or any property of the contractor or property owner or agents.

NOTICE: MY SIGNATURE BELOW INDICATES THAT I HAVE READ THE SAFETY AND HEALTH WARNING NOTICE AND ACCEPTANCE OF THE LOAD.

Release, Load and Terms Accepted By:

X

4000372

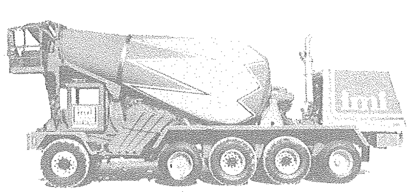

11849595

Concrete - Sand - Gravel - Stone "We're Proud Of Our Work" General Office (317) 326-3101

DRIVER COPY

Truck	Driver	User	Disp Ticket Num	Ticket ID	Time	Date
2336	2794	user	11849595	0	7:47	7/23/18

Load Size	Mix Code	Returned	Qty	Mix Age	Seq	Load ID
6.25 CYDS	9080IN				D	60435

Description	Design Qty	Adj.T	Required	Batched	Actual Wat
Batch: 1 -----	Start: 7:47:32		End:	------- Time (hh:mm:ss):	: : -----
STONE-8	1725 lb		10835 lb	10760 lb	6 gl
SAND-23	1225 lb		7924 lb	7940 lb	32 gl
Buzzi	658 lb		4113 lb	4100 lb	
WATER	255.0 lb	#	1271.9 lb	1264.0 lb	151.5 gl
MICROAIR	.50 /C		20.56 oz	21.00 oz	
DELVO	3.00 /C	#	123.38 oz	128.00 oz +	

Actual Num Batches: 1
Load 24073 lb Design W/C: 0.388 Water/Cement: 0.387 A Design 191.0 gl Actual 190.1 gl To Add: 0.9 gl
Slump: 4.00 in Water in Truck: 0.0 lb Adjust Water: 0.0 lb / Load Trim Water: 0.0 lb / CYD

Remit To: P.O. Box 7048, Group #2
Indianapolis, IN 46207-7048

Concrete Delivery Ticket

imi
Irving Materials, Inc.

Plant #	Ticket Number	Truck	Load Size	Mix	Slump	Use	Date	Customer
118	11849598	2347	6.25cy	9080IN	4.00	BRIDGE DECK	07/23/18	92914

Sold To	Tax Code	Driver	Project No.	Order No.
PURDUE UNIVERSITY	7	PARKER MITCHELL	0	1300

Delivery Address	P.O. Number
1040 W 750 N 2 TRUCKS ON EACH SIDE 1ST & 3RD TRUCKS PAST HARRISON THRU CURVE ON LEFT 2ND & 4TH TRUCKS 50 TO 600 T/L TO 225 T/R TO 750 T/R	4500612039

Job No.
GLORIA MULLI

Time Printed 07:49

Load Quantity	Total	Ordered Quantity	Product Code	Product Description	Unit Price	Amount
6.25	18.75cy	25.00cy	9080IN	CLASS C STONE		
6.25		1.00/y	18401	RETARDER 1		
				ENVIRONMENTAL FEE		

3

imi
www.irvmat.com

Water Added At Customer's Request				Total No. Gallons	Slump Meter Reading				

On Job Time	Finish Pour Time

Subtotal
Tax
Total

PROPERTY DAMAGE RELEASE / WARNING - Irritating To The Skin and Eyes

Dear Customer - The Seller is not responsible for slumps, strength or quality of concrete to which water or any other material has been added by the purchaser or at his request.

The undersigned hereby authorizes Irving Materials, Inc. to use private property for making the delivery shown here on and assumes full responsibility for any damage or injury due to the premises.

The undersigned agrees to reimburse said Company for loss of time and equipment by reason of such delivery and also to identify and save harmless said Company from any and all claims, demands and suits for or on account of or in any manner caused by or arising from private property delivery.

The undersigned assumes responsibility for a suitable roadway from public highway to point of delivery and is responsible for any needed wrecker service charges as a result.

SAFETY WARNING: Keep away from children. Contains Portland Cement. Irritating to the skin and eyes. Wear rubber boots, gloves and eye protection. Prolonged contact may cause burns. In case of contact with skin or eyes, flush thoroughly with water. If irritation persists, get medical attention. For additional information regarding the HAZARDS OF READY MIX CONCRETE, consult the Material Data Safety Sheet (MSDS) available upon request.

PRODUCT NOTICE: Seller will not be held responsible for the final appearance of exposed aggregate, integral coloring, stamped and decorative surfacing, and all other forms of architectural and design concrete.

DELIVERY NOTICE: Seller assumes no responsibility for deliveries beyond the public right of way. Buyer assumes responsibility for damages including but not limited to curb, sidewalk, driveway, or any property of the contractor or property owner or agents.

NOTICE: MY SIGNATURE BELOW INDICATES THAT I HAVE READ THE SAFETY AND HEALTH WARNING NOTICE AND ACCEPTANCE OF THE LOAD.

Release, Load and Terms Accepted By:
X

4000375

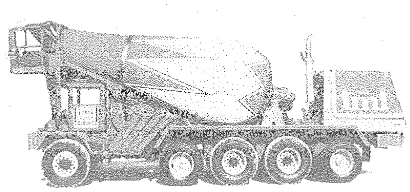

11849598

Concrete - Sand - Gravel - Stone "We're Proud Of Our Work" General Office (317) 326-3101

CUSTOMER COPY

Remit To: P.O. Box 7048, Group #2
Indianapolis, IN 46207-7048

Concrete Delivery Ticket

imi
Irving Materials, Inc.

Plant #	Ticket Number	Truck	Load Size	Mix	Slump	Use	Date	Customer
118	11849598	2347	6.25cy	9080IN	4.00	BRIDGE DECK	07/23/18	92914

Sold To	Tax Code	Driver	Project No.	Order No.
PURDUE UNIVERSITY	7	PARKER MITCHELL	0	1380

Delivery Address	P.O. Number
1040 W 750 N 2 TRUCKS ON EACH SIDE 1ST & 3RD TRUCKS PAST HARRISON THRU CURVE ON LEFT 2ND & 4TH TRUCKS 50 TO 600 T/L TO 225 T/R TO 750 T/R	4500612039

Job No.
GLORIA MULLI

Time Printed 07:49

Load Quantity	Total	Ordered Quantity	Product Code	Product Description	Unit Price	Amount
6.25	18.75cy	25.00cy	9080IN	CLASS C STONE		
6.25		1.00/y	18401	RETARDER 1		
				ENVIRONMENTAL FEE		

imi
www.irvmat.com

Water Added At Customer's Request				Total No. Gallons	Slump Meter Reading				

On Job Time	Finish Pour Time

Subtotal
Tax
Total

PROPERTY DAMAGE RELEASE / WARNING - Irritating To The Skin and Eyes

Dear Customer - The Seller is not responsible for slumps, strength or quality of concrete to which water or any other material has been added by the purchaser or at his request.

The undersigned hereby authorizes Irving Materials, Inc. to use private property for making the delivery shown here on and assumes full responsibility for any damage or injury due to the premises.

The undersigned agrees to reimburse said Company for loss of time and equipment by reason of such delivery and also to identify and save harmless said Company from any and all claims, demands and suits for or on account of or in any manner caused by or arising from private property delivery.

The undersigned assumes responsibility for a suitable roadway from public highway to point of delivery and is responsible for any needed wrecker service charges as a result.

SAFETY WARNING: Keep away from children. Contains Portland Cement. Irritating to the skin and eyes. Wear rubber boots, gloves and eye protection. Prolonged contact may cause burns. In case of contact with skin or eyes, flush thoroughly with water. If irritation persists, get medical attention. For additional information regarding the HAZARDS OF READY MIX CONCRETE, consult the Material Data Safety Sheet (MSDS) available upon request.

PRODUCT NOTICE: Seller will not be held responsible for the final appearance of exposed aggregate, integral coloring, stamped and decorative surfacing, and all other forms of architectural and design concrete.

DELIVERY NOTICE: Seller assumes no responsibility for deliveries beyond the public right of way. Buyer assumes responsibility for damages including but not limited to curb, sidewalk, driveway, or any property of the contractor or property owner or agents.

NOTICE: MY SIGNATURE BELOW INDICATES THAT I HAVE READ THE SAFETY AND HEALTH WARNING NOTICE AND ACCEPTANCE OF THE LOAD.

Release, Load and Terms Accepted By:
X

4000375

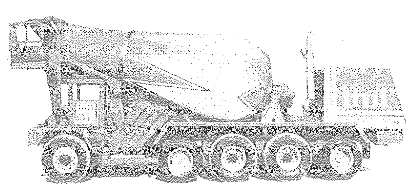

* 1 1 8 4 9 5 9 8 *

Concrete - Sand - Gravel - Stone "We're Proud Of Our Work" General Office (317) 326-3101

DRIVER COPY

Truck	Driver	User	Disp Ticket Num	Ticket ID	Time	Date
2347	3667	user	11849598	0	8:12	7/23/18

Load Size	Mix Code	Returned	Qty	Mix Age	Seq	Load ID
6.25 CYDS	9080IN				D	60438

Description	Design Qty	Adj.T	Required	Batched	Actual Wat
Batch: 1 -----	Start: 8:12:33		End:	------- Time (hh:mm:ss):	: : -----
STONE-8	1725 lb		10835 lb	10760 lb	6 gl
SAND-23	1225 lb		7924 lb	7920 lb	32 gl
Buzzi	658 lb		4113 lb	4120 lb	
WATER	274.9 lb		1396.2 lb	1386.0 lb	166.1 gl
MICROAIR	.50 /C		20.56 oz	20.50 oz	
DELVO	3.00 /C	#	123.38 oz	120.00 oz	

Actual Num Batches: 1

Load 24195 lb Design W/C: 0.418 Water/Cement: 0.414 A Design 205.9 gl Actual 204.6 gl To Add: 1.3 gl

Slump: 4.00 in Water in Truck: 0.0 lb Adjust Water: 0.0 lb / Load Trim Water: 0.0 lb / CYD

Remit To: P.O. Box 7048, Group #2
Indianapolis, IN 46207-7048

Concrete Delivery Ticket

imi
Irving Materials, Inc.

Plant #	Ticket Number	Truck	Load Size	Mix	Slump	Use	Date	Customer
118	11849599	2332	6.25cy	9080IN	4.00	BRIDGE DECK	07/23/18	92914

Sold To	Tax Code	Driver	Project No.	Order No.
PURDUE UNIVERSITY	Z	DOUG PHEBUS	0	1380

Delivery Address	P.O. Number
1040 W 750 N 2 TRUCKS ON EACH SIDE 1ST & 3RD TRUCKS PAST HARRISON THRU CURVE ON LEFT 2ND & 4TH TRUCKS 50 TO 600 T/L TO 225 T/R TO 750 T/R	4500612039

Job No.
GLORIA MULLI

Time Printed 08:16

Load Quantity	Total	Ordered Quantity	Product Code	Product Description	Unit Price	Amount
6.25	25.00cy	25.00cy	9080IN	CLASS C STONE		
6.25		1.00/y	18401	RETARDER 1		
				ENVIRONMENTAL FEE		

4

www.irvmat.com

Water Added At Customer's Request					Total No. Gallons	Slump Meter Reading				

On Job Time	Finish Pour Time

Subtotal
Tax
Total

PROPERTY DAMAGE RELEASE / WARNING - Irritating To The Skin and Eyes

Dear Customer - The Seller is not responsible for slumps, strength or quality of concrete to which water or any other material has been added by the purchaser or at his request.

The undersigned hereby authorizes Irving Materials, Inc. to use private property for making the delivery shown here on and assumes full responsibility for any damage or injury due to the premises.

The undersigned agrees to reimburse said Company for loss of time and equipment by reason of such delivery and also to identify and save harmless said Company from any and all claims, demands and suits for or on account of or in any manner caused by or arising from private property delivery.

The undersigned assumes responsibility for a suitable roadway from public highway to point of delivery and is responsible for any needed wrecker service charges as a result.

SAFETY WARNING: Keep away from children. Contains Portland Cement. Irritating to the skin and eyes. Wear rubber boots, gloves and eye protection. Prolonged contact may cause burns. In case of contact with skin or eyes, flush thoroughly with water. If irritation persists, get medical attention. For additional information regarding the HAZARDS OF READY MIX CONCRETE, consult the Material Data Safety Sheet (MSDS) available upon request.

PRODUCT NOTICE: Seller will not be held responsible for the final appearance of exposed aggregate, integral coloring, stamped and decorative surfacing, and all other forms of architectural and design concrete.

DELIVERY NOTICE: Seller assumes no responsibility for deliveries beyond the public right of way. Buyer assumes responsibility for damages including but not limited to curb, sidewalk, driveway, or any property of the contractor or property owner or agents.

NOTICE: MY SIGNATURE BELOW INDICATES THAT I HAVE READ THE SAFETY AND HEALTH WARNING NOTICE AND ACCEPTANCE OF THE LOAD.

Release, Load and Terms Accepted By:
X

4000376

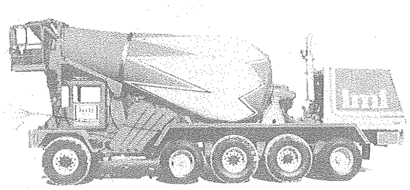

11849599

Concrete - Sand - Gravel - Stone "We're Proud Of Our Work" **General Office (317) 326-3101**

CUSTOMER COPY

Remit To: P.O. Box 7048, Group #2
Indianapolis, IN 46207-7048

Concrete Delivery Ticket

imi
Irving Materials, Inc.

Plant #	Ticket Number	Truck	Load Size	Mix	Slump	Use	Date	Customer
110	11849599	2332	6.25cy	9080IN	4.00	BRIDGE DECK	07/23/10	92914

Sold To	Tax Code	Driver	Project No.	Order No.
PURDUE UNIVERSITY	Z	DOUG PHEBUS	0	1300

Delivery Address	P.O. Number
1040 W 750 N 2 TRUCKS ON EACH SIDE 1ST & 3RD TRUCKS PAST HARRISON THRU CURVE ON LEFT 2ND & 4TH TRUCKS 50 TO 600 T/L TO 225 T/R TO 750 T/R	4500612039

Job No.
GLORIA MULLI

Time Printed 08:16

Load Quantity	Total	Ordered Quantity	Product Code	Product Description	Unit Price	Amount
6.25	25.00cy	25.00cy	9080IN	CLASS C STONE		
6.25		1.00/y	18401	RETARDER 1		
				ENVIRONMENTAL FEE		

www.irvmat.com

Water Added At Customer's Request					Total No. Gallons	Slump Meter Reading				

On Job Time	Finish Pour Time

Subtotal
Tax
Total

PROPERTY DAMAGE RELEASE / WARNING - Irritating To The Skin and Eyes

Dear Customer - The Seller is not responsible for slumps, strength or quality of concrete to which water or any other material has been added by the purchaser or at his request.

The undersigned hereby authorizes Irving Materials, Inc. to use private property for making the delivery shown here on and assumes full responsibility for any damage or injury due to the premises.

The undersigned agrees to reimburse said Company for loss of time and equipment by reason of such delivery and also to identify and save harmless said Company from any and all claims, demands and suits for or on account of or in any manner caused by or arising from private property delivery.

The undersigned assumes responsibility for a suitable roadway from public highway to point of delivery and is responsible for any needed wrecker service charges as a result.

SAFETY WARNING: Keep away from children. Contains Portland Cement. Irritating to the skin and eyes. Wear rubber boots, gloves and eye protection. Prolonged contact may cause burns. In case of contact with skin or eyes, flush thoroughly with water. If irritation persists, get medical attention. For additional information regarding the HAZARDS OF READY MIX CONCRETE, consult the Material Data Safety Sheet (MSDS) available upon request.

PRODUCT NOTICE: Seller will not be held responsible for the final appearance of exposed aggregate, integral coloring, stamped and decorative surfacing, and all other forms of architectural and design concrete.

DELIVERY NOTICE: Seller assumes no responsibility for deliveries beyond the public right of way. Buyer assumes responsibility for damages including but not limited to curb, sidewalk, driveway, or any property of the contractor or property owner or agents.

NOTICE: MY SIGNATURE BELOW INDICATES THAT I HAVE READ THE SAFETY AND HEALTH WARNING NOTICE AND ACCEPTANCE OF THE LOAD.

Release, Load and Terms Accepted By:
X

4000376

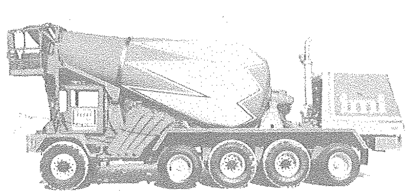

11849599

Concrete - Sand - Gravel - Stone "We're Proud Of Our Work" General Office (317) 326-3101

DRIVER COPY

Truck	Driver	User	Disp Ticket Num	Ticket ID	Time	Date
2332	1076	user	11849599	57582	8:18	7/23/18

Load Size	Mix Code	Returned	Qty	Mix Age	Seq	Load ID
6.25 CYDS	9080IN				D	60439

Description	Design Qty	Adj.T	Required	Batched	Actual Wat
Batch: 1 -----	Start: 8:18:21		End: 8:22:39	------- Time (hh:mm:ss): 00 : 04 : 18 -----	
STONE-8	1725 lb		10835 lb	10760 lb	6 gl
SAND-23	1225 lb		7924 lb	7920 lb	32 gl
Buzzi	658 lb		4113 lb	4110 lb	
WATER	274.9 lb		1396.2 lb	1388.0 lb	166.3 gl
MICROAIR	.50 /C		20.56 oz	20.50 oz	
DELVO	3.00 /C	#	123.38 oz	124.00 oz	

Actual Num Batches: 1

Load 24187 lb Design W/C: 0.418 Water/Cement: 0.416 A Design 205.9 gl Actual 204.8 gl To Add: 1.0 gl

Slump: 4.00 in Water in Truck: 0.0 lb Adjust Water: 0.0 lb / Load Trim Water: 0.0 lb / CYD

APPENDIX K. DETERIORATED CAPACITY CURVES

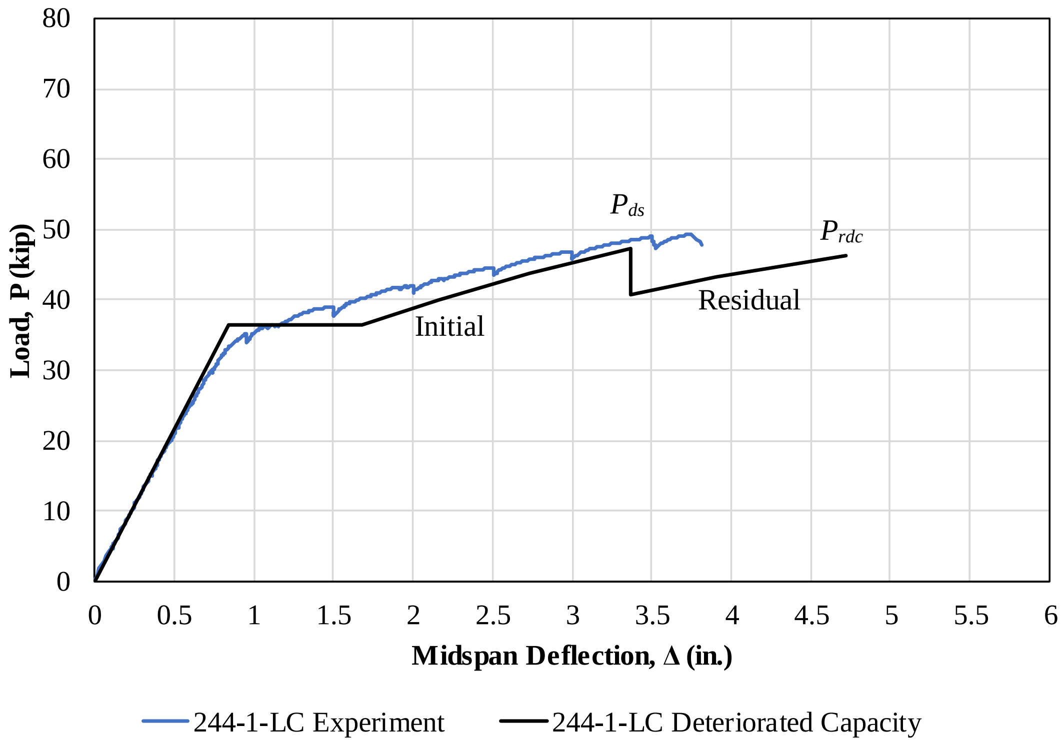

Figure K.1: Specimen 244-1-LC Deteriorated Capacity Load vs. Deflection

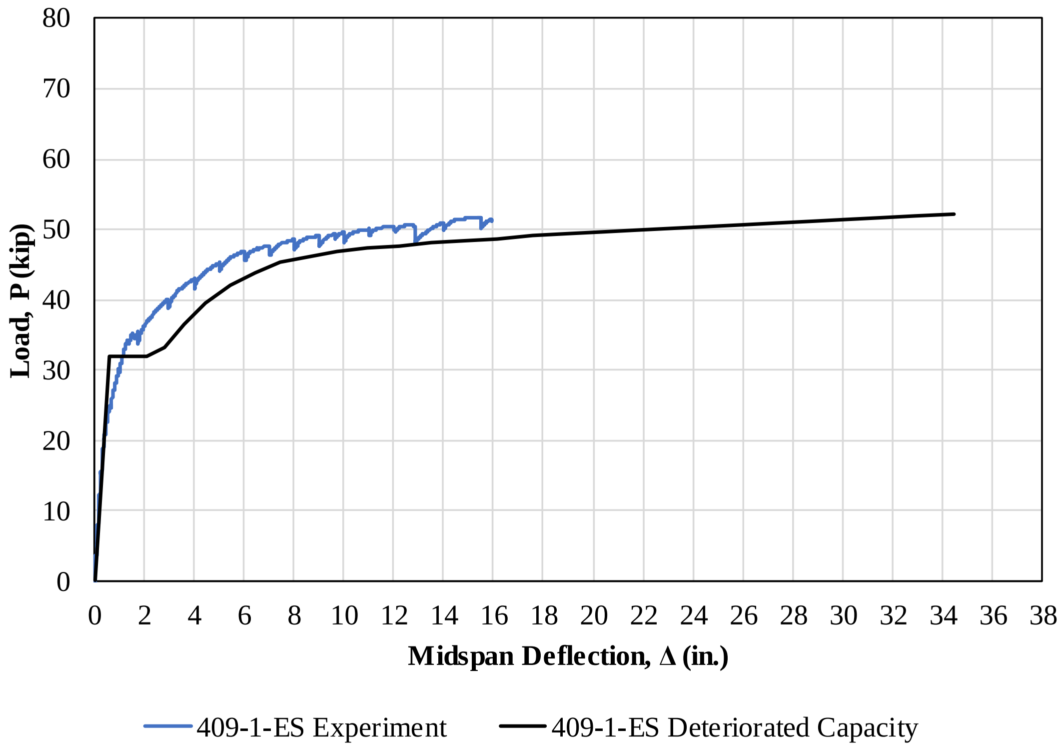

Figure K.2: Specimen 409-1-ES Deteriorated Capacity Load vs. Deflection

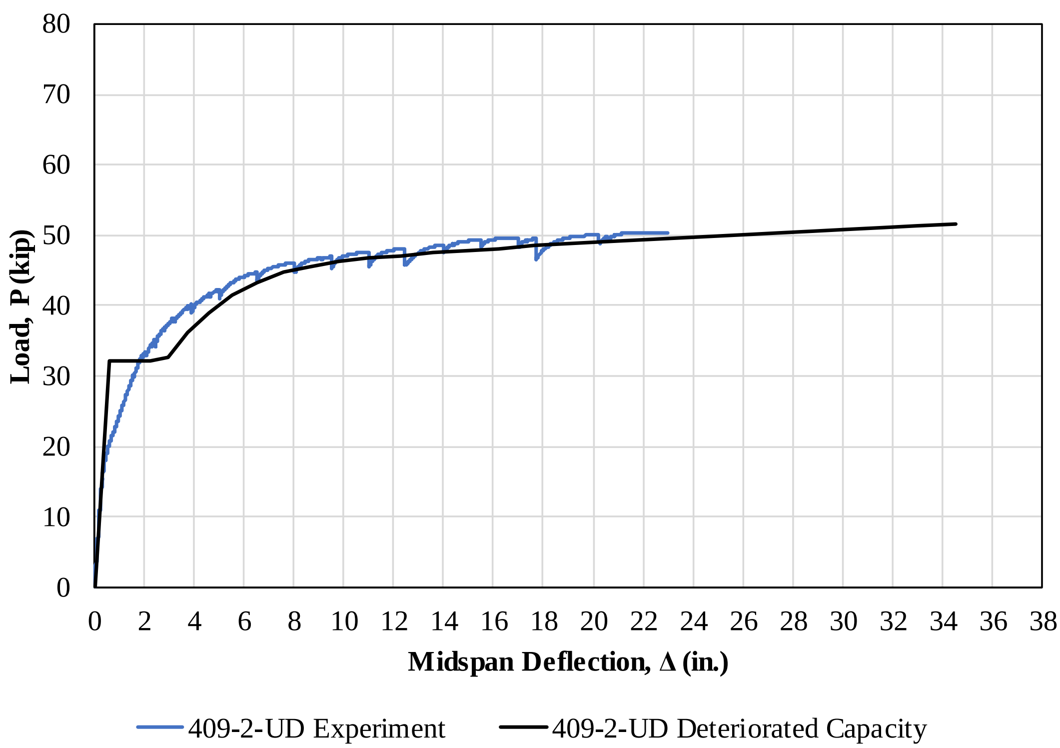

Figure K.3: Specimen 409-2-UD Deteriorated Capacity Load vs. Deflection

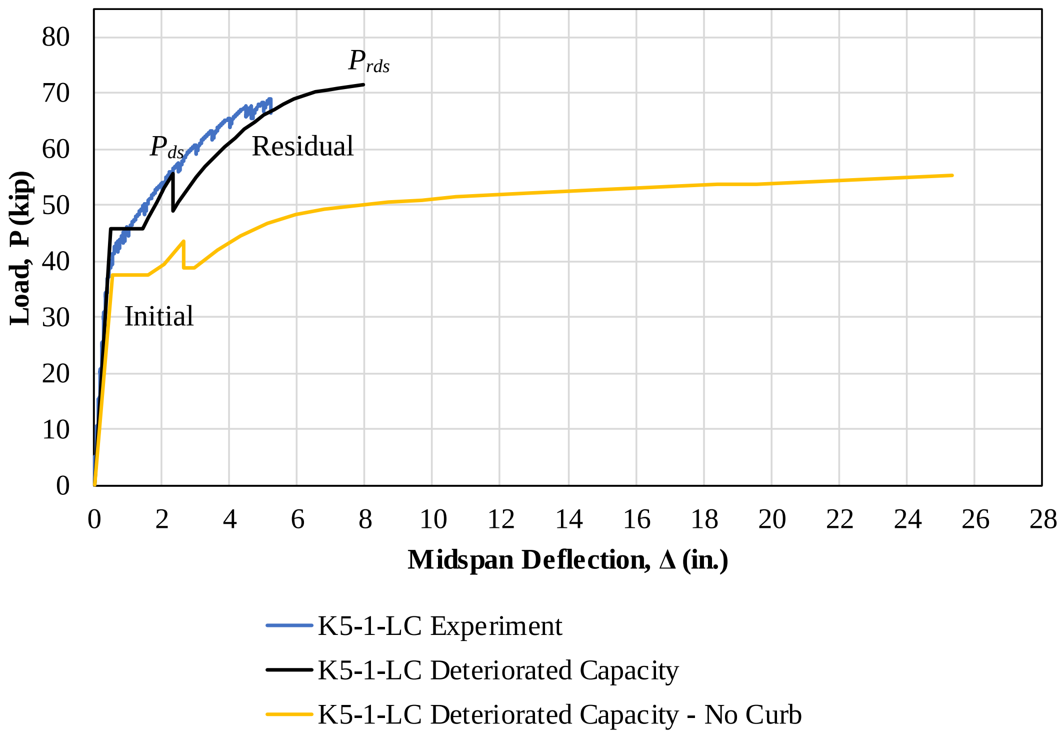

Figure K.4: Specimen K5-1-LC Deteriorated Capacity Load vs. Deflection

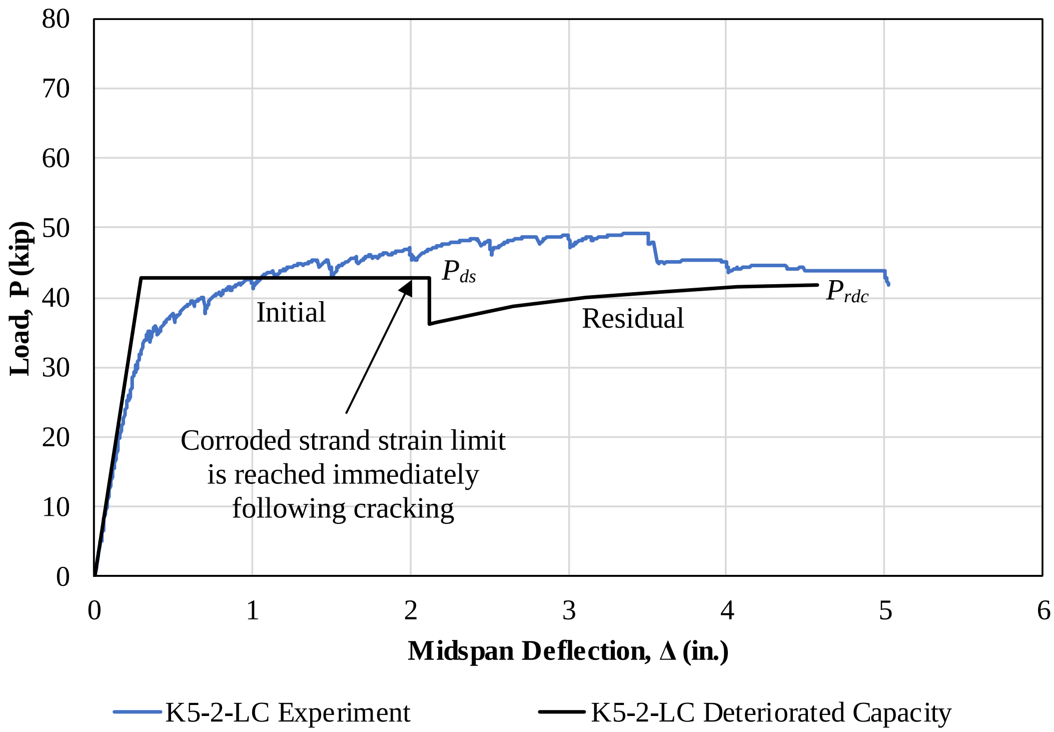

Figure K.5: Specimen K5-2-LC Deteriorated Capacity Load vs. Deflection

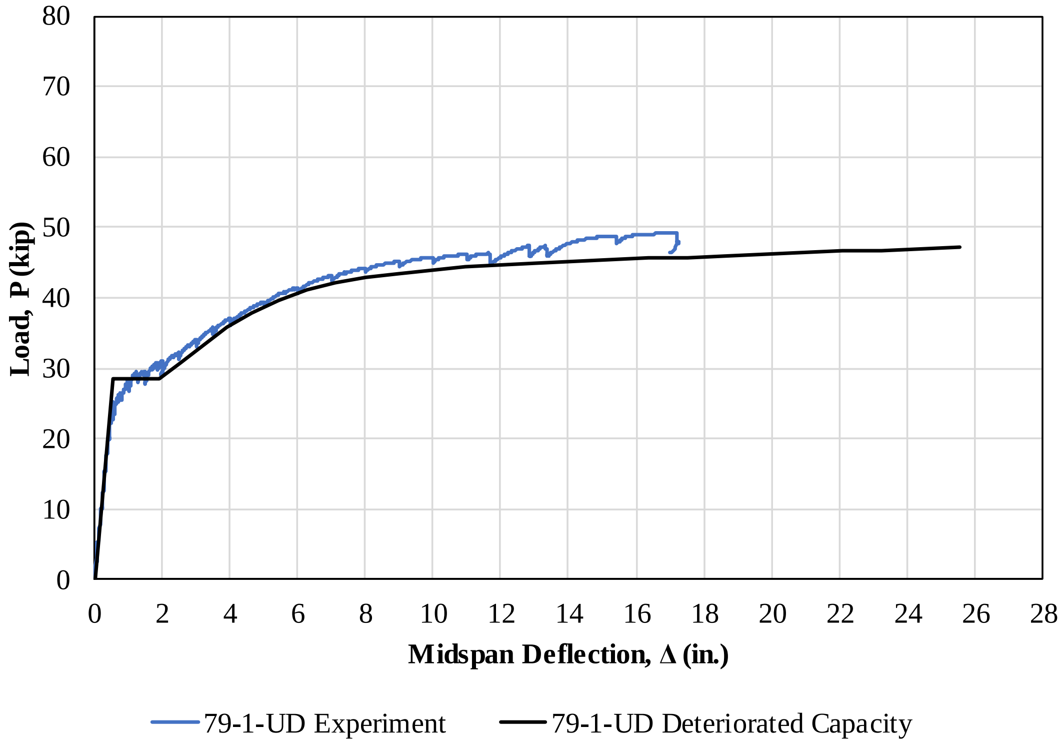

Figure K.6: Specimen 79-1-UD Deteriorated Capacity Load vs. Deflection

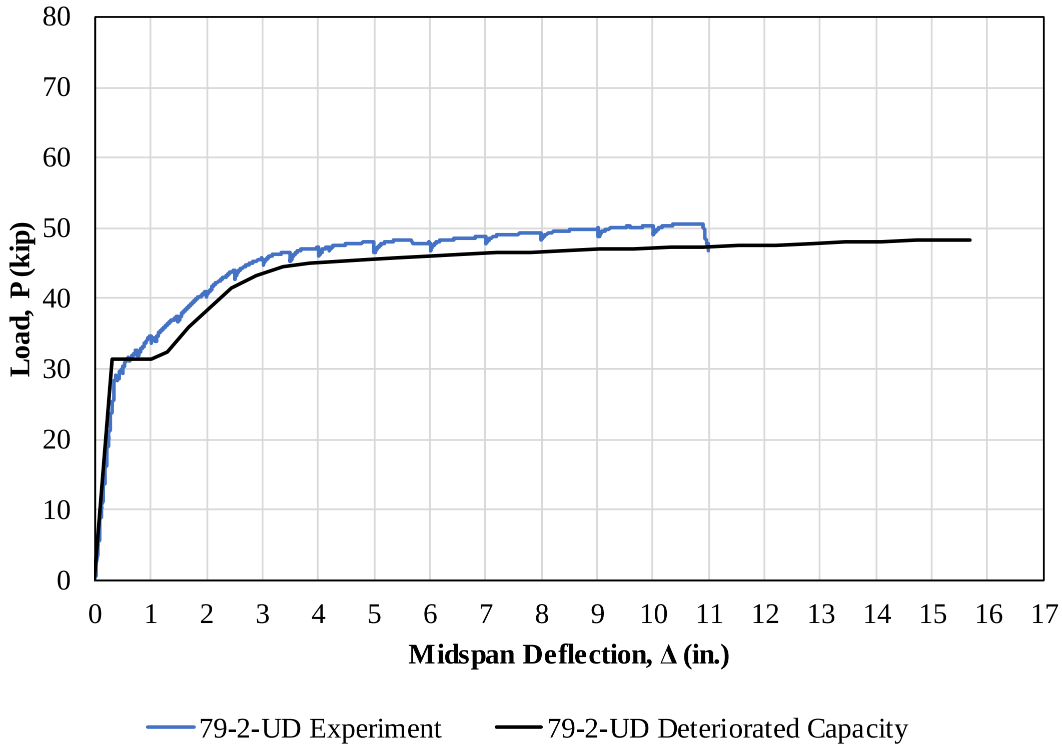

Figure K.7: Specimen 79-2-UD Deteriorated Capacity Load vs. Deflection

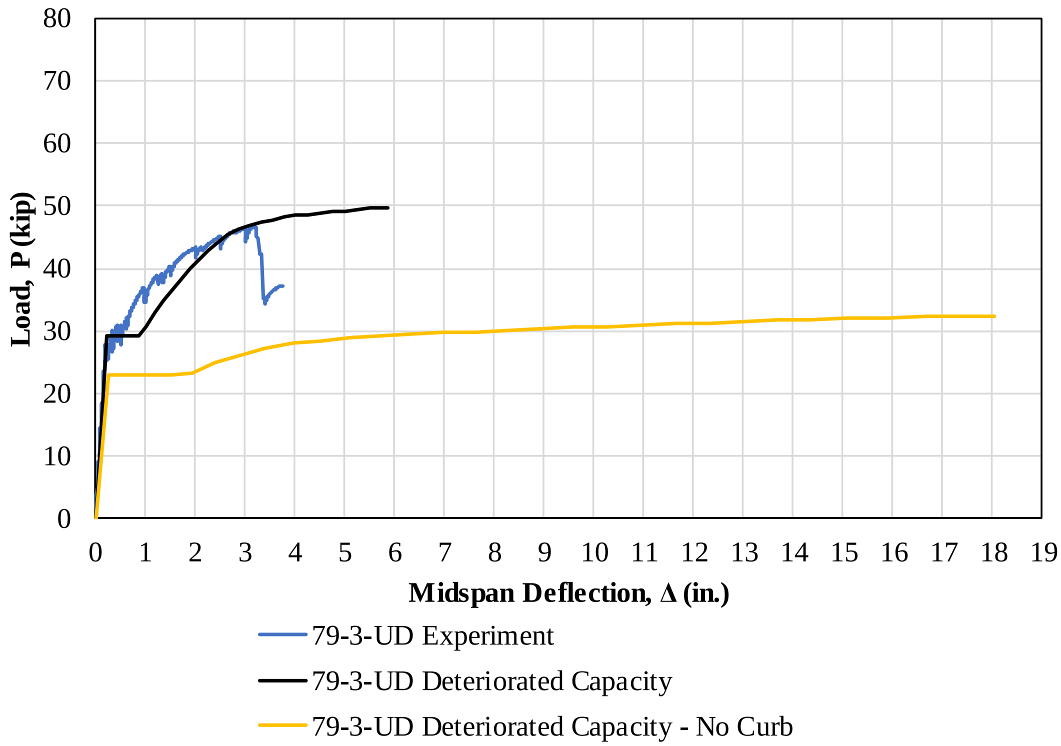

Figure K.8: Specimen 79-3-UD Deteriorated Capacity Load vs. Deflection

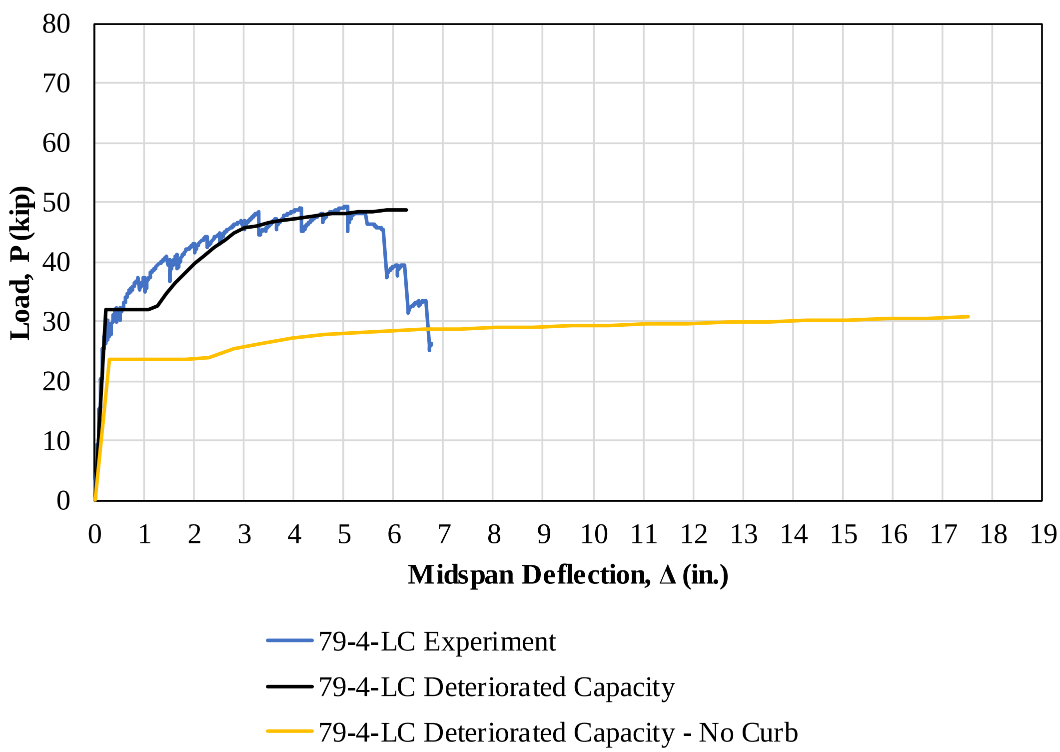

Figure K.9: Specimen 79-4-LC Deteriorated Capacity Load vs. Deflection

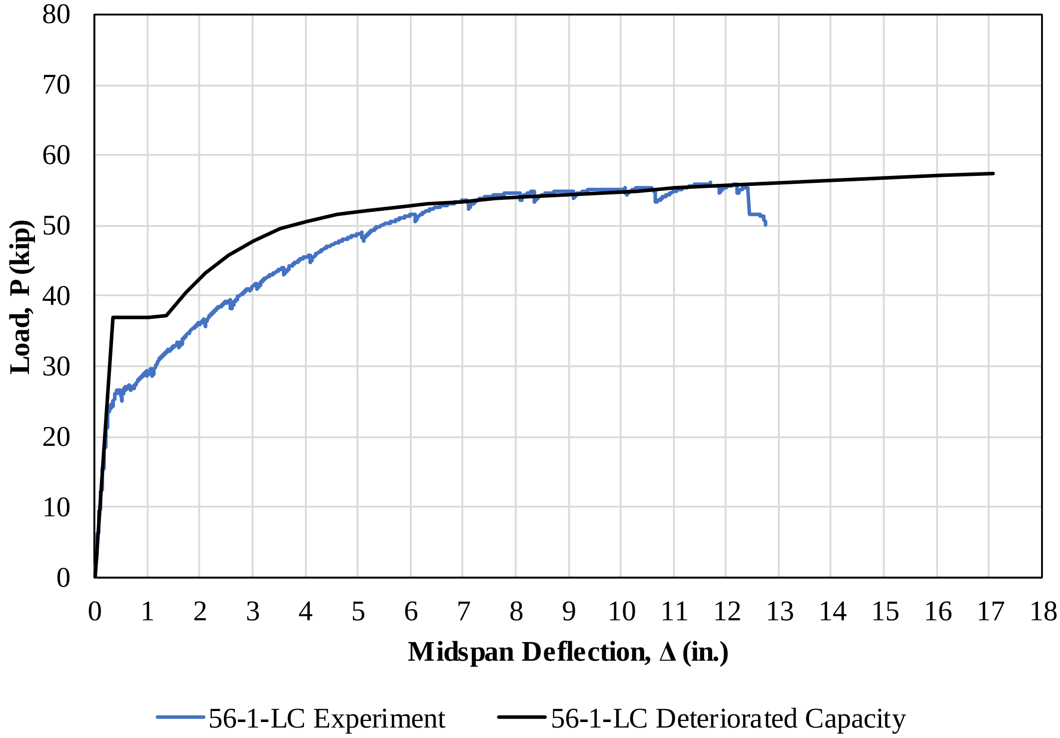

Figure K.10: Specimen 56-1-LC Deteriorated Capacity Load vs. Deflection

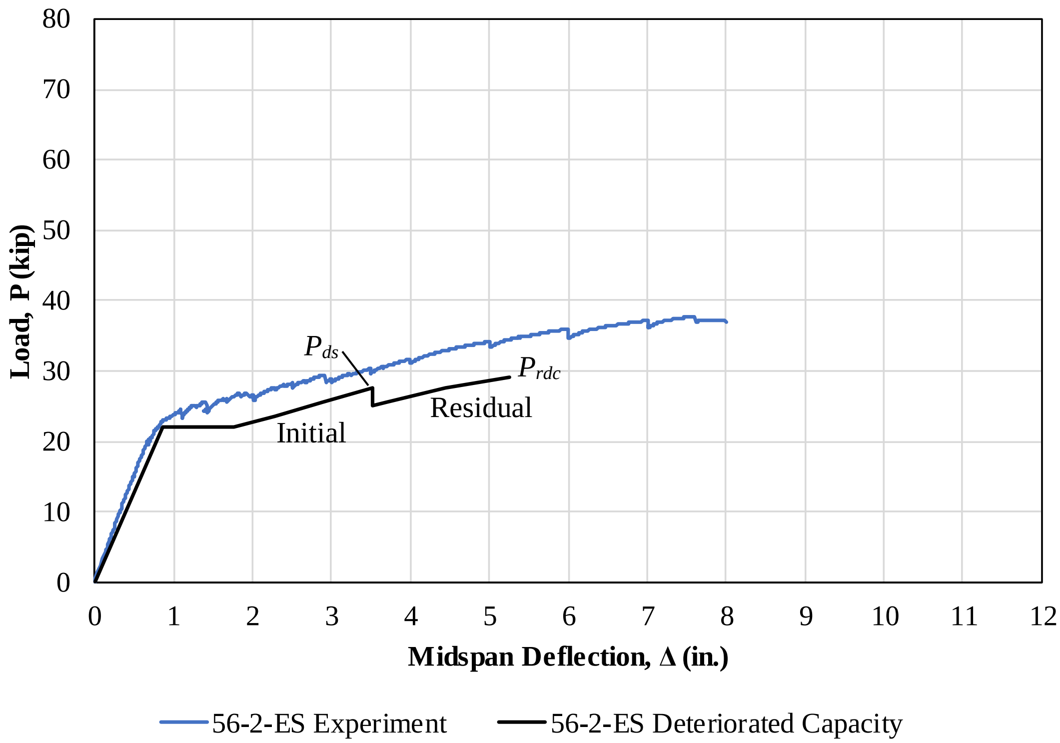

Figure K.11: Specimen 56-2-ES Deteriorated Capacity Load vs. Deflection

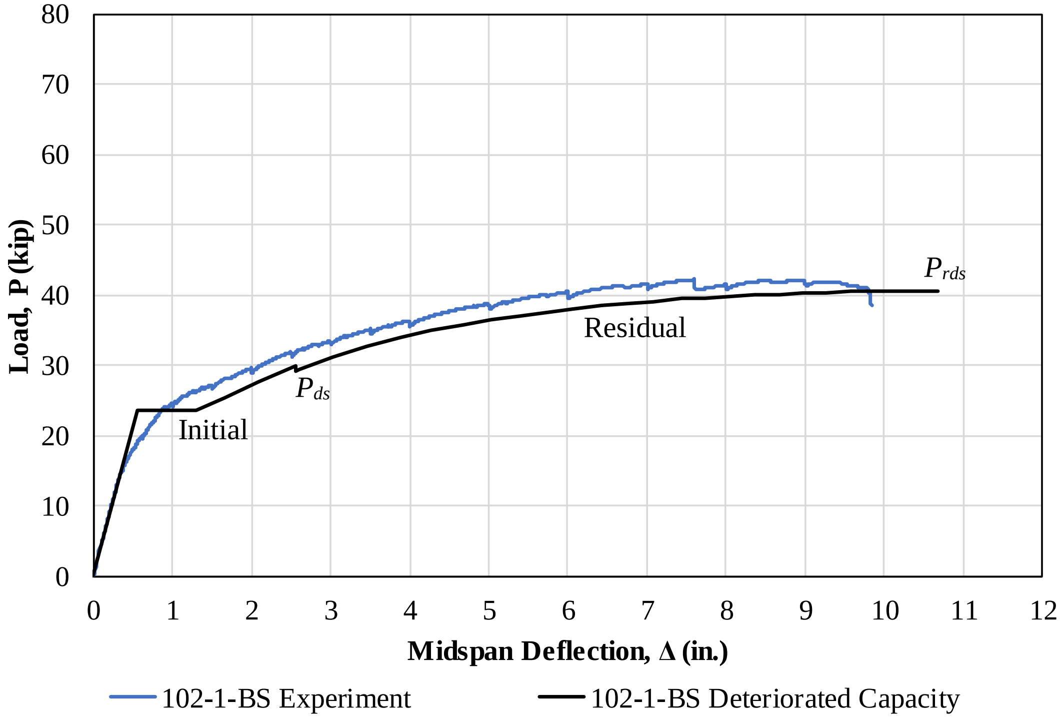

Figure K.12: Specimen 102-1-BS Deteriorated Capacity Load vs. Deflection

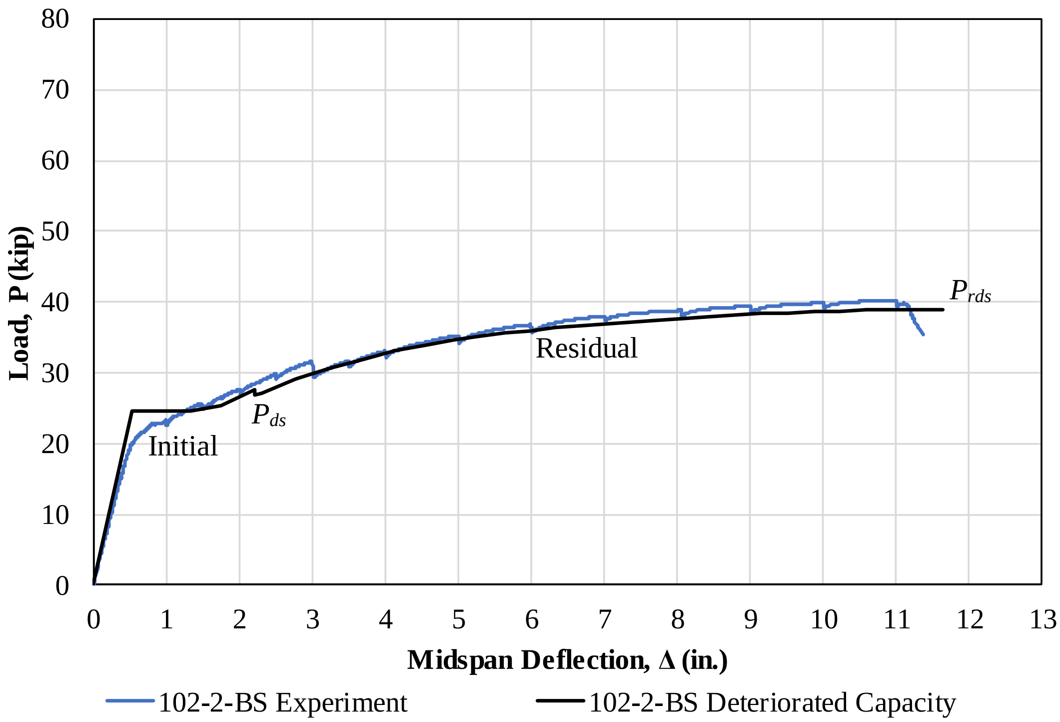

Figure K.13: Specimen 102-2-BS Deteriorated Capacity Load vs. Deflection

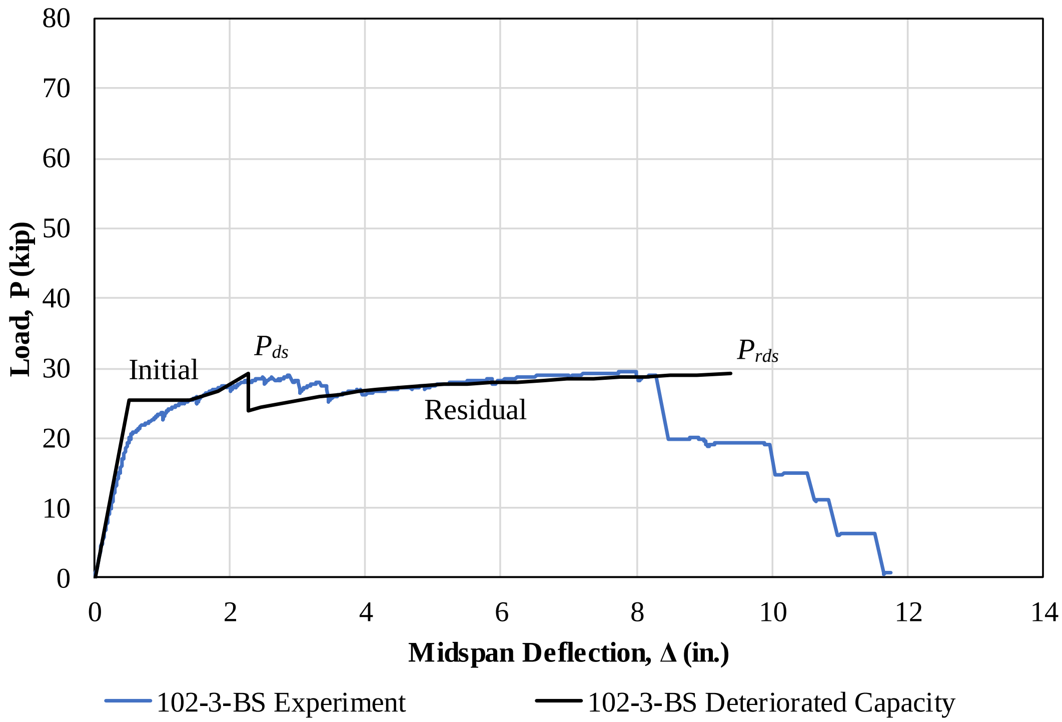

Figure K.14: Specimen 102-3-BS Deteriorated Capacity Load vs. Deflection

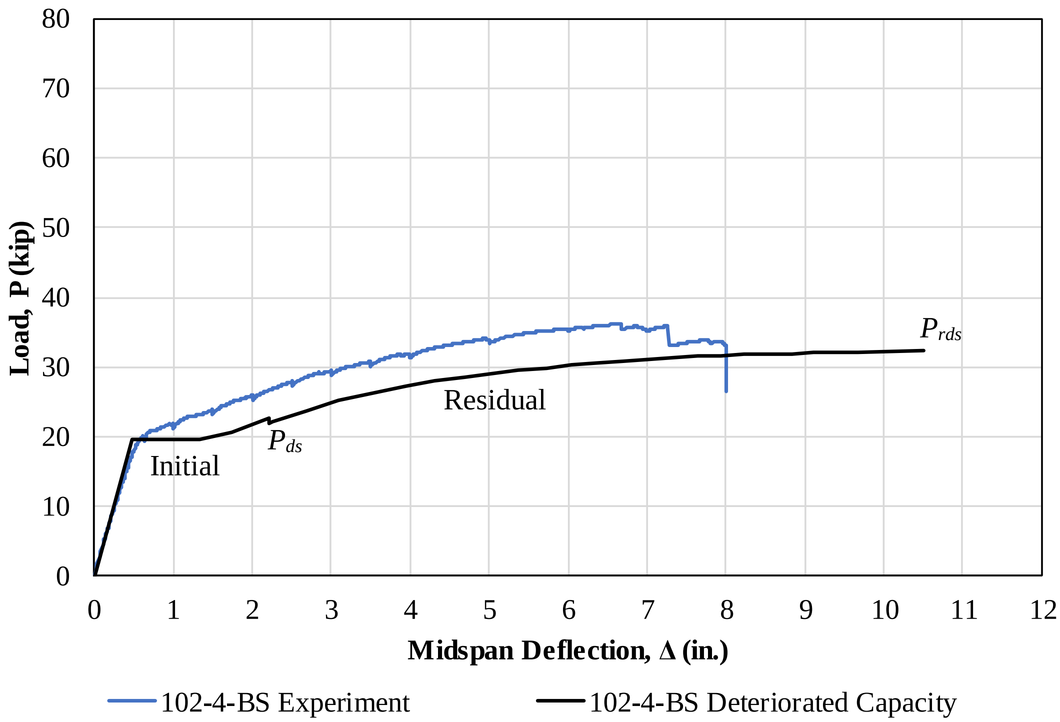

Figure K.15: Specimen 102-4-BS Deteriorated Capacity Load vs. Deflection